frontiers | Research Topics

Fish as model organism for skeletal diseases

Edited by
Erika Kague, Christoph Winkler and Ronald Kwon

Published in
Frontiers in Endocrinology
Frontiers in Physiology

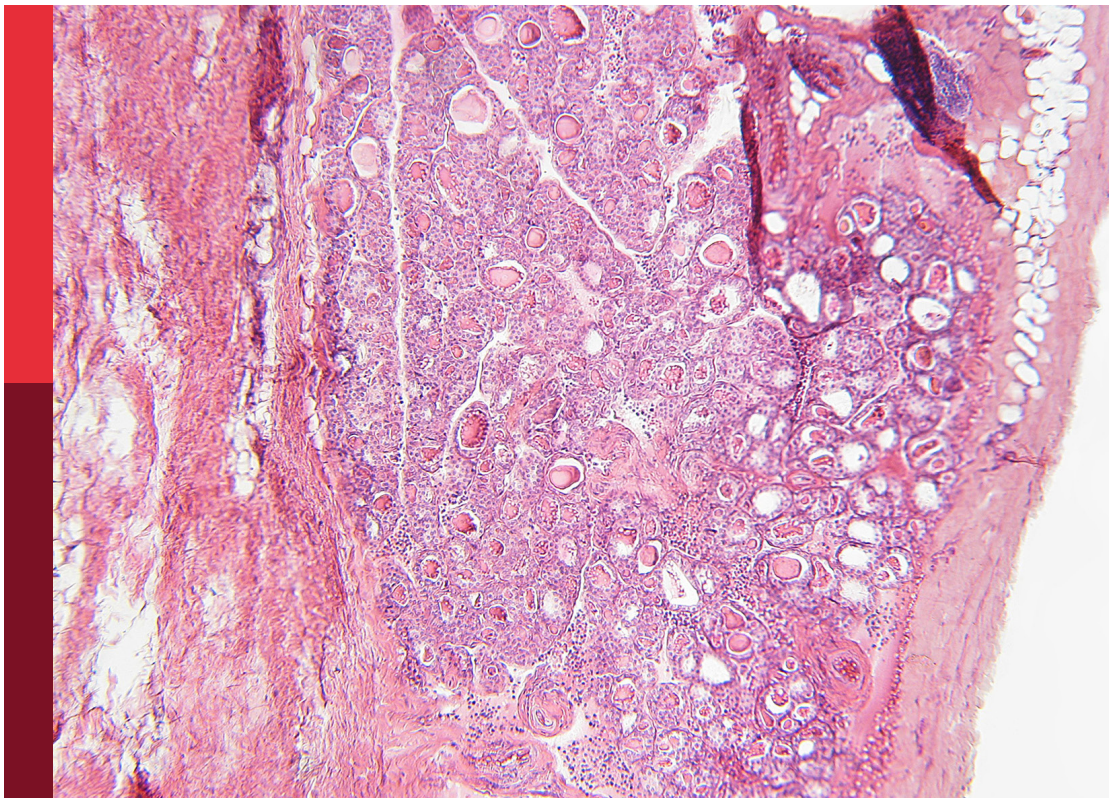

ISSN 1664-8714
ISBN 978-2-8325-4056-5
DOI 10.3389/978-2-8325-4056-5

About Frontiers

Frontiers is more than just an open access publisher of scholarly articles: it is a pioneering approach to the world of academia, radically improving the way scholarly research is managed. The grand vision of Frontiers is a world where all people have an equal opportunity to seek, share and generate knowledge. Frontiers provides immediate and permanent online open access to all its publications, but this alone is not enough to realize our grand goals.

Frontiers journal series

The Frontiers journal series is a multi-tier and interdisciplinary set of open-access, online journals, promising a paradigm shift from the current review, selection and dissemination processes in academic publishing. All Frontiers journals are driven by researchers for researchers; therefore, they constitute a service to the scholarly community. At the same time, the *Frontiers journal series* operates on a revolutionary invention, the tiered publishing system, initially addressing specific communities of scholars, and gradually climbing up to broader public understanding, thus serving the interests of the lay society, too.

Dedication to quality

Each Frontiers article is a landmark of the highest quality, thanks to genuinely collaborative interactions between authors and review editors, who include some of the world's best academicians. Research must be certified by peers before entering a stream of knowledge that may eventually reach the public - and shape society; therefore, Frontiers only applies the most rigorous and unbiased reviews. Frontiers revolutionizes research publishing by freely delivering the most outstanding research, evaluated with no bias from both the academic and social point of view. By applying the most advanced information technologies, Frontiers is catapulting scholarly publishing into a new generation.

What are Frontiers Research Topics?

Frontiers Research Topics are very popular trademarks of the *Frontiers journals series*: they are collections of at least ten articles, all centered on a particular subject. With their unique mix of varied contributions from Original Research to Review Articles, Frontiers Research Topics unify the most influential researchers, the latest key findings and historical advances in a hot research area.

Find out more on how to host your own Frontiers Research Topic or contribute to one as an author by contacting the Frontiers editorial office: frontiersin.org/about/contact

Fish as model organism for skeletal diseases

Topic editors

Erika Kague — University of Edinburgh, United Kingdom
Christoph Winkler — National University of Singapore, Singapore
Ronald Kwon — University of Washington, United States

Citation

Kague, E., Winkler, C., Kwon, R., eds. (2023). *Fish as model organism for skeletal diseases*. Lausanne: Frontiers Media SA. doi: 10.3389/978-2-8325-4056-5

Table of contents

frontiers | Frontiers in Endocrinology

TYPE Editorial
PUBLISHED 17 November 2023
DOI 10.3389/fendo.2023.1331690

OPEN ACCESS

EDITED AND REVIEWED BY
Jonathan H Tobias,
University of Bristol, United Kingdom

*CORRESPONDENCE
Erika Kague
ekague@ed.ac.ed

RECEIVED 01 November 2023
ACCEPTED 06 November 2023
PUBLISHED 17 November 2023

CITATION
Kague E, Kwon RY and Winkler C (2023) Editorial: Fish as model organism for skeletal diseases.
Front. Endocrinol. 14:1331690.
doi: 10.3389/fendo.2023.1331690

Editorial: Fish as model organism for skeletal diseases

Erika Kague[1]*, Ronald Young Kwon[2,3] and Christoph Winkler[4]

[1]Institute of Genetics and Cancer, Centre for Genomic and Experimental Medicine, University of Edinburgh, Edinburgh, United Kingdom, [2]Department of Orthopaedics and Sports Medicine, University of Washington School of Medicine, Seattle, WA, United States, [3]Institute for Stem Cell and Regenerative Medicine, University of Washington, Seattle, WA, United States, [4]Department of Biological Sciences and Centre for Bioimaging Sciences, National University of Singapore, Singapore, Singapore

KEYWORDS

medaka (Oryzias lapites), zebrafish (Brachydanio rerio), bone disease, osteoporosis, bone development, osteogenesis imperfecta

Editorial on the Research Topic
Fish as model organism for skeletal diseases

As our understanding of skeletal diseases continues to evolve, so does the need for innovative and versatile model organisms that can shed light on the intricate mechanisms underlying these conditions. In this context, the utilization of zebrafish and medaka, with their transparency during development, remarkable regenerative abilities, and genetic similarities with humans, provides unique opportunities to unravel the complexities of skeletal diseases. This Frontiers Research Topic on "*Fish as Model Organisms for Skeletal Diseases*" highlights the growing significance that fish species play in advancing our knowledge of skeletal development and diseases, offering new avenues for therapeutic discoveries.

Fish provide new insights into mechanisms of rare and common bone diseases

Rare bone diseases

Osteogenesis imperfecta (OI), also known as brittle bone disease, is a rare disease clinically characterised by short stature, skeletal deformities, low bone mass and bone fragility. In most cases, it is caused by autosomal mutations in collagen type I. Zebrafish *chihuahua (chi/-)* mutants carry a heterozygous mutation in *col1a1a* and have long been used as model for OI. Although *chihuahua* represents a very well characterised model, in which rib fractures have been described, Cotti et al. for the first-time report compression vertebral fractures associated with *chi/-*. Importantly, Cotti et al. tested whether low dietary phosphorus intake mitigates the skeletal phenotypes associated with this model, partially restoring bone shape variation of the vertebral bodies and osteoid layer of endplates. Their research suggests that reduced dietary phosphorus intake has therapeutic potential to improve bone matrix and alleviate the severe bone phenotypes of OI.

A recessive form of OI, classified as type XIV, is caused by mutations in *TMEM38B*, which encodes the trimeric intracellular cation channel Tric-b. Tonelli et al. report new

insights into *TMEM38B* function. They analysed spatiotemporal expression of *tmem38a* and *tmem38b* in zebrafish, and generated a zebrafish *tmem38b* loss-of-function mutant that developed a mild bone phenotype. Interestingly, collagen type I analyses revealed enlarged endoplasmic reticulum (ER) cisternae in *tmem38b* mutants. To investigate bone formation and remodelling, they performed TRAP staining after fin amputation, and showed differential staining in mutants, pointing to abnormal osteoclast activity. Abnormal actinotrichia formation in mutants after fin amputation supported a role for *tmem38b* in osteoclast activity.

Mutations in COMP (cartilage oligomeric matrix protein) lead to chondrodysplasias. Forte-Gomez et al. revealed that *comp* is expressed in myosepta and notochord but unexpectedly not in cartilage of larval zebrafish. When they targeted *comp* using CRISPR/Cas9, irregular staining for Comp protein was detected in myosepta. Electron microscopy beautifully revealed disorganised extracellular matrix in mutants, indicating that Comp plays a role in matrix assembly, similar to what had been proposed for a subgroup of human chondrodysplasia patients. This work thus depicts the suitability of zebrafish myosepta to study extracellular matrix organisation associated with bone diseases.

Collagen II is the most abundant collagen in cartilage, however, there are many questions regarding its secretory pathway *in vivo*. Ritter et al. generated loss-of-function mutants for *rgp1*. Prior to this study, the role of Rgp1 in protein trafficking had been examined *in vitro* and in yeast, however its role *in vivo* was unknown. Using multiple approaches including *in vivo* imaging of vesicular trafficking, electron microscopy, and overexpression, Ritter et al. found evidence for a Rgp1-regulated Rab6a-Rab8a pathway that directs secretion of collagen II. This study demonstrates how the favourable genetic and imaging attributes of zebrafish enable laboratories to pursue *in vivo* studies of collagen trafficking that may otherwise be considered too challenging or scientifically risky.

Common bone disease: osteoporosis

Other than the above-mentioned rare bone diseases, osteoporosis affects millions of people worldwide. It is characterised by impaired bone microarchitecture, commonly associated with reduced bone mineral density (BMD), and increased fracture risk.

LRP5, a co-receptor of the canonical Wnt pathway, has been associated with BMD through genome-wide association studies (GWASs). Diverse mutations in *LRP5* are causative of osteoporosis-pseudoglioma syndrome, high-bone mass, and craniofacial malformations. Khrystoforova et al. showed that zebrafish *lrp5* mutants recapitulated a loss-of-function mutation phenotype found in humans. Transcriptomic profiling of mutants surprisingly suggested the involvement of pathways implicated in osteoclast metabolism. Consistent with a role of Lrp5 in osteoclasts, they also observed increased osteoclast activity in mutant zebrafish scales. Given that osteoclasts act during fin lepidotrichia bifurcation, Khrystoforova et al. compared fins of wild-type and *lrp5* mutant fish, and found precocious fin bifurcation in *lrp5* mutants. Their work thus revealed an unexpected role of *lrp5* in osteoclasts.

Glucocorticoids (GCs) are therapeutic agents commonly used to treat immune-mediated diseases. However, their use is hampered by adverse effects in multiple organs including bone (inducing secondary osteoporosis), skin and intestine. The causes of this are not fully understood. Fleischhauer et al. surveyed the effects of GC administration in tissues with different levels of proliferation. They showed that adverse effects of GCs are particularly observed in regenerating (but not homeostatic) bone, as well as two highly proliferative tissues (skin and intestine). Because the effect of GC administration on fin regeneration mirrored effects on skin and intestine, the regenerating fin could be a useful model to understand the mechanisms underlying adverse effects of GCs in tissues with high cell turnover.

The paper by Imangali et al. provides a compelling proof of principle for a novel approach to modulate osteoclast activity *in vivo*. They used calcium phosphate (CaP) nanoparticles as carriers to efficiently deliver osteoprotegerin-b (Opgb) to osteoclasts to dampen their activity. First, the group injected fluorescently labelled CaP nanoparticles into the medaka heart, trunk or the caudal fin, showing nanoparticle stability for at least 35 hours post injection. Injecting CaP nanoparticles into transgenic reporter medaka allowed them to confidently determine CaP internalisation mostly by osteoclasts and their precursor cells, macrophages. Next, CaP nanoparticles were functionalised with a plasmid expressing Opgb specifically in macrophages, and injected into the medaka trunk muscle. These particles were successfully internalised by macrophages and expressed Opgb. To determine whether Opgb was functional, they induced bone resorption using their heat-shock inducible RankL model after nanoparticle injection. CaP nanoparticles expressing Opgb protected the bone against RankL-induced resorption.

Zebrafish and medaka as model organisms

As zebrafish and medaka are increasingly used for bone research, understanding bone development and mineralisation in these species is essential for establishing significant comparisons with mammalian systems and confidently assessing bone phenotype in functional studies.

Miao et al. used a cathepsin K reporter to assess osteoclast location during zebrafish skull formation. Surprisingly, osteoclasts were not associated with the osteogenic fronts of active growth, but were enriched around neuromasts and their associated nerves, indicating active remodelling of the areas around peripheral cranial nerves during skull development. The authors confirmed these findings through detecting a reduced diameter of nerve canals in *csf1ra* mutants that lack functional osteoclasts.

The Notch pathway is important for craniofacial development, with Jag1 being one of its major players. Mutations in *JAG1* lead to Alagille syndrome, characterised by craniofacial malformations. Other players in the Notch pathway include *HES1*, called *her6* in zebrafish. Contrary to mice, however, *her6* mutant zebrafish do not have a craniofacial phenotype. Stenzel et al. investigated *her6-her9* double knockouts in zebrafish and discovered that *her6* and *her9*

have redundant roles downstream of Jag1. Also, *her9* is vital for modulating mineralisation of the extracellular bone matrix.

In mammals and teleost models, increased bone morphogenic protein (BMP) or retinoic acid (RA) signalling causes vertebral fusions. However, the interplay between the two pathways and their targets was largely unknown. Pogoda et al. investigated the role of BMP signalling during early vertebral column formation in zebrafish. This research identified BMP as the initial pattern generator regulating the formation of the vertebral column. Using transgenic lines, drug treatment and genetic manipulations, they demonstrated that BMPs signal to notochord epithelial cells/chordoblasts to promote tissue mineralisation and notochord segmentation. Their work shed light onto the fundamental mechanisms underlying vertebral column formation in fish.

To better understand the mechanisms of bone development, it is important to standardize fish maintenance conditions and optimize imaging technologies that allow a robust assessment of the fish skeleton. Nguyen et al. used micro-computed tomography (microCT) to generate 3D models of zebrafish skeletons highlighting bone shape changes during development and in adults. With a focus on the craniofacial skeleton, this work also provides a comprehensive annotation of craniofacial bones through imaging segmentation. Standard microCTs fall short on resolution and visualisation of soft tissue. Leyhr et al. overcome these limitations by using phase-contrast synchrotron radiation microCT to image larvae and juvenile zebrafish treated with iodine-based contrast enhancer solution. They showcased the technique using wild-type and *nkx3.2-/-* mutant zebrafish, demonstrating soft tissue phenotypes in mutants. Finally, Di Biagio et al. demonstrated that fish rearing density has a phenotypic impact on the fish skeleton, independent of any genetic mutation. Medaka maintained at a rearing density greater than 5 fish/L reduced animal growth through reduction of bone mineralisation. Importantly, high density increased anomalies affecting the caudal fins and precaudal vertebral centra fusions.

A must-read literature review: endochondral growth zones in small fish

Finally, although small fish models lack long bones, they are still able to model human skeletal disorders associated with endochondral growth zones. In a must-read review, Le Pabic et al. revisited the literature on this topic, highlighting the differences and similarities of the growth zones between zebrafish and mammals. They dive deep into explaining the growth zone organisation, contribution to endochondral growth, cartilage maturation, their replacement by bone and the importance of cartilage proliferation rather than hypertrophy to control bone size in fish. The review emphasises the use of zebrafish for investigating causes of endochondral bone diseases and the identification of therapeutics.

Author contributions

EK: Conceptualization, Writing – original draft, Writing – review & editing. RK: Writing – review & editing. CW: Writing – review & editing.

Funding

The author(s) declare financial support was received for the research, authorship, and/or publication of this article. EK is funded by Versus Arthritis (Career Development Award, 23115). CW is supported by a grant from the Singapore Ministry of Education (MOE-T2EP30221-0008). RYK would like to acknowledge support from the National Institute of Arthritis and Musculoskeletal and Skin Diseases of the National Institutes of Health under Award Number AR074417.

Conflict of interest

The authors declare that the research was conducted in the absence of any commercial or financial relationships that could be construed as a potential conflict of interest.

Publisher's note

frontiers in Endocrinology

ORIGINAL RESEARCH
published: 24 February 2022
doi: 10.3389/fendo.2022.851879

Compression Fractures and Partial Phenotype Rescue With a Low Phosphorus Diet in the *Chihuahua* Zebrafish Osteogenesis Imperfecta Model

Silvia Cotti[1,2]*, *Ann Huysseune*[1], *Daria Larionova*[1], *Wolfgang Koppe*[3], *Antonella Forlino*[2] *and Paul Eckhard Witten*[1]

[1] Evolutionary Developmental Biology Group, Department of Biology, Ghent University, Gent, Belgium, [2] Biochemistry Unit, Department of Molecular Medicine, University of Pavia, Pavia, Italy, [3] SimplyFish AS, Stavanger, Norway

Osteogenesis imperfecta (OI) is a group of heritable disorders affecting bone and other connective tissues. Dominant OI forms are mainly caused by mutations in collagen type I. Patients suffer from skeletal deformities, fractures of long bones and vertebral compression fractures from early childhood onward. Altered collagen structure and excess mineralisation are the main causes for the bone phenotype. The *Chihuahua* (*Chi/+*) zebrafish has become an important model for OI. Given that reduced dietary phosphorus (P) intake reduces the bone mineral content and promotes bone matrix formation in teleosts, including zebrafish, we tested whether a low dietary P (LP) intake mitigates the OI phenotype in the *Chi/+* model. To answer this question, we characterised the *Chi/+* vertebral column phenotype at a morphological, cellular and subcellular level. We present the first description of vertebral compression fractures in *Chi/+* and assess the effects of LP diet on the *Chi/+* phenotype (*Chi/+*$_{LP}$). Compared to untreated *Chi/+*, two months of LP dietary treatment decreases vertebral deformities in the abdominal region and reduces shape variation of caudal vertebral bodies to a condition more similar to wild type (WT). At the histological level, the osteoid layer, covering the bone at the vertebral body endplates in WT zebrafish, is absent in *Chi/+*, but it is partially restored with the LP diet. Whole mount-stained specimens and histological sections show various stages of vertebral compression fractures in *Chi/+* and *Chi/+*$_{LP}$ animals. Both *Chi/+* and *Chi/+*$_{LP}$ show abundant osteoclast activity compared to WT. Finally, the ultrastructure analysis of WT, *Chi/+* and *Chi/+*$_{LP}$ shows *Chi/+* and *Chi/+*$_{LP}$ osteoblasts with enlarged endoplasmic reticulum cisternae and a high protein content, consistent with intracellular retention of mutated collagen. Nevertheless, the secreted collagen in *Chi/+*$_{LP}$ appears better organised concerning fibre periodicity compared to *Chi/+*. Our findings suggest that a reduced mineral content of *Chi/+* bone could explain the lower frequency of vertebral column deformities and the restored shape of the vertebral bodies in *Chi/+*$_{LP}$ animals. This, together with the improved quality of the bone extracellular matrix, suggests that two months of reduced dietary P intake can alleviate the severe bone phenotype in *Chi/+* zebrafish.

Keywords: osteogenesis imperfecta (OI), zebrafish, vertebral column deformities, compression fractures, osteoblasts, osteoclasts, collagen, dietary phosphorus

OPEN ACCESS

Edited by:
Erika Kague,
University of Bristol, United Kingdom

Reviewed by:
Katrin Henke,
Emory University, United States
Melissa M. Formosa,
University of Malta, Malta

***Correspondence:**
Silvia Cotti
silvia.cotti@ugent.be

Specialty section:
This article was submitted to Bone Research, a section of the journal Frontiers in Endocrinology

Received: *10 January 2022*
Accepted: *01 February 2022*
Published: *24 February 2022*

Citation:
Cotti S, Huysseune A, Larionova D, Koppe W, Forlino A and Witten PE (2022) Compression Fractures and Partial Phenotype Rescue With a Low Phosphorus Diet in the Chihuahua Zebrafish Osteogenesis Imperfecta Model. Front. Endocrinol. 13:851879. doi: 10.3389/fendo.2022.851879

INTRODUCTION

Osteogenesis imperfecta (OI), also known as 'brittle bone disease', is a clinically and genetically heterogeneous group of heritable disorders affecting bone and other connective tissues with collagen type I as main matrix component (1). Clinical features of OI patients are short stature, skeletal deformities, low bone mass and bone fragility. Frequent fractures also in absence of trauma can occur *in utero* and cause death before birth (2, 3). Scoliosis and compression fractures of the vertebral bodies are the most severe complications in human patients (4, 5). Vertebral compression fractures require surgery to stabilise the vertebral column and treatment with bisphosphonates to prevent bone loss (6–8).

In the majority of patients, OI is caused by autosomal dominant mutations in *COL1A1* and *COL1A2*, coding for α1 and α2 chains of the collagen type I (9). These OI forms, regarded as classical OI, were first classified in 1979 by Sillence and co-workers in 4 different types of OI (OI I-IV) based on clinical observations, radiographic features and the mode of inheritance (2). The types range from mild (type I), over moderate (type IV), severe (type III) to perinatally lethal (type II). The mildest form, OI type I, is caused by quantitative deficiency of structurally unaltered collagen. Patients have a normal or slightly short stature, deformities of long bones in the legs and are susceptible to bone fractures from early on. The moderate, severe and lethal OI forms are caused instead by alterations in the collagen structure. The most common mutations causing structural alterations of collagen type I are single-nucleotide variants that substitute glycine with a bulkier or with a charged residue within the Gly-X-Y repeat, either in the α1 or α2 chains (9). This results in delayed collagen folding and excess post-translational modifications (10).

Zebrafish (*Danio rerio*) has become an important model organism for the study of human skeletal disorders, due to its high reproduction rate and easy access to embryos. Moreover, basic processes of skeletal formation are conserved across gnathostomes (11–14). The first identified zebrafish mutant model for classical dominant OI is the *Chihuahua* (*Chi*/+). The mutant was isolated from a large N-ethyl-N-nitrosourea (ENU)-mutagenesis screen for skeletal dysplasias (15). *Chi*/+ carries a heterozygous glycine to aspartate substitution in position 736 in the α1 chain of collagen type I. Adult animals display typical OI characters, such as bending of the vertebral column, bone fragility (rib fractures), high bone mineral-to-matrix ratio and reduced bone elasticity (16, 17).

Next to structural alterations in collagen type I, also hypermineralisation leads to fragility and poor bone quality, both in OI patients and in zebrafish models (17). It is a common assumption that an increase in bone mineral content enhances the mechanical properties of bone. Proper mechanical function of bone requires, however, a balance between toughness, provided by the collagenous matrix, and stiffness, provided by the mineral phase (18). The antlers of deers and elks are examples for bones that withstand extreme mechanical forces. Yet, the bone mineral content of antlers is about half of that of a human femur (19). Excess mineralisation, on the other hand, makes bone stiff and brittle (18) and increases the risk of fractures (20, 21). Thus, while mutations in OI patients cannot be undone, lowering the bone mineral content could possibly alleviate skeletal defects in these patients. Recent studies on teleost fish, including wild type (WT) zebrafish (22), as well as farmed Atlantic salmon (23–25), have shown that periods of severely lowered dietary phosphorus (P) intake (-50%) reduce the bone mineral content and promote the formation of non-mineralised bone without causing vertebral column malformations. In contrast, but similar to OI patients and animal models, zebrafish with increased dietary P intake and animals with age-related increased bone mineral density show elevated rates of vertebral column malformations (22, 26).

We have used these new insights to investigate if a reduction of dietary P intake can mitigate deformities of the vertebral column in adult *Chi*/+ zebrafish. To answer this question we have characterised the *Chi*/+ vertebral column phenotype at a morphological, cellular and subcellular level and assessed the effect of a low P (LP) diet on the *Chi*/+ phenotype (further referred to as *Chi*/+$_{LP}$). The LP diet decreases vertebral deformities in the abdominal region and partially restores shape variation of the caudal vertebral bodies in the *Chi*/+ mutant. The osteoid layer covering the bone at the endplates in WT is absent in the *Chi*/+ mutants, but partially restored with the LP diet. Vertebral body fractures are observed in animals of both groups, *Chi*/+ and *Chi*/+$_{LP}$. In both groups, the bone shows evidence of fracture repair and remodelling, supported by the observation of abundant osteoclast activity in *Chi*/+ compared to WT fish. Finally, both *Chi*/+ and *Chi*/+$_{LP}$ display osteoblasts with enlarged endoplasmic reticulum (ER) cisternae and a high protein content consistent with intracellular retention of defective collagen. The secreted collagen in *Chi*/+$_{LP}$ appears, nevertheless, better organised concerning fibre periodicity than *Chi*/+.

RESULTS

Chihuahua Mutants Have Increased Frequency of Vertebral Column Deformities

Starting from 28 days post-fertilisation (dpf), WT were fed a regular P diet for two months. At 28 dpf, *Chi*/+ mutants were randomly divided in two groups and fed a 'LP diet' (low P content, *Chi*/+$_{LP}$) or a regular P diet (*Chi*/+) for two months. Three months old *Chi*/+ show severe deformities compared to WT fish on Faxitron X-ray images (**Figure 1A**), confirming earlier reports (15–17). Vertebral column deformities of WT, *Chi*/+ and *Chi*/+$_{LP}$ were assessed by whole mount Alizarin red S staining (details are described below). Compared to WT, *Chi*/+ mutants have an increased frequency of kyphosis and lordosis in the abdominal region of the vertebral column. Kyphosis and lordosis are reduced in the abdominal region of the vertebral column in *Chi*/+$_{LP}$ fish. However, compared to *Chi*/+ fish, *Chi*/+$_{LP}$ fish show increased

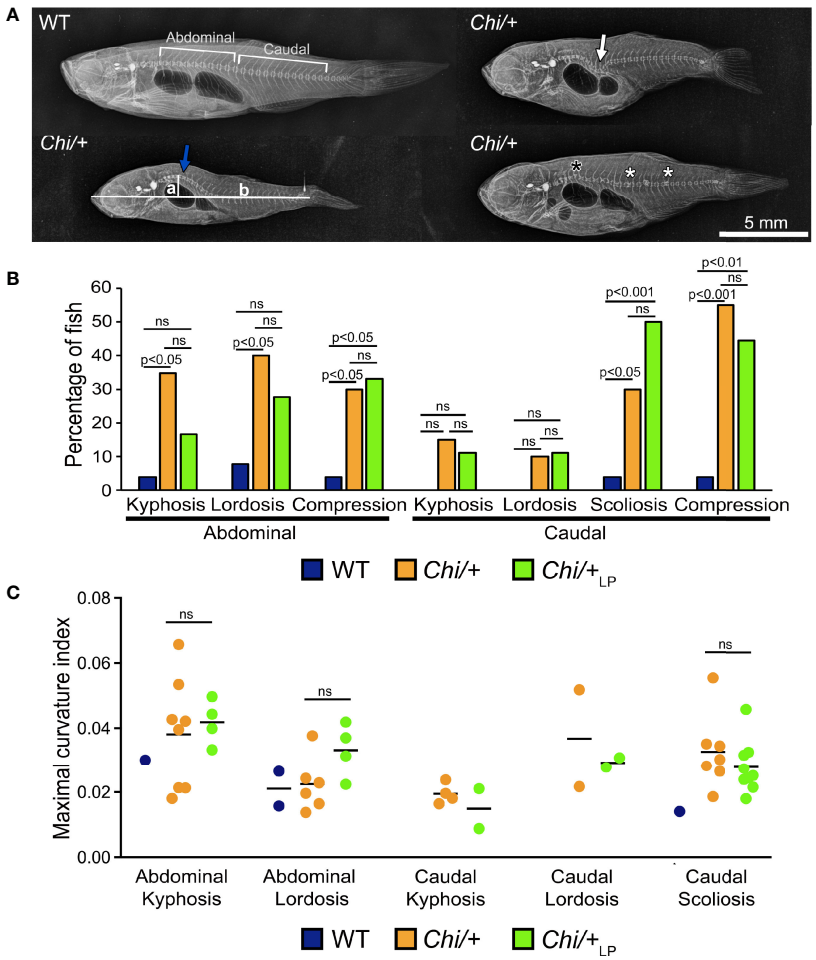

FIGURE 1 | Vertebral column deformities in *Chi*/+ and *Chi*/+$_{LP}$ mutants. **(A)** Representative X-rays of three months old WT and *Chi*/+ (representative also for the malformations diagnosed in *Chi*/+$_{LP}$) zebrafish show severe vertebral column deformities in mutants, i.e. abdominal kyphosis (blue arrow), abdominal lordosis (white arrow), vertebral body compressions (white asterisks) and hemivertebra (black asterisk). **(B)** Frequency of malformations. *Chi*/+ mutants (n=20) show increased frequency of kyphosis, lordosis, scoliosis and vertebral body compressions in the abdominal and caudal vertebral column compared to WT animals (n=26). *Chi*/+$_{LP}$ animals (n=18) display reduced kyphosis and lordosis of the abdominal, but increased scoliosis of the caudal vertebral column. Alterations were diagnosed based on Alizarin red S whole mount-stained specimens; only the abdominal and caudal region of the vertebral column were considered for the analysis. Chi-squared test followed by Bonferroni correction; p values are indicated; ns: non-significant. **(C)** Severity assessment of the maximal curvature index diagnosed in WT, *Chi*/+ and *Chi*/+$_{LP}$ related to abdominal kyphosis and lordosis, and to caudal kyphosis, lordosis and scoliosis. The graph shows individual data points and the mean value (black bar) for the maximal curvature index. The maximal kyphotic and lordotic indices were calculated in the sagittal plane of Alizarin red S stained specimens as the ratio (a/b) between the perpendicular distance from the axis (in correspondence of the maximal curvature, segment 'a' in **A**) and the standard length (segment 'b' in **A**). The same method but in the coronal plane was used to calculate the maximal scoliotic index. Mann-Whitney test was applied with a minimum of three values per group; ns, non-significant.

scoliosis in the caudal vertebral column. Both *Chi*/+ and *Chi*/+$_{LP}$ have a high frequency of compressed vertebral bodies; examples are shown in **Figure 1A**, frequency of deformities is shown in **Figure 1B**. To assess the severity of the curvature in those specimens diagnosed with kyphosis, lordosis and scoliosis, the maximal kyphotic, lordotic and scoliotic indices were measured, respectively. **Figure 1C** shows the maximal curvature indices in the abdominal and caudal region of affected WT, *Chi*/+ and *Chi*/+$_{LP}$ individuals. No statistical differences in the degree of curvature are detected between *Chi*/+ and *Chi*/+$_{LP}$ fish at three months of age (Mann-Whitney test: non-significant).

The general metrics for the analysis of the vertebral column malformations (**Table 1**) show that the frequency of specimens with at least one malformation is 19% in WT, 75% in *Chi*/+ and 89% in *Chi*/+$_{LP}$. The highest average malformation load is in the *Chi*/+ group (3.27 malformations/deformed specimen) where a total of 49 malformations were identified. The average malformation load in the *Chi*/+$_{LP}$ group is 2.5 with a total of 40 diagnosed malformations. These data indicate a tendency towards reduced number of malformations and average malformation load in the *Chi*/+$_{LP}$ compared to untreated *Chi*/+ (Chi-square test: p=0.27).

Partial Rescue of Vertebral Body Shape Variation in *Chihuahua* Mutants Under the LP Diet

To quantify shape variation of the caudal vertebral centra in WT, *Chi*/+ and *Chi*/+$_{LP}$ animals, landmark-based geometric morphometrics was applied, based on whole mount-stained specimens (**Figure 2A**). The scatterplot of 2D landmarks shows differences in location of corresponding landmarks between WT, *Chi*/+ and *Chi*/+$_{LP}$ animals. The scatterplot shows a high variation in the superimposition of Procrustes

TABLE 1 | General metrics for the analysis of vertebral column malformations in WT, *Chi*/+ and *Chi*/+$_{LP}$.

	WT	*Chi*/+	*Chi*/+$_{LP}$
Number of observed specimens	26	20	18
Total number of malformations	6	49	40
Frequency (%) of specimens with at least one malformation	19	75	89
Average malformation load	1.20	3.27	2.5

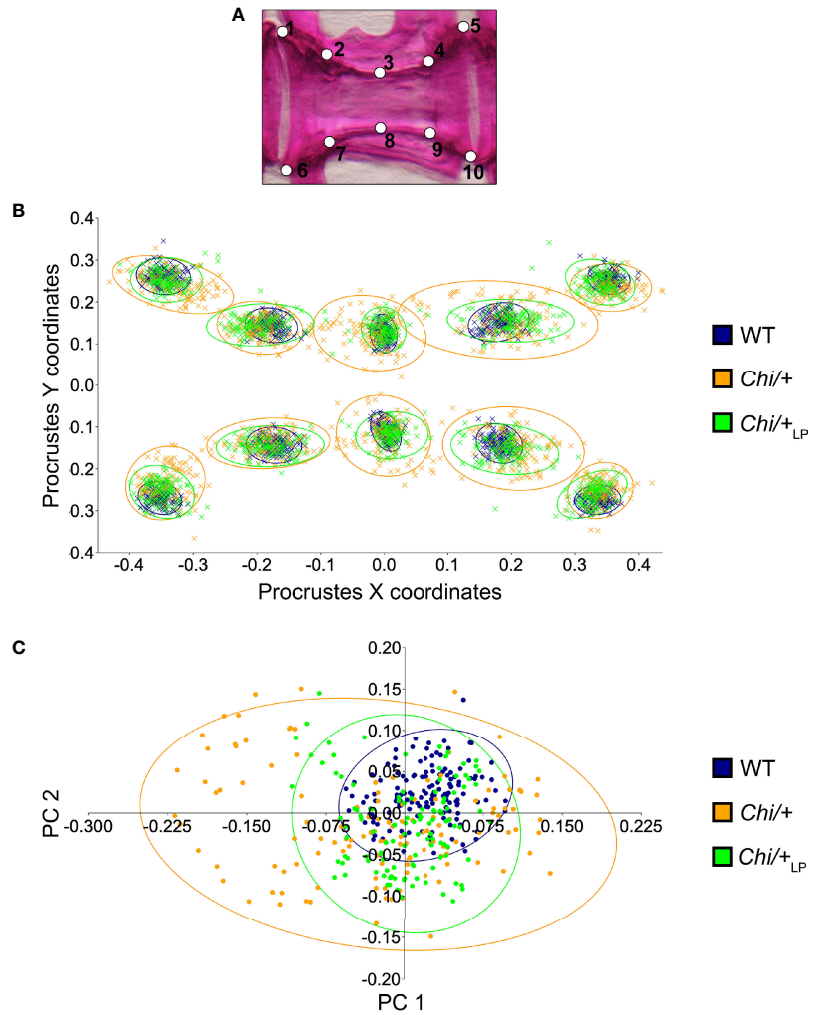

FIGURE 2 | Vertebral body shape variation in *Chi*/+ and *Chi*/+$_{LP}$ mutants. **(A)** Alizarin red S stained vertebral body of a WT animal with 2D landmark positions used for quantifying the shape variation by means of geometric morphometrics, represented in **(B)**. **(B)** The scatterplot of WT, *Chi*/+ and *Chi*/+$_{LP}$ 2D landmarks shows high variation in the superimposition of X,Y Procrustes coordinates of *Chi*/+ compared to WT animals. *Chi*/+$_{LP}$ animals display reduced landmark variation compared to *Chi*/+ and a distribution more similar to WT indicating a partial rescue of shape variation at three months of age. The first 10 caudal vertebral centra in WT (n=15), *Chi*/+ (n=13) and *Chi*/+LP (n=12) were analysed. The 95% confidence ellipses are shown. **(C)** Principal component analysis of vertebral centra shapes. Each symbol in the plot represents a vertebral body. PC indicates Principal Component and the values in the axis labels indicate the percentage of variation accounted for by each axis. *Chi*/+ animals show high variance compared to WT animals (*Chi*/+ versus WT, PC1 0.3321, PC2 0.1795; Chi-square test: $p < 0.001$). Variance is rescued in *Chi*/+$_{LP}$ animals (*Chi*/+$_{LP}$ versus WT, PC1 0.2484, PC2 0.2020; Chi-square test: non-significant). The 95% confidence ellipses are shown.

coordinates of *Chi*/+ compared to WT. *Chi*/+$_{LP}$ display reduced variation of landmarks compared to *Chi*/+ and a distribution more similar to WT (**Figure 2B**). Principal component analysis (PCA) of superimposed landmarks shows the amount of variation between WT, *Chi*/+ and *Chi*/+$_{LP}$. Only principal component 1 (PC1) and principal component 2 (PC2) were considered. Compared to WT, *Chi*/+ show a statistically significant higher variance (*Chi*/+ versus WT, PC1 0.3321, PC2 0.1795; Chi-square test: p<0.001). On the contrary, *Chi*/+$_{LP}$ animals show a non-statistically different variance compared to WT (*Chi*/+$_{LP}$ versus WT, PC1 0.2484, PC2 0.2020; Chi-square test: non-significant) (**Figure 2C**).

Histological assessment of the vertebral column in the sagittal plane confirmed the irregular shape of mutant vertebral bodies compared to WT vertebral bodies (**Figure 3**). Different from WT (**Figures 3A, B**), in *Chi*/+ animals vertebral body endplates of adjacent vertebral bodies are frequently shifted against each other along the dorsal-ventral axis (**Figure 3B**). Moreover, scoliosis of the vertebral column in *Chi*/+ and *Chi*/+$_{LP}$ animals, previously observed on whole mount-stained specimens is visible

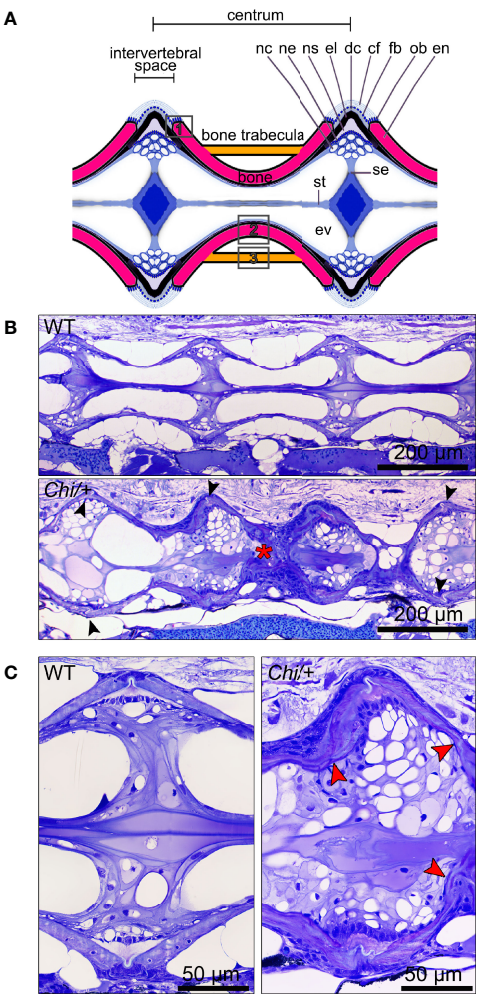

FIGURE 3 | Histology of vertebral column of WT, *Chi*/+ and *Chi*/+$_{LP}$ confirms the irregular shape of mutant vertebral bodies. **(A)** Schematic representation of the medio-sagittal plane of a zebrafish vertebral body centrum and two intervertebral spaces. Vertebral centra derive from segmental mineralisation of the notochord sheath and intramembranous bone formation around the notochord. Vertebral body endplates (en) are connected by intervertebral ligaments. Ligaments consist of the enlarged notochord sheath (ns, a collagen type II layer secreted by the cells of the notochord epithelium, ne), its outer elastin layer (el) and dense collagen type I fibre bundles (dc) produced by fibroblasts (fb) that surround the notochord. The collagen type I fibre bundles (cf) continue in the bone of the vertebral body endplates (en) as Sharpey fibres. Osteoblasts (ob) deposit new bone matrix that expands the vertebral body endplates in the bone growth zone. Inside, the notochord is composed of vacuolated notochord cells (nc) and extracellular vacuoles (ev). Condensed notochord cells constitute the notochord septum (se) and the notochord strand (st). Boxes indicate locations where the bone thickness was measured, i.e. endplates (1), central region of vertebrae (2) and trabecular bone (3). **(B)** Representative three months old WT and mutant sagittal sections of the vertebral column stained with toluidine blue. Compared to WT, Chi/+ mutants (representative also for *Chi*/+$_{LP}$) have several vertebral centra with deformed endplates that are shifted against each other along the dorsal-ventral axis (black arrowheads). *Chi*/+ animals also suffer from vertebral body compression fractures (red asterisk), scoliosis, lordosis and kyphosis. Scoliosis can be appreciated from the absence of a straight sagittal midline plane as seen in the WT animal. **(C)** Higher magnification of vertebral body endplates in WT and *Chi*/+ (representative also for *Chi*/+$_{LP}$) animals. Toluidine blue staining shows deformed endplates of adjacent vertebral bodies (red arrowheads) in *Chi*/+ mutants, yet with unaltered ligaments and unaltered intervertebral space as in WT.

on histological sections as the absence of a sagittal middle plane (**Figure 3B**). Histology reveals the presence of compression fractures in *Chi*/+ and *Chi*/+$_{LP}$ animals (see below for details) (**Figure 3B**). Vertebral centra of *Chi*/+ and *Chi*/+$_{LP}$ animals display distortions of the endplates not observed in WT zebrafish (**Figure 3C**). Despite these distortions, the endplates retain structurally unaltered intervertebral spaces with unaltered ligaments as in WT animals (**Figure 3C**).

Chihuahua Vertebrae Are Thin, Highly Mineralised and Lack an Osteoid. LP Diet Restores the Osteoid

Histological sections of non-demineralised vertebrae in the sagittal plane stained with Von Kossa/Van Gieson show the absence of a detectable osteoid layer (non-mineralised new bone matrix) in the growth zone of the vertebral endplates in *Chi*/+ animals (**Figure 4A**). In *Chi*/+$_{LP}$ animals the non-mineralised osteoid layer is restored (**Figure 4A**).

Vertebral body endplate mineralisation was assessed quantitatively based on the extent of the mineralised and non-mineralised bone matrix in whole mount specimens stained with Alizarin red S. In comparison to WT, *Chi*/+ mutants show higher mineralisation of the vertebral body endplates (Chi-square test: p<0.001), but the LP diet is capable of partially reducing endplate mineralisation in some *Chi*/+$_{LP}$ individuals (Chi-square test: *Chi*/+$_{LP}$ versus Chi/+, p<0.001; *Chi*/+$_{LP}$ versus WT, non-significant) (**Figure 4B**).

Finally, midline sections of the vertebral column were used to measure the thickness of bone structures in WT, *Chi*/+ and *Chi*/+$_{LP}$. Histomorphometry reveals that *Chi*/+ and *Chi*/+$_{LP}$ bone structures are significantly thinner compared to WT. This is the case for vertebral body endplates, the central region of the vertebral body and the trabecular bone (**Figure 4C**, **Table 2**).

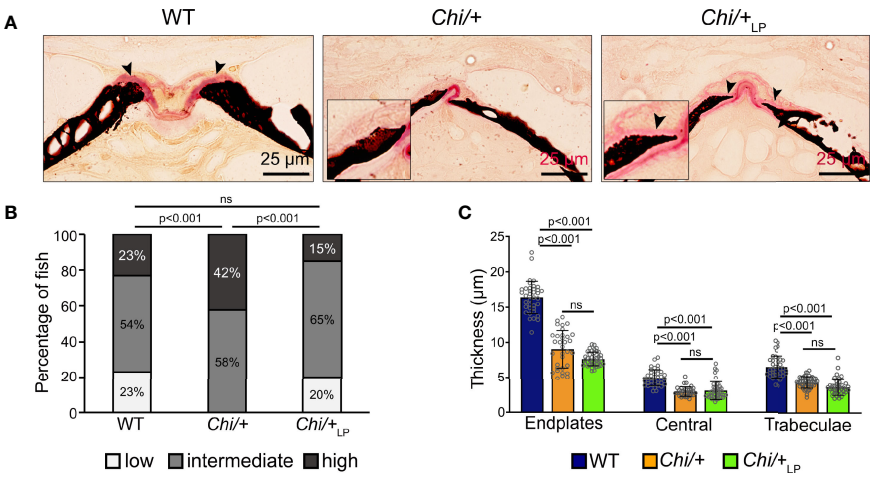

FIGURE 4 | *Chi*/+ vertebral bone structures are thin and highly mineralised. The LP diet restores the osteoid. **(A)** Sagittal histological non-demineralised sections stained with Von Kossa/Van Gieson show that three months old *Chi*/+ animals, compared to WT animals, have highly mineralised endplates. No osteoid layer can be identified. The osteoid (pink, black arrowheads) is restored in *Chi*/+$_{LP}$. Mineralised bone: black; dense collagen and non-mineralised bone: red. **(B)** Quantitative analysis of vertebral body endplate mineralisation (scored as low, intermediate or high) based on whole mount-stained specimens shows that *Chi*/+ animals exhibit a higher degree of mineralisation compared to WT animals. The LP diet reduces mineralisation of the vertebral body endplates in some *Chi*/+ individuals. The first 5 caudal vertebral centra in WT (n=15), *Chi*/+ (n=13) and *Chi*/+$_{LP}$ (n=12) were analysed. Chi-square test followed by Bonferroni correction, p values are indicated, ns: non-significant. **(C)** Measurements of bone structure thickness at three locations: (i) vertebral endplates, (ii) central region of vertebrae and (iii) trabecular bone (see **Figure 3A** for locations). Compared to WT animals, *Chi*/+ and *Chi*/+$_{LP}$ animals have thinner bone structures in all three locations (see also **Table 2**). Thickness of bone structures was measured on toluidine blue stained sections in 5 to 10 vertebral centra in WT (n=4), *Chi*/+ (n=4) and *Chi*/+$_{LP}$ (n=5). Mann-Whitney test followed by Bonferroni correction, p values are indicated, ns: non-significant.

TABLE 2 | Bone histomorphometry.

		Thickness, Mean ± SD (µm)	Pairwise p-values	
Vertebral body endplates	WT	16.39 ± 2.27	WT - *Chi*/+	4.6×10^{-12}
	Chi/+	9.03 ± 2.66	WT - *Chi*/+$_{LP}$	7.1×10^{-14}
	Chi/+$_{LP}$	7.63 ± 0.98	*Chi*/+ - *Chi*/+$_{LP}$	ns
Vertebral body central region	WT	4.95 ± 1.19	WT - *Chi*/+	3.5×10^{-10}
	Chi/+	2.90 ± 0.68	WT - *Chi*/+$_{LP}$	2.3×10^{-8}
	Chi/+$_{LP}$	3.10 ± 1.30	*Chi*/+ - *Chi*/+$_{LP}$	ns
Trabecular bone	WT	6.50 ± 1.58	WT - *Chi*/+	3.5×10^{-10}
	Chi/+	4.33 ± 0.78	WT - *Chi*/+$_{LP}$	2.3×10^{-8}
	Chi/+$_{LP}$	3.66 ± 1.14	*Chi*/+ - *Chi*/+$_{LP}$	ns

Statistical analysis is based on Mann-Whitney test followed by Bonferroni correction; ns, non-significant.

Compression Fractures and Fracture Repair in *Chihuahua* Vertebral Bodies

The analysis of whole mount-stained specimens reveals that *Chi*/+ and *Chi*/+$_{LP}$ animals have vertebral compression fractures that relate to the anteroposterior compression of vertebral centra (**Figure 5**). Compression fractures are absent in WT animals (**Figure 5A**). Different severity levels of compression fractures are observed in both *Chi*/+ and *Chi*/+$_{LP}$ individuals (**Figures 5B–D**). Some *Chi*/+$_{LP}$ animals present compression fractures that only affect one vertebral body (**Figure 5B**). Some *Chi*/+$_{LP}$ mutants show kyphosis associated with multiple compression fractures (**Figure 5C**). *Chi*/+ mutant fish display severely distorted vertebrae, as described above, and collapsed vertebral centra (**Figure 5D**). Regardless of the inter-individual variability among the fractures, the bone of fracture repair calli appears more dense than other bone elements when visualised with fluorescent light.

Histological sections in the sagittal plane of mutant vertebral columns confirm the presence of compression fractures in *Chi*/+ and *Chi*/+$_{LP}$ animals (**Figure 6**). A variety of fractured sites suggests that compression factures range from being in a status of repair (as evidenced by bone remodelling, see below) to

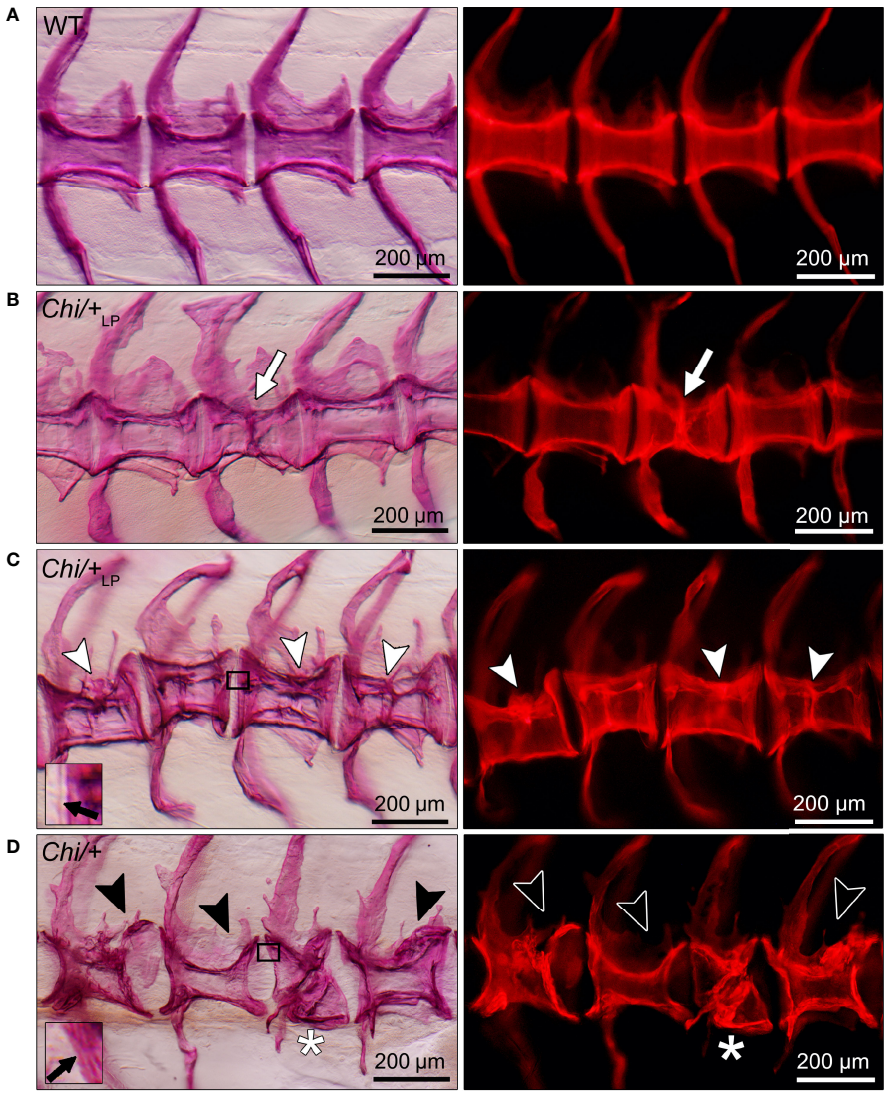

FIGURE 5 | Different grades of *Chi*/+ and *Chi*/+$_{LP}$ compression fractures. Whole mount Alizarin red S stained vertebral bodies of WT **(A)** and mutants **(B–D)** visualised in bright field (left) and with fluorescence (right). Inter-individual variability and different severity levels of compression fractures are observed in three months old mutant zebrafish. Bone calli associated to fractures appear more dense than other bone elements when visualised with fluorescent light. **(B)** Example of a mutant *Chi*/+$_{LP}$ showing a compression fracture affecting only one vertebral body, bone callus is visible (white arrow). **(C)** *Chi*/+$_{LP}$ zebrafish displaying kyphosis associated with multiple compression fractures and evident bone calli (white arrowheads). **(D)** Mutant *Chi*/+ fish displaying severely distorted vertebrae (black arrowheads) and a collapsed vertebral body (white asterisk). The inserts in **(C, D)** demonstrate the identification of osteoid on whole mount-stained specimens. Black arrows indicate the presence **(C)** and absence **(D)** of osteoid in *Chi*/+$_{LP}$ and *Chi*/+, respectively.

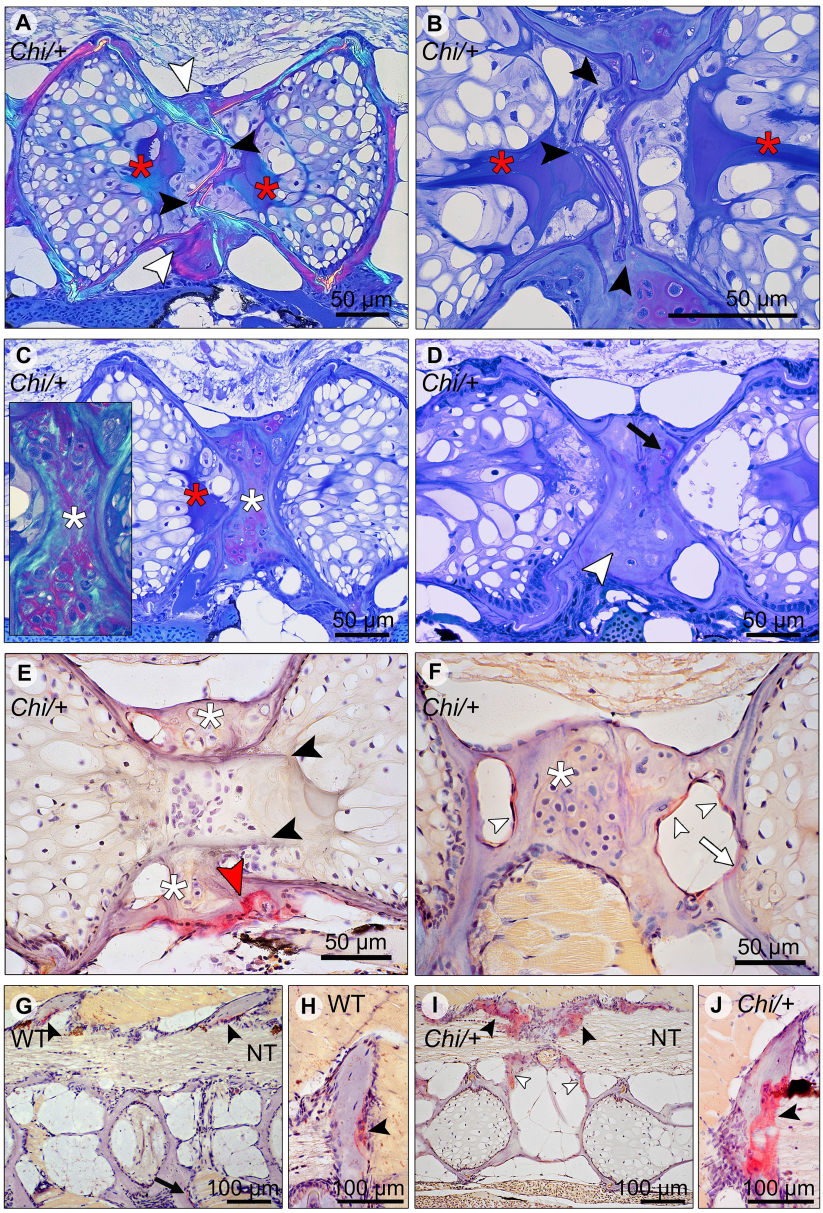

FIGURE 6 | Compression fractures and bone resorption in *Chi/+* and *Chi/+*$_{LP}$ vertebral bodies. **(A)** Toluidine blue stained medio-sagittal section of a compression fracture from three months old mutant zebrafish (representative for both *Chi/+* and *Chi/+*LP) observed with polarised light. The compression fracture is characterised by several fractures in the central region of the vertebral body (black arrowheads); a bone callus is present on the outside of the vertebral centrum (white arrowheads). The fracture also disrupts the notochord tissue and induces condensation of chordocytes into a fibrous tissue (a known reaction of notochord tissue to injuries) (red asterisks). **(B)** High magnification of the fractured bone (black arrowheads) inside the notochord. The reaction of the notochord tissue can be seen (red asterisks). **(C)** A fibrocartilaginous callus is present around the fractured central part of the vertebral body, the typical appearance for fracture callus at initial stages of repair (white asterisks). Polarised light (insert) shows collagen fibres (green) within the cartilaginous callus. Red asterisk indicates the notochord tissue condensation. **(D)** Sagittal section of a healed compression fracture. Fracture repair and remodelling processes replaced the fibrocartilaginous tissue by a bone callus (white arrowhead). Remnants of the fibrocartilaginous tissue are visible (black arrow). **(E)** Tartrate-resistant acid phosphatase (TRAP) staining confirms compression fracture repair. TRAP activity (red staining, red arrowhead) indicates resorption of the fibrous tissue (white asterisks) that is being replaced by a hard bone callus. The fractured bone fragments (black arrowheads) in the lumen of the notochord do not show resorption, which is consistent with the absence of blood vessels, lymphatic vessels and innervation inside the notochord. **(F)** TRAP activity is detected also in the trabecular bone (white arrowheads) and vertebral endplate (white arrow) of a vertebra showing a compression fracture in mutant zebrafish (representative for both *Chi/+* and *Chi/+*$_{LP}$). White asterisk indicates the fibrocartilaginous callus. **(G, H)** WT display TRAP activity (red) at sites of bone remodelling linked to bone growth, i.e. the endosteal surfaces of the neural (black arrowheads) and haemal arches (black arrow). NT, neural tube. **(I, J)** *Chi/+* animals (representative also for *Chi/+*$_{LP}$) show TRAP activity at the same locations as in WT, however mutants exhibit expanded TRAP activity at all endosteal and periosteal bone surfaces, i.e. arches (black arrowheads) and bone trabeculae connecting the endplates (white arrowheads). NT, neural tube.

fractures that do not, or not yet, display evidence of repair. Compression fractures affect the central region of the vertebral bodies. The fractured bone trabeculae become displaced into the chordocyte-filled lumen of the notochord (**Figures 6A, B**). When fractures injure the notochord, the notochord strand and the notochord septum (see **Figure 3A** for the anatomical terms) become condensed [keratinised in response to tissue damage according to (26)] (**Figures 6A, B**). Analysis of serial sections from several *Chi*/+ and *Chi*/+$_{LP}$ animals reveals that compression fractures display variable degrees of repair. Fractured sites show fibrocartilaginous calli at the outer surface of the compressed vertebral bodies (**Figure 6C**). Repair evidently continues with replacement of fibrocartilage tissue by a bone callus (**Figure 6D**). Repair at fracture locations is further confirmed by the demonstration of tartrate-resistant acid phosphatase (TRAP). TRAP is produced by osteoclasts and secreted onto the bone surface at the locations of bone resorption. TRAP activity is also linked to the resorption of fibrocartilage that is being replaced by a bone callus (**Figure 6E**) (27). Osteoclast activity is also observed at the bone trabeculae and vertebral endplates of vertebral compression fractures (**Figure 6F**). No signs of fracture repair or bone resorption are detected on bone elements inside the notochord (**Figure 6E**). This agrees with the fact that the notochord contains neither blood vessels, nor nerve fibres and no lymphatic vessels (28).

Chihuahua Mutants Have Increased Bone Resorption

Osteoclasts and locations of bone resorption (other than locations of fracture repair) in growing juvenile individuals were identified by the demonstration of TRAP. In WT zebrafish TRAP activity is typically restricted to locations within the vertebral column that require resorption for allometric growth (27), i.e. the endosteal surfaces of enlarging neural and haemal arches (**Figures 6G, H**). *Chi*/+ and *Chi*/+$_{LP}$ also display TRAP staining at the endosteal surfaces of the neural and haemal arches, but the enzymatic activity is increased and extends also to other bone structures such as the bone trabeculae (**Figures 6I, J**).

Transmission electron microscopy (TEM) confirms the presence of osteoclasts, attached to the endosteal surfaces of arches in WT, *Chi*/+ and *Chi*/+$_{LP}$ (**Figure 7A**). These cells, while attached to the bone surface, reside in resorption lacunae (as shown in **Figure 7A**, WT zebrafish). Actively resorbing osteoclasts exhibit a typical 'ruffled border', an electron-dense cytoplasm with abundant cytoplasmic vacuoles and resorption vesicles in proximity of the ruffled border (as shown in **Figure 7A**, *Chi*/+ zebrafish).

Chihuahua Mutants Show Signs of ER Stress and Altered Collagen Type I

The ultrastructure of bone cells and bone matrix in the vertebral column was analysed by TEM at the level of the medio-sagittal plane. Ultrathin sections of representative specimens show that *Chi*/+ and *Chi*/+$_{LP}$ have enlarged endoplasmic reticulum (ER) cisternae in osteoblasts located in the growth zone of the vertebral body endplates (**Figure 7B**, see **Figure 3A** for location). Likewise, ER cisternae in osteoblasts along the neural and haemal arches are enlarged. High magnification images show that *Chi*/+ ER cisternae are filled with protein (**Figure 7C**). Conversely, WT osteoblasts have numerous, yet not enlarged ER cisternae, indicative for high protein synthesis activity at the growth zone of the endplates (**Figure 7B**).

The collagen matrix appears altered in the *Chi*/+ mutants compared to WT. In WT, newly secreted collagen fibrils in the proximity of the osteoblasts (osteoid) are dispersed prior to maturation and assemble into larger fibres at a distance from the osteoblasts. In contrast, the *Chi*/+ bone matrix is characterised by densely packed collagen fibrils in the vicinity of the osteoblasts (**Figure 7C**). In *Chi*/+$_{LP}$, individual collagen fibrils are partly distinguishable in close proximity of the osteoblasts, indicative for less collagen packing and a more typical osteoid (**Figure 7C**).

Longitudinal sections of collagen fibres in WT zebrafish show a regular D-periodicity. The pattern is absent in *Chi*/+ mutants. In *Chi*/+$_{LP}$ the collagen D-periodicity is partially visible along the fibre (**Figure 7D**).

DISCUSSION

Chihuahua Zebrafish Suffer From Vertebral Column Deformities, Low Dietary P Partially Rescues the Bone Phenotype

Early reports on children and young patients diagnosed with OI described severe vertebral column deformities as the major complications of the disease. From very young age onwards, patients suffer from vertebral body deformities associated with progressive scoliosis, kyphosis or kyphoscoliosis (2, 4, 29). This condition is known to be age-dependent and usually worsens after the age of six (4, 30). Likewise, *Chi*/+ zebrafish display severe bending of the vertebral column, i.e. kyphosis and lordosis, at three months of age, as demonstrated by whole mount Alizarin red S staining and histological sections. Similar to human patients, such malformations progressively worsen in adult stages (16, 17). Vertebral body deformities, vertebral compressions and fractures represent other severe complications of young patients (4, 29). We show here for the first time that juvenile *Chi*/+ zebrafish suffer from vertebral body compressions in both the abdominal and caudal region of the vertebral column. Mutant vertebral bodies are distorted and characterised by increased shape variation compared to WT, as revealed by geometric morphometrics. On top of that, *Chi*/+ fish have highly mineralised vertebral body bone structures with no detectable osteoid (non-mineralised collagenous bone matrix), as confirmed by histology of non-demineralised specimens. Likewise, the osteoid thickness is reduced in the bone of human patients (31, 32) and murine OI models (33, 34). Moreover, hypermineralisation and bone brittleness are well documented in human patients (2, 4, 5, 29), OI mouse models (35) and OI zebrafish models (17, 36). Excess bone mineralisation related to increased dietary P intake or ageing is known to increase vertebral column malformations in WT zebrafish (22, 26). Hence, hypermineralisation alone can be considered a risk factor for bone deformities. In addition, OI bone is characterised by mutated collagen type I, which contributes to bone fragility. While mutations cannot be undone in OI patients or animal

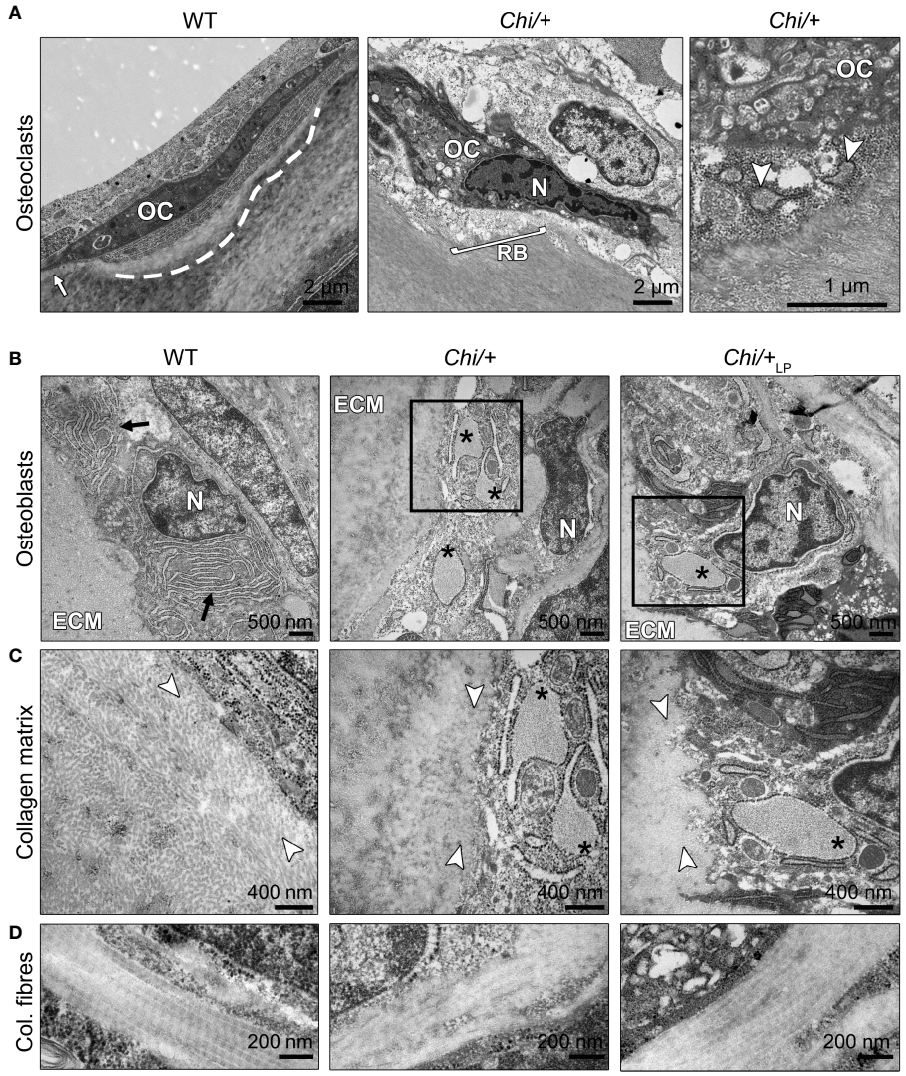

FIGURE 7 | Ultrastructure of bone cells and bone matrix in *Chi*/+ and *Chi*/+$_{LP}$ animals. **(A)** Transmission electron microscopy (TEM) of osteoclasts (OC) located at the arch surface of three months old WT and *Chi*/+ (representative for both *Chi*/+ and *Chi*/+$_{LP}$) vertebrae. The panel WT shows a typical flat-shaped teleost osteoclast (OC) characterised by its electrodense cytoplasm. The cell resides in a shallow resorption lacuna (dashed line), yet is attached to the bone surface (white arrow). The panel *Chi*/+ shows an osteoclast that resorbs the bone matrix and exhibits the typical 'ruffled border' (RB), an electron-dense cytoplasm with abundant cytoplasmic vacuoles and resorption vesicles (right panel, white arrowheads) in proximity of the ruffled border. N, nucleus. **(B)** TEM of WT, *Chi*/+ and *Chi*/+$_{LP}$ shows mutant osteoblasts with enlarged endoplasmic reticulum (ER) cisternae (asterisks). The osteoblasts are located in the growth zone of the vertebral body endplate (see **Figure 3A** for location). Higher magnification images in **(C)** show that *Chi*/+ osteoblast ER cisternae are filled with protein, likely mutated collagen type I WT osteoblasts have numerous, yet not enlarged ER cisternae (arrows). ECM: extracellular matrix of the bone surface; N: nucleus. **(C)** The newly secreted collagen fibrils (white arrowheads) in the proximity of the osteoblasts in WT are visibly separated prior to maturation and assemblage into collagen fibres. In contrast, the *Chi*/+ animal has densely packed collagen fibrils. No space can be recognised between the fibrils. In the *Chi*/+$_{LP}$ individual collagen fibres are densely packed and space between the fibrils is distinguishable in proximity to the osteoblasts. **(D)** Longitudinal sections of collagen fibres show a regular D-periodicity pattern in a WT animal, absence D-period pattern in a *Chi*/+ mutant, and a less regular D-periodicity pattern a *Chi*/+$_{LP}$ specimen.

models, lowering the bone mineral content could possibly alleviate their skeletal defects. Recent findings on teleosts including WT zebrafish (22) and Atlantic salmon (23–25) have shown that low dietary P administration reduces the bone mineral content and promotes the formation of non-mineralised bone without causing vertebral column malformations. To assess the effects of reduced dietary P intake on the mutant bone phenotype, *Chi*/+ were fed a low P diet (LP) from one month of age. *Chi*/+ zebrafish under LP conditions (*Chi*/+$_{LP}$) have reduced incidence of kyphosis and lordosis of the abdominal region of the vertebral column, and reduced shape variation of the caudal vertebral bodies. The reduced P intake restores the shape of vertebral bodies to a condition more similar to WT vertebral bodies. Moreover, the LP diet is shown to reduce the mineralisation of vertebral body endplates in some treated *Chi*/+ fish and to restore the osteoid layer, that is absent in untreated mutants. It is known that the presence of an osteoid

(non-mineralised collagen) has a beneficial effect on the mechanical properties of bone. The collagenous bone matrix itself is a very tough material that can withstand extreme mechanical forces and bend without fracturing. Examples for tough low mineralised bones that do not fracture are deer antlers and the bones of human infants (18), but also teleosts under reduced P intake show tough and deformable vertebral bodies with no signs of fractures (22, 24, 25). In contrast, high dietary P causes excess mineralisation and higher bone stiffness in teleosts (22, 24, 25), and results in reduced bone formation in humans (37, 38) and reduced ultimate strength (maximal load) in rats (39). Our findings suggest that the mineral content of *Chi*/+ bone likely was reduced by the LP diet, which could explain the reduced incidence of vertebral column deformities and the restored shape of the vertebral bodies.

Chihuahua Vertebrae Have Thin Bone Structures and Are Subjected to Compression Fractures

One of the most severe complications in OI patients are multiple compression fractures with collapse of the vertebral bodies (4, 29). Our findings show that *Chi*/+ zebrafish suffer from the same type of complications. Several compression fractures were identified on whole mount specimens and on histological sections. Which are the factors predicted to contribute to compression fractures? The first possible factor for compression fractures is the poor quality of OI bone, caused by mutated collagen production and excess mineralisation. As discussed above, over-mineralised bone fractures easily; both patients and *Chi*/+ zebrafish suffer from bone brittleness (5, 17). The second potential cause is reduced bone mass. Histological assessment of human biopsies showed that patients including children have thinner cortical bone and a reduced number of trabeculae in trabecular bone (4, 5). Likewise, two OI mice models (33, 34) and *Chi*/+ zebrafish have thinner bone elements compared to WT, thin vertebral body endplates, thin bone elements in the vertebral body central region and thin bone trabeculae. Thus, hypermineralised vertebral bodies with poor trabecular bone are at mechanical disadvantage and are easily subjected to compression fractures (5). Bone with low mass and excess of minerals cannot easily withstand mechanical forces exerted along the axial skeleton. The third potential factor contributing to compression fractures is the weakness of the spinal ligaments and intervertebral discs. Early reports described that OI patients lack vertebral stability because of the laxity of the spinal ligaments (2, 4) and intervertebral discs (40, 41). Similarly, the *Col1a*^{Jrt}/+ OI mouse model shows reduced cervical intervertebral space (42). Likewise, *Chi*/+ zebrafish show evidence of weak intervertebral ligaments. Although on histological sections the ligaments of *Chi*/+ fish display all the structural elements as in WT animals, *Chi*/+ vertebral endplates are often shifted against each other along the dorsal-ventral axis. In humans weak ligaments fail to provide sufficient support to the vertebral column and allow the progressive degeneration of the deformity into a compression fracture (4). It can be assumed that less severe complications appear first and subsequently progress into a severe compression fracture. To support this hypothesis, patients show microfractures of the vertebral body growth plates (4, 43). During growth in humans, vertebral growth plate microfractures can progress into complicated lesions such as compression fractures (29, 44).

Human OI patients show evidence of fracture repair, but often fractures heal with deformities (45). We show similar findings in *Chi*/+ zebrafish. Compression fractures in *Chi*/+ are also subjected to fracture repair but the vertebral bodies remain deformed. Analysis of histological sections from different specimens suggests the identification of fractures in different stages of repair and allows for the tentative reconstruction of the steps involved in vertebral fracture healing. Like in mammals, *Chi*/+ zebrafish fractures are initially stabilised by the formation of fibrocartilaginous calli, that subsequently become ossified. Despite the observation of fractures in different stages of repair, the design of our study does not allow to generate a timeline of fracture repair. In the goldfish (*Carassius auratus*), a cyprinid species like zebrafish, a bone fracture callus takes about 35 days to replace the fibrocartilaginous template (46). Thus, the presence of bone calli in compressed vertebral bodies of three months old *Chi*/+ indicates that mutants likely developed vertebral compression fractures before the start of the experiment. This could explain why both *Chi*/+ treated with the LP diet and untreated mutants show compression fractures. Compression fractures are therefore one of the most important complications during the initial stages of the disease, both in zebrafish and children affected by OI, and are crucial in the quick progression of the OI phenotype.

Chihuahua Zebrafish Have Increased Bone Resorption and Reduced Bone Formation, but the LP Diet Improves the Bone Matrix

Bone from individuals with OI is characterised by an increased bone turnover rate and an increased number of osteoclasts, associated to an increased eroded surface compared to controls (47–49). Analogous findings derive from studies on two OI mouse models, the *Oim* (33) and *Brtl* (34) mice. Likewise, *Chi*/+ zebrafish exhibit increased osteoclastic activity, as demonstrated by TRAP staining on histological sections. Resorption activity is increased at the endosteal surfaces of the neural and haemal arches compared to WT animals. TRAP activity extends also to other bone structures that are not subjected to resorption in WT zebrafish, such as the vertebral body endplates and the bone trabeculae that connect the vertebral body endplates (50). Trabecular bone surfaces display high osteoclast activity also in the *Oim* and *Brtl* mice (33, 34). The bone in zebrafish can be remodelled by multinucleated osteoclasts, but different from mammals, thin bony elements are typically resorbed by mononucleated cells (27). Flat, elongated mononucleated osteoclasts occur at endosteal surfaces, for example of neural and haemal arches (27, 50), as also observed in WT specimens in this study. Bone resorption in zebrafish is primarily related to the demands of allometric growth. The common type of mononucleated osteoclasts does not create deep resorption lacunae (27). TEM from *Chi*/+ specimens showed osteoclasts with abundant electrondense cytoplasm characterised by several cytoplasmic vacuoles. These cells exhibit the typical ruffled border, indicative for active resorption of the bone matrix. Also osteoclasts in bone from the *Oim* mouse exhibited cellular changes. *Oim* cells have a larger diameter and exhibit three times the number of nuclei compared to osteoclasts in WT mice (51). The abundant cytoplasmic vacuoles of osteoclasts and the larger amount

of TRAP-positive bone surfaces are indicative for increased resorptive activity in OI bone, both in *Chi*/+ zebrafish and mouse models (34, 51). While endosteal bone resorption is increased in human OI patients, osteoblasts produce less new bone, which results in a reduced osteoid thickness, as discussed above. The decrease in bone formation in human patients, reviewed by Fedarko (49), is consistent with data from the *Oim* and *Brtl* mouse models (33, 34). *In vitro* studies have shown that osteoblasts from human patients (reviewed by 49) and murine models (52) show decreased synthesis, processing and matrix incorporation of collagen compared to controls. The production of mutated collagen type I in OI osteoblasts results in delayed collagen folding and excess post-translational modifications, that cause intracellular retention of defective collagen and endoplasmic reticulum (ER) stress (10). At an ultrastructural level, *Chi*/+ zebrafish have osteoblasts in the vertebral growth zone with enlarged ER cisternae. Similar findings were previously described on osteoblasts from the caudal fin of adult *Chi*/+ (16). Here we show that ER cisternae in *Chi*/+ osteoblasts are filled with protein, likely mutated collagen type I. Intracellular collagen retention leads to collagen over modification and impairs collagen secretion in *Chi*/+ (16) and in OI models (52). The extracellular collagen matrix is also impaired. In close proximity of the osteoblasts, the collagen fibrils in *Chi*/+ fish are densely packed and lack the typical pattern of the osteoid collagen where the fibrils have a low density and are loosely arranged (53). In contrast, in *Chi*/+ the fibrils in the bone matrix have a high degree of compactness that is typical of fully mineralised bone (53). These findings correlate well with the lack of osteoid seams in *Chi*/+ and OI bone in general. It is widely accepted that insufficient osteoblast performance is at the basis of the severe OI phenotype. Thus, recent studies have targeted OI osteoblasts to relieve ER stress and improve cellular functions. The treatment with 4-phenylbutyrate, a chemical chaperone already approved by the FDA for urea cycle disorders, stimulates collagen secretion in murine OI osteoblasts *in vitro* (52), and improves the OI bone phenotype *in vivo* (16). In the present study, we show that two months of reduced dietary P administration partially rescue the OI phenotype in *Chi*/+. Mutants which received the LP diet show improved extracellular matrix with less dense collagen fibrils, indicative for a more typical osteoid. This finding together with the reduced incidence of vertebral column deformities and the rescue of the vertebral body shape, suggests that a reduced dietary P intake can alleviate the severe bone phenotype in juvenile *Chi*/+ zebrafish.

MATERIALS AND METHODS

Zebrafish Maintenance and Ethical Statement

Wild type AB (WT) and heterozygous *Chihuahua* (*col1a1a*$^{dc124/+}$, *Chi*/+) zebrafish were bred in-house. The mutant *Chi*/+ carries a heterozygous c.2207G>A mutation in *col1a1a* causing a p.G736D (G574D) substitution in the α1 chain of collagen type I (15). Zebrafish embryos were kept in petri dishes in fish water (1.2 mM $NaHCO_3$, 0.01% instant ocean, 1.4 mM $CaSO_4$, 0.0002% methylene blue) at 28°C until 7 days post-fertilisation (dpf), then housed in ZebTEC semi-closed recirculation housing systems (Techniplast, Buguggiate, Italy) at 28°C, pH 7.5 and conductivity 500 μS on a 14/10 light/dark cycle. Zebrafish from 7 to 21 dpf were fed three times a day alternating commercial dry food (ZM000, Zebrafish Management Ltd., Winchester, UK) and brine shrimp (Artemia cysts, Zebrafish Management Ltd., Winchester, UK). Fish were then fed for another week three times a day with a dry regular P diet (22), see also below), until 28 dpf, to adjust them to this type of dry feed. Starting from 28 dpf, WT were fed three times a day with a regular P diet for two months. At 28 dpf, *Chi*/+ were randomly divided in two groups and fed three times a day with a 'LP diet' (low P content) or a regular P diet for two months (see below for details). Specimens were collected after two months of dietary treatment, euthanised by tricaine (3-amino benzoic acidethylester) overdose (0.3%) and fixed for further analyses as described below. The experiments were conducted in the centralised animal facility of the University of Pavia (Pavia, Italy). All animal studies were conducted in agreement with EU Directive 2010/63/EU for animals. The experimental protocol was approved by the Italian Ministry of Health (Approval animal protocol No. 260/2020-PR, 26 March 2020).

Diet Composition

Diet composition and nutritional experiments are described in detail in (22). Briefly, the diets were formulated to have a total P content of 0.5% and 1.0%, termed low P (LP) diet and regular P diet, respectively (**Table 3**). Monoammonium phosphate (MAP) was used as dietary inorganic P supplement (54). In order to keep all diets equal in

TABLE 3 | Ingredients and chemical composition of the diets for zebrafish.

Ingredients (%)	Low P diet	Regular P diet
Rapeseed lecitin (Bergathin)	2.00	2.00
Krill meal	3.00	3.00
Wheat starch	18.77	18.77
Corn gluten meal	8.0	8.0
Wheat gluten meal	19.01	19.01
Soy protein concentrate	31.00	31.00
Capelin fish meal	5.00	5.00
Rapeseed oil	1.58	1.58
Peruvian fishoil	2.60	2.60
DL-Methionine	0.60	0.60
Biolys 54.6%	2.00	2.00
Lutavit C Aquastab 35%	0.10	0.10
Vitamin mix	0.50	0.50
Choline chloride 50%	1.50	1.50
Trace mineral mix (P free)	0.30	0.30
Monoammonium phosphate 26%	0.00	1.95
Diamol (diatomaceous earth)	4.00	2.05
Astaxanthin 10%	0.07	0.07
Total	100.00	100.00
Chemical composition (g/kg)		
Crude protein	497	508
Crude lipids	97	97
Crude ash	84	73
Calcium	4.84	4.79
Magnesium	1.96	1.98
Phosphorus	5.04	9.84

nutrients, except for P concentration, MAP replaced the inert filler diatomaceous earth (Diamol, Imerys, Denmark). The diets were formulated by SimplyFish AS (Stavanger, Norway, www.simplyfish.no) and produced by extrusion with subsequent crumbling to a suitable particle size by the Danish Technological Institute (Taastrup, Denmark, https://www.dti.dk). The P content of the product was verified at the University of Hohenheim (Stuttgart, Germany, https://www.uni-hohenheim.de) and determined with 5.04 g/kg diet and 9.84 g/kg diet for the low P and regular P diet, respectively (**Table 3**).

X-Rays

X-rays of WT, *Chi*/+ and *Chi*/+ under LP diet were acquired with a Faxitron Mx-20 (Faxitron, Tucson, Arizona, USA) using 25 kV for 10 sec. The Kodak DirectView Elite CR System and k-Pacs software (Kodak, Rochester, New York, USA) were used for image digitalisation.

Whole Mount Skeletal Staining

WT (n=26), *Chi*/+ (n=20) and *Chi*/+$_{LP}$ (n=18) were fixed for 24 h in 4% paraformaldehyde (PFA) in 1× phosphate-buffered saline (PBS) at C and were stained with Alizarin red S according to an established protocol (55). Fish were analysed and imaged using an Axio Zoom V16 stereomicroscope (Carl Zeiss, Oberkochen, Germany) with oblique illumination equipped with a 5MP CCD camera. Classification of the deformities was performed on whole mount-stained WT and mutants as defined by Martini et al. (56). Only the abdominal and caudal region of the vertebral column were analysed. The maximal curvature indices related to the abdominal and the caudal region of the vertebral column were calculated according to the method described by Marie-Hardy et al. (57). Briefly, the maximal kyphotic and lordotic indices were calculated in the sagittal plane of Alizarin red S stained specimens as the ratio (a/b) between the perpendicular distance from the axis in correspondence of the maximal curvature (segment 'a' in **Figure 1A**) and the standard length (described as the distance from the anterior most tip of the upper jaw to the posterior edge of the caudal peduncle where caudal fin rays insert (58), segment 'b' in **Figure 1A**). The same method but in the coronal plane was used to calculate the maximal scoliotic index. Moreover, for each group the following general metrics were calculated according to Martini et al. (56): the frequency (%) of specimens with at least one malformation, the total number of malformations identified, the average malformation load (total number of malformations diagnosed in a group/number of malformed individuals per group).

Lateral images of stained fish were used to quantitatively analyse mineralisation levels of vertebral endplates of WT, *Chi*/+ and *Chi*/+$_{LP}$ as described in (22). The first 5 caudal vertebral bodies (59) were considered for analysis in all specimens, following the established protocol (22). Briefly, the non-mineralised endplate was expressed as a percentage of the total non-mineralised endplate length over the total vertebral length. Vertebral endplates with a non-mineralised percentage value greater than 10% were classified as low mineralised, between 3% and 10% as intermediate mineralised, and less than 3% were considered high mineralised.

Geometric Morphometrics of Vertebral Centra

Lateral images of whole mount Alizarin red S stained specimens were used to quantify the shape variation of the first 10 caudal vertebral centra (59) in WT (n=15), *Chi*/+ (n=13) and *Chi*/+$_{LP}$ (n=12) by means of landmark-based geometric morphometrics. The landmarks, defined as biologically homologous anatomical loci recognisable on all specimens in the study (60), were selected on the vertebral centra as represented in **Figure 2A**: landmarks number 1, 5, 6 and 10 on the vertebral endplates; landmarks number 2, 4, 7 and 9 on the anterior and posterior cone of the centrum; landmarks number 3 and 8 in the central region of the centrum. A similar configuration of landmarks has been applied in a vertebral fracture assessment study in human patients (61). 2D landmarks were extracted from digital images using Fiji (NIH, Bethesda, Maryland, USA) and digitised in the same order for all vertebral centra analysed. Procrustes superimposition of digitised landmarks and visualisation of shape variations were performed using Past4.04 software (62). Principal component analysis was performed using PCAGen8 software as described in (60).

Histology and Bone Histomorphometry

WT (n=4), *Chi*/+ (n=4) and *Chi*/+$_{LP}$ (n=5) were fixed for 24 h in 2.5% PFA, 1.5% glutaraldehyde, 0.1 M sodium cacodylate buffer (pH 7.4) and 0.001% $CaCl_2$ at 4°C, decalcified in 0.1 M EDTA for 14 days at 4°C and embedded in glycol methacrylate (27). Sagittal 2 µm sections were cut on a Microm HM360 (Marshall Scientific, Hampton, New Hampshire, USA) automated microtome and were stained with toluidine blue (0.5% toluidine blue, 1% $Na_2B_4O_7$ in demineralised H_2O (dH_2O), pH 9 for 15 sec), rinsed in dH_2O and mounted with DPX. Images were acquired using an Axio Imager-Z1 microscope (Carl Zeiss, Oberkochen, Germany) equipped with an Axiocam 503 colour camera (Carl Zeiss, Oberkochen, Germany). Bone structure histomorphometry was analysed on images of toluidine blue stained sections of the middle plane of the vertebral column. Thickness of bone structures in the endplates, in the central region and in the trabeculae of 5 to 10 vertebral centra per specimen were measured using Fiji (NIH, Bethesda, Maryland, USA) (see **Figure 3A** for location). The mean values were considered for analysis.

For mineral detection on histological sections, WT and mutant zebrafish were selected based on X-rays to be representative for the phenotype. WT (n=1), *Chi*/+ (n=1) and *Chi*/+$_{LP}$ (n=1) were fixed as described above and embedded in glycol methacrylate without carrying out decalcification. Sections of 2 µm were stained according to the Von Kossa/Van Gieson protocol (63). Images were acquired using an Axio Imager-Z1 microscope (Carl Zeiss, Oberkochen, Germany) equipped with a 5MP CCD camera.

Transmission Electron Microscopy

WT (n=1), *Chi*/+ (n=1) and *Chi*/+$_{LP}$ (n=1) were selected based on X-rays to be representative for the phenotype, fixed and decalcified as described above for histology, and embedded in epon epoxy medium (64). Semi-thin 1 µm sagittal sections were cut on a Microm HM360 microtome (Marshall Scientific, Hampton, New Hampshire, USA), stained with toluidine blue

at pH 9 for 2 min, rinsed with dH_2O and mounted with DPX. For TEM analysis, ultrathin sections (about 70 nm) of the middle plane of the vertebral column were prepared on an UltracutE ultramicrotome (Reichert-Jung, Buffalo, New York, USA), contrasted with uranyl acetate and lead citrate and analysed with a Jeol JEM 1010 transmission electron microscope (Jeol Ltd., Tokyo, Japan) operating at 60 kV. Microphotographs were taken with a Veleta camera (Emsis, Muenster, Germany).

Enzyme Histochemistry

WT (n=2), *Chi*/+ (n=2) and *Chi*/+$_{LP}$ (n=2) were fixed in 4% PFA in 1× PBS, pH 7.4, for 1 h at RT and decalcified in 4% PFA, 10% EDTA, pH 7.4 for 14 days at 4°C. Specimens were embedded in glycol methacrylate (27). Sagittal 5 µm sections were cut on a Microm HM360 (Marshall Scientific, Hampton, New Hampshire, USA) automated microtome and demonstration of tartrate-resistant acid phosphatase (TRAP) was adapted from (27). Briefly, sections were pre-incubated at 37°C for 45 min in 50 mL acetate buffer (0.1 M sodium acetate, 50 mM L(+) di-sodium tartrate dehydrate, pH adjusted to 5.5 with acetic acid) to which is added 0.5 mL of enzyme substrate solution (2% Naphtol AS TR phosphate dissolved in ethylene glycol mono-butyl ether). Shortly before use, 1 mL of pararosaniline solution (4% pararosaniline chloride (CI. 42500) in 7% HCl solution) was mixed to 1 mL of fresh 5% sodium nitrite and, after hexazotiation, was added to the acetate-enzyme substrate solution. Enzymatic reaction took place in 30-60 min at 37°C. Subsequently, slides were rinsed in dH_2O, counterstained with Meyers haematoxylin for 10 min, rinsed in running tap water for 10 min, flushed in dH_2O, dried at 40°C and mounted with DPX.

Statistical Analysis

Quantitative variables are expressed as mean ± standard deviation, categories are expressed as percentages. Statistical analysis was performed using Past4.04 software (62). Differences in the occurrence of vertebral column deformities and in bone mineralisation levels were evaluated by means of Chi-square test followed by Bonferroni correction. Comparison of the maximal curvature indices was based on the non-parametric Mann-Whitney test. Differences in the thickness of bone structures were evaluated by means of Mann-Whitney non-parametric test followed by Bonferroni correction. For principal component analysis of geometric morphometrics data, significant differences in principal component 1 and principal component 2 were obtained using PCAGen8 software as described in (60) using Chi-square test (paired tests, WT-*Chi*/+ and WT-*Chi*/+$_{LP}$). A p value less than 0.05 was considered significant.

DATA AVAILABILITY STATEMENT

The raw data supporting the conclusions of this article will be made available by the authors, without undue reservation.

ETHICS STATEMENT

The animal study was reviewed and approved by Italian Ministry of Health.

AUTHOR CONTRIBUTIONS

SC, PEW, and AF designed the study. SC carried out the research. DL carried out TEM. WK designed the diets. SC, PW, and AH analysed the results and drafted the manuscript. PW and AH obtained the funding. All authors contributed to the article and approved the submitted version.

FUNDING

SC and PEW acknowledge funding by the European Union's Horizon 2020 Research and Innovation Programme under the Marie Skłodowska-Curie grant agreement No 766347 (Biomedaqu) and by Ghent University, Bijzonder Onderzoeksfonds grant code BOF.ITN.2021.0012.01. AH acknowledges Bijzonder Onderzoeksfonds grant from Ghent University in the frame of Concerted Research Actions funding No BOFGOA2021000407.

ACKNOWLEDGMENTS

We acknowledge the Ghent University TEM-Expertise Center (Life Sciences), facility Nematology Research Unit, where TEM was carried out; the animal facility "Centro di servizio per la gestione unificata delle attività di stabulazione e di radiobiologia" of the University of Pavia, Pavia, Italy where animals were hosted; the OPBA of the University of Pavia for support in animal protocol drawing up.

REFERENCES

1. Forlino A, Marini JC. Osteogenesis Imperfecta. *Lancet* (2016) 387:1657–71. doi: 10.1016/S0140-6736(15)00728-X
2. Sillence DO, Senn A, Danks DM. Genetic Heterogeneity in Osteogenesis Imperfecta. *J Med Genet* (1979) 16:101–16. doi: 10.1136/jmg.16.2.101
3. Marini JC, Forlino A, Bächinger HP, Bishop NJ, Byers PH, Paepe A, et al. Osteogenesis Imperfecta. *Nat Rev Dis Primers* (2017) 3:17052. doi: 10.1038/nrdp.2017.52
4. Benson DR, Newman DC. The Spine and Surgical Treatment in Osteogenesis Imperfecta. *Clin Orthop Relat Res* (1981) 159:147–53. doi: 10.1097/00003086-198109000-00020
5. Zeitlin L, Fassier F, Glorieux FH. Modern Approach to Children With Osteogenesis Imperfecta. *J Pediatr Orthop B* (2003) 12:77–87. doi: 10.1097/01.bpb.0000049567.52224.fa
6. Ben Amor IM, Roughley P, Glorieux FH, Rauch F. Skeletal Clinical Characteristics of Osteogenesis Imperfecta Caused by Haploinsufficiency Mutations in COL1A1. *J Bone Miner Res* (2013) 28:2001–7. doi: 10.1002/jbmr.1942
7. Wallace MJ, Kruse RW, Shah SA. The Spine in Patients With Osteogenesis Imperfecta. *J Am Acad Orthop Surg* (2017) 25:100–9. doi: 10.5435/JAAOS-D-15-00169
8. Castelein RM, Hasler C, Helenius I, Ovadia D, Yazici MEPOS Spine Study Group. Complex Spine Deformities in Young Patients With Severe

Osteogenesis Imperfecta: Current Concepts Review. *J Child Orthop* (2019) 13:22–32. doi: 10.1302/1863-2548.13.180185
9. Marini JC, Forlino A, Cabral WA, Barnes AM, San Antonio JD, Milgrom S, et al. Consortium for Osteogenesis Imperfecta Mutations in the Helical Domain of Type I Collagen: Regions Rich in Lethal Mutations Align With Collagen Binding Sites for Integrins and Proteoglycans. *Hum Mutat* (2007) 28:209–21. doi: 10.1002/humu.20429
10. Ishikawa Y, Bächinger HP. A Molecular Ensemble in the rER for Procollagen Maturation. *Biochim Biophys Acta* (2013) 1833:2479–91. doi: 10.1016/j.bbamcr.2013.04.008
11. Huysseune A. "Skeletal System". In: GK Ostrander, editor. *The Laboratory Fish. Part 4 Microscopic Functional Anatomy*. San Diego: Academic Press (2000). p. 307–17.
12. Witten PE, Harris MP, Huysseune A, Winkler C. Small Teleost Fish Provide New Insights Into Human Skeletal Diseases. *Methods Cell Biol* (2017) 138:321–46. doi: 10.1016/bs.mcb.2016.09.001
13. Tonelli F, Bek JW, Besio R, De Clercq A, Leoni L, Salmon P, et al. Zebrafish: A Resourceful Vertebrate Model to Investigate Skeletal Disorders. *Front Endocrinol* (2020) 11:489. doi: 10.3389/fendo.2020.00489
14. Dietrich K, Fiedler IAK, Kurzyukova A, López-Delgado AC, McGowan LM, Geurtzen K, et al. Skeletal Biology and Disease Modeling in Zebrafish. *J Bone Miner Res* (2021) 36:436–58. doi: 10.1002/jbmr.4256
15. Fisher S, Jagadeeswaran P, Halpern ME. Radiographic Analysis of Zebrafish Skeletal Defects. *Dev Biol* (2003) 264:64–76. doi: 10.1016/s0012-1606(03)00399-3
16. Gioia R, Tonelli F, Ceppi I, Biggiogera M, Leikin S, Fisher S, et al. The Chaperone Activity of 4PBA Ameliorates the Skeletal Phenotype of Chihuahua, a Zebrafish Model for Dominant Osteogenesis Imperfecta. *Hum Mol Genet* (2017) 26:2897–911. doi: 10.1093/hmg/ddx171
17. Fiedler IAK, Schmidt FN, Wölfel EM, Plumeyer C, Milovanovic P, Gioia R, et al. Severely Impaired Bone Material Quality in Chihuahua Zebrafish Resembles Classical Dominant Human Osteogenesis Imperfecta. *J Bone Miner Res* (2018) 33:1489–99. doi: 10.1002/jbmr.3445
18. Currey JD. The Many Adaptations of Bone. *J Biomech* (2003) 36:1487–95. doi: 10.1016/S0021-9290(03)00124-6
19. Veis A. "Mineralization in Organic Matrix Frameworks". In: PM Dove, JJ Yoreo and SW Weiner, editors. *Biomineralization. Reviews in Mineralogy and Geochemistry*. Chantilly, VA: Mineralogical Society of America (2003). p. 249–89.
20. Wilton TJ, Hosking DJ, Pawley E, Stevens A, Harvey L. Osteomalacia and Femoral Neck Fractures in the Elderly Patient. *J Bone Joint Surg Br* (1987) 69:388–90. doi: 10.1302/0301-620X.69B3.3584190
21. Guglielmi G, Muscarella S, Bazzocchi A. Integrated Imaging Approach to Osteoporosis: State-of-the-Art Review and Update. *Radiographics* (2011) 31:1343–64. doi: 10.1148/rg.315105712
22. Cotti S, Huysseune A, Koppe W, Rücklin M, Marone F, Wölfel EM, et al. More Bone With Less Minerals? The Effects of Dietary Phosphorus on the Post-Cranial Skeleton in Zebrafish. *Int J Mol Sci* (2020) 21:5429. doi: 10.3390/ijms21155429
23. Witten PE, Owen MA, Fontanillas R, Soenens M, McGurk C, Obach A. A Primary Phosphorus-Deficient Skeletal Phenotype in Juvenile Atlantic Salmon Salmo Salar: The Uncoupling of Bone Formation and Mineralization. *J Fish Biol* (2016) 88:690–708. doi: 10.1111/jfb.12870
24. Witten PE, Fjelldal PG, Huysseune A, McGurk C, Obach A, Owen MAG. Bone Without Minerals and its Secondary Mineralization in Atlantic Salmon. *J Exp Biol* (2019) 222:jeb188763. doi: 10.1242/jeb.188763
25. Drábiková L, Fjelldal PG, De Clercq A, Yousaf MN, Morken T, McGurk C, et al. Vertebral Column Adaptations in Juvenile Atlantic Salmon Salmo Salar, L. As a Response to Dietary Phosphorus. *Aquaculture* (2021) 541:736776. doi: 10.1016/j.aquaculture.2021.736776
26. Kague E, Turci F, Newman E, Yang Y, Brown KR, Aglan MS, et al. 3D Assessment of Intervertebral Disc Degeneration in Zebrafish Identifies Changes in Bone Density That Prime Disc Disease. *Bone Res* (2021) 9:39. doi: 10.1038/s41413-021-00156-y
27. Witten PE, Hansen A, Hall BK. Features of Mono- and Multinucleated Bone Resorbing Cells of the Zebrafish *Danio Rerio* and Their Contribution to Skeletal Development, Remodeling, and Growth. *J Morphol* (2001) 250:197–207. doi: 10.1002/jmor.1065
28. Witten PE, Hall BK. "The Ancient, Segmented, Active and Permanent Notochord". In: A Pradel, JSS Denton and P Janvier, editors. *Ancient Fishes and Their Living Relatives: A Tribute to John G. Maisey*. München, Germany: Verlag Dr. Friedrich Pfeil (2021). p. 215–24.
29. Shah SA, Wallace MJ. "Osteogenesis Imperfecta in the Spine". In: RW Kruse, editor. *Osteogenesis Imperfecta. A Case-Based Guide to Surgical Decision-Making and Care*. Cham, Switzerland: Springer (2020). p. 221–30. doi: 10.1007/978-3-030-42527-2
30. Benson DR, Donaldson DH, Millar EA. The Spine in Osteogenesis Imperfecta. *J Bone Joint Surg Am* (1978) 60:925–9. doi: 10.2106/00004623-197860070-00009
31. Stöß H, Pontz BF, Pesch H-J, Ott R. Heterogeneity of Osteogenesis Imperfecta. Biochemical and Morphological Findings in a Case of Type III According to Sillence. *Eur J Pediatr* (1986) 145:34–9. doi: 10.1007/BF00441849
32. Iwamoto J, Takeda T, Ichimura S. Increased Bone Resorption With Decreased Activity and Increased Recruitment of Osteoblasts in Osteogenesis Imperfecta Type I. *J Bone Miner Metab* (2002) 20:174–9. doi: 10.1007/s007740200025
33. Kalajzic I, Terzic J, Rumboldt Z, Mack K, Naprta A, Ledgard F, et al. Osteoblastic Response to the Defective Matrix in the Osteogenesis Imperfecta Murine (Oim) Mouse. *Endocrinology* (2002) 143:1594–601. doi: 10.1210/endo.143.5.8807
34. Uveges TE, Collin-Osdoby P, Cabral WA, Ledgard F, Goldberg L, Bergwitz C, et al. Cellular Mechanism of Decreased Bone in Brtl Mouse Model of OI: Imbalance of Decreased Osteoblast Function and Increased Osteoclasts and Their Precursors. *J Bone Miner Res* (2008) 23:1983–94. doi: 10.1359/jbmr.080804
35. Enderli TA, Burtch SR, Templet JN, Carriero A. Animal Models of Osteogenesis Imperfecta: Applications in Clinical Research. *Orthop Res Rev* (2016) 8:41–55. doi: 10.2147/ORR.S85198
36. Tonelli F, Cotti S, Leoni L, Besio R, Gioia R, Marchese L, et al. Crtap and *P3h1* Knock Out Zebrafish Support Defective Collagen Chaperoning as the Cause of Their Osteogenesis Imperfecta Phenotype. *Matrix Biol* (2020) 90:40–60. doi: 10.1016/j.matbio.2020.03.004
37. Kemi VE, Kärkkäinen MUM, Lamberg-Allardt CJE. High Phosphorus Intakes Acutely and Negatively Affect Ca and Bone Metabolism in a Dose-Dependent Manner in Healthy Young Females. *Br J Nutr* (2006) 96:545–52. doi: 10.1079/BJN20061838
38. Dermience M, Lognay G, Mathieu F, Goyens P. Effects of Thirty Elements on Bone Metabolism. *J Trace Elem Med Biol* (2015) 32:86–106. doi: 10.1016/j.jtemb.2015.06.005
39. Huttunen MM, Tillman I, Viljakainen HT, Tuukkanen J, Peng Z, Pekkinen M, et al. High Dietary Phosphate Intake Reduces Bone Strength in the Growing Rat Skeleton. *J Bone Miner Res* (2007) 22:83–92. doi: 10.1359/jbmr.061009
40. Brailsford JF. Osteogenesis Imperfecta. *Br J Radiol* (1943) 16:129–36. doi: 10.1259/0007-1285-16-185-129
41. Watanabe G, Kawaguchi S, Matsuyama T, Yamashita T. Correlation of Scoliotic Curvature With Z-Score Bone Mineral Density and Body Mass Index in Patients With Osteogenesis Imperfecta. *Spine* (2007) 32:E488–94. doi: 10.1097/BRS.0b013e31811ec2d9
42. Abdelaziz DM, Abdullah S, Magnussen C, Ribeiro-da-Silva A, Komarova SV, Rauch F, et al. Behavioral Signs of Pain and Functional Impairment in a Mouse Model of Osteogenesis Imperfecta. *Bone* (2015) 81:400–6. doi: 10.1016/j.bone.2015.08.001
43. McKusick VA. *Heritable Disorders of Connective Tissue. 4th ed*. CV Mosby, editor. St Louis: Mosby Company (1972).
44. Ishikawa S, Kumar SJ, Takahashi HE, Homma M. Vertebral Body Shape as a Predictor of Spinal Deformity in Osteogenesis Imperfecta. *J Bone Joint Surg Am* (1996) 78:212–9. doi: 10.2106/00004623-199602000-00007
45. McGreal C, Bober MB. "Patient Evaluation and Medical Treatment for Osteogenesis Imperfecta". In: RW Kruse, editor. *Osteogenesis Imperfecta. A Case-Based Guide to Surgical Decision-Making and Care*. Cham, Switzerland: Springer (2020). p. 11–9. doi: 10.1007/978-3-030-42527-2
46. Moss ML. Studies of the Acellular Bone of Teleost Fish. II. Response to Fracture Under Normal and Acalcemic Conditions. *Acta Anat* (1962) 48:46–602975–3015. doi: 10.1002/dvdy.22113
47. Baron R, Gertner JM, Lang R, Vignery A. Increased Bone Turnover With Decreased Bone Formation by Osteoblasts in Children With Osteogenesis Imperfecta Tarda. *Pediatr Res* (1983) 17:204–7. doi: 10.1203/00006450-198303000-00007
48. Rauch F, Travers R, Parfitt AM, Glorieux FH. Static and Dynamic Bone Histomorphometry in Children With Osteogenesis Imperfecta. *Bone* (2000) 26:581–9. doi: 10.1016/s8756-3282(00)00269-6

49. Fedarko NS. "Osteoblast/osteoclast Development and Function in Osteogenesis Imperfecta". In: JR Shapiro, PH Byers, FH Glorieux and PD Sponseller, editors. *Osteogenesis Imperfecta. A Translational Approach to Brittle Bone Disease*. San Diego: Academic Press (2014). p. 45–56. doi: 10.1016/B978-0-12-397165-4.00005-8
50. Witten PE, Huysseune A. A Comparative View on Mechanisms and Functions of Skeletal Remodelling in Teleost Fish, With Special Emphasis on Osteoclasts and Their Function. *Biol Rev Camb Philos Soc* (2009) 84:315–46. doi: 10.1111/j.1469-185X.2009.00077.x
51. Zhang H, Doty SB, Hughes C, Dempster D, Camacho NP. Increased Resorptive Activity and Accompanying Morphological Alterations in Osteoclasts Derived From the Oim/Oim Mouse Model of Osteogenesis Imperfecta. *J Cell Biochem* (2007) 102:1011–20. doi: 10.1002/jcb.21337
52. Garibaldi N, Contento BM, Babini G, Morini J, Siciliani S, Biggiogera M, et al. Targeting Cellular Stress In Vitro Improves Osteoblast Homeostasis, Matrix Collagen Content and Mineralization in Two Murine Models of Osteogenesis Imperfecta. *Matrix Biol* (2021) 98:1–20. doi: 10.1016/j.matbio.2021.03.001
53. Bonucci E. *Biological Calcification. Normal and Pathologicalpprocesses in the Early Stages*. Berlin, Germany: Springer-Verlag (2007).
54. Morales GA, Azcuy RL, Casaretto ME, Márquez L, Hernández AJ, Gómez F, et al. Effect of Different Inorganic Phosphorus Sources on Growth Performance, Digestibility, Retention Efficiency and Discharge of Nutrients in Rainbow Trout (*Oncorhynchus Mykiss*). *Aquaculture* (2018) 495:568–74. doi: 10.1016/j.aquaculture.2018.06.036
55. Taylor WR, Van Dyke GC. Revised Procedures for Staining and Clearing Small Fishes and Other Vertebrates for Bone and Cartilage Study. *Cybium* (1985) 9:107–19.
56. Martini A, Huysseune A, Witten PE, Boglione C. Plasticity of the Skeleton and Skeletal Deformities in Zebrafish (*Danio Rerio*) Linked to Rearing Density. *J Fish Biol* (2020) 98:971–86. doi: 10.1111/jfb.14272
57. Marie-Hardy L, Khalifé M, Slimani L, Pascal-Moussellard H. Computed Tomography Method for Characterising the Zebrafish Spine. *Orthop Traumatol Surg Res* (2019) 105:361–7. doi: 10.1016/j.otsr.2018.12.008
58. Parichy DM, Elizondo MR, Mills MG, Gordon TN, Engeszer RE. Normal Table of Postembryonic Zebrafish Development: Staging by Externally Visible Anatomy of the Living Fish. *Dev Dyn* (2009) 238:2975–3015. doi: 10.1002/dvdy.22113
59. Bird NC, Mabee PM. Developmental Morphology of the Axial Skeleton of the Zebrafish, *Danio Rerio* (Ostariophysi: Cyprinidae). *Dev Dyn* (2003) 228:337–57. doi: 10.1002/dvdy.10387
60. Webster M, Sheets H. "A Practical Introduction to Landmark-Based Geometric Morphometrics". In: J Alroy and G Hunt, editors. *The Paleontological Society Papers*. Cambridge: Cambridge University Press (2010). p. 163–88. doi: 10.1017/S1089332600001868
61. Jager PL, Slart RH, Webber CL, Adachi JD, Papaioannou AL, Gulenchyn KY. Combined Vertebral Fracture Assessment and Bone Mineral Density Measurement: A Patient-Friendly New Tool With an Important Impact on the Canadian Risk Fracture Classification. *Can Assoc Radiol J* (2010) 61:194–200. doi: 10.1016/j.carj.2009.12.012
62. Hammer Ø, Harper DAT, Ryan PD. Past: Paleontological Statistics Software Package for Education and Data Analysis. *Palaeontol Electron* (2001) 4:1–9.
63. Humason GL, Presnell JK, Schreibman MP. *Humason's Animal Tissue Techniques*. Baltimore, MD, USA: Johns Hopkins University Press (1997).
64. Spurr AR. A Low-Viscosity Epoxy Resin Embedding Medium for Electron Microscopy. *J Ultrastruct Res* (1969) 26:31–43. doi: 10.1016/S0022-5320(69)90033-1

Conflict of Interest: WK was employed by the company SimplyFish AS.

The remaining authors declare that the research was conducted in the absence of any commercial or financial relationships that could be construed as a potential conflict of interest.

Publisher's Note: All claims expressed in this article are solely those of the authors and do not necessarily represent those of their affiliated organizations, or those of the publisher, the editors and the reviewers. Any product that may be evaluated in this article, or claim that may be made by its manufacturer, is not guaranteed or endorsed by the publisher.

frontiers | Frontiers in Physiology

ORIGINAL RESEARCH
published: 26 May 2022
doi: 10.3389/fphys.2022.875866

Dynamics of the Zebrafish Skeleton in Three Dimensions During Juvenile and Adult Development

Stacy V. Nguyen[1], *Dominic Lanni*[2], *Yongqi Xu*[1], *James S. Michaelson*[3] *and Sarah K. McMenamin*[1]*

[1]Biology Department, Boston College, Chestnut Hill, MA, United States, [2]Biology Department, Vassar College, Poughkeepsie, NY, United States, [3]Department of Pathology, Massachusetts General Hospital, Boston, MA, United States

Zebrafish are a valuable model for normal vertebrate skeletogenesis and the study of myriad bone disorders. Bones grow, ossify and change shape throughout the zebrafish lifetime, and 3D technologies allow us to examine skeletogenic processes in detail through late developmental stages. To facilitate analysis of shape, orientation and tissue density of skeletal elements throughout ontogeny and adulthood, we generated a high-resolution skeletal reference dataset of wild-type zebrafish development. Using microCT technology, we produced 3D models of the skeletons of individuals ranging from 12 to 25 mm standard length (SL). We analyzed the dynamics of skeletal density and volume as they increase during juvenile and adult growth. Our resource allows anatomical comparisons between meristic units within an individual—e.g., we show that the vertebral canal width increases posteriorly along the spine. Further, structures may be compared between individuals at different body sizes: we highlight the shape changes that the lower jaw undergoes as fish mature from juvenile to adult. We show that even reproductively mature adult zebrafish (17–25 mm SL) continue to undergo substantial changes in skeletal morphology and composition with continued adult growth. We provide a segmented model of the adult skull and a series of interactive 3D PDFs at a range of key stages. These resources allow changes in the skeleton to be assessed quantitatively and qualitatively through late stages of development, and can serve as anatomical references for both research and education.

Keywords: skeletogenesis, zebrafish, microcomputed tomographic (micro-CT), skeletal anatomy, juvenile development

OPEN ACCESS

Edited by:
Ronald Kwon,
University of Washington,
United States

Reviewed by:
Kelly Diamond,
Seattle Children's Research Institute,
United States
Francesca Tonelli,
University of Pavia, Italy

***Correspondence:**
Sarah K. McMenamin
mcmenams@bc.edu

Specialty section:
This article was submitted to Skeletal Physiology, a section of the journal Frontiers in Physiology

Received: *14 February 2022*
Accepted: *06 May 2022*
Published: *26 May 2022*

Citation:
Nguyen SV, Lanni D, Xu Y, Michaelson JS and McMenamin SK (2022) Dynamics of the Zebrafish Skeleton in Three Dimensions During Juvenile and Adult Development. Front. Physiol. 13:875866. doi: 10.3389/fphys.2022.875866

INTRODUCTION

Zebrafish are an efficient and high-throughput model for studying development, and this system is emerging as a powerful tool for skeleton research (Raterman et al., 2020; Tonelli et al., 2020). Zebrafish skeletogenesis is similar in several ways to mammalian skeletal development, and the fish skeleton includes intramembranous and endochondrally ossifying elements (Krane, 2005; Ghayor et al., 2011), as well as both cellular and acellular bones (Weigele and Franz-Odendaal, 2016). The major signaling pathways that regulate skeletal development are highly conserved between mammals and teleosts (Witten and Huysseune, 2009), and zebrafish are a tractable model of vertebrate skeletogenesis with relevance to biomedicine (Hammond et al., 2012). Indeed, numerous studies have leveraged the zebrafish skeleton to investigate skeletal development and homeostasis (e.g. Witten et al., 2001; Crucke et al., 2015; Weigele and Franz-Odendaal, 2016; Machado and Eames, 2017; Parsons et al., 2018). Further,

a variety of mutant phenotypes in zebrafish model human bone disorders (Harris et al., 2014; Kwon et al., 2019; Dietrich et al., 2021).

The zebrafish skeleton is comprised of bones that form a dermal skeleton (which includes teeth, scales and fin rays) and an endoskeleton composed of the axial, craniofacial and appendicular elements (Tonelli et al., 2020). Previous work has focused on the sequence of ossification of these bones during early larval development (Cubbage and Mabee, 1996; Bird and Mabee, 2003; Kimmel et al., 2010). However, less is known about skeletal changes during later juvenile and adult stages of development. Several craniofacial bones—including the dermatocranium and infraorbitals—do not become fully ossified until adult stages in zebrafish (Chang and Franz-Odendaal, 2014; Mork and Crump, 2015). Histological stains (e.g., alcian blue and alizarin red) and transgenic reporter lines are valuable tools for imaging and analyzing the dynamic skeleton (Clément et al., 2008; Hammond et al., 2012; Pasqualetti et al., 2012; Rigueur and Lyons, 2014; Bensimon-Brito et al., 2016). More recent technologies—including confocal microscopy, optimal projection tomography and microcomputed tomography (microCT)—allow skeletal elements to be evaluated at high resolution in three dimensions (Bruneel and Witten, 2015; Kanther et al., 2019; Allalou et al., 2020; Bagwell et al., 2020).

Several resources detail the normal anatomical development of the zebrafish skeleton, focusing in particular on larval stages and the initial appearance of different bones. Groups have characterized ossification sequence in the craniofacial skeleton and pectoral girdle (Bird and Mabee, 2003) and the axial skeleton (Cubbage and Mabee, 1996), with a focus on larval stages. Many of the postembryonic stages of development are defined by the ossification of specific skeletal elements (Cubbage and Mabee, 1996; Parichy et al., 2009). FishFace is an online atlas of zebrafish craniofacial development, generated using fluorescent optical projection tomography (Eames et al., 2013). This database serves as a repository of confocal images that capture the development of individual craniofacial elements up to 21 days post fertilization (dpf) (Eames et al., 2013), roughly equivalent to the AR (anal rays) and DR (dorsal rays) stages of larval development according to the postembryonic normal table (Parichy et al., 2009). FishFace also includes an interactive 3D tool for viewing the entire head at three select developmental stages (Eames et al., 2013).

Over the past decade, microCT has served as a powerful tool for assessing phenotypes at a high resolution and in 3D (Charles et al., 2017; Hur et al., 2017). MicroCT has been used to capture the ways in which altered gene function affects skeletal phenotypes in zebrafish (Charles et al., 2017; Hur et al., 2017; Silvent et al., 2017; Caetano-Lopes et al., 2020). While microCT data provide researchers with valuable information, data-rich scans can require large amounts of storage space and access to costly analysis software (Tesařová et al., 2019). In recent years, several developmental atlases have been generated from microCT scans for other models and organs, including a 3D atlas of the developing human embryo and the developing mouse heart (de Bakker et al., 2012; de Boer et al., 2012).

To capture the changes which the zebrafish skeleton undergoes during juvenile and adult development, we generated an accessible skeletal reference from microCT scans of individuals ranging in size from 12 to 25 mm standard length (SL), ranging from J (juvenile) through A (adult) stages (Parichy et al., 2009). We demonstrate the use of this resource to quantify skeletal changes occurring with growth and development. Using this dataset, we examined the morphological changes of vertebrate along the anterior-posterior axis of the vertebral column during juvenile and adult stages. We tested whether density and volume of the skeleton increase with juvenile and adult growth. Further, we asked whether patterns of skeletal density along the anterio-posterior axis of the skeleton shifts with growth. This reference dataset of normal skeletal development can serve as a baseline to which disrupted developmental phenotypes can be compared. Moreover, we anticipate the dataset can be used as an anatomical reference in both educational and research settings.

MATERIALS AND METHODS

Fish Rearing and Measurement

All studies were performed on an approved protocol in accordance with the Boston College Institutional Animal Care and Use Committee (IACUC; Protocol #2020-005). Zebrafish were reared at 28°C on a 14:10 light:dark cycle and fed a diet of marine rotifers and adult pellet food flakes three times a day. Zebrafish were of the genetic background *Tg(tg:nVenus-2a-nfnB)*$^{wp.rt8}$ (McMenamin et al., 2014) and originated from several matings of the same parental breeding stock. Individuals were treated with 1% DMSO at 4 dpf, which does not activate the transgenic nitroreductase system (McMenamin et al., 2014). To ensure that these individuals were representative and that the transgenic background or the DMSO-treatment did not cause gross skeletal mis-patterning, we scanned representative stages from the Tübingen wild-type line for comparison. The two strains were overall comparable morphologically and in terms of relative density (see **Supplementary Figure S1**).

Capturing individuals at a range of developmental stages requires precise and repeatable methods for measuring development. Days post fertilization is an unreliable measure of developmental progress in zebrafish, particularly during later stages of development (Parichy et al., 2009; McMenamin et al., 2016). We used SL as a proxy for development, and samples were measured both before scanning and in the scans themselves (see **Supplementary Figure S2**). Although staging according to the postembryonic normal table is likely a more accurate measurement of developmental progress than length (Parichy et al., 2009; McMenamin et al., 2016), we chose to use fixed SL because it is a continuous and quantitative proxy for development which may be easily obtained from scans. On average, most of the 12 mm SL fish were 2 months old; 16 mm SL fish were between 4 and 5 months age and 24 mm SL fish were 6–9 months old when fixed. The sex of the individuals was also recorded when it was possible to discern sex, starting approximately around 17.5 mm SL (**Supplementary Figure S3**).

MicroCT Scanning and Reconstruction

Fish were euthanized by MS-222, and fixed in 4% paraformaldehyde for 24 h. SL was measured in fixed samples according to Parichy et al. (2009) before scanning, and was also measured digitally in the scans themselves (see **Supplementary Figure S1**). Fish samples shrink slightly during the fixation process; note that the reported fixed SL values may be converted to corresponding "fresh" SL by adding 0.29 mm (Parichy et al., 2009). A total of 62 specimens were scanned, ranging from 12 to 25 mm SL with a minimum of one scan for every half millimeter. Fixed specimens were placed in low-density foam molds and inserted into either a 1.5 ml centrifuge tube (for specimens 12–14 mm SL) or a 15 ml conical tube (for specimens >14 mm SL). Scans were performed on a SkyScan 1275 high resolution microCT system (Bruker, Kontich, Belgium) at a scanning resolution of 10.5 µm with an x-ray source voltage of 45 kV and current of 200 mA. Projection images were generated over 360° with a 0.1° rotation step and 6 averaging frames. Thresholding, ring artifact reduction, and beam hardening corrections were consistent across all scans during reconstruction using NRecon (Bruker, Kontich, Belgium).

Quantifications and Segmentation

Cross section images were generated in the open source software 3D slicer (Kikinis et al., 2014). Vertebral diameter measurements were taken using Amira 6.5 (Thermo Fisher Scientific FEI, Hillsboro, Oregon, United States) using the orthoslice module to view the transverse cross section and the canal width was quantified with the 2D measurement tool, measuring the diameter of the vertebral canals of all rib bearing vertebrae in zebrafish at four representative sizes (12, 16, 20, and 24 mm SL). Multi-level modeling was performed with pairwise post-hoc analysis to determine significant differences in vertebral diameters at each vertebra among the four standard length sizes. These measurements could alternatively be made using 3D Slicer.

Relative density heatmaps were generated with the volume rendering module and physics load transfer function in Amira with a threshold range of 20–120. Mean gray value was also used to show relative density between scans. Mean gray value was calculated from imported cross section slices using the measurement tool in ImageJ (Version 1.8.0_172, National Institutes of Health, Bethesda, Maryland, United States). Volume measurements were taken with the Material Statistics module in Amira.

Individual bones were segmented using the Segmentation Editor in Amira 6.5 (Thermo Fisher Scientific FEI, Hillsboro, Oregon, United States). Briefly, the entire scan volume was loaded into the program and a pixel threshold was determined to differentiate bone from soft tissue. The lasso tool was then used to select the corresponding pixels of a specific skeletal element and added to the appropriate material label. Segmented bones include the basibrachials, branchial arches, basioccipital, dentary, dermatocranium, ectopterygoid, exocciptal, entopterygoid, hyoid, hyomandibula, infraorbital, interopercle, kinethmoid, lateral ethmoid, maxilla, metapterygoid, opercle, orbitosphenoid, pharyngeal jaws, premaxilla, preopercle, parasphenoid, quadrate, supracleithrum, supraoccipital, subopercle, and supraorbital. Pearson correlation coefficients were calculated to show the correlation between density or volume and SL.

Interactive 3D PDFs

3D models of the microCT reconstructed scans were generated in Amira 6.5 using the Segmentation Editor and Generate Surface module (Thermo Fisher Scientific FEI, Hillsboro, Oregon, United States). Meshes were simplified using MeshLab (Cignoni et al., 2008; Callieri, 2013). These models were converted to .u3d files and imported as interactive 3D PDF using Acrobat Pro DC (Version 2021.005.20058, Adobe Inc., San Jose, CA, United States).

RESULTS

microCT Scan Data in Two Formats

Whole, raw microCT scans for individuals from every half mm SL are available for download (see **Table 1**; MorphoSource project URL https://www.morphosource.org/projects/000415918?locale=en).
When multiple scans were available for each size category (see **Supplementary Figure S3** and **Supplementary Table S1**), we selected the highest quality scan for upload to MorphoSource. Additionally, individuals of four representative sizes (12, 16, 20, and 24 mm SL) were used to generate 3D PDFs (see **Table 1**; **Supplementary Figures S5–S8**). These interactive PDFs can be viewed with any standard PDF viewer, including Adobe Acrobat Reader (Adobe Inc., San Jose, CA, United States). These 3D PDFs allow users to turn, rotate, and zoom in to the embedded 3D models.

Anatomical Measurements From microCT Cross Sections

The small size of the zebrafish can pose a barrier to measuring small anatomical elements in 3D. However, microCT technology allows visualization and analysis of elements of interest. MicroCT scans generate cross sections that can be accessed using a variety of programs such as DataViewer (Bruker, Kontich, Belgium), Amira (Thermo Fisher Scientific FEI, Hillsboro, Oregon, United States) or ImageJ (National Institutes of Health, Bethesda, Maryland, United States). Any of these programs will allow a user to scroll through the stacks of cross-section images from the scans in any anatomical plane (e.g., see **Figures 1A–D**). These cross-sections capture details at a resolution of 10.5 µm, which allows anatomical measurements even in relatively small bones. To test these types of measurements, we focused on the morphological changes of vertebrae along the anterio-posterior axis. We examined sagittal cross sections (as in **Figure 1D**) from scans of adult zebrafish at four representative sizes (12, 26, 20 and 24 mm SL), measuring the diameter of the vertebral canal of vertebrae 2 through 10 (the rib-bearing vertebrae; **Figure 1E**). These widths increase markedly in more posterior vertebrae (**Figure 1E**).

Zebrafish Skeletons Increase in Density and Volume Throughout Juvenile and Adult Growth

MicroCT datasets can be used to determine relative density. Our samples were all scanned under consistent parameters, so density can be directly compared between scans. We hypothesized that overall skeletal density would continue increasing throughout

TABLE 1 | Categories of sizes, sample numbers and scan ID. Full details of each individual may be found in **Supplementary Table S1**.

SL category (mm)	Number of individuals scanned	MorphoSource ID of representative individual	3D PDF of representative individual
12	2	000415877	**Supplementary Figure S5**
12.5	1	000416098	-
13	2	000416108	-
13.5	1	000416117	-
14	1	000416167	-
14.5	1	000416187	-
15	1	000416194	-
15.5	2	000416225	-
16	1	000416236	**Supplementary Figure S6**
16.5	1	000416257	-
17	3	000416263	-
17.5	2	000416291	-
18	1	000416305	-
18.5	1	000416322	-
19	2	000416327	-
19.5	4	000416332	-
20	5	000416337	**Supplementary Figure S7**
20.5	5	000416342	-
21	5	000416347	-
21.5	5	000416357	-
22	2	000416367	-
22.5	4	000416377	-
23	1	000416382	-
23.5	1	000416387	-
24	3	000416395	**Supplementary Figure S8**
24.5	2	000416402	-
25	1	000416412	-

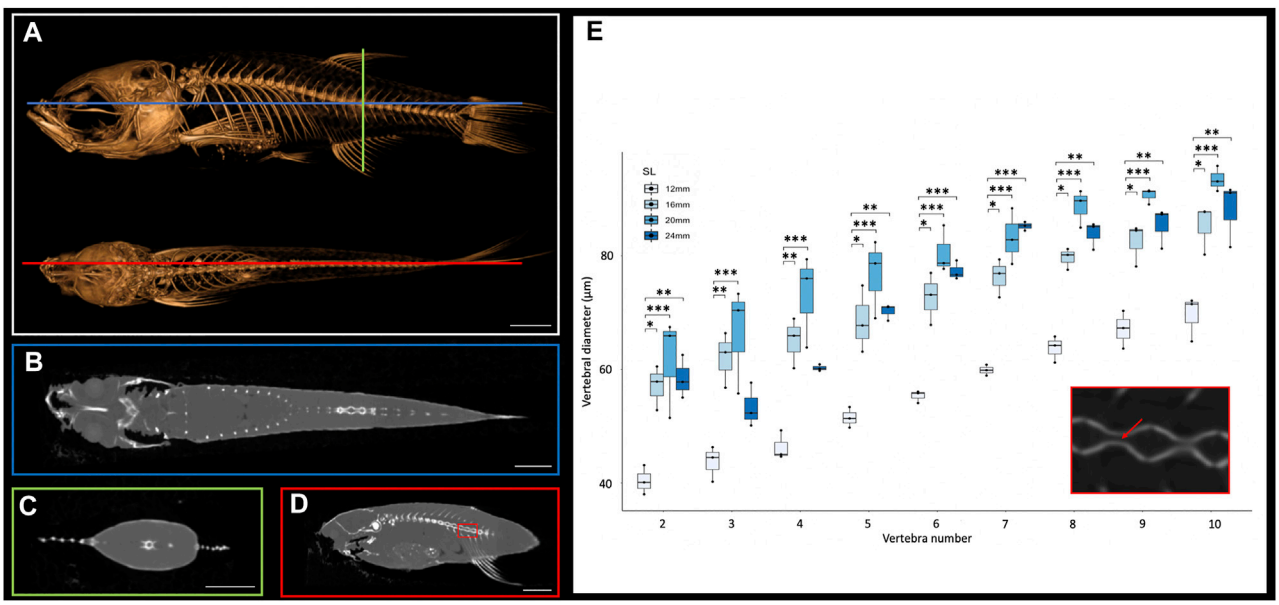

FIGURE 1 | Cross sections of microCT scans visualized in 3D Slicer. **(A)**, Surface rendering of 24 mm SL adult fish with lateral (top) and dorsal (bottom) views with coronal (blue), transverse (green), and sagittal (red) axes indicated. **(B)**, Coronal cross section image. **(C)**, Transverse cross section image. **(D)**, Sagittal cross section image. **(E)**, Quantification of vertebral canal width of 3 individual 24 mm SL adult fish; each individual differentiated with different shapes (circle, square, triangle). Inset shows higher resolution image through vertebrate (corresponding to the boxed detail in panel D). Red arrow indicates a canal from which interior width was measured. Scale bars, 2 mm.

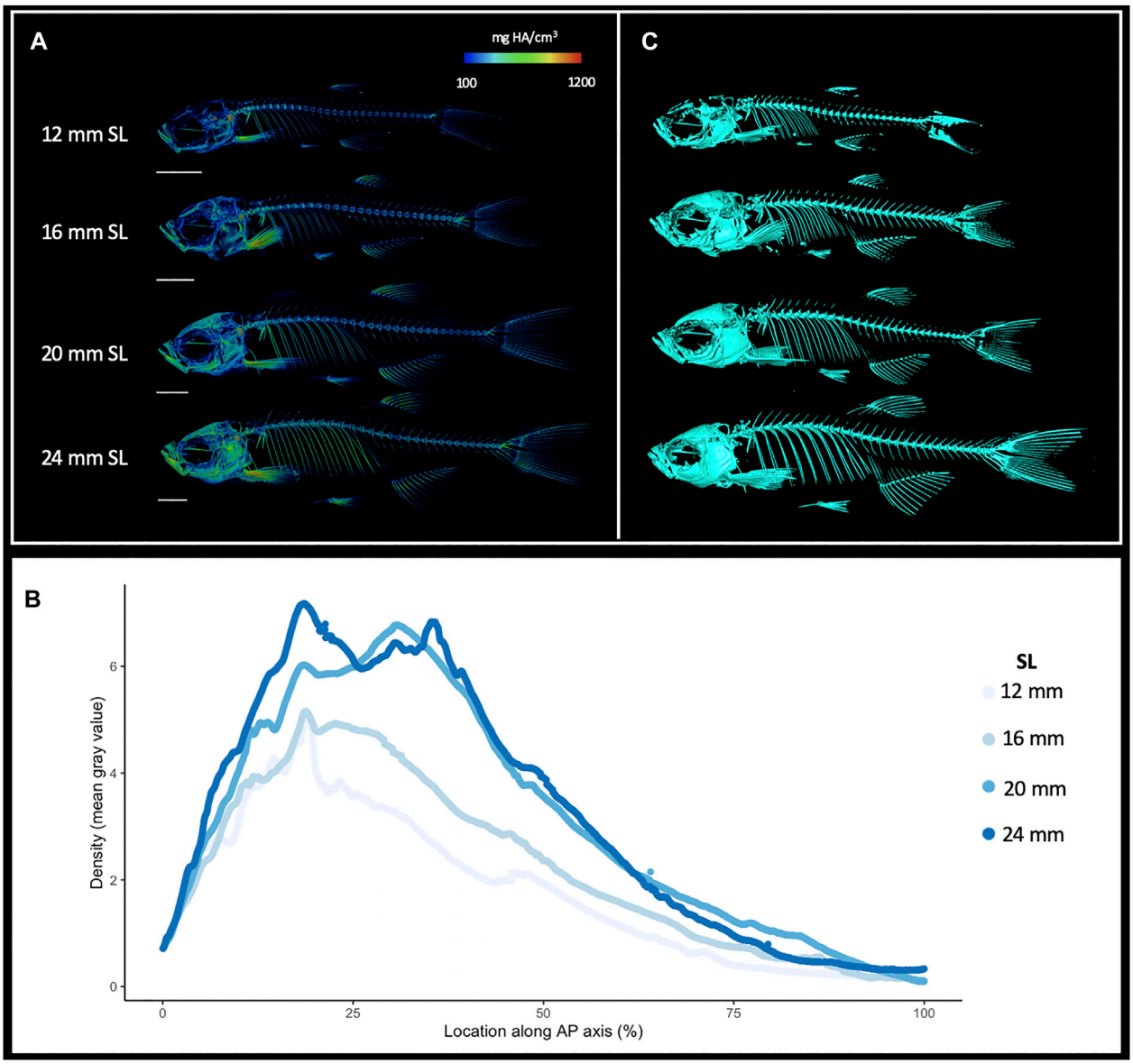

FIGURE 2 | Increasing skeletal density and volume with linear growth. **(A)**, Relative density renderings of skeletons from zebrafish at four different sizes (12, 16, 20, and 24 mm SL). Warmer colors indicate higher density regions. **(B)**, Average density of zebrafish skeleton along the body length of individual zebrafish at four sizes. **(C)**. Volume renderings of zebrafish at four sizes. Scale bars, 2 mm.

stages of adult growth. Indeed, density (as measured in mean grey values) increased markedly with increased size; regions of increasing density were particularly notable in the dermatocranium, ribs, and hypural complex (**Figure 2A**, **Supplementary Videos S1, S2**). Quantifying overall density of the skeleton as a function of body size (SL), we found that relative density increases roughly linearly throughout juvenile and adult development (**Figure 3A**). We next asked how density was distributed along the anterio-posterior axis of the skeleton, and whether such patterns change with growth. We found that density was highest in anterior regions of the body, corresponding to the craniofacial skeleton (**Figure 2B**). The high density of the head corresponds to the many plate bones in this region. The head also contains three pairs of otoliths; these dense, highly mineralized bony elements are used for hearing and vestibular function (Vasconcelos-Filho et al., 2019), and contribute to the overall density of the head. We note that while maximum density increases in increasingly large individuals, the distribution of density across the skeleton remains largely consistent (**Figure 2B**). Overall, we also see the same patterns of density distribution when comparing density to distance from the anterior portion of the zebrafish, and when normalizing density to the proportion of body length (**Supplementary Figure S4**).

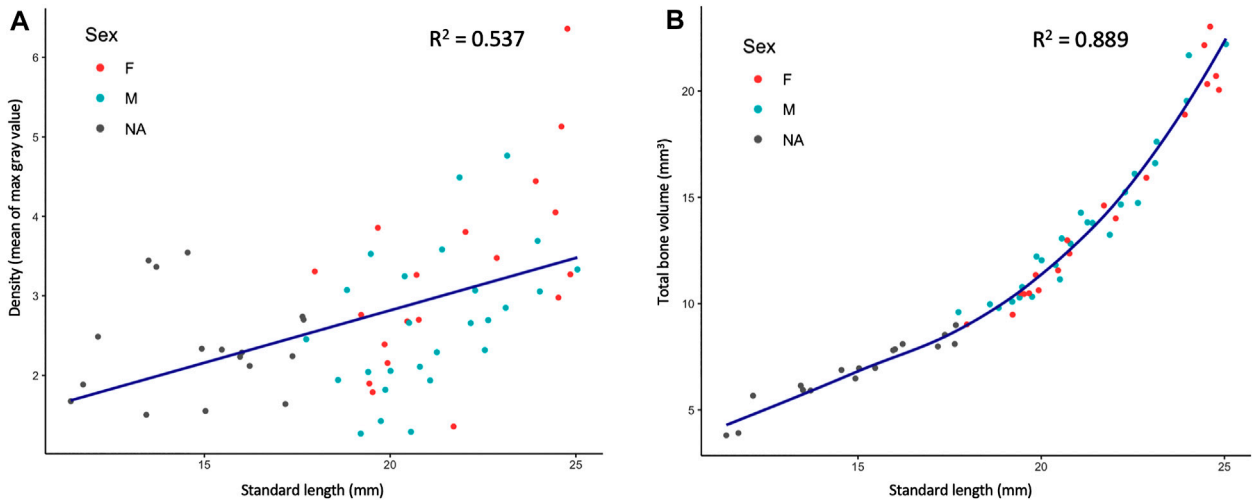

FIGURE 3 | Quantified skeletal density and volume relative to linear growth. **(A)**, Bone density relative to SL. **(B)**, Total bone volume relative to SL. Bone volume calculated from all cross sections of scan.

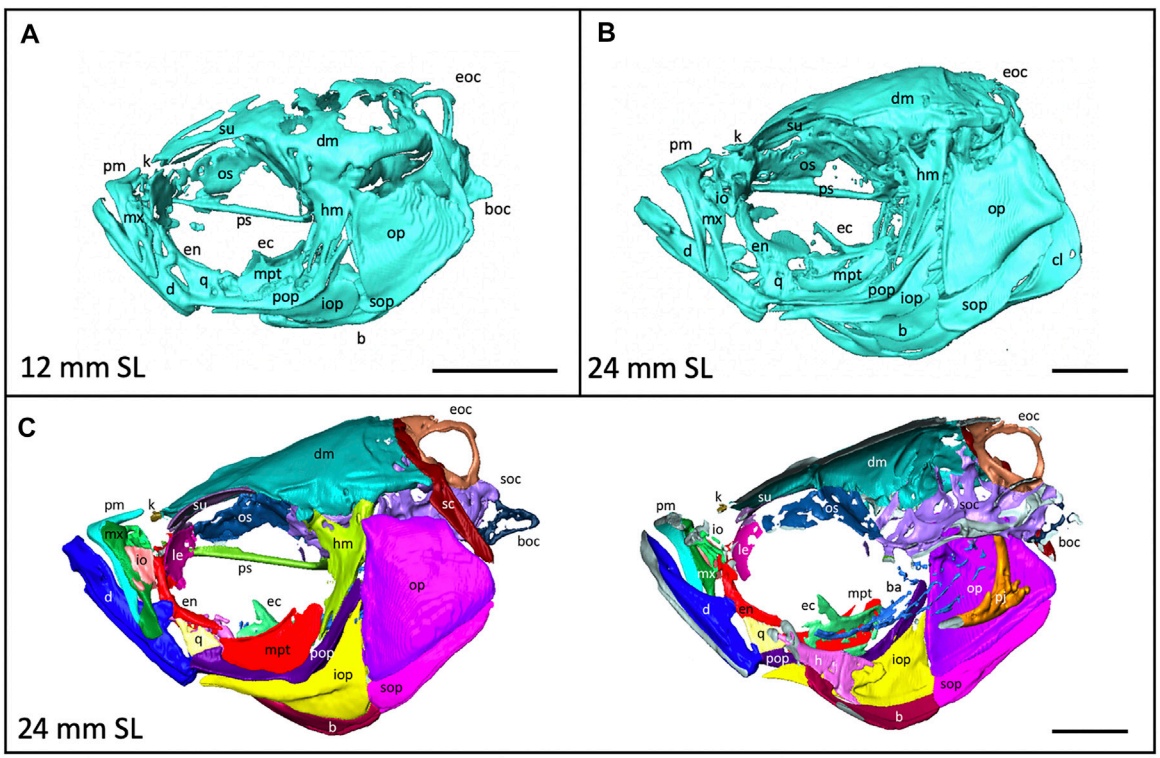

FIGURE 4 | Anatomy of the craniofacial skeleton. **(A)**, Volume rendering of the skull of a 12 mm SL zebrafish and **(B)**, a 24 mm SL zebrafish. **(C)**, Lateral view of skull of 24 mm SL zebrafish with segmented bones (left). Cross section of lateral view reveals some internal elements (right). b, basibrachials; ba, branchial arches; boc, basioccipital; d, dentary; dm, dermatocranium; ec, ectopterygoid; eoc, exoccipital; en, entopterygoid; h, hyoid; hm, hyomandibula; io, infraorbital; iop, interopercle; k, kinethmoid; le, lateral ethmoid; m, maxilla; mpt, metapterygoid; op, opercle; os, orbitosphenoid; pj, pharyngeal jaws; pm, premaxilla; pop, preopercle; ps, parasphenoid, q, quadrate; sc, supracleithrum; soc, supraoccipital; sop, subopercle, su, supraorbital. Scale bars, 1 mm.

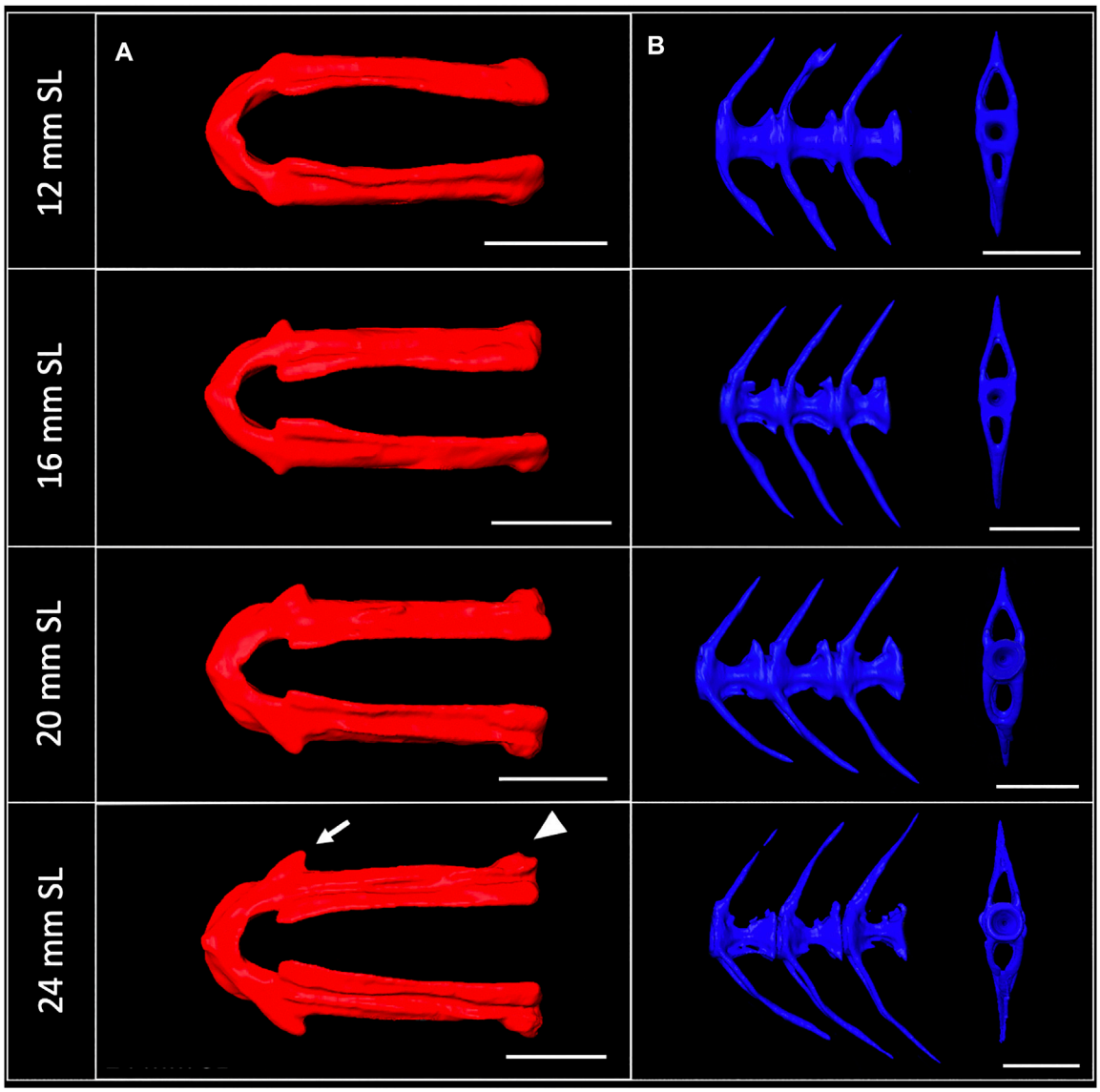

FIGURE 5 | Shape change of the lower jaw and caudal vertebrae. **(A)**, Segmented lower jaws from 12, 16, 20, and 24 mm SL individuals, viewed from the ventral perspective. In the largest individuals, note the pronounced anguloarticular prominence (arrow) and posterior end of lower jaw (arrowhead). **(B)**, Segmented first three caudal vertebrae from 12, 16, 20 and 24 mm SL individuals, viewed from a lateral perspective. Scale bars, 0.5 mm.

MicroCT scans can be used to calculate the volume of tissues within a specified density range. Volumetric renderings of the skeleton highlighted the new appearance of bones in the skull and fins as fish continue to grow (**Figure 2C**; also see **Figures 4A,B**). We further quantified the changes in overall skeletal volume, finding a roughly exponential increase in bone volume (a 3D measurement) with linear fish growth (a 2D measurement; **Figure 3B**).

Segmentation of Individual Bones Captures Shapes at a Fine Scale

3D models can be digitally segmented into individual elements. We segmented an adult skull into the 74 component bones. This segmented model captures the association of each element in 3D space and captures the anatomy of the adult craniofacial skeleton (**Figure 4C**). After segmentation, bones can be examined individually. To visualize how an individual bone changes shape as development progresses, we "virtually dissected" the lower jaws and caudal vertebrae from fish at a range of sizes (**Figures 5A,B**). We note that as adult zebrafish continue to grow, the anguloarticular prominence of the lower jaw becomes considerably more pronounced and the posterior end of the jaw widens (**Figure 5A**), while the caudal vertebrae do not undergo significant shape change during juvenile and adult development (**Figure 5B**).

DISCUSSION

The ability to capture shape changes in the skeleton at a fine scale is a powerful technique now being applied to developing organisms. The sensitivity of microCT technology makes it a powerful tool to examine subtle shape differences across developmental stages. In addition to capturing shape, microCT data can be used to quantify density and volume of skeletal elements. Isolating individual elements by segmentation can provide detailed information about spatial orientation and relationships between bones within the skeleton. Using consistent microCT settings at a range of developmental stages offers the ability to track changes in bone composition and morphology across development.

We generated a skeletal reference that allows assessment of skeletal morphology and composition throughout juvenile and adult development in zebrafish. Using this dataset, we showed that total bone volume and density progressively increase even during late stages of development. Additionally, we demonstrate that numerous skeletal elements continue to progressively grow and change shape during juvenile and adult growth, continuing into reproductive maturity. These results emphasize the importance of recording and matching SL between individuals. For the purposes of skeletal research, it is not sufficient to consider all "adult" zebrafish equivalent to one another: sizing and staging should be carefully considered.

This dataset contributes to a growing body of resources for zebrafish researchers, and may be used to examine bone shape during juvenile and adult development at a high resolution. In addition to the interactive 3D PDFs (**Supplementary Figures S5–S8**), all of the raw data from the microCT scans have been uploaded and made available online at MorphoSource, a repository for 3D data (Boyer et al., 2016) (see **Table 1**). These scans can be processed using Amira or 3D Slicer (Kikinis et al., 2014), which is open-source. Although here focus our analyses in this manuscript on the skeleton, users of the downloadable raw scans can change the thresholds to visualize and analyze other organs and systems, including the scales, liver and heart across late developmental stages.

Quantitative and qualitative assessment of the scans can highlight regions of the skeleton that are particularly dynamic during late stages of development: e.g., the dermatocranium—which increases in density (see **Figure 2A**), and the lower jaw—which changes in shape (see **Figure 5A**). These shifts can inform experimental design by suggesting specific anatomical regions for quantitative focus. Further, the labeled segmented scans (**Figure 4**) serve as a craniofacial anatomical reference in identifying skeletal elements.

For researchers using zebrafish as a model for skeletal disease, this reference can serve as a normal baseline to which aberrant skeletons can be compared in detail, in terms of morphology, density and skeletal volume. The reference provides a developmental framework for assessing disrupted phenotypes, allowing researchers to assess whether a model of interest shows skeletogenic processes that are accelerated or retarded relative to size. This developmental framework can assist researchers in selecting appropriate body size ranges to evaluate, and can add developmental context even when wild-type individuals (e.g., vehicle controls or non-mutant siblings) are analyzed side-by-side with a disease model. Finally, dynamic processes disrupted in a disease model can be compared to the normal rates of ossification and skeletal change established by this reference.

DATA AVAILABILITY STATEMENT

The original contributions presented in the study are included in the article/**Supplementary Materials**, further inquiries can be directed to the corresponding author.

ETHICS STATEMENT

The animal study was reviewed and approved by Boston College IACUC Committee.

AUTHOR CONTRIBUTIONS

SM, SN, and JM contributed to design of the study. SN, DL, and YX collected data, SN organized the database and performed analyses. SM and SN wrote the manuscript. All authors contributed to manuscript revision, read and approved the submitted version.

FUNDING

Funding provided by NSF CAREER 1845513, NIH R03HD091634, R00GM105874 and the Smith Family Foundation (to SM).

ACKNOWLEDGMENTS

Thank you to all members of the McMenamin Lab, past and present, for their support and input. Special thanks to Matthew Harris, Christopher Kenaley, Andrew Yang, Wendy Gupta, M. Shannon Fisher, and Alexander Browman for assistance and discussion. Thank you to the editor and two reviewers for helpful feedback.

SUPPLEMENTARY MATERIAL

The Supplementary Material for this article can be found online at: https://www.frontiersin.org/articles/10.3389/fphys.2022.875866/full#supplementary-material

Supplementary Figure 1 | DMSO-treated zebrafish have similar skeleton shape and bone density compared to wild-type zebrafish. **(A)**, Relative density renderings of skeletons from zebrafish of original dataset at four different sizes (12, 16, 20, and 24 mm SL) **(B)**, Relative density renderings of skeletons from wild-type zebrafish at the same four sizes (12, 16, 20, and 24 mm SL).

Supplementary Figure 2 | Manually measured standard lengths are closely correlated to digitally measured standard lengths. Digital length plotted against manual length for all individuals in the developmental skeletal reference dataset.

Supplementary Figure 3 | Histogram showing size distribution of samples scanned. Each dot represents a single individual; orange dots represent female fish and green dots represent male fish. Grey dots indicate fish that were too immature to be accurately sexed.

Supplementary Figure 4 | (A), Average density of individual slices along the anterio-posterior axis of individual zebrafish at four sizes. **(B)**, Normalized density plotted against the proportion of the body length.

Supplementary Figure 5 | Interactive PDF of 3D model of 12 mm SL zebrafish whole head (top) and whole body (bottom) scans.

Supplementary Figure 6 | Interactive PDF of 3D model of 16 mm SL zebrafish whole head (top) and whole body (bottom) scans.

Supplementary Figure 7 | Interactive PDF of 3D model of 20 mm SL zebrafish whole head (top) and whole body (bottom) scans.

Supplementary Figure 8 | Interactive PDF of 3D model of 24 mm SL zebrafish whole head (top) and whole body (bottom) scans.

Supplementary Video 1 | Density scans of the whole zebrafish skeleton ranging from 12 mm to 25 mm SL.

Supplementary Video 2 | Colored density scans of zebrafish craniofacial skeleton ranging from 12 mm to 25 mm SL. Warmer colors indicate higher density regions.

Supplementary Table 1 | Information about every individual scanned. Note that smaller individuals could not be accurately sexed. For individual scans available on MorphoSource, the ID is given in the last column.

REFERENCES

Bagwell, J., Norman, J., Ellis, K., Peskin, B., Hwang, J., Ge, X., et al. (2020). Notochord Vacuoles Absorb Compressive Bone Growth during Zebrafish Spine Formation. *Elife* 9, e51221. doi:10.7554/eLife.51221

Bensimon-Brito, A., Cardeira, J., Dionísio, G., Huysseune, A., Cancela, M. L., and Witten, P. E. (2016). Revisiting *In Vivo* Staining with Alizarin Red S - A Valuable Approach to Analyse Zebrafish Skeletal Mineralization during Development and Regeneration. *BMC Dev. Biol.* 16, 1–10. doi:10.1186/s12861-016-0102-4

Bird, N. C., and Mabee, P. M. (2003). Developmental Morphology of the Axial Skeleton of the Zebrafish,*Danio rerio* (Ostariophysi: Cyprinidae). *Dev. Dyn.* 228, 337–357. doi:10.1002/dvdy.10387

Boyer, D. M., Gunnell, G. F., Kaufman, S., and McGeary, T. M. (2016). Morphosource: Archiving and Sharing 3-D Digital Specimen Data. *Paleontol. Soc. Pap.* 22, 157–181. doi:10.1017/scs.2017.13

Bruneel, B., and Witten, P. E. (2015). Power and Challenges of Using Zebrafish as a Model for Skeletal Tissue Imaging. *Connect. Tissue Res.* 56 (2), 161–173. doi:10.3109/03008207.2015.1013193

Caetano-Lopes, J., Henke, K., Urso, K., Duryea, J., Charles, J. F., Warman, M. L., et al. (2020). Unique and Non-redundant Function of Csf1r Paralogues in Regulation and Evolution of Post-embryonic Development of the Zebrafish. *Dev.* 147, dev181834. doi:10.1242/dev.181834

Callieri, M. (2013). *Meshlab as a Complete Open Tool for the Integration of Photos and Colour with High-Resolution 3D Geometry Data*. Italy: Visual computing Lab.

Chang, C., and Franz-Odendaal, T. A. (2014). The Zebrafish Infraorbital Bones: a Descriptive Study. *Zebrafish* 11, 50–56. doi:10.1089/ZEB.2013.0907

Charles, J. F., Sury, M., Tsang, K., Urso, K., Henke, K., Huang, Y., et al. (2017). Utility of Quantitative Micro-computed Tomographic Analysis in Zebrafish to Define Gene Function during Skeletogenesis. *Bone* 101, 162–171. doi:10.1016/j.bone.2017.05.001

Cignoni, P., Callieri, M., Corsini, M., Dellepiane, M., Ganovelli, F., and Ranzuglia, G. (2008). MeshLab: an Open-Source Mesh Processing Tool, In Eurographics Italian Chapter Conference 2008, Italy.

Clément, A., Wiweger, M., von der Hardt, S., Rusch, M. A., Selleck, S. B., Chien, C.-B., et al. (2008). Regulation of Zebrafish Skeletogenesis by Ext2/dackel and Papst1/pinscher. *PLoS Genet.* 4, e1000136. doi:10.1371/journal.pgen.1000136

Crucke, J., Van De Kelft, A., and Huysseune, A. (2015). The Innervation of the Zebrafish Pharyngeal Jaws and Teeth. *J. Anat.* 227, 62–71. doi:10.1111/joa.12321

Cubbage, C. C., and Mabee, P. M. (1996). Development of the Cranium and Paired Fins in the zebrafishDanio Rerio (Ostariophysi, Cyprinidae). *J. Morphol.* 229, 121–160. doi:10.1002/(sici)1097-4687(199608)229:2<121::aid-jmor1>3.0.co;2-4

de Bakker, B. S., de Jong, K. H., Hagoort, J., Oostra, R.-J., and Moorman, A. F. M. (2012). Towards a 3-dimensional Atlas of the Developing Human Embryo: The Amsterdam Experience. *Reprod. Toxicol.* 34, 225–236. doi:10.1016/j.reprotox.2012.05.087

de Boer, B. A., van den Berg, G., de Boer, P. A. J., Moorman, A. F. M., and Ruijter, J. M. (2012). Growth of the Developing Mouse Heart: An Interactive Qualitative and Quantitative 3D Atlas. *Dev. Biol.* 368, 203–213. doi:10.1016/j.ydbio.2012.05.001

Dietrich, K., Fiedler, I. A., Kurzyukova, A., López-Delgado, A. C., McGowan, L. M., Geurtzen, K., et al. (2021). Skeletal Biology and Disease Modeling in Zebrafish. *J. Bone Min. Res.* 36, 436–458. doi:10.1002/JBMR.4256

Eames, B., DeLaurier, A., Ullmann, B., Huycke, T. R., Nichols, J. T., Dowd, J., et al. (2013). FishFace: Interactive Atlas of Zebrafish Craniofacial Development at Cellular Resolution. *BMC Dev. Biol.* 13, 23. doi:10.1186/1471-213X-13-23

Ghayor, C., Correro, R. M., Lange, K., Karfeld-Sulzer, L. S., Grätz, K. W., and Weber, F. E. (2011). Inhibition of Osteoclast Differentiation and Bone Resorption by N-Methylpyrrolidone. *J. of Biol. Chem.* 286, 24458–24466. doi:10.1074/jbc.M111.223297

Hammond, C. L., Moro, E., Eames, B., and Roehl, H. (2012). Using Transgenic Reporters to Visualize Bone and Cartilage Signaling during Development *In Vivo*. *Front. Endocrin.* 3, 91. doi:10.3389/fendo.2012.00091

Harris, M. P., Henke, K., Hawkins, M. B., and Witten, P. E. (2014). Fish Is Fish: The Use of Experimental Model Species to Reveal Causes of Skeletal Diversity in Evolution and Disease. *J. Appl. Ichthyol.* 30, 616–629. doi:10.1111/jai.12533

Hur, M., Gistelinck, C. A., Huber, P., Lee, J., Thompson, M. H., Monstad-Rios, A. T., et al. (2017). MicroCT-Based Phenomics in the Zebrafish Skeleton Reveals Virtues of Deep Phenotyping in a Distributed Organ System. *Elife* 6, e26014. doi:10.7554/eLife.26014

Kanther, M., Scalici, A., Rashid, A., Miao, K., Van Deventer, E., and Fisher, S. (2019). Initiation and Early Growth of the Skull Vault in Zebrafish. *Mech. of Dev.* 160, 103578. doi:10.1016/j.mod.2019.103578

Kikinis, R., Pieper, S. D., and Vosburgh, K. G. (2014). "3D Slicer: A Platform for Subject-Specific Image Analysis, Visualization, and Clinical Support," in *Intraoperative Imaging and Image-Guided Therapy* (New York, NY: Springer), 277–289. doi:10.1007/978-1-4614-7657-3_19

Kimmel, C. B., DeLaurier, A., Ullmann, B., Dowd, J., and McFadden, M. (2010). Modes of Developmental Outgrowth and Shaping of a Craniofacial Bone in Zebrafish. *PLoS One* 5, e9475. doi:10.1371/journal.pone.0009475

Krane, S. M. (2005). Identifying Genes that Regulate Bone Remodeling as Potential Therapeutic Targets. *J. Exp. Med.* 201, 841–843. doi:10.1084/jem.20050354

Kwon, R. Y., Watson, C. J., and Karasik, D. (2019). Using Zebrafish to Study Skeletal Genomics. *Bone* 126, 37–50. doi:10.1016/J.BONE.2019.02.009

Machado, R. G., and Eames, B. F. (2017). Using Zebrafish to Test the Genetic Basis of Human Craniofacial Diseases. *J. Dent. Res.* 96, 1192–1199. doi:10.1177/0022034517722776

McMenamin, S. K., Bain, E. J., McCann, A. E., Patterson, L. B., Eom, D. S., Waller, Z. P., et al. (2014). Thyroid Hormone-dependent Adult Pigment Cell Lineage and Pattern in Zebrafish. *Science* 345, 1358–1361. doi:10.1126/science.1256251

McMenamin, S. K., Chandless, M. N., and Parichy, D. M. (2016). Working with Zebrafish at Postembryonic Stages. *Methods Cell Biol.* 134, 587–607. doi:10.1016/bs.mcb.2015.12.001

Mork, L., and Crump, G. (2015). Zebrafish Craniofacial Development. *Curr. Top. Dev. Biol.* 115, 235–269. doi:10.1016/BS.CTDB.2015.07.001

Parichy, D. M., Elizondo, M. R., Mills, M. G., Gordon, T. N., and Engeszer, R. E. (2009). Normal Table of Postembryonic Zebrafish Development: Staging by Externally Visible Anatomy of the Living Fish. *Dev. Dyn.* 238, 2975–3015. doi:10.1002/dvdy.22113

Parsons, K. J., Son, Y. H., Crespel, A., Thambithurai, D., Killen, S., Harris, M. P., et al. (2018). Conserved but Flexible Modularity in the Zebrafish Skull:

Implications for Craniofacial Evolvability. *Proc. R. Soc. B* 285, 20172671. doi:10.1098/rspb.2017.2671

Pasqualetti, S., Banfi, G., and Mariotti, M. (2012). The Zebrafish Scale as Model to Study the Bone Mineralization Process. *J. Mol. Hist.* 43, 589–595. doi:10.1007/s10735-012-9425-z

Raterman, S. T., Metz, J. R., Wagener, F. A. D. T. G., and Von den Hoff, J. W. (2020). Zebrafish Models of Craniofacial Malformations: Interactions of Environmental Factors. *Front. Cell Dev. Biol.* 8, 600926. doi:10.3389/FCELL.2020.600926/BIBTEX

Rigueur, D., and Lyons, K. M. (2014). Whole-mount Skeletal Staining. *Methods Mol. Biol.* 1130, 113–121. doi:10.1007/978-1-62703-989-5_9

Silvent, J., Akiva, A., Brumfeld, V., Reznikov, N., Rechav, K., Yaniv, K., et al. (2017). Zebrafish Skeleton Development: High Resolution Micro-CT and FIB-SEM Block Surface Serial Imaging for Phenotype Identification. *PLoS One* 12, e0177731. doi:10.1371/journal.pone.0177731

Tesařová, M., Heude, E., Comai, G., Zikmund, T., Kaucká, M., Adameyko, I., et al. (2019). An Interactive and Intuitive Visualisation Method for X-Ray Computed Tomography Data of Biological Samples in 3D Portable Document Format. *Sci. Rep.* 9, 1–8. doi:10.1038/s41598-019-51180-2

Tonelli, F., Bek, J. W., Besio, R., De Clercq, A., Leoni, L., Salmon, P., et al. (2020). Zebrafish: A Resourceful Vertebrate Model to Investigate Skeletal Disorders. *Front. Endocrinol.* 11, 489. doi:10.3389/fendo.2020.00489

Vasconcelos-Filho, J. E., Thomsen, F. S. L., Stosic, B., Antonino, A. C. D., Duarte, D. A., Heck, R. J., et al. (2019). Peeling the Otolith of Fish: Optimal Parameterization for Micro-CT Scanning. *Front. Mar. Sci.* 6, 728. doi:10.3389/fmars.2019.00728

Weigele, J., and Franz-Odendaal, T. A. (2016). Functional Bone Histology of Zebrafish Reveals Two Types of Endochondral Ossification, Different Types of Osteoblast Clusters and a New Bone Type. *J. Anat.* 229, 92–103. doi:10.1111/JOA.12480

Witten, P. E., Hansen, A., and Hall, B. K. (2001). Features of Mono- and Multinucleated Bone Resorbing Cells of the zebrafishDanio Rerio and Their Contribution to Skeletal Development, Remodeling, and Growth. *J. Morphol.* 250, 197–207. doi:10.1002/jmor.1065

Witten, P. E., and Huysseune, A. (2009). A Comparative View on Mechanisms and Functions of Skeletal Remodelling in Teleost Fish, with Special Emphasis on Osteoclasts and Their Function. *Biol. Rev. Camb. Philos. Soc.* 84, 315–346. doi:10.1111/J.1469-185X.2009.00077.X

Zhang, H., Waldmann, L., Manuel, R., Boije, H., Haitina, T., Allalou, A., et al. (2020). zOPT: an Open Source Optical Projection Tomography System and Methods for Rapid 3D Zebrafish Imaging. *Biomed. Opt. Express* 11 (8), 4290–4305. doi:10.1364/BOE.393519

Conflict of Interest: The authors declare that the research was conducted in the absence of any commercial or financial relationships that could be construed as a potential conflict of interest.

Publisher's Note: All claims expressed in this article are solely those of the authors and do not necessarily represent those of their affiliated organizations, or those of the publisher, the editors and the reviewers. Any product that may be evaluated in this article, or claim that may be made by its manufacturer, is not guaranteed or endorsed by the publisher.

frontiers | Frontiers in Endocrinology

ORIGINAL RESEARCH
published: 30 June 2022
doi: 10.3389/fendo.2022.893699

A Baseline for Skeletal Investigations in Medaka (*Oryzias latipes*): The Effects of Rearing Density on the Postcranial Phenotype

Claudia Di Biagio[1,2*], *Zachary Dellacqua*[1,3], *Arianna Martini*[4], *Ann Huysseune*[2], *Michele Scardi*[4], *Paul Eckhard Witten*[2] *and Clara Boglione*[4]

[1] PhD Program in Evolutionary Biology and Ecology, Department of Biology, University of Rome 'Tor Vergata', Rome, Italy, [2] Laboratory of Evolutionary Developmental Biology, Gent University, Department of Biology, Gent, Belgium, [3] Aquaculture Research Group (GIA), Universidad de Las Palmas de Gran Canaria, Institute of Sustainable Aquaculture and Marine Ecosystems (ECOAQUA), Las Palmas, Spain, [4] Laboratory of Experimental Ecology and Aquaculture, University of Rome 'Tor Vergata', Department of Biology, Rome, Italy

Oryzias latipes is increasingly used as a model in biomedical skeletal research. The standard approach is to generate genetic variants with particular skeletal phenotypes which resemble skeletal diseases in humans. The proper diagnosis of skeletal variation is key for this type of research. However, even laboratory rearing conditions can alter skeletal phenotypes. The subject of this study is the link between skeletal phenotypes and rearing conditions. Thus, wildtype medaka were reared from hatching to an early juvenile stage at low (LD: 5 individuals/L), medium (MD: 15 individuals/L), and high (HD: 45 individuals/L) densities. The objectives of the study are: (I) provide a comprehensive overview of the postcranial skeletal elements in medaka; (II) evaluate the effects of rearing density on specific meristic counts and on the variability in type and incidence of skeletal anomalies; (III) define the best laboratory settings to obtain a skeletal reference for a sound evaluation of future experimental conditions; (IV) contribute to elucidating the structural and cellular changes related to the onset of skeletal anomalies. The results from this study reveal that rearing densities greater than 5 medaka/L reduce the animals' growth. This reduction is related to decreased mineralization of dermal (fin rays) and perichondral (fin supporting elements) bone. Furthermore, high density increases anomalies affecting the caudal fin endoskeleton and dermal rays, and the preural vertebral centra. A series of static observations on Alizarin red S whole mount-stained preural fusions provide insights into the etiology of centra fusion. The fusion of preural centra involves the ectopic formation of bony bridges over the intact intervertebral ligament. An apparent consequence is the degradation of the intervertebral ligaments and the remodeling and reshaping of the fused vertebral centra into a biconoid-shaped centrum. From this study it can be concluded that it is paramount to take into account the rearing conditions, natural variability, skeletal phenotypic plasticity, and the genetic background along with species-specific peculiarities when screening for skeletal phenotypes of mutant or wildtype medaka.

Keywords: skeleton, plasticity, vertebral body fusion, skeletal anomalies, meristic counts, mineralization

OPEN ACCESS

Edited by:
Jonathan H Tobias,
University of Bristol, United Kingdom

Reviewed by:
Sarah Kelly McMenamin,
Boston College, United States
Janine A Danks,
RMIT University, Australia

****Correspondence:***
Claudia Di Biagio
claudiadibiagio@gmail.com

Specialty section:
This article was submitted to Bone Research, a section of the journal Frontiers in Endocrinology

Received: *10 March 2022*
Accepted: *18 May 2022*
Published: *30 June 2022*

Citation:
Di Biagio C, Dellacqua Z, Martini A, Huysseune A, Scardi M, Witten PE and Boglione C (2022) A Baseline for Skeletal Investigations in Medaka (Oryzias latipes): The Effects of Rearing Density on the Postcranial Phenotype. Front. Endocrinol. 13:893699. doi: 10.3389/fendo.2022.893699

INTRODUCTION

Small teleost fish such as *Danio rerio* (zebrafish) and *Oryzias latipes* (medaka) are widely used as models for human skeletal diseases (1). Basic pathways of endoskeletal development and mineralization are highly conserved between mammals (i.e., humans) and teleost fish (1, 2) including molecular profiles of bone-inducing and regulating factors (3). Medaka belongs to the family of Adrianichthyidae (4) and has been used as a model species in Asia since the beginning of the 20th century (5–7). Medaka differs from zebrafish in several key features. Firstly, medaka are characterized by a longer ontogenetic period: embryos hatch after 7-9 days (26°C), whereas in zebrafish hatching occurs after 2-3 days (28°C) (8). Medaka can also withstand a wider temperature range, which can be employed in laboratory conditions to slow down the speed of development (9, 10). Fittingly, as descendant of marine ancestors, medaka is an euryhaline species, thus adults are capable of surviving in both limnic and marine conditions (11). As typically found in advanced teleosts, medaka's genome is small: with 700 Mb (12, 13), it represents about half the size of the zebrafish genome. The large availability of inbred medaka strains enables effective genetic screening and mutagenesis mapping. Another advantage of using medaka as a model organism is the physical transparency of the individuals up to the early juvenile stages: this facilitates visualization of vertebral column elements and rapid screening for defects over a long period of skeletogenesis. In contrast to zebrafish, which shares cellular bone with basal Osteichthyes and tetrapods, including mammals, medaka's bone is void of osteocytes (acellular bone), a characteristic of advanced teleosts. Nonetheless, bony structures are remodeled and respond to mechanical loading (14–16). The macro and nanostructure of the vertebral bodies as well as their mechanical properties are well conserved and comparable between zebrafish and medaka (17). In both species, and in contrast to mammals with a long intrauterine development, teleosts hatch as embryos (18) and skeletal development continues after hatching, subjected to the influence of multiple biotic and abiotic variables. Thus, the skeletal phenotype is substantially and continuously influenced by environmental factors that complement the genetic background (19, 20). There is comprehensive literature on the effects of the environment on the skeletal health of marine and freshwater teleosts. Rearing density has been described as an environmental variable that influences skeletal development in farmed fish and high densities have been reported as driving factors that induce skeletal anomalies. So far, relatively little attention has been given to study the effects of rearing density on model fish species held in laboratory conditions. For zebrafish, however, recent studies on wildtype (WT) animals have shown that high rearing density results in reduced size, increased variation of skeletal characters and skeletal anomalies in adults (21). Although variation is an intrinsic characteristic of biological entities, reliable wildtype individuals are a fundamental prerequisite for employing model organisms in biological investigations. When screening for mutant phenotypes or evaluating the effects of experimental variables, it is fundamental to discern between natural variation, unaccounted parameters and variations induced by the tested conditions. Textbooks report a thorough description of rearing techniques, maintenance, and rearing density requirements for different medaka life stages (9). Meristic counts of postcranial skeletal elements have been published for wild strains (22–24). For laboratory strains (or domestic/aquarium stocks), counts are available for vertebral centra and dermal fin rays (25–28), however the occurrence of density-dependent variations and anomalies and the extent of their prevalence has not yet been investigated. Given the growing utilization of juvenile and adult medaka in experiments, the aim of this paper is to provide baseline information for the postcranial skeleton based on an evaluation system that has been successfully applied to zebrafish (21, 29). For the purpose of this study, WT medaka were reared from hatching up to 40 days (hereafter dph) in a closed system with recirculating water at three different densities and the effects on survivorship, size, meristic counts, mineralization of skeletal elements, and variation in number and shape of elements are described. Deeper insights on cellular alterations, mineralization patterns, and occurrences of bone remodeling in the fusion of preural centra are reported.

MATERIALS AND METHODS

Ethical Statement

The animal study was reviewed and approved by the Italian Ministry of Health. The approval (N° 133/2021-PR) was issued pursuant to the Italian art. 31 of Legislative Decree 26/2014 and follows the Italian and European regulations.

Testing the Effect of Stocking Density: Experimental Rearing

The experimental rearing was carried out at the Experimental Biology and Aquaculture Laboratory, University of Rome 'Tor Vergata', Italy. The water for the experimental rearing was processed with an osmotic filtering system (Askoll, 4 Stages Pro System 75GPD), supplemented with salts (0.005% Sera Mineral Salts, 1 mM $NaHCO_3$) and UV sterilized (AQL, External Sterilizer Pro 18W). The aquaria shared water from a single centralized recirculating system provided with a heater (Eheim-Jager, ThermoControl) mechanical (Askoll Partiko), chemical (Askoll Adsorbor, active carbon), biological (Askoll Puremax), and UV filters to maintain constant temperature (26°C), pH (7.2-7.5), oxygen (> 90%), connectivity (300-500 μS) and reduce the level of ammonia. These controls were implemented in order to standardize identical rearing conditions in all of the aquaria, except for the stocking density. The photoperiod was 12:12 light-dark cycle. The levels of O_2, nitrites, nitrates, ammonia, pH, and water hardness were checked weekly (Hanna, HI9829, Sera NH3/NH4-Test and Sera Quick Test 6 in 1). Once a week, 1/3 of the recirculating water was renewed. Medaka of the CAB line were reared according to standard procedures (9, 30). The broodstock was maintained in 4 separate 3L tanks, each containing 5 females and 2 males, for a total of 20 females and 8 males. Egg spawning was induced by switching the light-dark cycle to 14:10. Eggs were collected from the belly of each female, transferred altogether to a petri dish and gently separated with tweezers under a stereomicroscope with cold light. The vital eggs were incubated in a thermostatic chamber at 26°C in 500 mL of filtered freshwater supplemented with 0.0002% methylene blue until hatching, at a density of 150-200 eggs/500

mL with a 12:12 light-dark photoperiod. To test the effects of rearing density, medaka from the same spawning event which hatched on the same day were utilized. To avoid any undesirable selection, the hatched medakas were collected in a 200 mL beaker with 30 mL water, mixed altogether and randomly transferred into 3L aquaria to obtain the following densities (**Table 1**): (1) LD or low density: 5 fish/L in 4 aquaria (total of 60 medaka); (2) MD or medium density: 15 fish/L in 1 aquarium (total of 45 medaka); (3) HD or high density: 45 fish/L in 1 aquarium (total of 135 medaka). The rationale underlying the choice of these experimental densities is based on guidelines available for this species (9). For 3L tanks, Kinoshita and colleagues suggest 16 medaka/L for rearing fish up to 30 dph; from 30-60 dph they suggest reducing the density to 10 medaka/L. Therefore, because individuals were reared from hatching up to 40 dph, an intermediate density of 15 medaka/L was chosen as a control and is referred to as medium density (MD). We tested a lower and a higher density by a factor of three. The fish were fed three times per day with a commercial diet ZEBRAFEED® (Sparos, Portugal), with increasing granulometry according to the size of fish, as indicated in the manufacturer's instructions. At the end of the experimental rearing (40 dph), all the juveniles were anaesthetized with tricaine (Sigma Aldrich) according to their size (MS-222 80-120 mg/L) and imaged with an Axiozoom V.16 camera (Zeiss, Germany). 3 HD individuals with vertebral body fusions and 3 controls were euthanized with a tricaine overdose (MS-222, 300 mg/L), fixed in 4% paraformaldehyde (PFA)/1.5% glutaraldehyde (GA)/0.1 M sodium cacodylate buffer (pH 7.4)/0.001% $CaCl_2$ and utilized for histological and enzyme histochemical analyses. The other individuals were euthanized, fixed in 4% PFA/1.5% GA overnight at 4°C and transferred through increasing ethanol concentrations up to 70% ethanol for anatomical inspections.

Terminology

In line with the terms used in comparative vertebrate anatomy (31) and enabling cross-comparisons with studies carried out on fish models, such as zebrafish, the axial skeleton was subdivided into cranial, abdominal, caudal, and caudal complex vertebrae (**Figure 1**). The cranial vertebrae, which are characterized by the absence of ribs, were not clearly discernable in all the specimens and were therefore not considered in the data analyses. The term abdominal is used to indicate vertebrae that carry ribs and/or open hemal arches (without hemal spines). The term caudal follows previously published studies on model fish, i.e., zebrafish. Concerning the caudal complex, the terminology we used is in accordance with Arratia and Schultze (32) and Bensimon-Brito et al. (33), and revised by Wiley et al. (34) in which preural centra are terminal vertebrae supporting the caudal fin and carrying modified hemal and neural arches; ural centra carry hypurals and epurals and the urostyle is the compound element of the vertebral column composed of preural 1 and all of the urals (32–36). As far as the caudal fin elements are concerned, we used the same terminology that is used for zebrafish which also applies to medaka (taking into consideration the different counts of hypurals and epurals) (34, 37). Epurals, hypurals, parhypural, modified hemal spine of PU2 (HPU2), and the extra caudal ossicle (EO) are endoskeletal elements that support the caudal fin. The underlining basis of the choice to include them among the caudal fin elements takes into consideration that their modified shape is a functional characteristic which support the principal caudal rays and could lead to increasing the stiffness of the caudal fin. This inclusion is in accordance with the other fin elements, which are made up of dermal rays and endoskeletal support (i.e., pterygophore, radials, basipterygia). The term 'malformation' refers to a morphological defect occurring during development. It is a broad term including congenital malformations as well as malformations with different etiologies, including environmental factors. The term 'anomalies' refers to both the defects that could be classified as malformations and natural variations which cannot be ascribed to a specific causative factor (38).

TABLE 1 | Rearing parameters.

Condition	Initial density (medaka/L)	Initial number (medaka/3L tank)	Survivorship (%)	Final density (medaka/L)	Final number (medaka/3L tank)
LD	5	15	91 (87, 93, 93, 93)	5 (4, 5, 5, 5)	14 (13, 14, 14, 14)
MD	15	45	98	15	44
HD	45	135	94	42	127

Initial and final number (medaka/3L tank) of individuals and density (medaka/L), and survivorship at 40 dph are reported for the tested densities: low (LD), medium (MD) and high (HD). For the LD group, data represents the average of the 4 LD tanks. The individual values of each tank are reported in parentheses.

Anatomical Survey: Meristic Counts, Mineralization State, Skeletal Anomalies

The fixed individuals were whole mount-stained with Alizarin red S (ARS), according to Taylor and Van Dyke (39). To properly visualize the vertebral column and the fin endoskeletal elements, the scales were completely removed. Imaging was performed with the Axiozoom V.16 stereomicroscope (Zeiss, Germany) equipped with a 5MP CCD camera. The standard length (SL) of all individuals was recorded on stained samples with Image J (Fiji, version 1.51), by measuring the distance between the tip of the upper jaw (premaxillary) and the insertion of the caudal fin rays. To investigate a potential effect of rearing density on skeletogenesis, the mineralization of all skeletal elements was examined. Caudal fin rays were considered fully mineralized if at least two segments were detected in at least 5 superior and 6 inferior dermal rays. This assumption was necessary considering the early juvenile stage. The frequencies (%) of individuals with fully, partially-, and non-mineralized skeletal elements were reported for all individuals belonging to the three density groups. The same analysis was performed only on individuals of the same size class SL: 11.5-15.5 mm (38 individuals for the LD group, 37 MD, and 63 HD). To statistically evaluate the link between the mineralization state and length, a logistic regression analysis was performed. For each skeletal region (i.e., vertebrae, fin rays, pterygophores), the score of 0 was assigned to the non- and/or partially mineralized elements, whereas a score of 1 was assigned to fully mineralized elements. The monitoring of the skeletal anomalies was carried out on the base of the alpha-numeric classification proposed by Martini *et al.* (21) for zebrafish and adapted to medaka (**Supplementary Table 1**). The vertebral region A in medaka refers to the cranial vertebrae and not

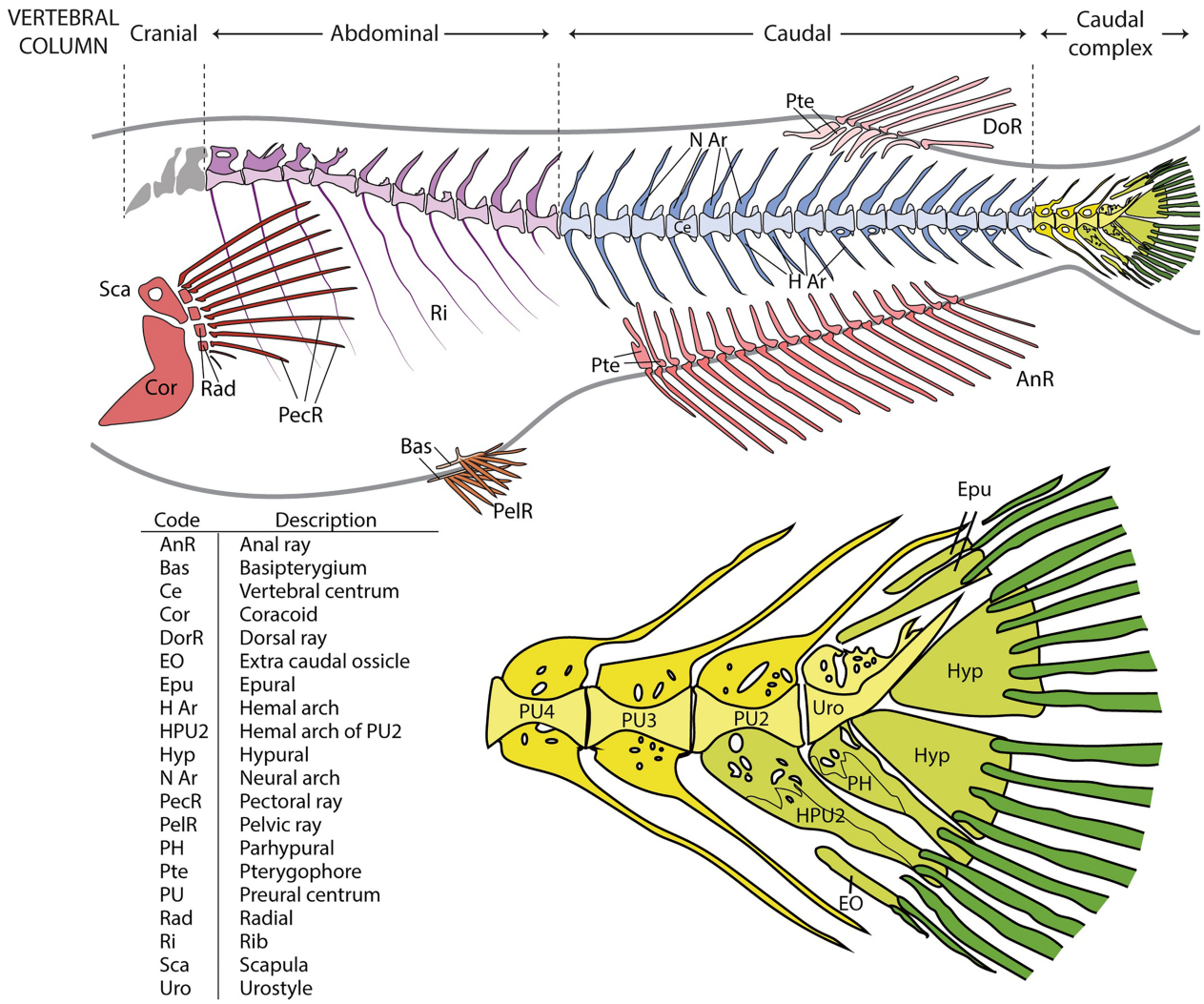

Code	Description
AnR	Anal ray
Bas	Basipterygium
Ce	Vertebral centrum
Cor	Coracoid
DorR	Dorsal ray
EO	Extra caudal ossicle
Epu	Epural
H Ar	Hemal arch
HPU2	Hemal arch of PU2
Hyp	Hypural
N Ar	Neural arch
PecR	Pectoral ray
PelR	Pelvic ray
PH	Parhypural
Pte	Pterygophore
PU	Preural centrum
Rad	Radial
Ri	Rib
Sca	Scapula
Uro	Urostyle

FIGURE 1 | Overview of the vertebral column and fins in medaka and close-up on the caudal complex skeleton. Medaka have two paired fins (pectoral fin: red; pelvic fin: orange) and three unpaired fins (anal fin: dark pink; dorsal fin: light pink; caudal fin: green). The vertebral column is divided into 4 regions: cranial (grey), abdominal (purple), caudal (blue), and caudal complex (yellow). The vertebral bodies are shown in a lighter tone, the neural and hemal arches in a darker tone. Similarly, the internal supports of the paired and unpaired fins (radials, scapula and coracoid of the pectoral fin, basipterygia of the pelvic fin, and pterygophores of the dorsal and anal fins) have a lighter tone, whereas the dermal fin rays a darker tone. In the bottom picture, the caudal complex vertebrae (in yellow) consist of 3 preural vertebrae (PU). The modified hemal arch (parhypural, PH) of the urostyle (Uro) and the modified hemal arch of PU2 (HPU2) are classified as part of the caudal fin, together with rays, epurals (Epu), hypurals (Hyp), and the extra caudal ossicle (EO). The PH and HPU2 have been modified to increase the stiffness of the fin and to support the caudal rays (dark green). The table represents an overview of all the investigated skeletal elements.

to the Weberian region (21), which is absent in medaka. It was decided to maintain the same terminology enabling a more efficient comparison between the two widely used fish models. The capital letter indicates the skeletal region, the number corresponds to a skeletal element, and the letter code specifies the type of anomaly. Skeletal anomaly data were expressed in a raw matrix (RM) and used to calculate the frequencies (%) of each type of anomaly over the total number of anomalies, in each group. The RM was subsequently transformed into a binary matrix (BM) which was used to calculate the prevalence of individuals affected by each anomaly type. The following descriptive metrics were calculated, for each group: 1) relative frequency (%) of individuals with at least one anomaly; 2) malformation index, i.e., the average anomalies' load (number of total anomalies over number of individuals with at least 1 anomaly); 3) relative frequency (%) of individuals with axis and/or vertebral body anomalies. The frequencies (%) of individuals affected by each type of anomaly over the total number of individuals are reported in **Supplementary Table 2**. The axis or vertebral centra anomalies reported in **Table 2** include both extended and localized deviations of the axis as well as variations in shape/size of vertebral centra (see **Supplementary Table 2** for a comprehensive list of the considered anomalies).

Statistics

Differences between median SL values at different rearing densities were analyzed by means of a Kruskal-Wallis test, with *a posteriori* pairwise Mann-Whitney tests and Bonferroni correction. Concerning the skeletal anomalies, statistical differences in proportions were analyzed by the "N-1" *chi-squared* test as recommended by Campbell (40) and Richardson (41) with the MedCalc software, followed by the Bonferroni correction for multiple testing. The confidence interval was calculated according to the recommended method given by Altman *et al.* (42). The independence between variables (i.e. vertebral numbers and rearing density or skeletal anomalies and rearing density) was tested with a *chi-squared* test, followed by the Bonferroni correction for multiple testing. The χ^2 components were calculated to determine which frequencies were significantly higher or lower than the expected values. For what concerns the mineralization data, logistic regression was calculated for each skeletal element and grouped by rearing density (LD, MD, and HD). The logistic function represents the probability (between 0 and 1) that a skeletal element is mineralized for a specific standard length. To obtain a linear relationship between SL and mineralization, the probability was transformed into the log odds of obtaining a fully mineralized skeletal element. To test whether the slope is significantly different from 0 (odds ratio ≠ 0), the Wald test and the likelihood ratio test were performed. All the statistical analyses except those about differences between proportions were performed with Past V 4.01 (43).

Histological Studies

The specimens employed for histological analyses were incubated in fixative for 2 hours, rinsed in PBS and decalcified (when necessary) in 10% EDTA/4% PFA at 4°C. Dehydration and embedding in glycol methacrylate was performed according to Witten *et al.* (44). In brief, the juveniles were rinsed with PBS, dehydrated with a graded series of acetone (30, 45–48) and stored at -20°C until embedding. Samples were pre-impregnated in monomer solution ((2-hydroxyethyl)-methacrylate, ethylene glycol monobuthyl ether, benzoyl peroxide) for 1 h on ice and transferred into fresh solution for 24 h at 4°C. The monomer solution was supplemented with 2% catalyst (N,N-dimethylaniline, poly-ethylenglycole-200) for embedding, which was incubated for 48 h at 4°C. The polymerization completes in the following 24 h at RT. 3 µm sections were cut on an automated microtome Microm HM 360 (Marshall Scientific, Hampton, NH, USA). Toluidine blue and Verhoeff Elastin staining were performed according to Humason et al. (49).

TABLE 2 | Descriptive skeletal metrics of the experimental groups.

	LD	MD	HD
Number of observed individuals	55	44	121
Frequency (%) of individuals with at least one anomaly	95[a]	98[a]	97[a]
Malformation index	5	5	5
Frequency (%) of individuals with axis deviations and/or vertebral centra anomalies	45[a]	59[a, b]	69[b]

The numbers are reported for each experimental group (LD, MD, HD). The malformation index refers to the average number of anomalies per observed individual. "N-1" chi-squared *test for proportions, followed by Bonferroni correction. Different letters (a, b) indicate statistically significant difference among groups (p <0.05).*

Enzyme Histochemical Procedures: Measuring TRAP and ALP Activity

Specimens used for the demonstration of tartrate-resistant acid phosphatase (TRAP) and alkaline phosphatase (ALP) activity were fixed, decalcified (only for TRAP), dehydrated and embedded as previously described. 4 µm sections were cut on an automated microtome Microm HM 360 (Marshall Scientific, Hampton, NH, USA). Demonstration of TRAP was performed according to Witten et al. (44) and Nemoto et al. (50). The ALP staining was based on the azo-dye-coupling method (51, 52) and performed according to Witten and Villwock (53).

RESULTS

Survivorship and Standard Length

The average survivorship of the individuals reared at low (LD), medium (MD), and high (HD) density conditions at 40 dph is 91%, 98%, and 94% respectively (**Table 1**). Due to the 6% mortality in the HD aquarium, the final density in this group was reduced to 42 individuals per liter. The density in the MD group remained unchanged, 15 individuals/L. For LD, the final density was maintained (5 individuals/L) in three of the aquaria replicates and was reduced to 4 individuals/L in one aquarium. Rearing density is found to be negatively related to the standard length (SL) of the animals. As shown in **Figure 2**, the SL of HD individuals (6.9-15.2 mm; median: 11.6 mm) is significantly lower compared to MD individuals (7.2-18 mm; median: 13.4 mm), and SL in MD individuals is significantly lower compared to LD individuals (11.8-17.5 mm; median: 14.9 mm).

The Postcranial Skeleton

The postcranial skeleton of medaka is composed of the vertebral column, paired fins, unpaired fins, and the endoskeletal fin support. The completely formed and mineralized vertebral column of medaka contains between 30 and 32 vertebrae, this includes the urostyle which is counted as a single unit. The vertebral column can be subdivided into 4 regions, as presented in **Figure 1**: cranial (2 vertebrae + basioccipital condyle), abdominal (9-11 vertebrae), caudal (14-16 vertebrae), and caudal complex (3-4 preural vertebrae plus urostyle). The last vertebra of the abdominal region that does not carry ribs and has open hemal arches is referred-to as a transitional region. The upper tips of the neural arches of the abdominal vertebrae are typically 'fan-shaped'. Iwamatsu (45) reports that the upper tips of the spines of the 2^{nd}-5^{th} vertebrae begin to develop this shape at 5.4 mm total length (TL), and that this process includes vertebrae 1-8 after the TL reaches 10 mm. A certain degree of variability is also observed in the shape of some hemal arches (**Figure 3**): i.e., the distal tip of ventral postzygapophysis connects to the arch by a bony bridge of variable thickness. This feature appears to be present in both the caudal and caudal complex vertebrae regardless of the rearing density but exhibits an increased occurrence when proceeding caudad. The position and frequency of these features is not significantly different between the experimental groups, except in the case of the last caudal vertebra, for which there are significant differences between LD and HD ($p < 0.05$).

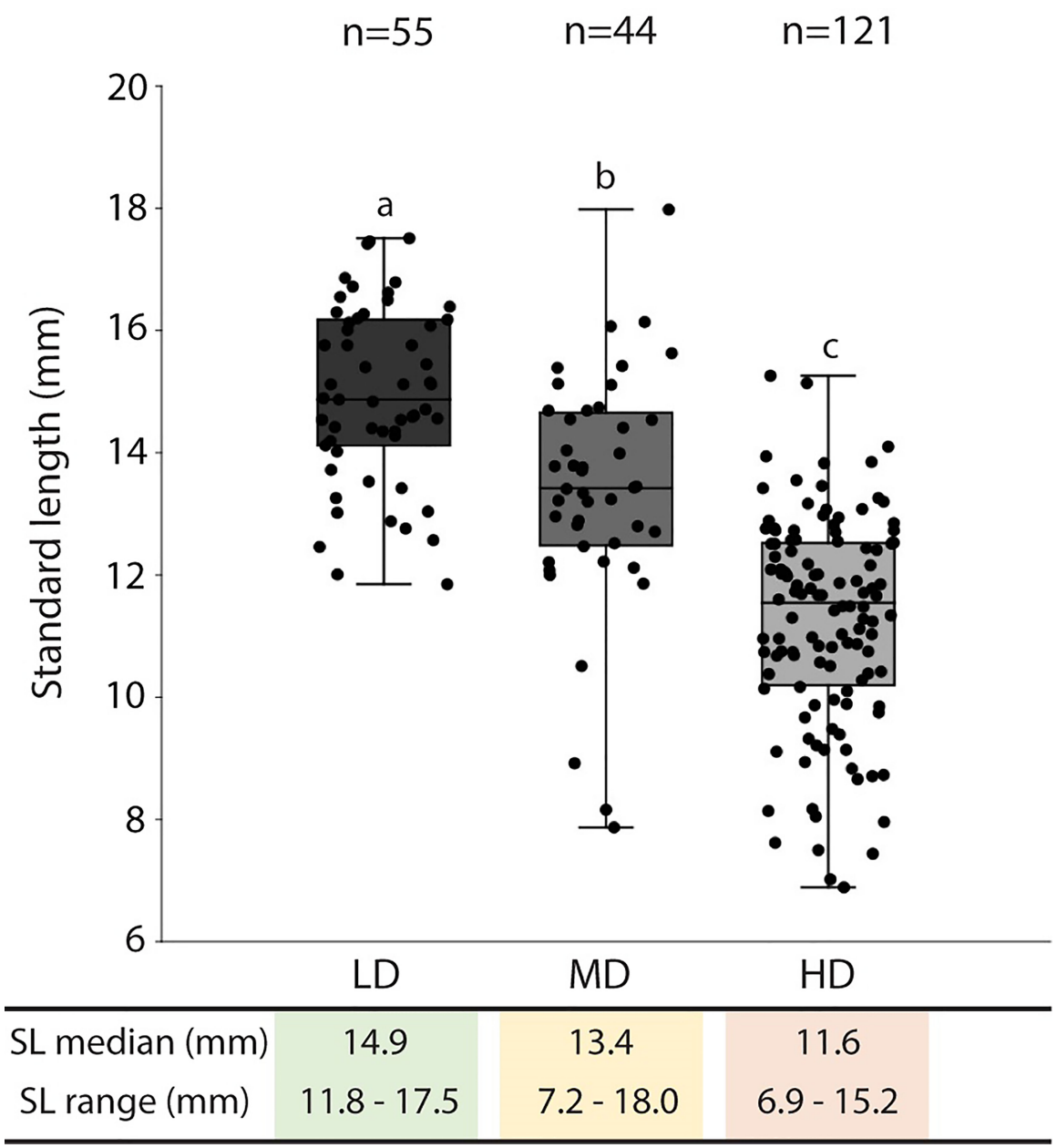

	LD	MD	HD
SL median (mm)	14.9	13.4	11.6
SL range (mm)	11.8 - 17.5	7.2 - 18.0	6.9 - 15.2

FIGURE 2 | Standard length in medaka reared at different densities. The standard length (SL: mm) median and range are presented in the table below the graph. The SL values are reported with box & whisker plots: the midline in each box is indicative of the median, whereas min and max values are shown with whiskers. The box represents the central percentile. Different letters indicate statistically significant differences among groups (Kruskall-Wallis test, followed by *a posteriori* pairwise Mann-Whitney tests with Bonferroni correction, $p < 0.0001$). SL, standard length (mm); n, number of samples; LD, low density; MD, medium density; HD, high density.

The meristic counts observed at the three experimental densities are reported in **Supplementary Table 3**. Counts that differ from those that have been previously published are: the numbers of dermal fin rays of the pectoral fins, 8-11 in this study vs. 9-10 or 9-11 in previous studies (22, 23, 26) and of the caudal fin, 6-7 inferior rays vs. 5-6 in a previous investigation (23). There are no remarkable differences in counts linked to density: a single HD medaka with 17 anal rays is observed and two HD individuals display only 29 vertebrae, due to vertebral centra fusions in the region of the caudal complex (**Figure 4**).

Effects of Rearing Density on Mineralization of Skeletal Elements

Bone formation involves the secretion of non-mineralized bone matrix while bone mineralization relates to the deposition of hydroxyapatite (16). We investigated if rearing density affects the

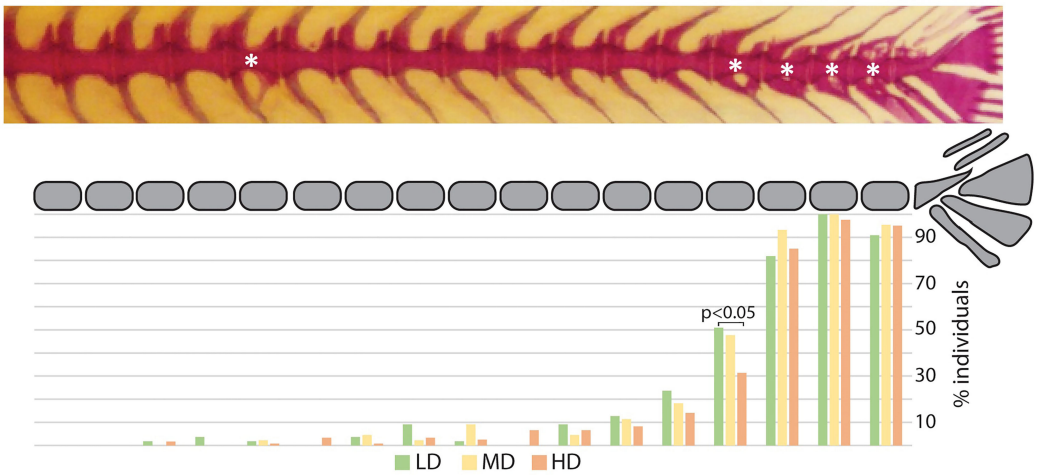

FIGURE 3 | Hemal arch variability. Representative whole mount Alizarin red S-stained vertebral column of medaka (top). The asterisks indicate arches with connections between the ventral postzygapophysis and the hemal arch of the same vertebral body. The lower diagram reports a schematic representation of the vertebral column (caudal region and caudal complex) with the percentage of individuals showing a ventral connection for the corresponding vertebral body. Green: LD (low density); yellow: MD (medium density); red: HD (high density). "N-1" *chi-squared* test for proportions, followed by Bonferroni correction; p values are indicated for significant differences only.

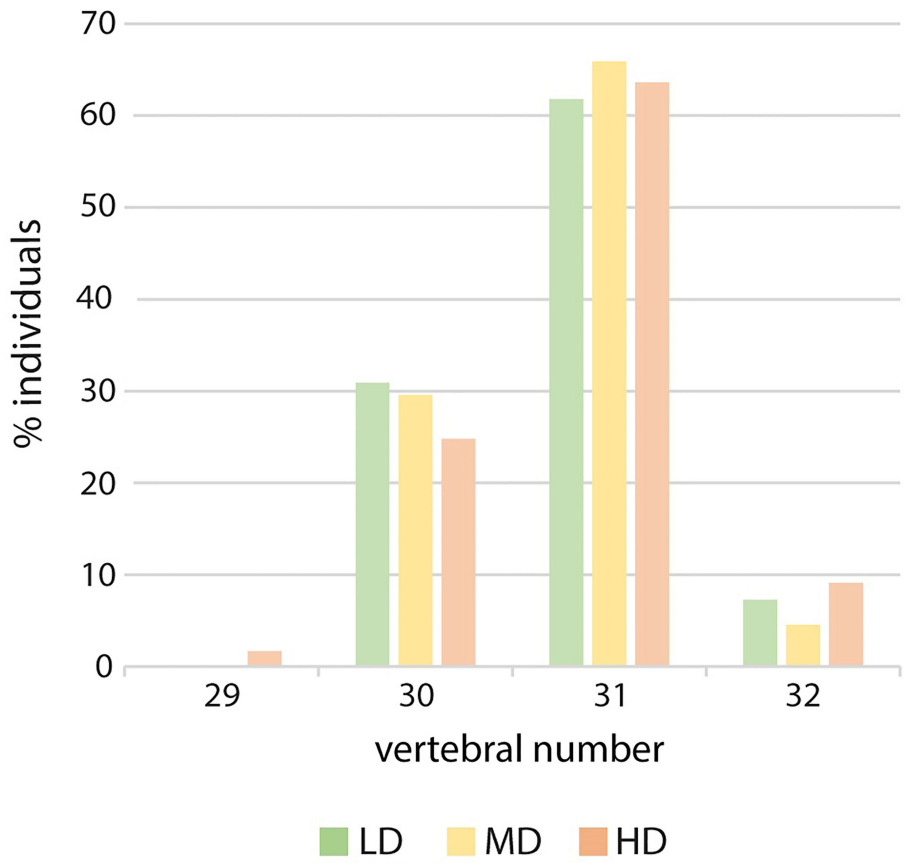

FIGURE 4 | Vertebral number variation in relation to rearing density. Percentage of individuals with 29, 30, 31 or 32 vertebral centra. LD: low density; MD: medium density; HD: high density. *Chi-squared* to test the independence of three out of four vertebral numbers (30, 31 and 32). The large p-value (0.82) does not allow to reject the hypothesis of independence.

mineralization of postcranial skeletal elements by examining the percentage of individuals with fully, partially-, and non-mineralized skeletal elements as indicated by the Alizarin red S staining. Vertebral centra and arches, parhypural (PH), modified hemal arch of PU2 (HPU2), and the dermal rays of the caudal fin are fully mineralized in all specimens, irrespective of the rearing density, therefore they are not shown in **Figure 5**. Conversely, the endoskeletal supports of all fins as well as the dermal fin rays of the dorsal, anal, pectoral and pelvic fins exhibit decreased levels of mineralization with increasing rearing density. The least mineralized skeletal element is the pelvic fin (LD: 51% of individuals with fully mineralized pelvic fin; MD: 36%; HD: 28%), followed by the pectoral, anal, dorsal, and caudal fin (**Figure 5A**). Taking into consideration that HD individuals are characterized by reduced size (**Figure 2**) compared to the other groups, the lower frequency of HD individuals with fully mineralized skeletal elements could be size-related. **Figure 5B** shows the mineralization levels of the individuals in the same size class (11.5-15.5 mm) for each density group. Although the HD condition appeared to be linked with reduced mineralization,

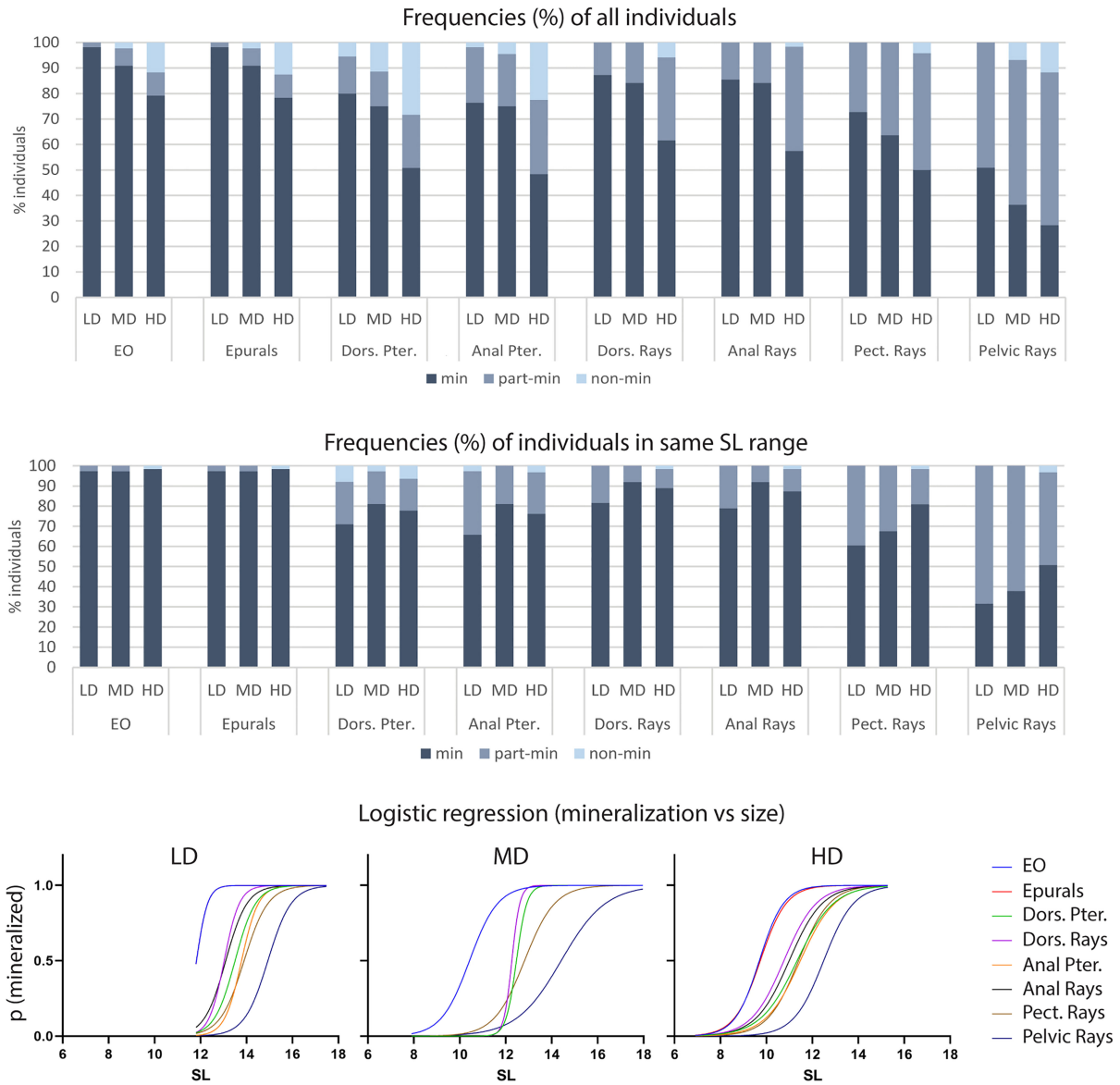

FIGURE 5 | Mineralization of skeletal elements in relation to rearing density. The frequency (%) of individuals with fully (min), partially- (part-min), and non-mineralized (non-min) skeletal elements is reported for all individuals **(A)** as well as for individuals in the same size range **(B)**. **(A)** The percentage of fully mineralized skeletal elements decreases with the increasing rearing density. However, this density-related trend is lost when analyzing only individuals in the same size range **(B)**. **(C)** Logistic regression. The probability of identifying a mineralized skeletal element according to the standard length is reported for each density group: low (LD, left), medium (MD, center) and high (HD, right) density. An "S" shaped logistic function indicates a clear correlation between mineralization and size, whereas straight lines would indicate independency. Dors., dorsal; Pter., Pterygophore; Pect, pectoral; LD, low density; MD, medium density; HD, high density.

these results were found to be confounding with the size of the fish. In fact, the stacked bar chart reveals the lack of a clear relationship between mineralization and rearing density. The dependency of the mineralization state on the size (SL) is statistically confirmed by a logistic regression analysis. The S-shape of the diagrams in **Figure 5C** signifies that the delay in mineralization for the partially- and non-mineralized elements is significantly dependent on the smaller SL (slope significantly different from 0 as tested with the Wald test and likelihood ratio test).

Effects of Rearing Density on Skeletal Anomalies

The results shown in **Table 2** reveal the presence of at least one skeletal anomaly in nearly all of the individuals from each group (95% in LD; 98% in MD; 97% in HD). Interestingly, the frequency of individuals with axis or vertebral centra anomalies progressively increases from the LD- to the MD- and HD group (45%, 59% and 69%, respectively), resulting in significant differences between the LD and HD groups. In medaka, we do not observe extended axis deviations such as kyphosis, scoliosis, saddle-back syndrome, nor mismatched fusion of arches, which have been reported to occur in WT zebrafish (21). Contrarily, vertebral fractures are observed in this study although they have not been reported in wildtype zebrafish. **Supplementary Table 2** reports the frequencies (%) of individuals affected by each of the 62 types of detected anomalies. The analysis of skeletal anomalies in different regions of the postcranial skeleton shows that the caudal complex is most variable, irrespective of rearing density (**Figure 6A**). Within the

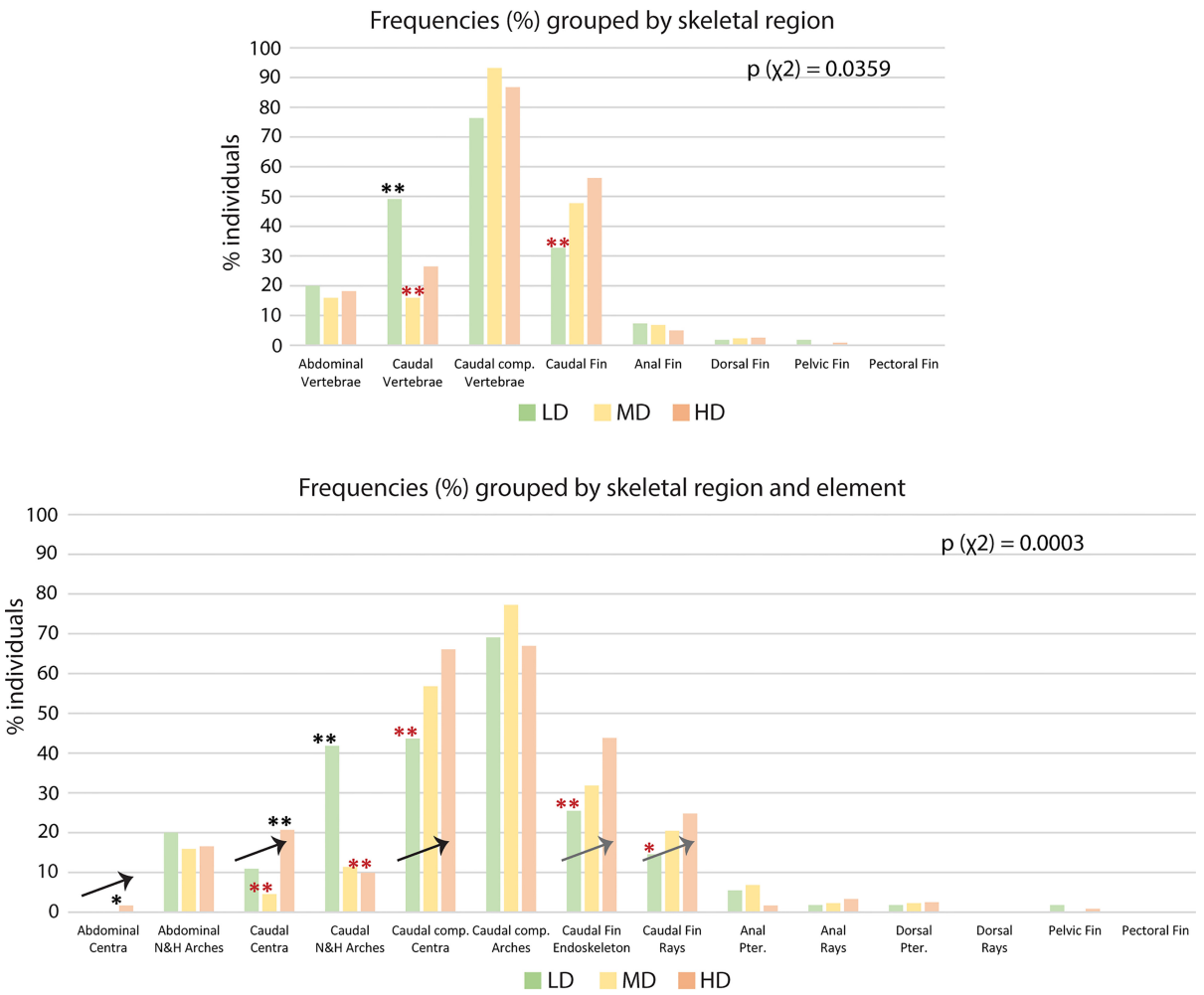

FIGURE 6 | Skeletal anomalies linked to rearing densities. **(A)** Frequency (%) of individuals showing skeletal anomalies, grouped by region. The bars for the abdominal, caudal, and caudal complex vertebrae include anomalies of the centra and the arches. The data for the pectoral, pelvic, dorsal, anal, and caudal fin refer to anomalies of the dermal fin rays and the fin endoskeleton. **(B)** Frequency (%) of individuals showing skeletal anomalies, grouped by region and element. Arrows indicate the increase in the frequency of individuals with anomalies with increased rearing density. N&H arches, neural and hemal arches; Caudal comp., caudal complex; Pter., Pterygophore; LD, low density; MD, medium density; HD, high density. *Chi-squared* test followed by the analysis of the χ^2 components, p-values are indicated on the respective graphs. Based on the analysis of the χ^2 components, frequencies significantly higher or lower (*: p <0.05; **: p <0.01) than the expected values are indicated by a black or red asterisk, respectively.

caudal complex, preural vertebrae display the highest number of anomalies (LD: 76%; MD: 95%; HD: 87%) (**Figure 6A**). These are followed by caudal fin rays and endoskeleton (LD: 33%; MD: 50%; HD: 56%), the caudal (LD: 49%; MD: 16%; HD: 26%) vertebrae and abdominal vertebrae (LD: 24%; MD: 23%; HD: 18%). Cases of lordosis are rare: less than 1% of the individuals are affected. Dermal rays and endoskeletal elements of pectoral, pelvic, dorsal, and anal fins show low occurrences of anomalies. One LD medaka displays absent right pelvic fin rays and the pelvic fin endoskeleton. One HD medaka displays the same anomaly on the opposite lateral side.

Interestingly, the number of anomalies per malformed individual does not differ among the groups, while the frequency of individuals with severe anomalies (*viz.* axis and/or vertebral centra anomalies) increases at high rearing density. Localized lordotic, scoliotic, and kyphotic deviations, involving up to 4 vertebral bodies, are more frequently found in the caudal vertebrae and preurals, and most prominently found in the HD individuals (up to 6%). In general, neural and hemal arches are more variable, with no clear trend linked to the rearing density.

If we analyze anatomical skeletal elements made up of multiple developmental units, it is possible to further differentiate the response to rearing density; i.e., vertebral bodies (anatomical units) consist of vertebral centra and arches, which are distinct developmental modules (54). Likewise, each fin (anatomical unit) consists of multiple endoskeletal elements and dermal fin rays (developmental units). The caudal fin endoskeleton includes the PH, HPU2, EO, hypurals, and epurals. From this more detailed perspective (**Figure 6B**), vertebral centra, but not neural and hemal arches, show increased variability coinciding with increased density. The percentage of individuals with at least one vertebral centrum anomaly increases with density, i.e., from 11% (LD) to 21% (HD) in the caudal region and from 44% (LD) to 66% (HD) in the caudal complex. Complete vertebral centra fusions are observed only in preural centra, increasing from 2% in the LD and MD groups to 7% in the HD group. The caudal fin endoskeleton displays a similar trend, with anomalies increasing from 26% in the LD group to 44% in HD group. Likewise, the caudal fin ray anomalies increase from 14% in LD group animals to 25% in HD group animals. Concerning the dorsal and anal fins, **Figure 6B** reveals that the variability shown in **Figure 6A** relates to the pterygophores, rather than the dermal rays. Fusions in the preural centra are observed at different phases of fusion and modeling, in different individuals. This allows a detailed morphological and cellular investigation, as described in the following.

Morphological and Histological Investigation of Vertebral Body Fusions in the Caudal Complex

Observations carried out on whole mount-stained samples (**Figure 7**) and histological sections (**Figure 8**) seem to indicate that vertebral centra fusion likely starts by the fusion of the hemal arches of the two neighboring centra (**Figures 7B, C**). Normal (**Figures 7A**, **8A**) consecutive vertebrae are separated by regular intervertebral spaces (IVS) with intervertebral ligaments and notochord tissue. The detailed structure of a typical IVS is presented in **Figures 8D**, **8H**. Vacuolated notochord cells and the cells of the notochord epithelium are surrounded by a ligament composed of the notochord sheath, the outer elastin layer of the notochord sheath, and collagen type I fiber bundles that connect the vertebral body endplates (54). In what is interpreted as an early-stage fusion, hemal arches of the adjacent vertebrae are intertwined, and the dorsal intervertebral space and neural arches are still separated (**Figure 7B**). In the case of an advanced or complete fusion (**Figure 7E**), the dorsal intervertebral spaces and neural arches fuse (**Figures 7D–F**). In **Figures 7E, F**, it is possible to observe a vertebral fusion remodeled and reshaped into a normal (albeit elongated) centrum.

In addition to a ventral-dorsal asymmetry occurring during fusion and remodeling, we also observe some fusions that exhibit a left-right asymmetry in the vertebral centra shape (**Figures 7H–K**). In these fusions, the centra appear to be laterally deviated, as in a localized scoliosis involving only two vertebrae. Centra in a status of fusion show a clear separation on one lateral side and a completely fused and modeled centrum on the opposite lateral side (compare **Figure 7J** with **Figure 7K**, white arrows). The arches are not modeled and remain distinguishable. Fusions that involve more than two vertebral bodies are an uncommon observation (2 out of 12 specimens present complete or partial fusions, **Figure 7F**, asterisk and arrowhead).

To elucidate the cellular processes involved in vertebral body fusions, sagittal sections of normal and fused preural vertebrae 2 and 3 are analyzed. **Figure 8** shows histological observations that reflect the dorsal-ventral asymmetry observed on whole mount Alizarin red S-stained specimens. In a normal vertebral centrum at 40 dph, the vacuolated notochord cells and extracellular vacuoles are present. Dorsal and ventral IVS are connected by the notochord septum, septa of neighboring vertebral bodies are connected by the notochord strand (**Figure 8A**), a typical situation for a mature teleost notochord (54). The elements of the intervertebral ligament between preural 2 and preural 3 (**Figures 8A, D, H**) are regularly shaped and no alterations are observed. **Figures 8B, C** show sagittal sections of partially and completely fused vertebral bodies, respectively. In the partial fusion, the dorsal intervertebral space is still unaltered although ventrally, the two vertebral bodies appear completely fused (**Figure 8B**); and the components of the intervertebral ligament are preserved inside the bony bridge that connects the ventral vertebral body endplates. In completely fused vertebral bodies the dorsal endplates are also fused by a bony bridge (**Figures 8C, E, I**). At this stage, the elements of the ventral intervertebral ligament are no longer distinguishable, except traces of the notochords' outer elastin layer (**Figure 8F, J**).

Based on these static observations of different degrees of vertebral fusion, we propose that the first step in the fusion process is the deposition of ectopic bone onto the IVS. This bone connects the endplates and bridges the IVS (**Figures 8E, I**). In this initial phase, the components of the intervertebral ligament, the collagen type-II based notochord sheath and its outer elastin layer are still present.

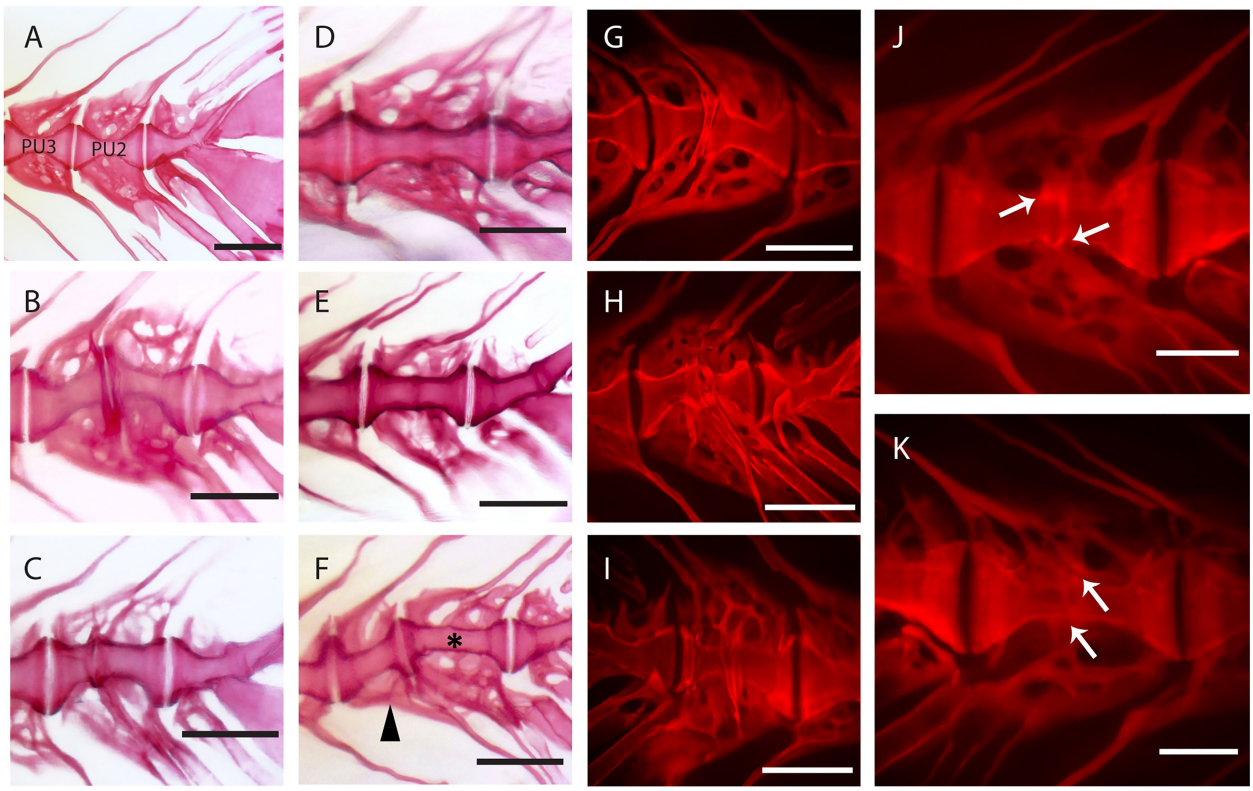

FIGURE 7 | Static observations of fusing preural centra in medaka. **(A)** Caudal complex with non-deformed centra. **(B–K)** Different degrees of fusion between two preural centra. **(H, I)** and **(J, K)** show the right and left side of the same fusions, respectively. White arrows point to a clearly separated IVS in J and to a reshaped IVS in **(K)**. **(F)** Multiple fusion of preural centra: a vertebral body (arrowhead) is fusing to two previously fused and reshaped vertebrae (asterisk). PU: preural vertebra. Whole mount-staining with Alizarin red S. Scale bars = 400 µm **(A–I)**, 200 µm **(J–K)**

The following stages, named as 'endplate remodeling', are shown in **Figures 8F** and **8J**, **Figures 8G** and **8K**. Parasagittal and sagittal sections reveal different levels of tissue reorganization: in the parasagittal plane (**Figures 8F, J**), small traces of elastin and collagen are detectable, but not in the sagittal plane (**Figures 8G, K**).

The reshaping of fused vertebral bodies, particularly bone formation and bone resorption, are revealed by the activity of ALP (alkaline phosphatase) as a marker for osteoblasts and TRAP (tartrate-resistant acid phosphatase) as a marker for osteoclasts (**Figures 9A–F**, respectively). ALP is expressed by mature osteoblasts and can be visualized by enzyme histochemistry as a strong red staining. TRAP is a lysosomal osteoclast-specific enzyme that is secreted by osteoclasts into the cells' subcellular space. Thus, TRAP not only labels bone resorbing cells but also sites of bone resorption. In a normal (i.e., non-fused) vertebral body, ALP is expressed by the osteoblasts on the growth zone of the vertebral body endplates (**Figure 9A**, arrows) and at the bone surfaces of the growing neural and hemal arches (**Figure 9C**, white asterisk). In fusing centra, ALP signal is detected on the surface of the fused IVS, thus bridging neighboring vertebral bodies (**Figure 9B**, arrow) and in unorganized bone structures that connect hemal arches (**Figure 9B**, arrowhead). The sections also highlight abundant vascularization in the region of the fusion (**Figure 9B**, black asterisks). In **Figures 9D–F**, TRAP can be identified based on a typical dark pink staining product. In a non-fused vertebral body, TRAP is visible at the endosteal bone surfaces of neural and hemal arches (**Figure 9D**, asterisks). At these locations, TRAP activity is required to facilitate the expansion of the arches during growth. In partially and completely fused vertebral bodies (**Figure 9E**), TRAP-positive osteoclasts are evidently involved in the reshaping of arches, individuated by the signal on the unorganized bone structures of fused hemal arches (**Figure 9F**). However, TRAP activity is absent on the surface of the fusing centra (**Figure 9E**).

DISCUSSION

This study analyzes the structure and variability of the postcranial skeleton in juvenile medaka raised at three different stocking densities. In particular, the focus is set on the effects of rearing density on growth, bone mineralization, meristic counts of skeletal elements, and skeletal anomalies. The results from this study could help distinguishing between skeletal variants that can occur in WT animals, anomalies related to laboratory rearing conditions and anomalies related to genetic strains. Thus, when screening for skeletal phenotypes resulting from gene editing, it is fundamental to take into account the rearing conditions (i.e., the influence of the

environment), natural variability, skeletal phenotypic plasticity, and the genetic background along with species-specific peculiarities.

The Response of the Skeleton to Rearing Density: Natural Variability or Malformations?

Almost all the observed medaka are affected by at least one skeletal anomaly (**Table 2**). Some of them appeared to be not significantly related to rearing density. For example, we observe variations in the hemal arches (**Figure 3**) that are possibly linked to SL rather than stocking density. This shape variability could be considered as a developmental feature that appears in larger medaka (for HD medaka: SL> 7.5 mm, median: 11.9 mm), as evidenced by the absence of significant differences in both the frequency and position of these features between the density groups. Generally, our data indicate that the frequency of individuals affected by anomalies of the arches and of all fins except the caudal fin, are not significantly dependent on rearing densities. Thus, these can be considered as natural variations. To discern which anomaly can be considered as natural variation and which is a deformation is difficult, to say the least. Following the definition of Mary West-Eberhard (19), "anomalies, or low-frequency discrete phenotypes, along with seemingly unpatterned variation called imprecision or noise, are often passed over in studies of variation, as if unusual variation were the enemy of insight" (19, page 205). Referred to as 'minor skeletal variants', numerous skeletal anomalies have been described in

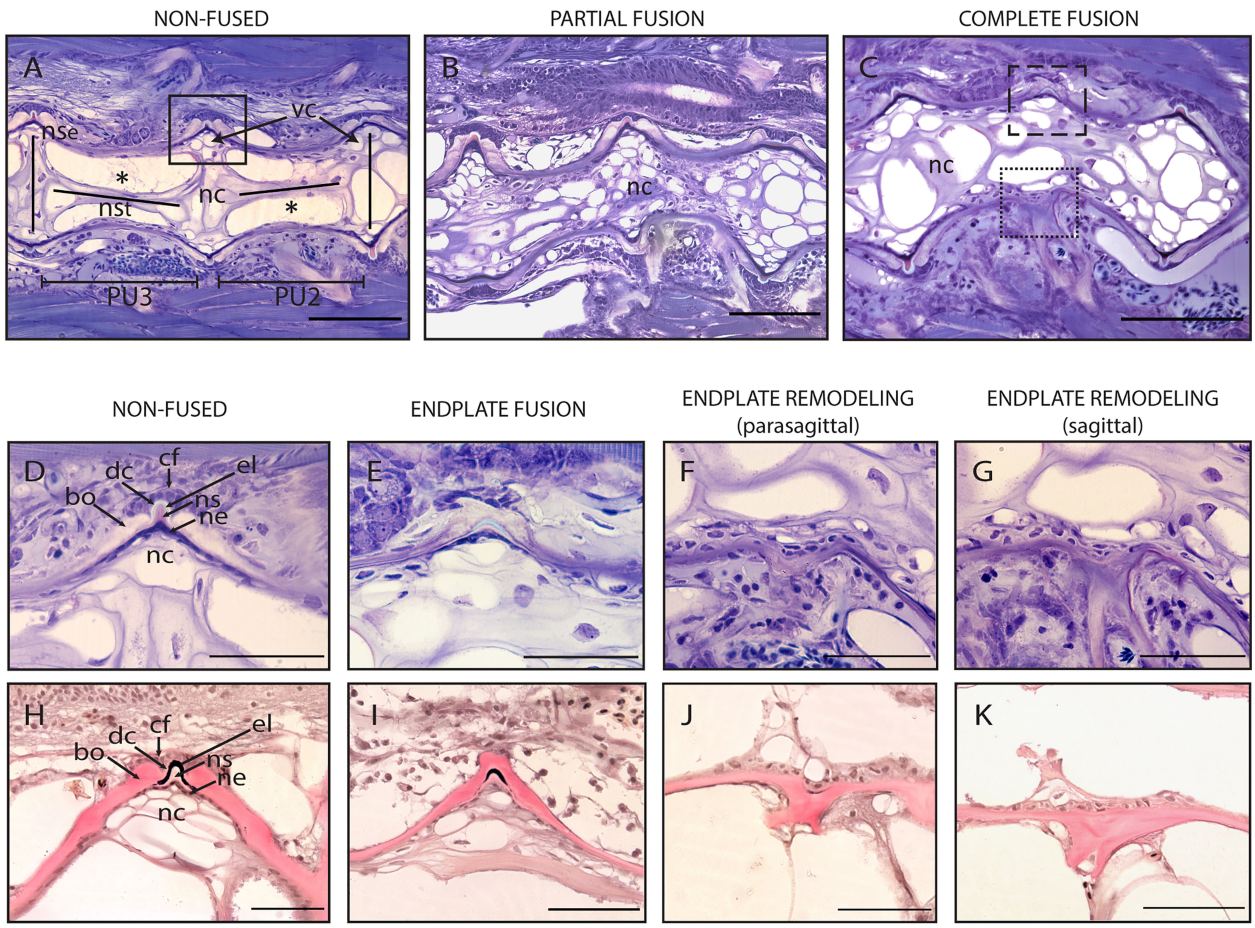

FIGURE 8 | Non-fused and fused vertebral centra. **(A–C)** Overview of non-fused preural centra, partial fusion and complete fusion. Sagittal sections through preural 2 and 3 (PU2, PU3). **(D–K)** Vertebral body endplates at different stages of vertebral body fusion. **(A)** Two non-fused vertebral centra. The box indicates an intact intervertebral ligament, similar to the one magnified in **(D, H)**. **(B)** Partial fusion between two centra. The dorsal IVS is still intact, ventrally the vertebral body endplates are fused. **(C)** Complete fusion. Dorsally (dashed box), the endplates are fused, the intervertebral ligament is still present. Ventrally (dotted box), the fusion is complete, and the intervertebral ligament has disappeared. **(D, H)** Non-fused dorsal endplates with regular intervertebral ligaments. **(E, I)** Beginning of vertebral body fusion, dorsal. Vertebral body endplates are bridged by bone, intervertebral ligaments are still present. **(F, J)** Endplate remodeling (parasagittal plane), advanced vertebral body fusion. Only remnants of the outer elastin layer as a trace of the ventral intervertebral ligament can be recognized. **(G, K)** Endplate remodeling (sagittal plane), advanced vertebral body fusion as in F,J. The elastin layer and any other traces of the ventral intervertebral ligament are completely absent. **(A–G)** Toluidine Blue staining. **(H–K)** Elastin staining (Verhoeff). nc, notochord; *, notochord vacuoles; PU2, preural 2; PU3, preural 3; bo, bone; cf, collagen type I fiber bundles; dc, dense collagen type I matrix; el, elastin; nc, notochord cells; ne, notochord epithelium; ns, notochord sheath; nse, notochord septum; nst, nochord strand; vc, vacuolated chordocytes. Scale bars = 100 µm **(A–C)** and 50 µm **(D–K)**.

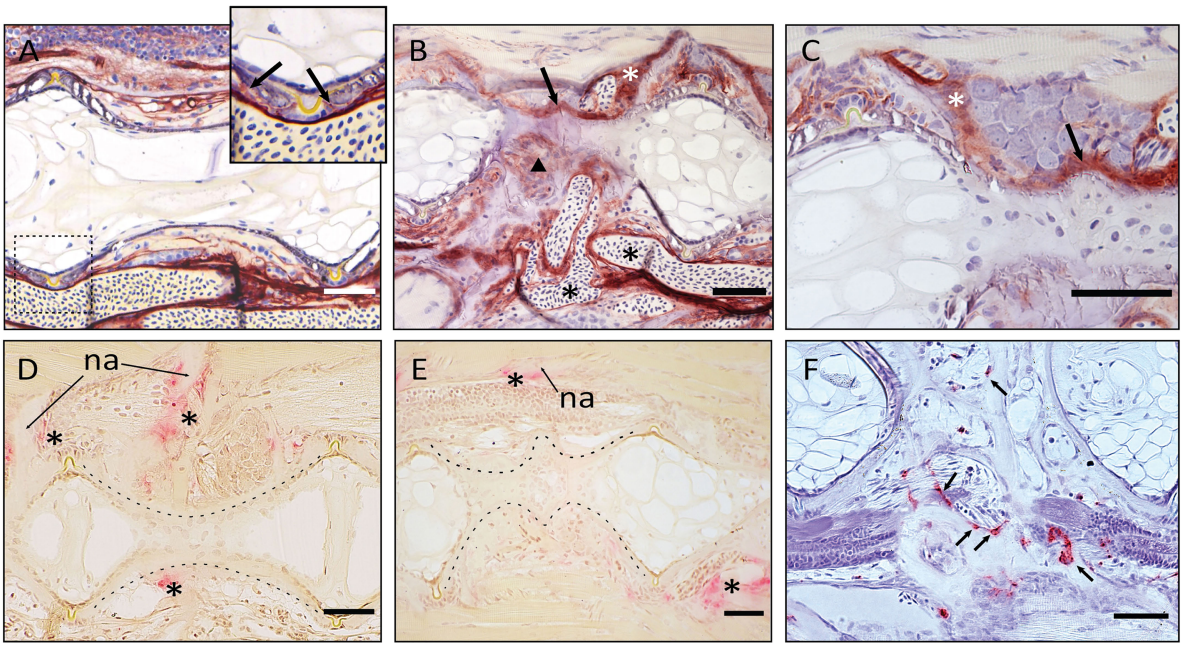

FIGURE 9 | Demonstration of ALP and TRAP activity on the fused vertebral bodies. **(A–C)** ALP staining of vertebral bodies, sagittal sections, at the level of the intervertebral space. Dark red is indicative of ALP activity. **(A)** normal vertebral body. The enlarged picture shows the ventral intervertebral ligament in the dashed box. ALP is regularly expressed by osteoblasts, as indicated by the arrows. **(B)** Fused vertebral bodies. ALP is detected over the intervertebral space, connecting the fusing vertebral bodies (arrow), in the unorganized fusing hemal arches (arrowhead), as well as along the arches (white asterisk). Highly unorganized blood vessels are indicated by the black asterisks. ALP in endothelial cells of blood vessels should not be confused with osteoblast-secreted ALP. **(C)** Fusion centrum, at larger detail. ALP signal bridges neighboring vertebral bodies (arrow) and is detected along the fusing neural arches (white asterisk). **(D–F)** TRAP activity in fusing vertebral bodies, the dashed lines help visualizing the normal and fusing centra. **(D–E)** TRAP staining according to Witten et al. (44). Asterisks mark TRAP activity, detectable only at the endosteum of neural (asterisks above the centrum) and hemal (asterisk below the centrum) arches in control and fusing vertebral bodies. TRAP-positive osteoclasts are not detectable on the fusing vertebral centra **(E)**. na: neural arch. **(F)** TRAP staining according to Nemoto et al. (50). Parasagittal section of fusing vertebral bodies. TRAP-positive osteoclasts (arrows) are involved in the modeling of hemal arches after fusion has occurred. Scale bars = 50 μm.

terrestrial mammals, including mice, small rodents, and humans (19, 55). In particular, in rodents, up to 98% of individuals showed at least one skeletal variant (56–59). These studies challenge the meaning of 'normal' because there are no 'normals' as such in nature (19). Likewise, also in some freshwater fish, minor skeletal variants have been described. Martini et al. (21) illustrates the existence of some skeletal variants (referred to as 'background anomalies') in wildtype zebrafish, whose occurrence is unaffected by the experimental conditions. Ferreri et al. (29) report that 87.2% of wild zebrafish display at least one skeletal anomaly, compared to 93.4% in the reared progeny of the same wild fish. In contrast, skeletal variability in marine species is rarely reported, except for fish sampled from polluted waters or aquaculture (60–62).

The Effects of Rearing Density on the Skeleton of Medaka

The first clear outcome of this study is that rearing densities greater than 5 medaka/L produce significantly shorter (SL) juveniles, whose length progressively decreases with increasing densities. The observation of decreased length as a consequence of high density is in line with similar studies performed on gilthead seabream (*Sparus aurata*), zebrafish, rainbow trout (*Oncorhynchus mykiss*), and halibut (*Hippoglossus hippoglossus L.*) (21, 62–64). However, it is challenging to determine whether density is the only factor influencing the growth or if there are other confounding factors at play. In this study, feeding *ad libitum* three times per day was meant to avoid the development of size differences due to food shortage. However, the possible instauration of some "size-hierarchy" in crowded aquaria (65) could have led to competition between smaller and larger individuals, thus reducing the access to food for smaller individuals.

At 40 dph (SL range: 7-18 mm), the vertebral column of all animals in this study is completely mineralized. This corresponds to the observation of Iwamatsu (45) who described a fully mineralized vertebral column in medaka (d-rR strain, reared at 26°C) starting from a TL of 10 mm. As shown in **Figure 5**, the delay in mineralization of dermal fin rays and fin endoskeletal elements observed at higher densities is significantly related to the reduced length of HD animals and not to the HD condition *per se*.

In this study, the meristic counts of all elements are reported for a laboratory wildtype strain (**Supplementary Table 3**). Our data are in line with those reported by Parenti (22) and Roberts (23) for wild adult medaka sampled in various regions of Asia. The minor differences we found

could be ascribed to particular traits from our laboratory strain, potential age differences (lower number of pectoral rays) or the possible influence of the natural environment (higher number of caudal rays). In this study, we observe only minor differences between the density groups: the number of vertebral bodies and the number of anal fin rays. The presence of 29 instead of 30-32 vertebrae is found in two HD individuals, however this is likely due to the complete fusion of preural 2 and 3. MD juveniles show higher median values for anal fin rays and pterygophores compared to LD and HD animals. A single HD medaka shows a minimum number of 17 anal rays, but this could be related to the small size of the individual (SL: 8 mm). Ali and Lindsey (25) report that in medaka, caudal and anal ray counts are the most susceptible to changes in response to varying environmental factors up to hatching, however in our study newly-hatched larvae are immediately subjected to different experimental conditions.

Similar to meristic counts that are found to have little variance, the percentage of medaka with at least one skeletal anomaly does not significantly vary between the three experimented densities (95% LD-, 98% MD-, and 97% HD-juveniles), with the lowest incidence found in the LD group (**Table 2**). The presence of at least 95% of medaka affected by skeletal anomalies can be explained by the methodology used. Our detailed analysis considers any detectable minor variation in size and shape of skeletal elements, which implies that diverse anomaly types (i.e., bifid neural spine, kypho-lordosis, vertebrae fusions, or misshapen caudal extra ossicle) are listed in the calculation of the metrics, regardless of their severity and associated functional impairment. Coherently, even the malformation index (number of anomalies per deformed individual) does not vary between the three groups.

Interestingly, the frequency of individuals with axis or vertebral centra anomalies progressively increases from the LD- to the MD- and HD group (45%, 59% and 69%, respectively; **Table 2**), with significant differences between the LD and HD group. Likewise, vertebral body anomalies and axis deviations are predominant in laboratory zebrafish reared at high density and gilthead seabream under intensive farming conditions (21, 66). Therefore, these anomalies could be considered as density-enhanced deformities.

In this study it was observed that the frequency of vertebral centra anomalies increases from cranial to caudal in all experimental groups. This pattern is also observed in both wild and reared zebrafish (29). In contrast, anomalies of neural and hemal arches in medaka do not show regional differences but generally display a higher degree of variability, regardless of the rearing density. In zebrafish, neural and hemal arches are also highly variable, affecting up to 50% of wild zebrafish. In captivity, this percentage can increase up to 80% (29) but Martini *et al.* (21) report that arch anomalies in the caudal complex increase at high densities. Morphological investigations on zebrafish or medaka mutants often highlight the independent response of vertebral centra and arches (15, 67–69).

Concerning the anomalies of paired and unpaired fins, this investigation identifies the caudal fin as the most variable and responsive to the tested densities. It is noteworthy that two medaka individuals (one from LD and one from HD group) lack the right or left pelvic fin rays and the basipterygium.

Rearing Density Increases Variation in Caudal and Caudal Complex Vertebrae and Caudal Fin Endoskeleton

The caudal complex vertebrae and the caudal fin endoskeleton of teleosts display a large degree of natural variation (70, 71). The results from this study show that increasing stocking density has an additional effect on the frequency of anomalies in the caudal and caudal complex vertebrae. Behavioral studies on rainbow trout demonstrated that high stocking density has a significant effect on several parameters, including swimming activity, oxygen consumption and muscular activity, compared to low rearing densities, with substantial changes in the swimming trajectories and the space utilization (46, 72). In zebrafish and other carp fishes (Cyprinids), pheromone release yield alarm reactions that stimulate agitated swimming and abrupt movements (73). Altered behavioral patterns involves burst swimming, circling, jumping and erratic movements, as a response to aggressive individuals (74). It could be hypothesized that such behavioral mechanisms are in place when zebrafish or medaka are reared at high density. During swimming, the vertebral column of fish flexes laterally. An *in vivo* x-ray motion analysis on striped bass (*Morone saxatilis)* reveals regional differences in lateral bending throughout the startle response (escape behavior), which results in large body bending generating vertebral rotations and translations. The study unveils greater bending in the caudal region, with the maximum attained angle in the caudal complex (75). Imaging of lateral displacement and curvature profiles during slow swimming and fast startle response in zebrafish reveal changes in the body curvature and strain distribution. During burst swimming the curvature of the caudal region increases, compared to a stiff head and abdominal region (76). Therefore, increased burst swimming due to the interactions between more individuals in high density could elicit greater mechanical loading on the caudal vertebrae. Mechanical stress is a fundamental player in bone formation and mineralization. Mechanical strain, primarily exerted through muscular activity, is required to maintain bone mass and reshape the bony structures (77–79). In zebrafish, swim-training during early development accelerates both perichondral and intramembranous bone formation (80). In adult zebrafish and medaka, daily sessions of physical training increase bone formation and mineralization, thereby promoting a healthy skeletal development (14, 81). In contrast, exhaustive training is shown to induce lordosis in zebrafish and seabass *Dicentrarchus labrax* (82, 83). Still, hemal lordosis has a great recovery potential in zebrafish juveniles: when transferred from a laminar flow to "static" water, over 90% of the lordotic individuals resume their straight vertebral column after one week (84). In Atlantic salmon (*Salmo salar*), altered mechanical load has been related to anterior-posterior compression of the vertebral column. The underlying hypothesis is a possible transformation of the bone growth zones and the concomitant replacement of the intervertebral notochord tissue by cartilaginous tissues (85). In light of all this, it can be proposed that distorted swimming

resulting from high density rearing affects muscular activity and can possibly increase anomalies with a significant impact on the skeletal phenotypes.

Fusion of Preural Centra: Insights Into the Formation and Remodeling Mechanisms of Acellular Bone

Vertebral body fusions can have different etiologies: they can be the result of injuries, infections (86), or abnormal posture. They can have unknown origins but they are also part of normal ontogenetic or phylogenetic processes. Non-pathological fusion of vertebrae is recorded in numerous extant and extinct vertebrates (87–90): the best-known examples are fusion of sacral vertebrae in tetrapods to provide support and rigidity (87, 88), and fusion of vertebrae in birds and oviraptorid dinosaurs to provide locomotion (89, 90). In some teleosts, vertebral body fusions in the caudal complex are an ontogenetic step in the development of the caudal fin endoskeleton (37, 70, 71).

Studies on zebrafish and Atlantic salmon have shown that fusions can occur *via* different processes, according to the stage of vertebral body development: (a) early fusions occur by continuous mineralization of the notochord sheath; (b) once bone has formed around the mineralized notochord sheath (autocentrum), fusions can occur by ectopic bone bridging the intervertebral space; (c) fusion of fully developed vertebral bodies typically involves the occurrence of ectopic cartilage located in the intervertebral space that is subsequently remodeled into bone (47, 91–93). Fusions of preural centra observed in this study are an example of the second fusion scenario (autocentrum fusion, **Figure 10A**).

The design of this study does not allow to follow the process of vertebral fusion in single individuals, but we observe a large number individuals in different stages of vertebral fusions. In view of the known fusion processes described in zebrafish and Atlantic salmon, it is possible to hypothesize about the sequence of events that lead to vertebral fusion in medaka (**Figure 10B**). The whole mount-staining reveals that the hemal arches fuse first and the ventral side of the fusion is remodeled and reshaped prior to the dorsal side. This leads to a dorsal-ventral asymmetry, which has been confirmed on a cellular level by the histological investigations. Assuming that the basis of the hemal arches fuses first, it could be speculated that the vertebral centra fuse as a secondary compensatory mechanism to the fusion of the arches. However, this latter hypothesis would require additional studies. The activity of the enzymes TRAP and ALP were investigated as proxies for osteoclasts and osteoblasts respectively, with the aim of gaining additional insights into the processes involved in the reshaping of the fused centra. In fact, remodeling and reshaping of teleost bone is based on the interplay between osteoblasts and osteoclasts (16), different from mammals where osteocytes regulate bone remodeling and osteoclast activity. In mammals, most osteoclasts are multinucleated giant cells that can easily be detected with standard histological procedures (94). Multinucleated osteoclasts can be absent in teleosts with acellular bone (as in medaka), yet acellular bone is resorbed, remodeled and responsive to mechanical load (14, 95, 96). According to Nemoto *et al.* (50) and Yu *et al.* (97), remodeling occurs in medaka by means of small and mononucleated osteoclasts. Indeed, acellular teleost bone must be remodeled in the frame of allometric growth, adaptation to mechanical load, and continuous tooth replacement (16, 48, 53, 95, 97–100). In growing teleosts, osteoclasts are present at endosteal bone surfaces enlarging skeletal elements, such as hemal and neural arches, but not on the vertebral centra (16, 44, 50, 53, 101). In our samples, partially and completely fused vertebral centra are negative for the osteoclast marker TRAP, even in locations that are evidently subjected to reshaping (**Figure 9**). Moreover, the lack of TRAP positive reversal lines renders the identification of previous remodeling events unfeasible (16). Possibly, at the vertebral centra, reshaping and fusion is only done by bone apposition. However, the absence of osteoclasts and bone remodeling demands further investigations.

Knowledge Applied to Biomedical Research

Large scale screens for zebrafish mutants with dominant effect on morphology reveal several skeletal defects (102). Interestingly, many of these defects are also observed in individuals from natural zebrafish populations and wildtype laboratory zebrafish strains (21, 29). If 'background' or rearing density-related skeletal anomalies in wildtype medaka resemble defects generated in disease models is discussed below.

Sporadic mutations that can cause curvatures of the vertebral column naturally occur in teleosts. The *curveback* guppy occasionally presents a spinal deformity that resembles human idiopathic scoliosis (103), and wildtype zebrafish frequently display scoliotic vertebrae in the region of the caudal complex (21). Several zebrafish and medaka mutants exist with phenotypes that resemble scoliosis in humans. Zebrafish with a mutation in a kinesin family 6 protein gene *kif6* reveal a marked curvature of the abdominal and caudal spine (104). The *col8a1a* zebrafish mutant (*leviathan* mutant) is another model, associated with notochord defects and congenital vertebral malformations (105). Motile ciliary defects are a further factor promoting scoliosis in both zebrafish and medaka (106, 107). Thus, ciliary defects are correlated with a more extended skeletal phenotype, referred to as lordokyphosis, including left-right asymmetry of the body axis. These mutants are designated as *wavy* medaka (108, 109). Our investigation in medaka reveals that extended axis deviations are rare: we do not observe scoliosis or kyphosis, and cases of lordosis affect less than 1% of the individuals. However, more localized lordotic, scoliotic and kyphotic deviations, involving up to 4 vertebral bodies, are more frequent, most prominently in high density conditions.

Vertebral fusions, commonly observed in wildtype fish models, can also result from mutations. In mutants, fusions are mainly observed in the abdominal and in the caudal region. In medaka, disruption of vesicle trafficking from the Golgi to the ER by a nonsense mutation in *sec24d* gene induces vertebral centra fusions (110). A similar effect is observed as the result of the knockout of a gene coding for a metal ion transporter (*SLC39A8*) in zebrafish (111). *osx/sp7* mutations in juvenile zebrafish lead to low bone mineral density and intervertebral disk degeneration (112). *sp7-/-*

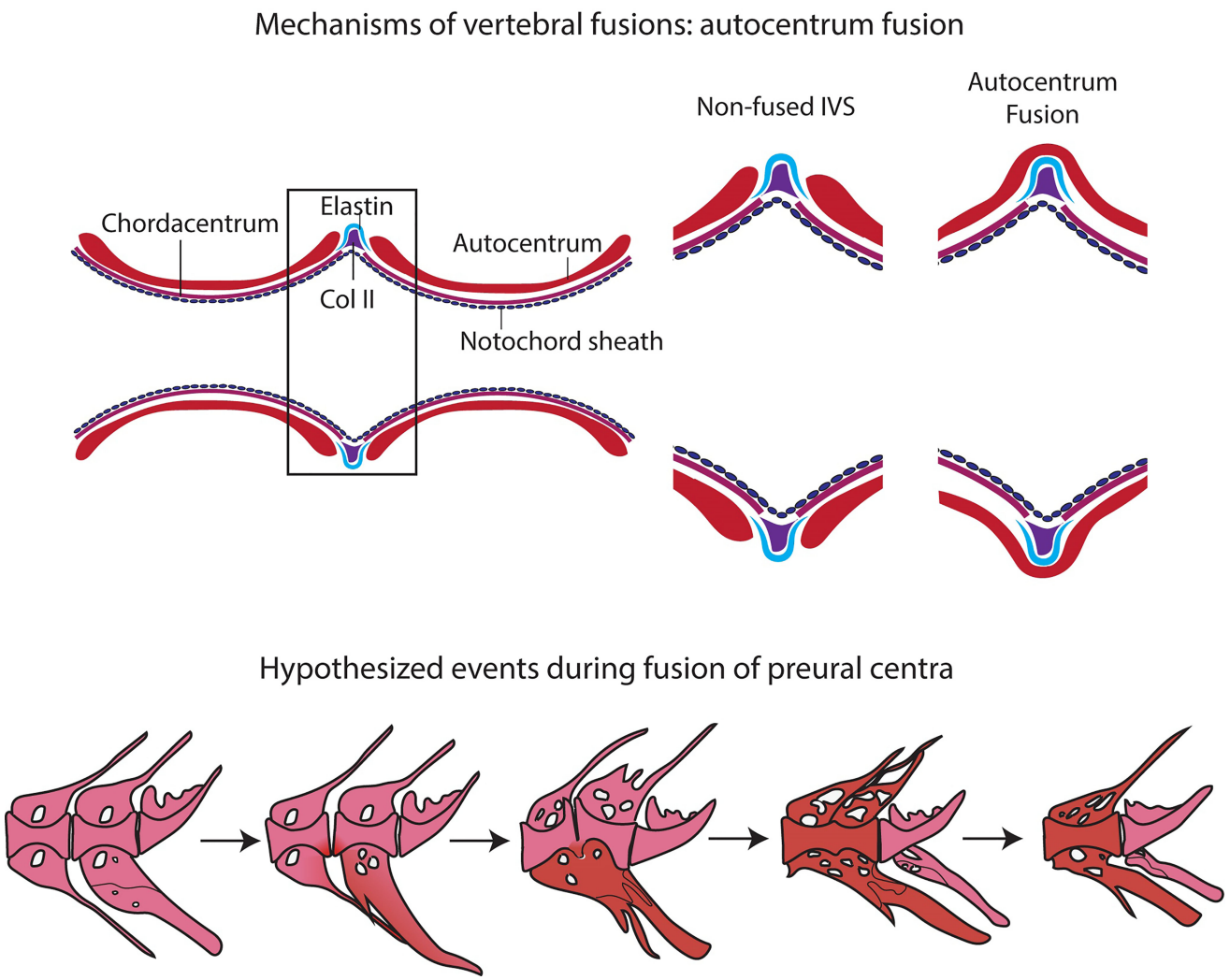

FIGURE 10 | Events in vertebral body fusions. **(A)** In normal conditions, two consecutive vertebrae are separated by regular intervertebral spaces, with intervertebral ligament and notochord tissue. Schematic representation of autocentrum fusion: ectopic bone (red) is deposited over the IVS, with the intervertebral ligament still intact. **(B)** Hypothesized events during vertebral body fusion based on static observations. It can be hypothesized that the fusion starts at the ventral side by fusion of the hemal arches. The vertebral bodies consequently fuse ventrally first, with a regularly shaped intervertebral space on the dorsal side. Next, the vertebral bodies fuse also dorsally, and the fused centrum is reshaped into a normally looking (albeit elongated) vertebral centrum. In pink: normal; in red: fusing/fused.

adults reveal bent regions of the spine, compromised osteocyte lacunar profile, alterations in mineral density and altered collagen organization (113, 114). Interestingly, *osx* knockout in zebrafish is not linked to embryonic and post-embryonic defects in bone formation (113). According to our work, vertebral fusions in early medaka juveniles are detected only in the caudal complex. Although abdominal and caudal vertebrae are affected by skeletal anomalies, no fusion is observed in the abdominal or caudal region, in contrast to mutants.

Genetic mutations can also affect the patterning of the arches. In medaka, disruption of *sp7* leads to the absence of neural and hemal arches, although it does not affect formation of vertebral centra anlagen, i.e., the segmented mineralization of the notochord sheath, remains normal (115, 116). Likewise, the zebrafish *fused somites/tbx6 (fss)* mutants display normal vertebral centra and misplaced neural and hemal arches (67, 117). In addition to *tbx6*, Lleras-Forero *et al.* (118) mutated several genes involved in the zebrafish segmentation clock. Regardless of a disrupted segmentation clock, the notochord is normally segmented with regular chordacentra formation. On the contrary, the mutants display disrupted myotome boundaries and completely misplaced and deformed neural and hemal arches. Interestingly, we have no references about such severe deformities of the arches in wildtype medaka and observation in wildtype zebrafish are rare (21).

Concerning the unpaired fins (caudal, dorsal and anal), severe defects are rarely observed in wildtype individuals of zebrafish and medaka. In contrast, these are a prevalent characteristic of some

severe mutant phenotypes. Henke and colleagues (102) report mutants with various degrees of phenotypes ranging from the reduction in ray number to the complete fin loss. Similarly, loss of function in the ectodysplasin (*eda*) and ectodysplasin receptor (*edar*) genes result in anomalies of the dermal skeleton (119). Anomalies of the paired fins (pectoral and pelvic) are more frequently observed in wild and wildtype zebrafish. Our investigation on wildtype medaka reveals that the pectoral fin is the least affected, whereas complete loss of pelvic fin rays and the supporting endoskeleton naturally occurred in two individuals.

In addition to considering the natural occurrence of skeletal anomalies in wild and wildtype individuals that might resemble defects resulting from genetic mutations, it is necessary to consider species-specific differences. The skeleton in medaka is overall more stable and less subject to anomalies and variations than zebrafish. According to this study, vertebral fusions are restricted to the caudal complex in medaka and are not detected in the caudal region. In contrast, partial and complete vertebral fusions are detected in wildtype zebrafish, however they are found less frequently in low-density rearing conditions (21). Likewise, axis deviations are rare in medaka, but more frequent in zebrafish, especially scoliosis affecting the preural vertebrae. A possible explanation to this reduced variability observed in medaka compared to zebrafish, is the smaller genome size but not the number of protein-coding genes (12, 13, 120). Variability is a fundamental process in development and evolution. However, as the organism complexity increases, the ability to alter a process or a character without effects on others processes and characters decreases (121). Organisms have the ability to reduce such variation. This tendency to buffer genetic and/or environmental perturbations is referred to as canalization (20, 122, 123). Thus, genetic or environmental canalization in advanced teleosts could explain the reduction in phenotypic plasticity of the skeleton.

DATA AVAILABILITY STATEMENT

The original contributions presented in the study are included in the article/**Supplementary Material**. Further inquiries can be directed to the corresponding author.

ETHICS STATEMENT

The animal study was reviewed and approved by Italian Ministry of Health, approval N° 133/2021-PR.

AUTHOR CONTRIBUTIONS

CDB performed the experiments, analyzed samples and data, and wrote the first draft of the manuscript. CB contributed to conception and design of the study and to data analyses. PW contributed to histological and histoenzymatic investigations. ZD and AM collaborated during the experimental rearing and setup. MS contributed to the statistical evaluation of the data. All authors contributed to manuscript revision, read, and approved the submitted version.

FUNDING

This project has received funding from the European Union's Horizon 2020 research and innovation program under the Marie Skłodowska-Curie grant agreement No. 766347 - BIOMEDAQU.

ACKNOWLEDGMENTS

We are grateful to the BIOMEDAQU network for inspiring and constructing discussions. We thank Massimiliano Graziani for the support provided in the fish care at University of Tor Vergata, Mieke Soenens for the valuable insights on histology. This work is part of the PhD thesis of CB.

SUPPLEMENTARY MATERIAL

The Supplementary Material for this article can be found online at: https://www.frontiersin.org/articles/10.3389/fendo.2022.893699/full#supplementary-material

REFERENCES

1. Harris MP, Henke K, Hawkins MB, Witten PE. Fish Is Fish: The Use of Experimental Model Species to Reveal Causes of Skeletal Diversity in Evolution and Disease. *J Appl Ichthyol* (2014) 30(4):616–29. doi: 10.1111/jai.12533
2. Witten PE, Harris MP, Huysseune A, Winkler C. Chapter 13 - Small Teleost Fish Provide New Insights Into Human Skeletal Diseases. In: HW Detrich, Westerfield M and LI Zon, editors. *Methods in Cell Biology* London: Academic Press (2017). 138:321–46.
3. Yasutake J, Inohaya K, Kudo A. Twist Functions in Vertebral Column Formation in Medaka, *Oryzias latipes*. *Mech Dev* (2004) 121(7-8):883–94. doi: 10.1016/j.mod.2004.03.008
4. Naruse K, Tanaka M, Takeda H. *Medaka: A Model for Organogenesis, Human Disease, and Evolution*. New York: Springer Science & Business Media (2011).
5. Ishikawa Y. Medakafish as a Model System for Vertebrate Developmental Genetics. *BioEssays* (2000) 22:487–95. doi: 10.1002/(SICI)1521-1878(200005)22:5<487::AID-BIES11>3.0.CO;2-8
6. Wittbrodt J, Shima A, Schartl M. Medaka - A Model Organism From the Far East. *Nat Rev Genet* (2002) 3(1):53–64. doi: 10.1038/nrg704
7. Yamamoto T. *Medaka (Killifish): Biology and Strains*. Tokyo: Yugakusha (1975).
8. Furutani-Seiki M, Wittbrodt J. Medaka and Zebrafish, an Evolutionary Twin Study. *Mech Dev* (2004) 121(7-8):629–37. doi: 10.1016/j.mod.2004.05.010
9. Kinoshita M, Murata K, Naruse K, Tanaka M. *Medaka - Biology, Management and Experimental Protocols*. Singapore: Wiley-Blackwell (2009).
10. Sampetrean O, Iida S, Makino S, Matsuzaki Y, Ohno K, Saya H. Reversible Whole-Organism Cell Cycle Arrest in a Living Vertebrate. *Cell Cycle* (2009) 8(4):620–7. doi: 10.4161/cc.8.4.7785
11. Miyanishi H, Uchida K. Establishment of a Simplified System to Evaluate Salinity Preference and Validation of Behavioral Salinity Selection in the Japanese Medaka, *Oryzias latipes*. *Fishes* (2021) 6(2):18. doi: 10.3390/fishes6020018

12. Gregory TR. Coincidence, Coevolution, or Causation? DNA Content, Cell Size, and the C-Value Enigma. *Biol Rev* (2001) 76:65–101. doi: 10.1017/S1464793100005595
13. Kasahara M, Naruse K, Sasaki S, Nakatani Y, Qu W, Ahsan B, et al. The Medaka Draft Genome and Insights Into Vertebrate Genome Evolution. *Nature* (2007) 447(7145):714–9. doi: 10.1038/nature05846
14. Ofer L, Dean MN, Zaslansky P, Kult S, Shwartz Y, Zaretsky J, et al. A Novel Nonosteocytic Regulatory Mechanism of Bone Modeling. *PloS Biol* (2019) 17 (2):e3000140. doi: 10.1371/journal.pbio.3000140
15. To TT, Witten PE, Huysseune A, Winkler C. An Adult Osteopetrosis Model in Medaka Reveals the Importance of Osteoclast Function for Bone Remodeling in Teleost Fish. *Comp Biochem Physiol C Toxicol Pharmacol* (2015) 178:68–75. doi: 10.1016/j.cbpc.2015.08.007
16. Witten PE, Huysseune A. A Comparative View on Mechanisms and Functions of Skeletal Remodelling in Teleost Fish, With Special Emphasis on Osteoclasts and Their Function. *Biol Rev Camb Philos Soc* (2009) 84 (2):315–46. doi: 10.1111/j.1469-185X.2009.00077.x
17. Ofer L, Zaslansky P, Shahar R. A Comparison of the Structure, Composition and Mechanical Properties of Anosteocytic Vertebrae of Medaka (*O. latipes*) and Osteocytic Vertebrae of Zebrafish (*D. Rerio*). *J Fish Biol* (2020) 98:995–1006. doi: 10.1111/jfb.14334
18. Balon EK. Alternative Ontogenies and Evolution: A Farewell to Gradualism. In: BK Hall, RD Pearson and GB Müller, editors. *Environment, Development, and Evolution Toward a Synthesis*. Cambridge: The MIT Press (2003). 37–66.
19. West-Eberhard MJ. *Developmental Plasticity and Evolution*. New York (USA: Oxford University Press (2002).
20. Debat V, David P. Mapping Phenotypes: Canalization, Plasticity and Developmental Stability. *Trends Ecol Evol* (2001) 16(10):555–61. doi: 10.1016/S0169-5347(01)02266-2
21. Martini A, Huysseune A, Witten PE, Boglione C. Plasticity of the Skeleton and Skeletal Deformities in Zebrafish (*Danio rerio*) Linked to Rearing Density. *J Fish Biol* (2021) 98:971–86. doi: 10.1111/jfb.14272
22. Parenti LR. A Phylogenetic Analysis and Taxonomic Revision of Ricefishes, *Oryzias* and Relatives (Beloniformes, Adrianichthyidae). *Zoolog J Linn Soc* (2008) 154(3):494–610. doi: 10.1111/j.1096-3642.2008.00417.x
23. Roberts TR. Systematic Observations on Tropical Asian Medakas or Ricefishes of the Genus *Oryzias*, With Descriptions of Four New Species. *Ichthyol Res* (1998) 45(3):213–24. doi: 10.1007/BF02673919
24. Uwa H, Parenti LR. Morphometric and Meristic Variation in Ricefish, Genus *Oryzias*: A Comparison With Cytogenetic Data. *Japanese J Ichthyology* (1988) 35(2):159–66. doi: 10.11369/jji1950.35.159
25. Ali MY, Lindsey CC. Heritable and Temperture-Induced Meristic Variation in the Medaka, *Oryzias latipes*. *Can J Zool* (1974) 52(8):959–76. doi: 10.1139/z74-128
26. Iwamatsu T, Nakamura H, Ozato K, Wakamatsu Y. Normal Growth of the "See-Through" Medaka. *Zoolog Sci* (2003) 20(5):607–15. doi: 10.2108/zsj.20.607
27. Iwamatsu T. Growth of the Medaka (II) – Formation of Fins and Fin Appendages. *Bull Aichi Univ Educ* (2013) 62:53–60.
28. Kimura T, Shinya M, Naruse K. Genetic Analysis of Vertebral Regionalization and Number in Medaka (*Oryzias latipes*) Inbred Lines. *G3 (Bethesda)* (2012) 2(11):1317–23. doi: 10.1534/g3.112.003236
29. Ferreri F, Nicolais C, Boglione C, Bertolini B. Skeletal Characterization of Wild and Reared Zebrafish: Anomalies and Meristic Characters. *J Fish Biol* (2000) 56(5):1115–28. doi: 10.1006/jfbi.2000.1233
30. Avdesh A, Chen M, Martin-Iverson MT, Mondal A, Ong D, Rainey-Smith S, et al. Regular Care and Maintenance of a Zebrafish (*Danio rerio*) Laboratory: An Introduction. *J Vis Exp* (2012) 69):e4196. doi: 10.3791/4196
31. Romer AS. *The Vertebrate Body*. Philadelphia: W.B. Sauders Company (1970).
32. Arratia G, Schultze HP. Reevaluation of the Caudal Skeleton of Certain Actinopterygian Fishes: III. Salmonidae. Homologization of Caudal Skeletal Structures. *J Morphol* (1992) 214:187–249. doi: 10.1002/jmor.1052140209
33. Bensimon-Brito A, Cancela ML, Huysseune A, Witten PE. The Zebrafish (*Danio rerio*) Caudal Complex - A Model to Study Vertebral Body Fusion. *J Appl Ichthyology* (2010) 26(2):235–8. doi: 10.1111/j.1439-0426.2010.01412.x
34. Wiley EO, Fuiten AM, Doosey MH, Lohman BK, Merkes C, Azuma M. The Caudal Skeleton of the Zebrafish, *Danio rerio*, From a Phylogenetic Perspective: A Polyural Interpretation of Homologous Structures. *Copeia* (2015) 103(4):740–50. doi: 10.1643/CG-14-105
35. Nybelin O. Zur Morphologie Und Terminologie Des Schwanzskelettes Der Actinopterygier. *Arkiv för Zoologi* (1963) 15:485–516.
36. Patterson C. The Caudal Skeleton in Lower Liassic Pholidophorid fishes. *Bull Br Mus Nat Hist Geol* (1968) 16:201–39.
37. Fujita K. Caudal Skeleton Ontogeny in the Adrianichthyid Fish, *Oryzias latipes*. *Japanese J Ichthyology* (1992) 39(1):107–09. doi: 10.11369/jji1950.39.107
38. Boglione C, Gisbert E, Gavaia P, E. Witten P, Moren M, Fontagné S, et al. Skeletal Anomalies in Reared European Fish Larvae and Juveniles. Part 2: Main Typologies, Occurrences and Causative Factors. *Rev Aquacult* (2013) 5:S121–S67. doi: 10.1111/raq.12016
39. Taylor WR, Van Dyke GC. Revised Procedures for Staining and Clearing Small Fishes and Other Vertebrates for Bone and Cartilage Study. *Cybium* (1985) 9:107–19.
40. Campbell I. Chi-Squared and Fisher-Irwin Tests of Two-By-Two Tables With Small Sample Recommendations. *Stat Med* (2007) 26:3661–75. doi: 10.1002/sim.2832
41. Richardson JTE. The Analysis of 2 X 2 Contingency Tables - Yet Again. *Stat Med* (2011) 30:890–92. doi: 10.1002/sim.4116
42. Altman DG, Machin D, Bryant TN, Gardner MJ. *Statistics With Confidence. 2nd Ed*. New York: BMJ Books (2000).
43. Hammer Ø, Harper DAT, Ryan PD. Past: Paleontological Statistics Software Package for Education and Data Analysis. *Palaeontol Electronica* (2001) 4 (1):1–9.
44. Witten PE, Hansen A, Hall BK. Features of Mono- and Multinucleated Bone Resorbing Cells of the Zebrafish Danio rerio and Their Contribution to Skeletal Development, Remodeling, and Growth. *J Morphol* (2001) 250 (3):197–207. doi: 10.1002/jmor.1065
45. Iwamatsu T. Growth of the Medaka (I) – Formation of Vertebrae, Changes in Blood Circulation, and Changes in Digestive Organs. *Bull Aichi Univ Educ* (2012) 61:55–63.
46. Cooke SJ, Chandroo KP, Beddow TA, Moccia RD, McKinley RS. Swimming Activity and Energetic Expenditure of Captive Rainbow Trout *Oncorhynchus mykiss* (Walbaum) Estimated by Electromyogram Telemetry. *Aquacult Res* (2000) 31(6):495–505. doi: 10.1046/j.1365-2109.2000.00470.x
47. Bensimon-Brito A, Cancela ML, Huysseune A, Witten PE. Vestiges, Rudiments and Fusion Events: The Zebrafish Caudal Fin Endoskeleton in an Evo-Devo Perspective. *Evol Dev* (2012) 14(1):116–27. doi: 10.1111/j.1525-142X.2011.00526.x
48. To TT, Witten PE, Renn J, Bhattacharya D, Huysseune A, Winkler C. Rankl-Induced Osteoclastogenesis Leads to Loss of Mineralization in a Medaka Osteoporosis Model. *Development* (2012) 139(1):141–50. doi: 10.1242/dev.071035
49. Humason GL, Presnell JK, Schreibman MP. *Humason's Animal Tissue Techniques*. Baltimore, MD, USA: Johns Hopkins University Press (1997).
50. Nemoto Y, Higuchi K, Baba O, Kudo A, Takano Y. Multinucleate Osteoclasts in Medaka as Evidence of Active Bone Remodeling. *Bone* (2007) 40(2):399–408. doi: 10.1016/j.bone.2006.08.019
51. Gruber H, Marshall G, Nolasco L, Kirchen M, Rimonin D. Alkaline and Acid Phosphatase Demonstration in Human Bone and Cartilage: Effects of Fixation Interval and Methacrylate Embedments. *Stain Technol* (1988) 63:299–306. doi: 10.3109/10520298809107604
52. Stibane F. Histochemical Investigations of the Ontogenetical Development of Acellular Teleost Bones With Special References of the Vertebral Column of *Aphanius mento* (Heckel, 1843). *Zool Jahrb Abt Anat* (1992) 122:449–77.
53. Witten PE, Villwock W. Growth Requires Bone Resorption at Particular Skeletal Elements in a Teleost Fish With Acellular Bone (*Oreochromis niloticus*, Teleostei: Cichlidae). *J Appl Ichthyol* (1997) 13(4):149–58. doi: 10.1111/j.1439-0426.1997.tb00115.x
54. Witten PE, Hall BK. The Ancient Segmented Active and Permanent Notochord. In: A Pradel, JSS Denton and P Janvier, editors. *Ancient Fishes and Their Living Relatives: A Tribute to John G Maisey*. München, Germany: Verlag Dr. Friedrich Pfeil (2021). p. 215–24.
55. Berry AC, Berry RJ. Epigenetic Variation in the Human Cranium. *J Anat* (1967) 101:361–79.

56. Weber W. Genetical Studies on the Skeleton of the Mouse. III. Skeletal Variation in Wild Populations. *J Genet* (1950) 50:174–8. doi: 10.1007/BF02986801
57. Berry RJ. Epigenetic Polymorphism in Wild Populations of *Mus musculus*. *Genet Res* (1963) 4(2):193–220. doi: 10.1017/s0016672300003566
58. Berry RJ, Searle AG. Epigenetic Polymorphism of the Rodent Skeleton. *Proc Zoolog Soc London* (1963) 140(4):577–615. doi: 10.1111/j.1469-7998.1963.tb01990.x
59. Howe WL, Parsons PA. Genotype and Environment in the Determination of Minor Skeletal Variants and Body Weight in Mice. *J Embryol Exp Morph* (1967) 17(2):283–92. doi: 10.1242/dev.17.2.283
60. Boglione C, Costa C. Skeletal Deformities and Juvenile Quality. In: MA Pavlidis and CC Mylonas, editors. *Sparidae* New Delhi: John Wiley & Sons Ltd. (2011).
61. Gavaia PJ, Domingues S, Engrola S, Drake P, Sarasquete C, Dinis MT, et al. Comparing Skeletal Development of Wild and Hatchery-Reared Senegalese Sole (*Solea senegalensis*, Kaup 1858): Evaluation in Larval and Postlarval Stages. *Aquacult Res* (2009) 40(14):1585–93. doi: 10.1111/j.1365-2109.2009.02258.x
62. Boglione C, Gagliardi F, Scardi M, Cataudella S. Skeletal Descriptors and Quality Assessment in Larvae and Post-Larvae of Wild-Caught and Hatchery-Reared Gilthead Sea Bream (*Sparus aurata* L. 1758). *Aquaculture* (2001) 192(1):0–22. doi: 10.1016/S0044-8486(00)00446-4
63. Björnsson B. Effects of Stocking Density on Growth Rate of Halibut (*Hippoglossus hippoglossus L.*) Reared in Large Circular Tanks for Three Years. *Aquaculture* (1994) 123(3-4):259–70. doi: 10.1016/0044-8486(94)90064-7
64. Holm JC, Refstie T, Bø S. The Effect of Fish Density and Feeding Regimes on Individual Growth Rate and Mortality in Rainbow Trout (*Oncorhynchus mykiss*). *Aquaculture* (1990) 89(3-4):225–32. doi: 10.1016/0044-8486(90)90128-A
65. Blaxter JHS. The Enhancement of Marine Fish Stocks. In: *Advances in Marine Biology*. London: Academic Press (2000). 38:1–54.
66. Prestinicola L, Boglione C, Makridis P, Spano A, Rimatori V, Palamara E, et al. Environmental Conditioning of Skeletal Anomalies Typology and Frequency in Gilthead Seabream (*Sparus aurata L.*, 1758) Juveniles. *PloS One* (2013) 8(2):e55736. doi: 10.1371/journal.pone.0055736
67. van Eeden FJM, Granato M, Schach U, Brand M, Furutani-Seiki M, Haffter P, et al. Mutations Affecting Somite Formation and Patterning in the Zebrafish, *Danio rerio*. *Development* (1996) 123:153–64. doi: 10.1242/dev.123.1.153
68. Kota I, Yusuke K, Norihiko M, Seigo H, Masayoshi A, Naho T, et al. Histopathology of a Wavy Medaka. *J Toxicol Pathol* (2016) 29:115–8. doi: 10.1293/tox.2015-0070
69. Takeuchi K. Wavy-Fused Mutants in Medaka *Oryzias latipes*. *Nature* (1966) 211:866–7. doi: 10.1038/211866b0
70. Arratia G. The Caudal Skeleton of Ostariophysan Fishes (Teleostei): Intraspecific Variation in Trichomycteridae (Siluriformes). *J Of Morphol* (1983) 177:213–29. doi: 10.1002/jmor.1051770208
71. Cumplido N, Allende ML, Arratia G. From Devo to Evo: Patterning, Fusion and Evolution of the Zebrafish Terminal Vertebra. *Front Zool* (2020) 17:18. doi: 10.1186/s12983-020-00364-y
72. Bégout Anras ML, Lagardère JP. Measuring Cultured Fish Swimming Behaviour: First Results on Rainbow Trout Using Acoustic Telemetry in Tanks. *Aquaculture* (2004) 240(1-4):175–86. doi: 10.1016/j.aquaculture.2004.02.019
73. Hall D, Suboski MD. Visual and Olfactory Stimuli in Learned Release of Alarm Reactions by Zebra Danio Fish (*BrachyDanio rerio*). *Neurobiol Learn Memory* (1995) 63(3):229–40. doi: 10.1006/nlme.1995.1027
74. Oliveira RF, Silva JF, Simoes JM. Fighting Zebrafish: Characterization of Aggressive Behavior and Winner-Loser Effects. *Zebrafish* (2011) 8(2):73–81. doi: 10.1089/zeb.2011.0690
75. Nowroozi BN, Brainerd EL. X-Ray Motion Analysis of the Vertebral Column During the Startle Response in Striped Bass, *Morone saxatilis*. *J Exp Biol* (2013) 216:2833–42. doi: 10.1242/jeb.085118
76. Muller UK, van Leeuwen JL. Swimming of Larval Zebrafish: Ontogeny of Body Waves and Implications for Locomotory Development. *J Exp Biol* (2004) 207:853–68. doi: 10.1242/jeb.00821
77. Duncan RL, Turner CH. Mechanotransduction and the Functional Response of Bone to Mechanical Strain. *Calcif Tissue Int* (1995) 57:344–58. doi: 10.1007/BF00302070
78. Haelterman N, Lim J. Sensing the Load. *Elife* (2019) 8:e47454. doi: 10.7554/eLife.50210
79. Yavropoulou MP, Yovos JG. The Molecular Basis of Bone Mechanotransduction. *J Musculoskelet Neuronal Interact* (2016) 16(3):221–36.
80. Fiaz AW, Leon-Kloosterziel KM, Gort G, Schulte-Merker S, van Leeuwen JL, Kranenbarg S. Swim-Training Changes the Spatio-Temporal Dynamics of Skeletogenesis in Zebrafish Larvae (*Danio rerio*). *PloS One* (2012) 7(4):e34072. doi: 10.1371/journal.pone.0034072
81. Suniaga S, Rolvien T, Vom Scheidt A, Fiedler IAK, Bale HA, Huysseune A, et al. Increased Mechanical Loading Through Controlled Swimming Exercise Induces Bone Formation and Mineralization in Adult Zebrafish. *Sci Rep* (2018) 8(1):3646. doi: 10.1038/s41598-018-21776-1
82. Kranenbarg S, Waarsing JH, Muller M, Weinans H, van Leeuwen JL. Lordotic Vertebrae in Sea Bass (*Dicentrarchus labrax L.*) Are Adapted to Increased Loads. *J Biomech* (2005) 38(6):1239–46. doi: 10.1016/j.jbiomech.2004.06.011
83. Printzi A, Fragkoulis S, Dimitriadi A, Keklikoglou K, Arvanitidis C, Witten PE, et al. Exercise-Induced Lordosis in Zebrafish *Danio rerio* (Hamilton, 1822). *J Fish Biol* (2020) 98:987–94. doi: 10.1111/jfb.14240
84. A Printzi, D Mazuraisz, PE Witten, J-L Zambonino-Infantez and GR Koumoundouros eds. Recovery of Haemal Lordosis in Juvenile Zebrafish (*Danio rerio*). In: *Aquaculture Europe 21*. Madeira, Portugal: European Aquculture Society.
85. Witten PE, Gil-Martens L, Hall BK, Huysseune A, Obach A. Compressed Vertebrae in Atlantic Salmon *Salmo salar*: Evidence for Metaplastic Chondrogenesis as a Skeletogenic Response Late in Ontogeny. *Dis Aquat Organisms* (2005) 64:237–46. doi: 10.3354/dao064237
86. Peh WCG. Cervical Spine Ankylosing Spondylitis. *Am J Orthop* (2004) 33:310.
87. Hildebrand M, Goslow G. *Analysis of Vertebrate Structure*. New York: Wiley (2001).
88. Abitbol MM. Evolution of the Sacrum in Hominoids. *Am J Phys Anthropol* (1978) 74(1):65–81. doi: 10.1002/AJPA.1330740107
89. Felice RN, O'Connor PM. Ecology and Caudal Skeletal Morphology in Birds: The Convergent Evolution of Pygostyle Shape in Underwater Foraging Taxa. *PloS One* (2014) 9(2):e89737. doi: 10.1371/journal.pone.0089737
90. Hildebrand M. Digging of Quadrupeds. In: M Hildebrand, DM Bramble, KF Liem and DB Wake, editors. *Functional Vertebrate Morphology*. Cambridge: Harvard University Press (1985).
91. Witten PE, Obach A, Huysseune A, Baeverfjord G. Vertebrae Fusion in Atlantic Salmon (*Salmo salar*): Development, Aggravation and Pathways of Containment. *Aquaculture* (2006) 258(1-4):164–72. doi: 10.1016/j.aquaculture.2006.05.005
92. Fjelldal PG, Hansen T, Breck O, Ørnsrud R, Lock EJ, Waagbø R, et al. Vertebral Deformities in Farmed Atlantic Salmon (*Salmo salar L.*) - Etiology and Pathology. *J Appl Ichthyology* (2012) 28(3):433–40. doi: 10.1111/j.1439-0426.2012.01980.x
93. Ytteborg E, Torgersen J, Baeverfjord G, Takle H. Morphological and Molecular Characterization of Developing Vertebral Fusions Using a Teleost Model. *BMC Physiol* (2010) 10:13. doi: 10.1186/1472-6793-10-13
94. Weiss RE, Watabe N. Studies on the Biology of Fish Bone. III. Ultrastructure of Osteogenesis and Resorption in Osteocytic (Cellular) and Anosteocytic (Acellular) Bones. *Calcif Tissue Int* (1979) 28:43–56. doi: 10.1007/BF02441217
95. Glowacki J, Cox KA, O'Sullivan J, Wilkie D, Deftos J. Osteoclasts Can Be Induced in Fish Having Acellular Bony Skeleton. *Proc Natl Acad Sci USA* (1986) 83:4104–7. doi: 10.1073/pnas.83.11.4104
96. Huysseune A. Phenotypic Plasticity in the Lower Pharyngeal Jaw Dentition of *Astatoreochromis alluaudi* (Teleostei: Cichlidae). *Archs Oral Biol* (1995) 40(11):1005–14. doi: 10.1016/0003-9969(95)00074-Y
97. Yu T, Witten PE, Huysseune A, Buettner A, To TT, Winkler C. Live Imaging of Osteoclast Inhibition by Bisphosphonates in a Medaka Osteoporosis Model. *Dis Model Mech* (2016) 9(2):155–63. doi: 10.1242/dmm.019091
98. Urasa F, Flik G, Wendelr-Bonga SE. Mobilization of Bone Minerals by Estrogens During Ovarian Growth in the Tilapia *Sarotherodon mossambicus*. *Gen Comp Endocr* (1984) 53(3):495.
99. Gunter HM, Meyer A. Molecular Investigation of Mechanical Strain-Induced Phenotypic Plasticity in the Ecologically Important Pharyngeal Jaws of Cichlid Fish. *J Appl Ichthyology* (2014) 30(4):630–5. doi: 10.1111/jai.12521

100. Huysseune A, Witten PE. Development Mechanisms Underlying Tooth Patterning in Continuously Replacing Osteichthyan Dentitions. *J Exp Zoology Part B: Mol Dev Evol* (2006) 306:204–15. doi: 10.1002/jez.b.21091
101. Witten PE, Villwock W. Bone Resorption by Mononucleated Cells During Skeletal Development in Fish With Acellular Bone. *J Bone Mineral Res* (1997) 12:149–58.
102. Henke K, Daane JM, Hawkins MB, Dooley CM, Busch-Nentwich EM, Stemple DL, et al. Genetic Screen for Postembryonic Development in the Zebrafish (*Danio rerio*): Dominant Mutations Affecting Adult Form. *Genetics* (2017) 207(2):609–23. doi: 10.1534/genetics.117.300187
103. Gorman KF, Tredwell SJ, Breden F. The Mutant Guppy Syndrome Curveback as a Model for Human Heritable Spinal Curvature. *Spine* (2007) 32:735–41. doi: 10.1097/01.brs.0000259081.40354.e2
104. Buchan JG, Gray RS, Gansner JM, Alvarado DM, Burgert L, Gitlin JD, et al. Kinesin Family Member 6 (Kif6) Is Necessary for Spine Development in Zebrafish. *Dev Dyn* (2014) 243(12):1646–57. doi: 10.1002/dvdy.24208
105. Gray RS, Wilm TP, Smith J, Bagnat M, Dale RM, Topczewski J, et al. Loss of *Col8a1a* Function During Zebrafish Embryogenesis Results in Congenital Vertebral Malformations. *Dev Biol* (2014) 386(1):72–85. doi: 10.1016/j.ydbio.2013.11.028
106. Grimes DT, Boswell CW, Morante NF, Henkelman RM, Burdine RD, Ciruna B. Zebrafish Models of Idiopathic Scoliosis Link Cerebrospinal Fluid Flow Defects to Spine Curvature. *Science* (2016) 352(6291):1341–4. doi: 10.1126/science.aaf6419
107. Kobayashi D, Iijima N, Hagiwara H, Kamura K, Takeda H, Yokoyama T. Characterization of the Medaka (*Oryzias latipes*) Primary Ciliary Dyskinesia Mutant, Jaodori: Redundant and Distinct Roles of *Dynein Axonemal Intermediate Chain 2 (Dnai2)* in Motile Cilia. *Dev Biol* (2010) 347(1):62–70. doi: 10.1016/j.ydbio.2010.08.008
108. Nagao Y, Cheng J, Kamura K, Seki R, Maeda A, Nihei D, et al. Dynein Axonemal Intermediate Chain 2 Is Required for Formation of the Left-Right Body Axis and Kidney in Medaka. *Dev Biol* (2010) 347(1):53–61. doi: 10.1016/j.ydbio.2010.08.001
109. Kobayashi D, Asano-Hoshino A, Nakakura T, Nishimaki T, Ansai S, Kinoshita M, et al. Loss of Zinc Finger Mynd-Type Containing 10 (Zmynd10) Affects Cilia Integrity and Axonemal Localization of Dynein Arms, Resulting in Ciliary Dysmotility, Polycystic Kidney and Scoliosis in Medaka (*Oryzias latipes*). *Dev Biol* (2017) 430(1):69–79. doi: 10.1016/j.ydbio.2017.08.016
110. Ohisa S, Inohaya K, Takano Y, Kudo A. *Sec24d* Encoding a Component of COPII Is Essential for Vertebra Formation, Revealed by the Analysis of the Medaka Mutant, *Vbi*. *Dev Biol* (2010) 342(1):85–95. doi: 10.1016/j.ydbio.2010.03.016
111. Haller G, McCall K, Jenkitkasemwong S, Sadler B, Antunes L, Nikolov M, et al. A Missense Variant in *SLC39A8* Is Associated With Severe Idiopathic Scoliosis. *Nat Commun* (2018) 9(1):4171. doi: 10.1038/s41467-018-06705-0
112. Kague E, Turci F, Newman E, Yang Y, Brown KR, Aglan MS, et al. 3d Assessment of Intervertebral Disc Degeneration in Zebrafish Identifies Changes in Bone Density That Prime Disc Disease. *Bone Res* (2021) 9(1):39. doi: 10.1038/s41413-021-00156-y
113. Kague E, Roy P, Asselin G, Hu G, Simonet J, Stanley A, et al. Osterix/sp7 Limits Cranial Bone Initiation Sites and Is Required for Formation of Sutures. *Dev Biol* (2016) 413(2):160–72. doi: 10.1016/j.ydbio.2016.03.011
114. Kague E, Witten PE, Soenens M, Campos CL, Lubiana T, Fisher S, et al. Zebrafish Sp7 Mutants Show Tooth Cycling Independent of Attachment, Eruption and Poor Differentiation of Teeth. *Dev Biol* (2018) 435(2):176–84. doi: 10.1016/j.ydbio.2018.01.021
115. Azetsu Y, Inohaya K, Takano Y, Kinoshita M, Tasaki M, Kudo A. The *Sp7* Gene Is Required for Maturation of Osteoblast-Lineage Cells in Medaka (*Oryzias latipes*) Vertebral Column Development. *Dev Biol* (2017) 431(2):252–62. doi: 10.1016/j.ydbio.2017.09.010
116. Yu T, Graf M, Renn J, Schartl M, Larionova D, Huysseune A, et al. A Vertebrate-Specific and Essential Role for *Osterix* in Osteogenesis Revealed by Gene Knockout in the Teleost Medaka. *Development* (2017) 144(2):265–71. doi: 10.1242/dev.139550
117. Fleming A, Keynes R, Tannahill D. A Central Role for the Notochord in Vertebral Patterning. *Development* (2004) 131(4):873–80. doi: 10.1242/dev.00952
118. Lleras Forero L, Narayanan R, Huitema LF, VanBergen M, Apschner A, Peterson-Maduro J, et al. Segmentation of the Zebrafish Axial Skeleton Relies on Notochord Sheath Cells and Not on the Segmentation Clock. *Elife* (2018) 7:e33843. doi: 10.7554/eLife.33843
119. Harris MP, Rohner N, Schwarz H, Perathoner S, Konstantinidis P, Nusslein-Volhard C. Zebrafish *Eda* and *Edar* Mutants Reveal Conserved and Ancestral Roles of Ectodysplasin Signaling in Vertebrates. *PloS Genet* (2008) 4(10):e1000206. doi: 10.1371/journal.pgen.1000206
120. Collins JE, White S, Searle SM, Stemple DL. Incorporating RNA-Seq Data Into the Zebrafish Ensembl Genebuild. *Genome Res* (2012) 22(10):2067–78. doi: 10.1101/gr.137901.112
121. Henn BM, Botigué LR, Bustamante CD, Clark AG, Gravel S. Estimating the Mutation Load in Human Genomes. *Nat Rev Genet* (2015) 16(6):333–43. doi: 10.1038/nrg3931
122. Waddington CH. Canalization of Development and the Inheritance of Acquired Characters. *Nature* (1942) 150(3811):563–5. doi: 10.1038/150563a0
123. Scharloo W. Canalization: Genetic and Developmental Aspects. *Annu Rev Ecol Systematics* (1991) 22(1):65–93. doi: 10.1146/annurev.es.22.110191.000433

Conflict of Interest: The authors declare that the research was conducted in the absence of any commercial or financial relationships that could be construed as a potential conflict of interest.

frontiers | Frontiers in Endocrinology

TYPE Original Research
PUBLISHED 02 September 2022
DOI 10.3389/fendo.2022.985304

OPEN ACCESS

EDITED BY
Erika Kague,
University of Bristol, United Kingdom

REVIEWED BY
Subburaman Mohan,
United States Department of Veterans Affairs, United States
Ryan Scott Gray,
University of Texas at Austin, United States

*CORRESPONDENCE
David Karasik
karasik@hsl.harvard.edu

SPECIALTY SECTION
This article was submitted to Bone Research, a section of the journal Frontiers in Endocrinology

RECEIVED 03 July 2022
ACCEPTED 16 August 2022
PUBLISHED 02 September 2022

CITATION
Khrystoforova I, Shochat-Carvalho C, Harari R, Henke K, Woronowicz K, Harris MP and Karasik D (2022) Zebrafish mutants reveal unexpected role of Lrp5 in osteoclast regulation. *Front. Endocrinol.* 13:985304. doi: 10.3389/fendo.2022.985304

Zebrafish mutants reveal unexpected role of Lrp5 in osteoclast regulation

Iryna Khrystoforova[1], Chen Shochat-Carvalho[1], Ram Harari[1], Katrin Henke[2], Katherine Woronowicz[3,4], Matthew P. Harris[3,4] and David Karasik[1]*

[1]Azrieli Faculty of Medicine, Bar-Ilan University, Safed, Israel, [2]Department of Orthopedics, Emory University, Atlanta, GA, United States, [3]Department of Orthopaedics, Boston Children's Hospital, Boston, MA, United States, [4]Department of Genetics, Harvard Medical School, Boston, MA, United States

Low-density Lipoprotein Receptor-related Protein 5 (*LRP5*) functions as a co-receptor for Wnt ligands, controlling expression of genes involved in osteogenesis. In humans, loss-of-function mutations in *LRP5* cause Osteoporosis-Pseudoglioma syndrome, a low bone mass disorder, while gain-of-function missense mutations have been observed in individuals with high bone mass. Zebrafish (*Danio rerio*) is a popular model for human disease research, as genetic determinants that control bone formation are generally conserved between zebrafish and mammals. We generated *lrp5*- knock-out zebrafish to study its role in skeletogenesis and homeostasis. Loss of *lrp5* in zebrafish leads to craniofacial deformities and low bone mineral density (total body and head) at adult ages. To understand the mechanism and consequences of the observed phenotypes, we performed transcriptome analysis of the cranium of adult *lrp5* mutants and siblings. Enrichment analysis revealed upregulation of *genes* significantly associated with hydrolase activity: *mmp9, mmp13a, acp5a*. *acp5a* encodes Tartrate-resistant acid phosphatase (TRAP) which is commonly used as an osteoclast marker, while Matrix metalloprotease 9, Mmp9, is known to be secreted by osteoclasts and stimulate bone resorption. These genes point to changes in osteoclast differentiation regulated by *lrp5*. To analyze these changes functionally, we assessed osteoclast dynamics in mutants and observed increased TRAP staining, significantly larger resorption areas, and developmental skeletal dysmorphologies in the mutant, suggesting higher resorptive activity in the absence of Lrp5 signaling. Our findings support a conserved role of Lrp5 in maintaining bone mineral density and revealed unexpected insights into the function of Lrp5 in bone homeostasis through moderation of osteoclast function.

KEYWORDS

lrp5, zebrafish, bone, osteoclast, osteoporosis

Introduction

Osteoporosis is a debilitating condition characterized by compromised bone architecture and decline of bone mineral density (BMD) associated with aging. Worldwide, osteoporosis affects millions of people and may result in bone fracture (1), causing heavy burden on the health, social and economic aspects of life (2, 3). Osteoporotic fractures require long-term immobilization and rehabilitation that consequently may contribute to loss of life (4). Over the last century, human lifespan has extended. A consequence of this extended lifespan is an enhanced emphasis on the skeletal system as a source of significant morbidity associated with aging (5). Continued turnover of bone extracellular matrix sustains skeletal integrity and maintains structure of bone as can be measured by mineral density of the bones (6). This turnover is controlled *via* a coupled interaction of bone-building osteoblasts and resorbing osteoclasts (7). The disparity of these integrated actions may result in low bone accrual and lead to BMD loss with age (8, 9).

Low-density Lipoprotein Receptor-related Protein 5 (LRP5), a co-receptor of the canonical Wnt-pathway, was identified as a locus associated with fracture risk and BMD by large-scale genome-wide association studies (GWAS) (10–13). Multiple studies have provided evidence that LRP5, is critical for bone development, growth, and maintenance (14–17). Together with Frizzled, LRP5 controls expression of genes involved in osteogenesis (18). These findings are supported by studies describing mutations in *LRP5* that underlie different pathological conditions and affect bone metabolism in humans (18). Loss-of-function mutations in LRP5 cause osteoporosis-pseudoglioma syndrome (OPPG), a low bone mass disorder, with severe low BMD and pathological vascularization of the retina (19), while point mutations having a gain-of-function affect have been observed in individuals with high bone mass (20). Mutations in *LRP5* are also known to be associated with cranial deformities, such as torus palatinus and thickening of frontal and mandible bones (Van Buchem disease) (21).

Animal models mirror the necessity of *lrp5* in postnatal bone metabolism and closely resemble human phenotypes. It has been shown that murine *Lrp5* knock-out models mimic the human OPPG phenotype with low BMD and appendicular limb deformities (16, 22). In murine *Lrp5* knock-outs the main cause of poor bone quality and low mineral deposition is mostly ascribed to reduced osteoblasts proliferation (14, 23). However, less is known about the effect of *Lrp5* knock-out on osteoclasts function. It was shown that high bone mineral density missense mutations in *Lrp5* reduce osteoclast differentiation and resorption activity in female mice (24). However, the systemic effect of *lrp5* deficiency on osteoclasts more broadly remains unknown.

The zebrafish has been a key vertebrate model to understand gene function in development and physiology (25). There are many advantages of zebrafish as an animal model: external development, high fecundity, optical clarity of embryos and larvae, short generation time, ease of genetic manipulations, availability of mutant and transgenic lines and, most importantly, high genetic similarity with humans (26, 27). Notably, zebrafish bones demonstrate similar cellular content and share molecular mechanisms with mammalian bones (28–30). As a result, zebrafish bones and tissues became a faithful model to study human bone disorders (28).

In the present study, we generated zebrafish *lrp5* knock-outs that allowed us to analyze bone phenotypes at various stages. Our model demonstrates delayed mineralization throughout the zebrafish skeleton at early stages with further deformation of the neuro- and viscerocranium in the adult craniofacial skeleton. We found that adult *lrp5*$^{-/-}$ fish had low BMD and displayed malformations of the craniofacial skeleton that may be a result of parasphenoid bone fractures. Surprisingly, transcriptome profiling of *lrp5*$^{-/-}$ cranial bones revealed the downregulation of genes in the bisphosphonate pathway together with mevalonate pathway genes, known as key pathways for controlling osteoclasts metabolism. Using the zebrafish model, we show that osteoclasts in *lrp5*$^{-/-}$ mutants are more active, resulting in increased bone resorption compared to *lrp5*$^{+/+}$. Thus, our work uncovers an unexpected role of Lrp5 in suppressing osteoclast regulation in addition to its effect previously identified on bone mineral density. We suggest that the *lrp5*$^{-/-}$ zebrafish model can contribute to identifying treatments to ameliorate symptoms of low BMD and prolong the health of aging bones.

Materials and methods

Zebrafish husbandry

All experiments were conducted according to institutional animal care and use committee (IACUC) approval for Bar-Ilan University zebrafish facility (protocol #b13213_40). Zebrafish (*Danio rerio*) of AB strain were maintained at 28°C under 14:10 light : dark cycle.

Generation of *lrp5*$^{-/-}$ line by CRISPR-Cas9

CRISPR-Cas9 was used to knock out *lrp5* in zebrafish. The plasmids pCS2-nCas9n (47929) and pT7-gRNA (46759) were purchased from Addgene (Cambridge, MA, USA). Two DNA oligomers 5`-TAGGGTCGCTCAGAGTCTGCAG-3` and 5`-AAACCTGCAGACTCTGAGCGAC-3` were annealed and ligated in to the pT7 gRNA plasmid after it was digested with BsmBI, BglII and SalI. gRNA was generated by *in vitro*

transcription of the pT7-gRNA digested with BamHI, using T7 RNA polymerase (New England Biolabs, Ipswich, MA, USA) followed by purification using MicroSpin G-50 Columns (GEHealthcare, San Diego, CA, USA). For making Cas9 mRNA, the template DNA (pCS2-nCas9n) was linearized by NotI, purified using a QIAprep column, capped Cas9 mRNA was synthesized using mMESSAGE mMACHINE SP6 kit (Invitrogen) and purified using Micro Spin G-50 Columns. A mix of *lrp5* gRNA (300ng/µL) and Cas9 mRNA (300ng/µL) was injected directly into zebrafish one-cell-stage embryos, using a pneumatic Pico Pump (WPI, Worcester, MA, USA).

After 24 hours the CRISPR efficiency was evaluated by PstI-HF (New England Biolabs) as the restriction site of this enzyme was located at the CRISPR-Cas9 target site. Next, CRISPR injected embryos were raised, and DNA was extracted from their fin tail and analyzed by PstI-HF to select founders carrying mutations. Founder fish were outcrossed to WT and DNA was extracted from several embryos of each founder and sequenced to decipher the mutation transmitted to F1 offspring. Further, F1 carrying an 8bp deletion in exon 2, were outcrossed with WT to generate F2 which were again outcrossed to WT to generate F3 to reduce off target effect. The $lrp5^{-/-}$ and $lrp5^{+/+}$ siblings were obtained by inbreeding of F3 $lrp5^{+/-}$.

Genotyping

For DNA extraction, embryo or adult fin tail were immersed in 100µL of 50mM NaOH heated to 95°C for 20 minutes and cooled down to 4°C. Afterwards, 1/10 volume of 1M Tris-HCL buffer at with pH8 was added (31). 5 µL of DNA was used for PCR with specific primers (Table S1) and PCR fragments were either cut by PstI-HF and run on a 2% agarose gel or sequenced (Hy-lab, Rehovot, Israel).

Western blot

The total proteins from caudal fins of adult fish were extracted by incubation in RIPA lysis buffer (Sigma-Aldrich, Burlington, MA, USA) with protease cocktail (Sigma-Aldrich) and separated in sodium dodecyl sulphate–polyacrylamide gel electrophoresis (SDS-PAGE). The proteins were transferred to polyvinylidene fluoride (PVDF) membrane (Merck Millipore Ltd, Tullagreen, Ireland) and blocked by 4% skim milk in Tris-buffered saline with 0.1% Tween-20 (TBST) v/v. Next, membrane was immunolabeled with anti-*LRP5* rabbit monoclonal antibodies (1:1000, D80F2, Cell Signaling Technology, Danvers, MA, USA) or anti-α-Tubulin mouse monoclonal IgM antibodies (1:1200, TU-02, sc-8035, (Santa Cruz Biotechnology, Dallas, TX, USA). Secondary antibodies (1:1500, ab97240, Goat Anti-Mouse, and 1:1500, ab97051, Goat Anti-Rabbit, Abcam) were incubated for 1 hour at room temperature. Membranes were developed using chemiluminescent substrate (Advansta Inc., San Jose, CA, USA) and imaged *via* UVITEC Alliance Q9 Imager (Cleaver Scientific, Warwickshire, UK).

Skeletal staining

Alizarin red alcian blue skeletal staining

To visualize bone and cartilage tissues at 7, 13 days post fertilization (dpf) and 1.5 month post-fertilization (mpf), $lrp5^{-/-}$ and $lrp5^{+/+}$ siblings were stained according to Walker and Kimmel protocol (32). In short, fish were euthanized and fixed in 4% paraformaldehyde (Sigma-Aldrich), for 2 h, washed with phosphate buffered saline (PBS), and dehydrated with 50% and 70% ethanol. Next, larvae were double stained with 0.5% alizarin red (Sigma-Aldrich) and 0.02% alcian blue (Sigma-Aldrich) or stained with alizarin red only, overnight, washed with distilled water and bleached with 3% H_2O_2 (Merck Millipore) and 2% potassium hydroxide (KOH, Sigma-Aldrich). Larvae were incubated at 37°C in 1% trypsin (Biological Industries, Beit HaEmek, Israel) in 2% borax (Sigma-Aldrich) solution with mild agitation for 45 min until 60% of the soft tissue was dissolved clear. Afterwards, larvae were serially washed with 20% glycerol mixed with 0.25% KOH, and 50% glycerol mixed with 0.25% KOH for 2 h. The larvae were photographed using Leica M165 FC microscope. Percentage of proximal notochord's calcification (stained red) was measured using ImageJ software (NIH, Bethesda, MD, USA).

Von Kossa staining

Elasmoid scales were collected from 10 mpf old fish and washed 3x in PBST, then stained in 2.5% of silver nitrate (2.5% $AgNO_3$ in dH_2O, Sigma) solution for 30 minutes. Stained scales were washed in PBST and then placed for 5 min in 5% sodium thiosulfate solution and washed again before transferred into 80% glycerol (33). Scales viewed under an automated upright slide scanning microscope, Axio Scan.Z1 (Zeiss, Oberkochen, Germany). The images were captured with 40×/0.95 objective at z-planes of 0.5 µm. Analysis of the resorbed area was done in ImageJ Software with use of ZFBONE toolset (34). 12 fish per group and at least 10 scales per fish were analyzed.

Tartrate-resistant acid phosphatase staining

To detect osteoclasts an acid phosphatase kit (387A; Sigma-Aldrich) was used. Scales were collected and fixed in fixative solution at room temperature and then washed 3x in PBST. TRAP staining solution was prepared following kit protocol. Scales were stained for 3h at 37°C in 500µL of TRAP stain. Then scales were washed in PBST and re-fixed in 4% PFA at 4°C overnight. Prior to imaging, scales were washed in PBST and moved to 80% glycerol in PBST. The images were captured with

10×/0.95 objective at z-planes of 0.5 µm. Analysis of the osteoclast's activity was done in ImageJ software with threshold application. 10 fish per group and at least 10 scales per fish were analyzed.

X-ray micro-computerized tomography

At 3 and 6mpf zebrafish were euthanized and fixed in 3.7% formaldehyde (Sigma-Aldrich) in PBS overnight. Length, weight and sex were recorded, and fish were stored in 70% ethanol until scanning. A total of 55 fish were scanned (3mpf: *lrp5*$^{-/-}$ n=15, *lrp5*$^{+/+}$ n=15; 6mpf: *lrp5*$^{-/-}$ n=12, *lrp5*$^{+/+}$ n=13) using a 1172 SkyScan micro-computed tomography (micro-CT) scanner (Bruker, Kontich, Belgium). The whole body of fish was scanned at pixel size of 12 µm (scan settings 49 kV, 100 µA, filter Al 0.25mm). The scanned files were reconstructed with NRecon Software (Bruker). The BMD was measured from reconstructed files using CTAnalyzer Software (Bruker) calibrated to the phantoms with known mineral density (0.25 and 0.75 g.cm^{-3} hydroxyapatite, Bruker). The 3D tomography images of zebrafish whole body were generated using CTvox software (Bruker). The morphometrical measurements of nasofacial angle (NA) and parasphenoid (PD) distance between two limits were done on 3D reconstructed micro-CT scanned zebrafish using Meshy online tool from GitHub platform (https://0x00019913.github.io/meshy/). Prior to the measurements, the reconstructed zebrafish heads were saved in 3D models using CTAnalyzer Software (Bruker).

RNA-sequencing and data analysis

Total RNA was extracted from 10mpf old zebrafish craniums (*lrp5*$^{-/-}$ n=8, *lrp5*$^{+/+}$ n=7). The tissue was lysed in Trizol (Sigma-Aldrich) and purified by Direct-Zol RNA kit (Zymo Research, Tustin, CA, USA). Integrity of the isolated RNA was tested using the Agilent TS HS RNA Kit and 4200 TapeStation at the Genome Technology Center at the Faculty of Medicine at Bar-Ilan University. 100 ng of total RNA was treated with the NEBNext poly (A) mRNA Magnetic Isolation Module (NEB, #E7490L). RNA-seq libraries were produced by using the NEBNext Ultra II RNA Library Prep Kit for Illumina NEB #E7770L. Quantification of the library was performed using dsDNA HS Assay Kit and QUBIT (Molecular Probes, Life Technologies Corporation, Gaithersburg, MD, USA) and qualification was done using the Agilent TS D1000 kit and 4200. 250nM of each library was pooled together and diluted to 4nM according to NextSeq manufacturer's instructions. 1.6pM was loaded onto the Flow Cell with 1% PhiX library control. Libraries were sequenced by Illumina NextSeq 500 platform with single end reads of 75 cycles according to the manufacturer's instructions.

Differential expression analysis

We compared the gene expression between *lrp5*$^{-/-}$ and *lrp5*$^{+/+}$ control siblings by mRNA differential expression (DE) analysis. The sequenced reads of all samples were aligned to the zebrafish genome (GRCz11) using TopHat2 (35), and the number of reads mapped within genes was quantified by Quantify to annotation model (Partek E/M) (36) of the Partek Flow software, v 10.0. This procedure resulted in a sequencing depth of 30–35 million reads per sample, out of which 80–81% were uniquely mapped to the zebrafish genome (GRCz11). Then, low expressed transcripts (<100 reads in all samples combined) were filtered out and data was normalized to trimmed mean of M-values in the Partek Flow. One outlier in the *lrp5*$^{-/-}$ group was detected by principle component analysis and removed. Differentially expressed genes were determined using the GSA (gene specific analysis) program from the Partek Flow package. P-values were corrected for multiple testing using the Benjamini–Hochberg method, with genes with a false discovery rate (FDR) < 0.05 and absolute value fold change (FC) >2 classified as differentially expressed. List of differentially expressed zebrafish genes was converted to their human orthologs using DIOPT (37), keeping only human orthologs with a DIOPT score >6. In cases where there were multiple zebrafish orthologs for one human gene, the gene with the highest log fold change in expression was used. Gene enrichment analysis was done using the online tool ShinyGO (http://bioinformatics.sdstate.edu/go/) with WikiPathways database.

Quantitative real-time PCR

For RNA extraction the tissue was lysed in Trizol (Sigma-Aldrich) and purified by Direct-Zol RNA kit (Zymo Research, Tustin, CA, USA). cDNA was synthesized from 1µg RNA by Takara PrimeScript kit (Takara, Mountain View, CA, USA). qPCR was performed with PowerUp SYBR Green Master Mix (Thermo Fisher Scientific, Waltham, MA, USA) using a ViiA^{TM} 7 Dx qPCR Instrument (Life Technologies Corporation). All reactions were performed as technical triplicates, and non-template controls were added in each PCR run. The relative expression values of the genes were normalized to the housekeeping control (primers are listed in Table S2).

Results

Generation of Lrp5 loss of function mutant zebrafish

LRP5 protein and function is highly conserved between human and zebrafish (38). The zebrafish Lrp5 protein (NP_001170929.1) consists of 1430 amino acids residues.

Using CRISPR-Cas9 mediated genome editing we induced an 8 base pair (bp) deletion in exon 2 of the *lrp5* gene (Figures 1A, B), which resulted in a frame shift at alanine 53 (Ala53fs), creating a premature stop codon after 54 amino acids. The truncation resulted in the absence of the functional protein domains, including the transmembrane region (Figure 1C). The LRP5 protein level in the *lrp5*$^{-/-}$ mutants was verified by western-blot, demonstrating a complete loss (Figure 1D). *lrp5*$^{-/-}$ zebrafish were further used to follow skeletogenesis from larval to adult stages to directly compare its role in regulating skeletal differentiation and development.

Very low numbers of homozygote fish were obtained through incrossing of carriers (Figure 1E) with only of 3.7% homozygotes surviving through adolescence (90 dpf); heterozygous fish did not display any reduction in survival rates. On closer inspection, we found that from 7 dpf the number of *lrp5*$^{-/-}$ fish decreased; daily manual water changes up to 1mpf increased survival of *lrp5*$^{-/-}$ mutants allowing for a broader analysis of the phenotype.

lrp5 is necessary for timing and extent of mineralization during development

As early as 7dpf several of the craniofacial skeleton elements start to mineralize, such as the notochord (Figures S1A, D, outlined in yellow) and can be easily observed by alizarin red staining for mineralized matrix. Using alizarin red staining alone (Figures S1A, D) or in combination with alcian blue (Figures S1B, E) which is specific for cartilage, we found that the ossification of the notochord was significantly lower in *lrp5*$^{-/-}$ fish at 7dpf and 13dpf compared with siblings. Interestingly, no obvious malformation or mispatterning of the cartilage was observed at these stages (Figures S1C, F). Whole-mount alizarin red staining of older juvenile stages (*e.g.* 1.5 mpf, Figure 2A), showed a distinct difference in the extent of mineralization in *lrp5* mutants. In planar intramembranous bones, such as the forming calvaria and lateral bones of the skull (opercle, subopercle) alizarin red stain was not uniform and much fainter than in wildtype siblings. (Figure 2A). The pattern of mineralization did not show a restricted pattern as would be expected in case of developmental delay, rather was mottled, showing variation across bones in a splotchy pattern (Figures 2A-D). We scanned adult *lrp5* mutants at 3 and 6mpf (Figure 2E) by X-ray micro-CT to assess changes in BMD in adults. *lrp5*$^{-/-}$ fish demonstrated a general lower whole-body BMD (Figures 2F, G) and skull BMD (Figures 2H, I) at 3 and 6mpf compared to sibling controls. Thus, consistent with findings from other vertebrates and mutant lines of zebrafish, *lrp5* is necessary to establish and maintain BMD.

As previously noted (39), adult *lrp5*$^{-/-}$ fish displayed an abnormal skull shape and body curvatures with variable degree of severity (Figure 2D). *lrp5*$^{-/-}$ displayed major deformities in the craniofacial skeleton as the cranial skeleton develops asymmetrically with malformations throughout the whole head (Figure 3A). To better characterize the deformities in the axial skeleton we segmented the reconstructed micro-CT scans of 3 and 6 mpf fish and performed morphometrical analysis (Figure 3B). At both ages, we observed a domed shape cranial vault with anterior protrusion of the frontal bone in *lrp5*$^{-/-}$. Following the same principle as Kague at al. we quantified midface dysmorphology (40) using the nasofacial angle between the maxilla and frontal bones. We measured the nasofacial angle between the parasphenoid, maxilla and frontal bone (Figure 3B, outlined in red) and found it was significantly larger in *lrp5* mutants compared to wildtype siblings at 3 (Figure 3C) and 6 mpf (Figure 3D). Normal frontonasal growth during development is dependent on appropriate extension of the paraphsenoid bone of the chondrocranium. Consistent with the domed shortened skulls of the mutant, we observed that the parasphenoid bone in *lrp5* mutants fish were severely bent, limiting the distance between rostral and caudal extension of the element (Figure 3B, blue dashed line; Figures 3E, F). Often, the defects were observed as a severe bend of the parasphenoid bone (Figure 3G, outlined in yellow) with varied penetrance, 40% of mutants at 3mpf (n=15) while *lrp5*$^{+/+}$ sibling fish did not show any abnormalities in the parasphenoid at comparable age.

lrp5 downstream Wnt-pathway members were not altered in adult *lrp5*$^{-/-}$ fish

Lrp5 is a co-receptor of the Wnt-pathway and known to control cell proliferation, migration and participate in expression of osteogenic genes (23, 38, 41). We decided to check the dynamics of Wnt-signaling regulators in response to loss of *lrp5* in the zebrafish. Protein expression levels of β-catenin and phospho-Gsk3β were not altered in *lrp5* mutants compared with *lrp5*$^{+/+}$ siblings (Figure S2A). Similar expression patterns were observed for β-catenin mRNA (Figure S2B). To further assess if the general response of Wnt signaling regulators was altered in the *lrp5* mutant, we checked gene expression response during fin regeneration, when active bone growth is taking place. Higher expression of Wnt-pathway genes, such as *axin2, dkk1a and lef1*, was found in 4 days post amputation (dpa) mutant and wildtype fins compared to intact fins. Interestingly, the expression of Wnt-pathway genes was significantly downregulated in 4dpa regenerate tissue of *lrp5*$^{-/-}$ compared to wildtype (Figures S2C-E).

10.3389/fendo.2022.985304

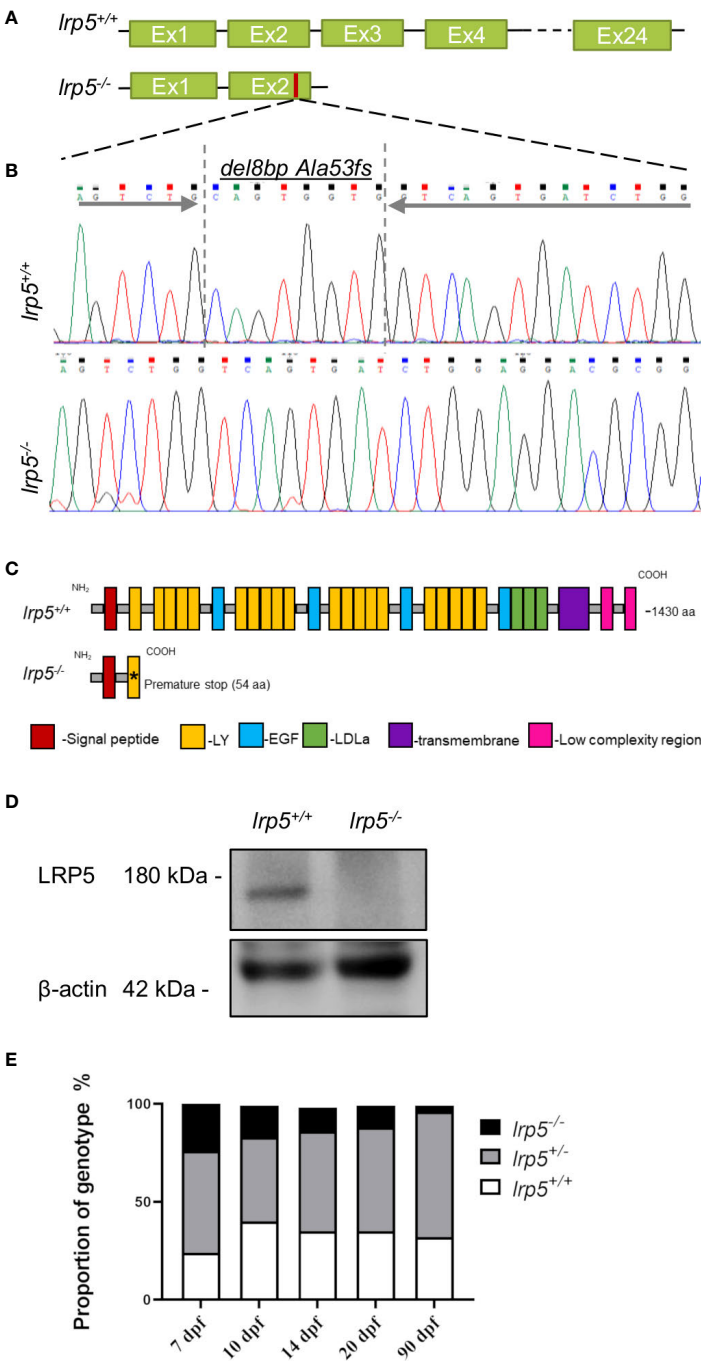

FIGURE 1
CRISPR-Cas9 induced *lrp5* zebrafish knockout line. **(A)** Schematic representation of the ZF *lrp5* gene structure with Sanger sequence chromatogram; **(B)** demonstrating the del8bp (Ala53fs) mutation, that results in a frameshift and a premature stops codon; **(C)** Schematic representation of the ZF LRP5 wild-type and mutated protein demonstrates the lack of functional domains in LRP5 of *lrp5*$^{-/-}$ (LY -low-density lipoprotein receptor; EGF – epidermal growth factor; LDLa- Low-density lipoprotein receptor domain class **(A, D)** Western-blot results demonstrated the absence of LRP5 protein in *lrp5*$^{-/-}$. **(E)** Each column in the graph represents the proportion of genotype (%) per developmental stage. Only 3.7% of *lrp5*$^{-/-}$ in survive and reach adolescence using instead of expected 25%.

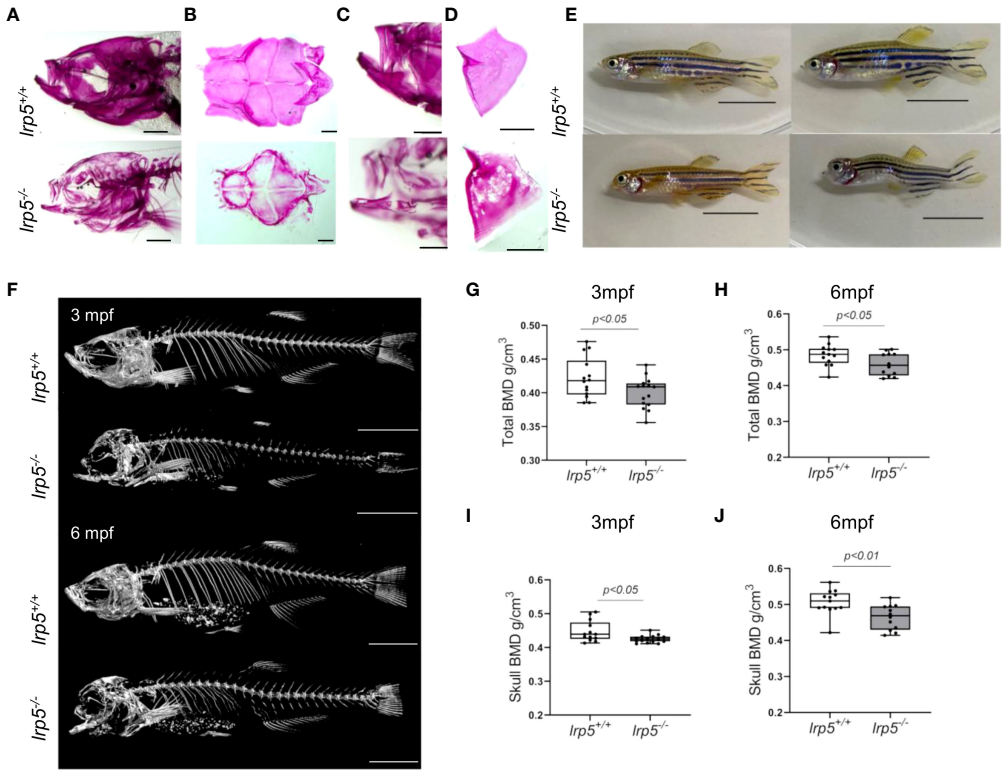

FIGURE 2
lrp5$^{-/-}$ adult fish display low bone mineral density. **(A)** Whole-mount alizarin red staining at 1.5 mpf display the distribution of mineralized matrix through the head bones. In the skull of *lrp5*$^{-/-}$ distribution of mineralized matrix throughout whole head bones differs from *lrp5*$^{+/+}$ Scale bar=1mm. **(B)** coronal view of the cranial vault. The alizarin red signal is distributed ubiquitously in *lrp5*$^{+/+}$ lower jaw **(C)** and opercle **(D)**, meanwhile in *lrp5*$^{-/-}$ fish the lower jaw demonstrated discontinues alizarin red signal. Scale bar=500µm. **(E)** Representative photos of *lrp5*$^{+/+}$ and *lrp5*$^{-/-}$ siblings at 4mpf; *lrp5*$^{-/-}$ present with deformed head and body curvatures. Scale bar=1cm. **(F)** 3D reconstruction of X-ray images of *lrp5*$^{+/+}$ and *lrp5*$^{-/-}$ skeleton at 3 and 6mpf. Scale bar= 1cm **(G, H)** Total BMD is decreased in adult *lrp5*$^{-/-}$ fish. **(I, J)** the skull BMD of *lrp5*$^{-/-}$ mutant fish is significantly lower both at 3 and 6mpf. Results in G-J are expressed as mean SD (3mpf n =13-15 fish, 6mpf n =12-13 fish, t-test).

Differential gene expression profiles in *lrp5*$^{-/-}$ mutants point to osteoclast deficiencies

These data suggest that specific signaling profiles were altered in the *lrp5* mutants during development. To further expand this analysis into bone growth and homeostasis, we assessed the transcriptome of the adult cranium in Lrp5 mutants (n=8) and wildtype siblings (n=6). In total 1044 genes were differentially expressed between *lrp5* mutant and wildtype adult skulls (Figure 4A): 725 upregulated and 319 downregulated. Volcano plots were constructed by integrating the p-value and fold change of each transcript to highlight differentially expressed genes (DEGs) between *lrp5* mutant and siblings (Figure 4B).

Using pathway analysis of differentially expressed genes, we observed a significant enrichment of genes involved in osteoblast signaling and function and in regulation of osteoclast differentiation such as mevalonate, TGF-beta, p38, MAPK pathways (Figure 4C). In parallel, we noted an increase in expression of genes implicated in osteoclast differentiation and activity such as *colony stimulating factor 1 receptor a (csf1ra)*, *acp5a* (encoding TRAP, tartrate resistant acid phosphatase), *tcirg1b* (encoding the a3 isoform of vacuolar H+-ATPase), matrix metalloproteases *mmp9*, *mmp13a*, and *osteoclast stimulation factor 1* (*ostf1*) (Table 1). RT-qPCR analysis was used to confirm the expression level of *acp5a, mmp9, mmp13a, mef2d, map3k5*, and *rps6k5* confirming these differential expression results (Figures 5A-F).

lrp5 function is necessary to restrict resorptive activity

The enrichment of DEGs with regulatory pathways of osteoclast function was unexpected. As such, we decided to check the osteoclast activity in the adult skeleton of *lrp5* mutants compared to wildtype siblings. As a proxy for general resorptive

10.3389/fendo.2022.985304

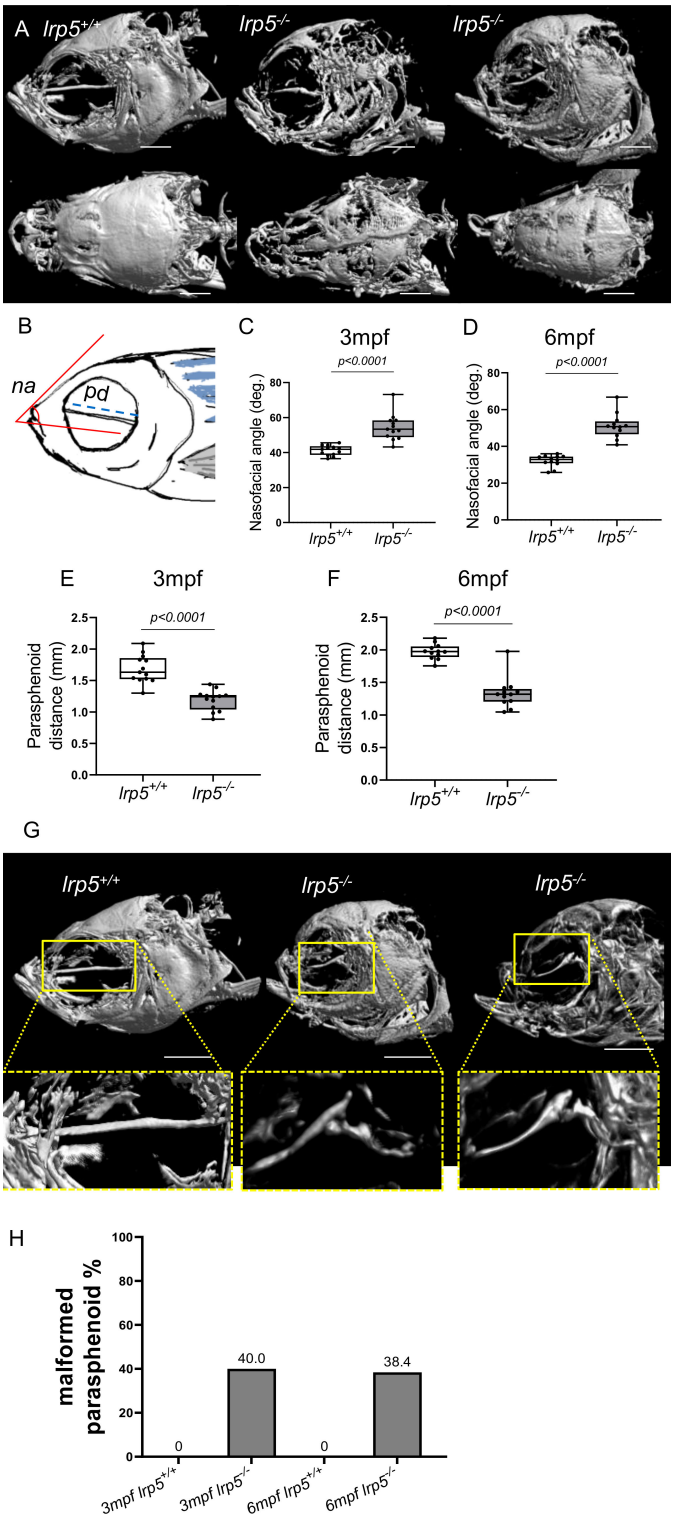

FIGURE 3
Craniofacial deformities of adult lrp5 mutant. **(A)** Adult *lrp5*$^{-/-}$ display major deformities of neuro- and viscera- craniums. **(B)** Schematic representation of morphometrical parameters measured na- nasofacial angle, pd- parasphenoid distance between its edges. **(C, D)** Nasofacial angle at 3mpf and 6mpf is significantly bigger in *lrp5*$^{-/-}$ compared to *lrp5*$^{+/+}$, meanwhile parasphenoid distance is significantly shorter in *lrp5*$^{-/-}$ adult fish at 3 and 6mpf **(E, F)**. **(G)** Parasphenoid bones of *lrp5*$^{-/-}$ are severely deformed and display a similar fracture pattern, outlined in yellow. **(H)** 40% of *lrp5*$^{-/-}$ fish displayed malformed parasphenoid at 3mpf and 38.4% at 6mpf within *lrp5*$^{-/-}$ group. At 3mpf and 6mpf *lrp5*$^{+/+}$ display no indication of parasphenoid deformities.(Scale bar 500μm, 3mpf n =13-15 fish, 6mpf n =12-13 fish, t-test).

10.3389/fendo.2022.985304

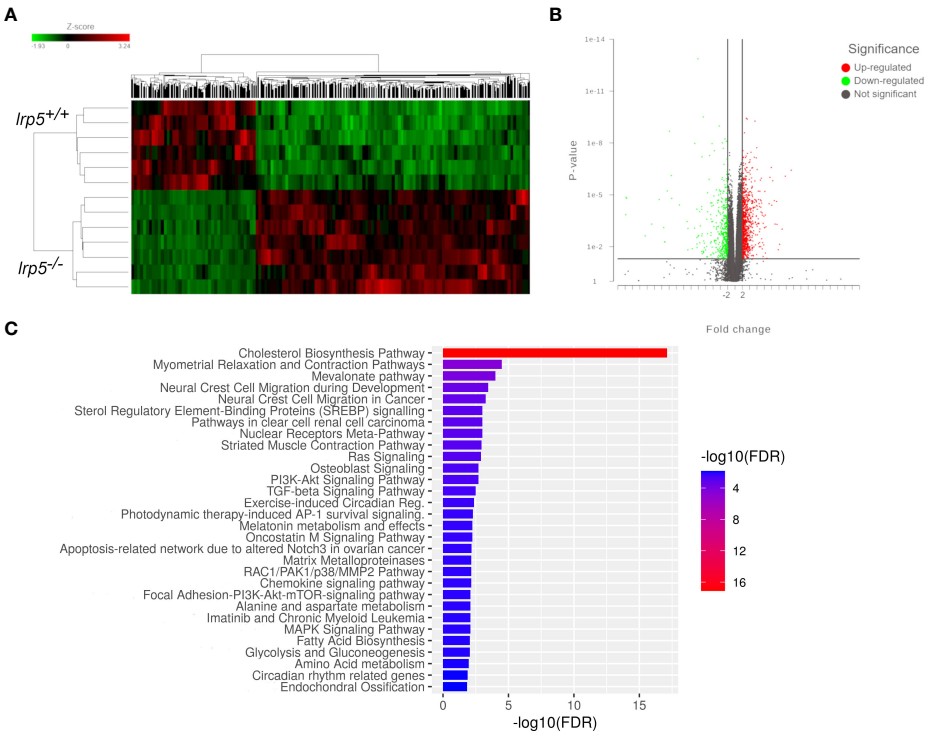

FIGURE 4
RNA-seq results. **(A)** The overall distribution of differentially expressed genes in the cranial bones between the *lrp5*$^{+/+}$ and *lrp5*$^{-/-}$ groups. Red and green represent up-regulated and down-regulated transcripts, respectively, in the clustering analysis. The color intensity is directly proportional to the change. **(B)** The volcano plot shows DEGs in the *lrp5*$^{-/-}$ cranial bones. The red part indicates up-regulated genes, and the green part indicates down-regulated genes. **(C)** Box plot of pathway analysis for all DEGs.

activity more broadly, we analyzed remodeling within zebrafish elasmoid scales. Zebrafish elasmoid scales are translucent mineralized structures of the dermal skeleton with osteoblasts and osteoclasts present (42). Over the last decade zebrafish scales have been used to exhibit the mechanism of bone remodeling (34, 43, 44). Using Von Kossa staining, we observed a distinctive demineralized area at the base of scales in 77% of *lrp5* mutant scales (n=134), compared to just 22% in wildtype siblings (n= 118) (Figure 6A). We quantified demineralization, normalizing it to the size of scales, and found that the demineralized area was significantly larger in mutant scales ($p=0.004386$, *t-test*) (Figure 6A). We further decided to check osteoclast activity using TRAP staining across an area supporting increased osteoclast activity. In line with the observed increase in bone resorption in the mutant, we observed a significant increase of TRAP staining in *lrp5*$^{-/-}$ scales suggesting higher osteoclast activity in the absence of Lrp5 signaling ($p<0.0001$, t-test) (Figure 6B).

TABLE 1 Differentially expressed genes related to osteoblasts and osteoclast signaling.

Osteoclast expressed			Osteoblast/osteocyte expressed		
Gene	**Foldchange**	**function**	***Gene***	**Fold change**	**function**
acp5a	3.5	Degradation of skeletal phosphoproteins	*bglap*	-2.78	Binds calcium and hydroxyapatite
mmp9	2.23	Collagenase, cleaves galectin-3 > suppressor of osteoclastogenesis	*col1a1*	-6.31	Structural component of bone matrix
fdps	-3.68	isoprenoid biosynthesis > catalyzes the formation of farnesyl diphosphate	*fgf23*	2.69	Inhibitor of mineralization
ostf1	2.09	osteoclast stimulating factor 1	*mmp13a*	10.69	Activates mmp9
tnfrsf11b	2.02	Osteoprotegerin acts as decoy receptor for TNFSF11 (RANKL)			

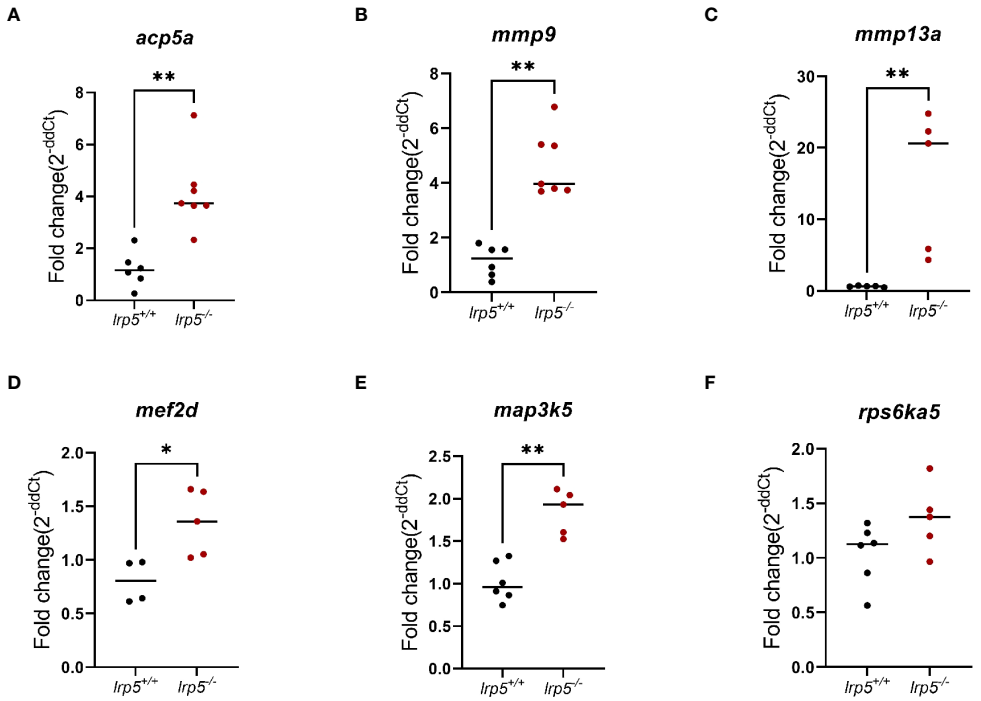

FIGURE 5
RT-qPCR validation of RNA-Seq data. Genes relevant to osteoclasts activity **(A-C)** and osteoclasts differentiation **(D-F)**. (n=6-7, Mann-Whitney test, dots represent each individual value distributed around mean (line): in black *lrp5*$^{+/+}$ control, dark red *lrp5*$^{-/-}$). Mann-Whitney test p-values: *p ≤ 0.05, **p≤ 0.01.

The dermal rays of fish fins show branching of the lepidotrichial skeletal elements

Recent work has shown that lepidotrichia branching process is sensitive to a balance between osteoblast-mediated bone growth and osteolytic tubules expressing *ctsk* and *trap* (45). The extent of branching is sensitive to drugs modifying osteoclast behavior and acts as a barometer of osteoclast activity in the development of the zebrafish skeleton. Consistent with this new finding, whole-mount alizarin red staining of adult *lrp5* mutant fish revealed abnormal branching of lepidotrichia in median fins (Figure 6C). In wildtype fins, the bifurcation or splitting of lepidotrichia demonstrates an organized pattern, occurring in a distal segment of the ray (Figure 6C, red arrow). Meanwhile in fins of *lrp5* mutants various fin rays lack 'stitching' of the hemirays (45) causing ray separation in the proximal segment of the lepidotrichia (Figure 6C). We quantified the number of normally branched fin rays in dorsal fins of mutants and compared it to wildtype siblings. We found that dorsal fins of *lrp5* mutant fish display significantly less normal branched fin rays compared to wildtype siblings (Figure 6C, p<0.0001, t-test). The precocious branching is consistent with the increased bone reworking and TRAP staining in scales and suggests activation of osteoclasts in *lrp5*-deficient mutant fish.

Discussion

In humans, recessive loss-of-function mutations in *LRP5*, a co-receptor in the Wnt signaling pathway, cause osteoporosis-pseudoglioma syndrome. Several GWAS studies identified *LRP5* as a major risk locus for osteoporosis-related phenotypes in the general population (10–12). Prior work detailed similar action of Lrp5 in the zebrafish regulating bone mineral density (39). However, the causes of these broad and systemic phenotypes have not been identified. To further address how Lrp5 regulates skeletal homeostasis, we created a zebrafish *lrp5* loss of function mutant, and looked at changes in timing of ossification and changes in transcriptional regulation that may provide insight into its action in patterning and remodeling of bone. Our findings point to a specific role of Lrp5 in suppressing osteoclast function during the development of new bone and in adult skeletal elements. Alteration of Lrp5 activity may also contribute to the loss of skeletal integrity.

We found that Lrp5 was essential for early viability as only 3.7% of homozygotes survived and reached sexual maturity.

10.3389/fendo.2022.985304

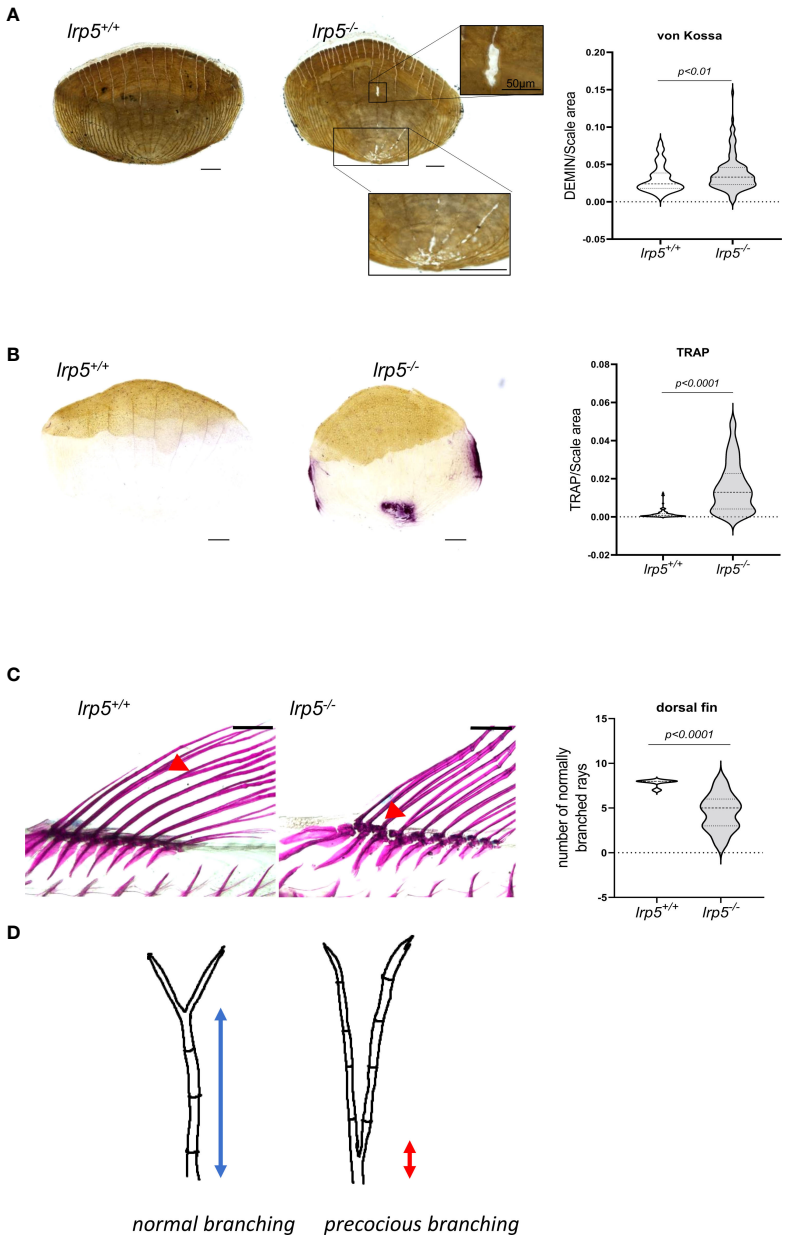

FIGURE 6
lrp5$^{-/-}$ scales display a larger demineralized area and TRAP positive area. **(A)** von Kossa staining of lrp5$^{-/-}$ scales revealed significantly more demineralized area (t-test, n of scales per group=120-130) than of control siblings scales. **(B)** TRAP staining of *lrp5*$^{-/-}$ scales indicates significantly larger TRAP area compared to *lrp5*$^{+/+}$ (t-test, n of scales=95-101). Scale bar=100µm. **(C)** Branching of lepidotrichia in *lrp5*$^{+/+}$ fins occurs in distal segments (red arrows), meanwhile *lrp5*$^{-/-}$ fish display bifurcation in proximal segments of lepidotrichia (C, red arrows). The number of normally branched fin rays is significantly lower in *lrp5*$^{-/-}$ compared to *lrp5*$^{+/+}$ siblings. **(D)** Schematic representation of excessive branching in *lrp5*$^{-/-}$. Results in A, B and C are expressed as mean SD.

The low survival rates in the mutants may be due to alterations in cranial neural crest specification (38) making *lrp5*$^{-/-}$ more vulnerable. However, we did not see any apparent cartilage patterning defects at these early stages. By avoiding constant water current and providing delicate feeding during the first 35 days, we were able to increase survival rates of *lrp5* mutant fish. The mutants that survived early development were then able to thrive into adulthood and reproduce.

Late skeletal roles of Lrp5 were apparent in the growth and differentiation of skeletal elements. In *lrp5* mutant juveniles, we observed an altered mineralization pattern of the craniofacial skeleton. At adult stages, *lrp5*$^{-/-}$ fish demonstrated a decrease in

whole-body BMD and a more drastic decrease in the BMD level of the head skeleton. These findings are consistent with a conserved role of Lrp5 in regulating mineralization and mineral density (46). The demonstration of progressive deficiencies in mineralization during development in the *lrp5* mutant provides an interesting experimental tool to assess progressive action of Lrp5 in regulating this trait.

Recently it was reported that *lrp5* mutant fish display craniofacial malformations in the adult, consistent with defects in skeletal integrity (39). However, we observed substantially more severe malformations in our *lrp5*$^{-/-}$ fish suggesting a role of Lrp5 in developmental patterning. It is plausible to assume that the higher penetrance of the craniofacial phenotype may be associated with the position of the induced mutation near the beginning of the protein, which results in appearance of a stop codon at the first LY domain, limiting the retention of all functional domains. In contrast, the previously reported zebrafish mutants carry the mutation in exon 5 that creates a stop codon at amino acid position 284, meanwhile zebrafish mutants we report here carry the mutation in exon 2 with stop codon at 54 aa. Although, early embryos look morphologically normal, adults have penetrant dysmorphologies of a domed cranial vault, anterior protrusion of the frontal bone and hypoplasia of facial bones. The nasofacial angle was significantly obtuse in crania of adult *lrp5* mutants consistent with decreased frontonasal growth and bossing. A key structural aspect of frontonasal growth is the formation and extension of the parasphenoid of the chondrocranium of the skull. In *lrp5* mutants, we observed severely bent and kinked parasphenoid bones. In similar vein, we find that the *lrp5* mutants have varied levels of fractures in craniofacial bones as seen in the dentary and in the parasphenoid, suggesting skeletal fragility in the mutants.

Insight into the mechanistic regulation of Lrp5 signaling in late development was brought out through our analysis of transcriptional regulation in resting bones of the skull. *lrp5* mutants exhibited lower expression of osteoblastic markers such as *bglap, fgf23* and *col1a1*. Extracellular matrix proteins such as *osteocalcin* (*bglap*) are generally expressed by mature and resting osteoblasts and by hypertrophic chondrocytes. Notably, in contrast, we observed upregulation of genes associated with osteoclast activity, such as *acp5a, tcirg* and *mmp9*.The *acp5a* gene in zebrafish encodes TRAP (tartrate-resistant acid phosphatase), which is secreted by macrophages, dendritic cells and most importantly by bone-resorbing osteoclasts (47, 48). TRAP is one of the key enzymes of the osteoclast resorption process and considered as a classical marker to measure osteoclast activity and number. No less importantly we observed the upregulation of the osteoclast-specific subunit of the v-ATPase *tcirg1*, which is essential for the acidification of the resorption lacuna (49, 50) and *mmp9* expression, an osteoclast-secreted protein known to degrade the bone collagenous matrix (51, 52). We show that pathways responsible for osteoclastogenesis are differentially expressed in *lrp5* mutants such as mevalonate, p38, MAPK and TGF-beta signaling pathways. One of the important roles of the mevalonate pathway is inhibition of osteoclast development *via* farnesyl diphosphate synthase (*fdps*) (53) and we found *fdps* 3.68-fold downregulated in cranial bones of *lrp5* mutant fish (Table 1). In addition, we found a significant increase in *csf1ra*. Csf1ra is the receptor for macrophage colony-stimulating factor 1 (m-csf) which is essential for macrophage differentiation to osteoclast (54). Together these data suggest that *lrp5* has an essential role in suppressing osteoclast regulation during bone homeostasis. To functionally assess this, we employed zebrafish scales as a model to observe osteoclast resorptive activity. The resorption area in *lrp5*$^{-/-}$ scales is significantly larger in mutants consistent with increased activity. This is further corroborated by detection of higher TRAP signal corresponding to increased osteoclast activity (Figure 6B). Osteoclasts are active in shaping developing and remodeled bone, as well as in repair of bone after damage. One emerging anatomical readout of osteoclast activity is the formation and the position of branch sites in the dermal rays of the zebrafish fin. Normally bifurcation of the fin rays occurs in the distal segments of lepidotrichia (Figure 6D). This process is mediated by bone resorption by osteolytic cells that facilitate the shaping of the lepidotrichia (55). Consistent with this morphological readout of osteoclast activity, we found that the number of normally branched fin rays was lower in *lrp5* mutants and deviated from the otherwise determinative pattern of branching within the fin.

The canonical Wnt-pathway is known to inhibit osteoclastogenesis *via* activated Wnt/β-catenin signals (56). Given our observed role of Lrp5 in suppressing osteoclast function we assessed the effect on Wnt downstream targets that may underlie these observations. In adult skeletal structures, we found that the protein expression levels of β-catenin and phospho-Gsk3β were similar in mutants and wildtype siblings. We further tested expression of selected Wnt-pathway genes during bone regeneration during phases of active bone growth (57). In contrast to the resting adult skeleton, during formation of new bone the expression of selected Wnt-pathway genes was significantly downregulated in *lrp5* mutant caudal fin regenerates compared to wildtype regeneration controls. In particular, the expression of *lef1* was significantly downregulated. Thus, we suggest that the canonical Wnt-pathway is attenuated in the developing skeleton of *lrp5* mutants suggesting potential mechanisms for regulation of osteoclast differentiation during development. This does not explain the difference in osteoclast activity in resting bones, however.

While we do show an increase in resorptive activity through von Kossa and TRAP staining of scales and dermal ray branching, it is unclear if this increase is caused by an elevated osteoclast number or increased cell' activity. Investigation of osteoclast number during development of *lrp5* mutants from early to adult stages will be important to

discern between a role of Lrp5 in osteoclastogenesis or in regulation of osteoclast activity.

In summary, our analysis demonstrates that *lrp5* deficiency results in delayed mineralization throughout the zebrafish skeleton during development consistent with loss of BMD at adult stages. This mineral deficiency is especially visible in the formation of the cranial skeleton, and results in the deformation of the viscerocranium and frontonasal shortening. We show that in-depth transcriptome analysis of cranial bones highlights differential regulation of genes associated with osteoclastogenesis in *lrp5* mutant tissues. We were able to confirm specific osteoclast regulation by demonstrating the increase of osteoclast activity and high resorption rate in *lrp5* mutant skeletal tissue that leads to a specific developmental readout of differential branching of dermal rays of the fin. Our study revealed unexpected insights into the role of Lrp5 in bone homeostasis through moderation of osteoclast function. Altogether our model permits characterization of the craniofacial skeleton and supports a new hypothesis for Lrp5 in the regulation of skeletal form and function. Thus, we propose *lrp5* knockout as an experimentally tractable model to examine post-embryonic bone development and the functional role of lrp5 signaling in osteoclast metabolism.

Data availability statement

The datasets presented in this study can be found in online repositories. The names of the repository/repositories and accession number(s) can be found in the article/Supplementary Material.

Ethics statement

The animal study was reviewed and approved by Institutional Animal Care and Use Committees of Israel.

Author contributions

IK: conceptualization, investigation, data curation, formal analysis, methodology, validation, visualization, writing-original draft, and writing-review and editing. CS-C: conceptualization, data curation, methodology, resources, visualization, and writing-review and editing. RH: formal analysis and investigation. KH: data analysis, methodology, and writing-review and editing. KW: data analysis and methodology. MH: conceptualization, supervision, and writing-review and editing. DK: conceptualization, data curation, funding acquisition, project administration, supervision, and writing-review and editing. All authors contributed to the article and approved the submitted version.

Funding

The study was supported by a grant No. 2017204 from US-Israel BSF and grant No. 1121/19 from Israel Science Foundation.

Acknowledgments

The authors express their gratitude to Inbar Ben-Zvi and Malka Kitainer, PhD for expert technical support. We also thank Dalia David for helpful discussions.

Conflict of interest

The authors declare that the research was conducted in the absence of any commercial or financial relationships that could be construed as a potential conflict of interest.

The handling editor EK declared a shared committee Consensus statement on bone-microCT measurement standardization with the author DK at the time of review.

Publisher's note

Supplementary material

The Supplementary Material for this article can be found online at: https://www.frontiersin.org/articles/10.3389/fendo.2022.985304/full#supplementary-material

SUPPLEMENTARY FIGURE 1
Lrp5 mutants display delayed mineralization at early developmental stages. Alizarin red staining together with alcian blue double staining shows significantly lower mineralization level of the notochord (yellow, dashed) and at 7 (A-C) and 13 (D-F) days post fertilization (dpf) compared with lrp5$^{+/+}$ siblings (7dpf n=37-44, 13dpf n=24-25, Mann-Whitney test, measured area outlined in yellow). Scale bar=100μm.

SUPPLEMENTARY FIGURE 2
Wnt-signaling pathway genes activity in lrp5$^{-/-}$ homozygous fish. (A) Wnt-pathway proteins in *lrp5*$^{-/-}$ fish, compared to *lrp5*$^{+/+}$ siblings. (B) RT-qPCR for expression of β-catenin gene in *lrp5*$^{-/-}$ caudal fins compared to *lrp5*$^{+/+}$ siblings. (C-E) mRNA level of Wnt-pathway genes is elevated in zebrafish regenerated caudal fins, compared to intact fins (n=5 fish in each group, Mann-Whitney test).

References

1. Li X, Xu Y, Lin W, Fan Y. The comparison of bone mineral density of femoral head between non-hip fracture side and hip fracture side. *Sci Rep* (2020) 10 (1):13015. doi: 10.1038/s41598-020-70144-5

2. Brink O. Hip fracture clearance: How much optimisation is necessary? *Injury* (2020) 51 Suppl 2:S111–7. doi: 10.1016/j.injury.2020.02.046

3. Cauley JA, Hochberg MC, Lui LY, Palermo L, Ensrud KE, Hillier TA, et al. Long-term risk of incident vertebral fractures. *JAMA* (2007) 298(23):2761–7. doi: 10.1001/jama.298.23.2761

4. Boonen S, Reginster JY, Kaufman JM, Lippuner K, Zanchetta J, Langdahl B, et al. Fracture risk and zoledronic acid therapy in men with osteoporosis. *N Engl J Med* (2012) 367(18):1714–23. doi: 10.1056/NEJMoa1204061

5. Coughlan T, Dockery F. Osteoporosis and fracture risk in older people. *Clin Med (Lond)* (2014) 14(2):187–91. doi: 10.7861/clinmedicine.14-2-187

6. Galea GL, Zein MR, Allen S, Francis-West P. Making and shaping endochondral and intramembranous bones. *Dev Dyn* (2021) 250(3):414–49. doi: 10.1002/dvdy.278

7. Kim JM, Lin C, Stavre Z, Greenblatt MB, Shim JH. Osteoblast-osteoclast communication and bone homeostasis. *Cells* (2020) 9(9):2073. doi: 10.3390/cells9092073

8. Salhotra A, Shah HN, Levi B, Longaker MT. Mechanisms of bone development and repair. *Nat Rev Mol Cell Biol* (2020) 21(11):696–711. doi: 10.1038/s41580-020-00279-w

9. Greenblatt MB, Tsai JN, Wein MN. Bone turnover markers in the diagnosis and monitoring of metabolic bone disease. *Clin Chem* (2017) 63(2):464–74. doi: 10.1373/clinchem.2016.259085

10. Trajanoska K, Morris JA, Oei L, Zheng HF, Evans DM, Kiel DP, et al. GEFOS/GENOMOS consortium and the 23andMe research team. assessment of the genetic and clinical determinants of fracture risk: genome wide association and mendelian randomisation study. *BMJ* (2018) 362:k3225. doi: 10.1136/bmj.k3225

11. Rivadeneira F, Styrkársdottir U, Estrada K, Halldórsson BV, Hsu YH, Richards JB, et al. Twenty bone-mineral-density loci identified by large-scale meta-analysis of genome-wide association studies. *Nat Genet* (2009) 41 (11):1199–206. doi: 10.1038/ng.446

12. Estrada K, Styrkarsdottir U, Evangelou E, Hsu YH, Duncan EL, Ntzani EE, et al. Genome-wide meta-analysis identifies 56 bone mineral density loci and reveals 14 loci associated with risk of fracture. *Nat Genet* (2012) 44(5):491–501. doi: 10.1038/ng.2249

13. Richards JB, Zheng HF, Spector TD. Genetics of osteoporosis from genome-wide association studies: advances and challenges. *Nat Rev Genet* (2012) 13(8):576–88. doi: 10.1038/nrg3228

14. Riddle RC, Diegel CR, Leslie JM, Van Koevering KK, Faugere MC, Clemens TL, et al. Lrp5 and Lrp6 exert overlapping functions in osteoblasts during postnatal bone acquisition. *PloS One* (2013) 8(5):e63323. doi: 10.1371/journal.pone.0063323

15. Sebastian A, Hum NR, Murugesh DK, Hatsell S, Economides AN, Loots GG. Wnt co-receptors Lrp5 and Lrp6 differentially mediate Wnt3a signaling in osteoblasts. *PloS One* (2017) 12(11):e0188264. doi: 10.1371/journal.pone.0188264

16. Holmen SL, Giambernardi TA, Zylstra CR, Buckner-Berghuis BD, Resau JH, Hess JF, et al. Decreased BMD and limb deformities in mice carrying mutations in both Lrp5 and Lrp6. *J Bone Miner Res* (2004) 19(12):2033–40. doi: 10.1359/JBMR.040907

17. Gong Y, Slee RB, Fukai N, Rawadi G, Roman-Roman S, Reginato AM, et al. Osteoporosis-pseudoglioma syndrome collaborative group. LDL receptor-related protein 5 (LRP5) affects bone accrual and eye development. *Cell* (2001) 107(4):513–23. doi: 10.1016/s0092-8674(01)00571-2

18. Norwitz NG, Mota AS, Misra M, Ackerman KE. LRP5, bone density, and mechanical stress: A case report and literature review. *Front Endocrinol (Lausanne)* (2019) 10:184. doi: 10.3389/fendo.2019.00184

19. Pekkinen M, Grigelioniene G, Akin L, Shah K, Karaer K, Kurtoglu S, et al. Novel mutations in the LRP5 gene in patients with osteoporosis-pseudoglioma syndrome. *Am J Med Genet A* (2017) 173(12):3132–5. doi: 10.1002/ajmg.a.38491

20. Frost M, Andersen T, Gossiel F, Hansen S, Bollerslev J, Van Hul W, et al. Levels of serotonin, sclerostin, bone turnover markers as well as bone density and microarchitecture in patients with high-bone-mass phenotype due to a mutation in Lrp5. *J Bone Mineral Res* (2011) 26(8):1721–8. doi: 10.1002/jbmr.376

21. van Lierop AH, Hamdy NA, van Egmond ME, Bakker E, Dikkers FG, Papapoulos SE. Van buchem disease: clinical, biochemical, and densitometric features of patients and disease carriers. *J Bone Mineral Res* (2013) 28(4):848–54. doi: 10.1002/jbmr.1794

22. Kelly OG, Pinson KI, Skarnes WC. The wnt co-receptors Lrp5 and Lrp6 are essential for gastrulation in mice. *Development* (2004) 131(12):2803–15. doi: 10.1242/dev.01137

23. Johnson ML. LRP5 and bone mass regulation: Where are we now? *BoneKEy Rep* (2012) 1:1. doi: 10.1038/bonekey.2012.1

24. Kang KS, Hong JM, Horan DJ, Lim KE, Bullock WA, Bruzzaniti A, et al. Induction of Lrp5 HBM-causing mutations in cathepsin-K expressing cells alters bone metabolism. *Bone* (2019) 120:166–75. doi: 10.1016/j.bone.2018.10.007

25. Grunwald DJ, Eisen JS. Headwaters of the zebrafish–emergence of a new model vertebrate. *Nat Rev Genet* (2002) 3(9):717–24. doi: 10.1038/nrg892

26. Suniaga S, Rolvien T, Vom Scheidt A, Fiedler IA, Bale HA, Huysseune A, et al. Increased mechanical loading through controlled swimming exercise induces bone formation and mineralization in adult zebrafish. *Sci Rep* (2018) 8(1):1–3. doi: 10.1038/s41598-018-21776-1

27. Tonelli F, Bek JW, Besio R, De Clercq A, Leoni L, Salmon P, et al. Zebrafish: a resourceful vertebrate model to investigate skeletal disorders. *Front Endocrinol* (2020) 11:489. doi: 10.3389/fendo.2020.00489

28. Bergen DJ, Kague E, Hammond CL. Zebrafish as an emerging model for osteoporosis: a primary testing platform for screening new osteo-active compounds. *Front Endocrinol* (2019) 10:6. doi: 10.3389/fendo.2019.00006

29. Witten PE, Harris MP, Huysseune A, Winkler C. Small teleost fish provide new insights into human skeletal diseases. *Methods Cell Biol* (2017) 138:321–46. doi: 10.1016/bs.mcb.2016.09.001

30. Busse B, Galloway JL, Gray RS, Harris MP, Kwon RY. Zebrafish: an emerging model for orthopedic research. *J Orthopaedic Res* (2020) 38(5):925–36. doi: 10.1002/jor.24539

31. Meeker ND, Hutchinson SA, Ho L, Trede NS. Method for isolation of PCR-ready genomic DNA from zebrafish tissues. *Biotechniques* (2007) 43(5):610–4. doi: 10.2144/000112619

32. Walker MB, Kimmel CB. A two-color acid-free cartilage and bone stain for zebrafish larvae. *Biotech Histochem* (2007) 82(1):23–8. doi: 10.1080/10520290701333558

33. De Vrieze E, Van Kessel MA, Peters HM, Spanings FA, Flik G, Metz JR. Prednisolone induces osteoporosis-like phenotype in regenerating zebrafish scales. *Osteoporosis Int* (2014) 25(2):567–78. doi: 10.1007/s00198-013-2441-3

34. Tarasco M, Cordelières FP, Cancela ML, Laizé V. ZFBONE: An ImageJ toolset for semi-automatic analysis of zebrafish bone structures. *Bone* (2020) 138:115480. doi: 10.1016/j.bone.2020.115480

35. Kim D, Pertea G, Trapnell C, Pimentel H, Kelley R, Salzberg SL. TopHat2: accurate alignment of transcriptomes in the presence of insertions, deletions and gene fusions. *Genome Biol* (2013) 14(4):R36. doi: 10.1186/gb-2013-14-4-r36

36. *Analysis of RNA-seq data with partek genomics suite 6.6 analysis of RNA-seq data with partek ® genomics SuiteTM 6.6.* Available at: https://biochem.slu.edu/bchm628/handouts/2015/PGS_RNASeqTutorial.pdf.

37. Hu Y, Flockhart I, Vinayagam A, Bergwitz C, Berger B, Perrimon N, et al. An integrative approach to ortholog prediction for disease-focused and other functional studies. *BMC Bioinf* (2011) 12:357. doi: 10.1186/1471-2105-12-357

38. Willems B, Tao S, Yu T, Huysseune A, Witten PE, Winkler C. The wnt Co-receptor Lrp5 is required for cranial neural crest cell migration in zebrafish. *PloS One* (2015) 10(6):e0131768. doi: 10.1371/journal.pone.0131768

39. Bek JW, Shochat C, De Clercq A, De Saffel H, Boel A, Metz J, et al. Lrp5 mutant and crispant zebrafish faithfully model human osteoporosis, establishing the zebrafish as a platform for CRISPR-based functional screening of osteoporosis candidate genes. *J Bone Miner Res* (2021) 36 (9):1749–64. doi: 10.1002/jbmr.4327

40. Kague E, Roy P, Asselin G, Hu G, Simonet J, Stanley A, et al. Osterix/Sp7 limits cranial bone initiation sites and is required for formation of sutures. *Dev Biol* (2016) 413(2):160–72. doi: 10.1016/j.ydbio.2016.03.011

41. Baron R, Kneissel M. WNT signaling in bone homeostasis and disease: from human mutations to treatments. *Nat Med* (2013) 19(2):179–92. doi: 10.1038/nm.3074

42. Bergen DJM, Tong Q, Shukla A, Newham E, Zethof J, Lundberg M, et al. Regenerating zebrafish scales express a subset of evolutionary conserved genes involved in human skeletal disease. *BMC Biol* (2022) 20(1):21. doi: 10.1186/s12915-021-01209-8

43. de Vrieze E, Sharif F, Metz JR, Flik G, Richardson MK. Matrix metalloproteinases in osteoclasts of ontogenetic and regenerating zebrafish scales. *Bone* (2011) 48(4):704–12. doi: 10.1016/j.bone.2010.12.017

44. Zang L, Kagotani K, Nakayama H, Bhagat J, Fujimoto Y, Hayashi A, et al. 10-gingerol suppresses osteoclastogenesis in RAW264.7 cells and zebrafish osteoporotic scales. *Front Cell Dev Biol* (2021) 9:588093. doi: 10.3389/fcell.2021.588093

45. Cardeira-da-Silva J, Bensimon-Brito A, Tarasco M, Brandão AS, Rosa J, Almeida PJ, et al. Fin ray branching is defined by TRAP+ osteolytic tubules. *bioRxiv* (2022). doi: 10.1101/2022.05.09.491182

46. Kato M, Patel MS, Levasseur R, Lobov I, Chang BH, Glass DA2nd, et al. Cbfa1-independent decrease in osteoblast proliferation, osteopenia, and persistent embryonic eye vascularization in mice deficient in Lrp5, a wnt coreceptor. *J Cell Biol* (2002) 157(2):303–14. doi: 10.1083/jcb.200201089

47. Hayman AR, Jones SJ, Boyde A, Foster D, Colledge WH, Carlton MB, et al. Mice lacking tartrate-resistant acid phosphatase (Acp 5) have disrupted endochondral ossification and mild osteopetrosis. *Development* (1996) 122 (10):3151–62. doi: 10.1242/dev.122.10.3151

48. He H, Wang C, Tang Q, Yang F, Xu Y. Possible mechanisms of prednisolone-induced osteoporosis in zebrafish larva. *BioMed Pharmacother* (2018) 101:981–7. doi: 10.1016/j.biopha.2018.02.082

49. Li YP, Chen W, Stashenko P. Molecular cloning and characterization of a putative novel human osteoclast-specific 116-kDa vacuolar proton pump subunit. *Biochem Biophys Res Commun* (1996) 218(3):813–21. doi: 10.1006/bbrc.1996.0145

50. Li YP, Chen W, Liang Y, Li E, Stashenko P. Atp6i-deficient mice exhibit severe osteopetrosis due to loss of osteoclast-mediated extracellular acidification. *Nat Genet* (1999) 23(4):447–51. doi: 10.1038/70563

51. Larrouture QC, Cribbs AP, Rao SR, Philpott M, Snelling SJ, Knowles HJ. Loss of mutual protection between human osteoclasts and chondrocytes in damaged joints initiates osteoclast-mediated cartilage degradation by MMPs. *Sci Rep* (2021) 11(1):22708. doi: 10.1038/s41598-021-02246-7

52. Bruni-Cardoso A, Johnson LC, Vessella RL, Peterson TE, Lynch CC. Osteoclast-derived matrix metalloproteinase-9 directly affects angiogenesis in the prostate tumor-bone microenvironment. *Mol Cancer Res* (2010) 8(4):459–70. doi: 10.1158/1541-7786.MCR-09-0445

53. Zaidi M. Skeletal remodeling in health and disease. *Nat Med* (2007) 13 (7):791–801. doi: 10.1038/nm1593

54. Dai XM, Ryan GR, Hapel AJ, Dominguez MG, Russell RG, Kapp S, et al. Targeted disruption of the mouse colony-stimulating factor 1 receptor gene results in osteopetrosis, mononuclear phagocyte deficiency, increased primitive progenitor cell frequencies, and reproductive defects. *Blood* (2002) 99(1):111–20. doi: 10.1182/blood.v99.1.111

55. Witten PE, Huysseune A. A comparative view on mechanisms and functions of skeletal remodelling in teleost fish, with special emphasis on osteoclasts and their function. *Biol Rev Camb Philos Soc* (2009) 84(2):315–46. doi: 10.1111/j.1469-185X.2009.00077.x

56. Wei W, Zeve D, Suh JM, Wang X, Du Y, Zerwekh JE, et al. Biphasic and dosage-dependent regulation of osteoclastogenesis by β-catenin. *Mol Cell Biol* (2011) 31(23):4706–19. doi: 10.1128/MCB.05980-11

57. Dietrich K, Fiedler IA, Kurzyukova A, López-Delgado AC, McGowan LM, Geurtzen K, et al. Skeletal biology and disease modeling in zebrafish. *J Bone Miner Res* (2021) 36(3):436–58. doi: 10.1002/jbmr.4256

frontiers | Frontiers in Endocrinology

TYPE Original Research
PUBLISHED 01 November 2022
DOI 10.3389/fendo.2022.969481

OPEN ACCESS

EDITED BY
Christoph Winkler,
National University of Singapore,
Singapore

REVIEWED BY
Franziska Knopf,
University Hospital Carl Gustav Carus,
Germany
Yann Gibert,
University of Mississippi Medical
Center, United States

*CORRESPONDENCE
Shannon Fisher
shanfish@bu.edu

†PRESENT ADDRESS
Joana Caetano-Lopes,
Blueprint Medicines, Cambridge, MA,
United States

SPECIALTY SECTION
This article was submitted to
Bone Research,
a section of the journal
Frontiers in Endocrinology

RECEIVED 15 June 2022
ACCEPTED 10 October 2022
PUBLISHED 01 November 2022

CITATION
Miao KZ, Cozzone A,
Caetano-Lopes J, Harris MP and
Fisher S (2022) Osteoclast activity
sculpts craniofacial form to permit
sensorineural patterning in the
zebrafish skull.
Front. Endocrinol. 13:969481.
doi: 10.3389/fendo.2022.969481

Osteoclast activity sculpts craniofacial form to permit sensorineural patterning in the zebrafish skull

Kelly Z. Miao[1], Austin Cozzone[1], Joana Caetano-Lopes[2,3†], Matthew P. Harris[2,3] and Shannon Fisher[1*]

[1]Department of Pharmacology and Experimental Therapeutics, Boston University Aram V. Chobanian & Edward Avedisian School of Medicine, Boston, MA, United States, [2]Department of Orthopaedic Surgery, Boston Children's Hospital, Boston, MA, United States, [3]Department of Genetics, Harvard Medical School, Boston, MA, United States

Efforts to understand the morphogenesis of complex craniofacial structures have largely focused on the role of chondrocytes and osteoblasts. Along with these bone–creating cells, bone–resorbing osteoclasts are critical in homeostasis of adult skeletal structures, but there is currently limited information on their role in the complex morphogenetic events of craniofacial development. Fundamental aspects of skull formation and general skeletal development are conserved from zebrafish to mammals. Using a *cathepsinK* reporter, we documented osteoclast location in the developing zebrafish skull over several weeks, from 5.18 mm to 9.6 mm standard length (approximately 15 to 34 days post fertilization). While broad distribution of osteoclasts is consistent across individuals, they are sparse and the exact locations vary among fish and across developmental time points. Interestingly, we observed osteoclasts concentrating at areas associated with neuromasts and their associated nerves, in particular the hyomandibular foramina and around the supraorbital lateral line. These are areas of active remodeling. In contrast, other areas of rapid bone growth, such as the osteogenic fronts of the frontal and parietal bones, show no particular concentration of osteoclasts, suggesting that they play a special role in shaping bone near neuromasts and nerves. In *csf1ra* mutants lacking functional osteoclasts, the morphology of the cranial bone was disrupted in both areas. The hyomandibular foramen is present in the initial cartilage template, but after the initiation of ossification, the diameter of the canal is significantly smaller in the absence of osteoclasts. The diameter of the supraorbital lateral line canals was also reduced in the mutants, as was the number of pores associated with neuromasts, which allow for the passage of associated nerves through the bone. Our findings define important and previously unappreciated roles for osteoclast activity in shaping craniofacial skeletal structures with a particular role in bone modeling around peripheral cranial nerves, providing a scaffold for wiring the sensioneural system during

craniofacial development. This has important implications for the formation of the evolutionarily diverse lateral line system, as well understanding the mechanism of neurologic sequelae of congenital osteoclast dysfunction in human craniofacial development.

KEYWORDS

osteoclast, neuromast, lateral line, foramen, live imaging, zebrafish, craniofacial development

Introduction

Craniofacial skeletal structures must create strong protection for the brain while allowing the peripheral nervous system to relay sensory inputs from the environment (1, 2). Disruptions to these processes underlie craniofacial birth defects, which broadly encompass the most common structural congenital defects in humans (3–5). In the context of understanding skeletal development of the skull, much of current research focuses on the evolutionary origin, growth and function of cells which build skeletal structures, such as chondrocytes and osteoblasts (6, 7) and in describing structural form and shape of individual bones during development and how they functionally integrate (8, 9). However, the form of individual bones and their final structural role also relies on the activity of bone-resorbing osteoclasts during development (10, 11). Relatively little is known of how these cells shape craniofacial development.

Osteoclasts are a specialized cell type in the hematopoietic lineage and can persist as mononucleate cells or form multinucleated cells by fusion of precursor cells (12, 13). Osteoclasts resorb bone in a tightly regulated homeostatic relationship with bone–generating osteoblasts to maintain general morphology and internal structure of bones in adulthood (14). Osteoclasts are typically stimulated by RANK/RANKL (15) and inhibited by OPG (16). Significant deviations from this homeostatic relationship contribute to adult diseases such as osteoporosis, arthritis, Paget's disease and periodontitis (17–19). Teleosts such as medaka have been successfully used to model the osteoclast dysfunction seen in these disorders (20, 21). Mutations leading to osteoclast dysregulation or dysfunction are the major cause of juvenile osteopetrosis (22–24), which can include significant neurologic sequelae. Understanding facial canal dehiscence caused by developmental abnormalities is important due to consequences for patients such as facial paralysis and hearing loss (25, 26), similar issues have been observed in relation to nerve compression by irregularities in the supraorbital foramen resulting in severe headaches (27, 28). There have been prior descriptions of the normal developmental role of osteoclasts in specific locations in the skull suggesting their overall importance (29–33).

The brain and associated cranial nerves are established prior to the formation of mineralized bone (9, 34, 35, 36) and need to be appropriately scaffolded to allow for function. This interaction adds further complexity to modeling craniofacial form. There is strong evidence in humans and other mammals that appropriate bone development and morphogenesis requires crosstalk between nerves and bone tissue (37–41). Osteoclasts possess nicotinic acetylcholine receptors (42) with agonists of these receptors causing apoptosis of osteoclasts (43) and the β2-adrenergic receptor has been shown to indirectly impact osteoclasts by modulating RANKL (44). Zebrafish provides an efficient means to model these interactions (45–47). The influence of nerves on the craniofacial skeleton has been established in both zebrafish and humans (39, 48). The zebrafish skull houses both cranial nerves and the anterior lateral line (aLL). The lateral line is a sensory system of aquatic vertebrates consisting of neuromasts with mechanosensory hair cells that sense changes in water pressure (49). In zebrafish, the afferent nerves of the cranial neuromasts pass through the hyomandibular foramen, which also houses the facial and auditory cranial nerves (50). After metamorphosis, as the fish transition into adulthood, a subset of cranial neuromasts and nerves become encased in bony lateral line canals (51).

To describe the normal distribution of osteoclasts during craniofacial development, we used a *cathepsinK* transgenic line to carry out serial confocal microscopy on developing zebrafish to localize osteoclasts in craniofacial structures. We find that osteoclasts during development are not distributed evenly and are absent from some highly dynamic structures, including the osteogenic fronts of the frontal and parietal bones. Instead, they cluster densely around areas associated with cranial nerves and sensory cells, including the aLL and the facial nerve (cranial nerve VII). Furthermore, mutants lacking osteoclasts (52) have dysregulation of neurological access and scaffolding, suggesting that bone remodeling, involving high levels of osteoclast activity, is important for specific functional attributes of cranial morphology. Our results highlight the important role of nervous system–bone crosstalk and show that the zebrafish provides a viable model system to understand these interactions.

Materials and methods

Animal husbandry and care

All zebrafish (*Danio rerio*) used for this study were maintained according to standard protocols (53). All experiments were conducted in strict accordance with the Guide for the Care and Use of Laboratory Animals of the National Institutes of Health and all protocols were approved by the Institutional Animal Care and Use Committee at Boston University. The transgenic line *Tg (Ola.ctsk:FRT-DsRed-STOP-FRT,Cre, cmlc2:GFP)* henceforth referred to as *ctsk:dsRed* consists of a medaka promoter active in osteoclasts (54) combined with a *cmlc2* heart marker for early embryo screening. The generation of the *ctsk:dsRed* and *csf1ra*^{mh5} mutant have been described previously (52).

Live calcein staining

A stock calcein solution of 2% in dH2O was adjusted to pH 7 (Sigma-Aldrich, cat: C0875) using NaOH. Stock solution was diluted 1:10 in zebrafish system water to generate fresh 0.2% staining solution. As previously described (55), fish were immersed in staining solution for 30 minutes, then transferred to clean water for 5 minutes three times to remove excess calcein. Post staining, fish were directly imaged or placed back onto the system for serial imaging. For successive imaging, fish were restained after each imaging session to integrate dye into newly formed bone.

Staging and measurements of standard length

Prior to confocal imaging, fish were anesthetized in Tricaine (MS-222, Sigma-Aldrich) and measured as previously described (9). Standard length was used as a proxy for developmental stage (56).

In-vivo imaging

For confocal imaging, fish were mounted in glass bottom dishes (MatTex Corporation) in 2% low melt SeaPlaque agarose in dH_2O (Lonza Catalog #: 50115). Once the agarose solidified within the dishes the fish were covered in fish water. The areas around the gills and mouth were carefully cleared of agarose with a dissecting probe to allow respiration. Total imaging time was around 10 min, after which fish were removed from the agarose and allowed to recover in water. Daily imaging of identified individual fish was conducted during early phases of rapid bone growth, and later reduced to once every 2-3 days as growth slowed (9). Individuals were imaged using the Leica TCS-LSI III macro-confocal microscope with 2× and 5× Plan APO objectives, generating.lif files which were converted into.tiff files using Fiji/ImageJ for further analysis. A total of 84 individual z-stacks were generated over a period of 22 days. Serial live-imaging is generally well tolerated as described previously (9). In this series one out of six original individuals failed to survive through the imaging period and required replacement with a sibling.

Alizarin red staining, dissection and imaging of fixed bone

Fish were fixed overnight in 4% PFA in PBS and Alizarin red staining was performed as previously described in the literature (57). Samples were then dissected to remove the bones from remaining tissue, mounted in 2% low melt agarose then imaged on the Leica TCS-LSI III macro-confocal microscope as described above.

Osteoclast overlay image creation

For composites, the imaging protocol was followed except that groups of individuals were matched by standard length and imaged at only one stage. To generate the overlaid images, max projections of the *ctsk:dsRed* channel were generated from the size-matched imaging files. These were processed in Fiji to despeckle, then threshold adjusted to obtain representations of osteoclast area, shape and location. Each individual was assigned a distinct color; the colorized images were overlaid in Adobe Photoshop on a greyscale max projection of the calcein–stained bone from a representative fish.

Quantification of bone pores

Maximum intensity projections of the calcein or Alizarin red staining were generated in Fiji. and adjusted for brightness and contrast. The pore diameters were obtained through manual tracing and measured in Fiji; statistical analysis was carried out in GraphPad Prism 9.

3D volume rendering of canals

Z-stacks were loaded into Fiji and adjusted for brightness/contrast. Canal limits were manually traced on selected images in the stack using the Segmentation Editor plugin, the interpolation function was then used to predict canal areas on images in between the manual traces in the Z-stack. 3D renderings were then created using the 3D Viewer function and images/videos were exported. For both still images and videos of the 3D rendering angles of imaging between both WT and mutants were matched.

Results

Imaging of *ctsk:dsRed* transgenic fish shows variations in osteoclast distribution in the developing skull

Previous studies of osteoclasts during development have generally captured information on cell distribution at single timepoints in fixed and stained individual animals. Using a previously described low-magnification confocal imaging methodology (9), we visualized the localization of osteoclasts during skull development in individual zebrafish over time. We used *ctsk:dsRed*, a previously established transgenic line which marks functional osteoclasts (52) combined with repeated calcein staining to capture bone growth throughout development (Figure 1A).

We imaged osteoclasts in six fish through live serial confocal microscopy, with individuals assigned into groups covering the ventral (3 individuals, 1 replacing an early death), dorsal (1 individual) or lateral (2 individuals) angles. Fish were imaged from 15dpf to 34dpf, initially on a daily basis, then transitioning to once every 2-3 days as growth slowed at later stages. This allowed us to follow the development of individuals ranging from SL5.18mm to SL9.6mm, generating 84 individual z-stacks with 17 z-stacks taken per individual; in the case of the early death, 10 initial z-stacks were completed and then a sibling replacement was imaged for an additional 6 z-stacks. The original imaging files are available for public access in the FaceBase database (**DOI:** 10.25550/1-X62C). Comparison of osteoclast distribution within individuals at different timepoints and between individuals (Figure 1B) shows that osteoclasts are sparse relative to the cells that make up the underlying bone. This sparsity is notable at the osteogenic fronts of the frontal and parietal bones, previously established as areas of high osteoblast activity (58). This implies that *ctsk*+ osteoclasts do not play a significant role in shaping the morphology of those regions of active bone growth. Comparisons of osteoclasts in different individuals imaged from the same angle at matched developmental timepoints (Figure 1C) also show variability in osteoclast distribution between developmentally matched individuals. This stands in contrast with osteoblasts which have a highly regular pattern between individuals throughout development (9).

Osteoclasts aggregate in specific areas during development across individuals and are associated with nerves and sensory cells

Through the course of the serial live imaging, we observed general patterns of osteoclast distribution across multiple individuals. To better visualize these patterns, we imaged groups of size–matched individuals and then overlaid osteoclast distributions (Figure 2A). The original imaging files used to create the composites are available for public access in the FaceBase database (**DOI:** 10.25550/6-F6XM). A table with nomenclature of bone structures in the skull is displayed in Table 1. Osteoclast clustering was first apparent at SL5.7mm along the branchiostegal rays and the mandibles, some of the first bones to mineralize within the zebrafish skull (8). The osteoclasts at these locations were most prominent at earlier stages and diminished during the imaging period (Figure 2B).

Osteoclasts also consistently clustered around the hyomandibular foramen which allows for the passage of the facial and auditory cranial nerves and aLL nerve (50) (Figure 2C). This dense concentration of osteoclasts is especially conspicuous around SL6.2mm and SL6.8mm, corresponding to previously described key points in the ossification of this structure from a cartilaginous template (8). Osteoclast activity around the hyomandibular foramen continues at SL8mm after this initial period of mineralization. The timing of osteoclast activity and timing of mineralization suggests that osteoclasts are involved in shaping the morphology of the canals both during and after the transition from cartilage to mineralized bone.

In the dorsal overlays at SL5.7mm and SL6.2mm there were no osteoclasts, consistent with the lack of mineralized bone. There is also little osteoclast activity at the timepoints most closely associated with early rapid growth at the osteogenic fronts of the major bones of the cranium the frontal and parietal bones, between SL6.8mm and SL8mm (9). Starting at SL9mm and continuing into SL10mm, stages when the frontal bones reach their final stages of growth and meet to form sutures, there is a notable increase in osteoclasts around the supraorbital lateral line canals. These canals have been previously observed to start forming with the neuromasts on the epithelium above the dermal bone, these neuromasts then sink down into a depression in the bone which is progressively enclosed by walls of ossifying bone until a closed channel is formed (51, 59). The concentration of osteoclasts continues along these canals at SL12mm but is nearly gone by SL14mm (Figure 2D). Our data implies that heightened osteoclast activity and bone resorption is associated with previously described key stages of supraorbital lateral line canal development.

csf1ra^{mh5} mutants display changes in the morphology of the hyomandibular foramen

We document a clear spatial and temporal relationship between osteoclasts and the formation and sculpting of structures associated with nerves and sensory cells. We infer that osteoclasts have an important role in the formation of these structures. To support our hypothesis, we examined mutants in *colony-stimulating factor 1 receptor*, a (*csf1ra*^{mh5}), a key regulator of the proliferation, differentiation and function of myelomonocytic cells, including

10.3389/fendo.2022.969481

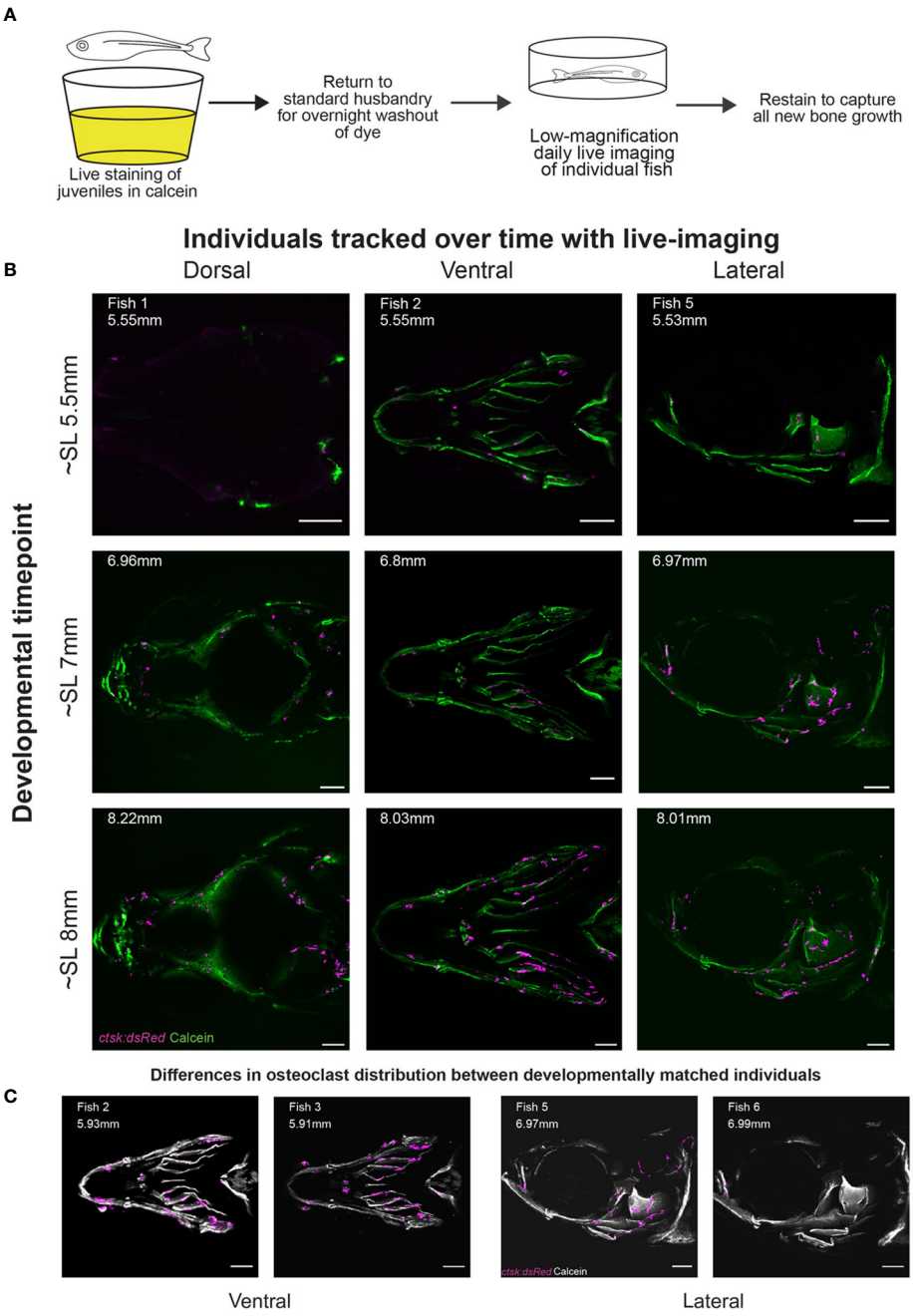

FIGURE 1
Daily live imaging shows changes in osteoclast distribution. Osteoclasts in six individuals were tracked throughout initiation and early growth of bone in the skull, all scale bars represent 200µm. **(A)** Diagram representing the workflow for daily live imaging of the transgenic *ctsk:dsRed* fish, fish were individually housed and then stained with calcein to capture bone growth, then returned to husbandry system to allow for both washout of dye and regular feedings between each daily live imaging session. **(B)** Osteoclast location and distribution is shown on calcein stained mineralized bone. Differences can be tracked within individuals over time and imaging capturing the dorsal, ventral and lateral angles allows for the tracking of osteoclasts on the entirety of the skull **(C)** Representative osteoclast distributions in magenta are displayed on a greyscale image of calcein staining showing that when comparing between individuals, though matched by developmental timepoint (as shown in SL), there is variation in distribution.

10.3389/fendo.2022.969481

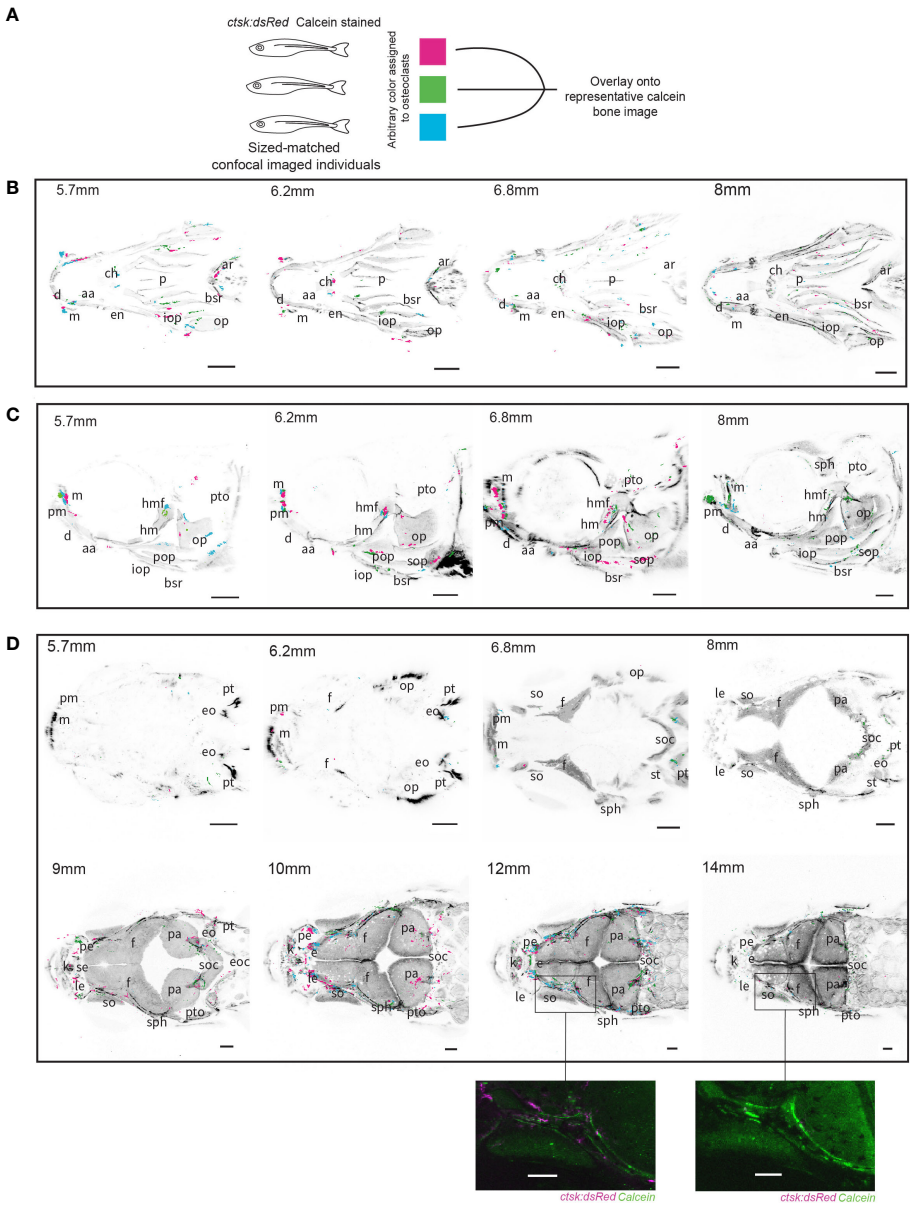

FIGURE 2
Overlays of osteoclasts from imaged individuals shows patterns in distribution. Three individuals were size-matched, stained and live-imaged to create each representation, all scale bars represent 200μm. **(A)** Diagram representing the methodology used to combine the three individuals in each image. **(B)** Ventral imaging shows that osteoclasts are distributed along the branchiostegal rays (bsr) throughout all of the tracked developmental timepoints, in addition concentrations of osteoclast can be seen on the mandibles (m) which house lateral line neuromasts **(C)** Lateral imaging of osteoclasts shows the same distributions as seen on the branchiostegal rays and mandibles but 6.8mm and 8mm images show concentrations of osteoclasts specifically around the hyomandibular foramina (hmf) and on the opercle (op) **(D)** Dorsal imaging of osteoclasts shows that osteoclasts are not highly active prior to growth of the frontal (f) and parietal bones (pa), with a notable concentration of osteoclasts around the supraorbital lateral line canals which run through the frontal bones around 10mm and 12mm which is comparatively reduced by 14mm, a detailed comparison of individuals at 12mm and 14mm is shown in unprocessed form. Abbreviations: aa (anguloarticular), ar (arches), bsr (branchiostegal ray), ch (ceratohyal), d (dentary), en (entopterygoid), eo (epioccipital), e (ethmoid), eoc (exoccipital), ff (facial nerve foramen), f (frontal), hm (hyomandibula), iop (interopercle), k (kinethmoid), le (lateral ethmoid), m (maxilla), op (opercle), p (parasphenoid), pa (parietal), pe (preethmoid), pm (premaxilla), pop (preopercle), pt (posttemporal), pto (pterotic), sph (sphenotic), se (supraethmoid), soc (supraoccipital), so (supraocciptal), so (supraorbital), sop (subopercle), st (supratemporal).

TABLE 1 Abbreviations for bone structures within the zebrafish skull as seen in Figure 2 utilizing terminology from Cubbage and Mabee (8).

List of abbreviations for skeletal elements

aa	anguloarticular	**eo**	epioccipital	**iop**	interopercle	**pa**	parietal	**sph**	sphenotic
ar	arches	**e**	ethmoid	**k**	kinethmoid	**pe**	preethmoid	**se**	supraethmoid
bsr	branchiostegal ray	**eoc**	exoccipital	**le**	lateral ethmoid	**pm**	premaxilla	**soc**	supraoccipital
ch	ceratohyal	**ff**	facial nerve foramen	**m**	maxilla	**pop**	preopercle	**so**	supraorbital
d	dentary	**f**	frontal	**op**	opercle	**pt**	posttemporal	**sop**	subopercle
en	entopterygoid	**hm**	hyomandibula	**p**	parasphenoid	**pto**	pterotic	**st**	supratempora

Companion diagram in Supplemental Material indicating location of abbreviated structures showing dorsal (A) at around SL9mm, ventral (B) at around SL8mm and lateral (C) at around 8mm.

osteoclasts (52). As previously described, *csf1ra* mutants lack osteoclasts and other myelomonocytic cells (56, 60).

Homozygous *csf1ra*^{mh5} mutants and wild-type siblings expressing *ctsk:dsRed* were vitally stained with calcein and observed during the period of osteoclast concentration at the hyomandibular foramen. At SL6.8mm the wild-type fish had a larger, more open canal at the hyomandibular foramen (Figure 3A), while the canal in the mutants had a significantly smaller cross sectional area (Figure 3B). By SL8mm, the canal in the wild–type fish was longer, defined by two deeper areas on each end with a high concentration of osteoclasts. In contrast, the mutants retained a rounder canal opening with a lower overall internal volume and different spacing of the sunken areas. On the surrounding opercle surface, these images also capture small clusters of osteoclasts in the WT fish associated with small additional foramina lacking in the mutants (61) (Figure 3C). We also documented close associations between osteoclasts and bone-forming osteoblasts in the hyomandibular foramen at this developmental timepoint (Supplemental Figure 1) (61). Our analyses indicate that the osteoclasts serve an essential, and specific role in shaping normal foramen morphology in the hyomandibula and opercle bones.

csf1ra^{mh5} mutants lack pores associated with the neuromasts of the supraorbital lateral line canals

Our data indicate a role for osteoclasts in sculpting the hyomandibular foramen; in their absence, the canal is smaller early in ossification, and less complex later in development (Figure 3). To determine if osteoclasts are similarly required to shape the supraorbital lateral line canals, we compared *csf1ra* mutants and siblings at stages of highest osteoclast concentration. At SL10mm and SL12mm, osteoclasts are not distributed evenly throughout the canals (Figures 4A, B). Instead, they tend to associate with small pores in the bone in and around the canals. In the mutants at the same stages, the most striking difference is the almost total absence of pores. To compare the structural differences in detail, we conducted confocal imaging on dissected and Alizarin red stained frontal bones from mutants and siblings and generated z-stacks capturing the entirety of the area of interest. The *csf1ra*$^{-/-}$ mutants had significantly narrower anterior lateral line canals compared to stage–matched siblings (Figure 4C). More strikingly, mutants and siblings showed a highly statistically significant difference in the number and area of pores (Figures 4D, E).

Discussion

We report here the first comprehensive description of osteoclast localization during vertebrate skull formation. Through serial live imaging, we described areas of high osteoclast concentration during development, and interrogated their functional roles in an osteoclast–deficient mutant.

Consistent with the motile nature of osteoclasts, their distribution is dynamic and varies within individual fish during development, and among fish at the same stage. We found the first osteoclasts marked by *ctsk:dsRed* line at around 5 dpf and this corresponds to previous research on osteoclast localization and bone formation during development in zebrafish (33, 55). Overall they are sparse, but tend to concentrate in several specific areas. To better visualize areas of concentration, we overlaid osteoclast positions from three separate fish, visualized from multiple angles and at several developmental stages. We observed areas of highest osteoclast concentration associated with cranial nerves and peripheral sensory cells, including the facial/auditory, lateral line nerves and the mandibular and supraorbital neuromasts (9).

One area with early clustering of osteoclasts was in and around the hyomandibular foramen, which allows passage of cranial nerves and thus connections with facial musculature, the inner ear and the neuromasts of the lateral line system (61–63). The foramen is already present in the hyomandibular cartilage, and is transversed by nerve fibers of facial nerve and aLL at 4 dpf (50). The final morphology of the hyomandibular foramen is shaped as development progresses in concert with ossification of the cartilage (6, 8). We find that the process of shaping is severely disrupted in the absence of osteoclasts in the *csf1ra* mutants. At the earliest stage of our imaging (SL6.8mm), the mutants have greatly reduced diameter of the foramen. By SL8mm, the foramen in the WT fish is more complex and curved, and while the diameter is increased in the mutants, the foramen retains a simple shape resembling the immature morphology.

Osteoclasts were also concentrated on the ventral side of the mandible and in the supraorbital canals, structures associated

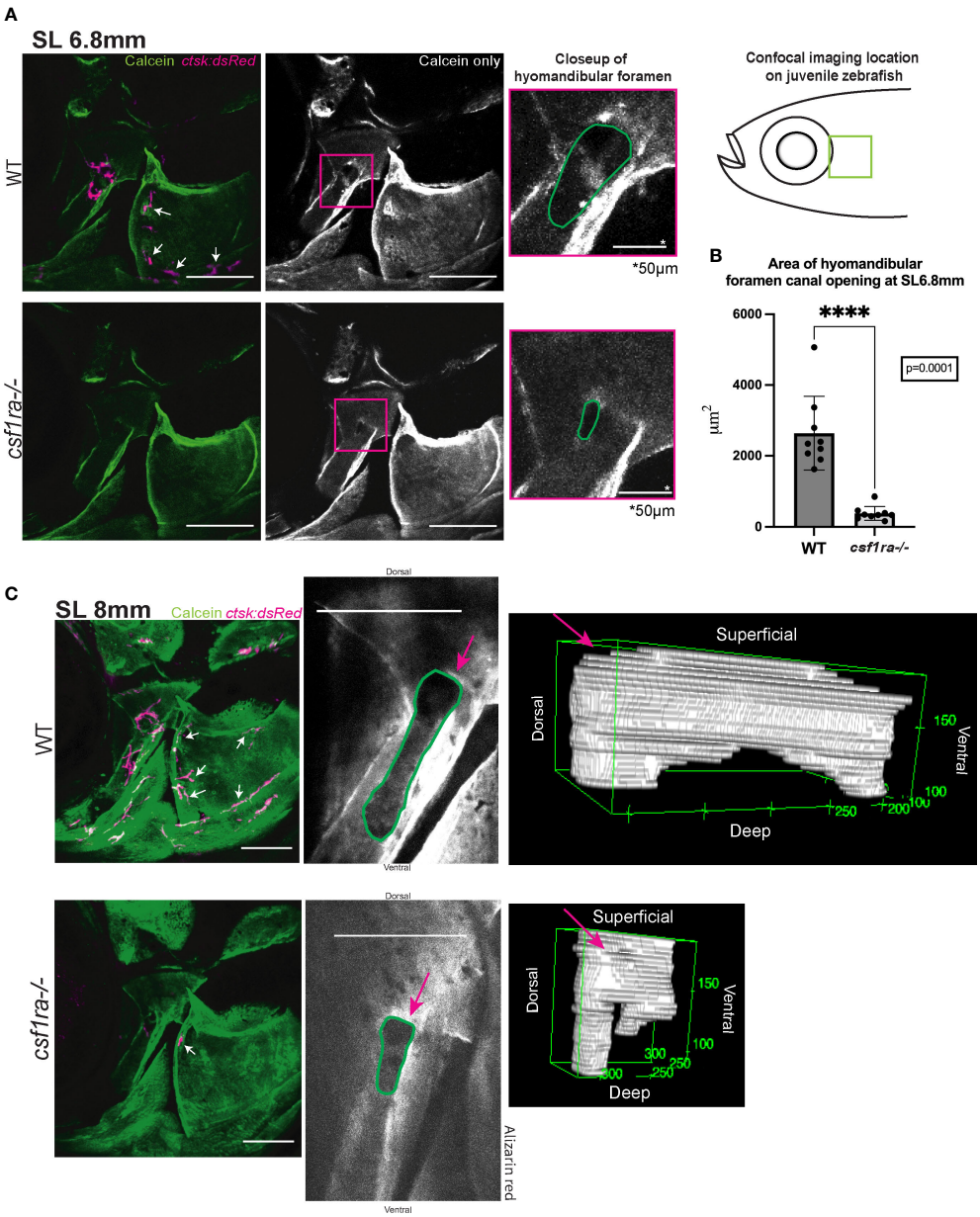

FIGURE 3
Imaging of hyomandibular foramen using calcein-stained *csf1ra* mutants with *ctsk:dsRed* and their wild-type siblings shows differences in canal opening morphology. Size matched individuals were imaged at SL6.8mm and SL8mm, all images are max projections of collected z-stacks, scale bars represent 200µm unless otherwise indicated. **(A)** Diagram represents location of the confocal imaging conducted on the lateral side of the fish focusing in on area of high osteoclast activity as seen in Figure 2. Lack of osteoclast activity in the foramen as seen in *csf1ra* mutants results in morphological differences in the foramen canal opening **(B)** Quantification of area of canal opening (WT n=9, *csf1ra*$^{-/-}$ n=9) lines indicate mean with SEM, Mann-Whitney U t-test (two-tailed) used for statistical analysis, 95% confidence interval **** indicates p-value = 0.0001 **(C)** Individuals at SL8mm display differences in canal morphology shown using representative 3D renderings of internal volume inside of the canals of WT siblings and *csf1ra* mutants, videos of these 3D renderings can be found in the Supplemental Figures.

respectively with the mandibular and supraorbital neuromasts of the aLL (4). The formation of the supraorbital canals housing the neuromasts is quite different from the formation of the hyomandibular foramen. The neuromasts sit on the lateral edge of the frontal bone, but their pattern and distribution is established prior to its formation. Subsequently the underlying bone forms canals that envelop the neuromasts, with external openings to allow sensing of water pressure (36, 50, 64–66). Pores also form in the bone below the neuromasts and allow passage of nerve fibers (51). We find that both processes are disrupted in the absence of

10.3389/fendo.2022.969481

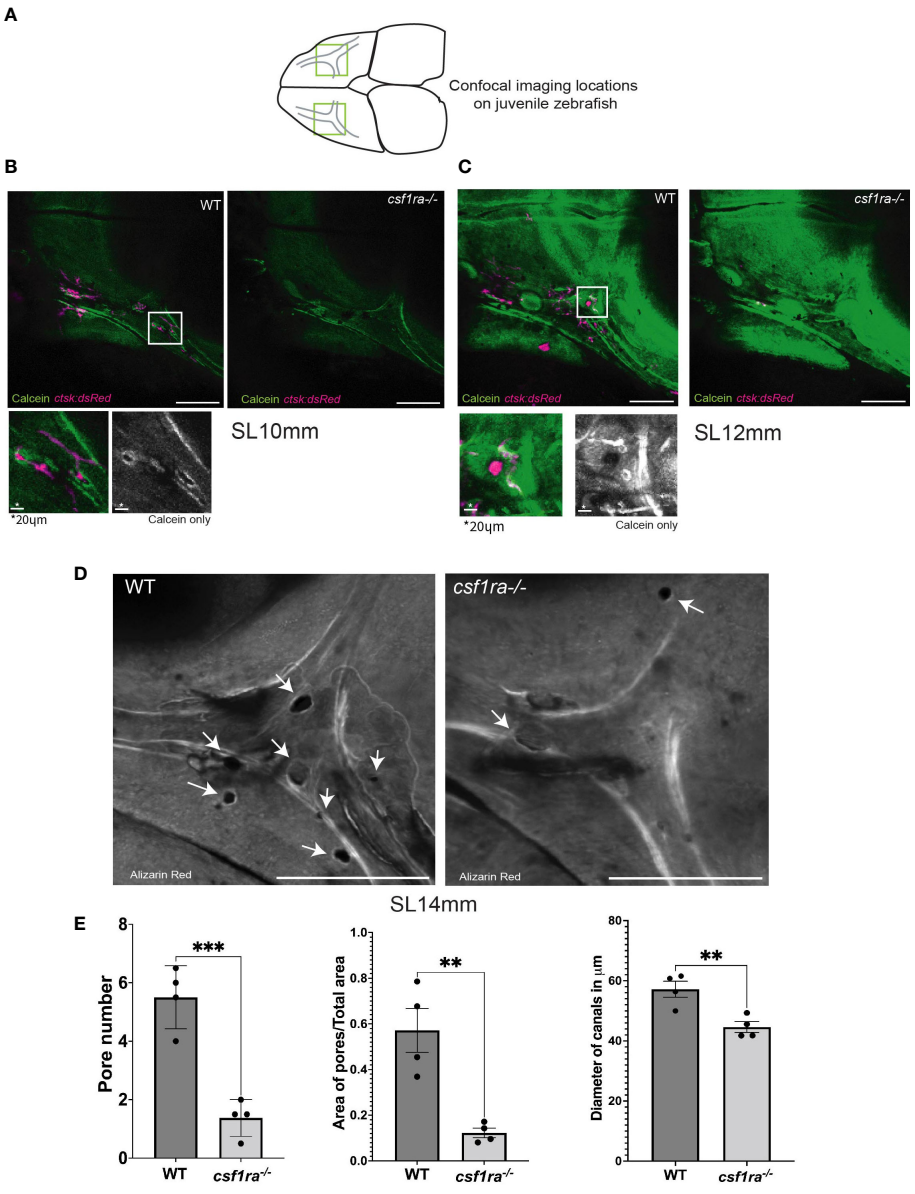

FIGURE 4
Imaging of supraorbital lateral line canals using calcein-stained *csf1ra* mutants with *ctsk:dsRed* and their wild-type siblings shows spatial associations between osteoclasts and foramina in the supraorbital lateral line canals. Individuals were size matched prior to imaging; all images are max projections of z-stacks and scale bars are 200μm unless otherwise indicated. **(A)** Highlighted areas on scheme represent locations of the confocal imaging conducted on the dorsal side of the skull in an area of high osteoclast activity as previously described in Figure 2. **(B)** SL10mm calcein-stained *ctsk:dsRed csf1ra*$^{-/-}$ mutants were live-imaged and wild type siblings show differences in osteoclast expression related to bone morphology. **(C)** SL12mm calcein-stained *ctsk:dsRed* live-imaged WT siblings and *csf1ra*$^{-/-}$ mutants show a continuing pattern from the earlier 10mm stage with activity around the pores **(D)** Bone from fixed alizarin red stained SL14mm individuals was imaged to capture a 3D representation, showing canals which lack pores in the mutant fish. **(E)** Quantification (WT n=4, *csf1ra*$^{-/-}$ n=4) of the number of pores (p=0.0006), followed by the area of the pores normalized using the total area (p=0.03). Measurements were taken from the canals on each frontal bone from the same individual. Since we cannot assume that the paired structures from each fish are independent these numbers were then averaged to generate one figure per individual prior to comparative analysis. Finally diameter of the canals at the juncture point was compared (p=0.008) with location of measurements taken marked in **(C)**, this generated 47 total measurements, 24 for the WT and 23 for the mutants (with one measurement missing due to irregularity of shape in mutant canal) the measurements from a single individual were averaged then statistical analysis conducted. For all charts lines indicate mean with SEM, Mann-Whitney U t-test (two-tailed) used for statistical analysis, 95% confidence interval. ** indicates p-value < 0.005, *** indicates p-value < 0.0005.

osteoclasts. The diameter of the canal is reduced during its formation, and more strikingly, the pores in the bone are largely absent. Our data highlights important parallels with the formation of the bony canals and the presence of osteoclasts around the posterior lateral line neuromasts (67). Positioning of neuromasts determine bone shape (59) and disruptions in neuromasts cause changes in the surrounding bone, implying a functional consequence (48, 50, 67). While we focused on two sites in the craniofacial skeleton, it is likely that the sculpting of bone associated with nerves is broadly disrupted in the absence of osteoclasts.

Prior work in many experimental systems has demonstrated the important instructive role of nerves in skeletal morphogenesis (37–39). Our results affirm the connection between nerves and bone, specifically during craniofacial development. We also demonstrate the critical role of osteoclasts in that connection. We speculate that possible signaling pathways involved could be CXCL12-CXCR4/CXCR7 (68–70) and/or Wnt-β-catenin (71, 72). Consistent with a broad role for osteoclasts in creating the scaffold for cranial nerves, patients with juvenile osteopetrosis frequently suffer neurologic sequelae associated with compression of the optic, facial, supraorbital and auditory nerves (27, 73–75). The overall architecture of the cranial nerves and their foramina are conserved between mammals and zebrafish (34, 76), which provides an accessible model to study these processes. Previous analysis of zebrafish *csf1ra* mutants has shown a general increase in bone mineral density, with an additive increase in fish also lacking the paralogue *csf1rb* (52), making these mutants a valuable model of osteoclast poor osteopetrosis. The presence of low amounts of *ctsk: dsRed* signal and smaller foramina in the mutants observed in our study (Figure 3C) could be attributed to the *csfr1b* paralogue. Homozygous *csf1ra* mutants are viable as adults, making feasible future examination of the hyomandibular and other foramina, and possible sequelae on nerve function and behavior. These detailed studies would expand the utility of the zebrafish model and provide insights into disrupted formation of cranial nerve foramina associated with osteopetrosis and other human diseases.

Data availability statement

The datasets presented in this study can be found in online repositories. The names of the repository/repositories and accession number(s) can be found below: The daily live imaging and osteoclast overlay datasets generated for this study are publicly accessible on the FaceBase site, at https://www.facebase.org, FB00001169 and FB00001240.

Ethics statement

The animal study was reviewed and approved by Boston University IACUC.

Author contributions

SF was responsible for project supervision. KM was responsible for the experiments conducted. KM and AC were responsible for data analysis. JC-L and MH contributed the *cstk: dsRed* and *csf1ra*$^{-/-}$ lines and assisted in experimental design. KM, AC, MH, and SF contributed to the writing and editing of the manuscript. All authors contributed to the article and approved the submitted version.

Funding

The work was supported by grants U01DE024434 to MH and SF, and R01DE022955 and R21DE021196 to SF from NIH/NIDCR, and T32GM008541 to KM.

Acknowledgments

The authors would like to thank the staff, especially Derek Walsh, of the aquatics facility at Boston University for their care of our fish stocks. We would also like to thank Dr. Jacqueline F. Webb for helpful discussions.

Conflict of interest

The authors declare that the research was conducted in the absence of any commercial or financial relationships that could be construed as a potential conflict of interest.

Publisher's note

Supplementary material

The Supplementary Material for this article can be found online at: https://www.frontiersin.org/articles/10.3389/fendo.2022.969481/full#supplementary-material

References

1. Abing W, Rauchfuss A. Fetal development of the tympanic part of the facial canal. *Arch Oto-rhino-laryngol* (1987) 243:374–7. doi: 10.1007/BF00464645

2. Edwards B, Wang JM, Iwanaga J, Loukas M, Tubbs RS. Cranial nerve foramina: Part II - a review of the anatomy and pathology of cranial nerve foramina of the posterior cranial fossa. *Cureus* (2018) 10:e2500. doi: 10.7759/cureus.2500

3. Twigg SR, Wilkie AO. New insights into craniofacial malformations. *Hum Mol Genet* (2015) 24:R50–9. doi: 10.1093/hmg/ddv228

4. Teng CS, Ting MC, Farmer DT, Brockop M, Maxson RE, Crump JG. Altered bone growth dynamics prefigure craniosynostosis in a zebrafish model of saethre-chotzen syndrome. *Elife* (2018) 7:e37024. doi: 10.7554/eLife.37024.041

5. Hamdan A-LH, Nabulsi MM, Farhat FT, Haidar RK, Fuleihan NS. When bone becomes marble: Head and neck manifestations of osteopetrosis. *Paedia Child Health* (2006) 11:37–40. doi: 10.1093/pch/11.1.37

6. Eames BF, DeLaurier A, Ullmann B, Huycke TR, Nichols JT, Dowd J, et al. FishFace: Interactive atlas of zebrafish craniofacial development at cellular resolution. *BMC Dev Biol* (2013) 13:23. doi: 10.1186/1471-213X-13-23

7. Mork L, Crump G. Zebrafish craniofacial development: A window into early patterning. *Curr Top Dev Biol* (2015) 115:235–69. doi: 10.1016/bs.ctdb.2015.07.001

8. Cubbage CC, Mabee PM. Development of the cranium and paired fins in the zebrafish danio rerio (Ostariophysi, cyprinidae). *J Morphol* (1996) 229:121–60. doi: 10.1002/(SICI)1097-4687(199608)229:2<121::AID-JMOR1>3.0.CO;2-4

9. Kanther M, Scalici A, Rashid A, Miao K, Van Deventer E, Fisher S. Initiation and early growth of the skull vault in zebrafish. *Mech Dev* (2019) 160:103578. doi: 10.1016/j.mod.2019.103578

10. Jacome-Galarza CE, Percin GI, Muller JT, Mass E, Lazarov T, Eitler J, et al. Developmental origin, functional maintenance and genetic rescue of osteoclasts. *Nature* (2019) 568:541–5. doi: 10.1038/s41586-019-1105-7

11. Kamakura T, Nadol JBJ. Evidence of osteoclastic activity in the human temporal bone. *Audiol Neurootol* (2017) 22:218–25. doi: 10.1159/000481279

12. Asagiri M, Takayanagi H. The molecular understanding of osteoclast differentiation. *Bone* (2007) 40:251–64. doi: 10.1016/j.bone.2006.09.023

13. Witten PE, Huysseune A. A comparative view on mechanisms and functions of skeletal remodelling in teleost fish, with special emphasis on osteoclasts and their function. *Biol Rev Camb Philos Soc* (2009) 84:315–46. doi: 10.1111/j.1469-185X.2009.00077.x

14. Kim JM, Lin C, Stavre Z, Greenblatt MB, Shim JH. Osteoblast-osteoclast communication and bone homeostasis. *Cells* (2020) 9:E2073. doi: 10.3390/cells9092073

15. Suda T, Takahashi N, Udagawa N, Jimi E, Gillespie MT, Martin TJ. Modulation of osteoclast differentiation and function by the new members of the tumor necrosis factor receptor and ligand families. *Endocr Rev* (1999) 20:345–57. doi: 10.1210/edrv.20.3.0367

16. Simonet WS, Lacey DL, Dunstan CR, Kelley M, Chang MS, Lüthy R, et al. Osteoprotegerin: a novel secreted protein involved in the regulation of bone density. *Cell* (1997) 89:309–19. doi: 10.1016/S0092-8674(00)80209-3

17. Charles JF, Aliprantis AO. Osteoclasts: more than 'bone eaters'. *Trends Mol Med* (2014) 20:449–59. doi: 10.1016/j.molmed.2014.06.001

18. Helfrich MH. Osteoclast diseases. *Microsc Res Tech* (2003) 61:514–32. doi: 10.1002/jemt.10375

19. Novack DV, Teitelbaum SL. The osteoclast: friend or foe. *Annu Rev Pathol* (2008) 3:457–84. doi: 10.1146/annurev.pathmechdis.3.121806.151431

20. To TT, Witten PE, Renn J, Bhattacharya D, Huysseune A, Winkler C. Rankl-induced osteoclastogenesis leads to loss of mineralization in a medaka osteoporosis model. *Development* (2012) 139:141–50. doi: 10.1242/dev.071035

21. To TT, Witten PE, Huysseune A, Winkler C. An adult osteopetrosis model in medaka reveals the importance of osteoclast function for bone remodeling in teleost fish. *Comp Biochem Physiol C Toxicol Pharmacol* (2015) 178:68–75. doi: 10.1016/j.cbpc.2015.08.007

22. Sobacchi C, Frattini A, Guerrini MM, Abinun M, Pangrazio A, Susani L, et al. Osteoclast-poor human osteopetrosis due to mutations in the gene encoding RANKL. *Nat Genet* (2007) 39:960–2. doi: 10.1038/ng2076

23. Stattin EL, Henning P, Klar J, McDermott E, Stecksen-Blicks C, Sandström, et al. SNX10 gene mutation leading to osteopetrosis with dysfunctional osteoclasts. *Sci Rep* (2017) 7:3012. doi: 10.1038/s41598-017-02533-2

24. Van Wesenbeeck L, Odgren PR, Coxon FP, Frattini A, Moens P, Perdu B, et al. Involvement of PLEKHM1 in osteoclastic vesicular transport and osteopetrosis in incisors absent rats and humans. *J Clin Invest* (2007) 117:919–30. doi: 10.1172/JCI30328

25. Yetiser S. The dehiscent facial nerve canal. *Int J Otolaryngol* (2012) 2012:679708. doi: 10.1155/2012/679708

26. Nomiya S, Kariya S, Nomiya R, Morita N, Nishizaki K, Paparella MM, et al. Facial nerve canal dehiscence in chronic otitis media without cholesteatoma. *Eur Arch Otorhinolaryngol* (2014) 271:455–8. doi: 10.1007/s00405-013-2431-2

27. Chepla KJ, Oh E, Guyuron B. Clinical outcomes following supraorbital foraminotomy for treatment of frontal migraine headache. *Plast Reconstr Surg* (2012) 129:656e–62e. doi: 10.1097/PRS.0b013e3182450b64

28. Tomaszewska A, Kwiatkowska B, Jankauskas R. The localization of the supraorbital notch or foramen is crucial for headache and supraorbital neuralgia avoiding and treatment. *Anatomical Rec Anat Rec* (2012) 295:1494–503. doi: 10.1002/ar.22534

29. Ealba EL, Jheon AH, Hall J, Curantz C, Butcher KD, Schneider RA. Neural crest-mediated bone resorption is a determinant of species-specific jaw length. *Dev Biol* (2015) 408:151–63. doi: 10.1016/j.ydbio.2015.10.001

30. Edamoto M, Kuroda Y, Yoda M, Kawaai K, Matsuo K. Trans-pairing between osteoclasts and osteoblasts shapes the cranial base during development. *Sci Rep* (2019) 9:1956. doi: 10.1038/s41598-018-38471-w

31. Kimmel CB, DeLaurier A, Ullmann B, Dowd J, McFadden M. Modes of developmental outgrowth and shaping of a craniofacial bone in zebrafish. *PloS One* (2010) 5:e9475. doi: 10.1371/journal.pone.0009475

32. Witten PE, Hansen A, Hall BK. Features of mono- and multinucleated bone resorbing cells of the zebrafish danio rerio and their contribution to skeletal development, remodeling, and growth. *J Morphol J Morphol* (2001) 250:197–207. doi: 10.1002/jmor.1065

33. Sharif F, de Bakker MA, Richardson MK. Osteoclast-like cells in early zebrafish embryos. *Cell J* (2014) 16:211–24.

34. Higashijima S, Hotta Y, Okamoto H. Visualization of cranial motor neurons in live transgenic zebrafish expressing green fluorescent protein under the control of the islet-1 promoter/enhancer. *J Neurosci* (2000) 20:206–18. doi: 10.1523/JNEUROSCI.20-01-00206.2000

35. Thomas ED, Cruz IA, Hailey DW, Raible DW. There and back again: development and regeneration of the zebrafish lateral line system. *Wiley Interdiscip Rev Dev Biol* (2015) 4:1–16. doi: 10.1002/wdev.160

36. Wada H, Kawakami K. Size control during organogenesis: Development of the lateral line organs in zebrafish. *Dev Growth Differ* (2015) 57:169–78. doi: 10.1111/dgd.12196

37. Abeynayake N, Arthur A, Gronthos S. Crosstalk between skeletal and neural tissues is critical for skeletal health. *Bone* (2021) 142:115645. doi: 10.1016/j.bone.2020.115645

38. Elefteriou F. Impact of the autonomic nervous system on the skeleton. *Physiol Rev* (2018) 98:1083–112. doi: 10.1152/physrev.00014.2017

39. Tomlinson RE, Christiansen BA, Giannone AA, Genetos DC. The role of nerves in skeletal development, adaptation, and aging. *Front Endocrinol (Lausanne)* (2020) 11:646. doi: 10.3389/fendo.2020.00646

40. Gerosa L, Lombardi G. Bone-to-Brain: A round trip in the adaptation to mechanical stimuli. *Front Physiol* (2021) 12. doi: 10.3389/fphys.2021.623893

41. Wan Q-Q, Qin W-P, Ma Y-X, Shen M-J, Li J, Zhang Z-B, et al. Crosstalk between bone and nerves within bone. *Advanced Sci Adv Sci* (2021) 8:2003390. doi: 10.1002/advs.202003390

42. Mandl P, Hayer S, Karonitsch T, et al. Nicotinic acetylcholine receptors modulate osteoclastogenesis. *Arthritis Res Ther* (2016) 18:63. doi: 10.1186/s13075-016-0961-x

43. Bajayo A, Bar A, Denes A, Bachar M, Kram V, Attar-Namdar M, et al. Skeletal parasympathetic innervation communicates central IL-1 signals regulating bone mass accrual. *Proc Natl Acad Sci U S A* (2012) 109:15455–60. doi: 10.1073/pnas.1206061109

44. Elefteriou F. Regulation of bone remodeling by the central and peripheral nervous system. *Arch Biochem Biophys* (2008) 473:231–6. doi: 10.1016/j.abb.2008.03.016

45. Schmidt R, Strähle U, Scholpp S. Neurogenesis in zebrafish - from embryo to adult. *Neural Dev* (2013) 8:3. doi: 10.1186/1749-8104-8-3

46. Tonelli F, Bek JW, Besio R, De Clercq A, Leoni L, Salmon P, et al. Zebrafish: A resourceful vertebrate model to investigate skeletal disorders. *Front Endocrinol (Lausanne)* (2020) 11:489. doi: 10.3389/fendo.2020.00489

47. Won SY, Choi BO, Chung KW, Lee JE. Zebrafish is a central model to dissect the peripheral neuropathy. *Genes Genomics* (2019) 41:993–1000. doi: 10.1007/s13258-019-00838-2

48. Chang CT, Franz-Odendaal TA. Perturbing the developing skull: using laser ablation to investigate the robustness of the infraorbital bones in zebrafish (Danio rerio). *BMC Dev Biol* (2014) 14:44. doi: 10.1186/s12861-014-0044-7

49. Piotrowski T, Baker CV. The development of lateral line placodes: taking a broader view. *Dev Biol* (2014) 389:68–81. doi: 10.1016/j.ydbio.2014.02.016

50. Wada H, Ghysen A, Satou C, Higashijima S, Kawakami K, Hamaguchi S, et al. Dermal morphogenesis controls lateral line patterning during postembryonic development of teleost fish. *Dev Biol* (2010) 340:583–94. doi: 10.1016/j.ydbio.2010.02.017

51. Webb JF, Shirey JE. Postembryonic development of the cranial lateral line canals and neuromasts in zebrafish. *Dev Dyn* (2003) 228:370–85. doi: 10.1002/dvdy.10385

52. Caetano-Lopes J, Henke K, Urso K, Duryea J, Charles JF, Warman ML, et al. Unique and non-redundant function of csf1r paralogues in regulation and evolution of post-embryonic development of the zebrafish. *Development* (2020) 147:dev181834. doi: 10.1242/dev.181834

53. Westerfield M. "General methods for Zebrafish care". *Eugene: Univ Oregon Press* (2007).

54. Chatani M, Takano Y, Kudo A. Osteoclasts in bone modeling, as revealed by *in vivo* imaging, are essential for organogenesis in fish. *Dev Biol* (2011) 360:96–109. doi: 10.1016/j.ydbio.2011.09.013

55. Du SJ, Frenkel V, Kindschi G, Zohar Y. Visualizing normal and defective bone development in zebrafish embryos using the fluorescent chromophore calcein. *Dev Biol* (2001) 238:239–46. doi: 10.1006/dbio.2001.0390

56. Parichy DM, Elizondo MR, Mills MG, Gordon TN, Engeszer RE. Normal table of postembryonic zebrafish development: staging by externally visible anatomy of the living fish. *Dev Dyn* (2009) 238:2975–3015. doi: 10.1002/dvdy.22113

57. Walker MB, Kimmel CB. A two-color acid-free cartilage and bone stain for zebrafish larvae. *Biotech Histochem* (2007) 82:23–8. doi: 10.1080/10520290701333558

58. Kague E, Roy P, Asselin G, Hu G, Simonet J, Stanley A, et al. Osterix/Sp7 limits cranial bone initiation sites and is required for formation of sutures. *Dev Biol* (2016) 413:160–72. doi: 10.1016/j.ydbio.2016.03.011

59. Powers AK, Boggs TE, Gross JB. Canal neuromast position prefigures developmental patterning of the suborbital bone series in astyanax cave- and surface-dwelling fish. *Dev Biol* (2018) 441:252–61. doi: 10.1016/j.ydbio.2018.04.001

60. Herbomel P, Thisse B, Thisse C. Zebrafish early macrophages colonize cephalic mesenchyme and developing brain, retina, and epidermis through a m-CSF receptor-dependent invasive process. *Dev Biol* (2001) 238:274–88. doi: 10.1006/dbio.2001.0393

61. Iwasaki M, Yokoi H, Suzuki T, Kawakami K, Wada H. Development of the anterior lateral line system through local tissue-tissue interactions in the zebrafish head. *Dev Dyn* (2020) 249:1440–54. doi: 10.1002/dvdy.225

62. Crucke J, Van de Kelft A, Huysseune A. The innervation of the zebrafish pharyngeal jaws and teeth. *J Anat* (2015) 227:62–71. doi: 10.1111/joa.12321

63. Sheets L, Holmgren M, Kindt KS. How zebrafish can drive the future of genetic-based hearing and balance research. *J Assoc Res Otolaryngol* (2021) 22:215–35. doi: 10.1007/s10162-021-00798-z

64. Alexandre D, Ghysen A. Somatotopy of the lateral line projection in larval zebrafish. *Proc Natl Acad Sci USA* (1999) 96:7558–62. doi: 10.1073/pnas.96.13.7558

65. Ghysen A, Dambly-Chaudière C. The lateral line microcosmos. *Genes Dev* (2007) 21:2118–30. doi: 10.1101/gad.1568407

66. Klein A, Bleckmann H. Function of lateral line canal morphology. *Integr Zool* (2015) 10:111–21. doi: 10.1111/1749-4877.12101

67. Wada H, Iwasaki M, Kawakami K. Development of the lateral line canal system through a bone remodeling process in zebrafish. *Dev Biol* (2014) 392:1–14. doi: 10.1016/j.ydbio.2014.05.004

68. Dambly-Chaudière C, Cubedo N, Ghysen A. Control of cell migration in the development of the posterior lateral line: antagonistic interactions between the chemokine receptors CXCR4 and CXCR7/RDC1. *BMC Dev Biol* (2007) 7:23. doi: 10.1186/1471-213X-7-23

69. David NB, Sapède D, Saint-Etienne L, Thisse C, Thisse B, Dambly-Chaudière C, et al. Molecular basis of cell migration in the fish lateral line: Role of the chemokine receptor CXCR4 and of its ligand, SDF1. *Proc Natl Acad Sci* (2002) 99:16297–302. doi: 10.1073/pnas.252339399

70. Shahnazari M, Chu V, Wronski TJ, Nissenson RA, Halloran BP. CXCL12/CXCR4 signaling in the osteoblast regulates the mesenchymal stem cell and osteoclast lineage populations. *FASEB J* (2013) 27:3505–13. doi: 10.1096/fj.12-225763

71. Kobayashi Y, Uehara S, Koide M, Takahashi N. The regulation of osteoclast differentiation by wnt signals. *Bonekey Rep* (2015) 4:713. doi: 10.1038/bonekey.2015.82

72. Jacques BE, Montgomery WH, Uribe PM, Yatteau A, Asuncion JD, Resendiz G, et al. The role of wnt/β-catenin signaling in proliferation and regeneration of the developing basilar papilla and lateral line. *Dev Neurobiol* (2014) 74:438–56. doi: 10.1002/dneu.22134

73. Benecke JE. Facial nerve dysfunction in osteopetrosis. *Laryngoscope* (1993) 103:494–7. doi: 10.1288/00005537-199305000-00002

74. McGonnell IM, Akbareian SE. Like a hole in the head: Development, evolutionary implications and diseases of the cranial foramina. *Semin Cell Dev Biol* (2019) 91:23–30. doi: 10.1016/j.semcdb.2018.08.011

75. Steward CG. Neurological aspects of osteopetrosis. *Neuropathol Appl Neurobiol* (2003) 29:87–97. doi: 10.1046/j.1365-2990.2003.00474.x

76. Mueller T, Vernier P, Wullimann MF. The adult central nervous cholinergic system of a neurogenetic model animal, the zebrafish danio rerio. *Brain Res* (2004) 1011:156–69. doi: 10.1016/j.brainres.2004.02.073

frontiers | Frontiers in Endocrinology

TYPE Original Research
PUBLISHED 14 November 2022
DOI 10.3389/fendo.2022.1000662

OPEN ACCESS

EDITED BY
Ronald Kwon,
University of Washington,
United States

REVIEWED BY
Daniel Youngstrom,
UCONN Health, United States
Andy Willaert,
Ghent University, Belgium

*CORRESPONDENCE
Raimund Wagener
raimund.wagener@uni-koeln.de

SPECIALTY SECTION
This article was submitted to
Bone Research,
a section of the journal
Frontiers in Endocrinology

RECEIVED 22 July 2022
ACCEPTED 07 October 2022
PUBLISHED 14 November 2022

CITATION
Forte-Gomez HF, Gioia R, Tonelli F, Kobbe B, Koch P, Bloch W, Paulsson M, Zaucke F, Forlino A and Wagener R (2022) Structure, evolution and expression of zebrafish cartilage oligomeric matrix protein (COMP, TSP5). CRISPR-Cas mutants show a dominant phenotype in myosepta. *Front. Endocrinol.* 13:1000662. doi: 10.3389/fendo.2022.1000662

Structure, evolution and expression of zebrafish cartilage oligomeric matrix protein (COMP, TSP5). CRISPR-Cas mutants show a dominant phenotype in myosepta

Helena Fabiana Forte-Gomez[1], Roberta Gioia[2], Francesca Tonelli[2], Birgit Kobbe[1], Peter Koch[3], Wilhelm Bloch[4], Mats Paulsson[5], Frank Zaucke[6], Antonella Forlino[2] and Raimund Wagener[5]*

[1]Center for Biochemistry, University of Cologne, Cologne, Germany, [2]Department of Molecular Medicine, Biochemistry Unit, University of Pavia, Pavia, Italy, [3]Department of Pharmacology, University Clinic Cologne, Cologne, Germany, [4]Institute of Cardiovascular Research and Sport Medicine, German Sport University, Cologne, Germany, [5]Center for Biochemistry, Center for Molecular Medicine, University of Cologne, Cologne, Germany, [6]Dr. Rolf M. Schwiete Research Unit for Osteoarthritis, Department of Orthopedics (Friedrichsheim), University Hospital Frankfurt, Goethe University, Frankfurt, Germany

COMP (Cartilage Oligomeric Matrix Protein), also named thrombospondin-5, is a member of the thrombospondin family of extracellular matrix proteins. It is of clinical relevance, as in humans mutations in COMP lead to chondrodysplasias. The gene encoding zebrafish Comp is located on chromosome 11 in synteny with its mammalian orthologs. Zebrafish Comp has a domain structure identical to that of tetrapod COMP and shares 74% sequence similarity with murine COMP. Zebrafish *comp* is expressed from 5 hours post fertilization (hpf) on, while the protein is first detectable in somites of 11 hpf embryos. During development and in adults *comp* is strongly expressed in myosepta, craniofacial tendon and ligaments, around ribs and vertebra, but not in its name-giving tissue cartilage. As in mammals, zebrafish Comp forms pentamers. It is easily extracted from 5 days post fertilization (dpf) whole zebrafish. The lack of Comp expression in zebrafish cartilage implies that its cartilage function evolved recently in tetrapods. The expression in tendon and myosepta may indicate a more fundamental function, as in evolutionary distant Drosophila muscle-specific adhesion to tendon cells requires thrombospondin. A sequence encoding a calcium binding motif within the first TSP type-3 repeat of zebrafish Comp was targeted by CRISPR-Cas. The heterozygous and homozygous mutant Comp zebrafish displayed a patchy irregular Comp staining in 3 dpf myosepta, indicating a dominant phenotype. Electron microscopy revealed that the endoplasmic reticulum of myosepta fibroblasts is not affected in homozygous fish. The disorganized extracellular matrix may indicate that this mutation rather interferes with extracellular matrix assembly, similar to what is seen in a subgroup of chondrodysplasia patients. The

early expression and easy detection of mutant Comp in zebrafish points to the potential of using the zebrafish model for large scale screening of small molecules that can improve secretion or function of disease-associated COMP mutants.

KEYWORDS

zebrafish, extracellular matrix, thrombospondins, comp, chondrodysplasia

Introduction

COMP is a homopentameric glycoprotein that was first isolated from different cartilage types and from the Swarm rat chondrosarcoma (1–3). At that time, it was considered to be a cartilage-specific protein. However, over the last decades a broader expression of COMP in many other mesenchymal tissues has been described, including tendon, muscle and dermis (4–6). Sequence analysis revealed that COMP belongs to the thrombospondin (TSP) family and is therefore also referred to as TSP5 (7).

COMP interacts with other extracellular matrix (ECM) components, including collagens from different collagen subfamilies (8). The binding to collagens and interconnection of ECM components makes a matrix-stabilizing function likely (9). In addition, COMP expression often correlates with fibrotic overexpression of collagens and increased matrix deposition, like in idiopathic pulmonary fibrosis and in different types of cancer (7). For fibrillar collagens, a role in collagen secretion and fibril formation has been suggested (10). In addition to these more structural functions, a binding to growth factors of the TGF-β superfamily, like TGF-β and different BMPs, has been described (11, 12). These interactions were shown to modulate the activity of the bound growth factor and their relevance has been demonstrated in chondrogenic (13) and osteogenic (14) differentiation of mesenchymal stem cells and in an animal model with aortic calcification (15). More recently, a protective role in the maintenance of the vascular ECM and the identification of COMP as a novel NOTCH ligand driving embryonic stem cell differentiation towards the smooth muscle lineage was reported (16).

COMP deficient mice do not show an obvious skeletal phenotype and it was speculated that the lack of COMP might be compensated by other members of the TSP family (17). However, the transgenic expression of mutant COMP variants in mice resulted in growth retardation and a chondrodysplasia-like phenotype (18). Mutations in COMP result in protein misfolding and accumulation in the endoplasmic reticulum, eventually leading to decreased cell proliferation and increased apoptosis (19, 20). In addition to skeletal alterations, a reduced tendon strength and a mild myopathy was reported in one of these mouse lines (21, 22).

Interestingly, the mutant mouse phenotype largely reflects the phenotype of human patients with mutations in the COMP gene. To date, more than 70 disease-causing mutations have been identified and associated with either the milder multiple epiphyseal dysplasia (MED) or the more severe pseudoachondroplasia (PSACH). The severity of the disease apparently depends on the specific mutation and it was shown in cell culture models that different mutations may cause the disease by different molecular mechanisms (23). MED and PSACH are rare diseases and currently, there is no treatment available for human patients (24).

In a first attempt to develop a treatment, transgenic mice were treated with anti-oxidant or anti-inflammatory compounds. Treatment with either resveratrol or aspirin reduced the amount of intracellularly accumulated COMP and the associated cellular stress as well as the extent of growth plate chondrocyte death (25). However, how these compounds affect the underlying disease mechanisms remains largely unclear (26).

Over the last years, zebrafish has been established as an attractive model organism to study human skeletal disorders (27). High fecundity, external development and the transparent early life stages are major advantages. In addition, the genome can be easily manipulated using CRISPR/Cas9 and the small size and fast development of the fish allows high throughput drug screening (28, 29). In zebrafish, functional analysis was so far performed only on Tsp4, the closest relative of COMP among the TSP family members (30). Interestingly, Tsp4b has been shown to be essential for ECM assembly and muscle attachment at myotendinous junctions (31). However, other members of the TSP family have not yet been investigated in detail.

In the present study, we therefore first characterized the structure of the zebrafish *comp* gene and analyzed the protein sequence and expression pattern in zebrafish. Second, we generated and phenotyped a zebrafish line in which a Comp mutation had been introduced by CRISPR/Cas9.

10.3389/fendo.2022.1000662

Materials and methods

Bioinformatic analysis

For the analysis of the orthologous gene loci the Ensembl *Danio rerio* (GRCz11), *Mus musculus* (GRCm39) and *Homo sapiens* (GRCh38.p13) genome databases were used. The potential signal peptide was predicted by SignalP v6.0 (https://services.healthtech.dtu.dk/service.php?SignalP-6.0) (32). Multiple sequence alignments were performed using the Pileup algorithm of the Wisconsin PackageTM and figures were prepared with the BOXSHADE 3.21 program. The phylogenetic analysis was done by protein distance as described in PHYLIP v3.695.

Fish husbandry

Zebrafish embryos were obtained by crossing Cologne (KOLN) strain wild type adult fish, raised at 28°C and staged as described (33). Animal protocols were approved by the veterinary agency of North-Rhine Westphalia (Landesamt für Natur, Umwelt und Verbraucherschutz [LANUV], Germany).

Expression and purification of recombinant zebrafish Comp and generation of specific antibodies

A cDNA construct encoding mature zebrafish Comp was generated by RT-PCR on whole zebrafish mRNA. Suitable primers introduced 5′ terminal NheI (5'caatgctagccaaggaatatctaga gatggagag3') and 3′ terminal BamHI restriction sites (5'caatgc ggccgcttaaaaaagctggatttgctg3'). The amplified PCR product was inserted into a modified pCEP-Pu vector (34) containing an N-terminal BM-40 signal peptide and a N-terminal Twin-Strep-tag upstream of the NheI restriction site. The recombinant plasmid was introduced into human embryonic kidney 293-EBNA cells (Invitrogen) using the FuGENE 6 transfection reagent (Roche). The cells were selected with puromycin (1 µg/mL) and when expressing the Strep-tagged protein transferred to serum free medium for harvest. After centrifugation, the cell culture supernatants were adjusted to pH 7.4, applied to a StrepTactin column (IBA) and eluted following the supplier's protocol.

The purified recombinant zebrafish Comp was used to immunize a rabbit and a guinea pig. The antisera were purified by affinity chromatography on a column with antigen coupled to CNBr-activated Sepharose (GE Healthcare). The specific antibodies were eluted with 0.1 M glycine, pH 2.5, the eluate neutralized with 1 M Tris-HCl, pH 8.8, and adjusted to 150 mM NaCl. An immunoblot of the recombinant protein detected with the affinity-purified antibodies is shown in Supplementary Figure 1.

Immunoprecipitation

For immunoprecipitation of endogenous Comp, whole 5 dpf zebrafish embryos were homogenized with a Dounce homogenizer and lysed for 30 min on ice in a solution containing 50 mM Tris-HCl, pH 7.4, 150 mM NaCl, 2 mM EDTA, 1% Nonidet P-40, and protease inhibitors. Tissue extracts were centrifuged and the supernatants recovered. Samples (1.5 mL) were first precleared by incubation for 5 h at 4°C with 50 µL of protein A-Sepharose (Roche). They were then centrifuged and the supernatants incubated overnight at 4°C with 4 µg affinity purified polyclonal guinea pig antibodies and 50 µL protein A-Sepharose. After centrifugation at 500 × g the beads were washed once with extraction buffer and twice with TBS, eluted in 2× Laemmli sample buffer containing β-mercaptoethanol, boiled for 3 min and analyzed by SDS-PAGE and western blot. For peptide mass fingerprint analysis gels were stained with Coomassie Brilliant Blue, bands cut out and MALDI-TOF mass spectrometry carried out by the Central Bioanalytic Core Unit in the Center for Molecular Medicine Cologne, University of Cologne, using a standard procedure (35, 36).

Protein extraction, SDS-PAGE, agarose/polyacrylamide composite gel electrophoresis and immunoblot

For one step protein extraction, zebrafish larvae were homogenized in 10 volumes 50 mM Tris, pH 7.4, 150 mM NaCl, 2 mM EDTA, 1% Nonidet P-40 and protease inhibitors, and put on ice for 15 min. 1/3 volume of 4x SDS Laemmli sample buffer (8% (w/v) SDS, 40% (v/v) glycerol, 0.2% (w/v) bromphenol blue, 250 mM Tris-HCl, pH 6.8) was added, the samples boiled for 5 min, centrifuged for 10 min and subjected to 4-10% (w/v) gradient gel SDS-PAGE. For sequential extraction, 178 wild type zebrafish larvae were frozen at -80°C. On the day of extraction, the larvae were thawed, 1.78 mL of chilled buffer I (0.15 M NaCl, 50 mM Tris-HCl, pH 7.4) (TBS) was added, the fish homogenized with a Dounce homogenizer and extracted on a roller shaker at 4°C for 10h. The extracts were clarified by centrifugation and the supernatants stored at -20°C. The pellets were re-extracted in an identical manner with buffer II (1 M NaCl, 10 mM EDTA, 50 mM

Tris, pH 7.4) and the remaining insoluble material was extracted with buffer III (8M urea, 10 mM EDTA, 50 mM Tris, pH 7.4). All extraction buffers contained Complete protease inhibitor (Roche). For agarose/polyacrylamide composite gel electrophoresis samples were supplemented with Laemmli SDS-sample buffer and urea to a final concentration of 2 M and subjected to electrophoresis on 0.5% (w/v) agarose/3% (w/v) polyacrylamide composite gels (37). Proteins were transferred to a nitrocellulose membrane and probed using affinity-purified polyclonal antibodies diluted in TBS/5% milk powder. Bands were detected by chemiluminescence using a peroxidase-conjugated swine anti-rabbit IgG secondary antibody (Dako).

Generation of zebrafish Comp mutants using CRISPR/Cas9

A guide RNA (gRNA) for *comp* (ENSDART00000171255) targeting the 5'- end of exon 8 (5'-GGAACTGACACCGAT ATCGATGG-3', 874-896 nt) was designed using the software CHOPCHOP (https://chopchop.cbu.uib.no/). The synthesis of target oligonucleotides (Eurofins Genomics) and the preparation of gRNAs were carried out as described (38). For the Cas9 mRNA *in vitro* transcription, the pT3TS-nCas9n vector (Addgene) was linearized by XbaI (New England BioLabs) digestion and purified using the Nucleospin Gel and PCR Clean-up Kit (Macherey-Nagel). DNA was transcribed using mMESSAGE mMACHINE T3 Kit (Invitrogen). mRNA polyadenylation was performed using the Poly (A) Tailing Kit (Ambion) and the Cas9 transcript was purified by RNeasy Mini Kit (Qiagen, Germany). The mRNA quality was checked by electrophoresis on a 1% (w/v) formaldehyde agarose gel. The gRNA (12.5 ng/µL) and Cas9 mRNA (300 ng/µL) were mixed in Danieau solution (58 mM NaCl, 0.7 mM KCl, 0.4 mM $MgSO_4$, 0.6 mM $Ca(NO_3)_2$, 5 mM Hepes, pH 7.6) with a tracer dye (0.5 mg/mL dextran conjugated with tetramethylrhodamine, Molecular Probes) in a final volume of 5 µL and pre-heated at 60° C for 10 min. Microinjection was carried out using an InjectMan micromanipulator (Eppendorf) assembled on a Leica M165 FC stereomicroscope. After 24 h the DNA from single embryos was extracted by proteinase K digestion (2.5 mg/mL, Sigma Aldrich) in lysis buffer (100 mM Tris HCl, pH 8.5, 5 mM EDTA, 0.2% (w/v) SDS, 200 mM NaCl) overnight (o/n) at 55°C, followed by isopropanol precipitation and resuspension in 20 mM Tris-HCl, 1 mM EDTA, pH 8.0. To evaluate targeting efficiency T7 Endonuclease Assay was performed (28). For genotyping the 283 bp amplicon obtained using 5'-CGCAATGGAAACAAACTGATTA-3' forward and 5'-GAGTTTGGAACAGTGAGGCAAT-3' reverse primers was digested with ClaI enzyme.

qPCR

RNA was extracted from RNA pools of 20 embryos at different stages of development (5, 12 and 24 hours post fertilization, hpf; 2, 3 and 4 days post fertilization, dpf, in duplicate) using Qiazol (Qiagen) and DNase digestion (Invitrogen) according to manufacturer's instructions. RNA quantity was determined by NanoDrop spectrophotometer and RNA quality by agarose gel electrophoresis. Reverse-transcription was performed using the High-Capacity cDNA Transcription kit (Applied Biosystems) according to manufacturer's protocol in a final volume of 20 µL. qPCR was performed in triplicate in a 25 µL final volume with SYBR Green Master mix (Applied Biosystems) using the QuantStudio 3 thermocycler and the QuantStudio Design & analysis software (Applied Biosystems).

The following primers were used: for Comp (ENSDAR T00000171255_2) forward, 5'-GAGTGTGAAGCCTGTGGCAT-3' and reverse, 5'-CACTCGTCAACGTCCTCACA-3' (334-353 nt), for β-actin (ENSDART00000054987_7) forward, 5-GAAGATCAAGATCATTGCTCCCCC -3' and reverse, 5'-GTTCTGTTTAGAAGCACTTCCTGTG -3' (1110-1135 nt) and for dna15ta1 forward, 5'-TACTGTGCTCAAATTGCTTCA-3' and reverse, 5'-AATGAGTACTGTGAACTTAATCCAT-3 ' (39). The annealing temperature was 60°C for the normalization with β actin and 58°C for the normalization with dna15ta1. ΔΔCt was used for quantitation.

Tissue labelling procedures

Zebrafish larvae were fixed overnight at 4°C in 4% paraformaldehyde (PFA) in PBS, pH 7.4, washed in PBS containing 0.1% Tween and finally washed and stored in methanol at −20°C. To bleach pigment and block endogenous peroxidases, larvae were incubated overnight in 3 mL of 10% H_2O_2 in methanol, then 10 mL of phosphate buffered tween (PBT) was added and the incubation continued for further 16 to 24 h. Larvae were washed in PBT, digested with 2 µg/mL proteinase K for 8 min and fixed again in 4% PFA for 15 min. After washing, larvae were treated with bovine testicular hyaluronidase (Sigma; 500 units/mL in 0.1 M NaH_2PO_4, 0.1 M sodium acetate, pH 5.0) at 37°C for 2h and blocked in 3% normal goat serum for 2 h. Affinity purified rabbit polyclonal antibodies were applied at appropriate dilutions and the specimens incubated for 2 h. The primary antibodies were visualized by consecutive treatment of larvae for 2 h each with biotinylated secondary antibody and a streptavidin–peroxidase

conjugate (ABC kit, Vectastain). All antibodies were diluted in 3% (w/v) normal goat serum in PBT. For color development, larvae were pre-soaked in diaminobenzidine (0.2 mg/mL PBT) for 30 min and 1 µL of 0.3% H_2O_2 solution was added while the larvae were observed under a dissection microscope. For whole-mount immunofluorescence analysis zebrafish were incubated with primary antibody overnight at 4°C, washed four times for 25 min at room temperature, incubated for 2 h at room temperature with fluorescently labelled secondary antibody and washed again four times. The embryos were cleared in 80% glycerol.

Paraffin-embedded sections were deparaffinized. After rehydration in PBS, the sections were digested with bovine testicular hyaluronidase (Sigma, 500 units/mL in 0.1 M NaH_2PO_4, 0.1 M sodium acetate, pH 5.0) at 37°C for 30 min and incubated with 0.2% Triton X-100 in TBS for 10 min. After washing, the sections were blocked with 1% (w/v) bovine serum albumin in TBS for 1 h and incubated with the affinity-purified rabbit polyclonal antibody overnight at 4°C. The primary antibodies were visualized by consecutive treatment with biotin-SP-conjugated goat anti-rabbit IgG (Dianova) and alkaline phosphatase-conjugated streptavidin (Dianova) for 1 h each. Antibodies and enzyme-conjugates were diluted in 1% (w/v) bovine serum albumin in TBS and the slides developed with Sigma FAST™ Fast Red TR/naphthol AS-MX (Sigma).

Electron microscopy

Zebrafish were fixed with 2% glutaraldehyde in 0.1 M sodium cacodylate, pH 7.2-7.3 overnight at 4°C and washed three times with PBS for 10-20 min. Thereafter, tissue was osmicated with 1% OsO4 in 0.1 M cacodylate and dehydrated in increasing ethanol concentrations. Araldite infiltration and flat embedding were performed following standard procedures. Toluidine blue was used to stain semithin sections of 0.5 µm. 70-nm-thick sections were cut with an Ultracut UCT ultramicrotome (Reichert) and stained with 1% aqueous uranylic acetate and lead citrate. Samples were analyzed with a Zeiss EM 109 electron microscope (Zeiss).

Results

The zebrafish genome contains duplicated genes coding for Thbs1-4 and a single gene coding for Comp

In the most recent version of the zebrafish genome database (GRCz11) and in ZFIN (https://zfin.org/) nine thrombospondin genes are listed, eight duplicated genes coding for thrombospondin 1-4 and a single gene coding Comp (Supplementary Table 1). *comp* is located on chromosome 11 (6,941,389-6,974,022 reverse strand) and *crtc1b* and *klhl26* which are located downstream of comp are in synteny with their ortholog genes in human and mouse (Figure 1). Like the genes coding for COMP in man and mouse, the zebrafish *comp* gene contains 19 coding exons and the intron-exon structure and the phase of the introns are completely conserved. The length of five exons is slightly different between zebrafish and mouse (Supplementary Table 2).

The protein sequence of zebrafish Comp is highly conserved and most similar to that of zebrafish Tsp4b

The zebrafish Comp protein consists of 749 amino acid residues (NP_001313279.1), the overall similarity to the murine COMP is 74% and the identity is 67% (Figure 2). An isoform lacking a single glycine residue as the consequence of alternative splicing is listed in the database. This glycine residue is located in the linker between the coiled coil and the first EGF like domain. However, the variant is most likely a minor form, as it is found

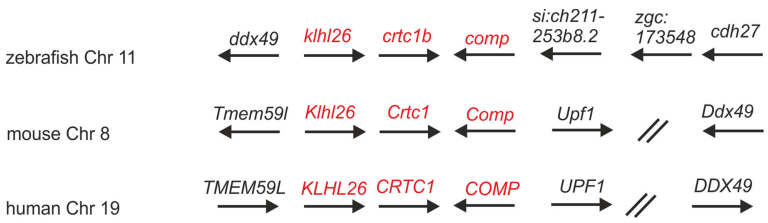

FIGURE 1
Syntenic relationships of Comp gene loci in zebrafish, mouse and human. Arrows indicate the 5' to 3' orientation of the genes. COMP genes and syntenic genes in the direct neighborhood are in red. Note that synteny is only present downstream of the Comp genes. ZFIN gene designations are used for genes lacking a gene name. The double slash indicates regions in the human and mouse genomes (52 and 29 Mbp, respectively) lacking synteny. Note, although not in the same order and direction, the ddx49 genes in zebrafish, mouse and human are all in the vicinity of the COMP genes.

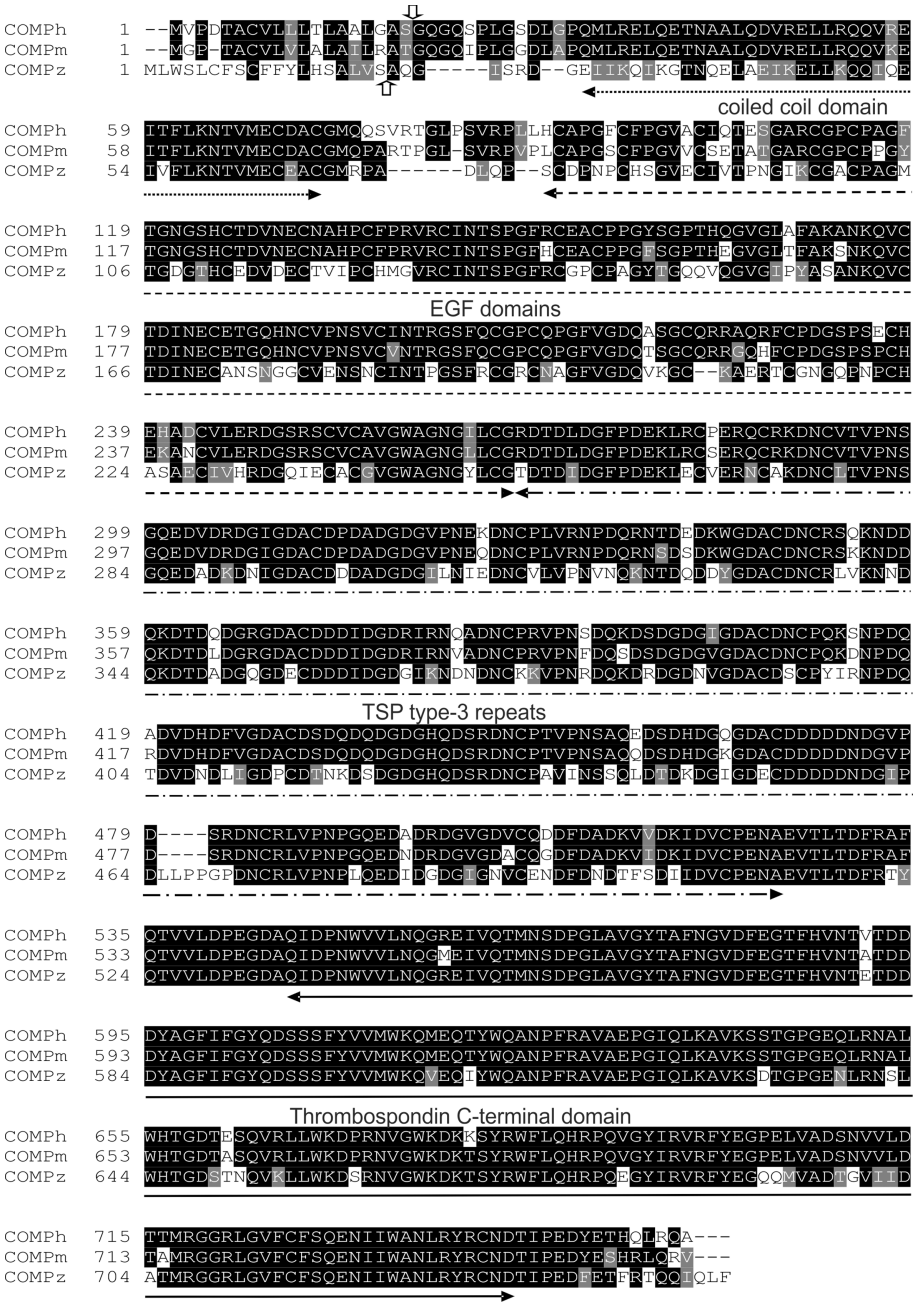

FIGURE 2
Alignment of amino acid sequences of the human, mouse and zebrafish COMP. The vertical arrows mark the potential signal peptide cleavage sites (up, zebrafish; down, human and mouse). The positions of the domains are indicated by horizontal arrows.

only in a single myoblast EST clone (CT608499.2). The domain structure of zebrafish Comp is completely conserved, consisting of an N-terminal coiled-coil domain, followed by four EGF-like domains, eight TSP type-3 repeats and the C-terminal domain. The predicted signal peptide sequence contains 20 amino acid residues (32) and the mature main isoform has a molecular mass of 79748 Da. All cysteine residues in the mature protein are conserved, while the EGF-like domains are the least, and the C-terminal domain the best conserved. The positions of aspartic acid residues in the TSP type-3 repeats that display a contiguous series of calcium binding sites (40) are, except for one residue, completely conserved. Most similar among the zebrafish thrombospondins is Tsp4b, having 60% similarity and 54% identity to zebrafish Comp. A phylogenetic tree based on the

alignment of the protein sequences of the shared parts of the thrombospondins from mouse and zebrafish was constructed by protein distance methods (Figure 3). The sequences of the duplicated zebrafish thrombospondins 1-4 are always located in the same branches as the respective mouse thrombospondins, clearly indicating that they are orthologs. Although zebrafish and mouse COMP are not in the Tsp4 sub-branch they are clearly part of the larger TSP4/TSP5 branch.

Zebrafish Comp forms pentamers and is easily extractable from tissue

Zebrafish Comp was recombinantly expressed in 293 EBNA cells to determine the oligomeric state, as pentameric coiled-coils are not detected by prediction programs, e.g. Multicoil. Indeed, non-reducing composite agarose/SDS-PAGE of the purified recombinant protein showed a prominent band at the calculated mass of a pentamer, similar to human or murine COMP (Figure 4A). The purified protein was used to immunize a rabbit and a guinea pig and the antisera purified by affinity chromatography on a column carrying the original antigen. As the quality of the antibodies is crucial, their specificity was tested on the Comp knockout strain sa12473, obtained from the European Zebrafish Resource Center (EZRC), as negative control. Sa12473 fish carry a stop codon in exon 13 of the *comp* gene. When applying the affinity purified antibodies, immunoblot bands were not visible for homozygous mutants in contrast to heterozygous and wild type siblings (Supplementary Figure 1). Also by immunofluorescence only heterozygous and wild type, but not homozygous Sa12473 fish were stained (Supplementary Figure 2) demonstrating the specificity of the antibodies. As the gels were run under reducing conditions monomeric Comp was detected. To study the structure of tissue-derived Comp and to identify similarities or differences to mammalian COMP, sequential extracts from 5 dpf wild type whole zebrafish were analyzed by immunoblotting using the affinity-purified antibodies. Nearly all Comp was extracted with TBS (Figure 4B). Here, composite agarose/polyacrylamide gel were run under non-reducing conditions to resolve the disulfide linked Comp oligomers. Like the recombinant zebrafish Comp (Figure 4A), the tissue Comp was present as pentamers. Further extraction with high salt/EDTA followed by 8M urea did not yield any substantial amounts of Comp (Figure 4B). To determine if Comp forms hetero-oligomers with Tsp4 (41) also in zebrafish, immunoprecipitation experiments were performed on 5 dpf wild type whole zebrafish TBS extracts using Comp antibodies. Indeed, analysis of the immunoprecipitates by peptide mass fingerprint mass spectrometry revealed that the only thrombospondin that co-immunoprecipitated with Comp (Supplementary Table 3) was Tsp4b, as seven specific peptides were detected (Supplementary Table 4), but no peptides derived from other thrombospondins (Supplementary Table 5).

Zebrafish Comp is strongly expressed in myosepta and notochord but not in cartilage

By RT-PCR, *comp* expression could be detected before 24 hpf (Supplementary Figure 3). The spatial expression pattern of

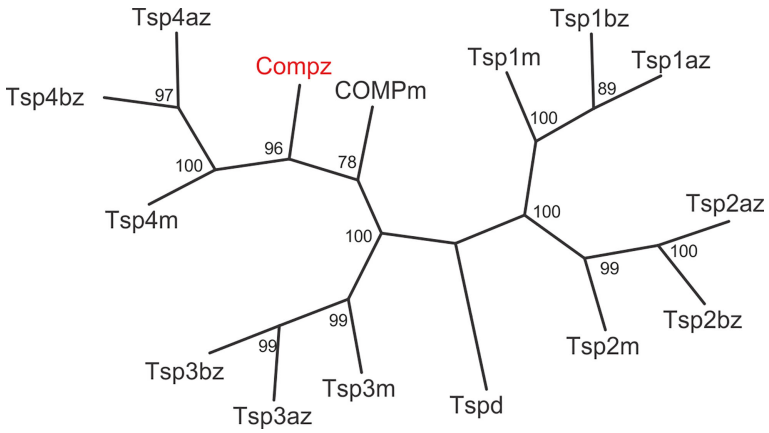

FIGURE 3
Phylogenetic tree of thrombospondins. Thrombospondin sequences comprising the EGF domains, TSP type-3 repeats and the C-terminal domains from zebrafish *(z)* and mouse *(m)* were aligned using the PILEUP program of the GCG package, using the default parameters. As a full-length sequence for zebrafish thrombospondin 1a was not present in the databases, we amplified the lacking N-terminal sequence by RT-PCR (see Supplementary Figure 4). The tree was constructed using the programs PROTEIN DISTANCE, Fitch-Margoliash and CONSENSE of the PHYLIP package version 3.695. Bootstrap analyses using 100 replicates were performed to show the significance. The numbers indicate the statistical weight of the individual branches. Drosophila *(d)* thrombospondin was used as outgroup.

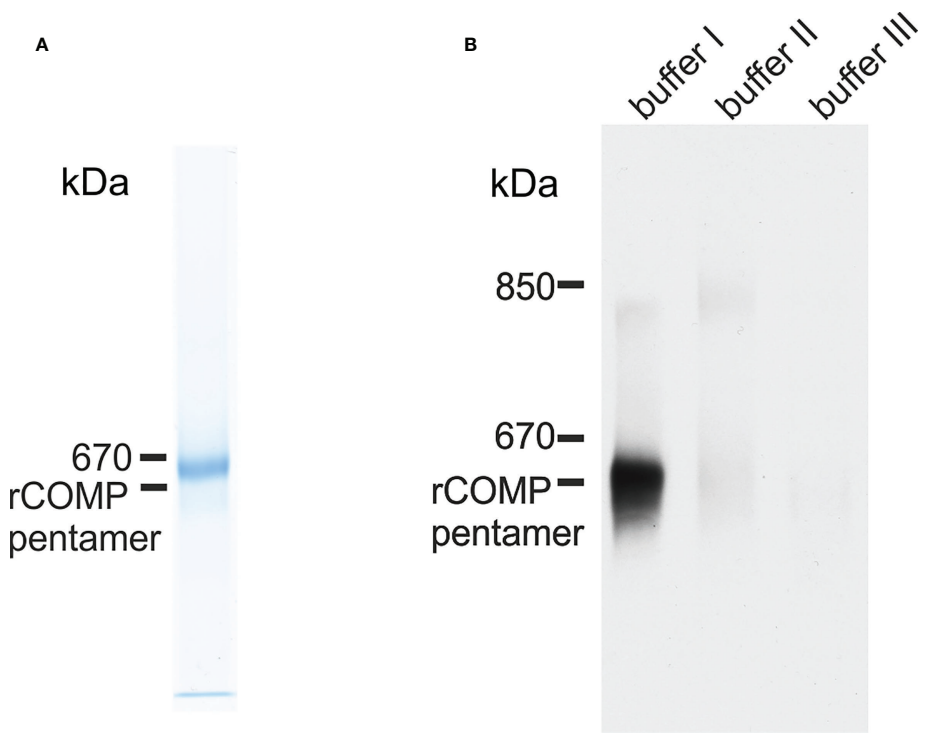

FIGURE 4
Immunoblot analysis of recombinant zebrafish Comp and Comp in extracts from zebrafish embryos. **(A)** Recombinant zebrafish COMP and **(B)** sequentially extracted proteins from whole 5 dpf zebrafish were separated in 0.5% (w/v) agarose/3% (w/v) polyacrylamide composite gels under non-reducing conditions and detected with guinea pig polyclonal antibodies specific for zebrafish Comp. Buffer I, TBS; buffer II, 50 mM Tris, pH 7.4, 10 mM EDTA, and 1M NaCl, buffer III, 50 mM Tris, pH 7.4, 10 mM EDTA and 8M urea. Recombinant rat COMP was used as a marker and the position of the pentamer is indicated.

Comp protein was studied by whole mount immunostaining and immunohistochemistry on sections, using the same antibodies as for the immunoblots. At 11 hpf Comp is expressed in the somites (Figures 5A–C), and at 72 hpf Comp is virtually exclusively and strongly expressed in myosepta (Figure 5D). At 100 hpf, Comp was also found in tendinous structures in the head (Figures 5E, F). Published *in situ* hybridization data (https://zfin.org/ZDB-GENE-060606-1/expression) confirm the expression pattern at the transcriptional level (42). In zebrafish, Comp was very strongly detected in the notochordal sheath and around vacuolated notochord cells in the intervertebral disc region (Figures 5G-J, see also Figure 7A). It was most clearly seen in transverse sections at positions where the diameter of the notochord is smaller (Figure 5J) Less prominent, Comp was also found in tendinous structures that attach muscles to the vertebra (Figure 5G-J), in a narrow zone surrounding ribs (Figures 5K, L) and in the myosepta (Figures 5K, L). However, in contrast to in mammals, Comp is not expressed in zebrafish articular cartilage or in cartilage anlagen of developing bones (Figures 5E, G, H, J).

Generation and characterization of mutant Comp zebrafish lines

In humans, mutations in the *COMP* gene lead to pseudoachondroplasia (PSACH) and multiple epiphyseal dysplasia (MED) (43). Mutations result either in retention of COMP in the rough endoplasmic reticulum (rER) of chondrocytes and subsequently premature chondrocyte death (44) or in the secretion of a dysfunctional COMP disturbing ECM assembly (23, 45). Although zebrafish do not express Comp in cartilage, due to the broad expression in larval myosepta they could represent a model both to study the consequences of COMP mutations and to test therapeutic approaches. Indeed, large scale screening is possible as the expression in myosepta can be easily monitored by whole mount immunofluorescence. A sequence encoding a calcium binding site in the first TSP type-3 repeat was targeted by CRISPR-Cas9 gene editing, to generate zebrafish Comp mutants. This TSP type-3 repeat was chosen, as mutations of the equivalent amino acid residues L272 and D273 (Figure 6A)

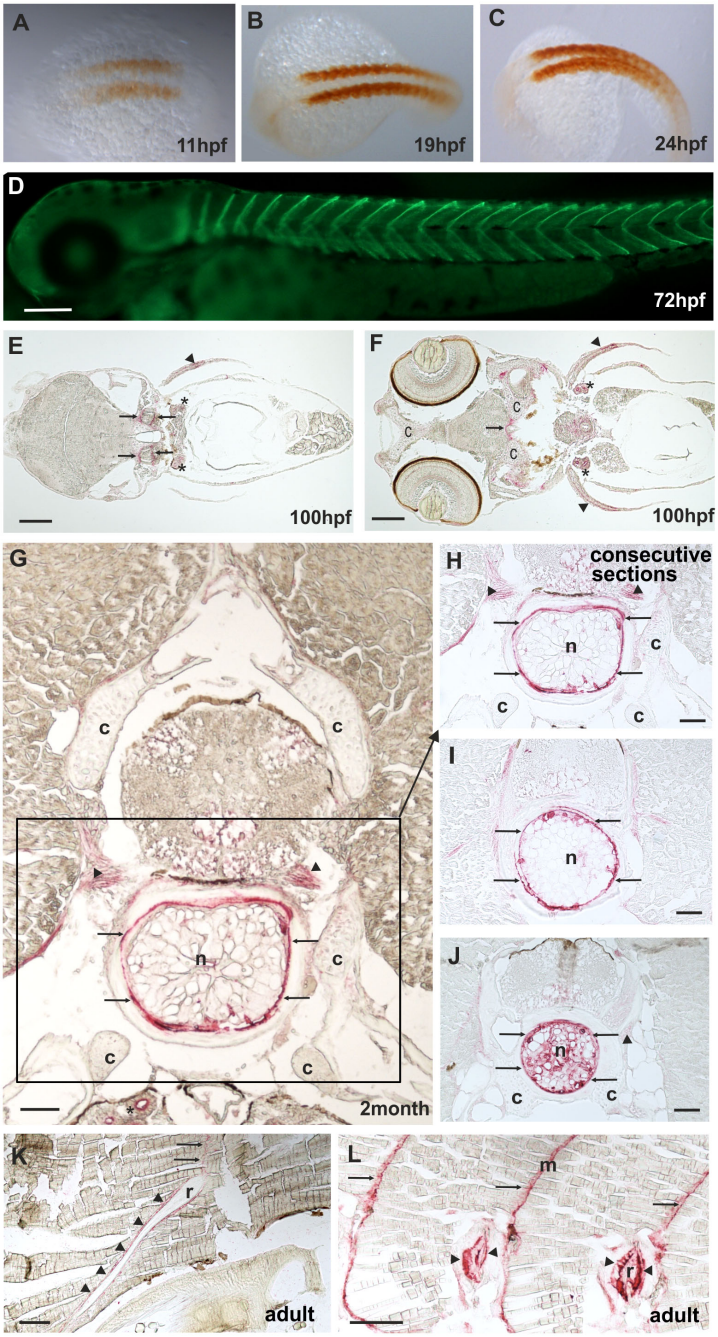

FIGURE 5
Comp distribution in zebrafish tissues at different stages of development. Immunostainings were performed using an affinity-purified rabbit antiserum directed against zebrafish Comp. **(A–D)**, whole mount staining of 11hpf **(A)**, 19hpf **(B)**, 24 hpf **(C)** and 72 hpf **(D)** zebrafish. At 11-24 hpf Comp is expressed in the somites (**A–C**, brown peroxidase staining) and at 72 hpf in the myosepta (**D**, green fluorescence). **E-L**, immunostaining was carried out on paraffin-embedded tissue sections from 100 hpf **(E, F)**, 2-month-old **(G–J)** and adult **(K, L)** zebrafish by alkaline phosphatase-conjugated streptavidin and Fast Red staining. In the head, at 100 hpf Comp is expressed in tendinous tissues (*arrows*), but not in cartilage (*c*) **(E, F)**. Comp is also found in the pectoral fin (arrowheads). A transverse section through a vertebral body displays Comp in the notochord (framed) most strongly in the notochord sheath (*arrows*), but not in vertebral cartilage (*c*) of 2-month-old zebrafish **(G, H, J)**. Consecutive transverse sections **(H-J)** show a variable expression around vacuolated notochord cells, most prominent at positions with a narrow notochord **(J)**. Comp was also found in tendinous structures that attach muscles to the vertebra **(G, H, J)** (*arrowheads*). In adult zebrafish **(K, L)** Comp is still expressed in myosepta (*m, arrows*) and around ribs (*r, arrowheads*) where the skeletal muscles are attached. (*Asterisks* in **E**, **F**) Unspecific staining of kidney tubules by the secondary antibody, see also Supplementary Figure 2. Bars: 50 µm in **(G–J)**, 100 µm in **(E, F, K, L)** and 200 µm in **(D)**.

are linked to PSACH and the D273 is proposed to be involved in Ca^{2+} binding (46). Four lines with frameshift mutations and two lines with small in frame deletions were generated. The lines with frameshift deletions were, as the sa12473 line (Supplementary Figure 1), complete Comp knockouts (Supplementary Figure 1). A line (ΔI258D259Comp) with an in-frame deletion resulting in the lack of I258 and D259 was further characterized. The homozygous and heterozygous mutant fish are viable and do not show an obvious phenotype (not shown). Immunoblotting of extracts from 2-month-old zebrafish revealed a slightly reduced Comp expression in heterozygous and a stronger reduction in homozygous mutant zebrafish, indicating that mutant ΔI258D259Comp is still expressed (Figure 6B). Interestingly, a band at approx. 100 kDa, most likely representing Comp lacking its coiled coil oligomerization domain, is lacking in heterozygous and homozygous fish (Figure 6B). Although Comp is also expressed in the notochord, the general architecture of the vertebral column in homozygous adult zebrafish was unaffected (Figure 7B), Interestingly, in wild type zebrafish Comp is strongly present in the fibrocartilaginous tissue in a very narrow zone at the base of the intervertebral discs and also lining the bone-shaped vacuolated tissue (Figure 7A). Whole mount immunofluorescence staining on 72 hpf zebrafish larvae from heterozygous breedings showed only two phenotypes. In one, the Comp antibody strongly and continuously stains the myosepta and irregularities are hardly seen. In the other phenotype, the myosepta are also stained, but the continuous staining is much weaker and, in contrast, irregular spots of strong staining appear within the myosepta indicating an irregular deposition of mutant Comp (Figure 6C). This pointed to a dominant phenotype and indeed genotyping revealed that only heterozygous and homozygous mutant zebrafish showed the distinct, patchy staining pattern of Comp (Figure 6C). Comp is absent in homozygous fish, but, as Comp forms pentamers, also in heterozygous mutant animals the presence/amount of pure wild type COMP is neglectable. Further, the similar staining pattern indicates that mutant ΔI258D259Comp pentamers and hybrid pentamers consisting of wild type and mutant ΔI258D259 Comp behave in a similar

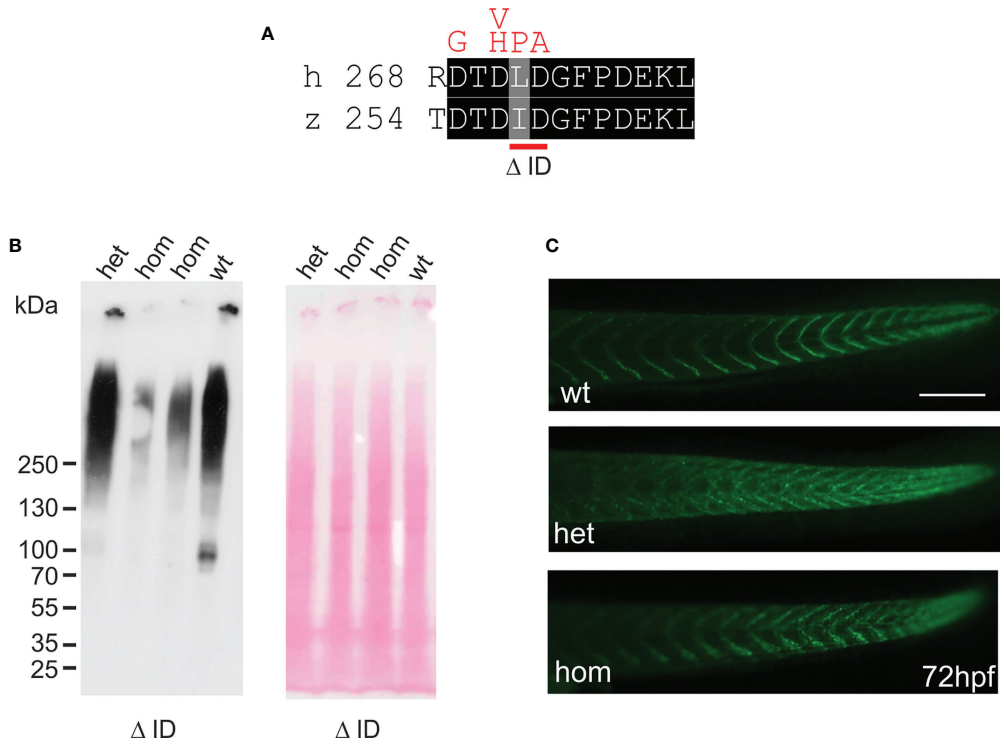

FIGURE 6
Mutant ΔI258D259Comp is expressed in zebrafish. **(A)** location of the CRISPR-Cas introduced deletion ΔI258D259 (*Δ ID*) in the first TSP type-3 repeat (red bar below) and comparison with mutations in chondrodysplasia patients (46) (above in red). **(B)** immunoblot analysis using an affinity-purified rabbit antiserum specific for zebrafish Comp (left) of direct extracts from 2-month-old wild type (*wt*), and heterozygous (*het*) or homozygous (*hom*) ΔI258D259Comp (*Δ ID*) zebrafish that were submitted to electrophoresis on 4-10% gradient SDS-polyacrylamide gels under non-reducing conditions. Ponceau staining shows equal loading (right). **(C)** whole mount immunofluorescence (green) staining of 72 hpf wild type (*wt*) (n=6), or heterozygous (*het*) (n=10) and homozygous (*hom*) (n=4) ΔI258D259Comp zebrafish mutants were performed using an affinity-purified guinea pig antiserum specific for zebrafish Comp and detected patchy Comp deposition in myosepta of heterozygous and homozygous mutants. Bar: 150 µm.

10.3389/fendo.2022.1000662

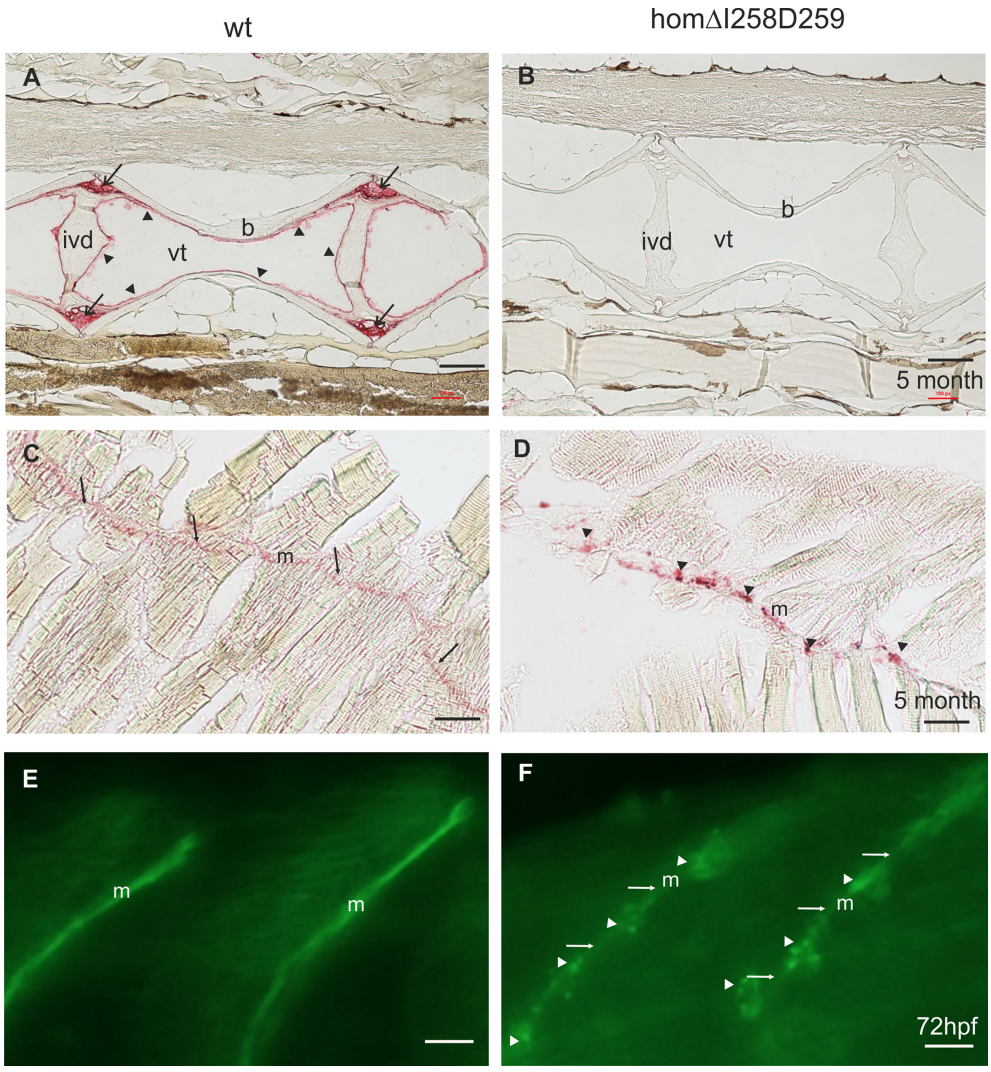

FIGURE 7
Mutant ΔI258D259Comp expression in vertebral column and muscle of zebrafish. Comp immunostainings were performed on paraffin-embedded tissue sections **(A-D)** from 5-month-old wild type (wt) **(A, C)** (n=4) and homozygous ΔI258D259Comp **(B, D)** (n=4) zebrafish by using affinity-purified rabbit **(A-D)** and guinea pig **(E, F)** antisera specific for zebrafish Comp, alkaline phosphatase-conjugated streptavidin and Fast Red staining **(A-D)** and secondary Alexa 488 conjugated antibodies **(E, F)**. **(A)** In the vertebral column of 5-month-old wt zebrafish, Comp is found in the fibrocartilaginous tissue at the base of the intervertebral discs (*ivd*) (*arrows*) and lining the inner part of the bones (b) (*arrowheads*), (*vt*, vacuolated tissue). **(B)** In mutant ΔI258D259Comp zebrafish this expression is nearly completely lacking. However, the architecture of the vertebral column is not altered. **(C)** In adult wild type zebrafish Comp is still uniformly found in myosepta (m). **(D)** Also in adult mutant ΔI258D259Comp zebrafish Comp is found in myosepta (*m*) but with an irregular patchy distribution (*arrowheads*). **(E, F)** This is similar in 72 hpf zebrafish where Comp is strongly and uniformly found in myosepta (*m*) of wt **(E)** and in irregular patches (*arrowheads*) interrupted by a much weaker uniform staining (*arrows*) in ΔI258D259Comp zebrafish as shown by whole mount immunofluorescence staining using an affinity-purified guinea pig antiserum specific for zebrafish Comp **(E, F)** (n=100), see also Figure 6C. Bars: 100 µm in **(A-D)** and 10 µm in **(E, F)**.

manner. Like in 72 hpf (Figures 7E, F), also in 5-month-old zebrafish mutant ΔI258D259 Comp is not continuously deposited within the myosepta, as is wild type Comp, and shows a patchy distribution (Figures 7C, D). To study the mutant phenotype at higher resolution, electron microscopy was performed on myosepta and adjacent muscle areas in 72 hpf homozygous mutants (Figure 8). The organization and structure of muscles adjacent to myosepta were not altered (Figures 8A, B) while the myosepta in the mutant fish appear more irregular and slightly enlarged compared to control. At higher magnification (Figures 8C, D), the disorganized ECM of the myosepta of mutant fish became obvious. In contrast to the largely homogenous myoseptal ECM of wild type, the myosepta of mutant fish revealed a disrupted, inhomogeneous and clustered ECM with different density. This may explain the patchy staining pattern while the structure of the endoplasmic

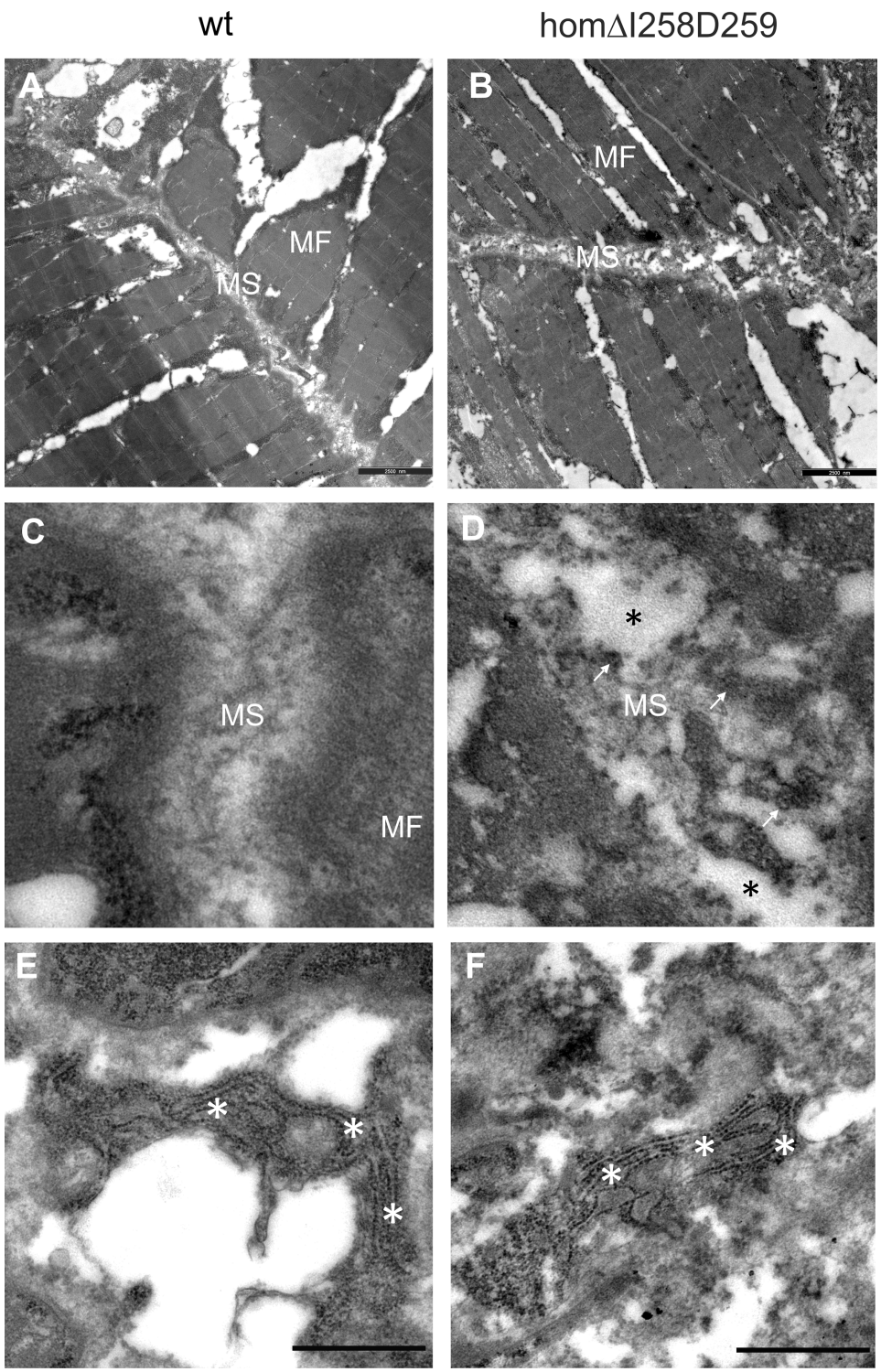

FIGURE 8
Electron microscopy of myosepta in wild type and mutant ΔI258D259Comp skeletal muscle of 72hpf zebrafish. The skeletal muscle fiber (*MF*) structure is comparable in wild type (*wt*) **(A)** and mutant ΔI258D259Comp **(B)** zebrafish while the myosepta (*MS*) in mutants are less dense and slightly enlarged compared to control. At higher magnification the myosepta of wild type **(C)** show a largely homogenous extracellular matrix (ECM) structure while myosepta of mutants **(D)** show disrupted (*black asterisks*), inhomogeneous and clustered ECM (*arrows*) structure with different density. The fibroblasts in wild type **(E)** and mutants **(F)** show an extensive endoplasmic reticulum (*white asterisks*) without obvious differences, indicating intact synthesis- active fibroblasts and no significant retention of mutant protein.

reticulum of myoseptal synthesis-active fibroblasts appeared unaltered (Figures 8E, F).

Discussion

COMP, a member of the thrombospondin family of ECM proteins, was first isolated from articular and tracheal cartilage as well as from the Swarm rat chondrosarcoma and was considered to be an abundant extracellular structural protein in cartilage (1–3). However, in recent years a much broader tissue distribution became obvious, including expression in tendon (4), skin (5), heart and skeletal muscle and vascular smooth muscle (6). It also became evident that COMP plays a role in collagen secretion (10). COMP is found in all vertebrates, but has not been well characterized in the zebrafish, a widely used model organism. Here we revisited more recent zebrafish genome assemblies and databases and unequivocally identified zebrafish Comp as the single ortholog of mammalian COMP. In contrast, ohnologs, duplicated genes that are common in zebrafish due to the whole genome duplication (WGD) that occurred in the last common ancestor in the teleost lineage (47), are found for the rest of the thrombospondin family.

Our characterization revealed that zebrafish Comp is highly conserved at the protein level and like mammalian COMP forms pentamers. However, it was very surprising that, although zebrafish Comp was found in the fibrocartilaginous matrix of intervertebral discs, Comp was not found in articular cartilage or in cartilage anlagen of developing bones. This is in clear contrast to other cartilage matrix proteins, like matrilin-3 (48). These, just as COMP, are linked to chondrodysplasias in humans (43). Our findings indicate that COMP has acquired a novel unique function in the cartilage of tetrapods, perhaps as the higher mechanical load to which land-living animals are exposed to demands a more strongly interconnected ECM. Further, the strong expression in myosepta, a tendon equivalent in zebrafish, may point to the more primordial and common function of COMP. Interestingly, Tsp4b, the closest Comp neighbour in the thrombospondin protein family of zebrafish, has a tissue distribution that is very similar to that of Comp (31).

In fact, our phylogenetic analysis revealed that Comp is found in the same branch as Tsp4 which makes it very likely that COMP originates from a duplication of an ancestral Tsp4 gene before the additional whole genome duplication occurring in teleosts, as proposed by others (30). It was shown that Tsp4 is essential for muscle attachment and ECM assembly at myotendinous junctions in zebrafish (31). In mammals, hetero-oligomers formed between COMP and TSP4 have been found in equine tendons (41), also reflecting a close functional relationship between COMP and Tsp4. Indeed, in the present study we co-immunoprecipitated Tsp4b using the Comp antibodies, indicating that such hetero-oligomers may exist also in zebrafish. Altogether our results indicate that Comp may play a similar role in zebrafish as in other vertebrates, except for its novel role in tetrapod cartilage.

Interestingly, a single thrombospondin is present already in Drosophila and its structure is most related to vertebrate COMP. The large isoform of Drosophila thrombospondin has been shown to form pentamers which indicates an early evolutionary origin of pentameric thrombospondins (49). Its major sites of expression in the Drosophila embryo are the muscle attachment sites and the precursors of the longitudinal visceral muscles. In larval stages it is expressed in wing imaginal discs (50). It was shown that Drosophila thrombospondin is a key ECM protein required for muscle-specific integrin-mediated adhesion to tendon cells. In thrombospondin mutant embryos muscles fail to attach to tendon cells and often aggregate and form ectopic integrin-mediated junctions with neighboring muscles. This leads to a nonfunctional somatic musculature and embryonic lethality (50).

In vertebrates, the absence of single members of the thrombospondin family does not result in severe phenotypes (30). Especially, mice lacking COMP have no obvious phenotype (17), perhaps due to redundancy between thrombospondins (51) or with other ECM proteins like matrilins (52). The zebrafish Comp knockout strains sa12473 (EZRC) and the CRISPR frame shift knockout generated here also have no obvious phenotype (not shown). In contrast, almost all mutations in COMP that lead to chondrodysplasias in humans are dominant missense or in frame deletion/insertion mutations with a broad spectrum of intracellular and extracellular phenotypes ranging from ER retention to collagen fibril organization (23, 53). Mouse strains carrying patient-derived mutations have been established and were helpful in the characterization of chondrodysplasia pathomechanisms (18, 21). However, use of the mouse system to study pathogenesis and potential treatment can be laborious and expensive. Cell culture models (23, 45) and micro-mass cultures (54) have also been employed, but are physiologically less relevant. The zebrafish, the simplest vertebrate model organism that is also suitable for CRISPR-Cas gene editing, could therefore serve as a valuable alternative to screen for pharmaceutical interventions in analogous PSACH/MED zebrafish Comp mutants. The advantage of this system would be the possibility to screen many compounds/treatments in large numbers of zebrafish larvae on microtiter plates by immunofluorescence microscopy (55). Indeed, in a zebrafish osteogenesis imperfecta model the chemical chaperone 4-phenylbutyrate was shown to ameliorate the skeletal phenotype (56). Recently, the treatment of cystic fibrosis was improved by the development of modulator therapies that target specific cystic fibrosis transmembrane conductance regulator protein malformations (57). Zebrafish has been used to identify altered protein expression by immunohistochemistry in a small molecule screen (58). Here we demonstrate that mutant Comp zebrafish lines will offer the possibility to perform large scale screens for chemical chaperones suitable

for correcting misfolded Comp, as we could clearly show that mutant fish can be distinguished from wild type and, therefore, efficacy of treatment can be easily monitored by analyzing the patchy myosepta staining by immunofluorescence microscopy.

Taken together we showed that, although well conserved, Comp is unexpectedly not a cartilage protein in zebrafish. Nevertheless, the expression in tendinous tissue is shared by zebrafish and mammals and the mutant zebrafish phenotype might reflect the tendino- and myopathy described in mice and patients. The easy detection and genomic manipulation by CRISPR-Cas and the very straightforward screening makes the zebrafish a promising model system to study pathogenesis and treatment of COMP-associated tissue pathologies in chondrodysplasias.

Data availability statement

The datasets presented in this study can be found in online repositories. The names of the repository/repositories and accession number(s) can be found in the article/Supplementary Material.

Ethics statement

The animal study was reviewed and approved by Veterinary agency of North-Rhine Westphalia (Landesamt für Natur, Umwelt und Verbraucherschutz [LANUV], Germany.

Author contributions

Conceptualization: AF, RW; Data Curation: AF, RW; Funding Acquisition: AF, FZ, MP, RW; Investigation: HF-G, RG, FT, BK, PK, WB; Supervision: AF, MP, RW; Validation: AF, RW; Visualization: WB, RW; Writing - Original Draft Preparation: AF, FZ, RW; Writing - Review and Editing: PK, FT, AF, FZ, MP, RW. All authors contributed to the article and approved the submitted version.

Funding

This study was supported by the European Community, FP7, 'Sybil' project grant No. 602300 and the German Research Foundation grants FOR2722-407164210 (MP and RW).

Conflict of interest

The authors declare that the research was conducted in the absence of any commercial or financial relationships that could be construed as a potential conflict of interest.

Publisher's note

Supplementary material

The Supplementary Material for this article can be found online at: https://www.frontiersin.org/articles/10.3389/fendo.2022.1000662/full#supplementary-material

References

1. Hedbom E, Antonsson P, Hjerpe A, Aeschlimann D, Paulsson M, Rosa-Pimentel E, et al. Cartilage matrix proteins - an acidic oligomeric protein (Comp) detected only in cartilage. *J Biol Chem* (1992) 267:6132–6. doi: 10.1016/S0021-9258(18)42671-3

2. Morgelin M, Heinegard D, Engel J, Paulsson M. Electron-microscopy of native cartilage oligomeric matrix protein purified from the swarm rat chondrosarcoma reveals a 5-armed structure. *J Biol Chem* (1992) 267:6137–41. doi: 10.1016/S0021-9258(18)42672-5

3. Oldberg A, Antonsson P, Lindblom K, Heinegard D. Comp (Cartilage oligomeric matrix protein) is structurally related to the thrombospondins. *J Biol Chem* (1992) 267:22346–50. doi: 10.1016/S0021-9258(18)41677-8

4. Dicesare P, Hauser N, Lehman D, Pasumarti S, Paulsson M. Cartilage oligomeric matrix protein (Comp) is an abundant component of tendon. *FEBS Lett* (1994) 354:237–40. doi: 10.1016/0014-5793(94)01134-6

5. Agarwal P, Zwolanek D, Keene DR, Schulz JN, Blumbach K, Heinegard D, et al. Collagen XII and XIV, new partners of cartilage oligomeric matrix protein in the skin extracellular matrix suprastructure. *J Biol Chem* (2012) 287:22549–59. doi: 10.1074/jbc.M111.335935

6. Riessen R, Fenchel M, Chen H, Axel DI, Karsch KR, Lawler J. Cartilage oligomeric matrix protein (thrombospondin-5) is expressed by human vascular smooth muscle cells. *Arterioscl Throm Vas* (2001) 21:47–54. doi: 10.1161/01.ATV.21.1.47

7. Halper J. Basic components of connective tissues and extracellular matrix: Fibronectin, fibrinogen, laminin, elastin, fibrillins, fibulins, matrilins, tenascins and thrombospondins. In: *Progress in heritable soft connective tissue diseases, 2nd Edition*, vol. 1348. Cham: Springer (2021). p. 105–26.

8. Acharya C, Yik JHN, Kishore A, Dinh VV, Di Cesare PE, Haudenschild DR. Cartilage oligomeric matrix protein and its binding partners in the cartilage extracellular matrix: Interaction, regulation and role in chondrogenesis. *Matrix Biol* (2014) 37:102–11. doi: 10.1016/j.matbio.2014.06.001

9. Zaucke F, Grassel S. Genetic mouse models for the functional analysis of the perifibrillar components collagen IX, COMP and matrilin-3: Implications for growth cartilage differentiation and endochondral ossification. *Histol Histopathol* (2009) 24:1067–79. doi: 10.14670/HH-24.1067

10. Schulz JN, Nüchel J, Niehoff A, Bloch W, Schönborn K, Hayashi S, et al. COMP-assisted collagen secretion–a novel intracellular function required for fibrosis. *J Cell Sci* (2016) 129:706–16. doi: 10.1242/jcs.180216

11. Haudenschild DR, Hong E, Yik JHN, Chromy B, Morgelin M, Snow KD, et al. Enhanced activity of transforming growth factor beta 1 (TGF-beta 1) bound to cartilage oligomeric matrix protein. *J Biol Chem* (2011) 286:43250–8. doi: 10.1074/jbc.M111.234716

12. Refaat M, Klineberg EO, Fong MC, Garcia TC, Leach JK, Haudenschild DR. Binding to COMP reduces the BMP2 dose for spinal fusion in a rat model. *Spine* (2016) 41:E829–36. doi: 10.1097/BRS.0000000000001408

13. Kipnes J, Carlberg AL, Loredo GA, Lawler J, Tuan RS, Hall DJ. Effect of cartilage oligomeric matrix protein on mesenchymal chondrogenesis *in vitro*. *Osteoarthr Cartil* (2003) 11:831–5. doi: 10.1016/S1063-4584(03)00055-4

14. Ishida K, Acharya C, Christiansen BA, Yik JHN, Dicesare PE, Haudenschild DR. Cartilage oligomeric matrix protein enhances osteogenesis by directly binding and activating bone morphogenetic protein-2. *Bone* (2013) 55:23–35. doi: 10.1016/j.bone.2013.03.007

15. Du Y, Wang Y, Wang L, Liu B, Tian Q, Liu CJ, et al. Cartilage oligomeric matrix protein inhibits vascular smooth muscle calcification by interacting with bone morphogenetic protein-2. *Circ Res* (2011) 108:917–28. doi: 10.1161/CIRCRESAHA.110.234328

16. Ma B, Yao F, Xie N, Mao C, Liu F, Gong Z, et al. Cartilage oligomeric matrix protein is a novel notch ligand driving embryonic stem cell differentiation towards the smooth muscle lineage. *J Mol Cell Cardiol* (2018) 121:69–80. doi: 10.1016/j.yjmcc.2018.07.002

17. Svensson L, Aszodi A, Heinegard D, Hunziker EB, Reinholt FP, Fassler R, et al. Cartilage oligomeric matrix protein-deficient mice have normal skeletal development. *Mol Cell Biol* (2002) 22:4366–71. doi: 10.1128/MCB.22.12.4366-4371.2002

18. Schmitz M, Niehoff A, Miosge N, Smyth N, Paulsson M, Zaucke F. Transgenic mice expressing D469 delta mutated cartilage oligomeric matrix protein (COMP) show growth plate abnormalities and sternal malformations. *Matrix Biol* (2008) 27:67–85. doi: 10.1016/j.matbio.2007.08.001

19. Pirog-Garcia KA, Meadows RS, Knowles L, Heinegard D, Thornton DJ, Kadler, et al. Reduced cell proliferation and increased apoptosis are significant pathological mechanisms in a murine model of mild pseudoachondroplasia resulting from a mutation in the c-terminal domain of COMP. *Hum Mol Genet* (2007) 16:2072–88. doi: 10.1093/hmg/ddm155

20. Suleman F, Gualeni B, Gregson HJ, Leighton MP, Pirog KA, Edwards S, et al. A novel form of chondrocyte stress is triggered by a COMP mutation causing pseudoachondroplasia. *Hum Mutat* (2012) 33:218–31. doi: 10.1002/humu.21631

21. Pirog KA, Katakura Y, Mironov A, Briggs MD. Mild myopathy is associated with COMP but not MATN3 mutations in mouse models of genetic skeletal diseases. *PloS One* (2013) 8. doi: 10.1371/journal.pone.0082412

22. Pirog KA, Jaka O, Katakura Y, Meadows RS, Kadler KE, Boot-Handford RP, et al. A mouse model offers novel insights into the myopathy and tendinopathy often associated with pseudoachondroplasia and multiple epiphyseal dysplasia. *Hum Mol Genet* (2010) 19:52–64. doi: 10.1093/hmg/ddp466

23. Dinser R, Zaucke F, Kreppel F, Hultenby K, Kochanek S, Paulsson M, et al. Pseudoachondroplasia is caused through both intra-and extracellular pathogenic pathways. *J Clin Invest* (2002) 110:505–13. doi: 10.1172/JCI0214386

24. Dennis EP, Greenhalgh-Maychell Pl, Briggs MD. Multiple epiphyseal dysplasia and related disorders: Molecular genetics, disease mechanisms, and therapeutic avenues. *Dev Dyn* (2021) 250:345–59. doi: 10.1002/dvdy.221

25. Posey KL, Coustry F, Veerisetty AC, Hossain M, Alcorn JL, Hecht JT. Antioxidant and anti-inflammatory agents mitigate pathology in a mouse model of pseudoachondroplasia. *Hum Mol Genet* (2015) 24:3918–28. doi: 10.1093/hmg/ddv122

26. Posey KL, Hecht JT. Novel therapeutic interventions for pseudoachondroplasia. *Bone* (2017) 102:60–8. doi: 10.1016/j.bone.2017.03.045

27. Busse B, Galloway JL, Gray RS, Harris MP, Kwon RY. Zebrafish: An emerging model for orthopedic research. *J Orthop Res* (2020) 38:925–36.

28. Tonelli F, Cotti S, Leoni L, Besio R, Gioia R, Marchese L, et al. Crtap and p3h1 knock out zebrafish support defective collagen chaperoning as the cause of their osteogenesis imperfecta phenotype. *Matrix Biol* (2020) 90:40–60. doi: 10.1016/j.matbio.2020.03.004

29. Wiley DS, Redfield SE, Zon LI. Chemical screening in zebrafish for novel biological and therapeutic discovery. *Method Cell Biol* (2017) 138:651–79. doi: 10.1016/bs.mcb.2016.10.004

30. Adams JC, Lawler J. The thrombospondins. *Csh Perspect Biol* (2011) 3. doi: 10.1101/cshperspect.a009712

31. Subramanian A, Schilling TF. Thrombospondin-4 controls matrix assembly during development and repair of myotendinous junctions. *Elife* (2014) 3. doi: 10.7554/eLife.02372

32. Teufel F, Armenteros JJA, Johansen AR, Gislason MH, Pihl SI, Tsirigos KD, et al. SignalP 6.0 predicts all five types of signal peptides using protein language models. *Nat Biotechnol* (2022) 40:1023–25. doi: 10.1038/s41587-021-01156-3

33. Kimmel CB, Ballard WW, Kimmel SR, Ullmann B, Schilling TF. Stages of embryonic-development of the zebrafish. *Dev Dynam* (1995) 203:253–310. doi: 10.1002/aja.1002030302

34. Maertens B, Hopkins D, Franzke CW, Keene DR, Bruckner-Tuderman L, Greenspan DS, et al. Cleavage and oligomerization of gliomedin, a transmembrane collagen required for node of ranvier formation. *J Biol Chem* (2007) 282:10647–59. doi: 10.1074/jbc.M611339200

35. Albert TK, Laubinger W, Muller S, Hanisch FG, Kalinski T, Meyer F, et al. Human intestinal TFF3 forms disulfide-linked heteromers with the mucus-associated FCGBP protein and is released by hydrogen sulfide. *J Proteome Res* (2010) 9:3108–17. doi: 10.1021/pr100020c

36. Sturmer R, Muller S, Hanisch FG, Hoffmann W. Porcine gastric TFF2 is a mucus constituent and differs from pancreatic TFF2. *Cell Physiol Biochem* (2014) 33:895–904. doi: 10.1159/000358662

37. Peacock AC, Dingman CW. Molecular weight estimation and separation of ribonucleic acid by electrophoresis in agarose-acrylamide composite gels. *Biochemistry* (1968) 7:668–&. doi: 10.1021/bi00842a023

38. Jao LE, Wente SR, Chen WB. Efficient multiplex biallelic zebrafish genome editing using a CRISPR nuclease system. *Proc Natl Acad Sci U States America* (2013) 110:13904–9. doi: 10.1073/pnas.1308335110

39. Vanhauwaert S, Van Peer G, Rihani A, Janssens E, Rondou P, Lefever S, et al. Expressed repeat elements improve RT-qPCR normalization across a wide range of zebrafish gene expression studies. *PloS One* (2014) 9. doi: 10.1371/journal.pone.0109091

40. Tan K, Duquette M, Joachimiak A, Lawler J. The crystal structure of the signature domain of cartilage oligomeric matrix protein: implications for collagen, glycosaminoglycan and integrin binding. *FASEB J* (2009) 23:2490–501. doi: 10.1096/fj.08-128090

41. Sodersten F, Ekman S, Schmitz M, Paulsson M, Zaucke F. Thrombospondin-4 and cartilage oligomeric matrix protein form heterooligomers in equine tendon. *Connect Tissue Res* (2006) 47:85–91. doi: 10.1080/03008200600584124

42. Thisse B, Thisse C. In situ hybridization on whole-mount zebrafish embryos and young larvae. *Methods Mol Biol* (2014) 1211:53–67. doi: 10.1007/978-1-4939-1459-3_5

43. Briggs MD, Chapman KL. Pseudoachondroplasia and multiple epiphyseal dysplasia: Mutation review, molecular interactions, and genotype to phenotype correlations. *Hum Mutat* (2002) 19:465–78. doi: 10.1002/humu.10066

44. Hecht JT, Makitie O, Hayes E, Haynes R, Susic M, Montufar-Solis D, et al. Chondrocyte cell death and intracellular distribution of COMP and type IX collagen in the pseudoachondroplasia growth plate. *J Orthop Res* (2004) 22:759–67. doi: 10.1016/j.orthres.2003.11.010

45. Hansen U, Platz N, Becker A, Bruckner P, Paulsson M, Zaucke F. A secreted variant of cartilage oligomeric matrix protein carrying a chondrodysplasia-causing mutation (p.H587R) disrupts collagen fibrillogenesis. *Arthritis Rheum-Us* (2011) 63:159–67. doi: 10.1002/art.30073

46. Briggs MD, Brock J, Ramsden SC, Belli PA. Genotype to phenotype correlations in cartilage oligomeric matrix protein associated chondrodysplasias. *Eur J Hum Genet* (2014) 22:1278–82. doi: 10.1038/ejhg.2014.30

47. Meyer A, Schartl M. Gene and genome duplications in vertebrates: the one-to-four (-to-eight in fish) rule and the evolution of novel gene functions. *Curr Opin Cell Biol* (1999) 11:699–704. doi: 10.1016/S0955-0674(99)00039-3

48. Ko YP, Kobbe B, Paulsson M, Wagener R. Zebrafish (Danio rerio) matrilins: shared and divergent characteristics with their mammalian counterparts. *Biochem J* (2005) 386:367–79. doi: 10.1042/BJ20041486

49. Adams JC, Monk R, Taylor AL, Ozbek S, Fascetti N, Baumgartner S, et al. Characterisation of drosophila thrombospondin defines an early origin of pentameric thrombospondins. *J Mol Biol* (2003) 328:479–94. doi: 10.1016/S0022-2836(03)00248-1

50. Subramanian A, Wayburn B, Bunch T, Volk T. Thrombospondin-mediated adhesion is essential for the formation of the myotendinous junction in drosophila. *Development* (2007) 134:1269–78. doi: 10.1242/dev.000406

51. Posey KL, Hankenson K, Veerisetty AC, Bornstein P, Lawler J, Hecht JT. Skeletal abnormalities in mice lacking extracellular matrix proteins, thrombospondin-1, thrombospondin-3, thrombospondin-5, and type IX collagen. *Am J Pathol* (2008) 172:1664–74. doi: 10.2353/ajpath.2008.071094

52. Groma G, Xin W, Grskovic I, Niehoff A, Brachvogel B, Paulsson M, et al. Abnormal bone quality in cartilage oligomeric matrix protein and matrilin 3 double-deficient mice caused by increased tissue inhibitor of metalloproteinases 3 deposition and delayed aggrecan degradation. *Arthritis Rheum-Us* (2012) 64:2644–54. doi: 10.1002/art.34435

53. Posey KL, Coustry F, Hecht JT. Cartilage oligomeric matrix protein: COMPopathies and beyond. *Matrix Biol* (2018) 71-72:161–73. doi: 10.1016/j.matbio.2018.02.023

54. Roman-Blas J, Dion AS, Seghatoleslami MR, Giunta K, Oca P, Jimenez SA, et al. MED and PSACH COMP mutations affect chondrogenesis in chicken limb bud micromass cultures. *J Cell Physiol* (2010) 224:817–26. doi: 10.1002/jcp.22185

55. Tonelli F, Bek JW, Besio R, De Clercq A, Leoni L, Salmon P, et al. Zebrafish: A resourceful vertebrate model to investigate skeletal disorders. *Front Endocrinol* (2020) 11. doi: 10.3389/fendo.2020.00489

56. Gioia R, Tonelli F, Ceppi I, Biggiogera M, Leikin S, Fisher S, et al. The chaperone activity of 4PBA ameliorates the skeletal phenotype of chihuahua, a zebrafish model for dominant osteogenesis imperfecta. *Hum Mol Genet* (2017) 26:2897–911. doi: 10.1093/hmg/ddx171

57. Guimbellot JS, Taylor-Cousar JL. Combination CFTR modulator therapy in children and adults with cystic fibrosis. *Lancet Resp Med* (2021) 9:677–9. doi: 10.1016/S2213-2600(21)00176-4

58. Murphey RD, Stern HM, Straub CT, Zon LI. A chemical genetic screen for cell cycle inhibitors in zebrafish embryos. *Chem Biol Drug Des* (2006) 68:213–9. doi: 10.1111/j.1747-0285.2006.00439.x

frontiers | Frontiers in Endocrinology

TYPE Review
PUBLISHED 06 December 2022
DOI 10.3389/fendo.2022.1060187

OPEN ACCESS

EDITED BY
Erika Kague,
University of Bristol, United Kingdom

REVIEWED BY
Ann Huysseune,
Ghent University, Belgium
James Nichols,
University of Colorado, United States
J. Gage Crump,
University of Southern California, United States

*CORRESPONDENCE
Pierre Le Pabic
lepabicp@uncw.edu
Thomas F. Schilling
tschilli@uci.edu

SPECIALTY SECTION
This article was submitted to Bone Research, a section of the journal Frontiers in Endocrinology

RECEIVED 02 October 2022
ACCEPTED 17 November 2022
PUBLISHED 06 December 2022

CITATION
Le Pabic P, Dranow DB, Hoyle DJ and Schilling TF (2022) Zebrafish endochondral growth zones as they relate to human bone size, shape and disease.
Front. Endocrinol. 13:1060187.
doi: 10.3389/fendo.2022.1060187

Zebrafish endochondral growth zones as they relate to human bone size, shape and disease

Pierre Le Pabic[1]*, Daniel B. Dranow[2], Diego J. Hoyle[2] and Thomas F. Schilling[2]*

[1]Department of Biology and Marine Biology, University of North Carolina Wilmington, Willmington, NC, United States, [2]Department of Developmental and Cell Biology, University of California, Irvine, Irvine, CA, United States

Research on the genetic mechanisms underlying human skeletal development and disease have largely relied on studies in mice. However, recently the zebrafish has emerged as a popular model for skeletal research. Despite anatomical differences such as a lack of long bones in their limbs and no hematopoietic bone marrow, both the cell types in cartilage and bone as well as the genetic pathways that regulate their development are remarkably conserved between teleost fish and humans. Here we review recent studies that highlight this conservation, focusing specifically on the cartilaginous growth zones (GZs) of endochondral bones. GZs can be unidirectional such as the growth plates (GPs) of long bones in tetrapod limbs or bidirectional, such as in the synchondroses of the mammalian skull base. In addition to endochondral growth, GZs play key roles in cartilage maturation and replacement by bone. Recent studies in zebrafish suggest key roles for cartilage polarity in GZ function, surprisingly early establishment of signaling systems that regulate cartilage during embryonic development, and important roles for cartilage proliferation rather than hypertrophy in bone size. Despite anatomical differences, there are now many zebrafish models for human skeletal disorders including mutations in genes that cause defects in cartilage associated with endochondral GZs. These point to conserved developmental mechanisms, some of which operate both in cranial GZs and limb GPs, as well as others that act earlier or in parallel to known GP regulators. Experimental advantages of zebrafish for genetic screens, high resolution live imaging and drug screens, set the stage for many novel insights into causes and potential therapies for human endochondral bone diseases.

KEYWORDS

Danio rerio, endochondral, skeleton, cartilage, growth plate

1 Introduction

Research on the growth plates (GPs) of endochondral bones in mice has greatly impacted our understanding of skeletal development as well as the causes of human skeletal disorders. Early studies showed that the epiphyses of limb long bones remain cartilaginous and proliferative, thereby allowing bone growth (1). Genetic studies showed

mechanisms regulating cartilage maturation, gradual replacement by osteoblasts, matrix deposition and continuous bone remodeling by osteoclasts (2). These discoveries laid the groundwork for much of modern skeletal research. Given the limited knowledge of the cellular and molecular mechanisms regulating the huge variety of sizes and shapes of other bones, such as those of the skull or vertebrae, much of our current understanding of skeletal development is based on work on GPs of long bones in the tetrapod limb.

Over the past several decades, the zebrafish has become a powerful system for genetic analysis of skeletal development. Despite having fins that lack the long bones found in tetrapod limbs and many other obvious anatomical differences in their skeletons, zebrafish have the same array of skeletal cell types found in humans. Furthermore, the work that has been done to date has shown that the molecular mechanisms that control skeletal development, growth and physiology are largely conserved despite over 400 million years since their lineages diverged from a common ancestor (3).

In this review, we present an overview of skeletal research in zebrafish with a special focus on endochondral growth zones (GZs), defined as regions of cartilage proliferation and maturation, which include the well-known GPs of long bones. For reviews covering other aspects of skeletal research in zebrafish (e.g. osteoblasts/osteoclasts, intramembranous skull bones, fin rays, scales), we refer the reader to the following (4–11). First, we provide a brief introduction to adult zebrafish skeletal anatomy with a specific focus on similarities with human endochondral bones. Next, we present the cellular architecture of GZs between zebrafish and humans and across the three major skeletal regions, cranial, axial and appendicular. Third, we compare endochondral development and physiology between zebrafish and mammals and review key recent studies that have led to insights into conserved cellular pathways that control bone size and shape in health and disease.

2 Skeletal anatomy in adult zebrafish and humans

2.1 Anatomical distribution of endochondral and intramembranous bones

2.1.1 Modes of ossification

Two modes of ossification produce the vertebrate skeleton: endochondral and intramembranous. In endochondral ossification, typified by long bones of the mammalian limb, mesenchymal condensations differentiate into cartilage that is eventually replaced by bone (2). In contrast, intramembranous bones, such as those of the skull vault, differentiate directly from mesenchyme (12). Some bones form by a combination of intramembranous and endochondral ossification, such as mammalian clavicles (13). The relative contributions of these two modes of ossification vary widely across different taxa, both in the axial skeleton, which consists of bones associated with the craniofacial complex and vertebrae, as well as the appendicular skeleton that supports the limbs and fins (Figure 1). Human and zebrafish skulls are both composed of a mixture of endochondral and intramembranous bones (14). While the mammalian calvaria occupies a large surface area, the chondrocranium and pharyngeal skeleton are composed of many smaller endochondral bones, just as in zebrafish (14, 15). In contrast, most of the zebrafish vertebral and limb skeletons are intramembranous while they are endochondral in humans. Despite these differences, zebrafish and humans are generally very similar in their development and basic structure. However, homologies between individual axial and appendicular bones of teleost fish and humans can be difficult to determine due to phylogenetic divergence and adaptation to different environments.

2.1.2 Bones of the axial and appendicular skeletons

In the skull, difficulty in identifying homologous bones between humans and other vertebrates is thought to be partly a consequence of progressive fusion of skeletal elements during mammalian evolution (16). The human skull contains 29 bones, all joined by fibrous joints known as sutures, except for the mandible, hyoid bone, and middle ear ossicles (17). Two thirds of these cranial bones are intramembranous, while the hyoid bone, middle ear ossicles, and several bones of the cranial base (ethmoid, body and lesser wings of the sphenoid, petrous portion and otic capsule of the temporal bone, and basal portion of the occipital bone) are endochondral (Figure 1). In contrast, the zebrafish skull contains 134 bones, 78 of which are endochondral (14). As in humans, the intramembranous bones of the zebrafish braincase suture together, while bones supporting the jaws, opercle, gills and other parts of the skull, articulate with each other by mobile joints (Figure 1).

The non-cranial portion of the axial skeleton includes the vertebral column and rib cage in both humans and zebrafish, in addition to the unpaired fins (dorsal, anal, caudal) in zebrafish (Figure 1). Vertebrae and ribs are endochondral in humans but intramembranous in zebrafish (4, 18–20). In addition, unlike in humans, the zebrafish ribcage remains open ventrally and lacks a sternum. The zebrafish axial skeleton also includes appendages with no homologs in humans: the dorsal, anal, and caudal fins. Fins consist of an exoskeleton of rays made of intramembranous bone, and a supporting internal skeleton made of endochondral hypurals in the caudal fin and radials in the dorsal and anal fins (Figure 1B). Lastly, the Weberian apparatus, an evolutionary innovation linking the ear to the swim bladder to enhance audition (a character found only in the Ostariophysan superorder), contains both intramembranous and endochondral bones (21) (Figure 1B).

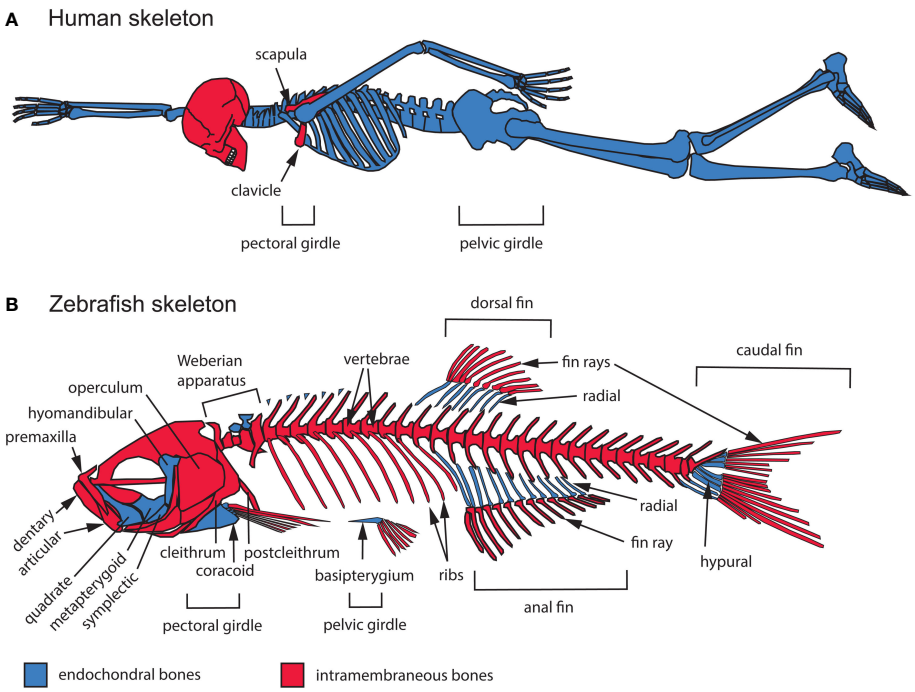

FIGURE 1
General overview of the intramembranous and endochondral composition of the zebrafish and human skeletons. **(A)** Human adult skeleton. In the head, intramembranous bones such as those of the calvaria (the top portion of the neurocranium) dominate the human skull in surface area, while endochondral bones mostly occupy the cranial base. All of the bones that compose the trunk and appendicular skeletons are endochondral, except for portions of the clavicle and scapula. **(B)** Zebrafish adult skeleton. The zebrafish skull, trunk and appendage skeletons are composed of both intramembranous and endochondral bones. The zebrafish skull is composed of 134 bones, 78 of which are endochondral. The zebrafish trunk skeleton is composed of intramembranous vertebrae and ribs. The zebrafish appendage skeleton is composed mostly of endochondral bones, while the fin ray exoskeleton is completely intramembranous.

Human and zebrafish appendicular skeletons consist of pectoral (shoulder) and pelvic (hip) girdles with associated appendages: fore- and hindlimbs in humans, pectoral and pelvic fins in zebrafish. Human limbs are entirely composed of endochondral bones, while paired fins in zebrafish consist of fin rays made of intramembranous bone supported proximally by endochondral radial bones (22). In humans, most of the pectoral and pelvic girdles are also endochondral, though portions of the clavicle (collar bone) and scapula (shoulder blade) form by intramembranous ossification (Figure 1A). Similarly, the zebrafish pectoral girdle contains a mixture of intramembranous (cleithrum, postcleithrum, supracleithrum) and endochondral (coracoid, mesocoracoid, scapula) bones, while the pelvic girdle is exclusively endochondral (basipterygium) (14).

2.2 Endochondral growth zone structure

2.2.1 Cellular architecture of endochondral growth zones

In endochondral GZs, step-by-step chondrocyte maturation regulates bone elongation (Figure 2) (1). The maturation process starts in the resting zone (RZ), which serves the role of stem-cell niche (Figure 2A). Slow-dividing RZ cells transit into the proliferative zone (PZ), where they proliferate at a higher rate and stack to form chondrocyte arrays characteristic of avian and murine long bone GPs. They subsequently stop dividing and enlarge as they enter the hypertrophic zone (HZ). Most undergo apoptosis at the chondro-osseous junction and are subsequently replaced by bone. In GPs with steady-state growth, pools of cells in each zone remain constant as: 1) the rate of PZ cell division offsets the rate of cells leaving the PZ, 2) the rate of cells leaving offsets the rate of cells entering the PZ, and 3) the rate of cells entering the HZ offsets the rate of cells lost at the chondro-osseous junction (25). These aspects of cartilage maturation appear broadly similar between mammalian and zebrafish endochondral GZs, though chondrocytes are not aligned into linear stacks in zebrafish PZs (26, 27).

Cartilage maturation can occur in one or both directions at GZs, parallel to the long axis of bone growth. In unidirectional (or epiphyseal) GZs (also known as GPs) typical of long bones, the RZ lies close to the distal-most region of the bone (epiphysis) and maturing cells progress medially toward the bone's central shaft (diaphysis), producing axial elongation at each end (1). In contrast,

10.3389/fendo.2022.1060187

bidirectional GZs produce growth in two opposite directions (28). This reflects a mirror-image organization where two sets of PZs and HZs flank a single RZ on either side (Figure 2B). Bidirectional GZs are often located within synchondroses or cartilaginous joints. In humans, they can be found in the skull base and vertebrae but in zebrafish are more common and found in multiple endochondral bones of the neurocranium and pharyngeal skeleton (Figure 3) (27).

2.2.2 Tissue architecture of endochondral bones

Although both human and zebrafish endochondral bones have GZs, they show several structural differences, including the fact that zebrafish lack: 1) secondary ossifications, 2) trabecular bone, and 3) a hematopoietic bone marrow (Figure 2). Human GPs often have "secondary" ossification centers distal to the RZ,

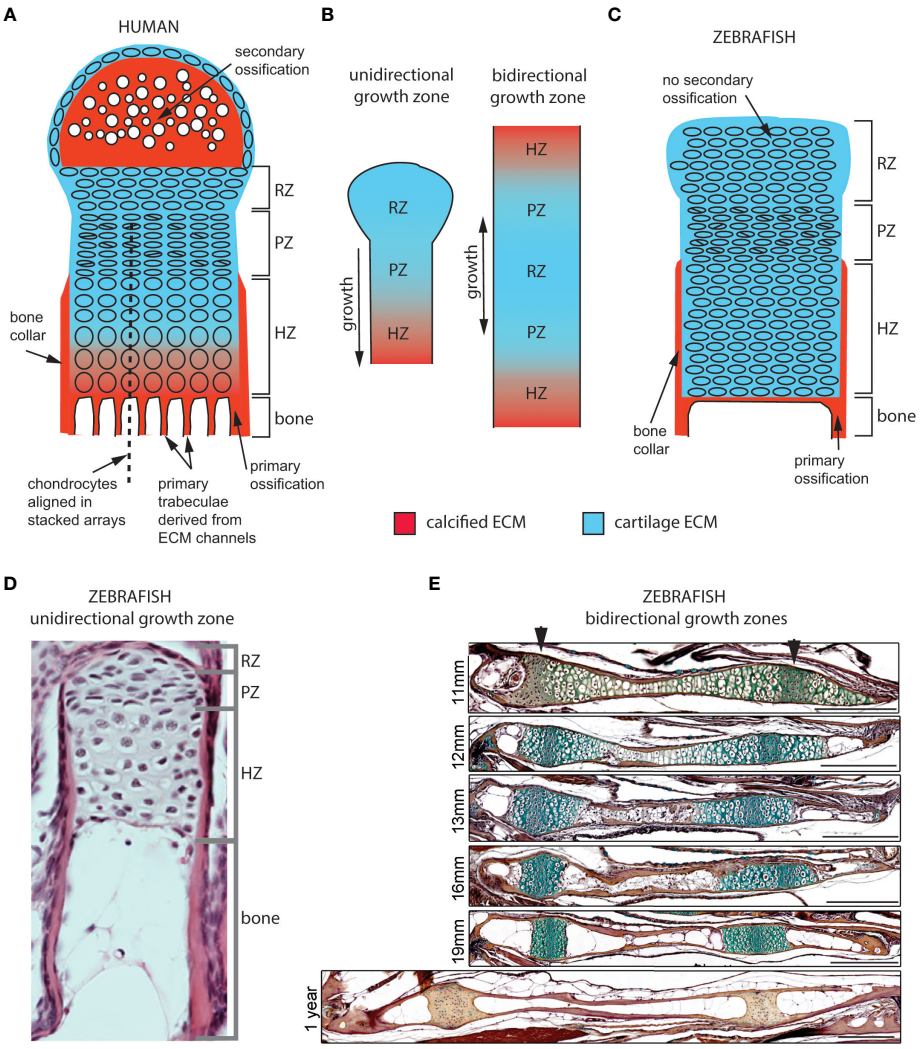

FIGURE 2
Cellular organization of epiphyseal and synchondroseal growth zones. **(A)** Human growth plate chondrocytes transition through resting-, proliferative- and hypertrophic zones (RZ, PZ, and HZ, respectively) before dying or transitioning to an osteoblast fate at the chondro-osseous junction. Cartilage cells stop dividing and enlarge in the hypertrophic zone. The bone collar forms a sheath around hypertrophic chondrocytes; the secondary ossification flanks the growth plate distally. Primary bone trabeculae derived from extracellular matrix channels populate the bone cavity. **(B)** In unidirectional (epiphyseal) growth zones, the resting zone is distal to the proliferative zone, itself distal to the hypertrophic zone; this layout produces unidirectional growth. In bidirectional (synchondroseal) growth zones, the resting zone is flanked by two proliferative zones and two hypertrophic zones in a mirror image organization; this layout produces bidirectional growth. **(C)** Stereotypical zebrafish unidirectional growth zone organization: chondrocytes transition through RZ, PZ and HZ, but they do not enlarge in the HZ. At the zebrafish resorption front, chondrocytes die or transition to either an osteocyte or adipocyte fate. A perichondral bone collar sheathes the zebrafish hypertrophic zone, but no secondary ossification is associated with zebrafish epiphyseal growth zones. Trabeculae are not observed in smaller teleosts such as zebrafish. **(D)** Histological section of zebrafish proximal radial showing unidirectional endochondral growth zone [originally published in (23)]. **(E)** Time series of maturation at two zebrafish bidirectional growth zones located within the ventral (left) and dorsal (right) ceratohyal synchondroses [originally published in (24)]. (scale bars = 50 μm).

which appear later in endochondral differentiation (Figure 2A) (2). In contrast, in zebrafish and other teleost GZs, maturing cartilage remains continuous with articular cartilage at the joints, similar to earlier stages of mammalian GP development (Figures 2C–E) (27, 29, 30). Secondary ossification centers in mammals were recently proposed to have evolved to protect hypertrophic chondrocytes from mechanical damage in load-bearing tetrapod bones (31). Another striking structural difference from mammals is the absence of primary bone trabeculae at the resorption front in zebrafish (32, 33). Primary trabeculae form parallel bone channels in mammals through the progressive replacement of extracellular matrix (ECM) tracks produced by chondrocyte stacks by bone ECM (Figure 2A), while secondary trabeculae appear later in response to mechanical stress (34, 35). Thus, the less well-aligned chondrocyte stacks of zebrafish GZs as well as the lower amount of ECM produced by GZ chondrocytes (also observed in other teleosts) may help explain the lack of primary trabeculae (Figures 2C–E) (29, 30, 36). However, trabeculae have been reported in the bones of larger teleosts, suggesting that their presence might simply reflect differences in bone size and strength requirements (37). In addition, zebrafish HZ chondrocytes are converted into osteoblasts at the resorption front, become part of the diaphyseal endosteum and differentiate into osteocytes embedded in the bone shaft (24). This supports the presence of endochondral ossification in zebrafish in the form of (1): a thin layer of bone matrix at the resorption front and (2) bone matrix deposition inside the bone shaft, instead of the bone spongiosa described in mammals and larger teleosts (24, 32, 37). Finally, zebrafish endochondral bones do not form a marrow that can support hematopoiesis. This instead occurs in the kidney marrow of zebrafish (38).

2.3 Anatomical distribution of endochondral growth zones

Rodents and humans have homologous skeletal GZs inherited from a shared common ancestor, as exemplified by long bone GPs such as the proximal tibial GP. Though zebrafish GZs are not individually homologous to any mammalian GZ, a growing body of research has revealed striking similarities in their GZ development and physiology. This demonstrates the relevance of zebrafish for understanding basic principles of skeletal biology and underlying causes of skeletal disease, including common chondrodysplasias associated with GPs. These similarities include the molecular and cellular mechanisms underlying endochondral differentiation. The genetic advantages of the zebrafish, along with its small size and optical accessibility, has led to a growing popularity for their use in testing new disease candidates discovered in humans and elucidating their mechanisms of action.

2.3.1 Bidirectional endochondral growth zone locations

Postembryonic growth of the human cranial base requires three bidirectional GZs: the spheno-ethmoidal, intersphenoid and spheno-occipital synchondroses (Figure 3A). Their importance in shaping the adult face is exemplified by the prominent forehead and flattened bridge of the nose associated with achondroplasia, the most common form of human dwarfism (39, 40). Reduced cell proliferation in the RZ of these GZs in achondroplasia results in reduced cranial base growth in patients, in addition to shortening of their arms and legs due to GP defects (Figure 3B) (41). The other anatomical location where bidirectional growth zones are found in humans are the vertebrae. Neurocentral synchondroses contribute to the growth of the vertebral body as well as the spinal canal (Figure 3B), and they fuse between ages 5 to 17 depending on their anterior-posterior location (42).

Zebrafish bidirectional growth zones are primarily located in the neurocranial and pharyngeal skeletons. As in mammals, the zebrafish neurocranium consists of both intramembranous and endochondral bones and numerous neurocranial synchondroses arise after the initial stages of chondrocranial ossification, yet their GZ activity has only recently been investigated (27). Growth of the zebrafish pharyngeal skeleton is supported by both uni- and bidirectional growth zones (Figure 3C). The pharyngeal skeleton derives from the pharyngeal arches (PA), which form by bilateral segmentation of the embryonic pharynx in vertebrates and their close relatives (16, 43, 44). Here we describe the PA-derived bidirectional GZs of the first (PA1, mandibular) and second (PA2, hyoid) arches, which develop first and produce the most skeletal growth, as these are most relevant to model human GZs in health and disease. For a more complete list of zebrafish pharyngeal GZs, see (27). In the dorsal PA1 skeleton, the palatoquadrate (PQ) synchondrosis mediates growth of the quadrate (QA) ventrally and metapterygoid (MP) dorsally (Figure 3C). In the dorsal PA2 skeleton, the hyosymplectic (HS) synchondrosis mediates growth of the symplectic (SY) ventrally and hyomandibular (HM) dorsally. In the ventral PA2 skeleton, the ventral ceratohyal (CH) synchondrosis mediates growth of the hypohyal (HH) bones ventrally and the CH dorsally, while the dorsal CH synchondrosis mediates growth of the CH (anterior CH) ventrally and epihyal (EH; posterior CH) dorsally (Figure 3C). In the PA3-6 (branchial arches 1-4) skeleton, basibranchial (BB) elongation is mediated by 2 bidirectional GZs (Figure 3C) (27).

The zebrafish PQ and CH synchondroses have been used to study developmental mechanisms that regulate GZ development (24, 26, 45, 46). These studies have shown that, like mammalian GPs, these GZs contain similar zones of cartilage maturation (RZ, PZ, HZ), though with some interesting differences in the timing of proliferation and hypertrophy. In addition, they share similar patterns of gene expression known to control GZ formation and size, as discussed below.

10.3389/fendo.2022.1060187

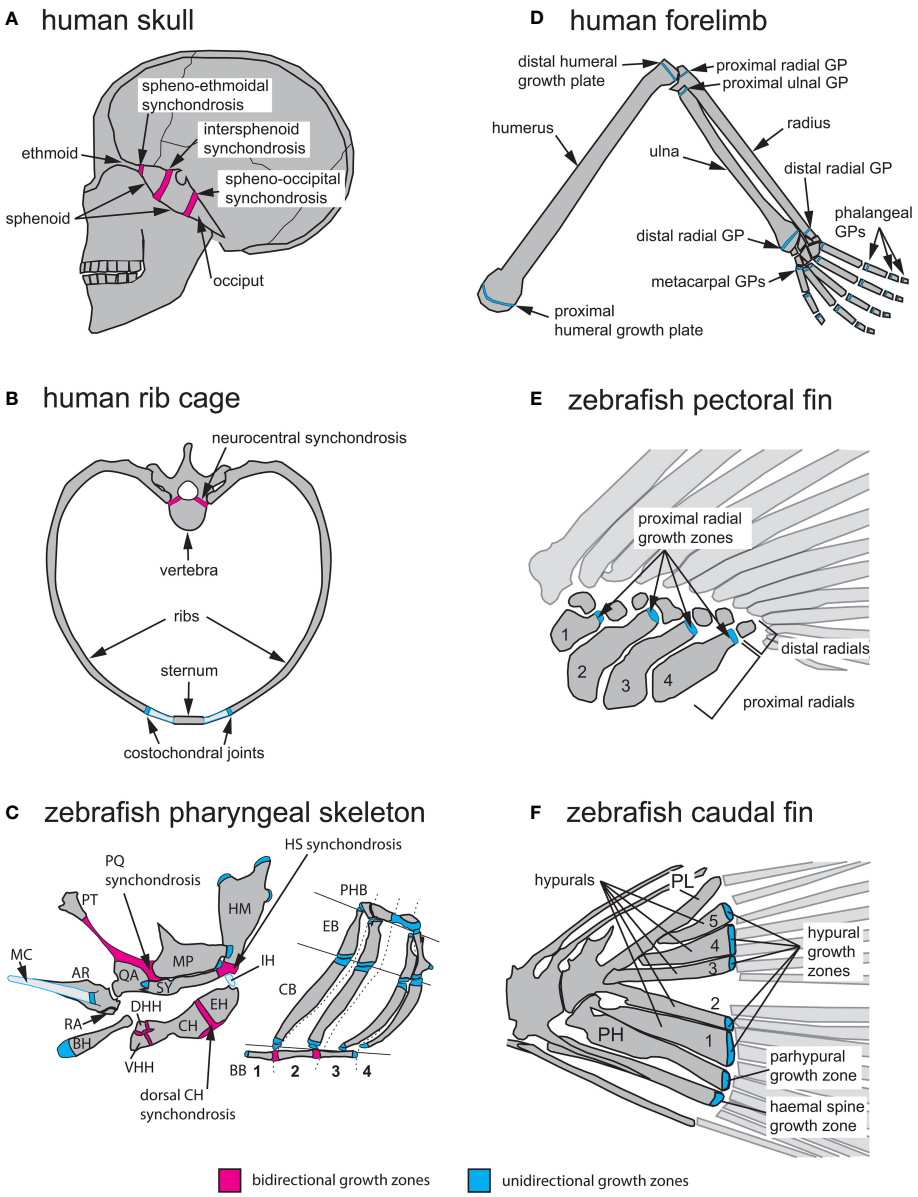

FIGURE 3
Anatomical locations of endochondral growth zones in human vs zebrafish. **(A)** Three synchondroses mediate growth of the human skull base (depicted in sagittal view): the spheno-ethmoidal-, intersphenoid- and spheno-occipital synchondroses. **(B)** Endochondral growth of human vertebrae and ribs (depicted in transverse view) takes place at neurocentral synchondroses and costochondral joints, respectively. **(C)** Over thirty endochondral growth zones mediate zebrafish pharyngeal skeleton growth. Three highly visible synchondroses mediate growth of first and second pharyngeal arch (PA1-2) skeletons. The PQ synchondrosis mediates growth of the QA and MP. The HS synchondrosis mediates growth of the SY and HM. The dorsal CH synchondrosis mediates growth of the CH and EH. In PA1 and 2, epiphyseal growth zones are found at the posterior MP, anterior SY, dorsal HM and anterior BH. In the gill supporting skeleton, epiphyseal growth zones are found at the ends of each CB and EB bone. **(D)** Axial growth of human stylopod (humerus, femur) and zeugopod (radius, ulna, tibia, fibula) bones is mediated by epiphyseal growth zones (=growth plates) located at each bone extremity. A single proximal epiphyseal growth zone mediates axial elongation of each autopod long bone (hand and foot phalanges). **(E)** In the zebrafish pectoral fin, epiphyseal growth zones are found at the distal end of each proximal radial. **(F)** In the zebrafish caudal fin, epiphyseal growth zones located at the distal end of each hypural bone (H1-5), the prehypural and two last haemal spines mediate axial elongation. AR, articular; BB, basibranchials; BH, basihyal; CB, ceratobranchial; CH, ceratohyal; DHH, dorsal hypohyal; EB, epibranchial; EH, epihyal; HM, hyomandibular; HS, hyosymplectic; IH, interhyal; MC, Meckel's cartilage; MP, metapterygoid; PH, parhypural; PHB, pharyngobranchials; PL, pleurostyle; PT, palatine; QA, quadrate; RA, retroarticular; SY, symplectic; VHH, ventral hypohyal. Red indicates bidirectional- and blue indicates unidirectional growth zones.

2.3.2 Unidirectional endochondral growth zone locations

In humans, unidirectional GZs are primarily found in the limbs and ribs (Figures 3B, D). Growth of ribs is mediated by GZs located within costochondral joints, which are synchondroses linking ribs to the costal cartilages of vertebrae (Figure 3B) (47, 48). In the limbs, epiphyseal GPs mediate elongation of the stylopod (humerus, femur) and zeugopod (radius/ulna, tibia/fibula) at the end of each long bone. In contrast, each bone of the autopod grows at a single GP (phalanges/metacarpals/metatarsals; Figure 3D).

Zebrafish unidirectional GZs are primarily found in the pharyngeal skeleton and fin endoskeleton (Figures 3C, E, F). In the PA3-6 (branchial arches 1-4) skeleton, the ceratobranchial (CB) and epibranchial (EB) bones of each arch possess a unidirectional GZ at each extremity (Figure 3C) (27). In the 2 sets of paired fins (pectoral and pelvic) the endoskeleton is reduced compared to that of human limbs, and its proximo-distal pattern is simplified. The endoskeleton of pectoral fins consists of 4 proximal radials and 6 to 8 distal radials (Figure 3E), while the pelvic fins contain 3 radials (22). The caudal fin endoskeleton consists of the pleurostyle of the caudal-most vertebrae, five hypurals, the parhypural, and the haemal spines of preural vertebrae 2 and 3 (Figure 3F) (49). Just as in mammalian limbs, all fin GZs are unidirectional. These are positioned at the distal ends of (1) proximal radials in the pectoral, dorsal and anal fins (2), radials in the pelvic fins, and (3) hypurals, parhypural and haemal spines in the caudal fin (Figures 3E, F) (50). Interestingly, mutations in conserved regulators of appendage development can lead to supernumerary bones in zebrafish consistent with radials and long bones having evolved from homologous structures in the common ancestor (23).

3 Development and cellular architecture of endochondral growth zones in teleost fish and humans

3.1 Developmental similarities and differences in endochondral growth zones between species

The stereotypical steps of mammalian endochondral long bone formation consist of: 1) mesenchymal condensation, 2) differentiation into cartilage, 3) formation of a perichondral bone collar at the diaphysis and concomitant hypertrophy of chondrocytes coupled with cartilage matrix mineralization, 4) blood vessel invasion, hypertrophic chondrocyte death and resorption of mineralized matrix by chondroclasts, all at the diaphysis 5) replacement of cartilage by endochondral bone and marrow, 6) appearance of distinct RZ, PZ, and HZ zones at each epiphysis, and lastly 7) epiphyseal formation of secondary ossification centers (2, 12). These features of GZs are largely conserved between teleost fish and tetrapods, at both the cellular and molecular levels, despite the later invasion of blood vessels in teleosts, lack of hematopoietic bone marrow or secondary ossifications. Notably, endochondral bone formation in smaller teleosts, such as zebrafish takes the form of (1) a thin layer of bone matrix at the resorption front and (2) bone matrix deposition on the inner surface of the bone shaft (24, 29, 30, 32, 36, 51).

3.1.1 From condensation to cartilage template

In tetrapods, the shape of the mesenchymal condensation determines the shape of the cartilage model (52). In contrast, cartilage elements differentiate within larger condensations in both the head and fins of teleosts (22, 53–55). Zebrafish embryonic and larval cartilage shapes generally prefigure the shape of adult skeletal elements (Figures 4A, B). One exception is the endoskeleton that supports the pectoral fins, in which a transient endoskeletal disc of cartilage supports the functional larval fin, but localized cartilage decomposition within the disc defines four proximal radials that prefigure the adult fin endoskeleton (Figures 3E, 4C) (56).

The shapes of pharyngeal cartilage elements in teleost embryos are regulated by complex morphogenetic cell behaviors such as localized cell-cell intercalations that take place hours before cartilage matrix deposition (56–59). Linear stacking of chondrocytes driven by such intercalations underlies the directionality of the GP or GZ as well as cartilage and bone elongation. Cartilage elements of mutants with cell-cell intercalation defects are shorter and wider than in wild-type individuals (26, 60). A growing body of research supports conserved control of cell-cell intercalation during cartilage morphogenesis in the RZs of vertebrate GPs (including mammals) by planar cell polarity (PCP) pathways (26, 58, 60–66).

Though initially studied in the context of epithelia, it has become clear that noncanonical Wnt/Wnt-PCP and Fat-Dchs/Fat-PCP signaling play important roles in regulating cell and tissue polarity in diverse cell and tissue types, including mesenchyme and cartilage. Several human syndromes that affect skeletal morphology are caused by mutations in Wnt-PCP and Fat-PCP signaling genes (67–77). Studies in zebrafish have successfully modeled craniofacial defects associated with loss-of-function of *gpc4*, *frizzled*, *wnt5b*, *fat3a* and *dchs2* in cartilage morphogenesis, and demonstrated requirements for these factors in mediating the polarized cell-cell intercalation of chondrocytes in the craniofacial skeleton (26, 58, 63, 64, 66).

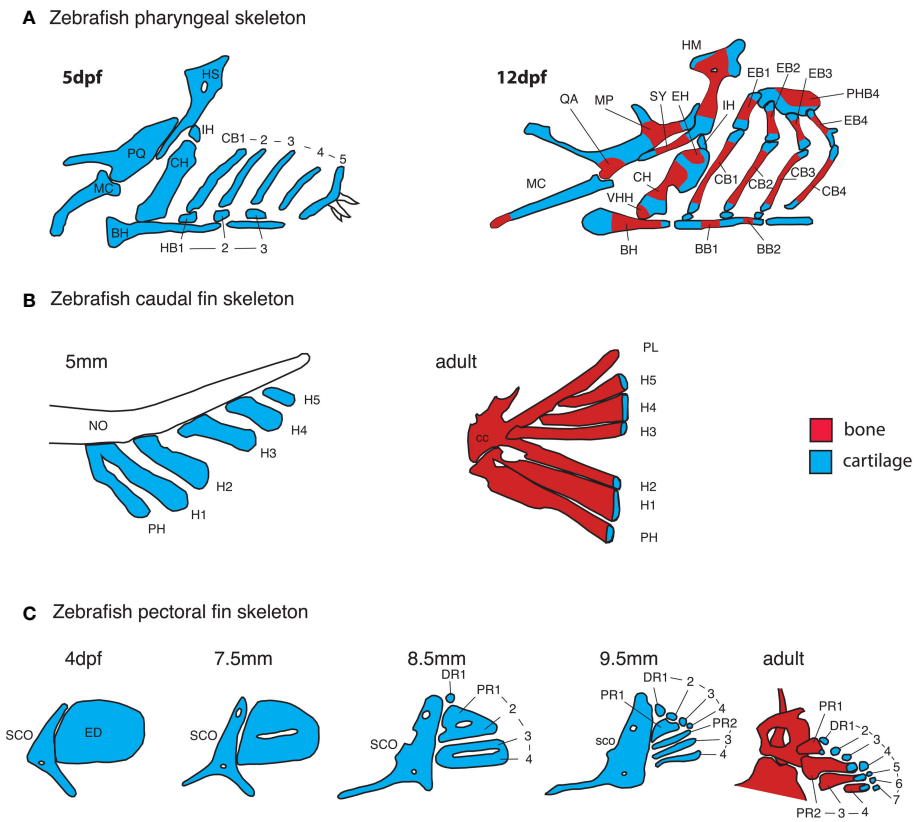

FIGURE 4
Early anatomy of zebrafish endochondral growth zones. **(A)** Endochondral growth zones start to appear in the zebrafish skeleton around 12days post-fertilization (dpf). One or more ossification centers appear on each bone. Unossified cartilage regions at bone ends become unidirectional growth zones, while those flanked by ossifying cartilage become bidirectional growth zones. In the 12dpf pharyngeal skeleton, the QA and MP bones ossify over the PQ cartilage, the HM and SY bones ossify over the HS cartilage, the HH, CH and EH bones ossify over the CH cartilage, BB1 and 2 ossify over the BB cartilage. Single ossifications appear on other pharyngeal bones. **(B)** In the caudal fin endoskeleton, single ossifications appear on each cartilage element, resulting in a single distal endochondral growth zone per element. **(C)** In the pectoral fin endoskeleton, the endoskeletal disc is progressively carved into four proximal- and seven distal radials. Ossification of each proximal radial leaves a single endochondral growth zone at the distal end. Distal radials do not ossify. BB, basibranchial; BH, basihyal; CB, ceratobranchial; CC, compound centrum; DR, distal radial; ED, endoskeletal disc; H, hypural; HB, hypobranchial; IH, interhyal; MC, Meckel's cartilage; NO, notochord; PH, parhypural; PHB, pharyngobranchials; PR, proximal radial; SCO, scapulocoracoid, VHH, ventral hypohyal.

3.1.2 Maturation of endochondral bones

The first signs of GZ development in the craniofacial skeleton in zebrafish are the simultaneous appearance of a perichondral bone collar and flattening of presumptive PZ chondrocytes during early metamorphosis (Standard Length = 6-7 mm) (26, 27). Unlike mammalian GZs, hypertrophic chondrocytes in zebrafish only enlarge slightly and transiently during zebrafish GZ development. Blood vessel invasion of the cartilage template coincides with the onset of HZ cell apoptosis, but unlike in mammals, it starts well after the onset of bone collar formation and GZ-mediated bone elongation (24, 27). It was long thought that osteocytes replacing HZ chondrocytes in GPs were introduced in the bone diaphysis by invading vasculature (2), but histological studies in chick and more recent lineage analyses using transgenic mice have shown a contribution to trabecular bone by HZ chondrocytes themselves (78–81). Similarly, recent clonal analysis using zebrafish transgenics has shown that HZ chondrocytes may undergo several fates at the resorption front: apoptosis, or transition into osteoblast or adipocyte fates (24). Unlike mammals, but similar to amphibians, reptiles and most bird species, secondary ossification centers do not develop in GZs of endochondral bones in zebrafish or other teleosts (1, 27, 29, 30).

3.1.3 Patterning of endochondral growth zones

Our understanding of GZ patterning mechanisms is largely based on studies of mouse limb GPs. Two signaling pathways activated by Indian Hedgehog (Ihh) and Parathyroid Hormone-like Hormone (Pthlh), respectively, interact at a distance to pattern long bone GPs (Figure 5A). *Ihh* is first expressed throughout the diaphysis of long bone cartilage templates before becoming restricted to chondrocytes in the pre-

hypertrophic zone (PHZ) (82, 86). Ihh activates *Pthlh* expression at a distance in periarticular chondrocytes, and Pthlh in turn represses *Ihh* expression. Mosaic analyses of *Ihh*, *Pthlh*, and *Pth1r* mutants have shown that this negative feedback loop effectively patterns the distance between RZ and HZ (83, 84). *Ihh* expression levels are also regulated by BMP and FGF signaling: *Smad1/5* promotes *Ihh* expression, while *Smad2/3* and *Fgfr3* repress its expression (87–90). In addition to their role in scaling the GP, Ihh promotes bone collar formation by inducing the differentiation of osteoblasts in the perichondrium (91, 92), while Pthlh promotes the proliferation of PZ chondrocytes and delays cell-cycle exit and the onset of chondrocyte enlargement, both in mice and zebrafish (82, 92). In contrast, little is known about the molecular pathways regulating HZ chondrocyte enlargement. Three phases of enlargement have been identified in mice, which include an initial three-fold volume increase through hypertrophy, that is, cell enlargement with a corresponding increase in organelle dry mass, followed by a four-fold increase through vacuole swelling by disproportionate intake of fluid, and a final two-fold increase through hypertrophy again. Interestingly, the duration of the last phase (hypertrophy) varies the most between rapidly and slowly expanding growth plates, and regulation of this phase requires *Insulin-like growth factor 1* (*Igf1*) (93).

The Ihh-Pthlh feedback loop appears to be conserved in mammalian cranial base synchondroses, although *Pthlh* is expressed throughout the RZ and PZ (94, 95). A few studies in zebrafish have shown the conservation of GZ patterning mechanisms between teleost fish and mammals (45, 96), and an earlier onset of *Pthlha* expression than previously described, namely at the onset of chondrogenesis and before the onset of *ihha* expression (Figure 5B) (46). Novel findings in zebrafish have also shown the potential of this model for expanding our understanding of GZ patterning, as they suggest that the Ihh-Pthlh feedback loop maintains but does not establish the GZ pattern, at least in some pharyngeal endochondral bones (46). Instead, the zebrafish *Pthlh* ortholog, *pthlha*, and mechanical force from muscle contraction initiate the HZ and the location of subsequent *ihha* expression, thereby establishing the negative feedback-loop that maintains GZs (Figure 5B) (46).

3.2 Cellular basis of similarities and differences in endochondral growth zones between species

3.2.1 Bone elongation and differential growth

The rate of bone elongation changes throughout the life of a GZ, and differs between GZs of an individual, as well as homologous GZs of different species. Such growth rate variation is referred to as differential growth (1). In rats, three cellular mechanisms mediate endochondral bone elongation: cell proliferation, cell enlargement, and ECM production. Cell proliferation takes place in the PZ and enlargement in the HZ, while ECM production takes place in both zones. These three cellular mechanisms contribute unequally to bone elongation in mammalian GPs: proliferation 7-10%, ECM production 32-49%, and cell enlargement 44-59% (25). The relatively minor contribution of proliferation to growth serves to compensate for the loss of chondrocytes at the chondro-osseous junction. Between mammalian species, as shown for bat metacarpal and jerboa metatarsal GZs, the largest driver of growth rate is the degree of cell enlargement of HZ chondrocytes (93, 97). In contrast, proliferation is the major contributor to endochondral bone elongation in zebrafish, as no significant cell enlargement or increase in ECM content are observed in active GZs (27). In other teleost fishes, the cellular basis of endochondral growth has been explored in several African cichlids: ECM production is the main driver of growth in *H. elegans*, while differences in cell proliferation and/or enlargement mediate differential growth in Lake Malawi cichlids (98, 99).

3.2.2 Life history differences

Mammals and teleost fishes also differ dramatically in the timing of growth over their lifespans. Human limb GPs are already active at birth and mediate axial elongation until the end of puberty, when estrogens trigger GP closure and growth arrest through complete replacement of epiphyseal cartilage by bone (100). In rats, GPs also become inactive at sexual maturity but they are not replaced by bone (1). Not all GPs become inactive at the same age: in humans, the three GZs of the cranial base ossify at different times: the intersphenoid GZ ossifies immediately before birth, the spheno-ethmoidal GZ ossifies at 6 years, and the spheno-occipital GZ remains active until the end of puberty (101–103). In contrast, most teleost fish grow throughout life, although the rate of growth slows with age, as described by the individual growth model of von Bertalanffy (104). Accordingly, zebrafish growth is indeterminate (105, 106), yet its pharyngeal GZs become inactive in adults and do not ossify, similar to rats. Further adult growth is mediated by intramembranous ossification (27).

3.3 Modeling human endochondral growth zone disorders in zebrafish

Despite the many similarities in development and physiology of their GZs, there have been relatively few studies modeling human GZ disorders in zebrafish. Recent reviews

10.3389/fendo.2022.1060187

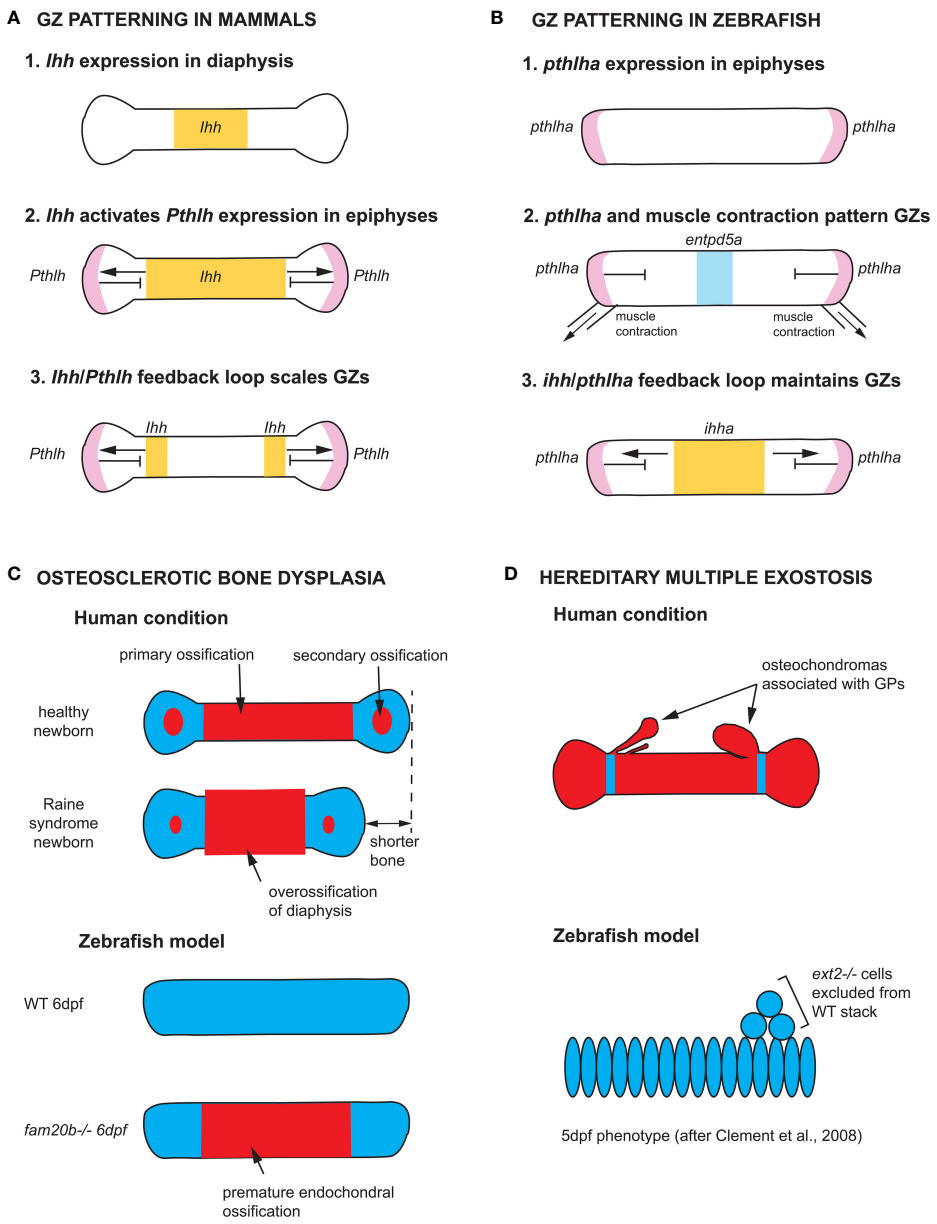

FIGURE 5
Zebrafish models of endochondral growth zone development and disease **(A)** Model for the patterning of growth zones (GZs) based on genetic studies of mouse long bones (82–84). *Indian hedgehog (Ihh)* is first expressed in the nascent diaphysis of the cartilage model. Its expression domain expands towards the epiphyses and activates *Parathyroid hormone-like hormone* (*Pthlh*) expression in periarticular cartilage. Pthlh represses Ihh at a distance, which sets the distance between the hypertrophic zone (HZ) and resting zone (RZ). **(B)** Model for the patterning of CH GZs in zebrafish based on (46). *pthlha* is expressed at the epiphyses of the differentiating CH. The HZ is then patterned by *pthlha* and muscle contractions before the onset of *ihha* expression. According to this model, *ihha* plays a role in the maintenance of GZs, not their patterning. **(C)** Zebrafish *fam20b* mutants recapitulates the skeletal phenotype of Raine syndrome, a particular form of osteosclerotic bone dysplasia (45). Short overossified long bones are observed in Raine syndrome newborns. Premature ossification of the CH diaphysis is observed in zebrafish *fam20b* mutants. **(D)** Zebrafish chimaeras recapitulate the formation of cartilage nodules observed in the human condition hereditary multiple exostosis, which results from a mutation in the *EXT2* gene. *ext2-/-* chondrocytes are excluded from WT cartilage stacks in zebrafish chimaeras, leading to the hypothesis that osteochondromas observed in *EXT2+/-* patients result from loss-of-heterozygosity (85). *Ihh* and *ihha* expression domains in yellow, *Pthlh* and *pthlha* expression domains in pink, *ectonucleoside triphosphate diphosphohydrolase 5a* (*entpd5a*) expression domain in light blue, cartilage in blue, and bone in red. CH, ceratohyal; GPs, growth plates; WT, wild type; dpf, days post-fertilization.

largely focus on the many models for other types of bone diseases such as osteogenesis imperfecta, osteoporosis, osteopetrosis and osteoarthritis, that alter ossification and osteoblasts (4–10). Notable exceptions include mutations in genes encoding proteoglycan core proteins or enzymes involved in their biosynthesis or assembly, as models for such cartilage diseases as Keipert syndrome (Glypican 4, GPC4; discussed in section 1a), osteosclerotic bone dysplasia (FAM20C), and hereditary multiple exostoses (Exostosin 2, EXT2).

Zebrafish provided some of the first insights into requirements for proteoglycans in craniofacial development (45, 96). A variety of Human conditions result from mutations in the proteoglycan biosynthesis pathway that builds chondroitin-sulfate- (CSPGs) and heparin-sulfate-proteoglycans (HSPGs) from UDP-glucose. Zebrafish mutants in seven of the nine enzymes of the O-linked-glycosylation pathway required for HSPG production have been described, several of which recapitulate endochondral skeletal defects of human patients (107).

A surprising discovery associated with the cartilage phenotypes of zebrafish mutants in *UDP-xylose synthase* (*uxs1*), *xylotransferase 1* (*xylt1*) and *glycosaminoglycan xylosyl kinase* (*fam20b*) is the premature maturation of hypertrophic chondrocytes and bone collar ossification (Figure 5C). This suggested a role for proteoglycans in regulating the timing of cartilage and bone differentiation, perhaps through the modulation of ligand-based cell-cell signaling (45, 96). Further, premature ossification in *fam20b* mutants provided a new etiology for Raine syndrome, a human disease resulting from mutations in *FAM20C*. Also known as osteosclerotic bone dysplasia, Raine syndrome patients have craniofacial defects such as low nasal bridge and midfacial hypoplasia indicative of defects in growth at synchondroses, as well as short and overossified long bones in newborns (Figure 5C). The zebrafish *fam20b* mutant phenotype suggests that Raine syndrome craniofacial and limb skeletal defects result from premature maturation of the skeleton (45).

Further down the HSPG biosynthetic pathway, *exostosin* (*ext*) *-1 and-2* code for glycosyltransferases involved in the polymerization of heparan sulfate chains. Mutations in *EXT1* or *EXT2* result in hereditary multiple exostoses (HME) in humans, a disease that causes the formation of benign bone tumors (osteochondromas) that are associated with GPs (Figure 5D). Most HME patients are heterozygous for mutations in either *EXT1* or *EXT2* (108–110). A study of zebrafish *ext2* mutants (*dackel*) supports a model where osteochondromas arise from local loss of heterozygosity (LOH): zebrafish $ext2^{-/-}$ embryos do not develop osteochondromas but their skeleton is generally misshapen, demonstrating a requirement for *ext2* in cartilage morphogenesis/stacking (85). Instead, $ext2^{-/-}$ cells form osteochondroma-like nodules when transplanted in wild type (WT) individuals: homozygous mutant cells are excluded from WT stacks, providing support to the LOH model for the etiology of HME (Figure 5D) (85).

4 Conclusions and future directions

In this review, we have highlighted the many similarities and differences between zebrafish and human skeletal anatomy, their endochondral GZs and recent studies of developmental and physiological mechanisms that control endochondral bone growth. Despite the apparent anatomical differences between human and teleost fish skeletons, the overwhelming conservation of different cell types and molecular mechanisms underlying skeletal development makes the zebrafish a powerful model for further studies of the causes and potential therapies for human skeletal diseases. This power lies in (1): the unique and well-known properties that have already made zebrafish a popular model system, which include ease of care, their small size, large number of offspring, suitability for large forward genetic screens and embryo transparency to name a few and (2) an ever-expanding toolkit to reach a diversity of research goals. CRISPR-Cas9-mediated mutagenesis is relatively easy in zebrafish and protocols have been developed for the rapid production of loss-of-function phenotypes in CRISPR-injected individuals (111, 112). Numerous transgenic lines labeling various skeletal cell lineages and their precursors have been used to image cartilage and bone morphogenesis *in vivo*, and also conduct lineage tracing in endochondral bones (24, 58, 113, 114). Transgenic zebrafish can also be utilized for cell-type and stage-specific ablation using the nitroreductase system (115), as well as in mosaic transgenic conditions to test the cell-autonomous and non-cell autonomous properties of particular genes and their mutant alleles (46, 116, 117). Lastly, recent improvements in single-cell RNAseq and ATACseq methodologies have allowed gene expression profiling of entire cell lineages and even whole organs or organisms at single cell resolution, made possible by the small size of zebrafish embryos and larvae (118–122). Future deployment of these single-cell techniques for the study of all skeletal cell types will undoubtedly lead to new insights into endochondral and GZ development in health and disease.

Author contributions

PL, DD, DH and TS all contributed to the conception and content covered in the manuscript. PL wrote the first draft of the manuscript. TS wrote sections of the manuscript. All authors contributed to manuscript revision, read, and approved the submitted version.

Funding

The authors of this work were supported by National Institutes of Health awards R01 DE013828 and R01 DE030565, as well as a National Science Foundation award MCB 2028424.

Conflict of interest

The authors declare that the research was conducted in the absence of any commercial or financial relationships that could be construed as a potential conflict of interest.

Publisher's note

References

1. Farnum C. *Postnatal growth of fins and limbs through endochondral ossification*. Chicago, IL, USA: University of Chicago Press (2007). p. 118–51.

2. Kronenberg HM. Developmental regulation of the growth plate. *Nature* (2003) 423(6937):332–6. doi: 10.1038/nature01657

3. Hurley IA, Mueller RL, Dunn KA, Schmidt EJ, Friedman M, Ho RK, et al. A new time-scale for ray-finned fish evolution. *Proc R Soc B-Biological Sci* (2007) 274 (1609):489–98. doi: 10.1098/rspb.2006.3749

4. Tonelli F, Bek JW, Besio R, De Clercq A, Leoni L, Salmon P, et al. Zebrafish: A resourceful vertebrate model to investigate skeletal disorders. *Front Endocrinol* (2020) 11:489. doi: 10.3389/fendo.2020.00489

5. Valenti MT, Marchetto G, Mottes M, Carbonare LD. Zebrafish: A suitable tool for the study of cell signaling in bone. *Cells* (2020) 9(8):1911. doi: 10.3390/cells9081911

6. Luderman LN, Unlu G, Knapik EW. Zebrafish developmental models of skeletal diseases. *Zebrafish at Interface Dev Dis Res* (2017) 124:81–124. doi: 10.1016/bs.ctdb.2016.11.004

7. Mari-Beffa M, Mesa-Roman ABB, Duran I. Zebrafish models for human skeletal disorders. *Front Genet* (2021) 12:675331. doi: 10.3389/fgene.2021.675331

8. Lleras-Forero L, Winkler C, Schulte-Merker S. Zebrafish and medaka as models for biomedical research of bone diseases. *Dev Biol* (2020) 457(2):191–205. doi: 10.1016/j.ydbio.2019.07.009

9. Carnovali M, Banfi G, Mariotti M. Zebrafish models of human skeletal disorders: Embryo and adult swimming together. *BioMed Res Int* (2019) 2019:1253710. doi: 10.1155/2019/1253710

10. Dietrich K, Fiedler IAK, Kurzyukova A, Lopez-Delgado AC, McGowan LM, Geurtzen K, et al. Skeletal biology and disease modeling in zebrafish. *J Bone Mineral Res* (2021) 36(3):436–58. doi: 10.1002/jbmr.4256

11. Witten PE, Huysseune A. A comparative view on mechanisms and functions of skeletal remodelling in teleost fish, with special emphasis on osteoclasts and their function. *Biol Rev Camb Philos Soc* (2009) 84(2):315–46. doi: 10.1111/j.1469-185X.2009.00077.x

12. Hall BK. *Bones and cartilage. 2nd ed*. Amsterdam, Netherlands: Academic Press (2015). p. 920.

13. DeSesso JM, Scialli AR. Bone development in laboratory mammals used in developmental toxicity studies. *Birth Defects Res* (2018) 110(15):1157–87. doi: 10.1002/bdr2.1350

14. Cubbage CC, Mabee PM. Development of the cranium and paired fins in the zebrafish danio rerio (Ostariophysi, cyprinidae). *J Morphology* (1996) 229(2):121–60. doi: 10.1002/(sici)1097-4687(199608)229:2<121::aid-jmor1>3.0.co;2-4

15. Kawasaki K, Richtsmeier JT. Association of the chondrocranium and dermatocranium in early skull formation. In: Percival C, Richtsmeier J, editors. *Building bones: Early bone development informing anthropological inquiry*. Cambridge, England: Cambridge University Press (2017). p. 52–78.

16. de Beer GR. *The development of the vertebrate skull*. London: Oxford University Press (1937). p. 552.

17. Netter FH. *Atlas of human anatomy. 7th ed*. Amsterdam, Netherlands: Elsevier (2018). p. 640.

18. Fleming A, Kishida MG, Kimmel CB, Keynes RJ. Building the backbone: The development and evolution of vertebral patterning. *Development* (2015) 142 (10):1733–44. doi: 10.1242/dev.118950

19. Peskin B, Henke K, Cumplido N, Treaster S, Harris MP, Bagnat M, et al. Notochordal signals establish phylogenetic identity of the teleost spine. *Curr Biol* (2020) 30(14):2805–14. doi: 10.1016/j.cub.2020.05.037

20. Bird NC, Mabee PM. Developmental morphology of the axial skeleton of the zebrafish, danio rerio (Ostariophysi : Cyprinidae). *Dev Dynamics* (2003) 228 (3):337–57. doi: 10.1002/dvdy.10387

21. Bird NC, Hernandez LP. Building an evolutionary innovation: Differential growth in the modified vertebral elements of the zebrafish weberian apparatus. *Zoology* (2009) 112(2):97–112. doi: 10.1016/j.zool.2008.05.003

22. Grandel H, Schulte-Merker S. The development of the paired fins in the zebrafish (Danio rerio). *Mech Dev* (1998) 79(1-2):99–120. doi: 10.1016/s0925-4773(98)00176-2

23. Hawkins MB, Henke K, Harris MP. Latent developmental potential to form limb-like skeletal structures in zebrafish. *Cell* (2021) 184(4):899–911. doi: 10.1016/j.cell.2021.01.003

24. Giovannone D, Paul S, Schindler S, Arata C, Farmer DT, Patel P, et al. Programmed conversion of hypertrophic chondrocytes into osteoblasts and marrow adipocytes within zebrafish bones. *Elife* (2019) 8:e42736. doi: 10.7554/eLife.42736

25. Wilsman NJ, Farnum CE, Leiferman EM, Fry M, Barreto C. Differential growth by growth plates as a function of multiple parameters of chondrocytic kinetics. *J Orthopaedic Res* (1996) 14(6):927–36. doi: 10.1002/jor.1100140613

26. LeClair EE, Mui SR, Huang A, Topczewska JM, Topczewski J. Craniofacial skeletal defects of adult zebrafish glypican 4 (Knypek) mutants. *Dev Dynamics* (2009) 238(10):2550–63. doi: 10.1002/dvdy.22086

27. Heubel BP, Bredesen CA, Schilling TF, Le Pabic P. Endochondral growth zone pattern and activity in the zebrafish pharyngeal skeleton. *Dev Dynamics* (2021) 250(1):74–87. doi: 10.1002/dvdy.241

28. Wei X, Hu M, Mishina Y, Liu F. Developmental regulation of the growth plate and cranial synchondrosis. *J Dental Res* (2016) 95(11):1221–9. doi: 10.1177/0022034516651823

29. Haines RW. Epiphysial growth in the branchial skeleton of fishes. *Q J Microscopical Sci* (1934) 77:77–97. doi: 10.1242/jcs.s2-77.305.77

30. Haines RW. The evolution of epiphyses and of endochondral bone. *Biol Rev* (1942) 17:267–92. doi: 10.1111/j.1469-185X.1942.tb00440.x

31. Xie M, Gol'din P, Herdina AN, Estefa J, Medvedeva EV, Li L, et al. Secondary ossification center induces and protects growth plate structure. *Elife* (2020) 9:e55212. doi: 10.7554/eLife.55212

32. Witten PE, Hansen A, Hall BK. Features of mono- and multinucleated bone resorbing cells of the zebrafish danio rerio and their contribution to skeletal

development, remodeling, and growth. *J Morphology* (2001) 250(3):197–207. doi: 10.1002/jmor.1065.abs

33. Weigele J, Franz-Odendaal TA. Functional bone histology of zebrafish reveals two types of endochondral ossification, different types of osteoblast clusters and a new bone type. *J Anat* (2016) 229(1):92–103. doi: 10.1111/joa.12480

34. White A, Wallis G. Endochondral ossification: A delicate balance between growth and mineralisation. *Curr Biol* (2001) 11(15):R589–R91. doi: 10.1016/s0960-9822(01)00359-1

35. Maisey JG. Phylogeny of early vertebrate skeletal induction and ossification patterns. *Evolutionary Biol* (1988) 22:1–36. doi: 10.1007/978-1-4613-0931-4_1

36. Haines RW. The posterior end of meckel's cartilage and related ossifications in bony fishes. *J Cell Sci* (1937) s2-80(317):1–38. doi: 10.1242/jcs.s2-80.317.1

37. Huysseune A. *Skeletal system*. London: Academic Press (2000) p. 307–17.

38. Amatruda JF, Zon LI. Dissecting hematopoiesis and disease using the zebrafish. *Dev Biol* (1999) 216(1):1–15. doi: 10.1006/dbio.1999.9462

39. Rousseau F, Bonaventure J, Legeaimallet L, Pelet A, Rozet JM, Maroteaux P, et al. Mutations in the gene encoding fibroblast growth-factor receptor-3 in achondroplasia. *Nature* (1994) 371(6494):252–4. doi: 10.1038/371252a0

40. Shiang R, Thompson LM, Zhu YZ, Church DM, Fielder TJ, Bocian M, et al. Mutations in the transmembrane domain of Fgfr3 cause the most common genetic form of dwarfism, achondroplasia. *Cell* (1994) 78(2):335–42. doi: 10.1016/0092-8674(94)90302-6

41. Stanescu R, Stanescu V, Maroteaux P. Homozygous achondroplasia - morphological and biochemical-study of cartilage. *Am J Med Genet* (1990) 37 (3):412–21. doi: 10.1002/ajmg.1320370323

42. Blakemore L, Schwend R, Akbarnia BA, Dumas M, Schmidt J. Growth patterns of the neurocentral synchondrosis (Ncs) in immature cadaveric vertebra. *J Pediatr Orthopaedics* (2018) 38(3):181–4. doi: 10.1097/bpo.0000000000000781

43. Graham A. Deconstructing the pharyngeal metamere. *J Exp Zoology Part B-Molecular Dev Evol* (2008) 310B(4):336–44. doi: 10.1002/jez.b.21182

44. Kimmel CB, Miller CT, Keynes RJ. Neural crest patterning and the evolution of the jaw. *J Anat* (2001) 199:105–20. doi: 10.1046/j.1469-7580.2001.19910105.x

45. Eames BF, Yan YL, Swartz ME, Levic DS, Knapik EW, Postlethwait JH, et al. Mutations in fam20b and xylt1 reveal that cartilage matrix controls timing of endochondral ossification by inhibiting chondrocyte maturation. *PloS Genet* (2011) 7(8):e1002246. doi: 10.1371/journal.pgen.1002246

46. Hoyle DJ, Dranow DB, Schilling TF. Pthlha and mechanical force control early patterning of growth zones in the zebrafish craniofacial skeleton. *Development* (2022) 149(2):dev199826. doi: 10.1242/dev.199826

47. Kampen WU, Claassen H, Kirsch T. Mineralization and osteogenesis in the human first rib cartilage. *Ann Anatomy-Anatomischer Anzeiger* (1995) 177(2):171–7. doi: 10.1016/s0940-9602(11)80069-5

48. Byers S, Moore AJ, Byard RW, Fazzalari NL. Quantitative histomorphometric analysis of the human growth plate from birth to adolescence. *Bone* (2000) 27(4):495–501. doi: 10.1016/s8756-3282(00)00357-4

49. Cumplido N, Allende ML, Arratia G. From devo to evo: Patterning, fusion and evolution of the zebrafish terminal vertebra. *Front Zoology* (2020) 17(1). doi: 10.1186/s12983-020-00364-y

50. Keer S, Cohen K, May C, Hu YN, McMenamin S, Hernandez LP. Anatomical assessment of the adult skeleton of zebrafish reared under different thyroid hormone profiles. *Anatomical Record-Advances Integr Anat Evolutionary Biol* (2019) 302(10):1754–69. doi: 10.1002/ar.24139

51. Huysseune A. Skeletal system. In: Ostrander GK, editor. *The laboratory fish*. London: Academic Press (2000). p. 307–17.

52. Hall BK, Miyake T. All for one and one for all: Condensations and the initiation of skeletal development. *Bioessays* (2000) 22(2):138–47. doi: 10.1002/(sici)1521-1878(200002)22:2<138::aid-bies5>3.0.co;2-4

53. Bertmar G. On the ontogeny of the chondral skull in characidae with a discussion on the chondrocranial base and visceral chondrocranium in fishes. *Acta Zoologica* (1959) 40:203–364. doi: 10.1111/j.1463-6395.1959.tb00397.x

54. Schilling TF, Kimmel CB. Musculoskeletal patterning in the pharyngeal segments of the zebrafish embryo. *Development* (1997) 124(15):2945–60. doi: 10.1242/dev.124.15.2945

55. Le Pabic P, Stellwag EJ, Scemama J-L. Embryonic development and skeletogenesis of the pharyngeal jaw apparatus in the cichlid Nile tilapia (Oreochromis niloticus). *Anatomical Record-Advances Integr Anat Evolutionary Biol* (2009) 292(11):1780–800. doi: 10.1002/ar.20960

56. Dewit J, Witten PE, Huysseune A. The mechanism of cartilage subdivision in the reorganization of the zebrafish pectoral fin endoskeleton. *J Exp Zoology Part B-Molecular Dev Evol* (2011) 316B(8):584–97. doi: 10.1002/jez.b.21433

57. Kimmel CB, Miller CT, Kruze G, Ullmann B, BreMiller RA, Larison KD, et al. The shaping of pharyngeal cartilages during early development of the zebrafish. *Dev Biol* (1998) 203(2):245–63. doi: 10.1006/dbio.1998.9016

58. Le Pabic P, Ng C, Schilling TF. Fat-dachsous signaling coordinates cartilage differentiation and polarity during craniofacial development. *PloS Genet* (2014) 10 (10):e1004726. doi: 10.1371/journal.pgen.1004726

59. Huysseune A, Sire JY. Development of cartilage and bone tissues of the anterior part of the mandible in cichlid fish - a light and tem study. *Anatomical Rec* (1992) 233(3):357–75. doi: 10.1002/ar.1092330304

60. Topczewski J, Sepich DS, Myers DC, Walker C, Amores A, Lele Z, et al. The zebrafish glypican knypek controls cell polarity during gastrulation movements of convergent extension. *Dev Cell* (2001) 1(2):251–64. doi: 10.1016/s1534-5807(01)00005-3

61. Gao B, Song H, Bishop K, Elliot G, Garrett L, English MA, et al. Wnt signaling gradients establish planar cell polarity by inducing Vangl2 phosphorylation through Ror2. *Dev Cell* (2011) 20(2):163–76. doi: 10.1016/j.devcel.2011.01.001

62. Li YW, Dudley AT. Noncanonical frizzled signaling regulates cell polarity of growth plate chondrocytes. *Development* (2009) 136(7):1083–92. doi: 10.1242/dev.023820

63. Rochard L, Monica SD, Ling ITC, Kong Y, Roberson S, Harland R, et al. Roles of wnt pathway genes wls, Wnt9a, Wnt5b, frzb and Gpc4 in regulating convergent-extension during zebrafish palate morphogenesis. *Development* (2016) 143(14):2541–7. doi: 10.1242/dev.137000

64. Kamel G, Hoyos T, Rochard L, Dougherty M, Kong Y, Tse W, et al. Requirement for frzb and Fzd7a in cranial neural crest convergence and extension mechanisms during zebrafish palate and jaw morphogenesis. *Dev Biol* (2013) 381 (2):423–33. doi: 10.1016/j.ydbio.2013.06.012

65. Li YW, Lie A, Junge J, Bronner M. Planar cell polarity signaling coordinates oriented cell division and cell rearrangement in clonally expanding growth plate cartilage. *Elife* (2017) 6:e23279. doi: 10.7554/eLife.23279

66. Sisson BE, Dale RM, Mui SR, Topczewska JM, Topczewski J. A role of Glypican4 and Wnt5b in chondrocyte stacking underlying craniofacial cartilage morphogenesis. *Mech Dev* (2015) 138:279–90. doi: 10.1016/j.mod.2015.10.001

67. Schwabe GC, Tinschert S, Buschow C, Meinecke P, Wolff G, Gillessen-Kaesbach G, et al. Distinct mutations in the receptor tyrosine kinase gene Ror2 cause brachydactyly type b. *Am J Hum Genet* (2000) 67(4):822–31. doi: 10.1086/303084

68. Oldridge M, Fortuna AM, Maringa M, Propping P, Mansour S, Pollitt C, et al. Dominant mutations in Ror2, encoding an orphan receptor tyrosine kinase, cause brachydactyly type b. *Nat Genet* (2000) 24(3):275–8. doi: 10.1038/73495

69. van Bokhoven H, Celli J, Kayserili H, van Beusekom E, Balci S, Brussel W, et al. Mutation of the gene encoding the Ror2 tyrosine kinase causes autosomal recessive robinow syndrome. *Nat Genet* (2000) 25(4):423–6. doi: 10.1038/78113

70. Afzal AR, Rajab A, Fenske CD, Oldridge M, Elanko N, Ternes-Pereira E, et al. Recessive robinow syndrome, allelic to dominant brachydactyly type b, is caused by mutation of Ror2. *Nat Genet* (2000) 25(4):419–22. doi: 10.1038/78107

71. White JJ, Mazzeu JF, Coban-Akdemir Z, Bayram Y, Bahrambeigi V, Hoischen A, et al. Wnt signaling perturbations underlie the genetic heterogeneity of robinow syndrome. *Am J Hum Genet* (2018) 102(1):27–43. doi: 10.1016/j.ajhg.2017.10.002

72. Lima AR, Ferreira BM, Zhang C, Jolly A, Du H, White JJ, et al. Phenotypic and mutational spectrum of Ror2-related robinow syndrome. *Hum Mutat* (2022) 43:900-18. doi: 10.1002/humu.24375

73. Person AD, Beiraghi S, Sieben CM, Hermanson S, Neumann AN, Robu ME, et al. Wnt5a mutations in patients with autosomal dominant robinow syndrome. *Dev Dyn* (2010) 239(1):327–37. doi: 10.1002/dvdy.22156

74. Waterson J, Stockley TL, Segal S, Golabi M. Novel duplication in glypican-4 as an apparent cause of Simpson-Golabi-Behmel syndrome. *Am J Med Genet A* (2010) 152A(12):3179–81. doi: 10.1002/ajmg.a.33450

75. Amor DJ, Stephenson SEM, Mustapha M, Mensah MA, Ockeloen CW, Lee WS, et al. Pathogenic variants in Gpc4 cause keipert syndrome. *Am J Hum Genet* (2019) 104(5):914–24. doi: 10.1016/j.ajhg.2019.02.026

76. Cappello S, Gray MJ, Badouel C, Lange S, Einsiedler M, Srour M, et al. Mutations in genes encoding the cadherin receptor-ligand pair Dchs1 and Fat4 disrupt cerebral cortical development. *Nat Genet* (2013) 45(11):1300–8. doi: 10.1038/ng.2765

77. Mansour S, Swinkels M, Terhal PA, Wilson LC, Rich P, Van Maldergem L, et al. Van maldergem syndrome: Further characterisation and evidence for neuronal migration abnormalities and autosomal recessive inheritance. *Eur J Hum Genet* (2012) 20(10):1024–31. doi: 10.1038/ejhg.2012.57

78. Yang L, Tsang KY, Tang HC, Chan D, Cheah KSE. Hypertrophic chondrocytes can become osteoblasts and osteocytes in endochondral bone formation. *Proc Natl Acad Sci United States America* (2014) 111(33):12097–102. doi: 10.1073/pnas.1302703111

79. Park J, Gebhardt M, Golovchenko S, Perez-Branguli F, Hattori T, Hartmann C, et al. Dual pathways to endochondral osteoblasts: A novel chondrocyte-derived osteoprogenitor cell identified in hypertrophic cartilage. *Biol Open* (2015) 4 (5):608–21. doi: 10.1242/bio.201411031

80. Roach HI. New aspects of endochondral ossification in the chick: Chondrocyte apoptosis, bone formation by former chondrocytes, and acid phosphatase activity in the endochondral bone matrix. *J Bone Mineral Res* (1997) 12(5):795–805. doi: 10.1359/jbmr.1997.12.5.795

81. Roach HI. Transdifferentiation of hypertrophic chondrocytes into cells capable of producing a mineralized bone-matrix. *Bone Mineral* (1992) 19(1):1–20. doi: 10.1016/0169-6009(92)90840-a

82. Vortkamp A, Lee K, Lanske B, Segre GV, Kronenberg HM, Tabin CJ. Regulation of rate of cartilage differentiation by Indian hedgehog and pth-related protein. *Science* (1996) 273(5275):613–22. doi: 10.1126/science.273.5275.613

83. Chung UI, Lanske B, Lee KC, Li E, Kronenberg H. The parathyroid hormone parathyroid hormone-related peptide receptor coordinates endochondral bone development by directly controlling chondrocyte differentiation. *Proc Natl Acad Sci United States America* (1998) 95(22):13030–5. doi: 10.1073/pnas.95.22.13030

84. Chung UI, Schipani E, McMahon AP, Kronenberg HM. Indian Hedgehog couples chondrogenesis to osteogenesis in endochondral bone development. *J Clin Invest* (2001) 107(3):295–304. doi: 10.1172/jci11706

85. Clement A, Wiweger M, von der Hardt S, Rusch MA, Selleck SB, Chien CB, et al. Regulation of zebrafish skeletogenesis by ext2/Dackel and papst1/Pinscher. *PloS Genet* (2008) 4(7):e1000136. doi: 10.1371/journal.pgen.1000136

86. St-Jacques B, Hammerschmidt M, McMahon AP. Indian Hedgehog signaling regulates proliferation and differentiation of chondrocytes and is essential for bone formation. *Genes Dev* (1999) 13(16):2072–86. doi: 10.1101/gad.13.16.2072

87. Retting KN, Song B, Yoon BS, Lyons KM. Bmp canonical smad signaling through Smad1 and Smad5 is required for endochondral bone formation. *Development* (2009) 136(7):1093–104. doi: 10.1242/dev.029926

88. Wang WG, Song B, Anbarchian T, Shirazyan A, Sadik JE, Lyons KM. Smad2 and Smad3 regulate chondrocyte proliferation and differentiation in the growth plate. *PloS Genet* (2016) 12(10):e1006352. doi: 10.1371/journal.pgen.1006352

89. Colvin JS, Bohne BA, Harding GW, McEwen DG, Ornitz DM. Skeletal overgrowth and deafness in mice lacking fibroblast growth factor receptor 3. *Nat Genet* (1996) 12(4):390–7. doi: 10.1038/ng0496-390

90. Naski MC, Colvin JS, Coffin JD, Ornitz DM. Repression of hedgehog signaling and Bmp4 expression in growth plate cartilage by fibroblast growth factor receptor 3. *Development* (1998) 125(24):4977–88. doi: 10.1242/dev.125.24.4977

91. Long FX, Chung UI, Ohba S, McMahon J, Kronenberg HM, McMahon AP. Ihh signaling is directly required for the osteoblast lineage in the endochondral skeleton. *Development* (2004) 131(6):1309–18. doi: 10.1242/dev.01006

92. Felber K, Croucher P, Roehl HH. Hedgehog signalling is required for perichondral osteoblast differentiation in zebrafish. *Mech Dev* (2011) 128(1-2):141–52. doi: 10.1016/j.mod.2010.11.006

93. Cooper KL, Oh S, Sung Y, Dasari RR, Kirschner MW, Tabin CJ. Multiple phases of chondrocyte enlargement underlie differences in skeletal proportions. *Nature* (2013) 495(7441):375–8. doi: 10.1038/nature11940

94. Young B, Minugh-Purvis N, Shimo T, St-Jacques B, Iwamoto M, Enomoto-Iwamoto M, et al. Indian And sonic hedgehogs regulate synchondrosis growth plate and cranial base development and function. *Dev Biol* (2006) 299(1):272–82. doi: 10.1016/j.ydbio.2006.07.028

95. Nagayama M, Iwamoto M, Hargett A, Kamiya N, Tamamura Y, Young B, et al. Wnt/Beta-catenin signaling regulates cranial base development and growth. *J Dental Res* (2008) 87(3):244–9. doi: 10.1177/154405910808700309

96. Eames BF, Singer A, Smith GA, Wood ZA, Yan YL, He XJ, et al. Udp xylose synthase 1 is required for morphogenesis and histogenesis of the craniofacial skeleton. *Dev Biol* (2010) 341(2):400–15. doi: 10.1016/j.ydbio.2010.02.035

97. Farnum CE, Tinsley M, Hermanson JW. Forelimb versus hindlimb skeletal development in the big brown bat, eptesicus fuscus: Functional divergence is reflected in chondrocytic performance in autopodial growth plates. *Cells Tissues Organs* (2008) 187(1):35–47. doi: 10.1159/000109962

98. Johnson S, Heubel B, Bredesen C, Schilling T, Le Pabic P. Cellular basis of differential endochondral growth in lake Malawi cichlids. *Dev Dynamics* (2022) 1-14. doi: 10.1002/dvdy.529

99. Huysseune A, Verraes W, Desender K. Mechanisms of branchial cartilage growth in astatotilapia elegans (Teleostei: Cichlidae). *J Anat* (1988) 158:13–30.

100. Borjesson AE, Lagerquist MK, Windahl SH, Ohlsson C. The role of estrogen receptor alpha in the regulation of bone and growth plate cartilage. *Cell Mol Life Sci* (2013) 70(21):4023–37. doi: 10.1007/s00018-013-1317-1

101. Ford E. Growth of the human cranial base. *Am J Orthodontics* (1958) 44:498–506. doi: 10.1016/0002-9416(58)90082-4

102. Scott JH. The cranial base. *Am J Phys Anthropology* (1958) 16:319–48. doi: 10.1002/ajpa.1330160305

103. Hayashi I. Morphological relationship between the cranial base and dentofacial complex obtained by reconstructive computer tomographic images. *Eur J Orthodontics* (2003) 25(4):385–91. doi: 10.1093/ejo/25.4.385

104. von Bertalanffy L. A quantitative theory of organic growth (Inquiries on growth laws. ii). *Hum Biol* (1938) 10:181–213. Available at: https://www.jstor.org/stable/41447359

105. Schilling TF. The morphology of larval and adult zebrafish. In: Nusslein-Volhard C, Dahm R, editors. *Zebrafish: A practical approach*. New York: Oxford University Press (2002).

106. Parichy DM, Elizondo MR, Mills MG, Gordon TN, Engeszer RE. Normal table of postembryonic zebrafish development: Staging by externally visible anatomy of the living fish. *Dev Dynamics* (2009) 238(12):2975–3015. doi: 10.1002/dvdy.22113

107. Brown DS, Eames BF. Emerging tools to study proteoglycan function during skeletal development. *Zebrafish: Cell Dev Biology Pt B: Dev Biol* (2016) 134:485–530. doi: 10.1016/bs.mcb.2016.03.001

108. Alvarez C, Tredwell S, De Vera M, Hayden M. The genotype-phenotype correlation of hereditary multiple exostoses. *Clin Genet* (2006) 70(2):122–30. doi: 10.1111/j.1399-0004.2006.00653.x

109. Francannet C, Cohen-Tanugi A, Le Merrer M, Munnich A, Bonaventure J, Legeai-Mallet L. Genotype-phenotype correlation in hereditary multiple exostoses. *J Med Genet* (2001) 38(7):430–4. doi: 10.1136/jmg.38.7.430

110. Xu L, Xia JH, Jiang HJ, Zhou JN, Li HJ, Wang DP, et al. Mutation analysis of hereditary multiple exostoses in the Chinese. *Hum Genet* (1999) 105(1-2):45–50. doi: 10.1007/s004390051062

111. Varshney GK, Pei WH, LaFave MC, Idol J, Xu LS, Gallardo V, et al. High-throughput gene targeting and phenotyping in zebrafish using Crispr/Cas9. *Genome Res* (2015) 25(7):1030–42. doi: 10.1101/gr.186379.114

112. Wu RS, Lam II, Clay H, Duong DN, Deo RC, Coughlin SR. A rapid method for directed gene knockout for screening in G0 zebrafish. *Dev Cell* (2018) 46 (1):112–25. doi: 10.1016/j.devcel.2018.06.003

113. Hammond C, Moro E. Using transgenic reporters to visualize bone and cartilage signaling during development in vivo. *Front Endocrinol* (2012) 3:91. doi: 10.3389/fendo.2012.00091

114. Kimmel CB, DeLaurier A, Ullmann B, Dowd J, McFadden M. Modes of developmental outgrowth and shaping of a craniofacial bone in zebrafish. *PloS One* (2010) 5(3):12. doi: 10.1371/journal.pone.0009475

115. Curado S, Stainier DYR, Anderson RM. Nitroreductase-mediated Cell/Tissue ablation in zebrafish: A spatially and temporally controlled ablation method with applications in developmental and regeneration studies. *Nat Protoc* (2008) 3 (6):948–54. doi: 10.1038/nprot.2008.58

116. Kawakami K, Shima A. Identification of the Tol2 transposase of the medaka fish oryzias latipes that catalyzes excision of a nonautonomous Tol2 element in zebrafish danio rerio. *Gene* (1999) 240(1):239–44. doi: 10.1016/s0378-1119(99)00444-8

117. Kwan KM, Fujimoto E, Grabher C, Mangum BD, Hardy ME, Campbell DS, et al. The Tol2kit: A multisite gateway-based construction kit for Tol2 transposon transgenesis constructs. *Dev Dyn* (2007) 236(11):3088–99. doi: 10.1002/dvdy.21343

118. Farrell JA, Wang YQ, Riesenfeld SJ, Shekhar K, Regev A, Schier AF. Single-cell reconstruction of developmental trajectories during zebrafish embryogenesis. *Science* (2018) 360(6392):979–85. doi: 10.1126/science.aar3131

119. Raj B, Wagner DE, McKenna A, Pandey S, Klein AM, Shendure J, et al. Simultaneous single-cell profiling of lineages and cell types in the vertebrate brain. *Nat Biotechnol* (2018) 36(5):442–50. doi: 10.1038/nbt.4103

120. Lencer E, Prekeris R, Artinger KB. Single-cell rna analysis identifies pre-migratory neural crest cells expressing markers of differentiated derivatives. *Elife* (2021) 10:e66078. doi: 10.7554/eLife.66078

121. Fabian P, Tseng KC, Thiruppathy M, Arata C, Chen HJ, Smeeton J, et al. Lifelong single-cell profiling of cranial neural crest diversification in zebrafish. *Nat Commun* (2022) 13(13). doi: 10.1038/s41467-021-27594-w

122. Wagner DE, Weinreb C, Collins ZM, Briggs JA, Megason SG, Klein AM. Single-cell mapping of gene expression landscapes and lineage in the zebrafish embryo. *Science* (2018) 360(6392):981–7. doi: 10.1126/science.aar4362

frontiers | Frontiers in Endocrinology

TYPE Original Research
PUBLISHED 12 December 2022
DOI 10.3389/fendo.2022.1033843

OPEN ACCESS

EDITED BY
Erika Kague,
University of Bristol, United Kingdom

REVIEWED BY
D'Juan Farmer, University of California, Los Angeles, United States
Tatjana Haitina,
Uppsala University, Sweden

*CORRESPONDENCE
James T. Nichols
James.Nichols@cuanschutz.edu

†These authors have contributed equally to this work and share first authorship

SPECIALTY SECTION
This article was submitted to Bone Research, a section of the journal Frontiers in Endocrinology

RECEIVED 01 September 2022
ACCEPTED 17 November 2022
PUBLISHED 12 December 2022

CITATION
Stenzel A, Mumme-Monheit A, Sucharov J, Walker M, Mitchell JM, Appel B and Nichols JT (2022) Distinct and redundant roles for zebrafish *her* genes during mineralization and craniofacial patterning.
Front. Endocrinol. 13:1033843.
doi: 10.3389/fendo.2022.1033843

Distinct and redundant roles for zebrafish *her* genes during mineralization and craniofacial patterning

Amanda Stenzel[1†], Abigail Mumme-Monheit[1†], Juliana Sucharov[1], Macie Walker[2], Jennyfer M. Mitchell[1], Bruce Appel[2] and James T. Nichols[1*]

[1]Department of Craniofacial Biology, University of Colorado-Anschutz Medical Campus, Aurora, CO, United States, [2]Department of Pediatrics, Section of Developmental Biology, University of Colorado-Anschutz Medical Campus, Aurora, CO, United States

The Notch pathway is a cell-cell communication system which is critical for many developmental processes, including craniofacial development. Notch receptor activation induces expression of several well-known canonical targets including those encoded by the *hes* and *her* genes in mammals and zebrafish, respectively. The function of these genes, individually and in combination, during craniofacial development is not well understood. Here, we used zebrafish genetics to investigate *her9* and *her6* gene function during craniofacial development. We found that *her9* is required for osteoblasts to efficiently mineralize bone, while cartilage is largely unaffected. Strikingly, gene expression studies in *her9* mutants indicate that although progenitor cells differentiate into osteoblasts at the appropriate time and place, they fail to efficiently lay down mineralized matrix. This mineralization role of *her9* is likely independent of Notch activation. In contrast, *her9* also functions redundantly with *her6* downstream of Jagged1b-induced Notch activation during dorsoventral craniofacial patterning. These studies disentangle distinct and redundant *her* gene functions during craniofacial development, including an unexpected, Notch independent, requirement during bone mineralization.

KEYWORDS

craniofacial, skeleton, *her*, mineralization, Notch, bone, osteoblast, patterning

Introduction

Notch signaling has diverse functions

The Notch signaling pathway is conserved across metazoans. Notch signaling is highly pleiotropic and functions in the development, homeostasis and regeneration of many different cells and tissues, including skeletal cells (1–3). During canonical vertebrate Notch activation, membrane-bound Jagged or Delta ligands bind to

membrane-bound Notch receptors to induce cell-cell communication (4). After binding, the Notch receptor is cleaved releasing the Notch intracellular domain (NICD) which translocates to the nucleus where it directly induces transcription of downstream target genes (5). Canonical Notch downstream targets include the homologs of the Drosophila genes hairy and enhancer of split. In mammals these genes are called *hairy and enhancer of split* (*hes*) (6). In zebrafish the homologous genes are called *hairy and enhancer of split related* (*her*) (7). The *hes* and *her* genes belong to a family of helix-loop-helix transcriptional repressors with Orange domain (8). The roles that these effectors play in various Notch signaling contexts are not yet clear. Further confounding our understanding, some *her* genes (like *her9*) have both Notch-dependent and Notch-independent expression in different situations (9–12). Thus, more work is needed to understand specific roles of the different *hes*/*her* genes, individually and in combination, and to explore contexts where their expression can be Notch dependent or independent.

Notch functions in craniofacial patterning

The vertebrate craniofacial skeleton is largely derived from post-migratory neural crest cells. After these cells migrate into the pharyngeal arches, various signaling pathways act upon them to confer dorsal versus ventral cellular identity. These dorsal and ventral cells then give rise to the diversely shaped cartilages and bones of the jaw and jaw support structures. The Notch pathway is one signaling system that functions during craniofacial development to specify dorsal versus ventral identity in zebrafish (1, 13–16). Much of our understanding of this process comes from studies of genetic mutants, overexpression conditions, and pharmacological inhibitors in zebrafish. In particular, the Notch ligand *jagged1b* (*jag1b*) is critical for zebrafish craniofacial development, and *jag1b* mutant phenotypes are phenocopied by the Notch cleavage inhibitor dibenzazepine (DBZ) (13). In *jag1b* mutants, dorsal craniofacial structures are shaped more like ventral structures suggesting identity transformations. In support, in *jag1b* mutants, expression of ventral identity genes like *dlx5a* are expanded into dorsal domains (1). These zebrafish studies offer insight into the mechanisms behind human craniofacial disease phenotypes. Humans with mutations in the human ortholog *JAG1* develop Alagille syndrome which is characterized by craniofacial abnormalities including a broad forehead, deep set eyes, small pointed chin, and midface hypoplasia (17). Midface hypoplasia, characterized by a reduction of bone, is observed in both humans and mouse models (18, 19). This dorsal bone reduction defect is similar to the reduced dorsal bone observed in zebrafish *jag1b* mutants. Thus, genetic studies in zebrafish inform the etiology of human genetic disease phenotypes.

Jag1b appears to be the most critical Notch ligand for zebrafish craniofacial development. In contrast, the roles of the various Notch target genes in craniofacial patterning are less clear. For example, *her6* expression is regionalized to the dorsal domain of the pharyngeal arches, making it a strong candidate for functioning downstream of *jag1b* during craniofacial patterning. However, zebrafish *her6* mutants are indistinguishable from wild types (14), indicating *her6* function is not required for dorsal identity patterning, or may function redundantly with other genes. Mice mutant for *Hes1*, the rodent ortholog of *her6*, develop dramatic craniofacial phenotypes (20) at least in part due to neural crest cell survival defects (21). To our knowledge, a patterning function of *Hes1* has not yet been demonstrated in mice. Another Notch target gene of this same family, *her9*, was reported to have overt craniofacial defects when mutagenized in zebrafish (22), but details of these defects were not analyzed, and no figures illustrating the skeletal phenotype were provided. Thus, the role of this gene in craniofacial development remains unknown. However, the human ortholog, *HES4*, is contained within a region deleted in chromosome 1p36 deletion syndrome, which is associated with a small, short and wide head, vision and hearing problems, abnormalities of the skeleton as well as abnormalities of the brain (23). Because there are many genes encompassed by this deletion, whether *HES4*/*her9* is involved in craniofacial patterning remains unknown. Adding to the confusion, there is no *HES4*/*her9* ortholog in the mouse genome. Therefore, the mouse system cannot inform the function of this gene.

Given that *her6* is specifically expressed in cranial neural crest cells from the dorsal pharyngeal arches, and that *her6* mutants do not develop overt phenotypes in zebrafish, we hypothesized that *her6* functions redundantly with other *her* genes downstream of *jag1b* during zebrafish craniofacial patterning. Double and triple mutant genetic experiments are needed to test this hypothesis.

Notch target genes regulate skeletal cell differentiation

The Notch pathway also plays a vital role in skeletal development occurring after craniofacial patterning. After regional identity is specified, precursor cells differentiate into chondrocytes and osteoblasts that make cartilage and bone, respectively. Numerous studies implicate Notch signaling and Notch target genes in both chondrocyte and osteoblast cell differentiation (3). Chondrogenic differentiation assays in human cells indicate that HES/HER proteins bind to *SOX9* binding sites in *COL2A1* enhancers, thereby suppressing expression of genes critical for chondrocyte differentiation (24). Similarly, in mouse cells these genes suppress *Sox9* and *Col2a1* expression and chondrogenesis (25). Thus, Notch

activation decreases chondrogenesis, at least in these experimental contexts. The role of Notch target genes during osteoblast differentiation is complicated and unclear. Specifically, some studies indicate Notch target genes, including *HES4/her9*, function to promote osteoblast formation (26). Meanwhile others indicate that Notch signaling, *via hes/her* genes, represses osteoblast differentiation (27, 28). Thus, *hes/her* genes are reported to have both an inductive and a suppressive effect on osteoblast differentiation. However, several of these studies were carried out with cell culture overexpression conditions, which may not inform *in vivo* function. A more complete understanding of the complicated role of these genes during osteoblast differentiation will likely arise from studies examining *in vivo* genetic models.

Here we used zebrafish genetics to discover that *her9* function is crucial for osteoblasts to efficiently mineralize bone. Surprisingly, osteoblasts differentiate in the correct time and place in *her9* mutants, yet mineralized matrix production is dramatically impaired. This mineralization role is independent of Notch cleavage. However, we did find a redundant role for *her9* and *her6* downstream of Jagged induced Notch activation during craniofacial patterning.

Results

Gene expression suggests *her9* and *her6* function downstream of *jag1b* during craniofacial development

jag1b functions in cranial neural crest cells of the dorsal anterior pharyngeal arches (arches 1 and 2) (1). We, and others, demonstrated that developing zebrafish heads express *her6*, in a *jag1b* dependent manner (14, 15). Yet, *her6* mutants do not produce overt craniofacial phenotypes (14). These results motivate the hypothesis that *her6* functions redundantly with other *her* genes downstream of *jag1b*. To explore what other *her* genes might be acting downstream of *jag1b* during craniofacial development, we searched for genes expressed in the same cranial neural crest cell population as *jag1b* and *her6*. We examined a 24 hours post fertilization (hpf) single cell RNA sequencing (scRNA-seq) dataset from sorted cranial neural crest cells. This dataset is an unpublished replicate to test for reproducibility of our previously published experiment (29). Both replicates are highly similar, and the results of this comparison will be reported elsewhere. We found that 16 *her* genes are detectibly expressed in this dataset (Figure S1), however *her9* and *her6* are the family members with the strongest expression in the skeletogenic, pharyngeal arch neural crest cells. In contrast, many of the other *her* genes are only weakly, or not detectably, expressed in the anterior pharyngeal arches. In fact, most of the other *her* genes in this dataset are restricted to the melanocyte population. Further examining *her9* and *her6* revealed that they are expressed in a subpopulation of anterior arch cranial neural crest cells along with *jag1b* (Figure 1A). While *her6* is broadly expressed among cranial neural crest cells, the *jag1b* expressing population is enriched for *her6*. *her9* is broadly, but more weakly, expressed in most cranial neural crest cells but the strongest expression is in the *jag1b* population. We further analyzed these expression data with side-by-side comparisons in two-color plots to look for co-expression between *jag1b*, *her9*, and *her6* (Figure S2). These plots further support our interpretation that *jag1b*, *her9* and *her6* are expressed in the same population, and in some cases in the same cells. We next re-clustered the anterior arch population to further analyze *jag1b* and *her9* and *her6* in these cells which give rise to the craniofacial skeleton. In these analyses we include UMAP plots with the expression of known "landmark" genes. These include the pan-anterior arch gene *dlx2a*, the intermediate and ventral anterior arch gene *dlx5a* and the extreme ventral anterior arch gene *hand2*. We observed in these studies, that *jag1b*, known to be expressed in the dorsal anterior arch population (1), is complementary to *dlx5a*, as expected. Moreover *jag1b* expression overlaps with *her9* and *her6* in these analyses. These data further support the finding that *her9* and *her6* are expressed in the same population of cells as *jag1b*. These results make *her9* and *her6* strong candidates for genes functioning downstream of *jag1b* during craniofacial development. To directly test if *her9* is dependent upon *jag1b* function, we performed RT-qPCR in wild types and *jag1b* mutants at 28 and 48 hpf. We previously demonstrated that *her6* is a transcriptional target of *jag1b* (15); expression is downregulated in *jag1b* mutants compared with wild-type controls at both 28 and 48 hpf (Figure 1B). Here, we find that *her9* expression is significantly decreased in *jag1b* mutants at 48 hpf compared with wild types. There is no significant difference at 28 hpf. These findings indicate that *her9* expression is *jag1b* independent at 28 hpf and *jag1b* dependent at 48 hpf. That both *her6* and *her9* expression are dependent upon *jag1b* in zebrafish heads at 48 hpf, motivates the hypothesis that they function redundantly downstream of Jag-induced Notch signaling at this stage.

her9 is required for timely bone mineralization

The *jag1b*-dependent *her6;her9* expression predicts that loss of function mutations in these genes will produce similar phenotypes to *jag1b* mutants. To test this prediction, we first examined *her9* individually. We recovered a *her9* mutant allele from an ENU mutagenesis screen (see Methods for details). The mutant allele produces a premature termination codon at amino acid 148 of 291, near the end of the region predicted to encode the Orange domain (Figure 2A). We detected reduced *her9* transcript levels in homozygous mutants suggesting that this

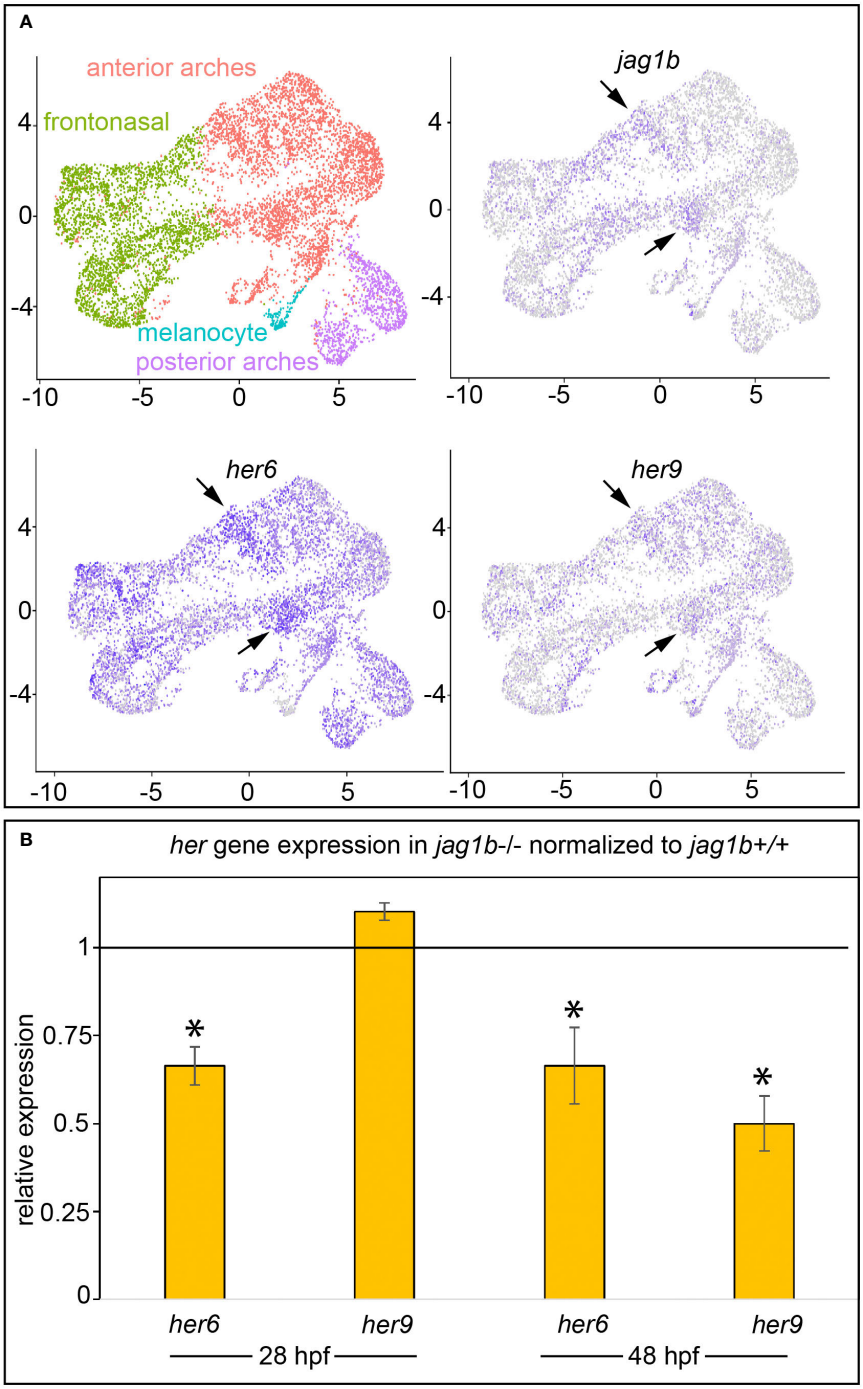

FIGURE 1
her6 and *her9* are expressed in the same subpopulation of cranial neural crest cells as *jag1b*, and their expression is dependent upon *jag1b* function. **(A)** UMAPs from single cell RNA-sequencing on 24 hpf sorted cranial neural crest cells. As in our previous work (29), cranial neural crest cells can be clustered into four distinct populations. Based on our previous study and the landmark genes enriched in each population we can identify where the cells reside in the intact animal. Arrows indicate *jag1b* enrichment in a subset of anterior arch cells. Although *her6* is broader, arrows indicate that some of the strongest expressing cells are the *jag1b* enriched populations. *her9* is also broadly expressed among cranial neural crest cells, but at lower levels than *her6*. Arrows indicate *her9* enrichment in the *jag1b*;*her6* expressing populations. **(B)** We performed qPCR on 28 and 48 hpf genotyped heads from wild type and *jag1b* homozygous mutant siblings. Expression of each *her* gene was normalized to *rps18*, then normalized to the relevant wild-type control. Reactions were performed in technical triplicate and the results represent three to six biological replicates. Each biological replicate was pooled heads from 5–6 genotyped homozygous wild types or homozygous mutants. Error bars are standard deviation. Asterisks indicate significant differences from wild type controls at $p < 0.05$ by students t-test.

10.3389/fendo.2022.1033843

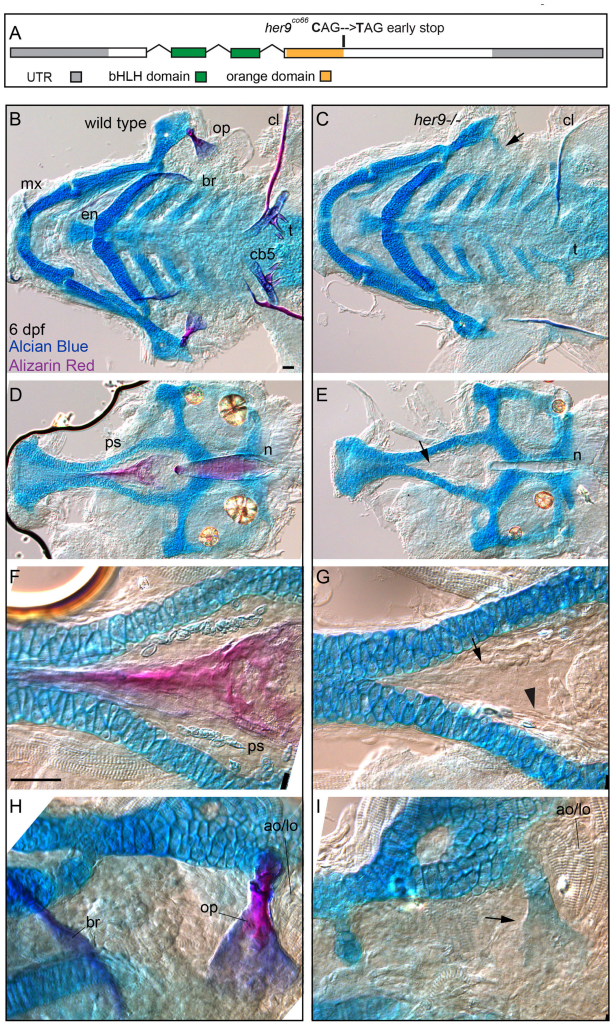

J AB strain	her9 +/+ n=14	her9 +/- n=36	her9- /- n=20
her9- phenotype	penetrance		
unmineralized op:	0%	0%	85% *
unmineralized ps:	0%	0%	100%*
unmineralized cl:	0%	0%	85% *

FIGURE 2
her9 is required for efficient mineralization. **(A)** Exon diagram for *her9* indicating the untranslated regions (UTR) and the regions predicted to encode the basic helix-loop-helix (bHLH) and Orange domains. The location of the early stop encoded by the *her9*^{co66} allele is indicated. **(B, C)** Zebrafish heterozygous for *her9* were pairwise intercrossed and six days post fertilization (dpf) larvae were stained with Alcian Blue and Alizarin Red to label cartilage and bone. The individuals were then genotyped, the viscerocrania were dissected, flat mounted, and then imaged. The following craniofacial skeletal elements are indicated in the wild-type individual: opercle bone (op), branchiostegal ray (br), maxilla (mx), entopterygoid (en), ceratobranchial 5 (cb5) bone, teeth (t), and the cleithrum (cl). Arrow in C indicates the unmineralized, Alcian Blue-positive opercle. Scale bar is 50 µm **(D, E)** The neurocrania from the same experiments as B and C were dissected, flat mounted, and then imaged. The parasphenoid bone (ps) and notochord (n) is indicated in the wild-type individual. Arrow in D indicates the shadow bone where the mineralized parasphenoid would be observable in wild types. **(F, G)** Enlargements from D and E. Arrow indicates the unmineralized shadow bone. Arrowhead denotes osteoblast-shaped cells surrounding the shadow bone. Scale bar is 50 µm **(H, I)** Enlargements from **(B, C)**. The adductor operculi and the levetor operculi muscles (ao/lo) are indicated. Arrow in I indicates the unmineralized, Alcian Blue-positive opercle with the adductor operculi and the levetor operculi muscles (ao/lo) attached. **(J)** The penetrance of *her9* mutant-associated phenotypes observed in 6 dpf larvae for each genotype are indicated. Asterisk indicates significant difference ($p<0.05$) in penetrance between the indicated genotype and wild type by Fishers exact test.

lesion impacts *her9* function (Figure S3). When we crossed adults heterozygous for this *her9* mutation we failed to recover homozygous mutants from these crosses at 12 dpf, indicating that the mutation is homozygous lethal, as reported previously (22). We next stained offspring from these crosses with Alcian Blue and Alizarin Red at 6 dpf. Alcian Blue labels cartilage by interacting with mucopolysaccharides (30). Alizarin Red stains bone by complexing with calcium in mineralized bone (31). We observed that cartilage staining in *her9* mutants was overtly normal (Figures 2B–I), although the overall size of the craniofacial skeleton, including the cartilage elements, was significantly smaller than wild type-controls (Figure S4). In contrast to the cartilage skeleton, which is strongly stained with Alcian Blue, we observed dramatic reductions in Alizarin Red-stained bone in these mutants. We found reduced mineralization in cranial neural crest cell-derived structures like the opercle bone, branchiostegal rays, maxilla, entopterygoid, ceratobranchial 5 (cb5) bones and teeth. The cleithrum, which is derived from mesoderm (32), was also weakly and variably stained in *her9* homozygous mutants (Figure 2C). We also observed that notochord mineralization was defective in *her9* mutants (Figures 2D, E). Thus, *her9* functions in the mineralization of structures derived from both cranial neural crest cells as well as mesoderm. Scoring the individual bones for mineralization defect penetrance revealed that parasphenoid mineralization loss is 100% penetrant, while the cleithrum and the opercle mineralization losses are more variable (Figure 2J). Thus, all bones require *her9* function, but some boney structures are more sensitive to *her9* loss than others. Both scRNA-seq and *in situ* gene expression studies indicate that *her9* is broadly expressed during the pharyngula period (Figures 1A, S3), consistent with the broad defects in bone mineralization.

We next aimed to determine if mineralization phenotype in *her9* mutants persists into later stages of skeletal development. To this end, we analyzed *her9* mutant and wild-type sibling control skeletons in 8 dpf zebrafish (Figure 3). Strikingly we observed that while bone mineralization was still reduced in *her9* mutants, some mineralization had occurred. Specifically, the opercle and parasphenoid had reduced, but clearly observable, Alizarin Red

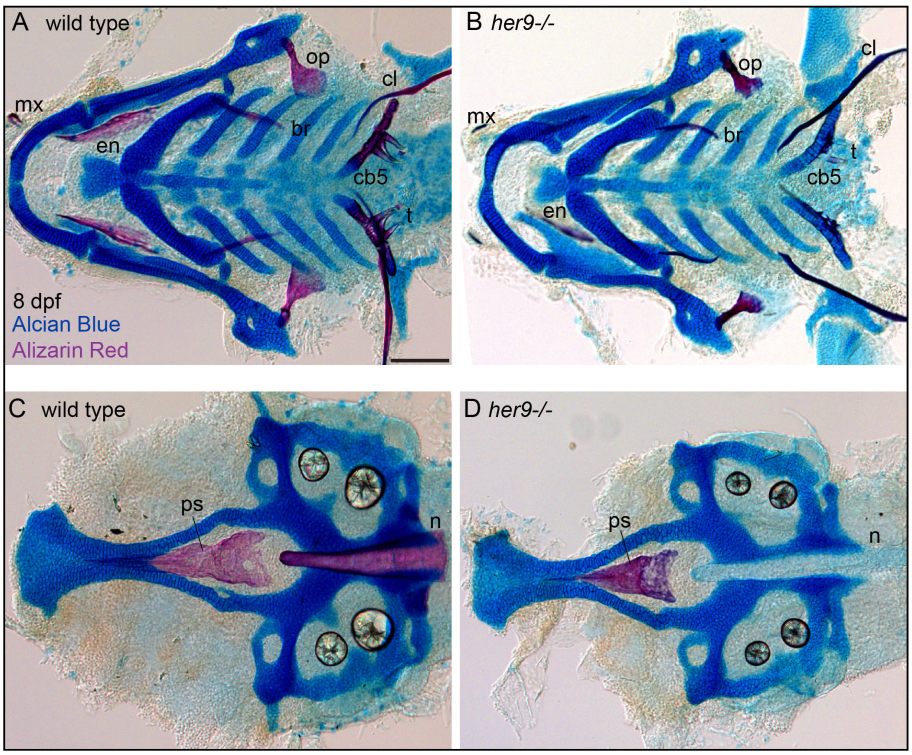

FIGURE 3
Mineralization defects in *her9* homozygous mutants partially recover at late stages of larval development. Zebrafish heterozygous for *her9* were pairwise intercrossed and at eight days post fertilization (dpf) larvae were stained with Alcian Blue and Alizarin Red to label cartilage and bone. The individuals were then genotyped, the viscerocrania and neurocrania were dissected, flat mounted, and then imaged. **(A, B)** Viscerocrania from wild-type and her9 homozygous mutant larvae. **(C, D)** Neurocrania from wild-type and her9 homozygous mutant larvae. The following craniofacial elements are indicated: opercle bone (op), branchiostegal ray (br), maxilla (mx), entopterygoid (en), ceratobranchial 5 (cb5) bone, teeth (t), cleithrum (cl), parasphenoid bone (ps), and notochord (n). Scale bar is 100 μm.

staining at this stage compared with wild-type controls. Thus, the early strong mineralization defects in *her9* mutants can partially recover at later stages of skeletal development.

To determine if this bone mineralization phenotype was due to *her9* function downstream of Notch signaling, we treated wild-type embryos with the pharmacological gamma secretase inhibitor DBZ, which inhibits Notch intramembranous cleavage and release of NICD, and phenocopies the *jag1b* mutant (13, 15). When we treated embryos during the craniofacial patterning stage (18-48 hpf), DBZ produced craniofacial phenotypes reminiscent of the *jag1b* mutant phenotype (Figure S5). Like *jag1b* mutants, there was no detectable bone mineralization phenotype in these treated animals. When we treated later stage animals during chondrocyte and osteoblast differentiation (48-72 hpf) with DBZ, there were no overt changes to the craniofacial skeleton. However, this treatment window produced a body-curvature phenotype indicating that DBZ is affecting Notch signaling outside the head during this stage. Finally, when we treated developing fish at later stages while the skeleton grows and becomes more elaborate (72-96 hpf) with DBZ, they were indistinguishable from untreated controls. Longer treatments from 18-72 hpf produce dramatic global defects and cannot be meaningfully interpreted for mineralization. These results indicate that inhibiting Notch cleavage and NICD release does not phenocopy the *her9* phenotype but does phenocopy the *jag1b* phenotype. Thus, the role that *her9* plays in bone mineralization is likely independent of Notch cleavage and *jag1b* function.

There was only weak or no Alizarin Red staining in 6 dpf *her9* mutant craniofacial bony elements. However, when we closely examined these preps, we observed 'shadow bones' or vacant spaces shaped like the wild type structures where the elements would normally develop in wild types. For some of these, like the opercle, there was Alcian Blue staining of the unmineralized element (Figure 2C). Interestingly, the adductor operculi and levator operculi muscle groups which articulate with the posterior edge of the opercle at this stage appeared to be present and articulated with the unmineralized opercle. For some structures like the parasphenoid, there was no detectable Alcian Blue, just a shadow bone in the shape of the wild-type bone observable by Nomarski imaging (Figure 2E). High magnification images of the shadow bones revealed osteoblast-shaped cells in the expected position surrounding the element (Figure 2G). These findings motivate the hypothesis that the cells which normally produce the affected bony elements in wild types, may be present in the correct location but are variably unable to produce mineralized matrix with the correct timing.

her9 is not required for osteoblast transcriptional identity

To determine whether the cells we observed surrounding the shadow bones are differentiated osteoblasts, we crossed the *her9* mutant into the *sp7:EGFP* transgenic line which faithfully labels active, bone-secreting osteoblasts (33). Fish with this transgene can be assayed with live Alizarin Red staining, which is a highly sensitive method of labeling mineralized bone (34). A strength of this approach is that the same bone can be longitudinally tracked in an individual over developmental time. We first examined the developing opercle at 3 dpf, when the initial opercle osteoblasts appear (35). In wild types, the first osteoblasts outline the early spicule-shaped opercle bone (Figure 4A) (36). By 6 dpf, the majority of osteoblasts are closely associated with the rapidly growing ventral edge. Examining the cells and bone matrix together at 6 dpf reveals that the early-forming spicule is the most mineralized and has the fewest osteoblasts, while the rapidly growing ventral edge, with the most osteoblasts, is more weakly mineralized. Similarly, the older, anterior end of the branchiostegal ray has fewer osteoblasts and more mineralized matrix, while the newly forming posterior end has the most osteoblasts and the least mineralized matrix. These observations indicate that we are tracking live, local mineralized matrix deposition by transgenic osteoblasts in areas of rapidly growing bone. In *her9* mutants, the earliest opercle osteoblasts are observable in a similar pattern to wild type, outlining a stick shape (Figure 4B). These results support our hypothesis that the cells surrounding the shadow bones (Figure 2) are indeed osteoblasts. Like wild types, by 6 dpf most of the *her9* mutant osteoblasts are located along the growing ventral edge. However, in contrast to wild types, the space outlined by osteoblasts is only very weakly stained with Alizarin Red at both 3 and 6 dpf (Figure 4B). Of note, the live fluorescent method of Alizarin Red staining was able to detect weakly mineralized matrix in *her9* mutants which was not observable in fixed skeletal preps imaged with transmitted light (Figure 2). Previous reports also indicate that Alizarin Red fluoresecence can reveal mineralized structures that are difficult to observe with visible light (37). This discovery that there was some mineralized bone in homozygous mutants are consistent with our late-stage study above (Figure 3) demonstrating that mineralized structures can be found in *her9* mutants at 8 dpf. Thus, mineralization is not completely absent in these mutants. Nevertheless, the amount of mineralized bone we are able to detect by both measures, at all stages, is severely reduced in *her9* mutants. In contrast to the bone, the otoliths are strongly stained with Alizarin red in both wild types and mutants, serving as an internal staining control and demonstrating that otolith mineralization is not dependent upon *her9* function. However, the otoliths are smaller in *her9* mutants compared with wild-type controls. Like other zebrafish craniofacial mutants (15, 35, 38), there is variation among mutant phenotypes; the shape of the opercle varies among *her9* mutant individuals (Figure 5). In spite of this variation, the *her9* mutant opercle bones are consistently smaller than wild-type opercles. Together with our cartilage measurements described above (Figure S4), we conclude that the entire craniofacial complex is smaller in *her9* mutants compared with wild types, and that *her9* mutants produce osteoblasts, which

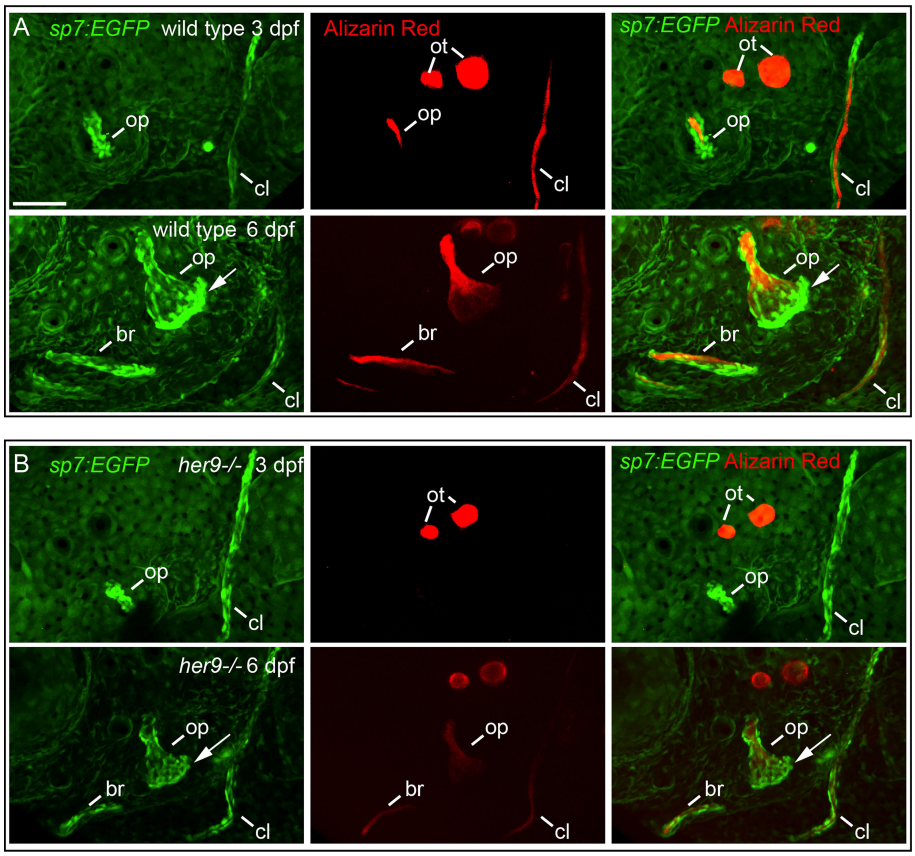

FIGURE 4
Osteoblasts differentiate in a spatiotemporal pattern similar to wild types in *her9* mutants, but only weakly mineralize bone. *sp7:EGFP;her9* heterozygotes were crossed to *her9* heterozygotes and offspring were sorted for transgene expression. 16 live transgenic animals were labeled with Alizarin Red and imaged at 3 dpf. After imaging, animals were recovered and grown in individual wells until 6 dpf when they were labeled with Alizarin Red and imaged again. Individual animals were recovered for genotyping to identify homozygous wild types **(A)** and homozygous *her9* mutants **(B)** that were imaged twice. The following structures are indicated: opercle bone (op), branchiostegal ray (br), cleithrum (cl), otoliths (ot). Arrows indicate osteoblasts prominently detected along the ventral edge of the opercle at 6 dpf. Scale bar is 50 µm.

appear with the same spatiotemporal dynamics as wild types, but *her9* mutant osteoblasts are not able to secrete mineralized matrix with the same spatiotemporal dynamics.

her9 expression is not enriched in osteoblasts

her9 function is required for fish to efficiently mineralize bone. Therefore, we hypothesized that *her9* would be strongly expressed in osteoblasts. We tested this hypothesis by performing *in situ* hybridization in the *sp7:EGFP* transgenic background to monitor *her9* expression while labeling osteoblasts. We found that *her9* is broadly expressed at 72 hpf, but expression was not concentrated in osteoblasts that are actively secreting matrix (Figure 6). Thus, while *her9* expression at this stage was detected in the pectoral fin, and in the trunk, surprisingly *her9* was not strongly expressed in the osteoblasts themselves.

her9 genetically interacts with *jag1b* during craniofacial patterning

By labeling osteoblasts and weakly mineralized bone with *sp7:EGFP* and live Alizarin Red staining, respectively, we are able to observe opercle shape even when mineralization defects are severe in *her9* mutants (Figures 4, 5). Using this protocol, we observed divergence from the characteristic fan-shaped opercle in some individuals. We discovered that, occasionally, *her9* mutant opercles at 6 dpf were less fan shaped, and instead were more stick-like, reminiscent of *jag1b* mutants (Figure 5). Similarly, the opercle bone was more stick shaped than wild-type controls at 8 dpf. These observations motivated the hypothesis that in addition to a Notch-

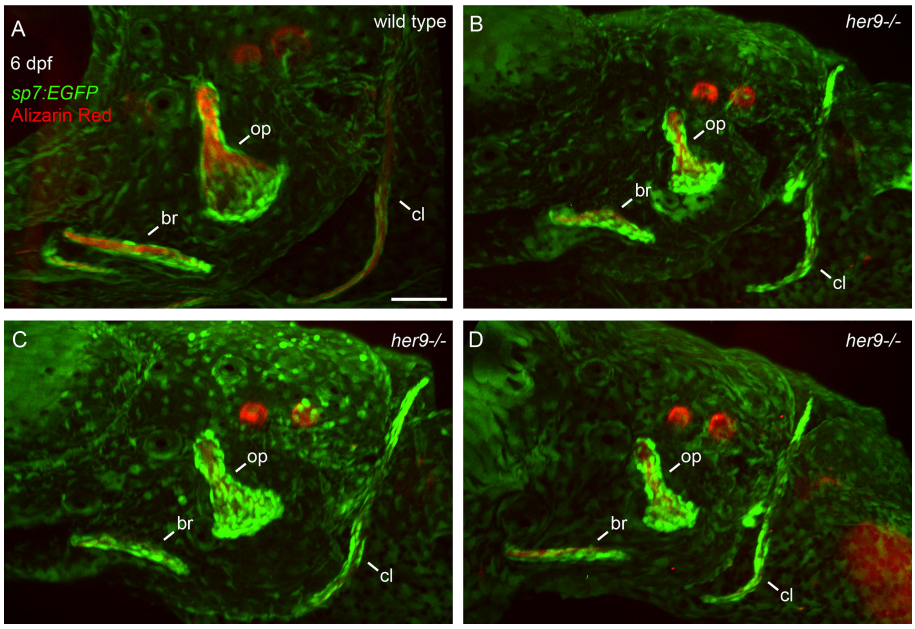

FIGURE 5
Opercle shapes are variable in *her9* mutants. *sp7:EGFP;her9* heterozygotes were crossed to *her9* heterozygotes and offspring were sorted for transgene expression. 24 live transgenic animals were labeled with Alizarin Red and imaged at 6 dpf. Imaged animals were genotyped. **(A)** Representative opercle region from a wild-type larva. **(B–D)** Three different her9 mutant larvae are shown. The following structures are indicated: opercle bone (op), branchiostegal ray (br), cleithrum (cl). Scale bar is 50 µm.

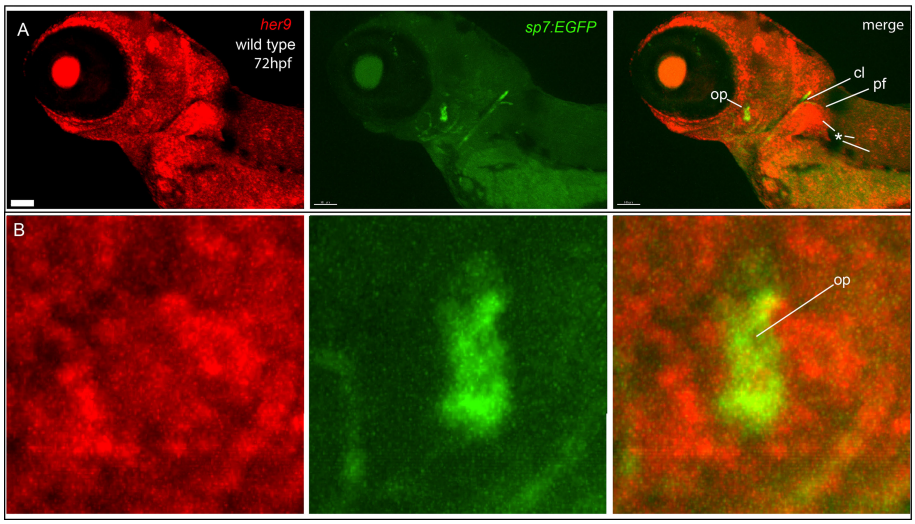

FIGURE 6
her9 is broadly expressed, but not enriched in osteoblasts. **(A)** *In situ* hybridization detects broad *her9* expression at 72 hpf. Asterisks indicate areas of strong *her9* expression. Opercle osteoblasts do not strongly express *her9*. **(B)** Enlargements of images in **(A)**. Images in **(B)** are enlargements of **(A)**. Scale bar is 80 µm.

10.3389/fendo.2022.1033843

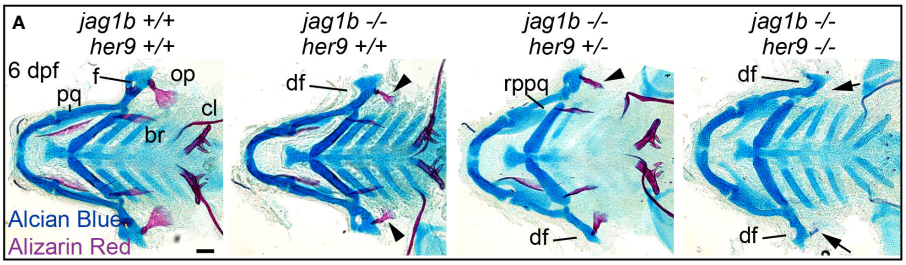

B

genotype:	***jag1b -/- her9 +/+*** **n=46**	***jag1b -/- her9 +/-*** **n=100**	***jag1b -/- her9 -/-*** **n=24**
jag1b- phenotype	penetrance		
dysmorpic foramen:	**9%**	**8%**	**33%** *
reduced posterior pq:	**83%**	**92%**	**95%**
small op bone:	**89%**	**66%**	**-**

C

genotype:	***her9 -/- jag1b +/+*** **n=10**	***her9 -/- jag1b +/-*** **n=33**	***her9 -/- jag1b - /-*** **n=12**
her9- phenotype	penetrance		
unmineralized op:	**100%**	**85%**	**75%**
unmineralized ps:	**100%**	**100%**	**100%**
unmineralized cl:	**100%**	**93%**	**83%**

FIGURE 7
Mutations in *her9* enhance *jag1b* mutant phenotypes. **(A)** *jag1b;her9* double heterozygotes were intercrossed and six days post fertilization (dpf) larvae were stained with Alcian Blue and Alizarin Red to label cartilage and bone. The individuals were then genotyped, the viscerocrania were dissected and flat mounted then imaged. The following craniofacial skeletal elements are indicated in the wild-type individual: opercle bone (op), branchiostegal ray (br), cleithrum (cl), foramen (f) palatoquadrate (pq). The dysmorphic foramen (df) and reduced posterior pq (rppq) phenotypes are indicated, and the small op bone phenotype is indicated by an arrowhead. Arrows mark the opercle mineralization defect associated with *her9* homozygous mutants. Poorly stained posterior arch derived cartilages and one missing entopterygoid bone in *jag1b-/-;her9+/-* are staining and mounting artifacts in this individual and not representative phenotypes associated with this genotype. Scale bar is 50 µm **(B)** Genotyped preps from A were scored for penetrance of *jag1b* mutant-associated phenotypes. Asterisk in dysmorphic foramen row indicates that *jag1b-/-;her9-/-* is significantly different from both *jag1b-/-;her9+/+* and *jag1b-/-;her9+/-* using a Fisher's exact test with $p<0.05$. **(C)** Genotyped preps from A were scored for penetrance of *her9* mutant-associated phenotypes.

independent role in osteoblast mineralization, *her9* may also function to pattern the craniofacial skeleton downstream of *jag1b*. To test this hypothesis, we performed a genetic interaction experiment between *jag1b* and *her9*. We intercrossed *jag1b;her9* double heterozygotes and stained offspring of these crosses with Alcian Blue and Alizarin red (Figure 7A). By scoring phenotypes in genotyped larvae at 6dpf, we discovered *her9* and *jag1b* genetically interact. Removing both copies of *her9* from *jag1b* homozygous mutants significantly increased the penetrance of an "dysmorphic foramen" phenotype in the dorsal hyomandibular cartilage (Figure 7B). This dysmorphic foramen class includes mildly affected animals with a larger foramen as well as more severe individuals no identifiable foramen. These more severe phenotypes were previously interpreted to be due to the dorsal hyomandibular cartilage transforming to be more rod shaped, partially resembling the ventral ceratohyal cartilage (1). However, we did not observe any significant changes in the penetrance of the dorsal arch 1 phenotype, a reduced palatoquadrate. We cannot meaningfully score double mutants for opercle bone phenotypes because the bone is not labeled with alizarin red in these fixed preps. We did not observe any changes in the penetrance of the *her9*-associated mineralization phenotype when *jag1b* was removed. These results indicate that *her9* and *jag1b* genetically interact during patterning of the dorsal hyomandibular skeleton, but not during bone mineralization.

her6 genetically interacts with *jag1b* and *her9*

Removing *her9* from *jag1b* mutants enhanced the *jag1b* craniofacial phenotype; double mutants had *jag1b* associated defects at higher penetrance than single mutants. However, penetrance was not increased to 100%. Therefore, we hypothesized that additional *her* genes might redundantly function downstream of *jag1b* during craniofacial patterning. *her6* is a known Notch target, and its cranial neural crest cell expression pattern makes it a strong candidate for functioning downstream of *jag1b* (Figure 1). A *her6* mutant was previously found to have a craniofacial skeleton indistinguishable from wild types (14). This mutant allele produces an eight-base pair deletion inducing a frameshift after amino acid 10 out of 270 then a premature termination codon after 12 missense amino acids. We speculated that this might not be a null allele, due to in-frame alternative start codons predicted in the transcript. Therefore, we generated a new mutation further downstream in *her6* that is a 4 base pair deletion causing a frameshift at amino acid 51, four nonsense amino acids, and an early stop at amino acid 55 (Figure 8A). Similar to the previously generated allele, our *her6* mutant also had a craniofacial skeleton that was indistinguishable from wild types (Figure 8B). We conclude that *her6* is not essential for craniofacial development in an otherwise wild-type background. Next, we tested whether the *her6* mutation genetically interacts with *jag1b*, like *her9* does. We crossed *jag1b;her6* double heterozygous mutants and stained offspring with Alcian Blue and Alizarin Red. When we scored genotyped, stained larvae, we found that no new phenotypes were produced. However, the penetrance of the *jag1b* mutant-associated reduced opercle bone was significantly increased bilaterally in *jag1b; her6* double homozygous mutants compared with *jag1b* single mutants (Figures 8B, C).

We next hypothesized that *her6* and *her9* might function redundantly during craniofacial patterning. To test this hypothesis, we combined the two mutations and intercrossed adults heterozygous for both *her6* and *her9*, and stained offspring with Alcian Blue and Alizarin Red (Figure 8D). Analyzing genotyped individuals revealed that the ceratohyal is occasionally misaligned at the midline in double homozygous mutants which is not observed in either single mutant. Further, fish double homozygous for both *her6* and *her9* developed eye phenotypes that were not present in either single mutant (Figure 8D). However, *her6;her9* double mutants did not phenocopy *jag1b* mutants, suggesting that other effectors provide further redundancy downstream of *jag1b*.

jag1b and *her6* and *her9* together regulate dorsal versus ventral skeletal identity

Our double mutant analyses demonstrated that *jag1b* genetically interacts with both *her9* and *her6*, and that *her9* and *her6* genetically interact with each other (Figures 7, 8). While *her6* enhanced the *jag1b*-associated opercle phenotype, *her9* enhanced the *jag1b*-associated foramen phenotype. Based on these findings, we hypothesized that *jag1b* triple mutant combinations would produce novel craniofacial defects. Specifically, if *her* genes genetically interact with *jag1b* then dramatic phenotypes, more severe than the sum of the single mutant phenotypes, would be predicted in the triple mutants. When we intercrossed triple heterozygous fish and stained for Alcian Blue and Alizarin Red, we found that triple homozygous mutants were severely affected by general delay and edema producing secondary defects (Figure S6). This genotype could not be meaningfully scored for skeletal phenotypes. However, when we examined *jag1b* and *her6* homozygous mutants in combination with *her9* heterozygotes, we uncovered a new phenotype not seen in any other allelic combination in this study, the opercle and branchiostegal ray shapes were reversed (Figure 9A). Rather than a fan-shaped opercle and stick shaped branchiostegal ray, we observed a stick shaped opercle and a fan shaped branchiostegal ray. We found the branchiostegal ray fan phenotype in 46% of fish with this triple-mutant genotype, which was never present in any other genotype (Figure 9B). In some cases, the expanded branchiostegal ray was fused with the opercle bone forming a large plate-like structure (Figure 9A). These fusions were reminiscent of transformation phenotypes found when the Endothelin pathway is manipulated (39), motivating the hypothesis that these phenotypes are dorsoventral identity transformations. To directly test for molecular evidence of identity transformation, we performed *in situ* hybridization for the ventral arch gene *dlx5a* on these families (Figure 9C). Consistent with previous reports (1), we found that *dlx5a* expression was expanded dorsally in *jag1b* single mutants compared with wild-type controls. Strikingly, in the triple mutant genotype, we found that *dlx5a* expression was shifted dorsally. That is, *dlx5a* expression was present in the dorsal-most aspect of the second arch and absent ventrally in this arch.

Discussion

Nonredundant *her9* function in bone mineralization

We discovered that zebrafish *her9* is critical for timely mineralization. This mineralization role is nonredundant with other genes since loss of *her9* in an otherwise wild-type background produces fully penetrant mineralization defects, for at least some bony elements. We discovered that bones derived from neural crest cells, as well as those derived from mesoderm, both require *her9* function for mineralization. However, some bones (like the parasphenoid) never mineralize in *her9* mutants at 6 dpf. Meanwhile others (like the cleithrum)

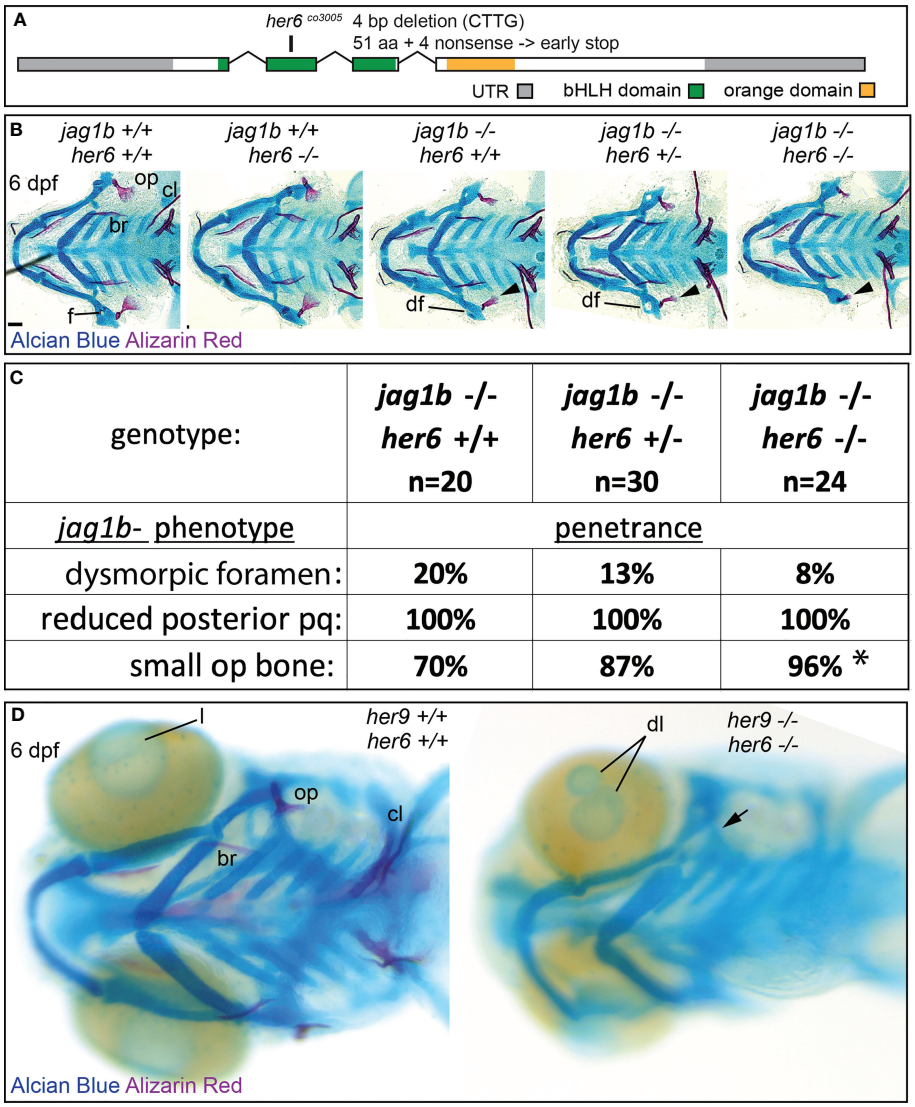

FIGURE 8
Mutations in *her6* enhance the *jag1b* mutant phenotype, *her6* and *her9* are redundantly required for eye development. **(A)** Exon diagram for *her6* indicating the untranslated regions (UTR) and the regions predicted to encode the basic helix-loop-helix (bHLH) and Orange domains. The location of the deletion encoded by the *her6*^{co3005} allele is indicated. **(B)** *jag1b;her6* double heterozygotes were intercrossed and six days post fertilization (dpf) larvae were stained with Alcian Blue and Alizarin Red to label cartilage and bone. The individuals were then genotyped, the viscerocrania were dissected and flat mounted then imaged. The following craniofacial skeletal elements are indicated in the wild-type individual: opercle bone (op), branchiostegal ray (br), cleithrum (cl), foramen (f). The dysmorphic foramen phenotype (df) is indicated, and the small op bone phenotype is indicated by an arrowhead. Scale bar is 50 µm **(C)** Genotyped preps from B were scored for penetrance of *jag1b* mutant-associated phenotypes. Asterisk in small op bone row indicates that penetrance in *jag1b-/-;her6-/-* is significantly different from *jag1b-/-;her6+/+* ($p<0.05$). **(D)** *her6;her9* double heterozygotes were intercrossed and six days post fertilization (dpf) larvae were stained with Alcian Blue and Alizarin Red to label cartilage and bone. The individuals were then genotyped and whole-mount imaged. An arrow indicates unmineralized opercle. The lens (l) is indicated in the wild type and a double lens phenotype is indicated in double homozygous mutants (dl).

partially mineralize at this stage. These findings indicate that some bones are more sensitive to *her9* loss than others. We propose that the ancestral role of *her/hes* genes is in both patterning and mineralization, but that these functions were subfunctionalized resulting in *her9* primarily functioning in bone mineralization while retaining vestigial, partially redundant patterning function. In support, we recently proposed that vestigial, redundant paralog function can be retained and function to buffer against loss of one of the paralogs (40). It would be interesting to determine if there is a nonredundant patterning role of *her9* later in development. Some mineralization mutants display correct patterning of

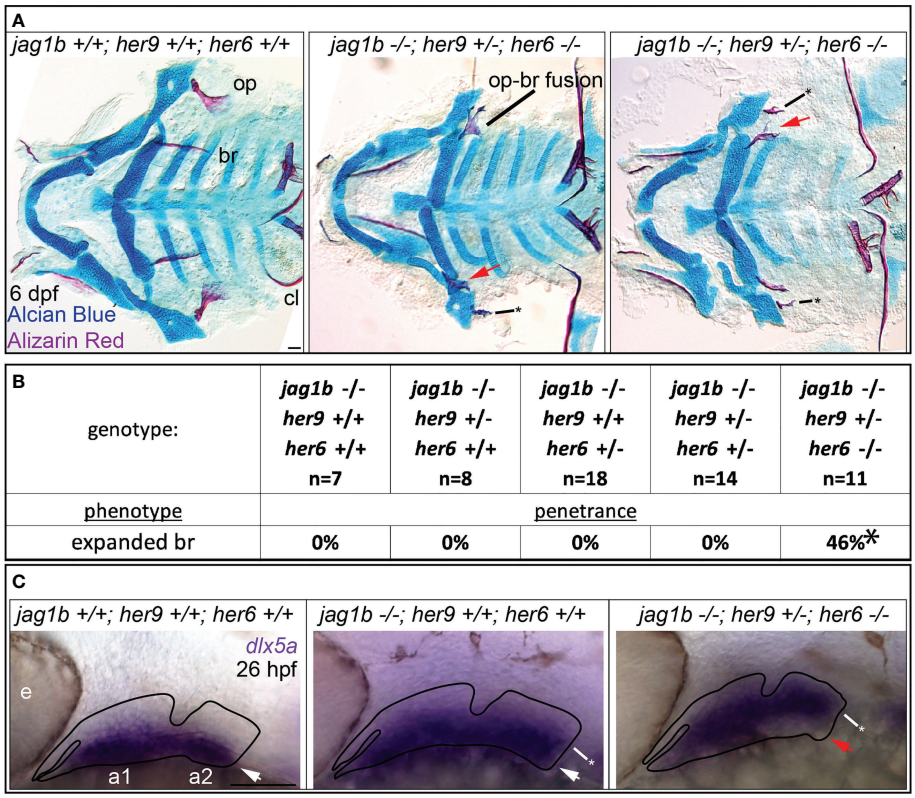

FIGURE 9
jag1b, *her9*, and *her6* redundantly regulate dorsal versus ventral identity. **(A)** *jag1b;her6;her9* triple heterozygotes were intercrossed and six days post fertilization (dpf) larvae were stained with Alcian Blue and Alizarin Red to label cartilage and bone. The individuals were then genotyped, the viscerocrania were dissected and flat mounted then imaged. The opercle (op), branchiostegal ray (br), and cleithrum (cl) are indicated in the wild type control. The bony fusion between the opercle and the branchiostegal ray is indicated. Red arrows indicate expanded, fan-shaped branchiostegal ray. Asterisk marks stick-shaped op phenotype **(B)** Genotyped preps from A were scored for penetrance of expanded branchiostegal ray. Asterisk indicates that penetrance of this phenotype in *jag1b-/-;her9+/-;her6-/-* is significantly different from all other genotypes, where it is never observed. **(C)** *jag1b;her6;her9* triple heterozygotes were intercrossed and 26 hours post fertilization (hpf) larvae were fixed for *in situ* hybridization experiments to label *dlx5a* expression. White arrows indicate ventral *dlx5a* expression, asterisks mark dorsally expanded *dlx5a* expression. Red arrow indicates reduced ventral *dlx5a* expression in triple mutants suggesting ventral-versus-dorsal identity reversal. This phenotype was observed on both sides of in 3/3 embryos examined with this genotype. Scale bars are 50 µm.

early-forming skeletal elements, but then develop late-stage defects in skull shape (41). However, we are unable to test for this possibility since the *her9* mutation is homozygous lethal. It is possible that generating new mutant *her9* alleles, or an allelic series, might produce different phenotypes and be informative for a more complete understanding of *her9* function.

It is interesting, and surprising, that *her9* expression is not enriched in osteoblasts. In *entpd5a* (*nob*) mutants, a mineralization phenotype similar to *her9* mutants develops (42). Unlike *her9* however, *entpd5a* is expressed in osteoblasts. Although expression of *entpd5a* in cells beyond osteoblasts is sufficient to rescue *entpd5a* mutants. Our data suggest that the mineralization role for *her9* is non cell-autonomous to the bone producing osteoblast cells. Determining the mechanism by which *her9* broadly controls mineralization, and any interaction with *entpd5a*, is a major focus for future study. We conclude that the *her9* cranial neural crest cell expression we detect by *in situ* and scRNAseq during early craniofacial development (24 hpf) functions in patterning downstream of *jag1b*, the mineralization function of *her9* is likely due to this gene functioning in other tissues, as broad expression is observed in *in situ* hybridization.

her9 and *her6* redundantly function in craniofacial patterning

Our study uncouples the mineralization and patterning roles of *her9*. In contrast to mineralization, the patterning role for *her9* is redundant with other family members since *her9* mutations do not affect patterning in an otherwise wild-type background, but do enhance patterning phenotypes when combined with other Notch

pathway mutants. There are likely other Notch target genes, along with *her6* and *her9*, functioning in a patterning role downstream of *jag1b* since *her6;her9* double mutants do not phenocopy the *jag1b* phenotype. We found some evidence to suggest spatially distinct roles for different Notch target genes. Specifically, removing *her6* from *jag1b* mutants increases the penetrance of the small opercle bone phenotype bilaterally. Meanwhile removing *her9* from *jag1b* mutants increases penetrance of the foramen phenotype. Thus, different functions downstream of *jag1b* activation of Notch may have been subfunctionalized among *her/hes* genes. One caveat of this interpretation is that fixed skeletal preps from *her9* mutants cannot be scored for bone shape phenotypes, so we don't know if homozygous *her9* mutants affect the penetrance of the stick opercle phenotype found in *jag1b* mutants. The *her* gene family is large, perhaps contributing to the extent of redundancy among family members. Future study disabling more *her* genes might reveal widespread redundancies during craniofacial development. Our previous work indicates that genes with stronger wild type expression are correlated with a larger buffering role when one family member is mutated (40). Therefore, our scRNA-seq dataset motivates examining *her8a* and *her11* next, since transcripts for these genes are detected, albeit weakly, in anterior arch cranial neural crest cells whereas many other family members are undetectable.

When *jag1b* and *her6* and *her9* function are disabled in combination, a branchiostegal ray phenotype develops that is not observed in any other combination. In this genotype, the branchiostegal ray was expanded into an opercle-like fan shape. At the same time, the opercle was reduced into a branchiostegal-like stick shape. These findings suggest both dorsal-to-ventral and ventral-to-dorsal homeotic transformations occur in this genotype. Consistently, we also found individuals with this genotype where the opercle and branchiostegal were fused, similar fusion phenotypes are observed in mutations in the *mef2ca* transcription factor encoding gene and are characterized as dorsoventral homeotic transformations (38, 43). Finally, we observed molecular evidence of homeotic transformation by examining *dlx5a* expression. *dlx5a* expression, which is ventrally restricted in wild types, is dorsally shifted in triple mutants. We interpret these data to indicate that dorsoventral identity is reversed in these triple mutants.

Mutations in *her6* do not produce an overt phenotype on their own but do genetically interact with other Notch pathway genes like *jag1b* and *her9*. Given this, it is curious that *her6* has been retained in the zebrafish genome. The *her/hes* genes can clearly be lost from genomes since the mouse ortholog of *her9*, *Hes4*, was lost. We propose that the *her/hes* family is highly redundant and interchangeable, and is therefore prone to gene losses and changes in functional requirement through evolutionary time.

The nonredundant and redundant roles of *her9* in mineralization and patterning, respectively, are also differentially dependent on Notch cleavage by gamma secretase. The mineralization role does not require Notch cleavage by gamma secretase since we are unable to phenocopy *her9* mutant phenotypes by inhibiting this enzyme. But this inhibitor does phenocopy the patterning phenotypes seen in *jag1b* mutants. Thus, it is possible that the mineralization role of *her9* is downstream of other signaling systems. For example, other reports indicate *her9* is in the Nodal and Retinoic Acid pathways (9, 22). This could be tested by inhibiting some of the other pathways associated with *her9* to test for phenocopy of the *her9* mineralization phenotype. Alternatively, *her9* may function downstream of gamma secretase-independent Notch activation (44). This alternative could be tested by mutating the relevant Notch receptors and ligands, or dominant-negative approaches to test for phenocopy of the mineralization phenotype, although previous studies utilizing these methods did not report a broad mineralization phenotype following Notch signaling blockade (16).

Is the unmineralized bone in *her9* mutants osteoid bone?

Normally, bones form from the stepwise production of mineralized matrix. As osteoblasts mature, they first make osteoid bone, then mineralized matrix. We find that *her9* is required for the proper timing of the mineralization stages of bone formation. In *her9* mutants, osteoblasts differentiate in the correct position, with the normal timing, but they don't mineralize the matrix with normal timing. However, there is detectible unmineralized matrix in some cases, like the opercle. Alcian Blue, which stains osteoid bone but not mature bone matrix (45), reproducibly labeled *her9* mutant opercles. Therefore, we interpret this *her9* mutant-associated phenotype as an extended osteoid stage. Intriguingly, extended osteoid stage opercles may occur naturally in some fish species, serving as a mechanism for generating bone shape diversity (46). In this work, the authors proposed that there are regions of extended osteoid in sculpin opercles contributing to opercle shape variation among different sculpin species. Thus, it is tempting to speculate that evolutionary changes in *her9* expression or function between different sculpin species underlie the extended osteoid observed in some sculpins. This would lead to naturally extended osteoid proposed to contribute to the diverse opercle bone shapes seen among sculpins. Further, that zebrafish *her9* mutants apparently produce an extended osteoid stage may inform human health. Rickets in children or osteomalacia in adults are disorders that arise when osteoid does not mineralize properly.

In this study we discovered a non-redundant, Notch-independent, bone mineralization requirement for *her9*. We also found a redundant role for *her9* and *her6* during Jag-Notch craniofacial patterning. These studies help us to understand human *HES4*-associated skeletal disease in an *in vivo* setting, which is not possible in rodent models. Our work helps to clarify the complex roles of *her/hes* genes during vertebrate skeletal development.

10.3389/fendo.2022.1033843

Materials and methods

Zebrafish strains and husbandry

All zebrafish were maintained and staged according to established protocols (47, 48). The *jag1b*^{b1105} allele and genotyping protocol has been previously described (1). The transgenic line *Tg(sp7:EGFP)b1212* has been previously described (33).

The *her9*^{co66} mutant line was generated by ENU mutagenesis and has a point mutation in exon 4 which produces an early stop codon near the predicted end of the Orange domain. The transition mutation converts the wild-type sequence GGGA**C**AGAT to GGGA**T**AGAT. The mutagenesis and mutant allele identification was performed as described (49). To identify the causative lesion, *co66* generated on the TU background was outcrossed to the AB strain for two generations and F3 embryos were screened. Heterozygous adults were intercrossed and 33 phenotypic wild type and 33 phenotypic mutant larvae were used to prepare pooled genomic DNA. Using 223 simple sequence-length polymorphism markers, we placed the *co66* locus on chromosome 23 between z7550, (31.6 centimorgan (cM), 13.6 megabase (mb)) and z7973 (34 cM, 26.0 mb). We identified *her9*, located at 23.4 mb as a candidate gene and found the mutation by Sanger sequencing which was homozygous only in phenotypically mutant individuals. The mutation was then maintained in our closed colony by outcrossing to AB for over seven generations, genotyping for *her9* heterozygotes at each generation. All individuals in this study were genotyped and the mineralization defect phenotype was 100% penetrant in *her9* homozygous mutants, and never present in heterozygotes or homozygous wild types. To genotype *her9*^{co66}, a DNA fragment was amplified using primers Her9-FW-exon2, 5'-TCTTCAAAGCCAATCATGGAAA-3', and Her9-RV-exon4, 5'-GAAGAGGCTGAGCCAAATGA-3', and then digested with BsmFI to produce a 604 bp fragment in mutants and 539/66 bp fragments in wild types. We generated the *her6*^{co3005} allele using CRISPR/Cas9 mutagenesis (50). We injected Cas9 mRNA along with two guide RNAs (5'- GCGAGAATCAACGAAAGCTT-3' and 5'-CCGTTCTTGGGAAGTACCGA-3') into single cell zebrafish embryos targeting exons 2 and 4 respectively. Injected zebrafish were screened for mutagenesis *via* PCR amplification using primers *her6* FW exon1 5'-GGCGAGCATGAACACTACA-3' and *her6* RV exon4 5'-GGTTCCTGTCCACATGTGAA-3'. Sanger sequencing revealed a 4 bp deletion in exon 2 (AAAGGGTC) which is predicted to cause a frameshift after amino acid 10 of 270 and a premature stop codon after 12 missense amino acids. Sanger sequencing also showed a naturally occurring 5bp deletion in intron 2. Genotyping for *her6* was done using PCR amplification with primers *her6* geno FW 5'- GAGCATGAACACT ACACCTGATA-3' and *her6* geno RV 5'- CGAAAGTCCG ACTGAGTCTTT-3'. The PCR product was then digested with HindIII to produce a 264bp fragment in mutants and 187/77 bp fragments in wild types. All zebrafish procedures have been approved by the University of Colorado Institutional Animal Care and Use Committee (IACUC), Protocol # 00188. Genomic DNA for genotyping was obtained by tail amputation. Fish were anesthetized by adding 0.01-0.2 mg/ml Tricaine (MS-222) to embryo media. Animals were euthanized by hypothermic shock followed by 1.5% sodium hypochlorite.

Tissue staining

Alcian Blue and Alizarin Red were used to stain cartilage and bone, respectively as previously described (30, 51). Live Alizarin Red staining was performed on zebrafish as described (35) at 3 dpf and 6 dpf. Zebrafish larvae were placed in 0.01% Alizarin Red and 0.01% HEPES solution in E2 media and allowed to swim for 30 minutes. The zebrafish were then transferred to clean E2 media and imaged.

Phenotype Scoring

Genotyped Alcian Blue and Alizarin Red stained zebrafish skeletons were scored for penetrance of relevant phenotypes. A Fisher's Exact test was used to determine significant differences in penetrance between genotypes.

Pharmacological Treatments

Notch cleavage inhibition using DBZ was performed similar to previously reported (13, 15). Wild-type zebrafish were treated with 10μM of DBZ or DMSO vehicle control from 18-48hpf, or 48-72hpf, or 72-96hpf. All treated zebrafish were raised to 6dpf and stained for bone and cartilage.

RNA *in situ* hybridization

Whole mount *in situ* hybridization with fluorescence was performed as previously described (52). The *her9* and *dlx5a* probes have been previously described (9, 53).

RT-qPCR

Gene expression studies were performed as previously described (15). Live individual 28 and 48 hpf embryos had their heads removed. Decapitated bodies were genotyped to identify homozygous wild-types and homozygous *jag1b* mutants. Heads from 5–6 identified homozygous wild types were pooled and total RNA was extracted with TRIzol Reagent

from ThermoFischer Scientific. cDNA was prepared with Superscript III from Invitrogen. qPCR experiments utilized a Real-Time PCR StepOnePlus system from Applied Biosystems and SYBR green. A standard curve was generated from serially diluted (1:2:10) cDNA pools, and primers with a slope of -3.3 +-0.3 were accepted. The relative quantity of target cDNA was calculated using Applied Biosystems StepOne V.2.0 software and the comparative Ct method. After surveying the expression of many housekeeping genes at multiple stages, we determined that *rps18* expression was the most consistent across stages and genotypes. Target gene expression in all experiments was normalized to *rps18*. Reactions were performed in technical triplicate, and the results represent two to six biological replicates. The following primers were used: *her9FW*, 5'-GAGAATCAACGAGAGCCTTG-3', *her9REV* 5'-CTCCAGAATATCAGCTTTCTCC-3', *her6FW* 5'-AACGAAAGCTTGGGTCAG-3', *her6REV* 5'-ACTGTCATCTCCAGGATGT-3', *rps18FW* 5'-CTGAACAGACAGAAGGACATAA-3', *rps18REV* 5'-AGCCTCTCCAGATCTTCTC-3'.

Cell sorting and sequencing

Cranial neural crest cells were sorted as described (29). Briefly, 60 wild-type 24 hpf *flia:EGFP;sox10:mRFP* double transgenic embryos were dissociated into single-cell suspension using cold-active protease from *Bacillus licheniformis*, DNase, EDTA, and trituration. Approximately 30,000 live, GFP/RFP double-positive cells were sorted into tubes pre-coated with fetal bovine serum with a MoFlo XDP100. Sorted cells at 2.08x10^6 cells/ml concentration with 70% viability were loaded into the 10x Chromium Controller aiming to capture 10000 cells. Using the NovaSEQ6000, 2×150 paired-end sequencing Chromium 10x Genomics libraries were sequenced at 100K reads per cell using 3prime NexGem V3.1 (Dual Index) sequencing.

scRNA-seq analysis

Recovered sequencing reads were mapped to a custom Cell Ranger reference based on the GRCz11/danRer11 genome assembly using the Cell Ranger pipeline (10X Genomics). The 10X Genomics Cell Ranger pipeline removed empty droplets from the dataset based on the distribution of cell barcodes. Additional analysis was performed in R using the Seurat package (54). Quality filtering of these data excluded cells with no genes detectable (>0 unique molecular identifiers (UMIs) per gene). Each gene in the dataset was required to be present in a minimum of five cells. Regarding the capture of dead or dying cells, a minimum presence of 250 genes (at <2.5% of mitochondrial UMIs detected) were required. After quality filtering, 7928 cells remained for analysis.

Microscopy and image analysis

Alcian Blue and Alizarin Red skeletons were dissected, flat mounted, and then imaged on a Leica DMi8 inverted microscope equipped with a Leica DMC2900. All fluorescent imaging was performed on a Leica DMi8 equipped with an Andor Dragonfly 301 spinning disk confocal system. Live imaging was performed as previously described (55).

Data availability statement

The sequencing dataset presented in this study can accessed from the GEO database (accession number GSE220081).

Ethics statement

The animal study was reviewed and approved by University of Colorado IACUC.

Author contributions

AS, AM-M, JS, MW and JMM designed performed and interpreted experiments and edited the manuscript. BA designed experiments. JN interpreted experiments wrote and edited the manuscript. All authors contributed to the article and approved the submitted version.

Funding

This work was funded by NIH R01DE029193 to JN, NIH F32DE029995 to JMM, NSF GRFP 1938058 to AMM.

Conflict of interest

The authors declare that the research was conducted in the absence of any commercial or financial relationships that could be construed as a potential conflict of interest.

Publisher's note

Supplementary material

The Supplementary Material for this article can be found online at: https://www.frontiersin.org/articles/10.3389/fendo.2022.1033843/full#supplementary-material

References

1. Zuniga E, Stellabotte F, Crump JG. Jagged-notch signaling ensures dorsal skeletal identity in the vertebrate face. *Development.* (2010) 137(11):1843–52. doi: 10.1242/dev.049056

2. Kraus JM, Giovannone D, Rydzik R, Balsbaugh JL, Moss IL, Schwedler JL, et al. Notch signaling enhances bone regeneration in the zebrafish mandible. *Development* (2022) 149(5):dev199995. doi: 10.1242/dev.199995

3. Pakvasa M, Haravu P, Boachie-Mensah M, Jones A, Coalson E, Liao J, et al. Notch signaling: its essential roles in bone and craniofacial development. *Genes diseases.* (2021) 8(1):8–24. doi: 10.1016/j.gendis.2020.04.006

4. Nichols JT, Miyamoto A, Weinmaster G. Notch signaling - constantly on the move. *Traffic.* (2007) 8(8):959–69. doi: 10.1111/j.1600-0854.2007.00592.x

5. Artavanis-Tsakonas S, Muskavitch MA. Notch: the past, the present, and the future. *Curr topics Dev Biol* (2010) 92:1–29. doi: 10.1016/S0070-2153(10)92001-2

6. Kageyama R, Ohtsuka T, Kobayashi T. The Hes gene family: repressors and oscillators that orchestrate embryogenesis. *Development (Cambridge, England)* (2007) 134.7:1243–51

7. Kuretani A, Yamamoto T, Taira M, Michiue T. Evolution of hes gene family in vertebrates: the hes5 cluster genes have specifically increased in frogs. *Evol* (2021) 21(1):1–15. doi: 10.1186/s12862-021-01879-6

8. Fisher AL, Ohsako S, Caudy M. The WRPW motif of the hairy-related basic helix-loop-helix repressor proteins acts as a 4-amino-acid transcription repression and protein-protein interaction domain. *Mol Cell Biol* (1996) 16(6):2670–7. doi: 10.1128/MCB.16.6.2670

9. Latimer AJ, Shin J, Appel B. her9 promotes floor plate development in zebrafish. *Dev dynamics: an Off Publ Am Assoc Anatomists.* (2005) 232(4):1098–104. doi: 10.1002/dvdy.20264

10. Radosevic M, Robert-Moreno À, Coolen M, Bally-Cuif L, Alsina B. Her9 represses neurogenic fate downstream of Tbx1 and retinoic acid signaling in the inner ear. *Development.* (2011) 138(3):397–408. doi: 10.1242/dev.056093

11. Bae Y-K, Shimizu T, Hibi M. Patterning of proneuronal and inter-proneuronal domains by hairy-and enhancer of split-related genes in zebrafish neuroectoderm. *Development (Cambridge, England)* (2005) 132.6:1375–85.

12. Leve C, Gajewski M, Rohr KB, Tautz D. Homologues of c-hairy1 (her9) and lunatic fringe in zebrafish are expressed in the developing central nervous system, but not in the presomitic mesoderm. *Dev Genes evolution.* (2001) 211(10):493–500. doi: 10.1007/s00427-001-0181-4

13. Barske L, Askary A, Zuniga E, Balczerski B, Bump P, Nichols JT, et al. Competition between jagged-notch and Endothelin1 signaling selectively restricts cartilage formation in the zebrafish upper face. *PloS Genet* (2016) 12(4):e1005967. doi: 10.1371/journal.pgen.1005967

14. Askary A, Xu P, Barske L, Bay M, Bump P, Balczerski B, et al. Genome-wide analysis of facial skeletal regionalization in zebrafish. *Development.* (2017) 144 (16):2994–3005. doi: 10.1242/dev.151712

15. Sucharov J, Ray K, Brooks EP, Nichols JT. Selective breeding modifies mef2ca mutant incomplete penetrance by tuning the opposing notch pathway. *PloS Genet* (2019) 15(12):e1008507. doi: 10.1371/journal.pgen.1008507

16. Paudel S, Gjorcheska S, Bump P, Barske L. Patterning of cartilaginous condensations in the developing facial skeleton. *Dev Biol* (2022) 486:44–55. doi: 10.1016/j.ydbio.2022.03.010

17. Oda T, Elkahloun AG, Pike BL, Okajima K, Krantz ID, Genin A, et al. Mutations in the human Jagged1 gene are responsible for alagille syndrome. *Nat Genet* (1997) 16(3):235–42. doi: 10.1038/ng0797-235

18. Suzuki A, Sangani DR, Ansari A, Iwata J. Molecular mechanisms of midfacial developmental defects. *Dev Dynamics.* (2016) 245(3):276–93. doi: 10.1002/dvdy.24368

19. Humphreys R, Zheng W, Prince LS, Qu X, Brown C, Loomes K, et al. Cranial neural crest ablation of Jagged1 recapitulates the craniofacial phenotype of alagille syndrome patients. *Hum Mol Genet* (2012) 21(6):1374–83. doi: 10.1093/hmg/ddr575

20. Akimoto M, Kameda Y, Arai Y, Miura M, Nishimaki T, Takeda A, et al. Hes1 is required for the development of craniofacial structures derived from ectomesenchymal neural crest cells. *J Craniofacial Surgery.* (2010) 21(5):1443–9. doi: 10.1097/SCS.0b013e3181ebd1a0

21. Kameda Y, Saitoh T, Nemoto N, Katoh T, Iseki S, Fujimura T. Hes1 is required for the development of pharyngeal organs and survival of neural crest-derived mesenchymal cells in pharyngeal arches. *Cell Tissue Res* (2013) 353(1):9–25. doi: 10.1007/s00441-013-1649-z

22. Coomer CE, Wilson SG, Titialii-Torres KF, Bills JD, Krueger LA, Petersen RA, et al. Her9/Hes4 is required for retinal photoreceptor development, maintenance, and survival. *Sci Rep* (2020) 10(1):1–20. doi: 10.1038/s41598-020-68172-2

23. Shimada S, Shimojima K, Okamoto N, Sangu N, Hirasawa K, Matsuo M, et al. Microarray analysis of 50 patients reveals the critical chromosomal regions responsible for 1p36 deletion syndrome-related complications. *Brain Dev* (2015) 37 (5):515–26. doi: 10.1016/j.braindev.2014.08.002

24. Grogan SP, Olee T, Hiraoka K, Lotz MK. Repression of chondrogenesis through binding of notch signaling proteins HES-1 and HEY-1 to n-box domains in the COL2A1 enhancer site. *Arthritis Rheumatism.* (2008) 58(9):2754–63. doi: 10.1002/art.23730

25. Dong Y, Jesse AM, Kohn A, Gunnell LM, Honjo T, Zuscik MJ, et al. RBPjκ-dependent notch signaling regulates mesenchymal progenitor cell proliferation and differentiation during skeletal development. *Development.* (2010) 137(9):1461–71. doi: 10.1242/dev.042911

26. Cakouros D, Isenmann S, Hemming SE, Menicanin D, Camp E, Zannetinno ACW, et al. Novel basic helix–loop–helix transcription factor Hes4 antagonizes the function of twist-1 to regulate lineage commitment of bone marrow stromal/stem cells. *Stem Cells Dev* (2015) 24(11):1297–308. doi: 10.1089/scd.2014.0471

27. Hilton MJ, Tu X, Wu X, Bai S, Zhao H, Kobayashi T, et al. Notch signaling maintains bone marrow mesenchymal progenitors by suppressing osteoblast differentiation. *Nat Med* (2008) 14(3):306–14. doi: 10.1038/nm1716

28. Zhang Y, Lian JB, Stein JL, Van Wijnen AJ, Stein GS. The notch-responsive transcription factor hes-1 attenuates osteocalcin promoter activity in osteoblastic cells. *J Cell Biochem* (2009) 108(3):651–9. doi: 10.1002/jcb.22299

29. Mitchell JM, Sucharov J, Pulvino AT, Brooks EP, Gillen AE, Nichols JT. The alx3 gene shapes the zebrafish neurocranium by regulating frontonasal neural crest cell differentiation timing. *Development* (2021) 148(7):dev197483. doi: 10.1242/dev.197483

30. Walker MB, Kimmel CB. A two-color acid-free cartilage and bone stain for zebrafish larvae. *Biotech Histochem* (2007) 82(1):23–8. doi: 10.1080/10520290701333558

31. Puchtler H, Meloan SN, Terry MS. On the history and mechanism of alizarin and alizarin red s stains for calcium. *J Histochem Cytochemistry.* (1969) 17 (2):110–24. doi: 10.1177/17.2.110

32. Kague E, Gallagher M, Burke S, Parsons M, Franz-Odendaal T, Fisher S. Skeletogenic fate of zebrafish cranial and trunk neural crest. *PloS One* (2012) 7(11): e47394. doi: 10.1371/journal.pone.0047394

33. DeLaurier A, Eames BF, Blanco-Sanchez B, Peng G, He X, Swartz ME, et al. Zebrafish *sp7:EGFP*: a transgenic for studying otic vesicle formation, skeletogenesis, and bone regeneration. *Genesis.* (2010) 48(8):505–11. doi: 10.1002/dvg.20639

34. Eames BF, DeLaurier A, Ullmann B, Huycke TR, Nichols JT, Dowd J, et al. FishFace: interactive atlas of zebrafish craniofacial development at cellular resolution. *BMC Dev Biol* (2013) 13(1):23. doi: 10.1186/1471-213X-13-23

35. Nichols JT, Blanco-Sanchez B, Brooks EP, Parthasarathy R, Dowd J, Subramanian A, et al. Ligament versus bone cell identity in the zebrafish hyoid skeleton is regulated by mef2ca. *Development.* (2016) 143(23):4430–40. doi: 10.1242/dev.141036

36. Kimmel CB, DeLaurier A, Ullmann B, Dowd J, McFadden M. Modes of developmental outgrowth and shaping of a craniofacial bone in zebrafish. *PloS One* (2010) 5(3):e9475. doi: 10.1371/journal.pone.0009475

37. Bensimon-Brito A, Cardeira J, Dionísio G, Huysseune A, Cancela M, Witten P. Revisiting *in vivo* staining with alizarin red s-a valuable approach to analyse zebrafish skeletal mineralization during development and regeneration. *BMC Dev Biol* (2016) 16(1):1–10. doi: 10.1186/s12861-016-0102-4

38. DeLaurier A, Huycke TR, Nichols JT, Swartz ME, Larsen A, Walker C, et al. Role of *mef2ca* in developmental buffering of the zebrafish larval hyoid dermal skeleton. *Dev Biol* (2014) 385(2):189–99. doi: 10.1016/j.ydbio.2013.11.016

39. Kimmel CB, Walker MB, Miller CT. Morphing the hyomandibular skeleton in development and evolution. *J Exp Zool B Mol Dev Evol* (2007) 308(5):609–24. doi: 10.1002/jez.b.21155

40. Bailon-Zambrano R, Sucharov J, Mumme-Monheit A, Murry M, Stenzel A, Pulvino AT, et al. Variable paralog expression underlies phenotype variation. *Elife.* (2022) 11:e79247. doi: 10.7554/eLife.79247

41. Kague E, Roy P, Asselin G, Hu G, Simonet J, Stanley A, et al. Osterix/Sp7 limits cranial bone initiation sites and is required for formation of sutures. *Dev Biol* (2016) 413(2):160–72. doi: 10.1016/j.ydbio.2016.03.011

42. Huitema LF, Apschner A, Logister I, Spoorendonk KM, Bussmann J, Hammond CL, et al. Entpd5 is essential for skeletal mineralization and regulates phosphate homeostasis in zebrafish. *Proc Natl Acad Sci* (2012) 109(52):21372–7. doi: 10.1073/pnas.1214231110

43. Miller CT, Swartz ME, Khuu PA, Walker MB, Eberhart JK, Kimmel CB. *mef2ca* is required in cranial neural crest to effect Endothelin1 signaling in zebrafish. *Dev Biol* (2007) 308(1):144–57. doi: 10.1016/j.ydbio.2007.05.018

44. Huppert SS, Ilagan MXG, De Strooper B, Kopan R. Analysis of notch function in presomitic mesoderm suggests a γ-secretase-independent role for presenilins in somite differentiation. *Dev Cell* (2005) 8(5):677–88. doi: 10.1016/j.devcel.2005.02.019

45. Baylink D, Wergedal J, Thompson E. Loss of proteinpolysaccharides at sites where bone mineralization is initiated. *J Histochem Cytochemistry.* (1972) 20 (4):279–92. doi: 10.1177/20.4.279

46. Cytrynbaum EG, Small CM, Kwon RY, Hung B, Kent D, Yan YL, et al. Developmental tuning of mineralization drives morphological diversity of gill cover bones in sculpins and their relatives. *Evol letters.* (2019) 3(4):374–91. doi: 10.1002/evl3.128

47. Westerfield M. *The zebrafish book: A guide for the laboratory use of zebrafish (Brachydanio rerio)*. Eugene OR: University of Oregon Press (1993).

48. Kimmel CB, Ballard WW, Kimmel SR, Ullmann B, Schilling TF. Stages of embryonic development of the zebrafish. *Dev Dynamics.* (1995) 203(3):253–310. doi: 10.1002/aja.1002030302

49. Kearns CA, Walker M, Ravanelli AM, Scott K, Arzbecker MR, Appel B. Zebrafish spinal cord oligodendrocyte formation requires boc function. *Genetics* (2021) 218(4):iyab082. doi: 10.1093/genetics/iyab082

50. Jao L-E, Wente SR, Chen W. Efficient multiplex biallelic zebrafish genome editing using a CRISPR nuclease system. *Proc Natl Acad Sci* (2013) 110(34):13904–9. doi: 10.1073/pnas.1308335110

51. Brooks E, Nichols J. Shifting zebrafish lethal skeletal mutant penetrance by progeny testing. *J visualized experiments: JoVE* (2017) 127:p.e56200. doi: 10.3791/56200

52. Nichols JT, Pan L, Moens CB, Kimmel CB. *barx1* represses joints and promotes cartilage in the craniofacial skeleton. *Development.* (2013) 140(13):2765–75. doi: 10.1242/dev.090639

53. Walker MB, Miller CT, Coffin Talbot J, Stock DW, Kimmel CB. Zebrafish *furin* mutants reveal intricacies in regulating Endothelin1 signaling in craniofacial patterning. *Dev Biol* (2006) 295(1):194–205. doi: 10.1016/j.ydbio.2006.03.028

54. Butler A, Hoffman P, Smibert P, Papalexi E, Satija R. Integrating single-cell transcriptomic data across different conditions, technologies, and species. *Nat Biotechnol* (2018) 36(5):411–20. doi: 10.1038/nbt.4096

55. Sasaki MM, Nichols JT, Kimmel CB. edn1 and hand2 interact in early regulation of pharyngeal arch outgrowth during zebrafish development. *PloS One* (2013) 8(6):e67522. doi: 10.1371/journal.pone.0067522

frontiers | Frontiers in Endocrinology

TYPE Original Research
PUBLISHED 23 January 2023
DOI 10.3389/fendo.2023.1002914

OPEN ACCESS

EDITED BY
Julian Lui,
Eunice Kennedy Shriver National Institute of Child Health and Human Development (NIH), United States

REVIEWED BY
Daiju Yamazaki,
National Institute of Health Sciences (NIHS), Japan
Emilie Dambroise (Mugniery)
Hôpital Necker-Enfants Malades, France

*CORRESPONDENCE
Antonella Forlino
aforlino@unipv.it

†These authors have contributed equally to this work and share first authorship

SPECIALTY SECTION
This article was submitted to Bone Research, a section of the journal Frontiers in Endocrinology

RECEIVED 25 July 2022
ACCEPTED 03 January 2023
PUBLISHED 23 January 2023

CITATION
Tonelli F, Leoni L, Daponte V, Gioia R, Cotti S, Fiedler IAK, Larianova D, Willaert A, Coucke PJ, Villani S, Busse B, Besio R, Rossi A, Witten PE and Forlino A (2023) Zebrafish Tric-b is required for skeletal development and bone cells differentiation. *Front. Endocrinol.* 14:1002914. doi: 10.3389/fendo.2023.1002914

Zebrafish Tric-b is required for skeletal development and bone cells differentiation

Francesca Tonelli[1†], Laura Leoni[1†], Valentina Daponte[1†], Roberta Gioia[1], Silvia Cotti[2], Imke A. K. Fiedler[3], Daria Larianova[2], Andy Willaert[4], Paul J. Coucke[4], Simona Villani[5], Björn Busse[3], Roberta Besio[1], Antonio Rossi[1], P. Eckhard Witten[2] and Antonella Forlino[1*]

[1]Department of Molecular Medicine, Biochemistry Unit, University of Pavia, Pavia, Italy, [2]Department of Biology, Ghent University, Ghent, Belgium, [3]Department of Osteology and Biomechanics, University Medical Center Hamburg-Eppendorf, Hamburg, Germany, [4]Department of Biomolecular Medicine, Center of Medical Genetics, Ghent University-University Hospital, Ghent, Belgium, [5]Department of Public Health and Experimental and Forensic Medicine, Unit of Biostatistics and Clinical Epidemiology, University of Pavia, Pavia, Italy

Introduction: Trimeric intracellular potassium channels TRIC-A and -B are endoplasmic reticulum (ER) integral membrane proteins, involved in the regulation of calcium release mediated by ryanodine (RyRs) and inositol 1,4,5-trisphosphate (IP_3Rs) receptors, respectively. While TRIC-A is mainly expressed in excitable cells, TRIC-B is ubiquitously distributed at moderate level. TRIC-B deficiency causes a dysregulation of calcium flux from the ER, which impacts on multiple collagen specific chaperones and modifying enzymatic activity, leading to a rare form of osteogenesis imperfecta (OI Type XIV). The relevance of TRIC-B on cell homeostasis and the molecular mechanism behind the disease are still unknown.

Results: In this study, we exploited zebrafish to elucidate the role of TRIC-B in skeletal tissue. We demonstrated, for the first time, that *tmem38a* and *tmem38b* genes encoding Tric-a and -b, respectively are expressed at early developmental stages in zebrafish, but only the latter has a maternal expression. Two zebrafish mutants for *tmem38b* were generated by CRISPR/Cas9, one carrying an out of frame mutation introducing a premature stop codon ($tmem38b^{-/-}$) and one with an in frame deletion that removes the highly conserved KEV domain ($tmem38b^{\Delta 120\text{-}7/\Delta 120\text{-}7}$). In both models collagen type I is under-modified and partially intracellularly retained in the endoplasmic reticulum, as described in individuals affected by OI type XIV. $Tmem38b^{-/-}$ showed a mild skeletal phenotype at the late larval and juvenile stages of development whereas $tmem38b^{\Delta 120\text{-}7/\Delta 120\text{-}7}$ bone outcome was limited to a reduced vertebral length at 21 dpf. A caudal fin regeneration study pointed towards impaired activity of osteoblasts and osteoclasts associated with mineralization impairment.

Discussion: Our data support the requirement of Tric-b during early development and for bone cell differentiation.

KEYWORDS

zebrafish, TRIC-B, osteogenesis imperfecta, bone, fin regeneration, collagen, endoplasmic reticulum

1 Introduction

The trimeric cation channels, TRICs, are responsible for the transport of K^+ ions across the endoplasmic or sarcoplasmic reticulum (ER/SR) membranes where they act as counter-ions to allow electroneutral Ca^{2+} exit from the ER/SR lumen to the cytosol. The mammalian family of TRICs is composed by TRIC-A and TRIC-B subtypes, encoded by *TMEM38A* and *TMEM38B*, respectively. TRIC-A mediated Ca^{2+} release throughout coupling with ryanodine receptors (RyRs) is particularly relevant in excitable cells, especially in striated muscle and brain (1), while TRIC-B, synchronizing with inositol trisphosphate receptors (IP_3Rs), ubiquitously mediates Ca^{2+} release (2).

Calcium plays important roles both as cofactor and stabilizing ion for several proteins with enzymatic and/or chaperone functions and as second messenger in various signal transduction pathways, thus its homeostasis affects multiple cell functions, including contraction and relaxation, motility, metabolism, protein synthesis, modification and folding, secretion, cell-cycle progression, apoptosis and gene expression (3, 4).

The impairment in RyRs- and IP_3Rs- mediated Ca^{2+} release observed in TRIC-A and TRIC-B knock-out mouse models, respectively, supports the tissue specific role of the channels in modulating calcium signaling. TRIC-A knock-out mice show reduced or irregular muscle contractile responses and develop hypertension (5, 6), while TRIC-B knock-out mice suffer from pulmonary dysfunction and die perinatally due to an insufficient alveoli surfactant production (7). Interestingly, TRIC-B knock-out mice reveal also skeletal abnormalities, such as reduced body size and impaired ossification associated with insufficient collagen matrix production (8).

A skeletal phenotype is similarly described in humans with loss of function mutations in *TMEM38B*, which are affected by a recessive form of osteogenesis imperfecta (OI), classified as OI type XIV (OMIM 615066) (9). They are characterized, similarly to the most OI individuals with dominant and other recessive forms (10), by wide phenotypical variability, ranging from asymptomatic to severe, with different degrees of bone deformities, low bone mass, mild to recurrent fractures, growth retardation and short stature (11). The primary fibroblasts and osteoblasts isolated from affected individuals display a reduced level of helical lysyl hydroxylation, suggesting a dysfunctional activity of lysyl hydroxylase 1 (LH1) that is a calcium dependent enzyme. LH1 is necessary for proper lysine hydroxylation in the collagen type I helical domain and formation of stable intermolecular cross-linking (12). Furthermore, hydroxylysines are substrates for collagen specific ER O-linked glycosylation process (13, 14). In OI type XIV individuals this results in the synthesis of under-modified collagen type I (15, 16), which is susceptible to cell retention causing ER stress and increased degradation. Furthermore, abnormally secreted molecules are not properly incorporated in the extracellular matrix fibers (17). Also, osteoblasts from TRIC-B knock-out mice present enlarged ER cisternae due to intracellular collagen retention (8).

In vitro long term cultured primary human OI type XIV osteoblasts display reduced expression of early markers of differentiation such as *RUNX2* and *SP7* and increased expression of the later markers *BGLAP* and *OPN*, which inhibit crystal growth (16, 18). Osteoclasts are also impaired, since their number and activity are reduced (16). In immortalized human Foetal Osteoblasts (hFOB) knock-out for *TMEM38B* a decreased proliferation and mineralization have been recently demonstrated (19).

In the last decade, zebrafish proved to be a very reliable animal model to reproduce human common and heritable disorders, including skeletal diseases. Its high reproductive rate, larvae transparency and small size together with the ease of manipulation of its genome made zebrafish a high throughput and low-cost model to understand the molecular basis of human diseases as well as to identify new targets and to test innovative pharmacological approaches. The development of high-resolution imaging techniques further strength the use of teleost in bone research (20).

Zebrafish can regenerate several organs and tissues including bone and indeed fin ray regeneration represents a powerful tool to investigate bone formation in adult animals.

In this study we mapped for the first time the spatial and temporal expression of *tmem38a* and *tmem38b* during zebrafish early developmental stages and their expression in adult tissues. By CRISPR/Cas9 targeting of *tmem38b* in zebrafish we proved the relevance of Tric-b for skeletal development and collagen biosynthesis. Using a caudal fin regeneration assay we demonstrated that lack of *tmem38b* affects both osteoblasts and osteoclasts activity.

2 Materials and methods

2.1 Zebrafish husbandry and ethical statement

Wild-type (WT) AB zebrafish were obtained by the European Zebrafish Research Center (EZRC) (Germany). Zebrafish embryos were kept in petri dishes in zebrafish water (1.2 mM $NaHCO_3$, instant ocean 0.1 g/L, 1.4 mM $CaSO_4$, methylene blue 0.00002% w/v) at 28°C until 6 days post fertilization (dpf), then housed in ZebTEC semi-closed recirculation housing systems (Techniplast) at 28°C, pH 7.5 and conductivity 500 µS on a 14/10 light/dark cycle. Adult zebrafish were fed three times a day alternating dry food and brine shrimps. For the experiments, larvae and adult zebrafish were anesthetized using 0.016% w/v tricaine (3-amino benzoic acidethylester, Sigma Aldrich) in zebrafish water and sacrificed by tricaine overdose (0.03% w/v). All the experiments were performed in agreement with EU Directive 2010/63/EU. The experimental protocol was approved by Italian Ministry of Health (Approval Animal Protocol No.1191/2016-PR).

2.2 *In silico* analysis

Synteny maps of the chromosomic regions surrounding transmembrane protein 38A and transmembrane protein 38B (*TMEM38A/B*) genes in *D. rerio*, *H. sapiens* and *M. musculus* were generated using the human genes as reference by combining PhyloView and AlignView from Genomicus 93.01 (http://www.genomicus.biologie.ens.fr) with Ensembl Comparative Genomics

data. Conserved domains between zebrafish, human and mouse proteins were identified using UniProt (https://www.uniprot.org).

2.3 *In situ* hybridization

Whole-mount *in situ* hybridization was carried out according to the standard protocol (21). An 841 bp amplicon was obtained by RT-PCR amplification of WT zebrafish *tmem38b* mRNA (ENSDART00000168983) using primers on exon 1 (5'-TCAATCTGAACGAGCTCGCATTT-3', 20-42 nt) and on exon 10 (5'- AAGAAGCAGAAGCCAGCAAAAAG-3', 839-861 nt) and subcloned in T7 pGEM-T-Easy vector (Promega). Plasmid DNA was linearized by enzymatic digestion with SacII (New England BioLabs) for the antisense RNA probe and with SpeI (Promega) for the sense probe. 48 and 72 hours post fertilization (hpf) embryos (n =10 for each group) were fixed in 4% (w/v) paraformaldehyde (PFA) o/n at 4°C, washed in PBS-T (PBS containing 0.1% Tween-20) and digested with 10 µg/mL proteinase K for a time depending on embryos' developmental stage. Digoxigenin uridine-5′ triphosphate (DIG) labeled RNA sense and antisense probes targeting *tmem38b* gene were used after incubation at 64°C. Finally, images were acquired using a Leica M165 FC microscope connected to a Leica DFC425 C digital camera.

2.4 Genotyping

The WT, *tmem38b*$^{-/-}$ and *tmem38b*$^{\Delta 120\text{-}7/120\text{-}7}$ genomic DNA was extracted depending on the experiment type, from single embryos, pool of embryos or caudal fin biopsies from adult zebrafish. Tissues were digested by proteinase K (2.5 mg/mL, Sigma Aldrich) in lysis buffer (100 mM Tris HCl, pH 8.5, 5 mM EDTA, 0.2% (w/v) SDS, 200 mM NaCl) overnight (o/n) at 55°C, followed by isopropanol precipitation and resuspension in 20 mM Tris-HCl, 1 mM EDTA, pH 8.0. DNA was PCR amplified using the following primers: forward 5'-TTACTGTCCGCTGGATGTGG-3' (11326-11345 nt) and reverse 5'–CAGAGCGTCGCTGTATTTGC-3' (11448-11467 nt) as described in Supplementary Methods. The different amplicon sizes were discriminated on 12% and 10% v/v electrophoresis acrylamide gel in TBE buffer (0.1 M Tris HCl, 0.1 M H_3BO_3, 2 mM EDTA, pH 8.2), respectively.

2.5 RNA extraction and qPCR

RNA was extracted from RNA pools of 20 embryos at different stages of development (from 2-4 cells to 96 hours post fertilization, hpf) and from caudal fins of adult WT, *tmem38b*$^{-/-}$ and *tmem38b*$^{\Delta 120\text{-}7/\Delta 120\text{-}7}$ (WT n = 3, *tmem38b*$^{-/-}$ n = 3, *tmem38b*$^{\Delta 120\text{-}7/\Delta 120\text{-}7}$ n = 3) or from pools of bones, brains, muscles, swim bladders, hearts (WT n = 3 pools, *tmem38b*$^{-/-}$ n = 3 pools, *tmem38b*$^{\Delta 120\text{-}7/\Delta 120\text{-}7}$ n = 3 pools, each pool included samples from 2 fish) using Qiazol (Qiagen) and DNase digestion (Invitrogen) according to manufacturer's instructions. All experiments were performed in triplicate, except when indicated in the figure legend. RNA quantity was determined by NanoDrop spectrophotometer and RNA quality by agarose gel electrophoresis. Reverse-transcription was performed using the High-Capacity cDNA Transcription kit (Applied Biosystems) according to manufacturer's protocol in a final volume of 20 µL. qPCR was performed in triplicate in a 25 µL final volume using Taqman Universal PCR Master mix (Applied Biosystems) and commercial TaqMan probes for *tmem38b*, *tmem38a*, *rpl13a* and *β actin* (Dr03434781_m1, Dr03075180_m1, Dr03119260_g1 and Dr03432610_m1, Applied Biosystems). The relative expression of each gene was calculated using the ΔΔCt method. qPCR for *acp5a* (ENSDART00000004716.10), *bglap* (ENSDART00000100845.5), *ctsk* (ENSDART00000179680.1), *mpeg* (ENSDART00000077637.5), *opg* (ENSDART00000184909.1), *rankl* (ENSDART00000098355.5), *sp7* (ENSDART00000128793.3) and the housekeeping *dna15ta1* (22) was performed in 25 µL reaction mixtures with 12.5 µL SYBR Green Mastermix (Applied Biosystems). Primer sequences are available upon request. The QuantStudio 3 thermocycler and the QuantStudio Design and analysis software (Applied Biosystems) were used. Samples were run in triplicate.

2.6 Collagen analysis

Skin and bone were dissected from adult WT (n=2), *tmem38b*$^{-/-}$ (n=2) and *tmem38b*$^{\Delta 120\text{-}7/\Delta 120\text{-}7}$ (n=2) following sacrifice. The tissues were defatted for 6 h in 0.1 N NaOH at 4°C. Bone was decalcified for 48 h in 0.5 M EDTA pH 7.4 at 4°C. The pepsin-soluble collagen fraction (PSC) was obtained as described in (23). Briefly, tissues were digested with 0.1 mg/mL pepsin in 0.5 M acetic acid at 4°C for 48 h. The PSC was precipitated by 0.9 M NaCl in 0.5 M acetic acid o/n at 4°C and quantified using Sircol Soluble Collagen assay (Biocolor). Equal amount of collagen from each sample (2 µg) was loaded on 6% SDS-Urea-PAGE in non-reducing conditions. Gels were stained overnight with 0.08 M picric acid, 0.04% Coomassie Brilliant Blue R250 (Sigma Aldrich), destained in water and acquired with ImageQuant LAS 4000 (GE Healthcare) using the ImageQuant LAS 4000 1.2 software.

2.7 Morphometric analysis

Images of anesthetized post hatching stages (7, 14, 21 dpf and 1, 2, 4, 6 mpf) WT (n ≥ 13) and *tmem38b*$^{-/-}$ (n ≥ 8) larvae and adult zebrafish were acquired with a M165FC stereomicroscope (Leica) connected to DFC425C digital camera (Leica). For *tmem38b*$^{\Delta 120\text{-}7/\Delta 120\text{-}7}$, images were taken at 21 dpf and 1 mpf (n ≥ 13). Measurements were performed as described (24) using the LAS v4.13 software (Leica). On lateral images, the Standard Length (SL) was measured as the distance from the snout to the caudal peduncle or, in pre-flexion larvae that do not have a caudal peduncle, to the posterior tip of the notochord. Vertebral length and height were evaluated at 21 dpf (WT n ≥22, *tmem38b*$^{-/-}$ n = 25, *tmem38b*$^{\Delta 120\text{-}7/\Delta 120\text{-}7}$ n = 19) and 1 mpf (WT n ≥18, *tmem38b*$^{-/-}$ n = 18, *tmem38b*$^{\Delta 120\text{-}7/\Delta 120\text{-}7}$ n = 18) in both mutants and also at 2 mpf in *tmem38b*$^{-/-}$ (WT n = 13, *tmem38b*$^{-/-}$ n = 14). For each vertebra, the mean of the length measured dorsally and ventrally, and the mean of the height measured anteriorly and posteriorly to the vertebral centrum were evaluated using the LAS v4.13 software (Leica). At 21 dpf, 10 vertebrae starting from the first ossified centrum were considered, while at 1 and 2 mpf the vertebral dimensions were evaluated by measuring from the second centrum articulated with the ribs. In addition, the level

10.3389/fendo.2023.1002914

of inflation of the swim bladder was evaluated in larvae by counting the numbers of lobes on lateral images at 21 dpf (WT n ≥27, *tmem38b*$^{-/-}$ n = 26, *tmem38b*$^{\Delta 120\text{-}7/\Delta 120\text{-}7}$ n = 21).

2.8 Skeletal staining

Bone was stained with Alizarin Red as previously described (25). Both larval and adult WT (n ≥ 28), *tmem38b*$^{-/-}$ (n ≥ 17) and *tmem38b*$^{\Delta 120\text{-}7/\Delta 120\text{-}7}$ (n = 8) zebrafish were sacrificed and fixed overnight in PFA 4% w/v in PBS (Sigma Aldrich) with 0.9 mM $CaCl_2$ and 0.49 mM $MgCl_2$, pH 7.4 at 4°C. Bleaching to remove the pigmentation was performed with 3% v/v H_2O_2, 0.5% w/v KOH at RT followed by two washes in glycerol 25% v/v, 0.1% w/v KOH. Soft tissues were digested with 1 mg/mL trypsin dissolved in a 30% v/v solution of saturated $B_4Na_2O_7$. After the staining in 0.01% w/v Alizarin Red S (Sigma Aldrich), 25% v/v glycerol, 100 mM Tris–HCl, pH 7.5 overnight at RT, fish were washed in increasing 0.1% series of glycerol/KOH and finally stored at 4°C in 100% glycerol, 0.1% KOH. Images were acquired using a Leica M165 FC microscope connected to a Leica DFC425 C digital camera. The mineralization of the notochord was evaluated describing the level of ossification as beginning, intermediate or complete ossification. The mineralization of Alizarin Red stained caudal fins was evaluated in the amputated samples and 5 days post amputation (dpa) (WT n ≥ 9, *tmem38b*$^{-/-}$ n ≥ 8, *tmem38b*$^{\Delta 120\text{-}7/\Delta 120\text{-}7}$ n ≥ 8) by measuring the real mineralized area (RMA) normalized to the ray width (RAY), according to literature (26). In addition, the length of segments per ray was measured on the amputated caudal fins (WT n = 6, *tmem38b*$^{-/-}$ n = 8, *tmem38b*$^{\Delta 120\text{-}7/\Delta 120\text{-}7}$ n = 3). Measurements were performed using the LAS v4.13 software (Leica).

2.9 Picro Sirius Red collagen staining

Amputated caudal fins of adult WT (n=3), *tmem38b*$^{-/-}$ (n=4) and *tmem38b*$^{\Delta 120\text{-}7/\Delta 120\text{-}7}$ (n=3) zebrafish were collected and fixed overnight in PFA 4% w/v in PBS. Caudal fins were stained 1 h in 0.1% w/v Sirius Red (Direct Red 80, Sigma Aldrich) in saturated aqueous solution of picric acid (Sigma Aldrich) (27). After staining, caudal fins were washed in 0.5% v/v acetic acid, and directly dehydrated three times in absolute ethanol. Samples were clarified with xylene and mounted with DPX (Sigma Aldrich). Slides were observed under polarized light with the DM2500 microscope (Leica) and acquired using the ICC50 W digital camera (Leica). Measurements were performed using Leica LAS v4.13 software on 20X images. First, the length of each actinotrichia per ray was measured by tracing a line from the most proximal red signal in the ray to the tip of the caudal fin. Then, all the actinotrichia whose length was measured were counted and the mean of the number of actinotrichia per ray was calculated.

2.10 Tartrate-resistant acid phosphatase staining

Tartrate-resistant Acid Phosphatase (TRAP) staining was performed (28). Caudal fins of adult WT (n = 7), *tmem38b*$^{-/-}$ (n = 9) and *tmem38b*$^{\Delta 120\text{-}7/\Delta 120\text{-}7}$ (n = 10) zebrafish were fixed in PFA 4% in PBS o/n at 4°C, washed in PBS containing 0.1% v/v Tween-20 and permeabilized in PBS containing 0.3% v/v Triton X-100 for 30 min. Fins were then equilibrated in TRAP buffer (0.1 M sodium acetate, 0.1 M acetic acid, 50 mM sodium tartrate) and colour reaction was performed in TRAP buffer containing 0.1 mg/ml Naphtol AS-MX phosphate (Sigma Aldrich) and 0.3 mg/ml Fast Red Violet LB (Sigma Aldrich). Fins were then bleached in 10% H_2O_2, 1% KOH o/n at RT to remove pigmentation and then stored in 70% glycerol at 4°C. Images were acquired using a Leica M165 FC microscope connected to a Leica DFC425 C digital camera. The number of TRAP+ cells in the regenerate was counted using the Cell Counter tool on the ImageJ software according to literature (29).

2.11 Transmission electron microscopy analysis

For transmission electron microscopy (TEM) analysis, 1 mpf WT (n= 3), *tmem38b*$^{-/-}$ (n=3) and *tmem38b*$^{\Delta 120\text{-}7/\Delta 120\text{-}7}$ (n=3) were fixed for 24 h at RT in 1.5% v/v PFA (Sigma Aldrich), 1.5% v/v glutaraldehyde (Sigma Aldrich), 0.1 M sodium cacodylate buffer (pH 7.4) and 0.001% w/v $CaCl_2$. The samples were decalcified in 0.1 M EDTA for 14 days at 4°C. Samples were rinsed in 0.1 M sodium cacodylate buffer containing 10% sucrose and post fixed for 2 h using 1% w/v OsO_4 in 0.1 M sodium cacodylate buffer at pH 7.4. Subsequently, zebrafish were infiltrated with low-viscosity epoxyembedding medium. Ultra-thin (70 nm) sections of the region of interest (vertebral endplate growth zone) were cut using a Reichert Ultracut E ultramicrotome (Reichert-Jung) with a diamond knife (Diatome Ltd.) and mounted on formvar-coated single slot copper grids. The sections were stained with uranyl acetate and lead citrate and viewed with a Jeol JEM-1010 (Jeol Ltd) TEM operating at 60 kV. Microphotographs were taken with a Veleta camera (Emsis, Germany) (30). TEM images were used to detect the endoplasmic reticulum cisternae enlargement. The area of ER cisternae in WT, *tmem38b*$^{-/-}$ and *tmem38b*$^{\Delta 120\text{-}7/\Delta 120\text{-}7}$ was measured using LAS v4.13 software (Leica).

2.12 4 phenylbutyrate treatment (4PBA)

WT, *tmem38b*$^{-/-}$ and *tmem38b*$^{\Delta 120\text{-}7/\Delta 120\text{-}7}$ embryos were manually dechorionated at 24 hpf. Fish were placed in 6 well plates (20 fish per well) in zebrafish water containing 0.003% 1-phenyl 2-thiourea (PTU) to prevent pigmentation and treated with 0.05 mM 4PBA from 1 dpf to 5 dpf. Half of the volume of water with or without 4PBA was replaced every day (23).

2.13 Whole-mount immunostaining

Whole mount immunostaining was performed as previously described (23). Briefly, *tmem38b*$^{-/-}$ (n=116) and WT (n=146) untreated and 4PBA treated *tmem38b*$^{-/-}$ (n=113); *tmem38b*$^{\Delta 120\text{-}7/\Delta 120\text{-}7}$ (n=19) and WT (n=43) untreated and 4PBA treated *tmem38b*$^{\Delta 120\text{-}7/\Delta 120\text{-}7}$ (n=34) were collected at 5 dpf, fixed overnight in 4% w/v PFA in PBS,

washed in PBS and stored in methanol at -20°C. After tissue digestion with 0.1% w/v proteinase K in PBS at 25°C for 15 min and 2% w/v hyaluronidase in PBS at 25°C for 20 min samples were blocked in 5% w/v bovine serum albumin (BSA, Sigma Aldrich) in PBS-T for 2 h at RT. Hsp47b affinity purified antibody (1:1000 in 5% BSA/PBS-T), kindly provided by Prof. Raimund Wagener, University of Cologne, Germany, and anti-rabbit secondary antibody (1:200 in 1% BSA/PBS-T, Cell Signaling) were used. DAB substrate (Thermo Scientific) was finally added until appearance of the staining. Fish were incubated in increasing glycerol series and stored at 4°C in 100% glycerol. Images were acquired using a Leica M165 FC microscope connected to a Leica DFC425 C digital camera. Three operators blinded to the genotype and to the treatment of the fish independently evaluated the intensity of the signal as zero, low (+) or high (++). Following imaging, samples underwent stepwise ethanol dehydration and soft epon embedding according to an established protocol (31). Sagittal 4 µm sections were cut on a Microm HM360 microtome (Marshall Scientific), mounted with DPX and observed with an Axio Imager-Z1 microscope (Carl Zeiss).

2.14 Statistical analysis

All quantitative variables were expressed as mean with standard deviation (SD) or standard error of the means (SEM), as indicated in figure legend, while qualitative variables using percentage. To evaluate gene expression across genotype (WT, *tmem38b*$^{-/-}$ and *tmem38b*$^{\Delta 120\text{-}7/\Delta 120\text{-}7}$) for each examined organ, non parametric analysis of variance (Kruskall Wallis) was applied, followed by non- parametric unpaired t test with multiple comparison correction. To separately describe the behaviour of WT with respect to each mutant in bone mineralization, swim bladder inflation and Hsp47 signal, chi-squared or Fisher's exact test, if the assumption for chi squared was not respected, was performed. The Bonferroni's correction for multiple tests was applied to adjust the p-value when the Hsp47 signal for untreated and treated mutants was compared to that of WT. Separately, by each time point a comparison between WT and *tmem38b*$^{-/-}$ standard length and vertebral measurements was evaluated using parametric or the equivalent non parametric unpaired t test, when the assumptions for parametric were violated. The same approach was applied to ray segment length, RMA/RAY width, number of TRAP positive cells and number and length of actinotrichia. A $p<0.05$ was considered significant apart from when multiple correction was used. Statistical analyses were performed using SigmaPlot and STATA15®.

3 Results

3.1 TRICs expression in zebrafish

A single copy of *tmem38a* and *tmem38b* encoding the trimeric intracellular cation channels (TRICs) Tric-a and Tric-b, respectively is present in the *D. rerio* genome. The zebrafish *tmem38a locus* is residing on chromosome 11 and similarly to the human and murine gene positioned on chromosome 19 and 8, respectively, consists of 6 exons. The zebrafish *tmem38b locus* is located on chromosome 21 and includes 10 exons, while the human and murine gene is located in chromosome 9 and 4, respectively and consist of 6 exons. The *in silico* analysis of the human, mouse and zebrafish genomic regions surrounding *tmem38a* and *tmem38b loci* supports their common ancestral origin (Figure 1A and Supplementary Table 1).

Zebrafish Tric-a consists of 295 amino acids and shows 70.6% and 68.1% identity with the human (299 aa) and the murine (298 aa) protein, respectively, whereas Tric-b (289 aa) shares only 45% and 48% identity with the human (291 aa) and the murine (292 aa) protein, respectively. Zebrafish Tric-a and Tric-b share 41.7% identity.

In all three species, homology data support that TRIC channels are symmetrical trimers of identical protomers crossing the endoplasmic reticulum membrane with 7 α helices and characterized by two inverted repeated regions and a C-terminal helix. Each protomer contains a lipid consensus binding sequence KEVXRXXK that likely confers to the channel the voltage-sensitivity and also includes the predicted pore-forming KEV, important to guarantee the K^+ flux (32). Also, the two glycine rich regions in TM2 and TM5 are conserved as well as Gly74 in TRIC-A and Ala74 in TRIC-B that are recognized as luminal calcium binding site relevant for pore opening (32, 33) (Figure 1B).

The expression of *tmem38b* at 48 and 72 hours post fertilization (hpf) in the region of cranio-facial cartilages was showed by whole mount *in situ* hybridization and supports also in teleosts the role of the channel in skeletal tissue starting from early developmental stage (Figure 1C and Supplementary Figure 1A). Temporal analysis of *tmem38a* and *tmem38b* expression in WT zebrafish at different embryonic developmental stages revealed a relevant increase of *tmem38a* expression from 24 hours post fertilization (hpf), while both a maternal and a zygotic expression were detected for *tmem38b* (Figure 1D). The two genes were expressed both in excitable (muscle, brain, heart) and in non-excitable (swim bladder, bone) adult tissues. As expected, the expression of *tmem38a* was particularly abundant in muscle, heart and brain, and surprisingly in bone as well, whereas the highest *tmem38b* expression was found in the swim bladder (Figures 2A, B).

3.2 *tmem38b* mutants generated by CRISPR/Cas9 gene editing

The skeletal phenotype described in osteogenesis imperfecta (OI) type XIV, and caused by *TMEM38B* loss-of-function mutations in mammals, demonstrated a relevant role of TRIC-B in bone homeostasis. Thus, to get further insight on *tmem38b* function in teleosts and to generate a zebrafish model for the human disease, CRISPR/Cas9 was used to target exon 7 (Supplementary Figure 1B, C and Supplementary Materials) which includes the consensus sequence KEVXRXXK important for the formation of the pore channel. Among the generated mutant F1 heterozygous zebrafish (Supplementary Figure 1D), two were selected and crossbred for further experiments. The one carrying a 7 nucleotides deletion (c.524_530delTGAAGGA) predicted to insert a premature stop codon at amino acid 122 of Tric-b was chosen to generate the F2 *tmem38b* knock out model (*tmem38b*$^{-/-}$). The mutant carrying a 24 nucleotides *in frame* deletion (c.517_540del24nt) predicted to remove the p.Ala120_Thr127 oligopeptide was selected to generate the F2 *tmem38b*$^{\Delta 120\text{-}7/\Delta 120\text{-}7}$ lacking the highly conserved KEV motif (Supplementary Figure 1D). qPCR showed that *tmem38b*

10.3389/fendo.2023.1002914

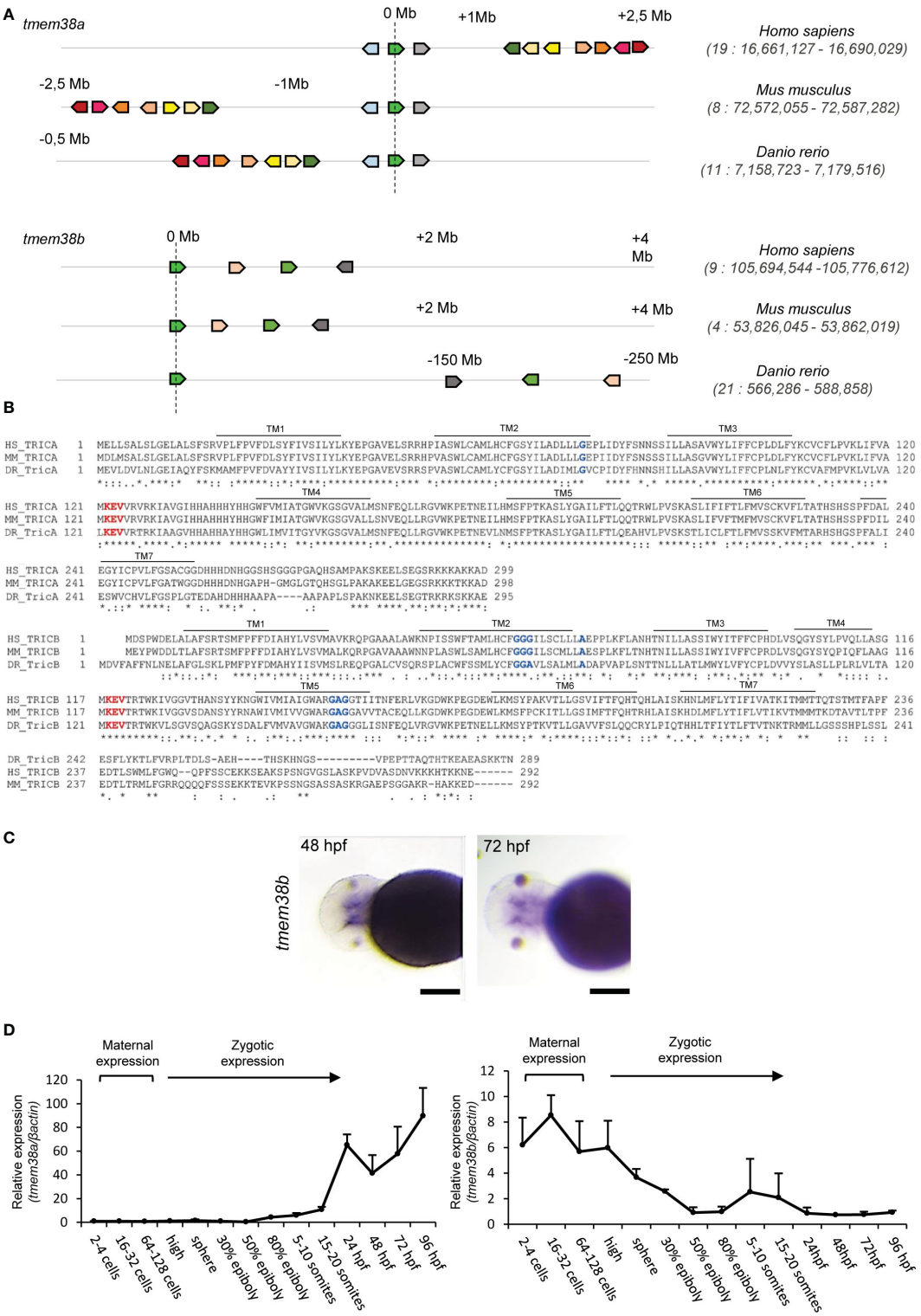

FIGURE 1
Analysis of *tmem38a/b* across species and of their spatio-temporal expression during zebrafish development. **(A)** The sinteny analysis performed on humans (*H. sapiens*), mice (*M. musculus*) and zebrafish (*D. rerio*) supported the existence of a common ancestral chromosomal origin for both *tmem38a* and *tmem38b*. The maps were obtained using the genome browser Genomicus. The human genes were used as roots. The position of the genes (Mb) relative to the investigated locus is based on Ensemble database and shown on top of the chromosome line. The exact chromosomal position of all the conserved genes is reported in the Supplementary Tables S1. The direction of the arrows indicates the gene orientation in respect to the reference gene. **(B)** Trimeric intracellular cation channel A (TRIC-A) and B (TRIC-B) domains are conserved among human, mouse and zebrafish. The 7 transmembrane domains (TM) are indicated. In red is shown the KEV pore channel domain, while in blue are indicated the two glycine reach regions in TM2 and TM5. **(C)** *In situ* hybridization analysis of 48 and 72 hpf WT embryos revealed the presence of *tmem38b* in the region of craniofacial cartilages. **(D)** Relative expression of *tmem38a* and *tmem38b* was evaluated by qPCR demonstrating a maternal expression only for *tmem38b*. The experiment was perfomed in duplicate. Scale bar: 500 µm. Human *TMEM38A* ENSG00000072954, murine *Tmem38a* ENSMUSG00000031791, zebrafish *tmem38a* ENSDARG00000024047; human *TMEM38B* ENSG00000095209, murine *Tmem38b* ENSMUSG00000028420, zebrafish *tmem38b* ENSDARG00000100549. Tric-a: human Q9H6F2, murine Q3PMT8, zebrafish Q6P2T0; Tric-b: human Q9NVV0, murine Q9DAV9, zebrafish Q7ZVP8.

10.3389/fendo.2023.1002914

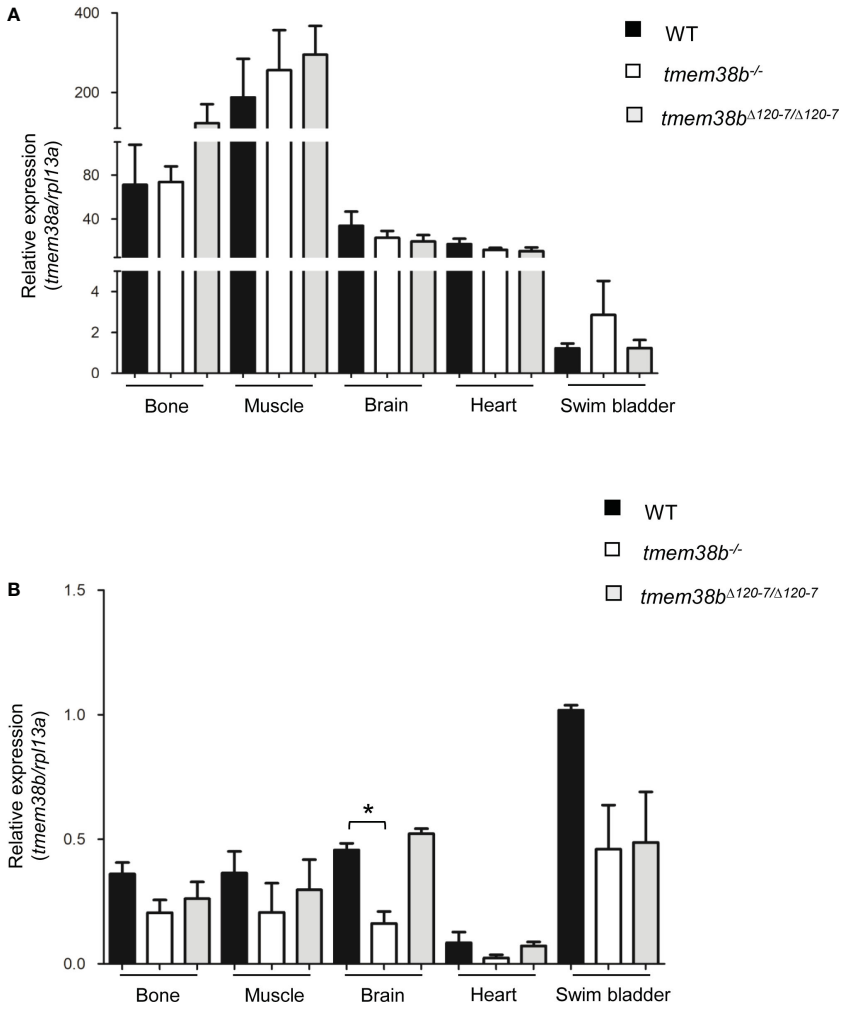

FIGURE 2
Expression analysis of *tmem38a* and *tmem38b* in excitable (muscle, brain, heart) and non-excitable tissues (bone, swim bladder) from adult WT and *tmem38b* mutants. **(A)** Relative expression of *tmem38a*. No difference in the transcript level was found between WT and *tmem38b* mutants by qPCR. **(B)** Relative expression of *tmem38b*. qPCR analysis revealed a reduced transcript level in almost all *tmem38b*$^{-/-}$ tissues respect to WT. Data are expressed as mean ± SEM. *p < 0.05 n = 3 RNA pools per group.

expression was significantly reduced in 24 hpf *tmem38b*$^{-/-}$ embryos compared to both WT (WT 1.19± 0.16, *tmem38b*$^{-/-}$ 0.40 ± 0.28, p=0.013) and *tmem38b*$^{\Delta 120\text{-}7/\Delta 120\text{-}7}$ (*tmem38b*$^{-/-}$ 0.40 ± 0.28, *tmem38b*$^{\Delta 120\text{-}7/\Delta 120\text{-}7}$ 2.11 ± 0.87; p= 0.031) while no difference in the expression of *tmem38a* was detected (WT 1.16± 0.14, *tmem38b*$^{-/-}$ 0.88 ± 0.12, *tmem38b*$^{\Delta 120\text{-}7/\Delta 120\text{-}7}$ 1.09 ± 0.17). In addition, the expression of *tmem38b* in various tissues revealed different levels of non-sense mediated mRNA decay (NMD) ranging from 41.2% in bone and muscle to 77.7% in heart for *tmem38b*$^{-/-}$ and from 16.6% in muscle and none in brain for *tmem38b*$^{\Delta 120\text{-}7/\Delta 120\text{-}7}$ (Figure 2A, B). Unfortunately, the lack of specific antibody against Tmem38b did not allow to evaluate the protein expression level.

3.3 Zebrafish juvenile skeleton is impaired in *tmem38b*$^{-/-}$

Both *tmem38b* mutants were viable, reached adulthood and were fertile. Nevertheless, an increased lethality was observed in *tmem38b*$^{-/-}$ from 7 days post fertilization (dpf) compared to both WT and *tmem38b*$^{+/-}$. Indeed, a significant difference from the expected 1:2:1 Mendelian ratio was observed at 2 and 3 weeks of age (Supplementary Table 2). The growth curve followed from 5 dpf to 6 months post fertilization (mpf) revealed a significant reduction in the standard length (SL) at 21 dpf and 1 mpf in *tmem38b*$^{-/-}$ compared to WT (Figure 3A) and a delay in the inflation of swim bladder lobes was detectable in mutant fish at 21dpf, suggesting a developmental delay rescued at older age (Figure 3B). No difference in SL and in the swim bladder inflation was evident in *tmem38b*$^{\Delta 120\text{-}7/\Delta 120\text{-}7}$ (Supplementary Figures 2A, B).

Whole mount Alcian Blue and Alizarin Red staining of 5 and 7 dpf larvae, respectively, did not reveal abnormality in cartilage or skeletal development in *tmem38b*$^{-/-}$ compared to WT (Supplementary Figures 3A-D). A reduced level of mineralization in the tip of notochord sheath was observed in *tmem38b*$^{-/-}$ compared to WT at 14 dpf (Figure 3C). An impaired mineralization of vertebra centra at 21 dpf and 1 mpf, as demonstrated by reduced vertebral length and vertebral height, the latter being smaller also at 2 mpf, was also

10.3389/fendo.2023.1002914

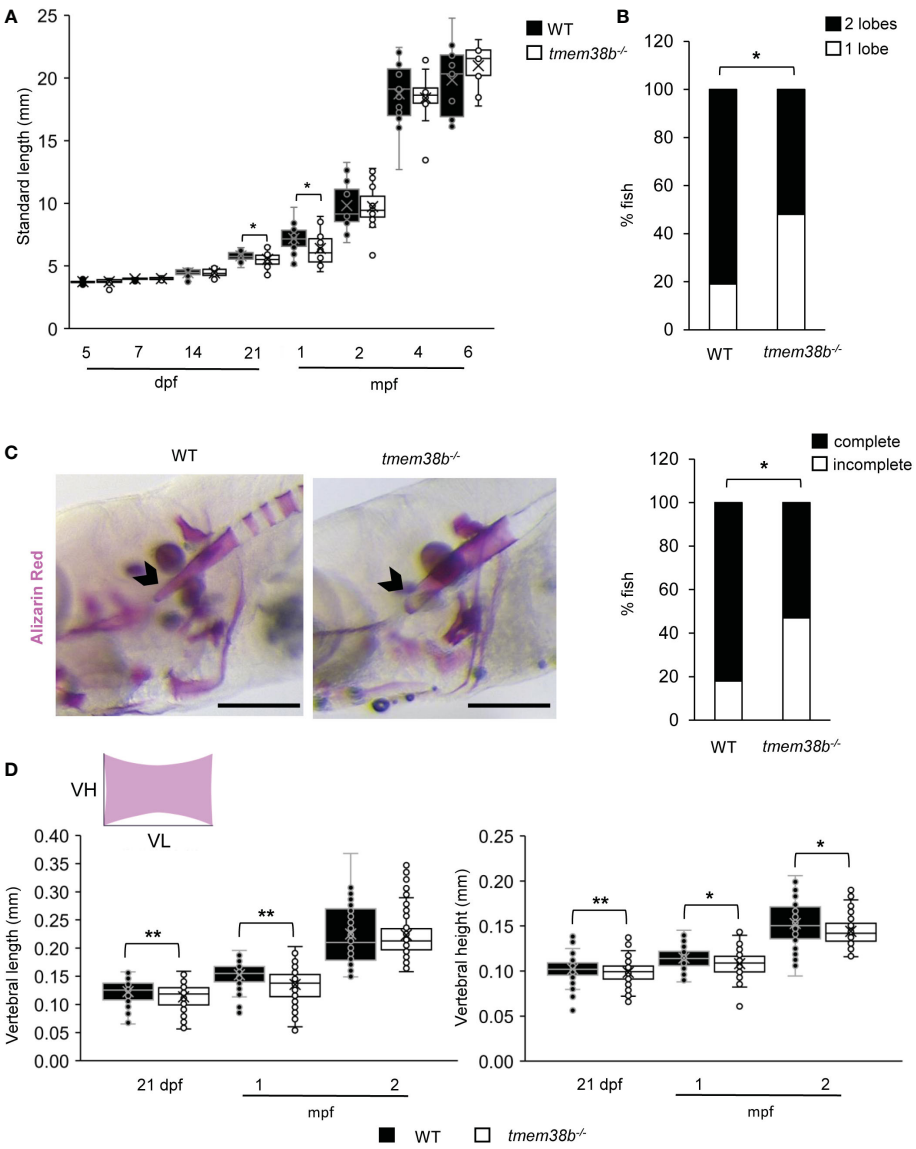

FIGURE 3
tmem38b$^{-/-}$ skeletal phenotype. **(A)** Growth curves representing WT and *tmem38b*$^{-/-}$ standard length measured at 5, 7, 14, 21 dpf, 1, 2, 4 and 6 mpf. At 21 dpf and 1 mpf *tmem38b*$^{-/-}$ were significantly shorter than WT. WT n ≥ 13, *tmem38b*$^{-/-}$ n ≥ 8. **(B)** At 21 dpf a significant delay in the inflation of the swim bladder was observed in *tmem38b*$^{-/-}$ (n = 27) with respect to WT (n = 28). **(C)** Representative lateral view (left panels) of 14 dpf alizarin red stained WT and *tmem38b*$^{-/-}$ fish. The notochord is indicated by the arrowhead. On the right the graph represents the level of the tip of the notochord mineralization, a delayed mineralization was evident in *tmem38b*$^{-/-}$ (*tmem38b*$^{-/-}$ n = 17) respect to WT (WT n = 28) Scale bar: 500 µm. **(D)** Vertebral length and vertebral height measurement in WT and *tmem38b*$^{-/-}$ zebrafish. Vertebral length (VL) was reduced in *tmem38b*$^{-/-}$ compared to WT at 21 dpf and 1 mpf. Vertebral height (VH) was reduced in *tmem38b*$^{-/-}$ compared to WT at 21 dpf, 1 and 2 mpf. 21 dpf: WT n= 29; *tmem38b*$^{-/-}$ n= 25; 1 mpf: WT n= 24; *tmem38b*$^{-/-}$ n= 18; 2 mpf: WT n= 13; *tmem38b*$^{-/-}$ n= 14. *,p < 0.05, **p ≤ 0.01.

detected (Figure 3D). Double staining with alizarin red and calcein did not show any difference in bone formation rate between WT and *tmem38b*$^{-/-}$ from 10 dpf to 1mpf (Supplementary Figure 4). The mineralization in mutant fish was partially rescued at 4 mpf, when only vertebral height was still reduced (Supplementary Figure 2C).

The vertebral size was unchanged in the *tmem38b*$^{\Delta 120\text{-}7/\Delta 120\text{-}7}$ at the analyzed time points, with the exception of a reduced vertebral length at 21 dpf (Supplementary Figure 2D).

MicroCT on both adult (9 mpf) fish models did not reveal any alteration in bone geometrical parameters compared to WT (Supplementary Figure 5 and data not shown). Also, nanoindentation analysis performed on vertebral bone cortex of 2 mpf mutants and control fish showed no differences either in hardness (*tmem38b*$^{-/-}$0.598 ± 0.050 GPa; *tmem38b*$^{\Delta 120\text{-}7/\Delta 120\text{-}7}$ 0.628 ± 0.068 GPa; WT 0.642 ± 0.052 GPa) or in elastic modulus (*tmem38b*$^{-/-}$ 13.704 ± 0.665 GPa; *tmem38b*$^{\Delta 120\text{-}7/\Delta 120\text{-}7}$ 13.895 ± 1.029 GPa; WT 14.391 ± 0.795 GPa).

Taken together, the skeletal characterization revealed a mild effect of Tric-b absence in zebrafish endoskeleton limited to late larval-juvenile developmental stage when a rapid bone growth is required. The lack of bone phenotype in *tmem38b*$^{\Delta 120\text{-}7/\Delta 120\text{-}7}$ supports either a possible residual activity of the *in frame* mutant Tric-b channel.

3.4 Collagen type I is retained in the endoplasmic reticulum of *tmem38b* mutants

Collagen type I extracted from WT and both mutants' skin and bone showed a slight faster electrophoretic migration (Figure 4A and Supplementary Figure 6A) supporting the presence of collagen under-modification, as reported in human OI type XIV cells (17). Electron microscopy analysis performed in the vertebral region revealed enlarged ER cisternae size in both fibroblasts and osteoblasts (Figure 4B) of *tmem38b* mutants compared to WT.

The expression of Hsp47b, the collagen specific chaperone known to assist procollagen assembly in the ER and its trafficking into the Golgi and whose expression is coupled with collagen synthesis (34), was evaluated by whole mount immunostaining on 5 dpf larvae.

Histological sections revealed that Hsp47b signal is intracellular and expressed in the outer epidermal layer (Figure 4C).

A stronger and significantly higher Hsp47b signal in mutants compared to WT was detected (Figures 4D–F).

Interestingly, the administration of 4 phenyl butyrate (4PBA), a chemical chaperone known to release ER stress in presence of collagen accumulation in dominant (23, 35) and some OI recessive forms (36), reduced Hsp47 signal in both mutants compared to controls supporting its positive role in restoring cell homeostasis also in presence of *tmem38b* mutations (Figures 4D-F).

3.5 Caudal fin rays and their regeneration are impaired in *tmem38b*$^{-/-}$

To evaluate the role of Tric-b during bone formation, caudal fin regeneration experiments were carried out. First, zebrafish amputated caudal fins were analyzed following Alizarin Red staining and a significantly increased segment length was detected in *tmem38b*$^{-/-}$ compared to controls (Figures 5A, B). In amputated and regrown samples stained with alizarin red the real mineralization area (RMA) was evaluated for all fin rays and normalized to ray width (RAY) (26). In *tmem38b*$^{-/-}$ a reduced RMA compared to WT was evident in the amputated samples, whereas at 5 days post amputation (dpa) it was significantly increased, suggesting a mineralization boost during early bone formation (Figures 5A, C).

qPCR analysis on WT and *tmem38b*$^{-/-}$ pools of caudal fins showed no difference in the expression of the early osteogenic marker *sp7* (*osterix*) at both time points. The increased expression trend of the late marker *osteocalcin* (*bglap*) in the mutant amputated fins compared to WT normalized in 5 dpa regenerates (Figure 5D).

No difference in bone mineralization during caudal fin regeneration as well as in the expression of specific markers of bone differentiation was detected in *tmem38b*$^{\Delta 120\text{-}7/\Delta 120\text{-}7}$ compared to WT (Supplementary Figures 6B–D).

3.6 Analysis of bone resorption during caudal fin regeneration in *tmem38b* mutants

Osteoblast and osteoclast activity in bone is tightly coupled and OI mutations frequently lead to an imbalance between bone formation and bone resorption (37). Indeed, in OI type XIV individuals a reduced number of osteoclasts associated to bone resorption was observed (16). To investigate bone resorption in *tmem38b* mutants both histomorphometric and molecular analyses were performed in regenerated caudal fins. Tartrate resistant acid phosphatase (TRAP) staining revealed a significant reduction in the number of TRAP+ cells in the 5 dpa *tmem38b*$^{-/-}$ regenerated caudal fin compared to WT. Interestingly, a strong TRAP staining signal was detected at the amputation plane and in the region corresponding to the new forming rays in *tmem38b*$^{\Delta 120\text{-}7/\Delta 120\text{-}7}$. On the contrary of WT and *tmem38b*$^{-/-}$, no signal was evident in the distal tip of the fin (Figure 6A). Nevertheless, *tmem38b*$^{\Delta 120\text{-}7/\Delta 120\text{-}7}$ and WT had similar number of TRAP+ cells.

No difference in the expression of the main osteoclast markers, *acp5a* (encoding for Trap), *ctsk* and in the ratio *rankl/opg* was detected in both mutants compared to WT (Figure 6B). An increased expression of the macrophage marker *mpeg1* was detected in *tmem38b*$^{\Delta 120\text{-}7/\Delta 120\text{-}7}$ respect to WT at 5 dpa, suggesting the presence of high number of osteoclast precursors (Figure 6B).

3.7 Actinotrichia formation is impaired in *tmem38b* mutants

Actinotrichia, spear-like structures made of collagen I, collagen II and actinodins 1 and 2 proteins located at the tip of each caudal fin ray, play a morphogenetic role in fin formation, representing a guide for osteoblasts distal migration although synthesized by different cell types, probably basal keratinocytes (27, 38, 39). Upon Picro Sirius Red staining of caudal fins WT and *tmem38b* actinotrichia number and length were evaluated. Polarized light microscopy demonstrated a reduced length of actinotrichia in both mutants compared to WT and limited to *tmem38b*$^{-/-}$ also a significant reduction in their number (Figure 6C).

4 Discussion

The present study demonstrates, for the first time to the best of our knowledge, the relevance of Tric-b in zebrafish bone during development and bone cells differentiation, providing further insight on the relevance of this channel for the skeleton and supporting a shared role between teleosts and mammals. Both *in silico* and *in vivo* approaches were applied.

4.1 Trics are conserved in zebrafish

The retention of trimeric intracellular cation-specific channels TRIC-A and TRIC-B in archaea, bacteria and eukaryotes underlines their relevance in the animal kingdom, and their high level of homology throughout species supports a common phylogenetic origin (40). Indeed, the synteny analysis performed around zebrafish *tmem38a* and *tmem38b loci* demonstrated the presence of conserved synteny blocks shared with *M. musculus* and *H. sapiens*. The identity is higher for TRIC-A than for TRIC-B, nevertheless, in

10.3389/fendo.2023.1002914

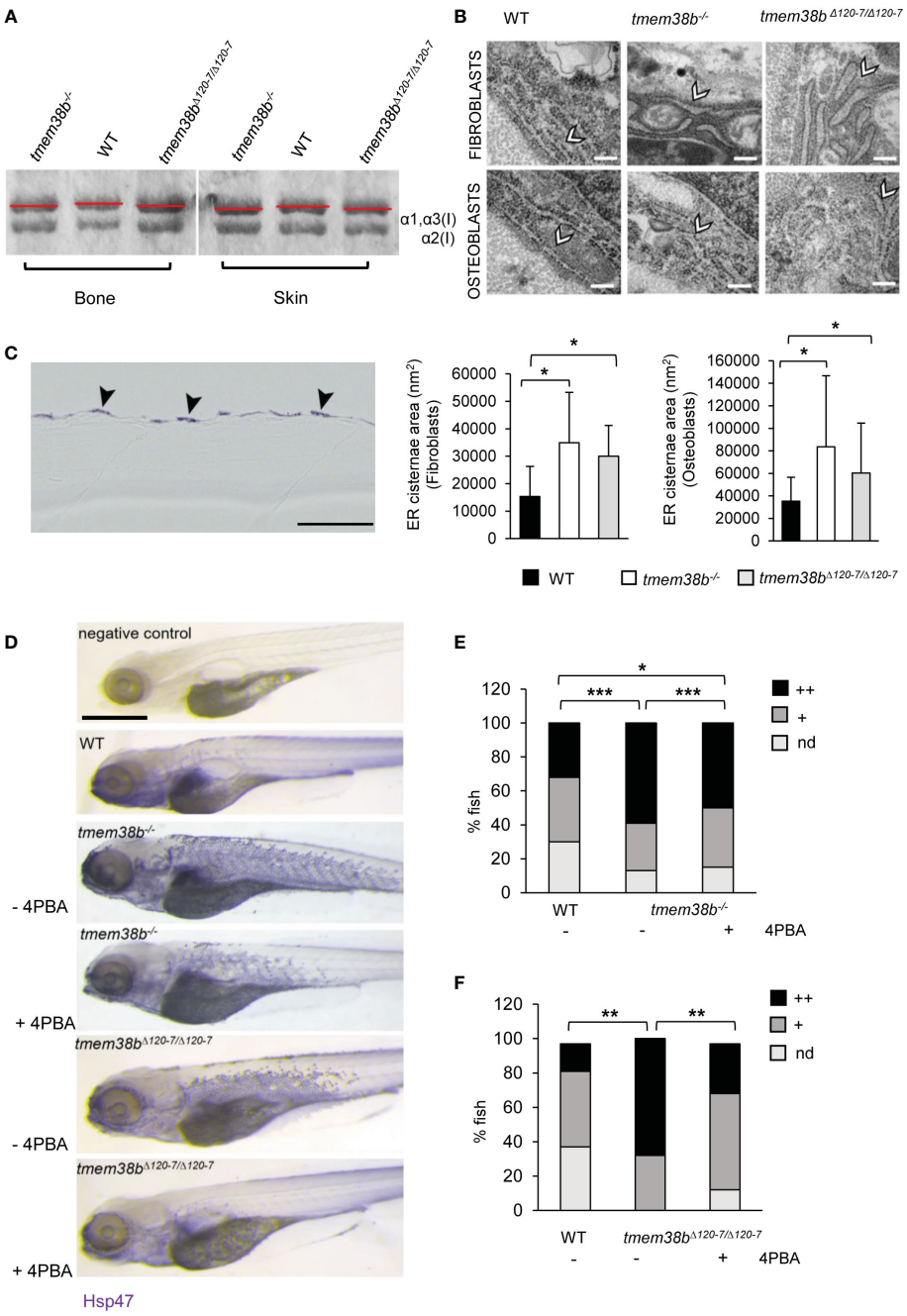

FIGURE 4
Collagen type I and ultrastructural analysis. **(A)** Representative Coomassie stained SDS-Urea-PAGE of collagen type I extracted from WT (n = 2) and mutants (*tmem38b*$^{-/-}$ n = 2; *tmem38b*$^{\Delta 120\text{-}7/\Delta 120\text{-}7}$ n = 2) bone and skin. Mutants' collagen α bands presented a slight faster migration compared to WT as highlighted by red lines. **(B)** Transmission electron microscopy images of 1 mpf WT (n = 3), *tmem38b*$^{-/-}$ (n = 3), and *tmem38b*$^{\Delta 120\text{-}7/\Delta 120\text{-}7}$ (n = 3) fibroblasts and osteoblasts at the vertebral endplate. ER cisternae enlargement was evident in mutants (arrowheads). Magnification 80000x. Scale bar: 200 nm. The ER cisternae area quantitation is shown in the graphs (bottom). **(C)** Immunohistochemistry of 5 dpf WT and *tmem38b*$^{-/-}$ with Hsp47b antibody. High magnification details of the skin of WT and *tmem38b*$^{-/-}$ following immunostaining with Hsp47b antibody revaled that Hsp47 signal was located in the fibroblasts of the skin (arrowheads). **(D)** Representative images of 5 dpf fish after whole mount immunohistochemistry with Hsp47b antibody, before and after 4PBA administration. Scale bar: 500 µm. **(E)** Analysis of Hsp47b expression by whole mount immunohistochemistry in WT and in *tmem38b*$^{-/-}$ before and after 4PBA administration. A significant increase of Hsp47 signal was detected in *tmem38*$^{-/-}$ compared to WT. 4PBA treatment significantly reduced the Hsp47b signal in *tmem38b*$^{-/-}$ compared to untreated mutant fish without reaching WT value (WT n = 146 and *tmem38b*$^{-/-}$ n = 116 untreated and 4PBA treated *tmem38b*$^{-/-}$ n = 113). **(F)** Analysis of Hsp47b expression by whole mount immunohistochemistry in WT and in *tmem38b*$^{\Delta 120\text{-}7/\Delta 120\text{-}7}$ before and after 4PBA administration. A significant increase of Hsp47 signal was present in *tmem38b*$^{\Delta 120\text{-}7/\Delta 120\text{-}7}$ compared to WT. 4PBA treatment significantly reduced the Hsp47b signal in *tmem38b*$^{\Delta 120\text{-}7/\Delta 120\text{-}7}$ compared to untreated mutant fish reaching WT value (WT n = 43 and *tmem38b*$^{\Delta 120\text{-}7/\Delta 120\text{-}7}$ n = 19 untreated and 4PBA treated *tmem38b*$^{\Delta 120\text{-}7/\Delta 120\text{-}7}$ n = 34). Zero (nd), low (+) and high (++) indicate the intensity of the signal. *p < 0.05, **p ≤ 0.01, ***p ≤ 0.001.

10.3389/fendo.2023.1002914

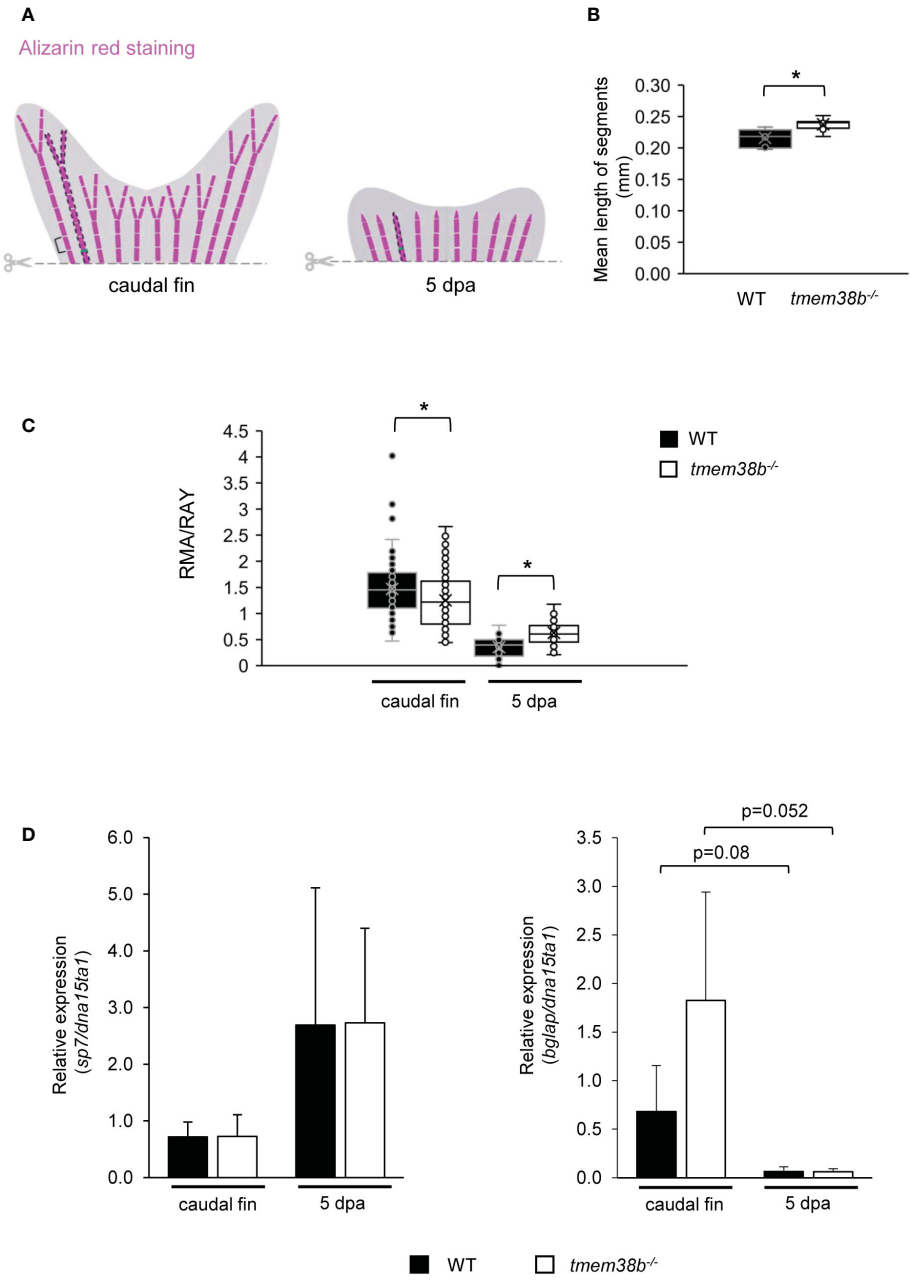

FIGURE 5
Morphometric and bone mineralization analyses during caudal fin regeneration in WT and *tmem38b*$^{-/-}$ mutants. **(A)** Schematic representation of morphometric measurements. Brackets indicate the length of fin ray segment, dashed areas represent the real mineralized areas (RMA) and the green lines indicate the ray widths (RAY). **(B)** The mean length of caudal fin ray segments was evaluated. Segments were significantly longer in *tmem38b*$^{-/-}$ compared to WT. **(C)** The ratio between the real mineralized area (RMA) and the mean ray width (RAY) was measured on alizarin red stained caudal fins to assess mineralization level. *tmem38b*$^{-/-}$ caudal fin was less mineralized respect to the WT. After 5 dpa, the regenerated mineralized area was larger in *tmem38b*$^{-/-}$ respect to the WT (WT n $\geq$ 9, *tmem38b*$^{-/-}$ n $\geq$ 8) *p < 0.05. **(D)** Relative expression of the early (*sp7*) and late (*bglap*) osteoblastic markers in WT and *tmem38b*$^{-/-}$ caudal fins in amputated and 5 dpa (WT n = 3, *tmem38b*$^{-/-}$ n = 3) samples. No significant difference was detected in *sp7* and *bglap* expression between WT and *tmem38b*$^{-/-}$ at both time points, even if a trend towards higher value was evident for *bglap* in mutant caudal fins with respect to controls. Data are shown as mean $\pm$ SEM.

each protomer all the critical amino acids necessary for pore formation and for protomer association into the homotrimeric channels are present (33). In particular, zebrafish Tric sequence contains the glycine rich domains, responsible for the intramembrane kinks interacting with diacylglycerol in the transmembrane helices (TM) 2 and 5 and the voltage sensing domain in TM4, where also the K129 gating residue, corresponding to K125 in *H. sapiens* and *M. musculus*, is conserved.

TRICs function in prokaryotes is still unclear, whereas in eukaryotes their localization as integral membrane protein of the sarcoplasmic/endoplasmic reticulum (SR/ER) and their specificity for monovalent cations, in particular potassium, support their function as counter ion channels contributing to maintain the SR/ER membrane electro-neutrality following calcium release. Indeed, *in vitro* and *in vivo* studies in human and murine cells, confirmed an impaired SR/ER calcium release in their absence (6, 8, 17, 41).

10.3389/fendo.2023.1002914

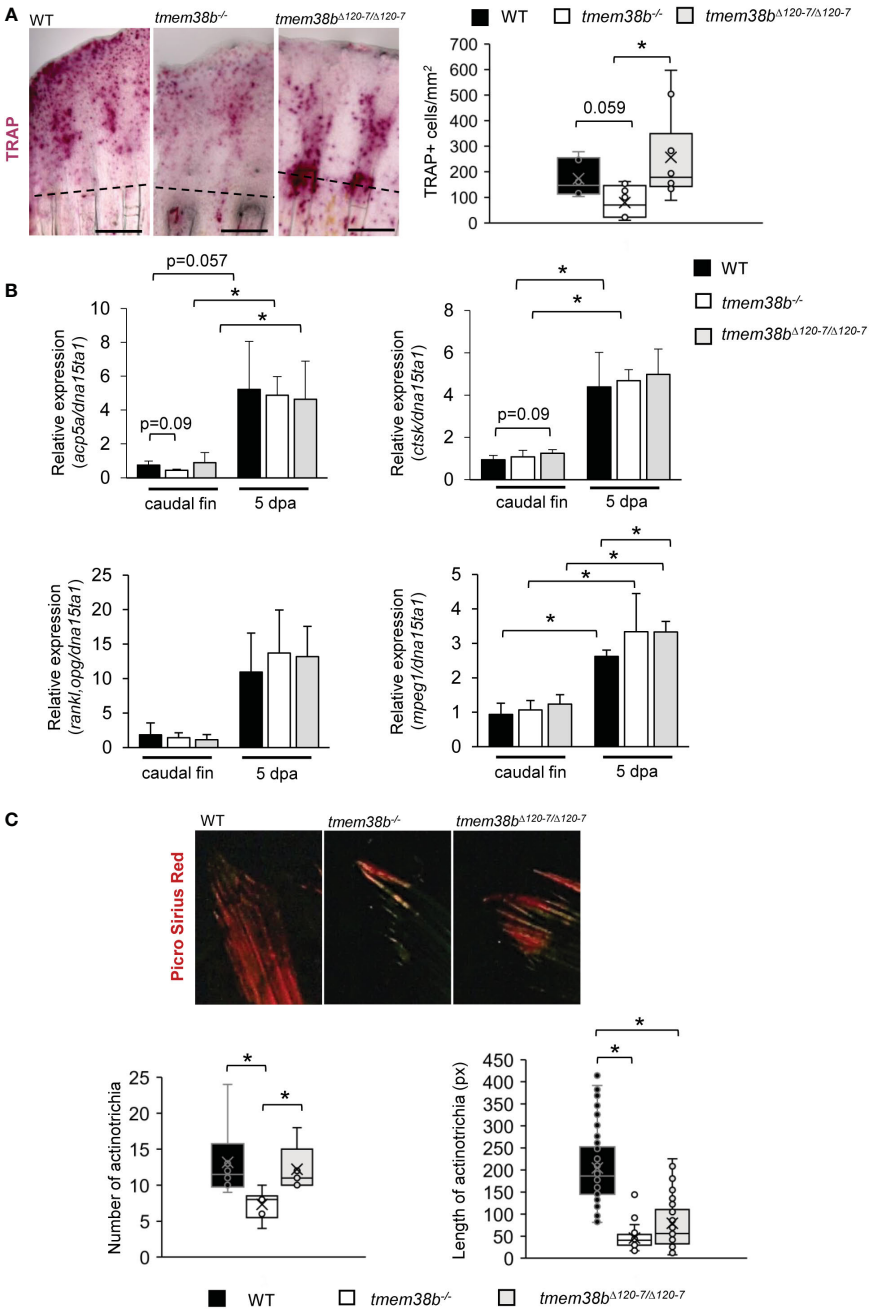

FIGURE 6
Osteoclast analysis during caudal fin regeneration in *tmem38b* mutants. **(A)** Representative images of TRAP staining of caudal fins of WT and *tmem38b* mutants at 5 dpa (WT n = 7, *tmem38b*$^{-/-}$ n = 9, *tmem38b*$^{\Delta 120\text{-}7/\Delta 120\text{-}7}$ n = 10). In WT, osteoclasts were present in the regenerate. Almost no TRAP activity could be detected in *tmem38b*$^{-/-}$, while in *tmem38b*$^{\Delta 120\text{-}7/\Delta 120\text{-}7}$ it seemed to be mostly localized along the regenerating fin rays. TRAP+ cells were significantly reduced in *tmem38b*$^{-/-}$ respect to the other two groups. **(B)** Relative expression of bone resorption-related markers *acp5a* and *ctsk*, of the macrophage marker *mpeg1* and *rankl*/*opg* ratio in amputated and 5 dpa caudal fin (WT n = 3, *tmem38b*$^{-/-}$ n = 3, *tmem38b*$^{\Delta 120\text{-}7/\Delta 120\text{-}7}$ n = 3). All markers were increased after amputation. *mpeg1* was significantly overexpressed in *tmem38b*$^{\Delta 120\text{-}7/\Delta 120\text{-}7}$ compared to WT at 5 dpa.*: p < 0.05. **(C)** Representative images of picro sirius red staining of actinotrichia in caudal fins of WT and *tmem38b* mutants (WT n = 3, *tmem38b*$^{-/-}$ n = 3, *tmem38b*$^{\Delta 120\text{-}7/\Delta 120\text{-}7}$ n = 3). *tmem38b*$^{-/-}$ revealed a reduced number of actinotrichia respect to WT and *tmem38b*$^{\Delta 120\text{-}7/\Delta 120\text{-}7}$, while the length of actinotrichia was reduced in both mutants compared to WT. *p < 0.05.

Of note, both in invertebrates and in vertebrates, after sperm fertilization Ca^{2+} waves regulate the polarization of cytoplasmic domains in oocytes and drive early embryo patterning and subsequent development (42–46). This early event depends largely on maternal gene products (47). The calcium responsible for egg activation originates from intracellular storage, mainly the endoplasmic reticulum, through the activity of phospholipase C (PLC) and inositol-tris-phosphate (IP3) (45, 48), the specific ligand allowing the opening of the inositol 3 phosphate receptor (IP3R) ER calcium channel. Between the TRIC channel subtypes, TRIC-A and TRIC-B, is the latter, ubiquitously distributed, that is coupled with IP3R, whereas TRIC-A, most abundantly present in excitable cells, is coupled with ryanodine receptors (RyRs) (2). We first demonstrated that in zebrafish both channels are expressed at early developmental

stages, but only *tmem38b* had a maternal expression, supporting its association with IP3R also in teleosts and its relevance during the first stage of embryo formation. On the contrary, *tmem38a* RNA was detectable only starting from 24 hpf at the appearance of somites, thus confirming the previous study on single-cell gene mapping expression (49), and in adult was present in all excitable and not-excitable analyzed tissue. As in mammals, the highest level of *tmem38a* mRNA in zebrafish is in skeletal muscle, but it is also expressed in bone (1, 50).

4.2 Tric-b is necessary in zebrafish for proper bone formation during fast growth developmental stages

In 2014, the identification of *TMEM38B* loss-of-function mutations in individuals affected by the recessive form of osteogenesis imperfecta (OI) type XIV demonstrated an unexpected and relevant role for the ER ion channel TRIC-B in mammalian bone homeostasis (8). Similarly, *Tmem38b* knock out mouse showed bone defects, even if mutant mice are perinatally lethal due to impairment in surfactant production, making difficult to characterize the murine skeletal outcome and its molecular basis (8).

Taking into account the high TRIC-B homology in teleosts and mammals and the suitability of zebrafish as a model for dominant and recessive OI forms (23, 25, 51), we targeted zebrafish *tmem38b* by CRISPR/Cas9 both to understand the role of Tric-b in *D. rerio* and to generate the first teleost model for the human disease. Two mutants were created and deeply characterized, the first one carrying a frameshift mutation (*tmem38b*$^{-/-}$) associated to the insertion of pre-termination codon and the second carrying a 24 bp *in frame* deletion causing the removal of a consensus sequence relevant for channel activity in the voltage-sensing TM4 domain (*tmem38b*$^{\Delta 120\text{-}7/\Delta 120\text{-}7}$). The highly conserved K122 and R126 amino acids are also lost in this model. On the other hand, the K129 residue with a relevant role in gating Tric channels is kept in *tmem38b*$^{\Delta 120\text{-}7/\Delta 120\text{-}7}$ leaving open the possibility of a residual activity for the translated protein.

The activation of nonsense mediated mRNA decay (NMD) of mutant mRNA, a process generally associated to the insertion of a premature stop codon, was proved in *tmem38b*$^{-/-}$, and absent in *tmem38b*$^{\Delta 120\text{-}7/\Delta 120\text{-}7}$. Interestingly, *tmem38b*$^{-/-}$ NMD was tissue dependent with a mean value of 69% in excitable tissues (muscle, brain, heart) and of 75% in non-excitable tissues (bone and swim-bladder). Tissue specific NMD was previously described in murine models and could indeed be relevant for understanding the genotype-phenotype relationship and the severity in heritable diseases (52, 53). Of note, NMD in bone was below 50% supporting the possibility of a certain level of translation of the truncated protein.

Unfortunately, despite the multiple attempts, in none of the models the protein expression could be evaluated due to the lack of specific antibody.

No compensatory effect of the *tmem38a* transcript was observed during early stage of development (24 hpf) in mutants compared to WT. Moreover, the increase of *tmem38a* expression (≥ 1.8 fold) detected in bone and muscle of *tmem38b*$^{\Delta 120\text{-}7/\Delta 120\text{-}7}$ during adulthood did not reach significant value.

Fish standard length and vertebrae size evaluated at several developmental stages were reduced in *tmem38b*$^{-/-}$ only at 21 dpf and 1 mpf. These time points overlap with the larval to juvenile transition that is associated to quick and significant body growth (24), likely demanding Tric-b activity and thus supporting a relevant role of *tmem38b* for early bone development rather than for adult skeletal homeostasis. Indeed, active skeletal growth implies a strong osteoblast activity and thus collagen synthesis and secretion, which indeed have been demonstrated to be altered in *TMEM38B* knock out human and mice cells (8, 17). Nevertheless, no difference in BFR was detectable between *tmem38b*$^{-/-}$ and WT from 10 dpf to 1mpf. *Tmem38b*$^{-/-}$ body length and vertebral size reach and maintain WT values in adult, in agreement with the reduced fracture frequency and bone properties amelioration after puberty described in OI patients (9, 54, 55). The skeletal phenotype in *tmem38b*$^{\Delta 120\text{-}7/\Delta 120\text{-}7}$, limited to reduced vertebral length at 21 dpf, supported a translation and likely a partial activity of Tric-b in the model and let us to hypothesize that a full active channel is necessary for proper bone formation.

Tmem38b$^{-/-}$ and *tmem38b*$^{\Delta 120\text{-}7/\Delta 120\text{-}7}$geometrical and material bone properties revealed by microCT and nanoindentation analysis at vertebral sites were in the normal range, but it should be taken into account that the very small zebrafish size at younger stages did not allow us, due to technical limitations, to evaluate bone properties at 21 dpf and 1 mpf, when differences in length and vertebral size were detectable.

4.3 Tric-b is required for proper swim bladder inflation

Fish swim bladder originates from the foregut endoderm, representing an evolutionary similarity with human lungs and, in addition, the presence of collagen type I was described at least in seabass (*Lates calcarifer*) (56). Mutations in *TMEM38B* are associated with pulmonary dysfunction both in OI type XIV individuals and in the *Tric-B* knock out mouse model, which dies immediately after birth due to respiratory failure (8, 16). Interestingly, *tmem38b*$^{-/-}$ revealed a delay in the inflation of the second lobe of the swim bladder in 21 dpf larvae compared to WT supporting Tric-b requirement for proper organ development, even if its direct role as potassium channel or indirect activity in collagen I synthesis are still unclear. A delayed swim bladder inflation was already described in the recessive OI type VII and VIII zebrafish models, carrying loss-of-function mutations in *crtap* and *p3h1*, respectively (25) and the complete lack of swim bladder inflation was reported in *col1a1a*$^{-/-}$ (51) proving that a normal amount and/or structure of collagen I in its extracellular matrix is necessary for proper swim bladder inflation. The lack of swim bladder defect in *tmem38b*$^{\Delta 120\text{-}7/\Delta 120\text{-}7}$ further supports in the model the presence of a translated and partial active Tric-b, pointing to its requirement for fish development.

4.4 Tric-b plays a role in dermal exoskeletal appendices

Histomorphometric analysis of caudal fin rays in adult mutants revealed a high variability in caudal fin ray segment length with an

overall significantly higher mean in *tmem38b*$^{-/-}$ compared to control and *tmem38b*$^{\Delta 120\text{-}7/\Delta 120\text{-}7}$. Fin ray segment length was associated to the conductance activity of Kcnk5b, a plasma membrane potassium channel belonging to the two pore family of channels. Gain-of-function mutations in *kcnk5b* are responsible for the *another longfin* (*alf*) zebrafish phenotype characterized by increased fin ray segment length (57). The hyperpolarization of the membrane consequent to these mutations represents a proof of the relevance of bioelectric signals not only in excitable tissues, but also for development and physiology in the non-excitable ones. Similarly to *tmem38b*$^{-/-}$, the *kcnk5b* mutants are viable and fertile. Interestingly, the activity of Kcnk5b is modulated by calcineurin that acts as channel inhibitor by binding to the cytosolic C-terminal end of the channel (58). Indeed, treatment of WT zebrafish with the calcineurin inhibitor FK506 well reproduces the *alf* phenotype (59). Calcineurin is a calcium dependent protein, whose activity is strongly dependent from intracellular calcium concentration (60). In mammals, the absence of TRIC-B, acting as counter ion for calcium flux from the ER, has been reported to decrease the calcium cytosolic concentration (17), thus the longer *tmem38b*$^{-/-}$ fin ray segments may indeed be the natural consequence of that, supporting a shared role of Tric-b between mammals and teleosts.

In *alf* mutants the longer segments are associated to an overall increase of caudal fin length whereas in *tmem38b*$^{-/-}$ mutant caudal fin size is within normal values (data not shown). Nevertheless, in *tmem38b* mutants a reduced length of actinotrichia is reported, and in *tmem38b*$^{-/-}$ also the number is reduced indicating that either reduction or lack of Tric-b impair their formation. The actinotrichia are spear-like structures containing collagen I located at the tip of each caudal fin ray (27). Fins grow through sequential addition of lepidotrichial segments at their distal tip *via* migration of mesenchymal cells along the actinotrichia, clusters of collagenous fibers that emerge from the tip of each lepidotrichium (61, 62). Thus, reduced length/number of actinotrichia could indeed negatively affect tail growth counteracting the longer segments.

4.5 Tric-b plays a role in osteoblasts differentiation

To address the effect of the absence of *tmem38b* on bone cells differentiation, caudal fin regeneration, a well-organized process that partially recapitulates the events occurring during bone development, was employed. The similar expression of *sp7* both in the amputated samples and 5 dpa regenerates in mutants and controls suggested that the reduced ray mineralization detected in *tmem38b*$^{-/-}$ caudal fin compared to WT was not a consequence of impairments on osteoblast de- and early re-differentiation. The overexpression of *bglap*, previously described in OI type XIV cultured primary osteoblasts as well as in the *TMEM38B* knock out human foetal osteoblasts (hFOB), may be related to the inhibition of hydroxyapatite crystal growth (16, 63) and could indeed explain the reduced alizarin red staining of caudal fin in the amputates samples. Less clear is the increased mineralization during early regeneration phase, suggesting an accumulation of minerals during bone modelling that could be due either to an impaired cellular function or to an increased inter-fibrillar spacing that undergoes remodelling during growth.

The effect of *tmem38b* targeting on osteoclasts (OCs) was also addressed using the amputation assay since osteoclasts are involved in zebrafish fin ray healing at the amputation site as well as at newly regenerated rays (28).

In *tmem38b*$^{-/-}$ mutant zebrafish Trap+ cells number was reduced compared to WT in presence of normal Rankl/Opg ratio resembling human and murine data (8, 16) and supporting a direct effect of Tric-b on osteoclast activity.

Of particular interest, in *tmem38b*$^{\Delta 120\text{-}7/\Delta 120\text{-}7}$ Trap+ cell number was unchanged compared to control, but their distribution was more abundant at the amputation site and along the neo-synthesized ray segment.

TRAP is an iron-containing enzyme expressed both in bone resorbing cells and in macrophages, that are one of the source of OCs (64). The increased expression of the macrophage marker *mpeg1* in *tmem38b*$^{\Delta 120\text{-}7/\Delta 120\text{-}7}$ compared to WT suggested that the Trap staining could indeed be due to immature OCs, possibly associated to a low level of anyway active mutant Tric-b (65).

4.6 Tric-b is necessary for zebrafish fibroblast and osteoblast homeostasis

Collagen type I extracted from bone and skin of both *tmem38b* zebrafish mutants showed a slightly faster electrophoretic migration resembling the pattern described for collagen type I synthesized by OI type XIV human fibroblasts and osteoblasts, for which a reduced lysine hydroxylation in the triple helical domain was demonstrated (16, 17). Thus, at a cellular level homozygosity for both mutant alleles affects collagen synthesis suggesting a need for a certain threshold of Tric-b conductance to guarantee proper cell homeostasis and that the mutant *in frame* protein likely conserves only a limited activity, sufficient for bone maintenance, but not enough for cell functionality. In human and murine OI *tmem38b* knock-out cells the collagen was mainly intracellularly retained causing severe matrix insufficiency. Interestingly, collagen extracellular deposition was also impaired in both zebrafish mutants in which reduced actinotrichia length was evident upon Picro Sirius red staining. A relevant role of lysine hydroxylase 1 in actinotrichia collagen post-translational modification was demonstrated in zebrafish using a knock down morpholino approach. Indeed, *lh1* morphants showed a dorsal curled tail phenotype, no actinotrichia development and defective formation of the fin fold (27). Since calcium regulates several post translational modifiers enzymes, including LH1, the correlation between defects in *TMEM38B* and impaired collagen folding already proposed by Cabral et al. (17) seems to hold up also in teleosts.

The mutant collagen retained inside the cells is responsible of enlarged ER cisternae in both zebrafish mutants and OI human and mouse cells. In *tmem38b*$^{-/-}$ and *tmem38b*$^{\Delta 120\text{-}7/\Delta 120\text{-}7}$ the upregulation of Hsp47 confirms impaired collagen secretion. Importantly, using the zebrafish models we demonstrated that the treatment with 4PBA partially rescues Hsp47 overexpression supporting its possible role as OI treatment also for OI type XIV as already demonstrated both *in vitro* and *in vivo* for dominant and some recessive OI forms (23, 35).

Data availability statement

The original contributions presented in the study are included in the article/Supplementary Material. Further inquiries can be directed to the corresponding author.

Ethics statement

The animal study was reviewed and approved by Italian Ministery of Health.

Author contributions

Conceptualization: AF, FT, LL, VD. Methodology: AF, FT, LL, VD, RG, SC, IAKF, DL, SV. Validation: FT, LL, VD, SC, IAKF. Formal analysis: AF, FT,VD, PEW, AW, PC. Resources: AF. Data curation: AF, FT, VD. Writing - original draft: AF, FT, VD, LL. Writing - review and editing: AF, FT, VD, LL, SC, IAKF, AW, PC, BB, RB, SV, AR. Supervision: AF. Project administration: AF. Funding acquisition: AF. All authors contributed to the article and approved the submitted version.

Funding

This research was funded by a Grant of the Italian Ministry of Education, University and Research (MIUR) to the Department of Molecular Medicine of the University of Pavia under the initiative "Dipartimenti di Eccellenza (2018–2022)" and Telethon Exploratory Grant GEP15066 to AF. The funders had no role in study design, data collection and analysis, decision to publish, or preparation of the manuscript.

Acknowledgments

We thank the animal facility "Centro di servizio per la gestione unificata delle attività di stabulazione e di radiobiologia" of the University of Pavia, Pavia, Italy to host the animals; the OPBA of the University of Pavia for supporting in animal protocol drawing up. We thank Dr Gabriella Nicoletta Giannini for initial *tmem38b* mutants characterization.

Conflict of interest

The authors declare that the research was conducted in the absence of any commercial or financial relationships that could be construed as a potential conflict of interest.

Publisher's note

Supplementary material

The Supplementary Material for this article can be found online at: https://www.frontiersin.org/articles/10.3389/fendo.2023.1002914/full#supplementary-material

References

1. Yazawa M, Ferrante C, Feng J, Mio K, Ogura T, Zhang M, et al. TRIC channels are essential for Ca2+ handling in intracellular stores. *Nature* (2007) 448(7149):78–82. doi: 10.1038/nature05928

2. Zhou X, Lin P, Yamazaki D, Park KH, Komazaki S, Chen SR, et al. Trimeric intracellular cation channels and sarcoplasmic/endoplasmic reticulum calcium homeostasis. *Circ Res* (2014) 114(4):706–16. doi: 10.1161/CIRCRESAHA.114.301816

3. Berridge MJ, Bootman MD, Roderick HL. Calcium signalling: dynamics, homeostasis and remodelling. *Nat Rev Mol Cell Biol* (2003) 4(7):517–29. doi: 10.1038/nrm1155

4. Marchi S, Patergnani S, Missiroli S, Morciano G, Rimessi A, Wieckowski MR, et al. Mitochondrial and endoplasmic reticulum calcium homeostasis and cell death. *Cell Calcium* (2018) 69:62–72. doi: 10.1016/j.ceca.2017.05.003

5. Yamazaki D, Tabara Y, Kita S, Hanada H, Komazaki S, Naitou D, et al. TRIC-a channels in vascular smooth muscle contribute to blood pressure maintenance. *Cell Metab* (2011) 14(2):231–41. doi: 10.1016/j.cmet.2011.05.011

6. Zhao X, Yamazaki D, Park KH, Komazaki S, Tjondrokoesoemo A, Nishi M, et al. Ca2+ overload and sarcoplasmic reticulum instability in tric-a null skeletal muscle. *J Biol Chem* (2010) 285(48):37370–6. doi: 10.1074/jbc.M110.170084

7. Yamazaki D, Komazaki S, Nakanishi H, Mishima A, Nishi M, Yazawa M, et al. Essential role of the TRIC-b channel in Ca2+ handling of alveolar epithelial cells and in perinatal lung maturation. *Development* (2009) 136(14):2355–61. doi: 10.1242/dev.036798

8. Zhao C, Ichimura A, Qian N, Iida T, Yamazaki D, Noma N, et al. Mice lacking the intracellular cation channel TRIC-b have compromised collagen production and impaired bone mineralization. *Sci Signal* (2016) 9(428):ra49. doi: 10.1126/scisignal.aad9055

9. Shaheen R, Alazami AM, Alshammari MJ, Faqeih E, Alhashmi N, Mousa N, et al. Study of autosomal recessive osteogenesis imperfecta in Arabia reveals a novel locus defined by TMEM38B mutation. *J Med Genet* (2012) 49(10):630–5. doi: 10.1136/jmedgenet-2012-101142

10. Garibaldi N, Besio R, Dalgleish R, Villani S, Barnes AM, Marini JC, et al. Dissecting the phenotypic variability of osteogenesis imperfecta. *Dis Model Mech* (2022) 15(5). doi: 10.1242/dmm.049398

11. Lv F, Xu XJ, Wang JY, Liu Y, Asan, Wang JW, et al. Two novel mutations in TMEM38B result in rare autosomal recessive osteogenesis imperfecta. *J Hum Genet* (2016) 61(6):539–45. doi: 10.1038/jhg.2016.11

12. Coe H, Michalak M. Calcium binding chaperones of the endoplasmic reticulum. *Gen Physiol Biophys* (2009) 28:F96–F103.

13. Ishikawa Y, Bächinger HP. A molecular ensemble in the rER for procollagen maturation. *Biochim Biophys Acta* (2013) 1833(11):2479–91. doi: 10.1016/j.bbamcr.2013.04.008

14. Perdivara I, Perera L, Sricholpech M, Terajima M, Pleshko N, Yamauchi M, et al. Unusual fragmentation pathways in collagen glycopeptides. *J Am Soc Mass Spectrom* (2013) 24(7):1072–81. doi: 10.1007/s13361-013-0624-y

15. Marini JC, Forlino A, Bächinger HP, Bishop NJ, Byers PH, Paepe A, et al. Osteogenesis imperfecta. *Nat Rev Dis Primers* (2017) 3:17052. doi: 10.1038/nrdp.2017.52

16. Webb EA, Balasubramanian M, Fratzl-Zelman N, Cabral WA, Titheradge H, Alsaedi A, et al. Phenotypic spectrum in osteogenesis imperfecta due to mutations in

TMEM38B: Unraveling a complex cellular defect. *J Clin Endocrinol Metab* (2017) 102 (6):2019–28. doi: 10.1210/jc.2016-3766

17. Cabral WA, Ishikawa M, Garten M, Makareeva EN, Sargent BM, Weis M, et al. Absence of the ER cation channel TMEM38B/TRIC-b disrupts intracellular calcium homeostasis and dysregulates collagen synthesis in recessive osteogenesis imperfecta. *PloS Genet* (2016) 12(7):e1006156. doi: 10.1371/journal.pgen.1006156

18. Fujisawa R, Tamura M. Acidic bone matrix proteins and their roles in calcification. *Front Biosci (Landmark Ed)* (2012) 17(5):1891–903. doi: 10.2741/4026

19. Leoni L, Tonelli F, Besio R, Gioia R, Moccia F, Rossi A, et al. Knocking out TMEM38B in human foetal osteoblasts hFOB 1.19 by CRISPR/Cas9: A model for recessive OI type XIV. *PloS One* (2021) 16(9):e0257254. doi: 10.1371/journal.pone.0257254

20. Tonelli F, Bek JW, Besio R, De Clercq A, Leoni L, Salmon P, et al. Zebrafish: A resourceful vertebrate model to investigate skeletal disorders. *Front Endocrinol (Lausanne)* (2020) 11:489. doi: 10.3389/fendo.2020.00489

21. Thisse C, Thisse B. High-resolution *in situ* hybridization to whole-mount zebrafish embryos. *Nat Protoc* (2008) 3(1):59–69. doi: 10.1038/nprot.2007.514

22. Vanhauwaert S, Van Peer G, Rihani A, Janssens E, Rondou P, Lefever S, et al. Expressed repeat elements improve RT-qPCR normalization across a wide range of zebrafish gene expression studies. *PloS One* (2014) 9(10):e109091. doi: 10.1371/journal.pone.0109091

23. Gioia R, Tonelli F, Ceppi I, Biggiogera M, Leikin S, Fisher S, et al. The chaperone activity of 4PBA ameliorates the skeletal phenotype of chihuahua, a zebrafish model for dominant osteogenesis imperfecta. *Hum Mol Genet* (2017) 26(15):2897–911. doi: 10.1093/hmg/ddx171

24. Parichy DM, Elizondo MR, Mills MG, Gordon TN, Engeszer RE. Normal table of postembryonic zebrafish development: staging by externally visible anatomy of the living fish. *Dev Dyn* (2009) 238(12):2975–3015. doi: 10.1002/dvdy.22113

25. Tonelli F, Cotti S, Leoni L, Besio R, Gioia R, Marchese L, et al. Crtap and p3h1 knock out zebrafish support defective collagen chaperoning as the cause of their osteogenesis imperfecta phenotype. *Matrix Biol* (2020) 90:40–60. doi: 10.1016/j.matbio.2020.03.004

26. Cardeira J, Gavaia PJ, Fernández I, Cengiz IF, Moreira-Silva J, Oliveira JM, et al. Quantitative assessment of the regenerative and mineralogenic performances of the zebrafish caudal fin. *Sci Rep* (2016) 6:39191. doi: 10.1038/srep39191

27. Durán I, Marí-Beffa M, Santamaría JA, Becerra J, Santos-Ruiz L. Actinotrichia collagens and their role in fin formation. *Dev Biol* (2011) 354(1):160–72. doi: 10.1016/j.ydbio.2011.03.014

28. Blum N, Begemann G. Osteoblast de- and redifferentiation are controlled by a dynamic response to retinoic acid during zebrafish fin regeneration. *Development* (2015) 142(17):2894–903. doi: 10.1242/dev.120204

29. Geurtzen K, Vernet A, Freidin A, Rauner M, Hofbauer LC, Schneider JE, et al. Immune suppressive and bone inhibitory effects of prednisolone in growing and regenerating zebrafish tissues. *J Bone Miner Res* (2017) 32(12):2476–88. doi: 10.1002/jbmr.3231

30. Huysseune A, Soenens M, Sire JY, Witten PE. High-resolution histology for craniofacial studies on zebrafish and other teleost models. *Methods Mol Biol* (2022) 2403:249–62. doi: 10.1007/978-1-0716-1847-9_17

31. Verstraeten B, Sanders E, Huysseune A. Whole mount immunohistochemistry and *in situ* hybridization of larval and adult zebrafish dental tissues. *Methods Mol Biol* (2012) 887:179–91. doi: 10.1007/978-1-61779-860-3_16

32. Yang H, Hu M, Guo J, Ou X, Cai T, Liu Z. Pore architecture of TRIC channels and insights into their gating mechanism. *Nature* (2016) 538(7626):537–41. doi: 10.1038/nature19767

33. Wang XH, Su M, Gao F, Xie W, Zeng Y, Li DL, et al. Structural basis for activity of TRIC counter-ion channels in calcium release. *Proc Natl Acad Sci U S A* (2019) 116 (10):4238–43. doi: 10.1073/pnas.1817271116

34. Ito S, Nagata K. Biology of Hsp47 (Serpin H1), a collagen-specific molecular chaperone. *Semin Cell Dev Biol* (2017) 62:142–51. doi: 10.1016/j.semcdb.2016.11.005

35. Garibaldi N, Contento BM, Babini G, Morini J, Siciliani S, Biggiogera M, et al. Targeting cellular stress *in vitro* improves osteoblast homeostasis, matrix collagen content and mineralization in two murine models of osteogenesis imperfecta. *Matrix Biol* (2021) 98:1–20. doi: 10.1016/j.matbio.2021.03.001

36. Besio R, Garibaldi N, Leoni L, Cipolla L, Sabbioneda S, Biggiogera M, et al. Cellular stress due to impairment of collagen prolyl hydroxylation complex is rescued by the chaperone 4-phenylbutyrate. *Dis Model Mech* (2019) 12(6). doi: 10.1242/dmm.038521

37. Uveges TE, Collin-Osdoby P, Cabral WA, Ledgard F, Goldberg L, Bergwitz C, et al. Cellular mechanism of decreased bone in brtl mouse model of OI: imbalance of decreased osteoblast function and increased osteoclasts and their precursors. *J Bone Miner Res* (2008) 23(12):1983–94. doi: 10.1359/jbmr.080804

38. König D, Page L, Chassot B, Jaźwińska A. Dynamics of actinotrichia regeneration in the adult zebrafish fin. *Dev Biol* (2018) 433(2):416–32. doi: 10.1016/j.ydbio.2017.07.024

39. Kuroda J, Iwane AH, Kondo S. Roles of basal keratinocytes in actinotrichia formation. *Mech Dev* (2018) 153:54–63. doi: 10.1016/j.mod.2018.08.010

40. Silverio AL, Saier MH. Bioinformatic characterization of the trimeric intracellular cation-specific channel protein family. *J Membr Biol* (2011) 241(2):77–101. doi: 10.1007/s00232-011-9364-8

41. El-Ajouz S, Venturi E, Witschas K, Beech M, Wilson AD, Lindsay C, et al. Dampened activity of ryanodine receptor channels in mutant skeletal muscle lacking TRIC-a. *J Physiol* (2017) 595(14):4769–84. doi: 10.1113/JP273550

42. Fuentes R, Tajer B, Kobayashi M, Pelliccia JL, Langdon Y, Abrams EW, et al. The maternal coordinate system: Molecular-genetics of embryonic axis formation and patterning in the zebrafish. *Curr Top Dev Biol* (2020) 140:341–89. doi: 10.1016/bs.ctdb.2020.05.002

43. Whitaker M. Calcium at fertilization and in early development. *Physiol Rev* (2006) 86(1):25–88. doi: 10.1152/physrev.00023.2005

44. Charbonneau M, Moreau M, Picheral B, Vilain JP, Guerrier P. Fertilization of amphibian eggs: a comparison of electrical responses between anurans and urodeles. *Dev Biol* (1983) 98(2):304–18. doi: 10.1016/0012-1606(83)90361-5

45. Steinhardt RA, Epel D. Activation of sea-urchin eggs by a calcium ionophore. *Proc Natl Acad Sci U S A* (1974) 71(5):1915–9. doi: 10.1073/pnas.71.5.1915

46. Steinhardt RA, Epel D, Carroll EJ, Yanagimachi R. Is calcium ionophore a universal activator for unfertilised eggs? *Nature* (1974) 252(5478):41–3. doi: 10.1038/252041a0

47. Solnica-Krezel L. Maternal contributions to gastrulation in zebrafish. *Curr Top Dev Biol* (2020) 140:391–427. doi: 10.1016/bs.ctdb.2020.05.001

48. Crossley I, Swann K, Chambers E, Whitaker M. Activation of sea urchin eggs by inositol phosphates is independent of external calcium. *Biochem J* (1988) 252(1):257–62. doi: 10.1042/bj2520257

49. Wagner DE, Weinreb C, Collins ZM, Briggs JA, Megason SG, Klein AM. Single-cell mapping of gene expression landscapes and lineage in the zebrafish embryo. *Science* (2018) 360(6392):981–7. doi: 10.1126/science.aar4362

50. O'Brien F, Eberhardt D, Witschas K, El-Ajouz S, Iida T, Nishi M, et al. Enhanced activity of multiple TRIC-b channels: an endoplasmic reticulum/sarcoplasmic reticulum mechanism to boost counterion currents. *J Physiol* (2019) 597(10):2691–705. doi: 10.1113/JP277241

51. Gistelinck C, Kwon RY, Malfait F, Symoens S, Harris MP, Henke K, et al. Zebrafish type I collagen mutants faithfully recapitulate human type I collagenopathies. *Proc Natl Acad Sci U S A* (2018) 115(34):E8037–E46. doi: 10.1073/pnas.1722200115

52. Zetoune AB, Fontanière S, Magnin D, Anczuków O, Buisson M, Zhang CX, et al. Comparison of nonsense-mediated mRNA decay efficiency in various murine tissues. *BMC Genet* (2008) 9:83. doi: 10.1186/1471-2156-9-83

53. Bateman JF, Freddi S, Nattrass G, Savarirayan R. Tissue-specific RNA surveillance? nonsense-mediated mRNA decay causes collagen X haploinsufficiency in schmid metaphyseal chondrodysplasia cartilage. *Hum Mol Genet* (2003) 12(3):217–25. doi: 10.1093/hmg/ddg054

54. Ramzan K, Alotaibi M, Huma R, Afzal S. Detection of a recurrent TMEM38B gene deletion associated with recessive osteogenesis imperfecta. *Discov (Craiova)* (2021) 9(1): e124. doi: 10.15190/d.2021.3

55. Volodarsky M, Markus B, Cohen I, Staretz-Chacham O, Flusser H, Landau D, et al. A deletion mutation in TMEM38B associated with autosomal recessive osteogenesis imperfecta. *Hum Mutat* (2013) 34(4):582–6. doi: 10.1002/humu.22274

56. Sinthusamran S, Benjakul S, Kishimura H. Comparative study on molecular characteristics of acid soluble collagens from skin and swim bladder of seabass (Lates calcarifer). *Food Chem* (2013) 138(4):2435–41. doi: 10.1016/j.foodchem.2012.11.136

57. Perathoner S, Daane JM, Henrion U, Seebohm G, Higdon CW, Johnson SL, et al. Bioelectric signaling regulates size in zebrafish fins. *PloS Genet* (2014) 10(1):e1004080. doi: 10.1371/journal.pgen.1004080

58. Yi C, Spitters TW, Al-Far EAA, Wang S, Xiong T, Cai S, et al. A calcineurin-mediated scaling mechanism that controls a k+-leak channel to regulate morphogen and growth factor transcription. *Elife* (2021) 10. doi: 10.7554/eLife.60691

59. Daane JM, Lanni J, Rothenberg I, Seebohm G, Higdon CW, Johnson SL, et al. Bioelectric-calcineurin signaling module regulates allometric growth and size of the zebrafish fin. *Sci Rep* (2018) 8(1):10391. doi: 10.1038/s41598-018-28450-6

60. Creamer TP. Calcineurin. *Cell Commun Signal* (2020) 18(1):137. doi: 10.1186/s12964-020-00636-4

61. Goss RJ, Stagg MW. The regeneration of fins and fin rays in fundulus heteroclitus. *J Exp Zool* (1957) 136(3):487–507. doi: 10.1002/jez.1401360306

62. Haas HJ. Studies on mechanisms of joint and bone formation in the skeleton rays of fish fins. *Dev Biol* (1962) 5:1–34. doi: 10.1016/0012-1606(62)90002-7

63. Romberg RW, Werness PG, Riggs BL, Mann KG. Inhibition of hydroxyapatite crystal growth by bone-specific and other calcium-binding proteins. *Biochemistry* (1986) 25(5):1176–80. doi: 10.1021/bi00353a035

64. Hayman AR. Tartrate-resistant acid phosphatase (TRAP) and the osteoclast/immune cell dichotomy. *Autoimmunity* (2008) 41(3):218–23. doi: 10.1080/08916930701694667

65. Paredes LC, Olsen Saraiva Camara N, Braga TT. Understanding the metabolic profile of macrophages during the regenerative process in zebrafish. *Front Physiol* (2019) 10:617. doi: 10.3389/fphys.2019.00617

frontiers | Frontiers in Endocrinology

TYPE Original Research
PUBLISHED 09 February 2023
DOI 10.3389/fendo.2023.1120420

OPEN ACCESS

EDITED BY
Christoph Winkler,
National University of Singapore,
Singapore

REVIEWED BY
Hans-Martin Pogoda,
University of Cologne, Germany
Atsuki Nara,
Nagahama Institute of Bio-Science
and Technology, Japan

*CORRESPONDENCE
Ela W. Knapik
ela.knapik@vumc.org

†PRESENT ADDRESS
Gokhan Unlu,
Laboratory of Metabolic Regulation and
Genetics, The Rockefeller University,
New York, NY, United States

SPECIALTY SECTION
This article was submitted to
Bone Research,
a section of the journal
Frontiers in Endocrinology

RECEIVED 09 December 2022
ACCEPTED 24 January 2023
PUBLISHED 09 February 2023

CITATION
Ritter DJ, Choudhary D, Unlu G and
Knapik EW (2023) Rgp1 contributes to
craniofacial cartilage development and
Rab8a-mediated collagen II secretion.
Front. Endocrinol. 14:1120420.
doi: 10.3389/fendo.2023.1120420

Rgp1 contributes to craniofacial cartilage development and Rab8a-mediated collagen II secretion

Dylan J. Ritter[1,2], Dharmendra Choudhary[2], Gokhan Unlu[1,2†] and Ela W. Knapik[1,2*]

[1]Department of Cell and Developmental Biology, Vanderbilt University, Nashville, TN, United States, [2]Division of Genetic Medicine, Department of Medicine, Vanderbilt University Medical Center, Nashville, TN, United States

Rgp1 was previously identified as a component of a guanine nucleotide exchange factor (GEF) complex to activate Rab6a-mediated trafficking events in and around the Golgi. While the role of Rgp1 in protein trafficking has been examined *in vitro* and in yeast, the role of Rgp1 during vertebrate embryogenesis and protein trafficking *in vivo* is unknown. Using genetic, CRISPR-induced zebrafish mutants for Rgp1 loss-of-function, we found that Rgp1 is required for craniofacial cartilage development. Within live *rgp1*$^{-/-}$ craniofacial chondrocytes, we observed altered movements of Rab6a^{+} vesicular compartments, consistent with a conserved mechanism described *in vitro*. Using transmission electron microscopy (TEM) and immunofluorescence analyses, we show that Rgp1 plays a role in the secretion of collagen II, the most abundant protein in cartilage. Our overexpression experiments revealed that Rab8a is a part of the post-Golgi collagen II trafficking pathway. Following loss of Rgp1, chondrocytes activate an Arf4b-mediated stress response and subsequently respond with nuclear DNA fragmentation and cell death. We propose that an Rgp1-regulated Rab6a-Rab8a pathway directs secretion of ECM cargoes such as collagen II, a pathway that may also be utilized in other tissues where coordinated trafficking and secretion of collagens and other large cargoes is required for normal development and tissue function.

KEYWORDS

Rgp1, collagen, chondrocytes, zebrafish, cartilage, extracellular matrix

Introduction

The extracellular matrix (ECM) is a complex network of proteins that provides architectural support for cellular and tissue development (1–3). Among ECM proteins, collagens are the most abundant in vertebrates, composing over a quarter of the dry body mass in humans (4, 5). In order for collagen to function, it must be trafficked from the site of synthesis, the endoplasmic reticulum (ER), to the Golgi complex before being secreted to the extracellular space (6–8). Previous studies have identified components of the secretory machinery contributing to collagen trafficking from the ER to the Golgi, including TANGO1, CREB3L2, and the Coat Proteins II (COPII) complex components Sec13-31, Sec23A, and Sec24D (9–17). Fewer studies addressed the role of the secretory machinery components in collagen transit through the Golgi complex (18, 19). Thus, this stretch of the collagen secretory pathway is less well understood. Consistently, studies in animal models, including zebrafish, have revealed that proper functioning secretory pathway is essential for craniofacial development (3, 20–22). Following initial mesenchymal condensations, chondroblasts are normally positioned and form individual cartilage elements (23–25). However, later steps of cartilage development depend on ECM secretion and isometric growth of cells. Chondroblasts at this stage are most affected by defects in the secretion of collagen and other cargoes to ECM, resulting in a thin matrix and clinically brittle skeletal elements (26).

Fibrillar collagens oligomerize extracellularly into cable-like fibrils and are indispensable for three-dimensional structural stability of cartilage and other tissues (27–29). Mutations in the collagen II α1 peptide, the predominant fibrillar collagen in cartilage, contribute to a category of diseases known as type II collagenopathies (30–34). In addition to mutations in the collagen II α1 peptide itself, mutations in its processing enzymes, including *LH2* and *LH3*, have also been found to cause developmental defects in skeletal tissues (9–11, 18, 35–38). Despite considerable knowledge of the early, ER-to-Golgi trafficking of fibrillar collagens, the mechanisms governing collagen transit from Golgi-to-plasma membrane remain relatively unknown (39–42).

The central regulators of the secretory pathway are small GTPases that need to be activated by selective GEFs (43). Like other Rabs, Rab6a is only active in intracellular traffic when it is bound to GTP and a cellular membrane following interactions with its cognate heterodimer GEF composed of Rgp1 and Ric1 (43–49). When bound to GDP, Rabs are inactive, cytosolic proteins and do not participate in trafficking processes. Previous biochemical studies and cell culture experiments identified the obligatory nature of this GEF complex and its role in activation of Rab6a (44, 45). The UniProt database associates RGP1 with ECM organization and vesicular transport (50). However, Mendelian diseases were not linked to *RGP1* deficiency and the impact on clinical phenome was only tested as part of genome wide analyses. Thus, little is known about the role of *RGP1* in clinical and developmental settings.

To address the biological function of Rgp1, we generated CRISPR-edited zebrafish knockout models and found that mutants have abnormal craniofacial cartilage development and defective collagen II secretion from chondrocytes. Furthermore, we show that Rab6a and Rab8a are critical contributors to the Rgp1-dependent secretion of collagen II in chondrocytes. Specifically, our results suggest that Rgp1, Rab6a, and Rab8a coordinate the traffic of collagen II to the extracellular space as part of a post-Golgi Rab pathway. We expect that our *in vivo* findings at the cellular and tissue levels will contribute to a greater understanding of protein trafficking across tissues specialized for large cargo secretion.

Materials and methods

Fish maintenance and breeding

Zebrafish were raised under standard laboratory conditions at 28.5°C with a constant photoperiod (14 h light: 10 h dark) as previously described (18).

CRISPR/Cas9 genome editing

CRISPR/Cas9 target sites within the zebrafish *rgp1* gene were identified using the CHOPCHOP web tool (51). sgRNA templates were generated as previously described (52). gRNAs were synthesized with the MEGAshortscript T7 transcription kit (AM1354, ThermoFisher Scientific; Waltham, MA).

To generate mutations with CRISPR/Cas9 system, a mixture of 500 pg purified Cas9 protein (CP01, PNA Bio Inc.; Newbury Park, CA) and 150 pg gRNA was injected into one-cell stage WT AB embryos. Injected embryos were grown to 5 dpf for phenotypic analysis and to identify founders carrying mutant alleles in the germline. Founders were then outcrossed to transgenic or WT lines to generate stable lines carrying the listed mutations (Figure 1B). *In silico* protein translation was based on cDNA sequences obtained from mutant larvae (Figure 1C).

Live imaging of larvae for body length analysis

Larvae were anesthetized at 5 dpf in 0.15 mg/mL Tricaine (TRS1, Pentair; Cary, NC) and mounted in 3% methylcellulose on a bridge slide. Body lengths were measured from jaw protrusion to caudal fin fold from dorsal views in FIJI software (53). Head lengths were measured from jaw protrusion to the pectoral fin attachment point.

Cartilage staining

Larvae at 5 dpf were fixed in 2% PFA and stained overnight in 0.02% Alcian Blue (A5268, Sigma; St. Louis, MO) and 60 mM $MgCl_2$ in 70% EtOH as previously described (54). Larvae were then bleached (1.5% H_2O_2, 1% KOH), washed in 0.25% KOH/25% glycerol, and cleared in 0.25% KOH/50% glycerol.

RNA isolation and cDNA synthesis

RNA was isolated from at least 30 3 dpf larvae from independent mating crosses of fish. Larvae were homogenized in TRIzol Reagent (15596018, ThermoFisher Scientific; Waltham, MA), and RNA extraction was performed as previously described (55). RNA (1 μg)

10.3389/fendo.2023.1120420

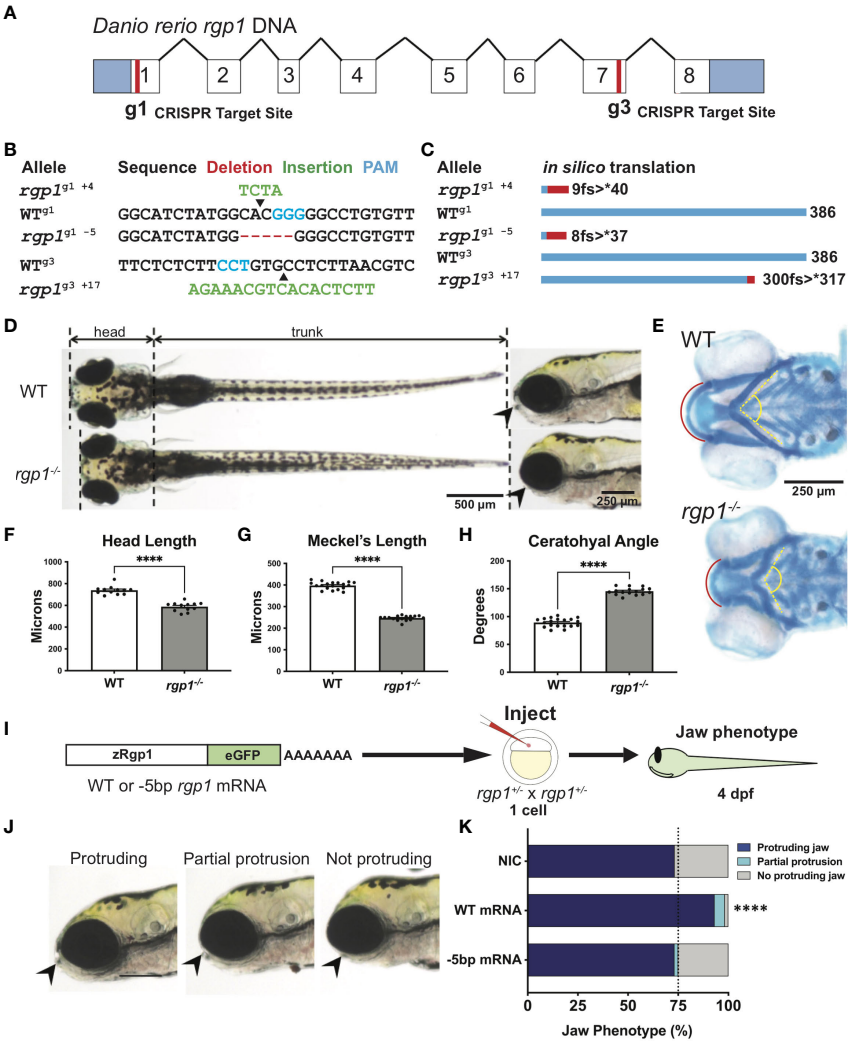

FIGURE 1
Rgp1 is required for zebrafish craniofacial skeletal development. **(A)** Zebrafish *rgp1* intron/exon map showing locations of g1 and g3 gRNA target sites. **(B)** Sequences from three different alleles isolated from the use of g1 and g3 gRNAs. **(C)** Predicted peptide lengths for alleles shown in **(B)**. **(D)** Live imaging of 5 dpf WT and *rgp1*$^{-/-}$ larvae from ventral and lateral view showing jaw protrusions (black arrowhead). **(E)** Alcian blue staining and imaging of 5 dpf WT and *rgp1*$^{-/-}$ cartilage in the ventral craniofacial head skeleton. The Meckel's cartilage (red), and ceratohyal (yellow, dashed) are marked. **(F)** Quantification of larva head length. **(G)** Quantification of Meckel's cartilage length. **(H)** Quantification of ceratohyal cartilage angle. **(I)** Schematic for zebrafish *rgp1* mRNA injection and rescue experiment. **(J)** Lateral images of larvae showing jaw protrusion, partial protrusion, and no protrusion phenotypes (black arrowheads). **(K)** Quantification of jaw phenotype percentages in groups of injected and non-injected embryos. Significance is presented by ****p<0.0001.

obtained from samples was treated with DNase I before inactivation by EDTA chelation. Samples were mixed with an 18-nucleotide poly-T primer and allowed to anneal before adding dNTPs and M-MLV Reverse Transcriptase (M1701, Promega; Madison, WI).

mRNA overexpression and phenotypic assessment

rgp1 cDNA was isolated from total WT zebrafish cDNA by PCR amplification and purification (28104, Qiagen; Hilden, Germany). The cDNA was inserted into pGEM-T using TA subcloning (A1360, Promega; Madison, WI). Following restriction enzyme digestion, the insert was moved into pCS2+ and linearized by NotI digestion. Synthesized capped mRNA transcripts were produced *via in vitro* transcription with mMESSAGE mMACHINE SP6 transcription kit (AM1340, ThermoFisher Scientific; Waltham, MA). 400 pg of mRNA diluted in 0.3X Danieau Buffer was micro-injected into single cell-stage embryos. Embryos were grown to 4 dpf for subsequent visualization and live imaging. An observer blinded to injection content scored larvae for the extent of the protruding jaw phenotype.

Generation of transgenic constructs for injection

Transgenic constructs for overexpression of zRgp1, zRab6a, and hRAB8A were generated as previously described using the Gateway cloning-based Tol2kit method (56). Full-length constructs for pME were PCR-amplified with attB1 and attB2 sequences and cloned into

pDONR221 using BP clonase II (11789020, ThermoFisher Scientific; Waltham, MA). p3E constructs were PCR-amplified with attB2R and attB3 sites and cloned into pDONR p2R-p3 using BP clonase II. A Multisite Gateway Cloning LR reaction was performed using the p5E-1.7-kb Col2a1a promoter, pME vectors, p3E vectors, pDEST-Tol2pA2, and LR clonase II enzyme mix (11791020, ThermoFisher Scientific; Waltham, MA) (57, 58). The resulting destination clones were used for mosaic overexpression experiments.

Zebrafish embryos at the one-cell stage were injected with 50-100 pg medaka transposase mRNA and 10-100 pg recombined pDEST plasmid. Larvae were collected at 3 dpf for sample processing and imaging.

Site-directed mutagenesis

Site-directed mutagenesis was performed on plasmids using the Q5 Site-Directed Mutagenesis Kit (E0554S, NEB; Ipswich, MA) as previously described with the following modifications (59). Template DNA was combined with sequence-specific SDM primers generated using NEBaseChanger online software (Table 1). Following Q5 PCR amplification, template DNA was degraded, and the newly synthesized product was ligated using the included Kinase/Ligase/DpnI enzyme mix. The final plasmid product was transformed into DH5α E. coli for subsequent plasmid isolation.

Cryosectioning and immunohistochemistry

Larvae at 3 dpf were fixed overnight in 4% PFA, washed, and moved to 30% sucrose overnight. The following day, larvae were mounted in OCT embedding medium (6769006, ThermoFisher Scientific; Waltham, MA), frozen, cryosectioned, and transferred onto Superfrost slides (12-550-15, ThermoFisher Scientific; Waltham, MA) as previously described (60). Slides were dried on a heat block, rehydrated in PBS, and mounted onto a Sequenza staining rack. Sections were incubated with Proteinase K for antigen retrieval and permeabilized in PBS+0.5% Triton X-100, then blocked in 2% BSA and 2% NGS. Samples were stained with primary antibodies (Table 2) diluted in blocking solution and incubated overnight at 4°C. The following day, samples were rinsed and incubated in secondary antibodies (Table 2), rinsed again, and incubated in DAPI before being mounted using Prolong Gold Antifade Agent (P36930, ThermoFisher Scientific; Waltham, MA). Fluorescent imaging was carried out using an AxioImager Z1 equipped with an Apotome and an EC Plan Neofluar 100X/1.30 Oil objective and ORCA-Flash4.0

TABLE 1 Primers.

Name	Forward	Reverse
sgRNA Oligo	TTTTGCACCGACTCGGTGCCACTTTTTCAAGTTGATAACGGACTAGCCTTATTTTAACTTGCTATTTCTAGCTCTAAAAC	
zrgp1 g1 sequencing	CGTCTCCGGTTGTTTTGTTT	GGTGTGACATTGGGTTTGTG
zrgp1 g3 sequencing	AGGAGCAGTATCAGAGACGACC	ATACTCATGTGACTGGCTTTGTG
zrgp1 cDNA	CGTCTCCGGTTGTTTTGTTT	CGGCACAAGGTAAAACCAGT
zrgp1 coding sequence	ATGATTGAGGTGGTGGCATC	TCAAATATTGATGCTGTTTG
zrgp1-eGFP pCS2+ cloning	CTTAAGATGATTGAGGTGGTGGCATC	CTCGAGCTTGTACAGCTCGTCCATGC
zrgp1 B1-B2	GGGGACAAGTTTGTACAAAAAAGCAGGCTATGATTGAGGTGGTGGC	GGGGACCACTTTGTACAAGAAAGCTGGGTTGCAAATATTGATGCTGTT
zrgp1 B2-B3	GGGGACAGCTTTCTTGTACAAAGTGGCCATGATTGAGGTGGTGGCATC	GGGGACAACTTTGTATAATAAAGTTGCTCAAATATTGATGCTGTTTG
zrgp1 Δ5bp SDM	GGGCCTGTGTTTTTGGCC	CCATAGATGCCACCACCTC
zRab6a B2-B3	GGGGACAGCTTTCTTGTACAAAGTGGTTATGTCTGCAGCAGGAGATTT	GGGGACAACTTTGTATAATAAAGTTGCTTACATTCAGTTCTTTGGCT
hRAB8A B2-B3	GGGGACAGCTTTCTTGTACAAAGTGGCCATGGCGAAGACCTACGA	GGGGACAACTTTGTATAATAAAGTTGCTCACAGTAGCACACAGC
hRAB8A Q67L SDM	ACGGCAGGACtGGAACGATTT	GTCCCATATCTGTAACTTTATCTTC
hRAB8A T22N SDM	GTCGGGAAGAaCTGTGTGCTG	TCCGGAATCCCCGATTAAC
zrgp1 g1 gRNA	AATTAATACGACTCACTATAggtggtggcatctatggcacGTTTTAGAGCTAGAAATAGC	
zrgp1 g3 gRNA	AATTAATACGACTCACTATAggtgtgacgttaagaggcacGTTTTAGAGCTAGAAATAGC	
edem1 qPCR	ATCCAAAGAAGATCGCATGG	TCTCTCCCTGAAACGCTGAT
hspa5 qPCR	AAGAGGCCGAAGAGAAGGAC	AGCAGCAGAGCCTCGAAATA
ddit3p qPCR	AAGGAAAGTGCAGGAGCTGA	TCACGCTCTCCACAAGAAGA
ef1 qPCR	GCATACATCAAGAAGATCGGC	GCAGCCTTCTGTGCAGACTTTG
arf4a qPCR	CCCATCAGCGAGTTGACAGA	CCCTCGTATAAACCCGTCCC
arf4b qPCR	AGAGAATCTCAGCCTCGCAC	ACAGACGCGTCCAAAGGTTA
tfe3a qPCR	CGCACGCTGATAGAGGAACT	ACCGATAGCAACCTGTGAGC
tfe3b qPCR	AGCCCCATGGCACATCTTAAT	CTCTGGCCTCTGTTTCGATCA
acbd3 qPCR	AAACCCTGAGCAGAGTGTCG	AGCATCTGGGTTGTAAGGGC

TABLE 2 Antibodies/IF Reagents.

Antibody	Catalog No.	Vendor	RRID	Dilution	Species
Collagen II	II-II63B	DSHB	AB_528165	1:250	Mouse IgG1
mCherry	16D7	ThermoFisher Scientific	AB_2536611	1:250	Rat IgG2a
GFP	A10262	Vanderbilt Molecular and Cell Biology Core	AB_2534023	1:500	Chicken IgY
GFP-488	A21311	Invitrogen	AB_221477	1:250	Rabbit IgG
WGA-488	W11261	Invitrogen	N/A	1:500	N/A
CHP-Biotin	B-CHP	3Helix	N/A	1.4μM	N/A
LBPA	Z-PLBPA	Echelon Biosciences	AB_11129226	1:100	Mouse IgG1
Rhodamine-phalloidin	R415	ThermoFisher Scientific	N/A	1:500	N/A
DAPI	D1306	Invitrogen	N/A	1:4000	N/A
Mouse IgG-Alexa647	A32787	Invitrogen	AB_2762830	1:500	Donkey
Rat IgG-Alexa555	A21434	Invitrogen	AB_2535855	1:500	Goat
Mouse IgG-Alexa555	A21422	Life Technologies	AB_2535844	1:500	Goat
Chicken IgY-Alexa488	A11039	Invitrogen	AB_2534096	1:500	Goat
Streptavidin-Alexa555	S32355	Invitrogen	N/A	1:500	N/A

N/A, not applicable.

Digital CMOS Camera. Co-localization analysis of CHP and LBPA was performed using FIJI's Coloc2 function. Cell boundaries were used to highlight a region of interest, which was then used to make a mask. Pearson's R values were collected from cells across WT and *rgp1*$^{-/-}$ larvae.

Intracellular Col2 quantification

Images of collagen IF were analyzed in FIJI. For collagen accumulation in chondrocytes, the intracellular area of each cell (demarcated by caax-eGFP signal), collagen area (Col2 signal), and nuclear area (DAPI) were measured. The following formula was used to calculate the percent intracellular collagen area per cell (18):

$$\%\ \ intracellular\ \ collagen\ \ II = \frac{collagen\ \ II\ \ area}{(intracellular\ \ area - nuclear\ \ area)} \times 100$$

Electron microscopy

Larvae were fixed at 3 dpf in 2.5% glutaraldehyde in 0.1 M sodium cacodylate by incubating at room temperature for 1 hour first, then overnight at 4°C, as previously described (18). After rinsing in 0.1 M sodium cacodylate, samples were post-fixed with 1% osmium tetroxide in 0.1 M sodium cacodylate for 1 hour. After additional rinsing, specimens were sequentially dehydrated in increasing concentrations of ethanol and then propylene oxide, infiltrated with resin step-wise, and then embedded in resin for 48 hours at 60°C. Coronal sections of 10 μm were collected until craniofacial chondrocytes were visible under low magnification microscopy based on their location in the jaw, characteristic stacking arrangement, and surrounding ECM. 70-nm sections were collected on TEM grids following sectioning on a Leica Ultracut Microtome and analyzed on a Phillips CM-12 Transmission Electron Microscope provided by the Vanderbilt Cell Imaging Shared Resource. Images of the hyosymplectic element were acquired from tiled images and stitching across single sections. Individual ultrastructural elements were identified by morphological characteristics and were pseudo colored.

Live vesicle movement and tracking

Live vesicle movement in WT and *rgp1*$^{-/-}$ transgenic larvae was performed on a Zeiss LSM880 confocal microscope. Embryos obtained from gRNA-generated stable mutant lines crossed to mosaic (Col2a1a:caax-eGFP) adults were injected with a Tol2 construct expressing Col2a1a:mCherry-zRab6a for transient, transposon-mediated DNA integration. Zebrafish larvae at 3 dpf that were grown in PTU were selected for imaging if they expressed caax-eGFP and expressed substantial mCherry-zRab6a in the hyosymplectic cartilage. Larvae were anesthetized in 0.15 mg/mL Tricaine, embedded in 1.2% low-melt agarose (A20070, RPI; Mount Prospect, IL) on glass-bottom confocal dishes, and overlaid with embryo media containing 0.4 mg/mL Tricaine. For time-lapse imaging, larvae were imaged under a 40X/1.1 LD C-Apochromat water-immersion objective. Frame intervals of 300 ms were collected over the course of 300 frames for each sample with 300 ms delay between acquisitions. Individual frames were deconvolved using Airyscan (Zeiss; Jena, Germany). Supplemental Movies 1, 2 are sped up to 100 frames/second for display purposes.

Confocal time-lapse images from live transgenic larvae were analyzed in Imaris 9.7.2 (Oxford Instruments; Abingdon, United

Kingdom). Analysis was performed using the automated Spots feature. Spots in the red channel were filtered by their quality and fit to the autoregressive motion-tracking algorithm. Tracks generated over longer than 5 frames were selected for analysis. All tracks collected were measured for track length and mean track speed.

TUNEL assay

To identify double-stranded DNA breaks indicative of cell death, TUNEL assays were performed as previously described with the following modifications (61). Larvae were fixed overnight in 4% PFA, moved to 30% sucrose in PBS, and cryosectioned. TUNEL was performed using the Roche *In Situ* Death Detection Kit (12156792910, Sigma; St. Louis, MO). Larvae were co-stained with WGA-488 or GFP-488 and DAPI.

qPCR

Synthesized cDNA was diluted 1:1 with water before use in qPCR. Three biological replicates were performed, with each biological replicate consisting of an independent RNA extraction. qPCR was performed using forward and reverse primers (Table 1), cDNA, and 2X SYBR Green PCR Master Mix (4309155, ThermoFisher Scientific; Waltham, MA) as previously described (62). Samples were run in technical triplicates, and curves were normalized to *ef-1* transcript levels.

Statistical analysis

Statistical analyses were performed with GraphPad Prism 9.3.1 (63). Statistical significance between WT and *rgp1*$^{-/-}$ larva gross morphology was assessed by Mann-Whitney U-test (two-tailed) with 95% confidence intervals. For head length and cartilage size measurements, symbols on the graph represent individual larvae, with lines representing means ± SEM.

Statistical significance for jaw protrusion phenotypes following mRNA injection was analyzed by Chi-Square analysis. Numbers on the graph represent larvae across pooled clutches from injections across at least three independent mating crosses.

Statistical significance between mCherry-zRab6a puncta dynamics in WT and *rgp1*$^{-/-}$ chondrocytes was assessed by Mann-Whitney U-test (two-tailed) with 95% confidence intervals. Symbols on graph represent individual vesicles with red lines representing means.

Comparisons of intracellular collagen II staining between fluorescent and non-fluorescent chondrocytes was determined by one-way ANOVA with Tukey's multiple comparison test. Symbols on the graph represent measurements of individual chondrocytes with lines representing means ± SEM.

Statistical analysis of cell death phenotypes in TEM of chondrocytes was not performed. Numbers on the graph represent the fraction of total individual chondrocytes with each phenotype.

Statistical analysis between qPCR expression levels was assessed by Mann-Whitney U-test (two-tailed) with 95% confidence intervals. Symbols on the graph represent individual biological replicates from technical triplicates with lines representing means ± SEM.

No data points or measurements were omitted across any experiment. The number of larvae, vesicles, or cells required for each experiment was determined based on power analysis with 95% confidence intervals. Significance is represented by *p<0.05; **p<0.01; ***p<0.001; ****p<0.0001; ns, not significant.

Results

CRISPR-generated *rgp1*$^{-/-}$ zebrafish larvae have craniofacial defects

Zebrafish begin to develop a protruding jaw around 3 days post-fertilization (dpf), a process essential for feeding that begins at 5 dpf. Previous work from our laboratory noted that mosaically reduced Rgp1 expression contributes to defects in jaw morphology and craniofacial development (18). However, it remains unknown how genetic mutations in Rgp1 affect craniofacial cartilage development. To generate stable mutant lines, we used CRISPR/Cas9 genome editing and two guide RNAs (gRNAs) targeting exons one (g1) and seven (g3) to generate three independent *rgp1* mutant alleles (Figures 1A, B). All three zebrafish alleles are predicted to induce frameshift mutations, which would likely result in the translation of a shorter peptide or nonsense mediated decay (Figure 1C). All three *rgp1*$^{-/-}$ alleles showed a lack of a protruding jaw and were shorter when compared to wild-type (WT) controls (Figure 1D). The embryonic zebrafish craniofacial skeleton is primarily cartilaginous until 5 dpf (64). To assess the cartilage structure and integrity, we stained larvae with Alcian blue, a dye that binds glycosaminoglycans commonly found in the cartilage extracellular matrix (Figure 1E) (54). In *rgp1*$^{-/-}$ larvae, we found malformed craniofacial cartilage elements, leading to an overall shortening of the head skeleton by approximately 20% compared to WT controls (Figure 1F, p<0.0001). The Meckel's cartilage, corresponding to the lower jaw, is significantly shorter in *rgp1*$^{-/-}$ larvae (Figures 1E, G, p<0.0001). Additionally, the ceratohyal cartilage element, a ventral structure of the head skeleton, was bent at a wider angle in mutants compared to WT controls (Figures 1E, H, p<0.0001).

To validate our new model and rule out the possibility of CRISPR-induced off-target effects, we performed an mRNA genetic replacement experiment and assessed jaw morphology in live larvae to determine if clutches overexpressing *rgp1* had a majority of larvae with normal protruding jaws (Figures 1I–J) (65–67). There was an increase in the proportion of larvae showing a protruding jaw in WT mRNA injected larvae, compared to the non-injected control of 75% larvae with protruding jaws, typical for a recessive phenotype (Figure 1K, p<0.0001). On the contrary, injection of an mRNA coding for the mutant *rgp1*$^{g1\ -5}$ allele did not result in phenotypic jaw rescue (Figure 1K, p=0.502). The *rgp1*$^{g1\ -5}$ allele was used in panels D-K, although all three alleles presented with a similar phenotype. Similarly, trans-heterozygote larvae for different *rgp1* mutant alleles had similar jaw protrusion defects to homozygous mutant alleles, further ruling out the possibility of off-target effects in individual *rgp1* mutant lines (data not shown). From the mRNA genetic replacement experiment, we concluded that the observed craniofacial skeletal

defects were due to mutations in *rgp1* and its subsequent loss of function.

Rab6a activation is reduced in *rgp1*$^{-/-}$ chondrocytes

Rgp1 was previously identified as a component of the Rab6a GEF complex in yeast and mammalian cells (44, 45). To test whether mutations in *rgp1* disrupt Rab6a activation and vesicle movement in our zebrafish model, we generated and injected a Tol2 DNA construct to overexpress mCherry-fused WT zebrafish Rab6a (WT zRab6a) under a Col2a1α promoter (57, 58, 68). We co-injected the construct along with transposase into the single-cell progeny of heterozygote mutant fish carrying a transgene that labels chondrocyte membrane with caax-eGFP (Figure 2A) (69). Because transposase integration is mosaic, not all cells express the construct, and the mCherry fusion protein highlights specific vesicular compartments. This gave us the opportunity to compare activation of Rab6a and vesicular compartment movements as puncta in movies. We chose to analyze hyosymplectic chondrocytes that stack horizontally, develop around 3 dpf, and are close to the zebrafish skin, making them amenable to *in situ* live imaging (Figures 2B, C) (64). We found that the mCherry-zRab6a^{+} vesicular compartments in *rgp1* mutants traveled shorter distances (Figure 2D, p<0.0001) and moved slower (Figure 2E, p<0.0001) than WT controls (Supplemental Movies 1, 2). These data suggest that Rgp1 is needed for Rab6a^{+} vesicular compartment dynamics within chondrocytes.

Rgp1 is required for collagen II secretion

Craniofacial chondrocytes predominantly secrete collagen II during larval craniofacial development (68). To assess secretion of collagen II, we performed immunofluorescence with a collagen II antibody in WT and *rgp1*$^{-/-}$ larvae crossed to a transgenic zebrafish line expressing membrane-bound caax-eGFP under the Col2a1α promoter (Figure 3A) (57, 69, 70). The caax-eGFP transgene labeled the cell membrane boundary to distinguish intracellular from extracellular space. We identified two prominent phenotypes in the *rgp1*$^{-/-}$ chondrocytes: collagen II secretion defects and an abnormal cell shape; we have chosen to focus on the collagen II secretion phenotype. We found that *rgp1*$^{-/-}$ chondrocytes had significantly higher amounts of intracellular collagen II when compared to WT controls (Figures 3B, C, p<0.0001). We also observed reduced extracellular collagen II staining in *rgp1*$^{-/-}$ cartilage. Thus, we conclude that Rgp1 is required for secretion of collagen II in chondrocytes.

To test whether the intracellular collagen II accumulations stem specifically from loss of Rgp1, we overexpressed WT zebrafish Rgp1 (zRgp1) under a Col2a1α promoter using a Tol2 construct (Figure 3D). We took advantage of a viral p2A self-cleavable peptide sequence to identify cells over-expressing WT zRgp1 (56, 71). Single-cell embryos were injected, and the construct mosaically integrated, with cytosolic mCherry expression only visible in cells where the Tol2 construct integrated (Figure 3E). WT chondrocytes had no significant difference in the amount of intracellular collagen II regardless of whether they overexpressed zRgp1 or not (Figure 3F,

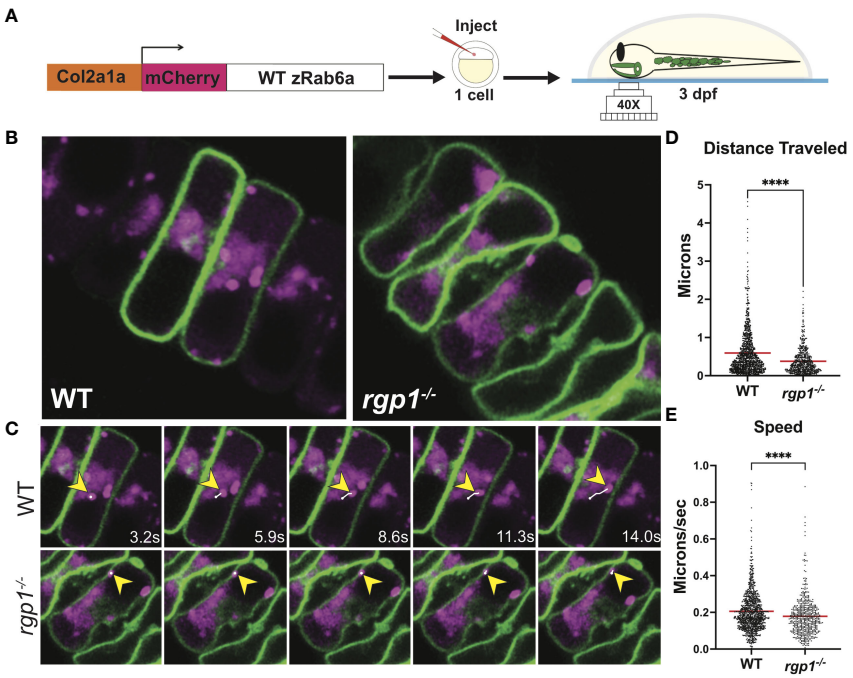

FIGURE 2
Rab6a vesicle trafficking is reduced in *rgp1*$^{-/-}$ chondrocytes **(A)** Experimental design for mosaic overexpression of WT mCherry-zRab6a fusion protein in Tg(Col2a1α:caax-eGFP) transgenic zebrafish chondrocytes for live imaging. **(B)** Representative images from movies of mCherry-zRab6a vesicular compartment movement in chondrocytes (Supplemental Movies 1, 2). **(C)** Montage of mCherry-zRab6a puncta progression at specific times in WT and *rgp1*$^{-/-}$ chondrocytes (yellow arrowheads) showing path of indicated vesicle over time (white line). **(D)** Quantification of vesicular compartment distances traveled in WT and *rgp1*$^{-/-}$ chondrocytes. Red lines indicate means. **(E)** Quantification of vesicular compartment speeds in WT and *rgp1*$^{-/-}$ chondrocytes. Red lines indicate means. Significance is presented by ****p<0.0001.

10.3389/fendo.2023.1120420

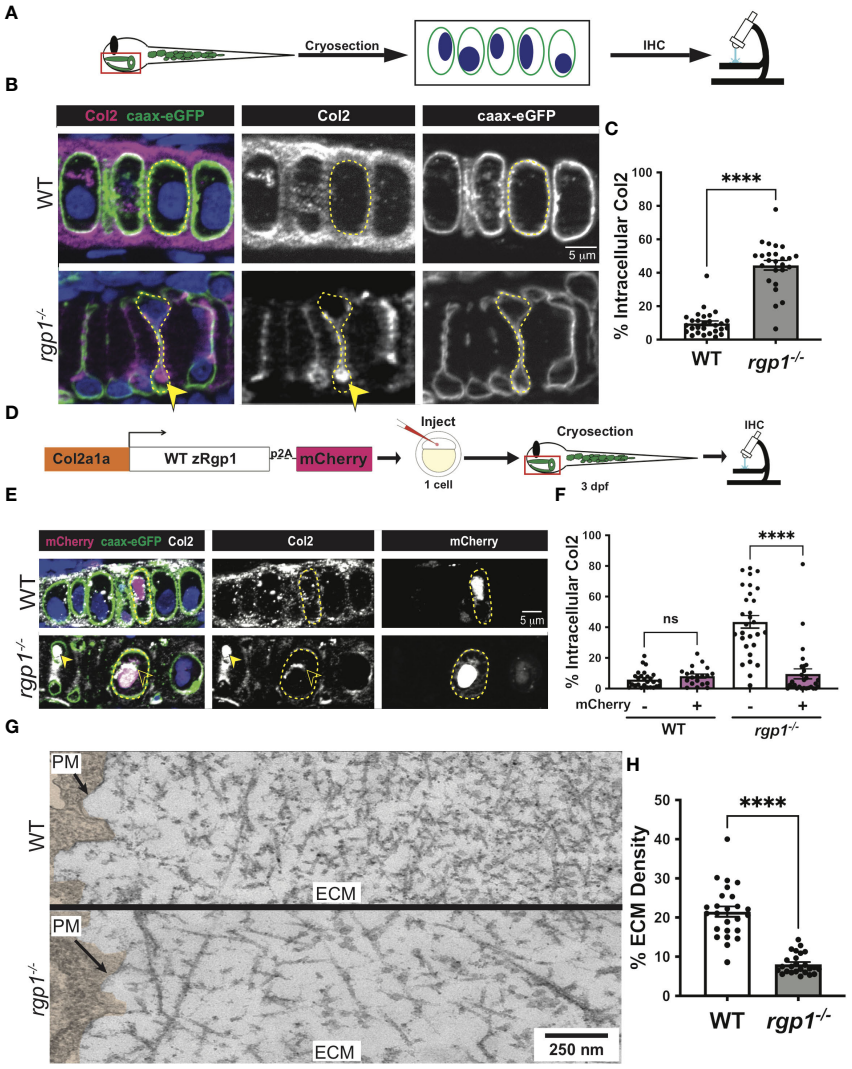

FIGURE 3
Rgp1$^{-/-}$ chondrocytes accumulate collagen II intracellularly. **(A)** Experimental design for immunohistochemical analysis of chondrocytes in the craniofacial head skeleton. **(B)** Representative images of Tg(Col2a1α:caax-eGFP) transgenic larvae in WT and *rgp1*$^{-/-}$ cartilage (Col2, magenta; eGFP, green). Yellow arrowhead identifies intracellular collagen II. **(C)** Quantification of the percentage of cytosolic area occupied by collagen II signal in chondrocytes. **(D)** Experimental design for mosaic overexpression of zRgp1-p2A-mCherry in zebrafish chondrocytes. **(E)** Representative images of Tg (Col2a1α:caax-eGFP) transgenic chondrocytes in WT and *rgp1*$^{-/-}$ cartilage (TEM images of chondrocyte membranes (PM) and adjacent mCherry, magenta; eGFP, green; Col2, white). Yellow arrowhead identifies collagen II in mCherry^{-} cells while empty arrowhead identifies collagen II in mCherry^{+} cells. **(F)** Quantification of the percentage of cytosolic area occupied by collagen II signal in chondrocytes. **(G)** TEM images of chondrocyte membranes and adjacent ECM proteins. **(H)** Quantification of TEM staining density from craniofacial chondrocyte plasma membrane to edge of cartilage tissue using ImageJ. Significance is presented by ****p<0.0001; ns, not signficant.

p=0.960). In *rgp1*-deficient chondrocytes, expression of zRgp1-p2A-mCherry (Figure 3E) reduced accumulations of intracellular collagen II compared to mCherry^{-} chondrocytes (Figures 3E, F, p<0.0001). Thus, overexpression of WT zRgp1 in *rgp1*$^{-/-}$ chondrocytes was sufficient to rescue collagen II secretion defects in a cell-autonomous manner.

To assess the abundance of extracellular matrix proteins in an antibody-independent method, we used TEM. We found that at 3 dpf, WT chondrocytes have secreted a large amount of protein to the ECM, with increasing crosslinking further away from the cell membrane (Figure 3G). However, *rgp1*-deficient cartilage ECM was significantly less dense compared to WT (Figure 3H, p<0.0001), although there were ECM proteins present in the extracellular space. This supports our observation that although collagen II is likely not secreted by *rgp1*$^{-/-}$ chondrocytes, other ECM proteins are secreted to the extracellular space.

Collagen II accumulates in an endolysosomal compartment

To assess where collagen II accumulates in *rgp1*$^{-/-}$ chondrocytes, we compared TEM images of WT and *rgp1*$^{-/-}$ hyosymplectic chondrocytes (Figure 4A). In *rgp1*$^{-/-}$ cells, we found large vacuolar-like structures, (Figure 4B) some of which were filled with striated assemblies (Figure 4B'-B"). Previous studies have identified this striated TEM ultrastructure as a fully assembled, mature collagen fibril, which is typically found exclusively extracellularly (72, 73).

10.3389/fendo.2023.1120420

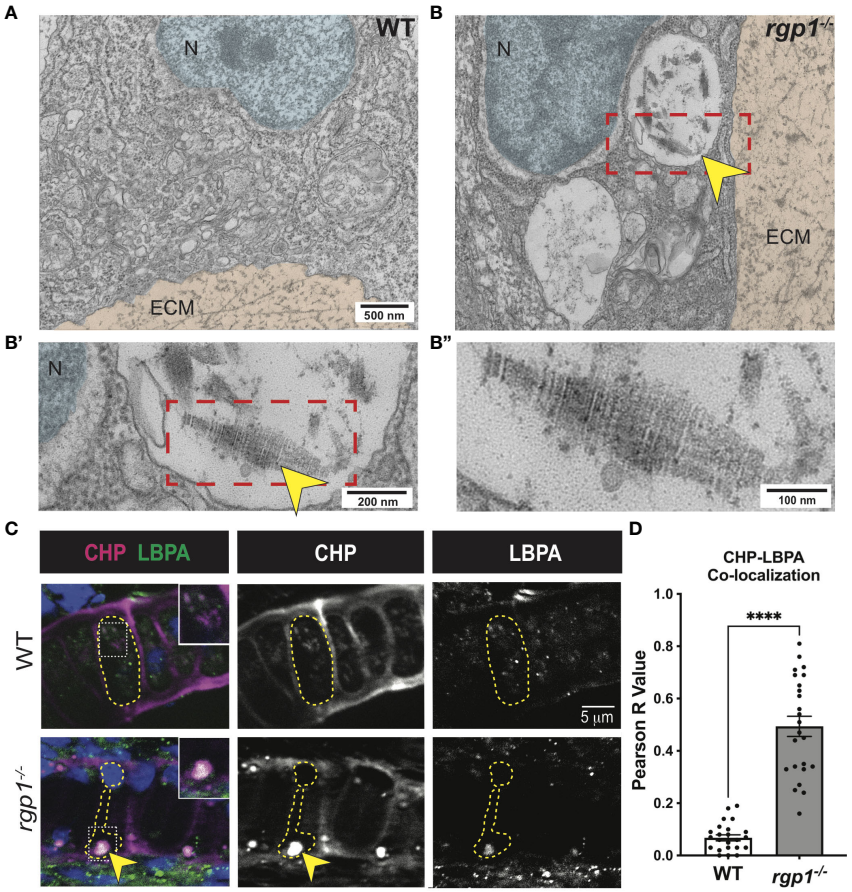

FIGURE 4
Collagen II accumulations in *rgp1*$^{-/-}$ chondrocytes localize to endolysosomes **(A)** TEM images of 3 dpf WT craniofacial chondrocytes. **(B)** TEM images of 3 dpf *rgp1*$^{-/-}$ craniofacial chondrocytes showing vacuolar structures (yellow arrowhead) **(B')** Enlarged image of boxed area showing striated ultrastructure of intracellular collagen fibrils (yellow arrowhead). **(B")** Further enlargement of boxed area. **(C)** Representative images of chondrocytes in WT and *rgp1*$^{-/-}$ cartilage (CHP, magenta; LBPA, green). Insets are enlargements of white dashed boxes, and an intracellular accumulation is labeled with a yellow arrowhead. **(D)** Quantification of the Pearson R value for co-localization in individual chondrocytes. Significance is presented by ****p<0.0001.

Collagen II is normally trafficked with N- and C-terminal telopeptide domains that prevent aberrant oligomerization intracellularly (4, 74, 75). The presence of striated collagen intracellularly suggests that endopeptidases cleaved the procollagen trimer, thus allowing for spontaneous fibril assembly within the observed vacuolar-like structures.

Lysosomes are small, vacuolar compartments that concentrate proteolytic peptidases for enzymatic digestion (76). To test whether the structures observed in TEM carry hallmarks of lysosomal membranes containing collagen, we co-stained for markers of endolysosomal compartments and collagen. To perform this co-localization assay, we used an antibody against a lipid enriched in endolysosomal membranes, lysobisphosphatidic acid (LBPA), and a collagen hybridizing peptide (CHP; Figure 4C) (77, 78). We chose to use CHP instead of a collagen II antibody since the collagen II antibody and the LBPA antibody were generated in the same host species. In WT chondrocytes, we found LBPA staining in small puncta, consistent with staining of endolysosomal compartments; we also found very little co-localization between LBPA and CHP, suggesting that collagen is not normally found in LBPA^{+} compartments (Figure 4C). However, CHP and LBPA staining often co-localized in *rgp1*$^{-/-}$ chondrocytes (Figures 4C, D, p<0.0001) and was as large as the inclusions in the TEM images. This suggests that collagen II accumulates in an endolysosomal compartment in *rgp1*$^{-/-}$ chondrocytes.

Rab8a is required for collagen II trafficking, and constitutive activation of Rab8a partially rescues *rgp1*$^{-/-}$ collagen II secretion defects

Rab8a has been shown to mainly associate with exocytic trafficking from the *trans*-Golgi network (TGN) to the plasma membrane and co-localizes with Rab6a^{+} vesicular carriers (79–83). To test whether overexpression of hRAB8A is sufficient to affect collagen II secretion in zebrafish chondrocytes, we used WT mCherry-hRAB8A under a Col2a1α promoter (Figure 5A). In WT larvae, there was no difference in intracellular collagen II levels between mCherry^{+} and mCherry^{-} cells (Figure 5B, C, p=0.9999). In *rgp1*$^{-/-}$ chondrocytes, we found that overexpression of the WT mCherry-hRAB8A also had no effect on intracellular collagen II when compared to mCherry^{-} cells (Figures 5B, 5C, p=0.9993). Thus, simple overexpression of WT hRAB8A does not alter collagen II secretion.

10.3389/fendo.2023.1120420

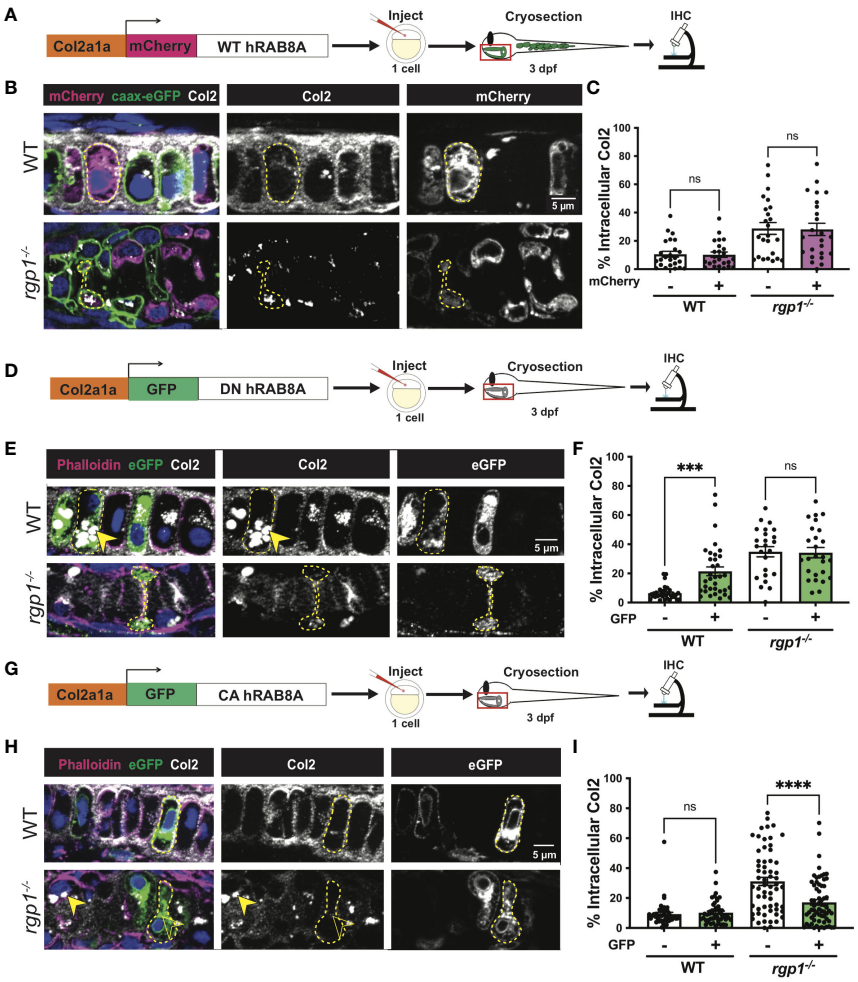

FIGURE 5
Collagen II trafficking is regulated by Rab8a. **(A)** Experimental design for mosaic overexpression of WT mCherry-hRAB8A fusion protein in zebrafish chondrocytes. **(B)** Representative images of Tg(Col2a1α:caax-eGFP) transgenic chondrocytes in WT and *rgp1*$^{-/-}$ cartilage (mCherry, magenta; caax-eGFP, green; Col2, white). **(C)** Quantification of the percentage of cytosolic area occupied by collagen II signal in chondrocytes. **(D)** Experimental design for mosaic overexpression of DN GFP-hRAB8A fusion protein in zebrafish chondrocytes. **(E)** Representative images of chondrocytes in WT and *rgp1*$^{-/-}$ cartilage (phalloidin, magenta; eGFP, green; Col2, white). Yellow arrowhead identifies intracellular collagen II. **(F)** Quantification of the percentage of cytosolic area occupied by collagen II signal in chondrocytes. **(G)** Experimental design for mosaic overexpression of CA GFP-hRAB8A fusion protein in zebrafish chondrocytes. **(H)** Representative images of chondrocytes in WT and *rgp1*$^{-/-}$ cartilage (phalloidin, magenta; eGFP, green; Col2, white). Yellow arrowhead identifies collagen II in GFP^{-} cells while empty arrowhead identifies collagen II in GFP^{+} cells. **(I)** Quantification of the percentage of cytosolic area occupied by collagen II signal in chondrocytes. Significance is presented by ***p<0.001; ****p<0.0001; ns, not signficant.

Point mutations in Rab proteins can alter their affinity for GTP or GDP to lock it in the "constitutively-active" (CA), GTP-bound conformation or the "dominant-negative" (DN), GDP-bound conformation (48, 84–86). To test whether inactivating Rab8a blocks collagen II secretion in zebrafish chondrocytes, we expressed a Tol2 fusion construct of GFP and DN human RAB8A (T22N) under a Col2a1α promoter (Figure 5D) (85). We found that GFP^{+} WT chondrocytes accumulated large inclusions of collagen II in higher amounts compared to their adjacent GFP^{-} counterparts (Figures 5E, F, p=0.0004). In *rgp1*$^{-/-}$ chondrocytes that already accumulate large collagen II inclusions, there was no change in intracellular collagen II staining in GFP^{+} vs GFP^{-} cells (Figure 5F, p>0.9999). This result is consistent with Rab8a being required for cargo secretion, including collagen II in chondrocytes.

To test whether constitutive activation of hRAB8A would be sufficient to rescue collagen II accumulations in *rgp1*$^{-/-}$ chondrocytes, we expressed a Tol2 fusion construct of GFP and CA hRAB8A (Q67L) under a Col2a1α promoter (Figure 5G) (86). In WT chondrocytes, there was no difference in intracellular collagen II levels between GFP^{+} and GFP^{-} cells (Figures 5H, I, p=0.9890). In *rgp1*$^{-/-}$ chondrocytes, we found that expression of CA GFP-hRAB8A (Figure 5H) reduced levels of intracellular collagen II compared to GFP^{-} cells (Figures 5H, I, p<0.0001). Therefore, overexpression of CA Rab8a is sufficient to partially rescue secretion of intracellular collagen II in *rgp1*$^{-/-}$ chondrocytes, suggesting that Rgp1 functions upstream of the Rab8a activation step.

Rgp1$^{-/-}$ chondrocytes activate Golgi stress and undergo cell death

In TEM analysis at 3 dpf, we observed *rgp1*$^{-/-}$ chondrocytes with abnormal nuclei when compared to WT cells (Figures 4A, B). The observed mixture of electron-dense and electron-sparse material

within the nucleus is suggestive of nuclear condensations, an early sign of cell death. To identify hallmarks of cell death, we further assessed chondrocyte ultrastructure using TEM on hyosymplectic chondrocytes (87, 88). While WT chondrocytes did not have any abnormalities in nuclear structure, *rgp1*$^{-/-}$ chondrocytes had begun to undergo nuclear condensation and presented with clear cytoplasmic vacuolar structures (Figures 6A, B). Specifically, binary scoring for the presence or absence of these phenotypes revealed that hallmarks of cell death were only sporadically observed in the WT chondrocytes (Figure 6C). As such, these findings suggest that *rgp1*$^{-/-}$ chondrocytes undergo cell death at higher rates than WT chondrocytes.

To test if *rgp1*$^{-/-}$ chondrocytes underwent DNA fragmentation consistent with the nuclear condensation observed in TEM, we performed a TUNEL assay. As a co-stain, we used wheat germ agglutinin (WGA) to label N-glycosylated proteins in the extracellular matrix and to help detect cell boundaries (Figure 6D). We found more TUNEL^{+} nuclei in *rgp1*$^{-/-}$ chondrocytes compared to WT nuclei, indicative of higher levels of DNA fragmentation (Figure 6E, p<0.0001). Together, the nuclear changes detected by TEM and TUNEL staining support the increase in chondrocyte cell death in Rgp1-deficient cells.

It remained unclear whether the observed cell death occurred as a result of collagen II accumulations or if another Rgp1-related phenotype induced cell death. To test whether collagen II accumulation induced cell death, we overexpressed DN GFP-hRAB8A (Figure 5D) in WT chondrocytes and compared TUNEL staining in GFP^{+} cells with intracellular collagen II accumulations to GFP^{-} chondrocytes with no collagen II backlogs (Figure 6F). We found no difference in the percentage of nuclei with DNA fragmentation between the GFP^{+} and GFP^{-} chondrocytes at 3 dpf (Figure 6G, p>0.9999); this observation was consistent even after prolonged accumulation of collagen II at 4 dpf (Figure 6G, p=0.3294). Thus, we conclude that the chondrocyte cell death in *rgp1*$^{-/-}$ chondrocytes is caused independently from collagen II accumulation.

Since collagen II accumulation was not sufficient to induce cell death, we investigated whether defects in Golgi trafficking could cause cellular stress responses along the secretory pathway. To test this possibility, we used qPCR to measure transcript levels of three ER

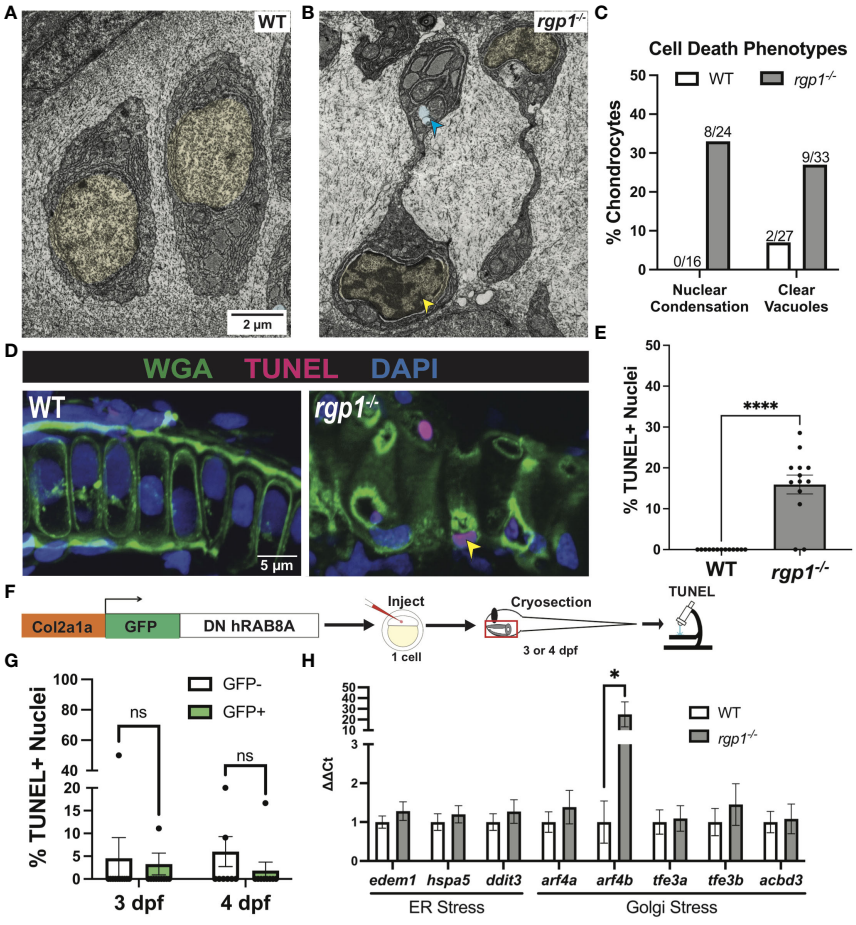

FIGURE 6
rgp1$^{-/-}$ chondrocytes undergo cell death and induce a Golgi stress marker. **(A)** TEM images of 3 dpf WT chondrocytes showing normal cellular morphology. **(B)** *rgp1*$^{-/-}$ craniofacial chondrocytes showing partial nuclear condensation (yellow shading, blue arrow) and clear cytoplasmic vacuoles (blue shading, blue arrow). **(C)** Quantification of cell death-associated TEM phenotypes. **(D)** Representative images of chondrocytes labeled with TUNEL and WGA in WT and *rgp1*$^{-/-}$ cartilage (TUNEL, magenta; WGA, green). Yellow arrowhead identifies TUNEL^{+} nucleus. **(E)** Quantification of the percentage of nuclei that were TUNEL^{+} in each image. **(F)** Experimental design for mosaic overexpression of DN GFP-hRAB8A fusion protein in zebrafish chondrocytes, as used in Figure 5A. **(G)** Quantification of the percentage of nuclei that were TUNEL^{+} in each image at 3 dpf or 4 dpf **(H)** qPCR panel of ER stress transcripts (*edem1, bip, chop*) and Golgi stress transcripts (*arf4a, arf4b, tfe3a, tfe3b, acbd3*) normalized to *ef-1* transcript levels in 3 dpf larvae. Significance is presented by *p<0.05; ****p<0.0001; ns, not signficant.

stress transcripts, *edem1*, *hspa5* (BiP), and *ddit3* (CHOP), and five Golgi stress transcripts, *arf4a, arf4b, tfe3a, tfe3b, and acbd3* in 3 dpf larvae (Figure 6H). However, *rgp1*$^{-/-}$ larvae significantly upregulated expression of *arf4b* (Figure 6H, p=0.0286), an ortholog of human ARF4 (GTPase of the Ras superfamily of small G proteins), that was previously shown to be upregulated in response to Golgi stress conditions impinging on Golgi integrity and homeostasis (89). Upregulation of Arf4b and the fact that TEM imaging of *rgp1*$^{-/-}$ chondrocytes failed to identify canonical Golgi stacks (data not shown) similar to those observed in WT siblings, suggests that *rgp1* loss-of-function leads to Golgi stress and Golgi fragmentation.

Discussion

While studies of trafficking mechanisms *in vitro* and in yeast have been informative, studies in multicellular organisms are critical to identify the trafficking mechanisms required for tissue organization. This is especially true in vertebrates where the coordinated secretion of large cargoes is essential for normal development. Prior work in the field recognized that the TGN serves as a sorting hub for exocytic vesicles shown to be heterogeneous in their cargoes, trafficking regulators, and destinations (90). Here, we show that Rgp1 is required for the post-Golgi secretion of select protein cargoes. As a result, Rgp1-deficient zebrafish larvae present with prominent craniofacial cartilage phenotypes including (i) disrupted collagen II trafficking and protein backlogs within chondrocytes, (ii) activation of a Golgi stress response and increased chondrocyte death, and (iii) altered chondrocyte cell shape.

Studies in yeast and mammalian cells in culture identified Rgp1 as part of a GEF complex for Rab6a (44, 45). In our study, we show that Rgp1 is essential for Rab6a activation *in vivo* in zebrafish chondrocytes (Figure 2). Consistent with a conserved mechanism of Rgp1 function among vertebrates from zebrafish to humans, our *in vivo rgp1*$^{-/-}$ model revealed an essential role for Rgp1 in craniofacial development and collagen II secretion.

Our results revealed that in chondrocytes, Rgp1 is required for the trafficking of a subset of ECM cargoes from the TGN. Using TEM imaging of *rgp1*$^{-/-}$ cartilage, we found a limited amount of protein in the extracellular space (Figure 3). Additionally, immunofluorescence experiments revealed a small amount of collagen II present in the *rgp1*$^{-/-}$ cartilage extracellular space. These findings suggest that collagen II secretion is inefficient following reduced Rab6a pathway activation or there exists a potential compensatory mechanism for collagen II secretion. Previous work in the field has shown that the ER contacts the plasma membrane at distances sufficient for direct trafficking (91–93). It is plausible that in *rgp1*$^{-/-}$ cartilage, a small amount of collagen II is secreted directly from the ER to the extracellular space as an adaptive mechanism during Golgi stress. Alternatively, some collagen II in the Golgi could be packaged into exocytic vesicles regulated by other proteins, like Arf GTPases (40, 94). Arf proteins, like Rabs, regulate trafficking from the *trans*-Golgi to different compartments within the cell, including the plasma membrane (95).

Previous findings from mammalian cell culture experiments show that Rab6a coordinates vesicle trafficking through a post-Golgi Rab cascade together with Rab8a (80, 96). By overexpressing DN hRAB8A, we showed that Rab8a is required to traffic collagen II in zebrafish chondrocytes. Overexpression of CA hRAB8A rescued collagen II accumulations in *rgp1*$^{-/-}$ chondrocytes, suggesting that Rab8a acts downstream of Rgp1 within the secretory pathway. It has been appreciated that Rab8a regulates post-Golgi trafficking of small cargoes such as the transferrin receptor, vesicular stomatitis virus G protein, and matrix metalloproteinase 14 (81, 86, 97). Rab8a is also required in polarized cells to traffic collagen IV, a network collagen important for basement membrane organization (98). Here, we provide evidence that in non-polarized chondrocytes, Rab8a regulates the trafficking of collagen II, a large fibrillar collagen in cartilage ECM. This suggests that in other tissues, Rab8a might also be involved in the traffic of diverse large cargoes, expanding the essentiality of Rab8a during development.

We found that in Rgp1-deficient chondrocytes, type II collagen accumulates in the endolysosomal compartment. Potentially, collagen II arrives at the late Golgi but is unable to continue along the secretory pathway because of the dysfunctional TGN. Stalled membrane bound compartments are likely recognized by a stress response mechanism (e.g. Arf4), leading to fusion with lysosomes to clear intracellular accumulations. Our TEM findings confirmed the presence of a large number of small, membrane-bound compartments loaded with electron dense material and large vacuolar-like structures containing processed and assembled collagen fibers. TEM images showing reduced cartilage ECM density further correlate the two findings. Furthermore, DN hRAB8A overexpression to block collagen II secretion was not sufficient to induce cell death, suggesting that another Rgp1-mediated process causes cell death.

Our identification of an Arf4b-specific Golgi stress response aligns well with a previous study in human cells in culture that found Arf4 upregulation following application of Golgi-disrupting drugs (89). While intriguing, that study used drugs known to induce both Golgi stress and ER stress (99, 100). In contrast, our model identifies a Golgi-specific stress response in the absence of an ER stress response. Arf4 has been implicated in regulating transport between the recycling endosome and TGN, and increased *arf4* expression levels were shown to correlate with Golgi fragmentation (89, 101). Thus, it is not surprising that in the absence of Rgp1 activity, leading to a dysfunctional TGN and buildup of matrix proteins in the endolysosomal compartment, *arf4* becomes upregulated.

Extensive analyses of TEM images from *rgp1*$^{-/-}$ chondrocytes failed to identify canonical Golgi stacks similar to those observed in WT counterparts. It is conceivable that disturbed Rab6a-mediated traffic contributes to Golgi disorganization or even dispersion (102). Since Rgp1 GEF activity is associated with the TGN, it is feasible that Rgp1 deficiency could lead to Golgi dispersion and stress, despite a normally functioning ER (44). This is consistent with our live imaging data tracking Rab6a^{+} compartments, where WT chondrocytes showed perinuclear and condensed structures, while *rgp1*$^{-/-}$ chondrocytes showed more dispersed structures. Future studies will be needed to understand the relationship of Golgi morphology and Golgi stress.

Our study also poses new questions regarding mechanisms regulating cargo trafficking and developmental cell shape changes in mesenchymal cells such as chondrocytes. This highlights the existence of alternative pathways as compared to those identified in polarized, basement membrane oriented epithelial cells. Chondrocyte shape

variation was observed in cells deficient in various components of the secretory pathway machinery including COPII (Sec23, Sec24) or post-Golgi elements (Ric1, Kif5b, Erc1) (9, 10, 18, 23, 103). Unlike genetic replacement of Rgp1 in *rgp1*$^{-/-}$ larvae that rescued all cellular phenotypes, overexpression of constitutively activated hRAB8A was not able to overcome the *rgp1*$^{-/-}$ cell shape phenotype, suggesting that increased exocytic pathway activation is not sufficient to restore cell shape (Figure 5). This suggests that there are yet unknown processes in cell shape determination regulated by Rgp1.

Despite a growing body of knowledge in the field of cartilage and bone biology, surprisingly few diseases have been described involving the secretory machinery, particularly in the post-Golgi compartment (8). Recently, we have described the novel CATIFA syndrome, where subjects carry variants in RIC1, the binding partner of RGP1 (18). Deficiencies of RIC1 in CATIFA and Rgp1 in zebrafish models are consistent with type II collagenopathies, affecting collagen II secretion, and their common presentation includes scoliosis, cleft palate and a shorter jaw (31, 104). Although, no syndromes have been currently linked to the *RGP1* gene, the zebrafish models presented here will provide a valuable tool to test other non-skeletal phenotypes potentially associated with RGP1 variants that might emerge from Whole Exome Sequencing of clinical cases.

In closing, regulation of post-Golgi trafficking is an essential process in the development and function of tissues such as cartilage. The coordination of Rgp1, Rab6a, and Rab8a to regulate collagen II secretion demonstrates the complexity of intracellular interactions that govern vesicle dynamics. The continued identification of the individual components and pathways that regulate protein trafficking offers insight into biological mechanisms that are likely to apply broadly across tissues during development.

Data availability statement

The data presented in this study are deposited in Genbank (accession numbers OQ305607, OQ305608, OQ305609, OQ305610) and Figshare (accession numbers 21944015, 21944093).

Ethics statement

The animal study was reviewed and approved by Institutional Animal Care and Use Committee at Vanderbilt University Medical Center.

Author contributions

DR, GU, and EK conceived the project and designed the analysis. DR and DC collected the data. DR, DC, and GU contributed analysis tools. DR performed most of the research and analysis described. DR and EK wrote the paper with contributions and input from all authors. All authors contributed to the article and approved the submitted version.

Funding

EK gratefully acknowledges financial support from the National Institutes of Health (NIH) (R01MH113362) (R56AG068026). DC was supported by NIH R01MH113362. DR was supported by National Research Service Award (NRSA) 1F31DE030007 and the T32GM008554 Training Program in Cellular, Biochemical, and Molecular Sciences. GU was supported by the Vanderbilt International Scholar Program and American Heart Association predoctoral fellowship (15PRE22940041). The Vanderbilt University Cell Imaging Shared Resource was supported by NIH grant DK020593.

Acknowledgments

We are grateful to Sarah Naguib, James Hayes, Alex Pfannenstein, and the members of the Knapik Laboratory for their helpful discussions and feedback. We thank the Vanderbilt University Cell Imaging Shared Resource for technical support with confocal imaging, data analysis, and electron microscopy, and we thank Cory Guthrie and the Zebrafish Core Facility for fish care.

Conflict of interest

The authors declare that the research was conducted in the absence of any commercial or financial relationships that could be construed as a potential conflict of interest.

Publisher's note

Supplementary material

The Supplementary Material for this article can be found online at: https://www.frontiersin.org/articles/10.3389/fendo.2023.1120420/full#supplementary-material

References

1. Frantz C, Stewart KM, Weaver VM. The extracellular matrix at a glance. *J Cell Sci* (2010) 123:4195–200. doi: 10.1242/jcs.023820

2. Rozario T, DeSimone DW. The extracellular matrix in development and morphogenesis: A dynamic view. *Dev Biol* (2010) 341:126. doi: 10.1016/J.YDBIO.2009.10.026

3. Luderman LN, Unlu G, Knapik EW. Zebrafish developmental models of skeletal diseases. *Curr Top Dev Biol* (2017) 124:81–124. doi: 10.1016/BS.CTDB.2016.11.004

4. Ishikawa Y, Bächinger HP. A molecular ensemble in the rER for procollagen maturation. *Biochim Biophys Acta - Mol Cell Res* (2013) 1833:2479–91. doi: 10.1016/J.BBAMCR.2013.04.008

5. Gordon MK, Hahn RA. Collagens. *Cell Tissue Res* (2010) 339:247. doi: 10.1007/S00441-009-0844-4

6. Melville DB, Knapik EW. Traffic jams in fish bones: ER-to-Golgi protein transport during zebrafish development. *Cell Adh Migr* (2011) 5:114. doi: 10.4161/CAM.5.2.14377

7. Emr S, Glick BS, Linstedt AD, Lippincott-Schwartz J, Luini A, Malhotra V, et al. Journeys through the golgi–taking stock in a new era. *J Cell Biol* (2009) 187:449–53. doi: 10.1083/JCB.200909011

8. Hellicar J, Stevenson NL, Stephens DJ, Lowe M. Supply chain logistics - the role of the golgi complex in extracellular matrix production and maintenance. *J Cell Sci* (2022) 135. doi: 10.1242/JCS.258879

9. Lang MR, Lapierre LA, Frotscher M, Goldenring JR, Knapik EW. Secretory COPII coat component Sec23a is essential for craniofacial chondrocyte maturation. *Nat Genet* (2006) 38:1198–203. doi: 10.1038/ng1880

10. Sarmah S, Barrallo-Gimeno A, Melville DB, Topczewski J, Solnica-Krezel L, Knapik EW. Sec24D-dependent transport of extracellular matrix proteins is required for zebrafish skeletal morphogenesis. *PloS One* (2010) 5:e10367. doi: 10.1371/journal.pone.0010367

11. Melville DB, Montero-Balaguer M, Levic DS, Bradley K, Smith JR, Hatzopoulos AK, et al. The feelgood mutation in zebrafish dysregulates COPII-dependent secretion of select extracellular matrix proteins in skeletal morphogenesis. *Dis Model Mech* (2011) 4:763–76. doi: 10.1242/dmm.007625

12. Malhotra V, Erlmann P. Protein export at the ER: loading big collagens into COPII carriers. *EMBO J* (2011) 30:3475. doi: 10.1038/EMBOJ.2011.255

13. Saito K, Chen M, Bard F, Chen S, Zhou H, Woodley D, et al. TANGO1 facilitates cargo loading at endoplasmic reticulum exit sites. *Cell* (2009) 136:891–902. doi: 10.1016/J.CELL.2008.12.025

14. Raote I, Chabanon M, Walani N, Arroyo M, Garcia-Parajo MF, Malhotra V, et al. A physical mechanism of TANGO1-mediated bulky cargo export. *Elife* (2020) 9:1–41. doi: 10.7554/ELIFE.59426

15. Saito K, Yamashiro K, Ichikawa Y, Erlmann P, Kontani K, Malhotra V, et al. cTAGE5 mediates collagen secretion through interaction with TANGO1 at endoplasmic reticulum exit sites. *Mol Biol Cell* (2011) 22:2301–8. doi: 10.1091/MBC.E11-02-0143

16. Townley AK, Feng Y, Schmidt K, Carter DA, Porter R, Verkade P, et al. Efficient coupling of Sec23-Sec24 to Sec13-Sec31 drives COPII-dependent collagen secretion and is essential for normal craniofacial development. *J Cell Sci* (2008) 121:3025–34. doi: 10.1242/JCS.031070

17. McCaughey J, Stevenson NL, Mantell JM, Neal CR, Paterson A, Heesom K, et al. A general role for TANGO1, encoded by MIA3, in secretory pathway organization and function. *J Cell Sci* (2021) 134. doi: 10.1242/JCS.259075/271201

18. Unlu G, Qi X, Gamazon ER, Melville DB, Patel N, Rushing AR, et al. Phenome-based approach identifies RIC1-linked mendelian syndrome through zebrafish models, biobank associations and clinical studies. *Nat Med* (2020) 26:98–109. doi: 10.1038/s41591-019-0705-y

19. Bergen DJM, Stevenson NL, Skinner REH, Stephens DJ, Hammond CL. The golgi matrix protein giantin is required for normal cilia function in zebrafish. *Biol Open* (2017) 6:1180–9. doi: 10.1242/BIO.025502

20. Fromme JC, Ravazzola M, Hamamoto S, Al-Balwi M, Eyaid W, Boyadjiev SA, et al. The genetic basis of a craniofacial disease provides insight into COPII coat assembly. *Dev Cell* (2007) 13:623–34. doi: 10.1016/J.DEVCEL.2007.10.005

21. Marí-Beffa M, Mesa-Román AB, Duran I. Zebrafish models for human skeletal disorders. *Front Genet* (2021) 12:675331. doi: 10.3389/FGENE.2021.675331

22. Kague E, Roy P, Asselin G, Hu G, Simonet J, Stanley A, et al. Osterix/Sp7 limits cranial bone initiation sites and is required for formation of sutures. *Dev Biol* (2016) 413:160–72. doi: 10.1016/J.YDBIO.2016.03.011

23. Levic DS, Unlu G, Melville DB, Knapik EW. Regulated extracellular matrix trafficking shapes cell growth during cartilage morphogenesis. *bioRxiv* (2022). doi: 10.1101/2022.06.08.495337

24. Hall BK, Miyake T. Divide, accumulate, differentiate: Cell condensation in skeletal development revisited. *Int J Dev Biol* (2004) 39:881–93. doi: 10.1387/IJDB.8901191

25. Kague E, Gallagher M, Burke S, Parsons M, Franz-Odendaal T, Fisher S. Skeletogenic fate of zebrafish cranial and trunk neural crest. *PloS One* (2012) 7. doi: 10.1371/JOURNAL.PONE.0047394

26. Claeys L, Storoni S, Eekhoff M, Elting M, Wisse L, Pals G, et al. Collagen transport and related pathways in osteogenesis imperfecta. *Hum Genet* (2021) 140:1121–41. doi: 10.1007/S00439-021-02302-2

27. Bella J, Hulmes DJS. Fibrillar collagens. *Subcell Biochem* (2017) 82:457–90. doi: 10.1007/978-3-319-49674-0_14

28. Exposito J-Y, Valcourt U, Cluzel C, Lethias C. The fibrillar collagen family. *Open Access Int J Mol Sci* (2010) 11:11. doi: 10.3390/ijms11020407

29. Steplewski A, Hintze V, Fertala A. Molecular basis of organization of collagen fibrils. *J Struct Biol* (2007) 157:297–307. doi: 10.1016/J.JSB.2006.10.009

30. Nenna R, Turchetti A, Mastrogiorgio G, Midulla F. COL2A1 gene mutations: Mechanisms of spondyloepiphyseal dysplasia congenita. *Appl Clin Genet* (2019) 12:235. doi: 10.2147/TACG.S197205

31. Spranger J, Winterpacht A, Zabel B. The type II collagenopathies: A spectrum of chondrodysplasias. *Eur J Pediatr* (1994) 153:56–65. doi: 10.1007/BF01959208

32. Barat-Houari M, Sarrabay G, Gatinois V, Fabre A, Dumont B, Genevieve D, et al. Mutation update for COL2A1 gene variants associated with type II collagenopathies. *Hum Mutat* (2016) 37:7–15. doi: 10.1002/HUMU.22915

33. Kannu P, Bateman J, Savarirayan R. Clinical phenotypes associated with type II collagen mutations. *J Paediatr Child Health* (2012) 48:E38–E43. doi: 10.1111/J.1440-1754.2010.01979.X

34. Xu L, Qiu X, Zhu Z, Yi L, Qiu Y. A novel mutation in COL2A1 leading to spondyloepiphyseal dysplasia congenita in a three-generation family. *Eur Spine J* (2014) 23 Suppl 2:271–277. doi: 10.1007/S00586-014-3292-0

35. Reddi AH, Gay R, Gay S, Miller EJ. Transitions in collagen types during matrix-induced cartilage, bone, and bone marrow formation. *Proc Natl Acad Sci U.S.A.* (1977) 74:5589–92. doi: 10.1073/PNAS.74.12.5589

36. Li SW, Prockop DJ, Helminen H, Fässler R, Lapveteläinen T, Kiraly K, et al. Transgenic mice with targeted inactivation of the Col2 alpha 1 gene for collagen II develop a skeleton with membranous and periosteal bone but no endochondral bone. *Genes Dev* (1995) 9:2821–30. doi: 10.1101/GAD.9.22.2821

37. Salo AM, Cox H, Farndon P, Moss C, Grindulis H, Risteli M, et al. A connective tissue disorder caused by mutations of the lysyl hydroxylase 3 gene. *Am J Hum Genet* (2008) 83:495. doi: 10.1016/J.AJHG.2008.09.004

38. Mumm S, Gottesman GS, Wenkert D, Campeau PM, Nenninger A, Huskey M, et al. Bruck syndrome 2 variant lacking congenital contractures and involving a novel compound heterozygous PLOD2 mutation. *Bone* (2020) 130:115047. doi: 10.1016/J.BONE.2019.115047

39. Gorur A, Yuan L, Kenny SJ, Baba S, Xu K, Schekman R. COPII-coated membranes function as transport carriers of intracellular procollagen I. *J Cell Biol* (2017) 216:1745. doi: 10.1083/JCB.201702135

40. Stalder D, Gershlick DC. Direct trafficking pathways from the golgi apparatus to the plasma membrane. *Semin Cell Dev Biol* (2020) 107:112–125. doi: 10.1016/j.semcdb.2020.04.001

41. Di Martino R, Sticco L, Luini A. Regulation of cargo export and sorting at the trans-golgi network. *FEBS Lett* (2019) 593:2306–18. doi: 10.1002/1873-3468.13572

42. Bonfanti L, Mironov AA, Martínez-Menárguez JA, Martella O, Fusella A, Baldassarre M, et al. Procollagen traverses the golgi stack without leaving the lumen of cisternae: Evidence for cisternal maturation. *Cell* (1998) 95:993–1003. doi: 10.1016/S0092-8674(00)81723-7

43. Ishida M, Oguchi ME, Fukuda M, E. Oguchi M, Fukuda M. Multiple types of guanine nucleotide exchange factors (GEFs) for rab small GTPases. *Cell Struct Funct* (2016) 41:61–79. doi: 10.1247/csf.16008

44. Pusapati GV, Luchetti G, Pfeffer SR. Ric1-Rgp1 complex is a guanine nucleotide exchange factor for the late golgi Rab6A GTPase and an effector of the medial golgi Rab33B GTPase. *J Biol Chem* (2012) 287:42129–37. doi: 10.1074/jbc.M112.414565

45. Siniossoglou S, Peak-Chew SY, Pelham HR. Ric1p and Rgp1p form a complex that catalyses nucleotide exchange on Ypt6p. *EMBO J* (2000) 19:4885–94. doi: 10.1093/emboj/19.18.4885

46. Pfeffer SR. Rab GTPases: master regulators that establish the secretory and endocytic pathways. *Mol Biol Cell* (2017) 28:712–5. doi: 10.1091/mbc.E16-10-0737

47. Schwartz SL, Cao C, Pylypenko O, Rak A, Wandinger-Ness A. Rab GTPases at a glance. *J Cell Sci* (2007) 120:3905–10. doi: 10.1242/jcs.015909

48. Hattula K, Furuhjelm J, Arffman A, Peränen J. A Rab8-specific GDP/GTP exchange factor is involved in actin remodeling and polarized membrane transport. *Mol Biol Cell* (2002) 13:3268–80. doi: 10.1091/mbc.E02-03-0143

49. Homma Y, Fukuda M. Rabin8 regulates neurite outgrowth in both GEF activity-dependent and -independent manners. *Mol Biol Cell* (2016) 27:2107–18. doi: 10.1091/MBC.E16-02-0091

50. Consortium TU, Bateman A, Martin M-J, Orchard S, Magrane M, Ahmad S, et al. UniProt: The universal protein knowledgebase in 2023. *Nucleic Acids Res* (2023) 51:D523–31. doi: 10.1093/NAR/GKAC1052

51. Montague TG, Cruz JM, Gagnon JA, Church GM, Valen E. CHOPCHOP: a CRISPR/Cas9 and TALEN web tool for genome editing. *Nucleic Acids Res* (2014) 42:W401–W407. doi: 10.1093/NAR/GKU410

52. Bayraktar EC, La K, Karpman K, Unlu G, Ozerdem C, Ritter DJ, et al. Metabolic coessentiality mapping identifies C12orf49 as a regulator of SREBP processing and cholesterol metabolism. *Nat Metab* (2020) 2:1–12. doi: 10.1038/s42255-020-0206-9

53. Schindelin J, Arganda-Carreras I, Frise E, Kaynig V, Longair M, Pietzsch T, et al. Fiji - an open source platform for biological image analysis. *Nat Methods* (2012) 9:676–82. doi: 10.1038/NMETH.2019

54. Walker MB, Kimmel CB. A two-color acid-free cartilage and bone stain for zebrafish larvae. *Biotech Histochem* (2009) 82:23–8. doi: 10.1080/10520290701333558

55. Müller II, Knapik EW, Hatzopoulos AK. Expression of the protein related to Dan and Cerberus gene–prdc—During eye, pharyngeal arch, somite, and swim bladder development in zebrafish. *Dev Dyn* (2006) 235:2881–8. doi: 10.1002/DVDY.20925

56. Cox NJ, Unlu G, Bisnett BJ, Meister TR, Condon B, Luo PM, et al. Dynamic glycosylation governs the vertebrate COPII protein trafficking pathway HHS public access SEC23A-dependent *in vivo* collagen trafficking and skeletogenesis in a zebrafish model of CLSD. *Biochemistry* (2018) 57:91–107. doi: 10.1021/acs.biochem.7b00870

57. Dale RM, Topczewski J. Identification of an evolutionarily conserved regulatory element of the zebrafish col2a1a gene. *Dev Biol* (2011) 357:518–31. doi: 10.1016/j.ydbio.2011.06.020

58. Kawakami K. Tol2: a versatile gene transfer vector in vertebrates. *Genome Biol* (2007) 8 Suppl 1:S7. doi: 10.1186/gb-2007-8-s1-s7

59. Granero-Moltó F, Sarmah S, O'Rear L, Spagnoli A, Abrahamson D, Saus J, et al. Goodpasture antigen-binding protein and its spliced variant, ceramide transfer protein, have different functions in the modulation of apoptosis during zebrafish development. *J Biol Chem* (2008) 283:20495–504. doi: 10.1074/jbc.M801806200

60. Luderman LN, Michaels MT, Levic DS, Knapik EW. Zebrafish Erc1b mediates motor innervation and organization of craniofacial muscles in control of jaw movement. *Dev Dyn* (2022) 252:104–123. doi: 10.1002/DVDY.511

61. Liu D, Wang WD, Melville DB, Cha YI, Yin Z, Issaeva N, et al. Tumor suppressor lzap regulates cell cycle progression, doming, and zebrafish epiboly. *Dev Dyn* (2011) 240:1613–25. doi: 10.1002/DVDY.22644

62. Unlu G, Gamazon ER, Qi X, Levic DS, Bastarache L, Denny JC, et al. GRIK5 genetically regulated expression associated with eye and vascular phenomes: Discovery through iteration among biobanks, electronic health records, and zebrafish. *Am J Hum Genet* (2019) 104:503–19. doi: 10.1016/j.ajhg.2019.01.017

63. GraphPad. *GraphPad prism software*. GraphPad (2012). Available at: www.graphpad.com.

64. Eames B, DeLaurier A, Ullmann B, Huycke TR, Nichols JT, Dowd J, et al. FishFace: interactive atlas of zebrafish craniofacial development at cellular resolution. *BMC Dev Biol* (2013) 13:23. doi: 10.1186/1471-213X-13-23

65. El-Brolosy MA, Kontarakis Z, Rossi A, Kuenne C, Günther S, Fukuda N, et al. Genetic compensation triggered by mutant mRNA degradation. *Nature* (2019) 568:193–7. doi: 10.1038/s41586-019-1064-z

66. Rossi A, Kontarakis Z, Gerri C, Nolte H, Hölper S, Krüger M, et al. Genetic compensation induced by deleterious mutations but not gene knockdowns. *Nature* (2015) 524:230–3. doi: 10.1038/nature14580

67. Ma Z, Zhu P, Shi H, Guo L, Zhang Q, Chen Y, et al. PTC-bearing mRNA elicits a genetic compensation response *via* Upf3a and COMPASS components. *Nature* (2019) 568:259–63. doi: 10.1038/s41586-019-1057-y

68. Yan Y-LY -L, Hatta K, Riggleman B, Postlethwait JH. Expression of a type II collagen gene in the zebrafish embryonic axis. *Dev Dyn* (1995) 203:363–76. doi: 10.1002/AJA.1002030308

69. Gao J, Liao J, Yang GY. CAAX-box protein, prenylation process and carcinogenesis. *Am J Transl Res* (2009) 1:312–25.

70. Linsenmayer TF, Hendrix MJC. Monoclonal antibodies to connective tissue macromolecules: Type II collagen. *Biochem Biophys Res Commun* (1980) 92:440–6. doi: 10.1016/0006-291X(80)90352-6

71. Kim JH, Lee S-R, Li L-H, Park H-J, Park J-H, Lee KY, et al. High cleavage efficiency of a 2A peptide derived from porcine teschovirus-1 in human cell lines, zebrafish and mice. *PloS One* (2011) 6:e18556. doi: 10.1371/journal.pone.0018556

72. Piez KA, Miller A. The structure of collagen fibrils. *J Supramol Struct* (1974) 2:121–37. doi: 10.1002/JSS.400020207

73. Shoulders MD, Raines RT. COLLAGEN STRUCTURE AND STABILITY. *Annu Rev Biochem* (2009) 78:929–58. doi: 10.1146/ANNUREV.BIOCHEM.77.032207.120833

74. Hirata Y, Matsui Y, Wada I, Hosokawa N. Endoplasmic reticulum-to-Golgi trafficking of procollagen III via conventional vesicular and tubular carriers. *Mol Biol Cell* (2022) 33:ar21. doi: 10.1091/MBC.E21-07-0372

75. Prockop DJ, Kivirikko KI, Tuderman L, Guzman NA. The biosynthesis of collagen and its disorders (second of two parts). *N Engl J Med* (1979) 301:77–85. doi: 10.1056/NEJM197907123010204

76. Ballabio A, Bonifacino JS. Lysosomes as dynamic regulators of cell and organismal homeostasis. *Nat Rev Mol Cell Biol* (2020) 21:101–18. doi: 10.1038/S41580-019-0185-4

77. Wherrett JR, Huterer S. Enrichment of bis-(monoacylglyceryl) phosphate in lysosomes from rat liver. *J Biol Chem* (1972) 247:4114–20. doi: 10.1016/S0021-9258(19)45047-3

78. Gruenberg J. Life in the lumen: The multivesicular endosome. *Traffic* (2020) 21:76–93. doi: 10.1111/TRA.12715/

79. Grigoriev I, Splinter D, Keijzer N, Wulf PS, Demmers J, Ohtsuka T, et al. Rab6 regulates transport and targeting of exocytotic carriers. *Dev Cell* (2007) 13:305–14. doi: 10.1016/J.DEVCEL.2007.06.010

80. Shibata S, Kawanai T, Hara T, Yamamoto A, Chaya T, Tokuhara Y, et al. ARHGEF10 directs the localization of Rab8 to Rab6-positive executive vesicles. *J Cell Sci* (2016) 129:3620–34. doi: 10.1242/JCS.186817

81. Huber LA, Pimplikar S, Parton RG, Virta H, Zerial M, Simons K. Rab8, a small GTPase involved in vesicular traffic between the TGN and the basolateral plasma membrane. *J Cell Biol* (1993) 123:35–45. doi: 10.1083/jcb.123.1.35

82. Markgraf DF, Peplowska K, Ungermann C. Rab cascades and tethering factors in the endomembrane system. *FEBS Lett* (2007) 581:2125–30. doi: 10.1016/j.febslet.2007.01.090

83. Hutagalung AH, Novick PJ. Role of rab GTPases in membrane traffic and cell physiology. *Physiol Rev* (2011) 91:119–49. doi: 10.1152/physrev.00059.2009

84. Del Nery E, Miserey-Lenkei S, Falguières T, Nizak C, Johannes L, Perez F, et al. Rab6A and Rab6A′ GTPases play non-overlapping roles in membrane trafficking. *Traffic* (2006) 7:394–407. doi: 10.1111/J.1600-0854.2006.00395.X

85. Moritz OL, Tam BM, Hurd LL, Peränen J, Deretic D, Papermaster DS. Mutant rab8 impairs docking and fusion of rhodopsin-bearing post-golgi membranes and causes cell death of transgenic xenopus rods. *Mol Biol Cell* (2001) 12:2341. doi: 10.1091/MBC.12.8.2341

86. Bravo-Cordero JJ, Marrero-Diaz R, Megías D, Genís L, García-Grande A, García MA, et al. MT1-MMP proinvasive activity is regulated by a novel Rab8-dependent exocytic pathway. *EMBO J* (2007) 26:1499–510. doi: 10.1038/SJ.EMBOJ.7601606

87. Burattini S, Falcieri E. Analysis of cell death by electron microscopy. *Methods Mol Biol* (2013) 1004:77–89. doi: 10.1007/978-1-62703-383-1_7

88. Elmore S. Apoptosis: A review of programmed cell death. *Toxicol Pathol* (2007) 35:495. doi: 10.1080/01926230701320337

89. Reiling JH, Olive AJ, Sanyal S, Carette JE, Brummelkamp TR, Ploegh HL, et al. A CREB3–ARF4 signalling pathway mediates the response to golgi stress and susceptibility to pathogens. *Nat Cell Biol* (2013) 15:1473–85. doi: 10.1038/ncb2865

90. Ford C, Parchure A, von Blume J, Burd CG. Cargo sorting at the trans-golgi network at a glance. *J Cell Sci* (2021) 134. doi: 10.1242/JCS.259110/273634

91. Wu H, Carvalho P, Voeltz GK. Here, there, and everywhere: The importance of ER membrane contact sites. *Science (80-)* (2018) 361. doi: 10.1126/SCIENCE.AAN5835

92. Zaman MF, Nenadic A, Radojičić A, Rosado A, Beh CT. Sticking with it: ER-PM membrane contact sites as a coordinating nexus for regulating lipids and proteins at the cell cortex. *Front Cell Dev Biol* (2020) 8:675. doi: 10.3389/FCELL.2020.00675

93. Li C, Qian T, He R, Wan C, Liu Y, Yu H, et al. Endoplasmic reticulum–plasma membrane contact sites: Regulators, mechanisms, and physiological functions. *Front Cell Dev Biol* (2021) 9:627700. doi: 10.3389/FCELL.2021.627700

94. Adarska P, Wong-Dilworth L, Bottanelli F. ARF GTPases and their ubiquitous role in intracellular trafficking beyond the golgi. *Front Cell Dev Biol* (2021) 0:679046. doi: 10.3389/FCELL.2021.679046

95. Donaldson JG, Jackson CL. ARF family G proteins and their regulators: roles in membrane transport, development and disease. *Nat Rev Mol Cell Biol* (2011) 12:362–75. doi: 10.1038/nrm3117

96. Grigoriev I, Lou Y, Martinez-Sanchez E, Serra-Marques A, Smal I, Meijering E, et al. Rab6, Rab8, and MICAL3 cooperate in controlling docking and fusion of exocytotic carriers. *Curr Biol* (2011) 21:967–74. doi: 10.1016/J.CUB.2011.04.030

97. Henry L, Sheff DR. Rab8 regulates basolateral secretory, but not recycling, traffic at the recycling endosome. *Mol Biol Cell* (2008) 19:2059–68. doi: 10.1091/MBC.E07-09-0902

98. Devergne O, Sun GH, Schüpbach T. Stratum, a homolog of the human GEF Mss4, partnered with Rab8, controls the basal restriction of basement membrane proteins in epithelial cells. *Cell Rep* (2017) 18:1831–9. doi: 10.1016/J.CELREP.2017.02.002

99. Prasad V, Suomalainen M, Pennauer M, Yakimovich A, Andriasyan V, Hemmi S, et al. Chemical induction of unfolded protein response enhances cancer cell killing through lytic virus infection. *J Virol* (2014) 88:13086–98. doi: 10.1128/JVI.02156-14

100. Shinjo S, Mizotani Y, Tashiro E, Imoto M. Comparative analysis of the expression patterns of UPR-target genes caused by UPR-inducing compounds. *Biosci Biotechnol Biochem* (2013) 77:729–35. doi: 10.1271/BBB.120812

101. Nakai W, Kondo Y, Saitoh A, Naito T, Nakayama K, Shin HW. ARF1 and ARF4 regulate recycling endosomal morphology and retrograde transport from endosomes to the golgi apparatus. *Mol Biol Cell* (2013) 24:2570–81. doi: 10.1091/MBC.E13-04-0197

102. Liu S, Storrie B. How rab proteins determine golgi structure. *Int Rev Cell Mol Biol* (2015) 315:1–22. doi: 10.1016/bs.ircmb.2014.12.002

103. Santos-Ledo A, Garcia-Macia M, Campbell PD, Gronska M, Marlow FL. Kinesin-1 promotes chondrocyte maintenance during skeletal morphogenesis. *PloS Genet* (2017) 13:e1006918. doi: 10.1371/JOURNAL.PGEN.1006918

104. Nishimura G, Haga N, Kitoh H, Tanaka Y, Sonoda T, Kitamura M, et al. The phenotypic spectrum of COL2A1 mutations. *Hum Mutat* (2005) 26:36–43. doi: 10.1002/HUMU.20179

frontiers | Frontiers in Endocrinology

TYPE Original Research
PUBLISHED 22 February 2023
DOI 10.3389/fendo.2023.1101758

OPEN ACCESS

EDITED BY
Gudrun Stenbeck,
Brunel University London, United Kingdom

REVIEWED BY
Antonella Forlino,
University of Pavia, Italy
Farhath Sultana,
Icahn School of Medicine at Mount Sinai, United States

*CORRESPONDENCE
Christoph Winkler
dbswcw@nus.edu.sg

SPECIALTY SECTION
This article was submitted to Bone Research, a section of the journal Frontiers in Endocrinology

RECEIVED 18 November 2022
ACCEPTED 31 January 2023
PUBLISHED 22 February 2023

CITATION
Imangali N, Sokolova V, Kostka K, Epple M and Winkler C (2023) Functionalized calcium phosphate nanoparticles to direct osteoprotegerin to bone lesion sites in a medaka (*Oryzias latipes*) osteoporosis model.
Front. Endocrinol. 14:1101758.
doi: 10.3389/fendo.2023.1101758

Functionalized calcium phosphate nanoparticles to direct osteoprotegerin to bone lesion sites in a medaka (*Oryzias latipes*) osteoporosis model

Nurgul Imangali[1], Viktoriya Sokolova[2], Kathrin Kostka[2], Matthias Epple[2] and Christoph Winkler[1]*

[1]Department of Biological Sciences and Centre for Bioimaging Sciences, National University of Singapore, Singapore, Singapore, [2]Inorganic Chemistry and Center for Nanointegration Duisburg-Essen (CENIDE), University of Duisburg-Essen, Essen, Germany

Calcium phosphate (CaP) is the inorganic part of hard tissues, such as bone, teeth and tendons, and has a high biocompatibility and good biodegradability. Therefore, CaP nanoparticles functionalized with DNA encoding bone anabolic factors are promising carrier-systems for future therapeutic development. Here, we analysed CaP nanoparticles in a genetically modified medaka fish model, where osteoporosis-like lesions can be induced by transgenic expression of receptor activator of nuclear factor kappa-B ligand (Rankl). Rankl-transgenic medaka were used to visualize and understand effects of microinjected functionalized CaP nanoparticles during modulation of osteoclast activity *in vivo*. For this, we synthetized multi-shell CaP nanoparticles by rapid precipitation of calcium lactate and ammonium hydrogen phosphate followed by the addition of plasmid DNA encoding the osteoclastogenesis inhibitory factor osteoprotegerin-b (Opgb). An additional layer of poly(ethyleneimine) was added to enhance cellular uptake. Integrity of the synthesized nanoparticles was confirmed by dynamic light scattering, scanning electron microscopy and energy dispersive X-ray spectroscopy. Fluorescently labelled CaP nanoparticles were microinjected into the heart, trunk muscle or caudal fins of Rankl-transgenic medaka embryos that expressed fluorescent reporters in various bone cell types. Confocal time-lapse imaging revealed a uniform distribution of CaP nanoparticles in injected tissues and showed that nanoparticles were efficiently taken up by macrophages that subsequently differentiated into bone-resorbing osteoclasts. After Rankl induction, fish injected with Opg-functionalized nanoparticles showed delayed or absent degradation of mineralized matrix, i.e. a lower incidence of osteoporosis-like phenotypes. This is proof of principle that CaP nanoparticles can be used as carriers to efficiently deliver modulatory compounds to osteoclasts and block their activity.

KEYWORDS

osteoporosis, nanoparticles, bone resorption, Rankl, osteoprotegerin, OPG

Introduction

Bone is constantly remodelled to maintain its rigidity and bone mineral density (reviewed in 1). This requires repeated rounds of bone resorption by osteoclasts that are derived from the monocyte/macrophage lineage. Bone resorption is immediately followed by formation of new bone matrix, which is deposited by osteoblasts that originate from mesenchymal progenitor cells. Osteoclast formation and activity is tightly controlled by a triad consisting of receptor-activator of nuclear kappa-B ligand (Rankl), Rank and osteoprotegerin (OPG). Rankl binds to Rank on the surface of osteoclast precursors to induce differentiation, while osteoblast-derived OPG serves as a secreted decoy receptor that binds to Rankl to prevent its interaction with Rank (2). Formation and activation of osteoblasts and osteoclasts needs to be coordinated to prevent excessive bone resorption and maintain homeostatic bone remodeling. Any disruption results in skeletal diseases such as osteoporosis, a chronic disorder characterized by reduced bone mass, deterioration of bone microarchitecture and fracture-prone bones. Women and men over the age of 50 have an increased risk for osteoporotic fractures, with up to 9 million osteoporotic fractures reported globally (3, 4). Current osteoporosis treatments either use inhibitors of bone resorption or enhancers of bone formation. Anti-resorptive drugs such as bisphosphonates represent a frequently used first-line therapy to reduce resorption by blocking overall osteoclast activity. However, prolonged bisphosphonate exposure reduces bone-cell coupling and impairs bone remodelling to result in more fracture-prone bones (reviewed in 5). Therefore, more targeted therapies are needed that maintain bone quality in a controlled manner especially after long-term use.

Nanoparticles have gained increasing attention as delivery vehicles in therapy, e.g. of cancer (reviewed in 6). They offer deep tissue penetration and efficiently deliver chemicals, growth factors or nucleic acids to target tissues, including bone (reviewed in 7). Historically, calcium phosphate nanoparticles (CaP) were first used as gene carriers in 1973 with reasonable transfection rates *in vitro* (8). The transfection efficiency of triple-shell CaP was shown to be similar to commercially available Polyfect transfection agents and CaP nanoparticles were reported to be safe and non-toxic (9). In a bone context, previous *in vitro* studies suggested that particles could induce synthesis of various cytokines such as Rankl within osteoblasts, which in turn enhanced formation of osteoclasts (10, 11). Nanoparticles were also used to deliver osteoblast-inducing proteins BMP2 and Runx2 to bone matrix, which resulted in increased osteogenesis *in vitro* (12–14). *In vivo*, a scaffold coated with CaP nanoparticles and implanted into mice released bisphosphonates as well as plasmid DNA encoding BMP2, which both enhanced bone formation (15, 16). Thus, an osteogenic effect of functionalized nanoparticles has been established. However, these approaches so far have not been used under osteoporotic conditions and the efficacy of applied nanoparticles under such conditions remains unknown.

Small fish models have become popular for bone research and modelling human bone disorders, including osteoporosis (17, 18). Our lab previously established a medaka fish osteoporosis model, where inducible expression of Rankl triggered ectopic formation of osteoclasts, excessive bone resorption and osteoporosis-like bone lesions (19, 20). In the present study, we took advantage of translucent medaka larvae and used live confocal imaging to visualize dynamics and distribution of injected CaP nanoparticles under osteoporosis-like conditions. Nanoparticles were functionalized with plasmid DNA encoding mCherry or osteoprotegerin-b (Opgb), and assessing bone cell activity and mineralization revealed a protective effect of functionalized nanoparticles. Our findings suggest an efficient osteomodulatory capacity of functionalized CaP nanoparticles as vehicles *in vivo*.

Materials and methods

Fish maintenance and transgenic lines

All animal experiments were performed in accordance with protocols approved by the Institutional Animal Care and Use Committee (IACUC) of NUS (protocol numbers: R14-293, R18-0562, BR15-0119, BR19-0120). Medaka strains were kept in the fish facility at the National University of Singapore (NUS), Department of Biological Sciences (DBS) under a controlled photoperiod of 14 hours light/10 hours darkness at 28°C to induce spawning. Collected embryos were raised in 0.3 x Danieau's solution (fish medium; 0.23 mM KCl, 19.3 mM NaCl, 0.2 mM $Ca(NO_3)_2$, 0.13 mM $MgSO_4$ and 1.7 mM HEPES, pH 7.0) in a 30°C incubator, and staged according to Iwamatsu (21). Fish medium was changed daily and embryos were screened for fluorescence reporter expression from 5 days post fertilization (dpf) onwards. Hatchlings were raised at 30°C until 14 dpf, and 28°C from 14 dpf onwards. Wild-type (Cab) and transgenic medaka lines labelling macrophages (*mpeg1*:mCherry), osteoclasts (*ctsk*:mCherry), osteoblasts (*osx*:GFP) and their precursors (*col10a1*:nlGFP), as well as carrying a heat-shock inducible Rankl transgene are described in Supplemental Table 1. Transgenic fish were maintained as homozygous carriers. Double and triple transgenic lines were generated through cross-breeding of single transgenic lines.

Cloning of plasmids expressing osteoprotegerin-b

For generation of cDNA encoding osteoprotegerin-b (*opgb*; ENSORLT00000006170), total RNA was extracted from wild-type medaka larvae (10 to 15 larvae pooled per biological replicate; 9 to 18 dpf) or adult medaka fins. Total cDNA synthesis was performed using a RevertAid First Strand cDNA Synthesis kit (Thermo Scientific K1621) with oligo(dT)18 primers and 500 ng to 1 µg of total RNA, according to the manufacturer's protocol. The medaka *opgb* coding sequence (881 bp) was amplified from cDNA using primers opgF (5'-GGGGAATTCCCACCATGACAGTGCTTTACC-3') and opgR (5'-CAGCAGGCT GAAGTTTGTAGCTGGAAAAATCAAGCTAC-3'). To generate a *mpeg1*:*opgb*-p2a-EGFP plasmid, a p2a-EGFP-PolyA sequence was amplified from *osx*:*cxcl9l*-p2a-EGFP (20). The *opgb* cDNA and p2a-EGFP-SV40 fragments were fused by overlap extension PCR using primers that introduced a 5'-*EcoRI* site, followed by a Kozak sequence and a 3'-*ApaI* site. The obtained *opgb*-p2a-EGFP-SV40 fragment was digested with *EcoRI* and *ApaI*

restriction enzymes and ligated in frame into a *pI-SceI* plasmid containing the *mpeg1* promoter digested with *EcoRI* and *ApaI* (22). The *mpeg1:opgb*-p2a-EGFP plasmid (Supplementary Figure S1) allows ectopic expression of *opgb*, linked to EGFP *via* a self-cleaving p2a peptide, in *mpeg1*-expressing macrophages in medaka. Primers used are listed in Supplementary Table 2. For a functionality test, the plasmid was injected into medaka embryos at one-cell stage together with *I-Sce-I* meganuclease and hatchlings were imaged to visualize EGFP expression in macrophages in the aorta-mesonephros-gonad region (AGM) from 6 dpf onwards (Supplementary Figure S2).

Preparation and characterization of nanoparticles

Triple-shell CaP nanoparticles were prepared by a co-precipitation from water according to earlier protocols (23). A 0.1 M NaOH solution (p.a.; Merck, Darmstadt, Germany) was used to adjust the pH of aqueous solutions of calcium-L-lactate (18 mmol L^{-1}; p.a., Sigma Aldrich, Waltham, MA, USA) and diammonium hydrogen phosphate (10.8 mmol L^{-1}; p.a., Merck, Darmstadt, Germany) to 10. Ultrapure water (Purelab ultra instrument, ELGA) with a specific resistivity of 18.2 MΩ was used for all syntheses. For the colloidal stabilization of CaP nanoparticles and additional fluorescent labelling, the Cy5-labelled cationic polymer polyethyleneimine (PEI-Cy5, 2 mg mL^{-1}, M_w = 25 kDa, Surflay Nanotec GmbH, Berlin, Germany) was used. The three solutions described above were rapidly pumped with peristaltic pumps in a volume ratio 5 mL: 5 mL: 7 mL into a glass vessel containing 3.3 mL ultrapure water to obtain CaP/PEI-Cy5 nanoparticles. To synthesize pDNA-functionalized CaP/PEI-Cy5-nanoparticles, two different plasmids were added to this dispersion, respectively, after stirring for 20 min at room temperature. The first plasmid was pDNA-mCherry, encoding mCherry together with a ubiquitously active CMV enhancer (23), to obtain CaP/PEI-Cy5/pDNA-mCherry nanoparticles. The second plasmid was *mpeg1:opgb*-p2a-EGFP to obtain CaP/PEI-Cy5/*mpeg1:opgb*-p2a-EGFP nanoparticles. Plasmid DNA (pDNA) was purified by column purification following the manufacturer's instructions (Qiagen Plasmid Maxi Kit; Qiagen, Hilden, Germany). Next, an outer silica shell was attached to protect the pDNA from enzymatic degradation. For this, 5 mL of the pDNA-loaded calcium phosphate nanoparticle dispersion was added to a mixture of 25 µL tetraethoxysilane (TEOS, 98%, Sigma Aldrich, CorpWaltham, MA, USA), 50 µL ammonia solution (7.8 wt %, Carl Roth, Karlsruhe, Germany), and 20 mL ethanol (EtOH, p.a., VWR, Darmstadt, Germany) in a round-bottom flask. The resulting dispersion was stirred at room temperature for 16 h. Particles were isolated at room temperature with a 5430/5430 R centrifuge (Eppendorf AG, Hamburg, Germany) at 30,000 rpm for 35 min, followed by redispersion in 5 mL ultrapure water accompanied by 12 s ultrasonication with a sonotrode (UP50H, sonotrode N7, amplitude 70%, pulse duration 0.8 s, Hielscher Ultrasonics GmbH, Teltow, Germany).

Atomic absorption spectroscopy (AAS) was performed with an M-Series AA spectrometer (Thermo Electron Corporation, Waltham, MA, USA) to determine the calcium concentration in a given dispersion. 0.5 mL of the sample was dissolved in diluted HCl. For the size distribution of the nanoparticles, dynamic light scattering (DLS) and for stability studies, zeta potential measurements were performed with a Zetasizer Nano ZS (λ= 633 nm, Malvern Nano ZS ZEN 3600, UK). Scanning electron microscopy (SEM) images were taken with an Apreo S LoVac microscope (ThermoFisher Scientific Inc., Waltham, MA, USA) to show the size and shape of the particles. UV-Vis measurements to determine the Cy5 concentration in the dispersion were performed with a Varian Cary 300 bio-spectrophotometer (Agilent Technologies, Santa Clara, California, USA) in a 400 µL Suprasil® quartz cuvette. To determine the pDNA concentration in the particles, a Microvolume UV-Vis spectrophotometer (λ= 260 nm, "Nanodrop", DS-11 FX+, DeNovix, Wilmington, DE, USA) was used by dropping 2 µL of the resulting dispersion (after purification by centrifugation) onto the measurement surface.

For a longer shelf-life, 250 µL of nanoparticle dispersion were mixed with 10 µL of a d-(+)-trehalose solution (20 mg/mL) as cryoprotectant and freeze-dried in a Christ Alpha 2-4 LSC device (Martin Christ GmbH, Osterode am Harz, Germany). The freeze-dried particles were stable, also for shipping. For application of the nanoparticles, they were redispersed in water or cell culture medium (cell experiments) by gentle sonication/vortexing.

Injection of nanoparticles

Lyophilized CaP nanoparticles were dispersed in water to a final concentration of 100 µM calcium in water solution. The solution was placed on ice and sonicated with a probe sonicator at 70% amplitude for 10 sec twice with a 10 sec interval to disperse agglomerates into individual nanoparticles. Around 300 nL of nanoparticle dispersion was injected into the heart ventricle, the trunk muscle region above the egg yolk extension or between the fin rays of the caudal fin of medaka larvae. Most injections were done at 9 to 13 days post fertilization (dpf; with one exception at 21 dpf), when macrophages, osteoblasts and osteoclasts can be imaged efficiently by confocal microscopy.

Live fluorescent bone staining

Live staining of mineralized bone matrix was done by immersing medaka hatchlings (12 to 18 dpf) in either Alizarin Complexone solution (ALC; 0.1% in fish medium, Sigma A3882) for two hours or in a Calcein solution (0.01% in fish medium; Sigma C0875) for one hour in the dark at room temperature (RT). Stained hatchlings were rinsed with fish medium three times (15 mins per rinse, at RT) and mounted in 1.5% low melting agarose on a glass bottom petri dish for live fluorescence imaging (488 nm laser/GFP filter for Calcein; 568 nm laser/mCherry filter for ALC).

Fluorescence imaging

Live fluorescence imaging was performed using a stereomicroscope (Nikon SMZ18) equipped with the NIS-Elements BR 3.0 software or confocal microscopes (Zeiss Meta 500; Olympus

FluoView FV3000; Zeiss LSM900). Medaka hatchlings (8 to 23 dpf) were anaesthetized with 0.005% ethyl 3-aminobenzoate methane sulfonate (Tricaine; Sigma MS-222) and mounted in 1.5% low-melting-point agarose on a glass bottom petri dish. Confocal pictures were taken using 405, 488, 543 or 633 nm laser lines for CFP, GFP, mCherry and Cy5 fluorescent signals, respectively. Time-lapse imaging was performed with Olympus FV3000 or Zeiss LSM900 microscopes by imaging the region of interest for 15-20 hours with 5-10 mins intervals. Imaging data were processed using Olympus FV31S-SW 2.1.1.98, Bitplane Imaris 9.0, ImageJ and Adobe Photoshop CC 2018 software.

Statistical analyses

The numbers of hatchlings with the indicated phenotype were recorded. Results were presented as percentages with mean (SEM) as determined using Prism 7.2. A Two-tailed Student's t-test was used to compare individual groups and to determine the significance. The level of significance was set as follows: *0.01<P<0.05, **P<0.01, ***P<0.001 and ****P<0.0001.

Results

Characterization of CaP nanoparticles

CaP nanoparticles were synthesised with the fluorescently labelled polymer PEI-Cy5. This allowed the tracking of the particles in biological experiments. The fluorescent polymer was quantified by UV spectroscopy after preparing a calibration row of dissolved PEI-Cy5 (absorption maximum at λ = 670 nm). The hydrodynamic diameter and the stability of the particles were investigated by dynamic light scattering (DLS) (Figure 1A). With a polydispersity index (PDI) below 0.3, the dispersion can be considered as well-dispersed. The zeta potential of +20 mV indicated an electrostatic stabilization with a positive charge due to the presence of PEI, which was obviously not compensated by the negative charge of plasmid DNA. Based on the SEM images (Figures 1B–D), the morphology of particles was uniform and approximately spherical. Table 1 summarises all analytical results of CaP/PEI-Cy5/SiO_2 and CaP/PEI-Cy5/pDNA/SiO_2 nanoparticles (for extended details on calculations, see 23).

Nanoparticles are stable after injection into medaka embryos

CaP nanoparticles were microinjected into medaka larvae at different stages (8 to 21 days post fertilization, dpf) into the following regions: i) the heart ventricle, ii) into the trunk muscle region positioned next to the aorta-gonad-mesonephros (AGM; a region where macrophages reside that differentiate into osteoclasts after Rankl induction (22)), and iii) between the bony fin rays of the caudal fin (Figure 2A). The stability of CaP nanoparticles was assessed by injection of Cy5-labelled nanoparticles into the heart ventricle and subsequent live fluorescent imaging of blood vessels at 1, 13 and 35 hours post injection (hpi). At 1 hpi, nanoparticles were observed in the heart (Figure 2B), and at 13 hpi in blood vessels of the trunk (Figure 2C, C'), and fin (Figure 2D, D'). This pattern suggested that

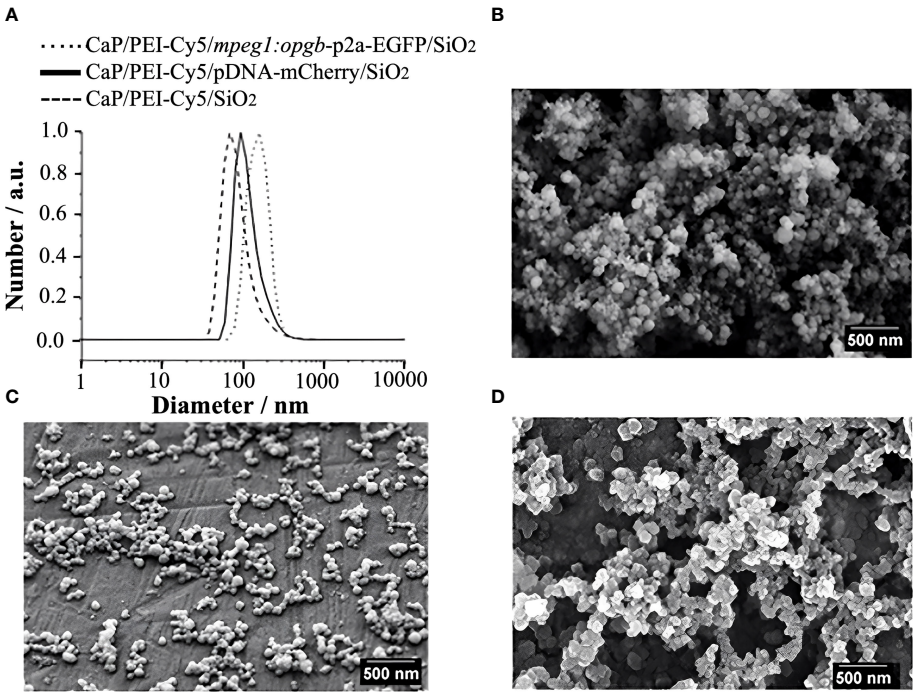

FIGURE 1
Characterization of CaP nanoparticles. **(A)** Dynamic light scattering (particle size distribution by number) of water-dispersed nanoparticles. **(B)** SEM image of CaP/PEI-Cy5/SiO_2 nanoparticles. **(C)** SEM image of CaP/PEI-Cy5/pDNA-mCherry/SiO_2 nanoparticles. **(D)** SEM image of CaP/PEI-Cy5/*mpeg1:opgb*-p2a-EGFP/SiO_2 nanoparticles. Scale bars = 500 nm.

nanoparticles distributed efficiently throughout the whole body and persisted in dispersed form. Nanoparticles were evident in the bloodstream for up to 35 hpi but the fluorescent signal was strongly reduced by this stage (Figure 2D"). This showed that injected nanoparticles are stable for at least 35 hours. This time window thus appeared optimal for assessing whether plasmid-functionalized nanoparticles are able to transfect tissue cells.

Nanoparticles are internalized by osteoclasts and macrophages in the caudal fin

To determine whether nanoparticles are internalized by medaka bone cells, nanoparticles were functionalized with an mCherry reporter plasmid (CaP/PEI-Cy5/pDNA-mCherry/SiO_2) and injected into transgenic medaka larvae that expressed the following bone cell reporters: *col10a1*-nlGFP in osteoblast progenitors (24), *osx*-GFP in pre-mature osteoblasts (25), and *ctsk*-mCherry in osteoclasts (26).

First, nanoparticles were injected into the caudal fin in close proximity to bony fin rays. Interestingly, only sparse, if any, colocalization of Cy5 or mCherry from functionalized nanoparticles with signals for *col10a1:nlGFP* or *osx:GFP* could be observed with live fluorescent imaging (Supplementary Figures S3, S4). Thus, osteoblast progenitors (*col10a1*) and pre-mature osteoblasts (*osx*) are unlikely to efficiently internalize CaP nanoparticles. Importantly, however, mCherry reporter expression was detected in some distinct non-osteoblast cells in the caudal fin as early as 5 hpi (Supplementary Figures S3, S4) and remained stable at 18 hpi (Figures 3A, A", B, B") and 38 hpi (Figure 3C, C"). Most of the cells that had taken up nanoparticles and expressed mCherry reporter were small and round-shaped and were localized on the outer surface of the bony fin rays (Figure 3A; Supplementary Figures S3, S4). Some of these cells were *ctsk*:nlGFP positive and showed a colocalization of Cy5 and mCherry with nlGFP signals, indicating that they had taken up the functionalized nanoparticles and expressed the introduced plasmid reporter (Figures 3A, A"; arrowheads). Some of the *ctsk*:nlGFP cells that had internalized nanoparticles were large and dynamic (Figures 3B, C", arrowheads). Based on their morphology and migratory behaviour, we hypothesized that these cells are macrophages that had switched on the *ctsk*:nlGFP reporter. To test this, nonfunctionalized Cy5 labelled nanoparticles (CAP/PEI-Cy5/SiO_2) were injected into the caudal fin of *mpeg1*:mCherry transgenic medaka larvae and fluorescent reporter expression was analyzed over 24 hours (Figure 4). After injection, a colocalization of nanoparticle derived Cy5 and the macrophage reporter mCherry was observed as early as 3 hpi, which confirmed internalization of nanoparticles by *mpeg1* positive macrophages. Live fluorescence time-lapse imaging showed that mCherry macrophages were recruited to the injection site in the caudal fin and efficiently phagocytosed nanoparticles within 24 hpi, which resulted in a depletion of Cy5 signal over time (Figure 4; Supplementary Movie 1). These anti-inflammatory *mpeg1*:mCherry macrophages were recruited in response to tissue damage induced by injection, as they were also detected after injection of water as control (Supplementary Figure S5).

TABLE 1 Characterization of nanoparticles.

Sample	CaP/PEI-Cy5/SiO_2 M_w (PEI-Cy5) = 25.0 kDa	CaP/PEI-Cy5/ pDNA-mCherry/SiO_2 M_w (mCherry) = 28.8 kDa	CaP/PEI-Cy5/ *mpeg1:opgb*-p2a-EGFP/SiO_2 M_w (*opgb*-p2a-EGFP) = 112.1 kDa
Solid core particle diameter by SEM/nm	87 ± 10	88 ± 11	82 ± 15
V(one nanoparticle; only CaP)/m^3	$3.45 \cdot 10^{-22}$	$3.57 \cdot 10^{-22}$	$2.89 \cdot 10^{-22}$
m(one nanoparticle; only CaP)/kg	$1.08 \cdot 10^{-18}$	$1.12 \cdot 10^{-18}$	$9.06 \cdot 10^{-19}$
w(Ca^{2+}) in the dispersion by AAS/kg m^{-3}	0.099	0.079	0.081
w($Ca_5(PO_4)_3OH$) in the dispersion/kg m^{-3}	0.248	0.198	0.203
N(nanoparticles) in the dispersion/m^{-3}	$2.29 \cdot 10^{+17}$	$1.77 \cdot 10^{+17}$	$2.24 \cdot 10^{+17}$
w(pDNA) in the dispersion/kg m^{-3}	–	0.141 (94%)	0.132 (98%)
N(pDNA)/m^{-3}	–	$2.95 \cdot 10^{+20}$	$7.09 \cdot 10^{+19}$
m(pDNA) per nanoparticle in the dispersion/kg	–	$7.97 \cdot 10^{-20}$	$5.89 \cdot 10^{-20}$
N(pDNA) molecules per nanoparticle	–	$1.67 \cdot 10^{+3}$	$3.16 \cdot 10^{+2}$
w(PEI-Cy5) in the dispersion/kg m^{-3}	$1.60 \cdot 10^{-2}$	$1.33 \cdot 10^{-2}$	$1.04 \cdot 10^{-2}$
N(PEI-Cy5)/m^{-3}	$3.85 \cdot 10^{+20}$	$3.20 \cdot 10^{+20}$	$2.51 \cdot 10^{+20}$
m(PEI-Cy5) per nanoparticle in the dispersion/kg	$6.98 \cdot 10^{-20}$	$7.52 \cdot 10^{-20}$	$4.64 \cdot 10^{-20}$
N(PEI-Cy5) molecules per nanoparticle	$1.68 \cdot 10^{+3}$	$1.81 \cdot 10^{+3}$	$1.12 \cdot 10^{+3}$
Hydrodynamic particle diameter by DLS/nm (number)	68	93	159
Polydispersity index (PDI) by DLS	0.3	0.2	0.4
Zeta potential by DLS/mV	+22	+20	+18

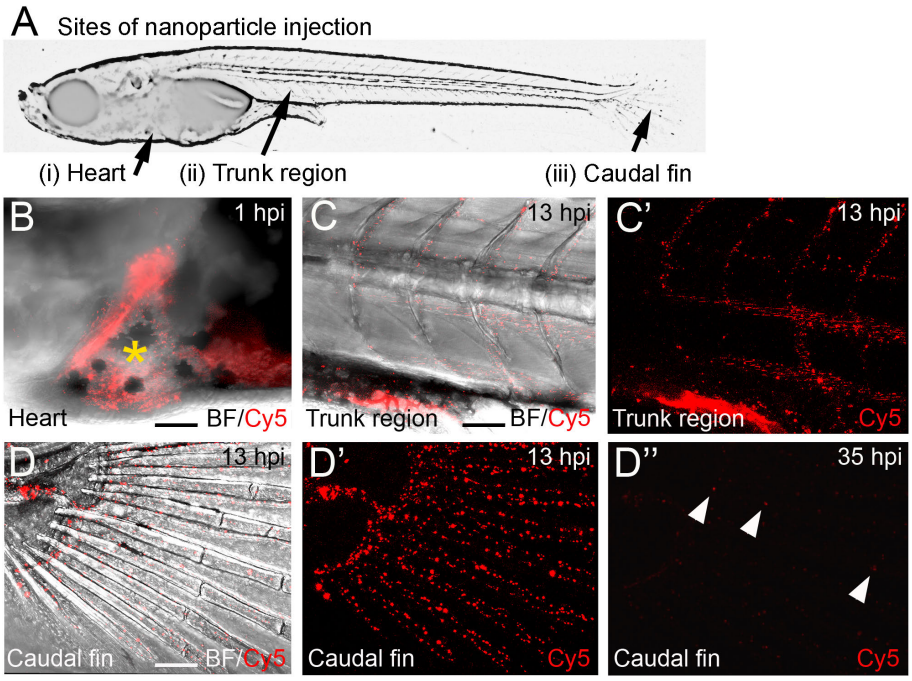

FIGURE 2
Distribution of Cy5-labelled calcium phosphate nanoparticles after injection into medaka larvae. **(A)** Schematic image of a medaka embryo at 11 days post fertilization (dpf) indicating sites of nanoparticle injection, i.e. heart, muscle fiber region in the rostral trunk and between bony rays of the caudal fin. **(B)** Merged image of brightfield (BF) and Cy5 channel of larval medaka heart at 1 hour post injection (hpi). Cy5 (red) indicates nanoparticles around injection site marked by yellow asterisk. **(C, C')** After heart injection, Cy-5-labeleld nanoparticles are detectable in blood vessels of the trunk at 13 hpi. A merge of brightfield and fluorescence image **(C)** and the fluorescence image alone are shown **(C')**. **(D, D")** After heart injection, Cy5-labelled nanoparticles are detectable in blood vessels of the caudal fin at 13 hpi **(D- D')** and show strongly reduced fluorescence at 35 hpi **(D")**. Arrowheads mark remaining fluorescently labeled particles. Ten embryos were analysed and showed this phenotype. Scale bars = 90 µm.

Macrophages internalize nanoparticles and differentiate into osteoclasts along the vertebral column

Next, non-functionalized Cy5 nanoparticles were injected into the muscle region above the AGM and close to the vertebral column of *rankl:HSE*:CFP/*mpeg1*:mCherry/*ctsk*:nlGFP transgenic fish (Figure 5). These fish report the presence of *mpeg1* macrophages in the AGM, as well as their differentiation into *ctsk* positive osteoclasts upon heat-shock-induced Rankl expression (22).

Live imaging revealed that nanoparticle injection after Rankl induction caused most macrophages to migrate from the AGM to the injection site (Figure 5A). Recruited as well as resident macrophages at the injection site were found to take up Cy5-labelled nanoparticles and to differentiate into *ctsk*:nlGFP positive osteoclasts (Figures 5B, C; Supplementary Movie 2). Importantly, the newly differentiated *ctsk* positive osteoclasts retained Cy5 signal (Figures 5B, C, arrowheads) indicating that the non-functionalized nanoparticles did not interfere with differentiation of Rankl-induced macrophages. In summary, while osteoblast progenitors and pre-osteoblasts and most of the *ctsk* positive cells were found to not take up injected CaP nanoparticles, *mpeg1* positive macrophages efficiently internalized non-functionalized and functionalized nanoparticles. Upon injection, these macrophages were efficiently recruited to injection sites, internalized nanoparticles and then differentiated into *ctsk* osteoclasts upon Rankl induction. Thus, CaP nanoparticles are potent delivery vehicles to osteoclast progenitors in medaka.

Nanoparticles deliver osteoprotegerin-b to medaka bone matrix

Next, nanoparticles were functionalized with *mpeg1:opgb*-p2a-EGFP plasmid to express Opgb specifically in macrophages. Successful transfection of macrophages was monitored by expression of EGFP, which was linked to Opgb through a self-cleavable p2A peptide (Supplementary Figures S1, S2). Functionalized nanoparticles were injected into the trunk muscle region close to the vertebral column of *mpeg1*:mCherry transgenic fish at 13 dpf. At 7 hpi, macrophages had taken up nanoparticles but did not yet express detectable levels of *opgb*-p2a-EGFP (Figure 6A). At 15 hpi, however, several *mpeg1*:mCherry macrophages had a Cy5 label, demonstrating presence of internalized nanoparticles, and. co-expressed mCherry and EGFP (Figure 6B, B"', arrowheads). This suggested successful expression of CaP-delivered Opgb in these macrophages. Unexpectedly, EGFP signal was also detected outside macrophages suggesting either a possible leakage of the *mpeg1* promoter or inefficient cleavage of the p2A peptide resulting in secretion of EGFP-tagged Opgb.

Next, we addressed whether the expressed Opgb was functional and could modulate excessive bone resorption triggered by Rankl induction. For this, *rankl:HSE*:CFP/*ctsk*:mCherry double transgenic medaka larvae were heat-shocked at 9 dpf to induce Rankl induction.

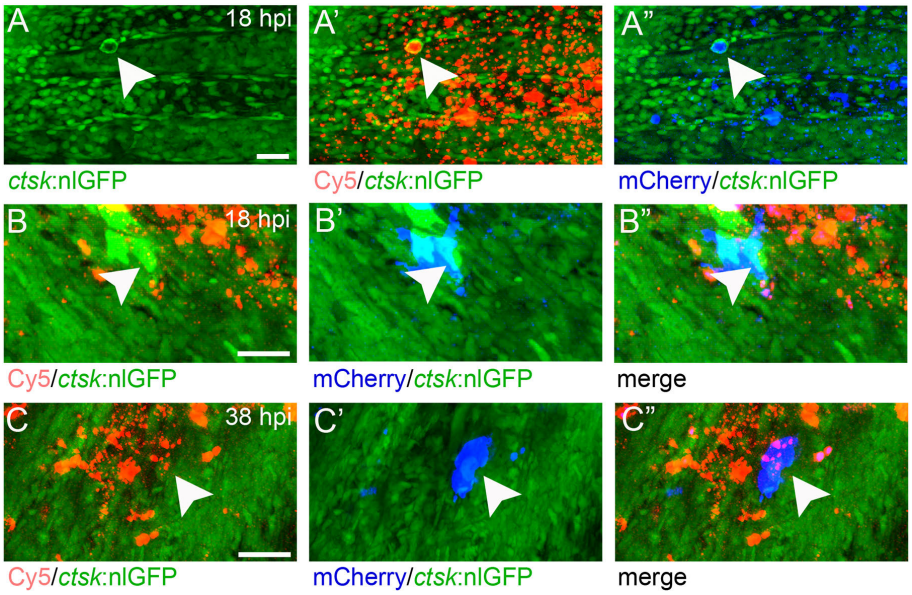

FIGURE 3
ctsk:nlGFP positive cells in the medaka caudal fin internalize plasmid-functionalized CaP nanoparticles and express mCherry protein. **(A, A")** Caudal fin of *ctsk*:nlGFP transgenic medaka at 12 dpf and 18 hours after injection of CAP/PEI-Cy5/pDNA-mCherry/SiO2 nanoparticles into the fin. Panels show *ctsk*: nlGFP positive cells **(A)**, colocalization of nlGFP and Cy5 **(A')**, and colocalization of nlGFP and plasmid-encoded mCherry **(A")**; arrowhead). **(B, C")** Large and dynamic mCherry expressing cell (arrowheads) at 18 hpi **(B, B")** and 38 hpi **(C, C")**. Panels show nlGFP positive cells colocalized with Cy5 **(B, C)**, colocalization of nlGFP with plasmid-encoded mCherry **(B', C')** and merge **(B", C")**. Cy5 marks nanoparticles (red) and mCherry (blue) marks cells that took up nanoparticles and express reporter protein. 6 out of 10 analysed embryos showed this phenotype. Scale bars = 20 µm **(A)**.

At 1 hour after Rankl induction, larvae were then injected with *mpeg1:opgb*-p2a-EGFP nanoparticles and then analyzed at 10 and 12 dpf (Figure 7). Nanoparticle injected larvae without heat shock (-Rankl, +Opgb) and Rankl-induced larvae without injection of nanoparticles (+Rankl) were used as controls (Figures 7A, B). Injection of *opgb*-functionalized nanoparticles resulted in an increased recruitment of *ctsk* positive cells to the injection site even without Rankl induction (Figure 7A). The small rounded morphology and dynamic behavior of these recruited cells suggested that these were activated macrophages that had turned on the *ctsk* reporter transgene in response to CaP without fully differentiating into osteoclasts. Live bone staining with calcein showed normal bone mineralization

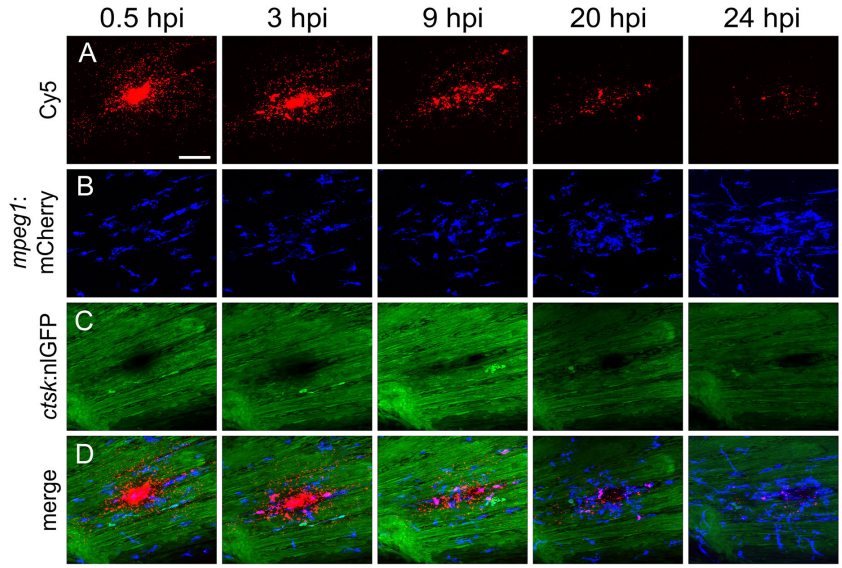

FIGURE 4
Macrophages are recruited to the injection site and internalize CaP nanoparticles within 24 hours. Cy5-labelled nanoparticles were injected into the caudal fin of *mpeg1*:mCherry/*ctsk*:nlGFP double transgenic medaka larvae at 12 dpf. **(A-D)** Lateral views of a caudal fin showing Cy5-labelled nanoparticles **(A)**, *mpeg1*:mCherry positive macrophages **(B)**, *ctsk*:nlGFP positive osteoclasts **(C)** and merged image **(D)** at 0.5, 3, 9, 20 and 24 hours post injection (hpi), respectively. Scale bar = 40 µm. 3 out of 3 analysed fish showed this phenotype.

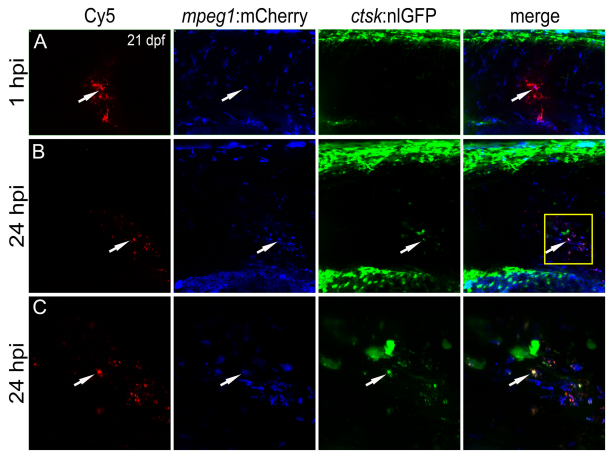

FIGURE 5
CaP nanoparticles are internalized by Rankl-induced macrophages that subsequently differentiate into osteoclasts. Cy5-labelled CaP nanoparticles were injected into trunk muscle of *mpeg1*:mCherry/*ctsk*:nlGFP/*rankl*:*HSE*:CFP transgenic medaka larvae at 21 dpf after a heat shock had been applied at 20 dpf to induce Rankl expression. **(A)** Lateral view of trunk region showing Cy5-labelled nanoparticles, *mpeg1*:mCherry positive macrophages, *ctsk*:nlGFP positive osteoclasts and merged image at 1 hpi. **(B)** Same larva at 24 hpi. **(C)** High magnification view of region indicated as box in **(B)** Colocalization of Cy5, mCherry and/or nlGFP signals is indicated by white arrowheads. 5 out of 5 analyzed embryos showed this phenotype.

without Rankl induction and no enhanced lesions as in Rankl-induced larvae, despite the presence of *ctsk*:mCherry cells. This supported the idea that recruited *ctsk* positive cells had not differentiated into activated osteoclasts (Figure 7A). In contrast, heat shock-induced Rankl expression in control larvae that had not been treated with nanoparticles resulted in increased osteoclast differentiation at vertebral bodies, which led to excessive bone resorption and absent neural and hemal arches as reported earlier (Figure 7B; see 19, 20). In larvae injected with nanoparticles after Rankl induction, the recruitment of *ctsk* positive cells started at 24 hpi (10 dpf) and had increased by 72 hpi (12 dpf; Figure 7C, D). At 12 dpf, some *ctsk* positive cells were recruited to the injection site and took up nanoparticles (Figure 7D, magenta arrowheads), while the majority of newly differentiated *ctsk* positive osteoclasts remained at the vertebral bodies (Figure 7D, white arrowheads; Supplementary Figure S6). The average fluorescent density of mCherry marking *ctsk* positive cells at the injection site was not significantly different among the three groups (Figure 7E). Importantly, neural arches and vertebral centra were largely preserved after Rankl induction in larvae injected with *opgb*-functionalized nanoparticle, which was evident by live bone staining with calcein at 12 dpf (Figure 7D, neural arches marked with yellow arrowheads). Statistical analysis showed that compared to Rankl-induced larvae without nanoparticles, the nanoparticle-injected larvae had significantly more vertebral bodies with evident

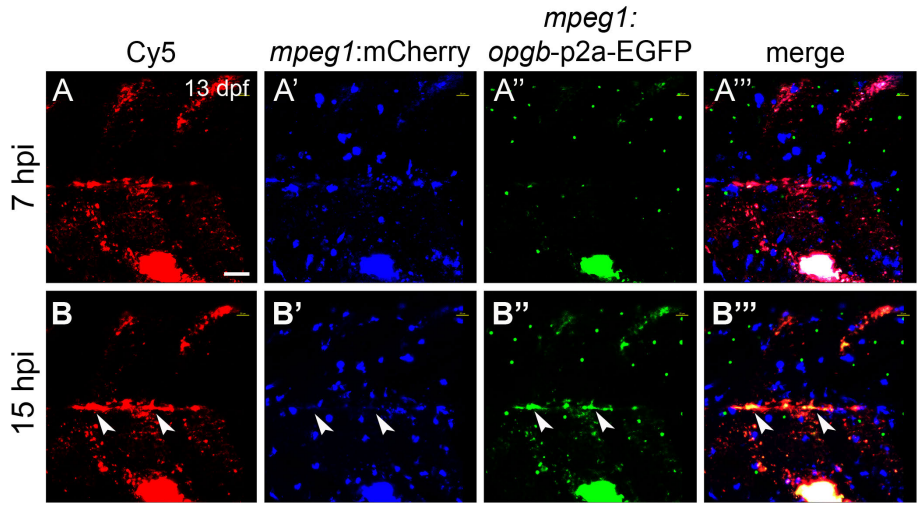

FIGURE 6
CaP nanoparticles deliver *mpeg1*:*opgb*-p2a-EGFP plasmid to macrophages. Cy5-labelled CaP nanoparticles functionalized with *mpeg1*:*opgb*-p2a-EGFP plasmid were injected into trunk muscle above the yolk extension of *mpeg1*:mCherry transgenic larvae at 13 dpf. **(A, A'")** Lateral view of trunk region at 7 hpi showing Cy5-labelled nanoparticles **(A)**, *mpeg1*:mCherry-expressing macrophages (A'), *mpeg1*:*opgb*-p2a-EGFP expressing cells **(A")** and a merged image **(A'")**. Note that some macrophages internalized CaP nanoparticles but did not express *opgb*-p2a-EGFP at this early stage. **(B, B'")** Same larva at 15 hpi. Note colocalization of Cy5, *mpeg1*:mCherry and *mpeg1*:*opgb*-p2a-EGFP (arrowheads), suggesting that macrophages have internalized CaP nanoparticles and express *opgb*-p2a-EGFP. Scale bar = 40 µm. 6 out of 6 analyzed embryos showed this phenotype.

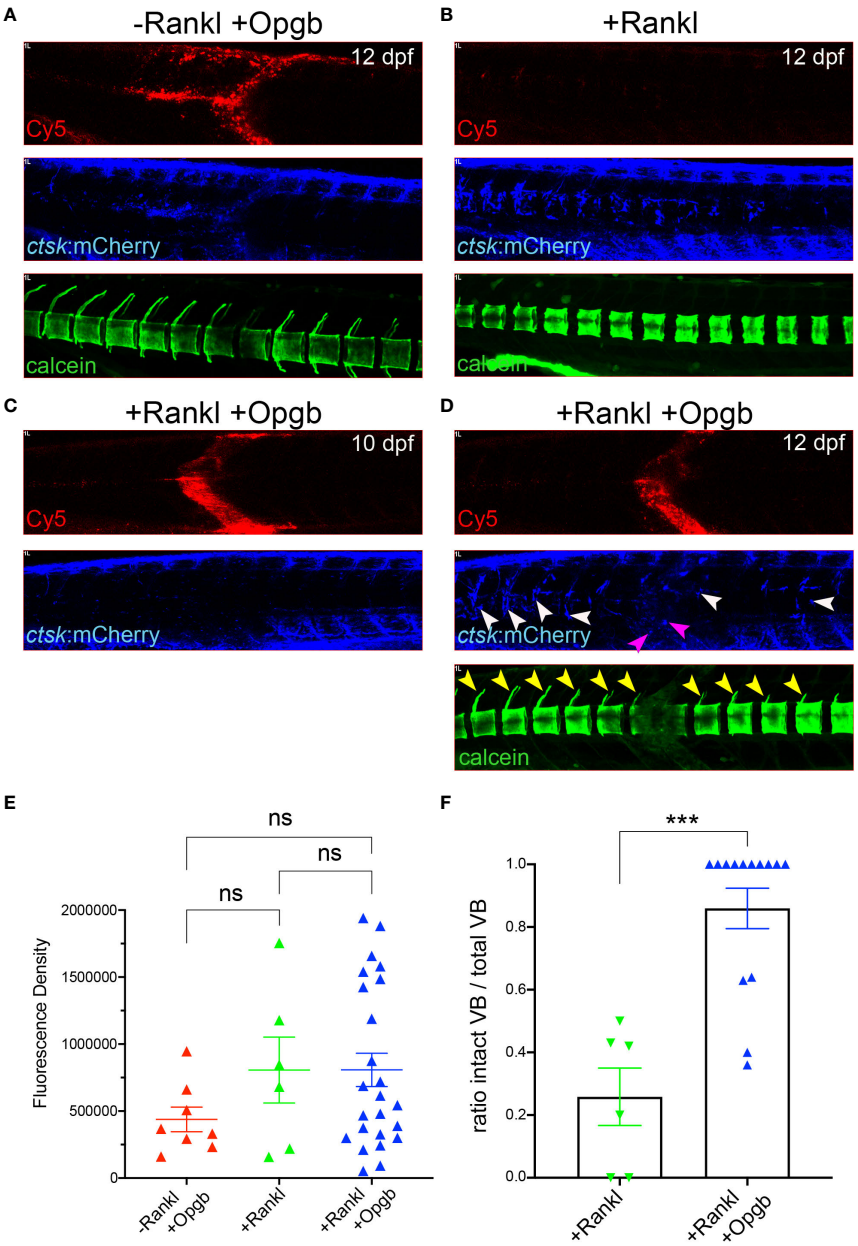

FIGURE 7
Nanoparticle-derived *opgb*:GFP protects mineralized vertebral arches from resorption by Rankl-induced osteoclasts. Cy5-labelled CaP nanoparticles functionalized with *mpeg1:opgb*-p2a-EGFP plasmid were injected into trunk muscle of *ctsk*:nlGFP/*rankl:HSE*:CFP double transgenic larvae at 9 dpf and imaged at 10 and 12 dpf. **(A)** Lateral view of trunk region. In the absence of Rankl induction, Cy5-labelled nanoparticles (top) recruit *ctsk*:mCherry positive cells to the injection site at 72 hpi (middle). Calcein staining at 12 dpf indicates normal mineralization of vertebral arches (bottom, n=4). **(B)** After Rankl induction at 9 dpf and in the absence of CaP nanoparticle injection (top), *ctsk*:mCherry expressing osteoclasts form along vertebral bodies (middle). Calcein staining indicates complete resorption of neural vertebral arches (bottom). **(C)** After Rankl induction at 9 dpf and injection of *mpeg1:opgb*-p2a-EGFP-functionalized nanoparticles at 1 hour after Rankl induction, no *ctsk*:mCherry cells are recruited at 10 dpf (i.e., 24 hpi). **(D)** Same larva as in C at 72 hpi showing formation of Rankl-induced ectopic *ctsk*:mCherry osteoclasts. Calcein staining indicates that despite abundant osteoclasts, mineralization of vertebral neural arches is preserved (n=14 larvae). **(E)** Statistical analysis of relative fluorescence density of mCherry signal at 12 dpf within specified region of interest at injection area, i.e. vertebral bodies (VBs) 8-10, indicative for recruitment of *ctsk* positive cells. **(F)** Statistical analysis of the ratio of calcein-stained VBs with neural arches present over total number of VBs. Only VBs with *ctsk* positive osteoclasts present after Rankl induction were counted. ***, p<0.005; ns, not significant.

neural arches after Rankl induction (Figure 7F). This suggests that although Opgb delivered by nanoparticles did not reduce the density of *ctsk* positive cells (macrophages or osteoclasts), it protected bone integrity from Rankl-induced resorption. In conclusion, we show that CaP nanoparticles functionalized with *opgb*-expressing plasmids were internalized by macrophages in the presence or absence of Rankl induction. Expression of the delivered plasmid protected mineralized bone from Rankl-induced osteoclasts and excessive resorption. This suggests that CaP nanoparticles can act as efficient delivery vehicles of bone-modulating compounds in medaka *in vivo*.

Discussion

Calcium phosphate (CaP) nanoparticles are regarded as safe and efficient carriers of biomolecules across cell membranes *in vitro* and *in*

vivo (9, 27, 28) Their promising potential for bone repair was demonstrated when a nanoparticulate CaP-containing paste was used to successfully deliver osteogenic growth factors to bone in rabbits (28). Compared to other transport vehicles, such as titanium oxide, CaP nanoparticles exhibit no toxic effects but may increase intracellular calcium levels. Hence, high concentrations and prolonged treatment with standard CaP nanoparticles, especially in their non-functionalized form, may cause particle aggregation and accumulation of calcium (29). Accordingly, we previously demonstrated that CaP nanoparticles internalized by HeLa cells did not affect cell proliferation and viability (23) but were degraded in lysosomes within 3 hours after uptake (27).

In the present study, we assessed the effect of CaP nanoparticles *in vivo* in a transgenic medaka model expressing various fluorescent bone cell reporters. We found that non-functionalized (CaP/PEI-Cy5/SiO2) and functionalized (CaP/PEI-Cy5/pDNA-mCherry/SiO_2; CaP/PEI-Cy5/*mpeg1*:*opgb*-p2a-EGFP/SiO_2) nanoparticles did not affect the viability of nanoparticle-treated larvae. Cy5-labelled non-functionalized CaP nanoparticles were stable and circulated in the bloodstream for up to 35 hours after injection into the heart of medaka larvae. This suggested that CaP nanoparticles can be used as safe delivery vehicles to medaka bone cells *in vivo*.

Medaka macrophages internalize CaP nanoparticles

CaP nanoparticles were shown to enter cells *via* macropinocytosis and their internalization depended on the nanoparticle morphology, size and coating (27). The CaP nanoparticles used in the present study were spherical, less than 100 nm in diameter and coated with silica to prevent agglomeration (30). All these properties are known to improve uptake by cells (31). While oral administration of nanoparticles results in high absorption in the intestine (32), the injection of nanoparticles in this study allowed a more targeted delivery to bone cells positioned along the vertebral column and bony fin rays. To assess which type of bone cell internalized the nanoparticles, Cy5-labeled and pDNA:mCherry-functionalized CaP nanoparticles (CaP/PEI-Cy5/pDNA-mCherry/SiO_2) were injected into transgenic medaka expressing different fluorescent reporters in osteoblast progenitors, pre-osteoblasts, macrophages or osteoclasts. Although injections were done in close proximity to bone and bone cells, very sparse if any uptake of nanoparticles by *col10a1*:nlGFP osteoblast progenitors and *osx*:mGFP pre-osteoblasts was detectable. Our *in vivo* findings are in contrast to several *in vitro* studies that showed that inorganic nanoparticles including hydroxyapatite-based nanoparticles and CaP nanoshells were efficiently internalized by mammalian pre-osteoblasts and osteoblasts and stimulated their differentiation, proliferation and activities (33–40). Future studies are therefore needed to better understand whether a particular differentiation state of osteoblasts is needed *in vivo* to allow uptake of CaP nanoparticles.

Osteoclasts and their macrophage/monocyte progenitors efficiently phagocytose biological particles. Consistent with this, Cy5-labelled CaP nanoparticles were rapidly internalized by *ctsk*:nlGFP expressing cells in the caudal fin. Injection of CaP nanoparticles into muscle tissue also induced an increased density of *ctsk*:nlGFP cells that took up nanoparticles. Based on their morphology and dynamics, as evident by live imaging, these *ctsk*:nlGFP cells most likely represented macrophages that had initiated differentiation into osteoclasts possibly as a response to elevated CaP levels at the injection site. While some inorganic nanoparticles, such as gold nanoparticles, were shown to inhibit osteoclastogenesis *in vitro* (41), CaP nanoparticles might induce differentiation of recruited macrophages into *ctsk*-expressing cells in medaka. To test this hypothesis, Cy5-labelled CaP nanoparticles (CaP/PEI-Cy5/SiO_2) were injected into *mpeg1*:mCherry transgenic medaka that exhibit fluorescently labelled pro-inflammatory (M1) macrophages (22). This confirmed that *mpeg1*:mCherry macrophages were recruited to injection sites and efficiently internalized CaP nanoparticles within a few hours after injection. How these macrophages internalized several Cy5-labelled particles, however, remains unclear. *In vitro*, human macrophages were shown to take up large amounts of hydroxyapatite or other nanoparticles using a highly branched membranous compartment (the surface connected compartment, SCC) with several openings to the extracellular space (42). Whether a similar mechanism is responsible for nanoparticle internalization in medaka *in vivo* remains to be tested.

Most immature and non-activated *mpeg1*:mCherry macrophages in medaka reside within the aorta-gonadal mesonephros (AGM). In response to Rankl, they relocate to the vertebral column, where they differentiate into *ctsk*:nlGFP expressing osteoclasts (22). In this study, Cy5-labeled nanoparticles (CaP/PEI-Cy5/SiO_2) were injected close to the medaka AGM after Rankl induction. We found that approximately 30-50 of the Rankl-induced *mpeg1*:mCherry macrophages accumulated at the injection site and internalized nanoparticles. Afterwards, these macrophages differentiated into *ctsk*:nlGFP expressing osteoclasts and retained Cy5 signal within their cytoplasm. This strongly suggests that internalized CaP nanoparticles do not interfere with osteoclast differentiation. Together, our study showed that pro-inflammatory medaka macrophages were recruited to sites of nanoparticle injection, efficiently internalized CaP nanoparticles and differentiated into actively resorbing osteoclasts in response to Rankl induction. This opens the possibility to use nanoparticles as vehicles to introduce bone modulatory compounds into osteoclasts.

Functionalized nanoparticles prevent excessive bone resorption in a medaka Rankl model

We thus assessed whether medaka macrophages also internalize functionalized CaP nanoparticles and can express sufficient levels of osteomodulatory proteins such as the osteoclast-inhibiting osteoprotegerin (Opg) from the internalized nanoparticles. During bone remodelling, Opg acts as a Rankl decoy receptor and prevents excessive bone resorption (2). Consequently, a deficiency in Opg increases bone turnover and leads to osteoporosis-like phenotypes (43, 44). On the other hand, administration of recombinant Opg reduced osteoporotic bone loss in ovariectomized or Opg-deficient mice (45, 46), confirming the bone protective effect of Opg. Opg was also shown to inhibit osteoblast apoptosis through binding to TNF-related apoptosis-inducing ligand (TRAIL) (47). Thus, Opg reduces osteoclastogenesis and promotes osteoblast survival, which makes it a potent therapeutic

target for osteoporosis. Slow or intermittent release of exogenous Opg might diminish bone resorption without strongly affecting bone remodelling. In medaka, there are two *opg* genes, *opga* and *opgb*, with highly conserved cysteine-rich N-terminal domains that are important for Rankl binding, and less conserved C-terminal domains, which are shorter compared to mammalian Opg (48). In the present study, we loaded CaP nanoparticles with a plasmid expressing *opgb* under control of the *mpeg1* macrophage promoter (CaP/PEI-Cy5/*mpeg1*:*opgb*-p2a-EGFP/SiO_2). These nanoparticles were injected into medaka larvae with normal bone development (in the absence of ectopic Rankl induction) or with induced osteoporotic lesions (after ectopic Rankl induction). The used *mpeg1* promoter restricted ectopic *opgb* expression to macrophages. Under Rankl-induced conditions, we hypothesized that a subset of macrophages internalized the functionalized nanoparticles, differentiated into osteoclasts and secreted *opgb* into the surrounding tissues. Consistently, we found that the expression of *opgb*-p2a-EGFP partially colocalized with Cy5, indicating that the majority of the injected nanoparticles efficiently delivered cargo DNA to macrophages, which subsequently expressed the functionalized plasmid. We also found that *opgb* delivered by nanoparticles did not affect bone development in the absence of Rankl induction. This is consistent with the fact that bone homeostasis at the analysed larval stages (11-13 days) does not rely on endogenous osteoclasts, which only form at later stages (21 days; 19). In stark contrast, *opgb* functionalized nanoparticles protected mineralized bone under osteoporotic conditions when excessive osteoclast formation was induced by transgenic Rankl expression. Interestingly after Rankl induction, the density of *ctsk*:nlGFP cells at the vertebral column was similar in untreated and nanoparticle-treated fish. Despite this, the mineralized matrix of neural arches was preserved after injection of Opgb nanoparticles, while it was almost completely resorbed in untreated controls. This suggests that nanoparticle-delivered Opgb did not interfere with the formation of Rankl-induced *ctsk*:nlGFP osteoclasts, but rather blocked their activity. It is likely that the levels of nanoparticle-derived Opgb were insufficient to entirely compete with transgenic Rankl and block osteoclast formation but these levels appeared sufficient to block osteoclast activity. This is consistent with a previous report showing that Opg inhibits the bone-resorbing activity of osteoclasts in giant cell tumours of bone (49).

One of the limitations of the current study is that we were not able to directly visualize the differentiation of *mpeg1*:mCherry macrophages carrying Cy5-labelled nanoparticles functionalized with *mpeg1*:*opgb*-p2a-EGFP into *ctsk*:nlGFP or *ctsk*:mCherry positive osteoclasts. This was not possible as emission wavelengths of the four fluorescence reporters overlapped. Nevertheless, our study provides strong evidence that functionalized CaP nanoparticles are stable in medaka larvae and are efficiently taken up by macrophages that differentiate into osteoclasts under osteoporotic conditions. After targeted injection into tissue adjacent to bone, these nanoparticles served as efficient vehicles to deliver Opgb at sufficient levels to block osteoclast activity and protected bone from Rankl-induced osteoporotic insult.

Data availability statement

The original contributions presented in the study are included in the article/Supplementary Material. Further inquiries can be directed to the corresponding author.

Ethics statement

The animal study was reviewed and approved by National University of Singapore IACUC.

Author contributions

NI, VS, ME and CW contributed to conception and design of the study. NI, VS and KK generated the data. NI, VS, KK, ME and CW analyzed the data. NI performed the statistical analysis. NI, VS and KK wrote the first draft of the manuscript. VS, ME and CW revised and edited the manuscript. All authors contributed to manuscript revision, read, and approved the submitted version. All authors contributed to the article and approved the submitted version.

Funding

This work was funded by grants from the Ministry of Education Singapore (MOE2016-T2-2-086 and MOE-T2EP30221-0014) and National Research Foundation Singapore (NRF2017-NRF-ISF002-2671) to CW. NI was supported by a Singapore International Graduate Award (SINGA).

Acknowledgments

We thank Giorgia Pastorin, Cynthia He and Phan Quang Tien for critical comments, suggestions and for providing reagents. We are grateful to the Centre for Bioimaging Sciences (CBIS) confocal unit and the fish facility at Department of Biological Sciences (DBS), National University of Singapore for continued support. We thank Dr Kateryna Loza (Essen) for recording SEM images and Robin Meya (Essen) for AAS measurements.

Conflict of interest

The authors declare that the research was conducted in the absence of any commercial or financial relationships that could be construed as a potential conflict of interest.

Publisher's note

Supplementary material

The Supplementary Material for this article can be found online at: https://www.frontiersin.org/articles/10.3389/fendo.2023.1101758/full#supplementary-material

References

1. Clarke B. Normal bone anatomy and physiology. *Clin J Am Soc Nephrol* (2008) 3 Suppl 3:S131–139. doi: 10.2215/CJN.04151206

2. Takahashi N, Udagawa N, Suda T. A new member of tumor necrosis factor ligand family, ODF/OPGL/TRANCE/RANKL, regulates osteoclast differentiation and function. *Biochem Biophys Res Commun* (1999) 256:449–55. doi: 10.1006/bbrc.1999.0252

3. Johnell O, Kanis JA. An estimate of the worldwide prevalence and disability associated with osteoporotic fractures. *Osteoporosis Int* (2006) 17:1726–33. doi: 10.1007/s00198-006-0172-4

4. Johnston CB, Dagar M. Osteoporosis in older adults. *Med Clinics North America* (2020) 104:873–84. doi: 10.1016/j.mcna.2020.06.004

5. Charles JF, Aliprantis AO. Osteoclasts: More than 'bone eaters'. *Trends Mol Med* (2014) 20:449–59. doi: 10.1016/j.molmed.2014.06.001

6. Mitchell MJ, Billingsley MM, Haley RM, Wechsler ME, Peppas NA, Langer R. Engineering precision nanoparticles for drug delivery. *Nat Rev Drug Discovery* (2021) 20:101–24. doi: 10.1038/s41573-020-0090-8

7. Chen Y, Wu X, Li J, Jiang Y, Xu K, Su J. Bone-targeted nanoparticle drug delivery system: An emerging strategy for bone-related disease. *Front Pharmacol* (2022) 13:909408. doi: 10.3389/fphar.2022.909408

8. Graham FL, van der Eb AJ. Transformation of rat cells by DNA of human adenovirus 5. *Virology* (1973) 54:536–9. doi: 10.1016/0042-6822(73)90163-3

9. Sokolova V, Epple M. Biological and medical applications of calcium phosphate nanoparticles. *Chemistry* (2021) 27:7471–88. doi: 10.1002/chem.202005257

10. Pioletti DP, Kottelat A. The influence of wear particles in the expression of osteoclastogenesis factors by osteoblasts. *Biomaterials* (2004) 25:5803–8. doi: 10.1016/j.biomaterials.2004.01.053

11. Tautzenberger A, Kreja L, Zeller A, Lorenz S, Schrezenmeier H, Mailänder V, et al. Direct and indirect effects of functionalised fluorescence-labelled nanoparticles on human osteoclast formation and activity. *Biomaterials* (2011) 32(6):1706–14. doi: 10.1016/j.biomaterials.2010.10.053

12. Zhang S, Kucharski C, Doschak MR, Sebald W, Uludag H. Polyethylenimine-PEG coated albumin nanoparticles for BMP-2 delivery. *Biomaterials* (2010) 31:952–63. doi: 10.1016/j.biomaterials.2009.10.011

13. Kong Z, Lin J, Yu M, Yu L, Li J, Weng W, et al. Enhanced loading and controlled release of rhBMP-2 in thin mineralized collagen coatings with the aid of chitosan nanospheres and its biological evaluations. *J Mater Chem B* (2014) 2:4572–82. doi: 10.1039/C4TB00404C

14. Park JS, Yi SW, Kim HJ, Kim SM, Park KH. Regulation of cell signaling factors using PLGA nanoparticles Coated/Loaded with genes and proteins for osteogenesis of human mesenchymal stem cells. *ACS Appl Mater Interfaces* (2016) 8:30387–97. doi: 10.1021/acsami.6b08343

15. Krebs MD, Salter E, Chen E, Sutter KA, Alsberg E. Calcium phosphate-DNA nanoparticle gene delivery from alginate hydrogels induces *in vivo* osteogenesis. *J BioMed Mater Res A* (2010) 92:1131–8. doi: 10.1002/jbm.a.32441

16. Alghamdi HS, Bosco R, Both SK, Iafisco M, Leeuwenburgh SCG, Jansen JA, et al. Synergistic effects of bisphosphonate and calcium phosphate nanoparticles on peri-implant bone responses in osteoporotic rats. *Biomaterials* (2014) 35:5482–90. doi: 10.1016/j.biomaterials.2014.03.069

17. Witten PE, Harris MP, Huysseune A, Winkler C. Small teleost fish provide new insights into human skeletal diseases. *Methods Cell Biol* (2017) 138:321–46. doi: 10.1016/bs.mcb.2016.09.001

18. Lleras-Forero L, Winkler C, Schulte-Merker S. Zebrafish and medaka as models for biomedical research of bone diseases. *Dev Biol* (2019) 457:191–205. doi: 10.1016/j.ydbio.2019.07.009

19. To TT, Eckhard Witten P, Renn J, Bhattacharya D, Huysseune A, Winkler C. Rankl-induced osteoclastogenesis leads to loss of mineralization in a medaka osteoporosis model. *Development* (2012) 139:141–50. doi: 10.1242/dev.071035

20. Phan QT, Liu R, Tan WH, Imangali N, Cheong B, Schartl M, et al. Macrophages switch to an osteo-modulatory profile upon RANKL induction in a medaka (Oryzias latipes) osteoporosis model. *JBMR* (2020) 4:e10409. doi: 10.1002/jbm4.10409

21. Iwamatsu T. Stages of normal development in the medaka oryzias latipes. *Mech Dev* (2004) 121:605–18. doi: 10.1016/j.mod.2004.03.012

22. Phan QT, Tan WH, Liu R, Sundaram S, Buettner A, Kneitz S, et al. Cxcl9l and Cxcr3.2 regulate recruitment of osteoclast progenitors to bone matrix in a medaka osteoporosis model. *Proc Natl Acad Sci U.S.A.* (2020) 117:19276–86. doi: 10.1073/pnas.2006093117

23. Sokolova V, Rojas-Sanchez L, Bialas N, Schulze N, Epple M. Calcium phosphate nanoparticle-mediated transfection in 2D and 3D mono- and co-culture cell models. *Acta Biomater* (2019) 84:391–401. doi: 10.1016/j.actbio.2018.11.051

24. Renn J, Buttner A, To TT, Chan SJ, Winkler C. A col10a1:nlGFP transgenic line displays putative osteoblast precursors at the medaka notochordal sheath prior to mineralization. *Dev Biol* (2013) 381:134–43. doi: 10.1016/j.ydbio.2013.05.030

25. Renn J, Winkler C. Osterix-mCherry transgenic medaka for *in vivo* imaging of bone formation. *Dev Dyn* (2009) 238:241–8. doi: 10.1002/dvdy.21836

26. Yu T, Witten PE, Huysseune A, Buettner A, To TT, Winkler C. Live imaging of osteoclast inhibition by bisphosphonates in a medaka osteoporosis model. *Dis Model Mech* (2016) 9:155–63. doi: 10.1242/dmm.019091

27. Sokolova V, Kozlova D, Knuschke T, Buer J, Westendorf AM, Epple M. Mechanism of the uptake of cationic and anionic calcium phosphate nanoparticles by cells. *Acta Biomater* (2013) 9:7527–35. doi: 10.1016/j.actbio.2013.02.034

28. Schlickewei C, Klatte TO, Wildermuth Y, Laaff G, Rueger JM, Ruesing J, et al. A bioactive nano-calcium phosphate paste for in-situ transfection of BMP-7 and VEGF-a in a rabbit critical-size bone defect: results of an *in vivo* study. *J Materials Science: Materials Med* (2019) 30:15. doi: 10.1007/s10856-019-6217-y

29. Epple M. Review of potential health risks associated with nanoscopic calcium phosphate. *Acta Biomaterialia* (2018) 77:1–14. doi: 10.1016/j.actbio.2018.07.036

30. Kozlova D, Chernousova S, Knuschke T, Buer J, Westendorf AM, Epple M. Cell targeting by antibody-functionalized calcium phosphate nanoparticles. *J Mater Chem* (2012) 22:396. doi: 10.1039/C1JM14683A

31. Patel S, Kim J, Herrera M, Mukherjee A, Kabanov AV, Sahay G. Brief update on endocytosis of nanomedicines. *Adv Drug Delivery Rev* (2019) 144:90–111. doi: 10.1016/j.addr.2019.08.004

32. Jani P, Halbert GW, Langridge J, Florence AT. Nanoparticle uptake by the rat gastrointestinal mucosa: Quantitation and particle size dependency. *J Pharm Pharmacol* (1990) 42:821–6. doi: 10.1111/j.2042-7158.1990.tb07033.x

33. Albers CE, Hofstetter W, Siebenrock KA, Landmann R, Klenke FM. *In vitro* cytotoxicity of silver nanoparticles on osteoblasts and osteoclasts at antibacterial concentrations. *Nanotoxicology* (2013) 7:30–6. doi: 10.3109/17435390.2011.626538

34. Hadjicharalambous C, Kozlova D, Sokolova V, Epple M, Chatzinikolaidou M. Calcium phosphate nanoparticles carrying BMP-7 plasmid DNA induce an osteogenic response in MC3T3-E1 pre-osteoblasts. *J BioMed Mater Res A* (2015) 103:3834–42. doi: 10.1002/jbm.a.35527

35. Carles-Carner M, Saleh LS, Bryant SJ. The effects of hydroxyapatite nanoparticles embedded in a MMP-sensitive photoclickable PEG hydrogel on encapsulated MC3T3-E1 pre-osteoblasts. *BioMed Mater* (2018) 13:045009. doi: 10.1088/1748-605X/aabb31

36. Tran N, Webster TJ. Increased osteoblast functions in the presence of hydroxyapatite-coated iron oxide nanoparticles. *Acta Biomaterialia* (2011) 7:1298–306. doi: 10.1016/j.actbio.2010.10.004

37. Pauksch L, Hartmann S, Rohnke M, Szalay G, Alt V, Schnettler R, et al. Biocompatibility of silver nanoparticles and silver ions in primary human mesenchymal stem cells and osteoblasts. *Acta Biomaterialia* (2014) 10:439–49. doi: 10.1016/j.actbio.2013.09.037

38. Santos C, Gomes P, Duarte JA, Almeida MM, Costa MEV, Fernandes MH. Development of hydroxyapatite nanoparticles loaded with folic acid to induce osteoblastic differentiation. *Int J Pharmaceutics* (2017) 516:185–95. doi: 10.1016/j.ijpharm.2016.11.035

39. Xu Z, Liu C, Wei J, Sun J. Effects of four types of hydroxyapatite nanoparticles with different nanocrystal morphologies and sizes on apoptosis in rat osteoblasts. *J Appl Toxicol* (2012) 32(6):429–35. doi: 10.1002/jat.1745

40. Zhang D, Liu D, Zhang J, Fong C, Yang M. Gold nanoparticles stimulate differentiation and mineralization of primary osteoblasts through the ERK/MAPK signaling pathway. *Materials Sci Eng C* (2014) 42:70–7. doi: 10.1016/j.msec.2014.04.042

41. Zeng L, Geng H, Gu W, Ma S, Qin Y, Xia S, et al. Au nanoparticles attenuate RANKL-induced osteoclastogenesis by suppressing pre-osteoclast fusion. *J Nanoscience Nanotechnology* (2018) 19:2166–73. doi: 10.1166/jnn.2019.15764

42. Motskin M, Müller KH, Genoud C, Monteith AG, Skepper JN. The sequestration of hydroxyapatite nanoparticles by human monocyte-macrophages in a compartment that allows free diffusion with the extracellular environment. *Biomaterials* (2011) 32:9470–82. doi: 10.1016/j.biomaterials.2011.08.060

43. Bucay N, Sarosi I, Dunstan CR, Morony S, Tarpley J, Capparelli C, et al. Osteoprotegerin-deficient mice develop early onset osteoporosis and arterial calcification. *Genes Dev* (1998) 12:1260–8. doi: 10.1101/gad.12.9.1260

44. Mizuno A, Amizuka N, Irie K, Murakami A, Fujise N, Kanno T, et al. Severe osteoporosis in mice lacking osteoclastogenesis inhibitory factor/osteoprotegerin. *Biochem Biophys Res Commun* (1998) 247:610–5. doi: 10.1006/bbrc.1998.8697

45. Simonet WS, Lacey DL, Dunstan CR, Kelley M, Chang MS, Luthy R., et al. Osteoprotegerin: A novel secreted protein involved in the regulation of bone density. *Cell* (1997) 89:309–19. doi: 10.1016/S0092-8674(00)80209-3

46. Min H, Morony S, Sarosi I, Dunstan CR, Capparelli C, Scully S, et al. Osteoprotegerin reverses osteoporosis by inhibiting endosteal osteoclasts and prevents vascular calcification by blocking a process resembling osteoclastogenesis. *J Exp Med* (2000) 192:463–74. doi: 10.1084/jem.192.4.463

47. Emery JG, McDonnell P, Burke MB, Deen KC, Lyn S, Silverman C, et al. Osteoprotegerin is a receptor for the cytotoxic ligand TRAIL. *J Biol Chem* (1998) 273:14363–7. doi: 10.1074/jbc.273.23.14363

48. Wagner TU, Renn J, Riemensperger T, Volff JN, Koster RW, Goerlich R, et al. The teleost fish medaka (Oryzias latipes) as genetic model to study gravity dependent bone homeostasis *in vivo*. *Adv Space Res* (2003) 32:1459–65. doi: 10.1016/S0273-1177(03)90381-4

49. Atkins GJ, Bouralexis S, Haynes DR, Graves SE, Geary SM, Evdokiou A, et al. Osteoprotegerin inhibits osteoclast formation and bone resorbing activity in giant cell tumors of bone. *Bone* (2001) 28:370–7. doi: 10.1016/S8756-3282(01)00404-5

frontiers | Frontiers in Endocrinology

TYPE Original Research
PUBLISHED 06 March 2023
DOI 10.3389/fendo.2023.1108916

OPEN ACCESS

EDITED BY
Erika Kague,
University of Bristol, United Kingdom

REVIEWED BY
Felix Loosli,
Karlsruhe Institute of Technology (KIT), Germany
Elis Newham,
Queen Mary University of London, United Kingdom

*CORRESPONDENCE
Tatjana Haitina
tatjana.haitina@ebc.uu.se
Sophie Sanchez
sophie.sanchez@ebc.uu.se

SPECIALTY SECTION
This article was submitted to Bone Research, a section of the journal Frontiers in Endocrinology

RECEIVED 26 November 2022
ACCEPTED 10 February 2023
PUBLISHED 06 March 2023

CITATION
Leyhr J, Sanchez S, Dollman KN, Tafforeau P and Haitina T (2023) Enhanced contrast synchrotron X-ray microtomography for describing skeleton-associated soft tissue defects in zebrafish mutants.
Front. Endocrinol. 14:1108916.
doi: 10.3389/fendo.2023.1108916

Enhanced contrast synchrotron X-ray microtomography for describing skeleton-associated soft tissue defects in zebrafish mutants

Jake Leyhr[1], Sophie Sanchez[1,2]*, Kathleen N. Dollman[2], Paul Tafforeau[2] and Tatjana Haitina[1]*

[1]Department of Organismal Biology, Uppsala University, Uppsala, Sweden, [2]European Synchrotron Radiation Facility, Grenoble, France

Detailed histological analyses are desirable for zebrafish mutants that are models for human skeletal diseases, but traditional histological techniques are limited to two-dimensional thin sections with orientations highly dependent on careful sample preparation. On the other hand, techniques that provide three-dimensional (3D) datasets including µCT scanning are typically limited to visualizing the bony skeleton and lack histological resolution. We combined diffusible iodine-based contrast enhancement (DICE) and propagation phase-contrast synchrotron radiation micro-computed tomography (PPC-SRµCT) to image late larval and juvenile zebrafish, obtaining high-quality 3D virtual histology datasets of the mineralized skeleton and surrounding soft tissues. To demonstrate this technique, we used virtual histological thin sections and 3D segmentation to qualitatively and quantitatively compare wild-type zebrafish and *nkx3.2*$^{-/-}$ mutants to characterize novel soft-tissue phenotypes in the muscles and tendons of the jaw and ligaments of the Weberian apparatus, as well as the sinus perilymphaticus associated with the inner ear. We could observe disrupted fiber organization and tendons of the adductor mandibulae and protractor hyoideus muscles associated with the jaws, and show that despite this, the overall muscle volumes appeared unaffected. Ligaments associated with the malformed Weberian ossicles were mostly absent in *nkx3.2*$^{-/-}$ mutants, and the sinus perilymphaticus was severely constricted or absent as a result of the fused exoccipital and basioccipital elements. These soft-tissue phenotypes have implications for the physiology of *nkx3.2*$^{-/-}$ zebrafish, and demonstrate the promise of DICE-PPC-SRµCT for histopathological investigations of bone-associated soft tissues in small-fish skeletal disease models and developmental studies more broadly.

KEYWORDS

iodine staining, propagation phase-contrast synchrotron microtomography, virtual histology, zebrafish mutant, 3D segmentation, inner ear, Weberian apparatus, nkx3.2

Introduction

Skeletal diseases primarily affect bones and are genetically determined or caused by developmental abnormalities (1). In addition to bones, joints and cartilages can also be affected in skeletal diseases as endochondral bones are formed on the basis of cartilage anlagen during the development (2). Furthermore, some bone disorders like *osteogenesis imperfecta* can also display weakened muscle phenotypes (3) and in several diseases the associated tissues like bone-to-bone connecting ligaments and muscle-to-bone connecting tendons are also affected (4).

Genetic mutations that cause skeletal diseases can be linked to the genes that function as building blocks of cartilage and/or bone, but also as contributors to the structural and mechanical properties of the attached muscles or other associated tissues (e.g. collagen type I) (4). In addition, the absence, reduction, or deformation of skeletal components can also affect the associated tissue that requires direct interaction with the skeletal component during development. This interaction can be primarily mechanical, such as between the brain and skull in craniosynostosis (5), but can also involve inter-tissue crosstalk *via* signaling molecules (6). Furthermore, connective tissue diseases linked to bone metabolism and its endocrine function can trigger the immune system and manifest phenotypes in musculoskeletal, cardiovascular, respiratory, and ocular systems (7).

Together with the mouse, the zebrafish (*Danio rerio*) is an important and well-established model organism for human skeletal diseases (8, 9). There is at least one zebrafish orthologue for ~80% of human genes involved in disease (10), and many genes are conserved in their function, displaying overlapping expression patterns during skeletal development in zebrafish and human (11). This knowledge facilitated the generation of zebrafish gene mutants that was further accelerated by the development of CRISPR/Cas9 genome editing knock-out, knock-in, and genomic deletion approaches (12, 13), leading to a dramatic expansion of available zebrafish gene mutants in recent years. As a large number of mutants lack an easily detectable phenotype, a thorough examination approach at a histological level is needed in order to identify and link the mutant phenotypes to the human pathologies, and to understand their mechanistic basis (14–16). However, while traditional histology can provide extremely detailed information (17), it is constrained by slice orientation and physical section thickness that provides poor z-resolution, limiting attempts to understand morphological structures in 3D.

Skeletal phenotypes are most often described by investigating mutants in a transgenic background of fluorescently-labeled skeletal cells or by applying fluorescent and/or chromogenic stains of cartilage and bone, however detailed characterization in 3D by using these methods is often very limited. Confocal, light-sheet, and other advanced 3D optical microscopy techniques rely on optically transparent specimens and specific labelling of cells/tissues intended to be visualized, both of which can require complex preparation protocols and imaging setups when the specimens in question are relatively large and pigmented. As the skeleton mineralizes and becomes X-ray dense, imaging by X-ray micro-computed tomography (μCT) has proven to be a simple and powerful technique for the characterization of adult skeletal structures in 3D, useful in describing normal development and mutant phenotypes (e.g. 18–20).

3D phenotypic characterization using μCT is optimized for the visualization of highly dense mineralized structures while other tissues are barely detectable, limiting our understanding of how skeletal phenotypes interact with the surrounding soft tissues. By using tissue contrasting agents such as phosphotungstic acid (PTA) or iodine (I_2E, I_2M, or I_2KI), the soft tissue density can be enhanced and visualized together with the mineralized structures by X-ray imaging (21–23). This enhances contrast by increasing the attenuation of X-rays passing through the soft tissues. The use of propagation phase-contrast imaging can complement this method to obtain sharp images at submicron resolution (24). This technique relies on the detection of changes in the phase of a coherent X-ray beam caused by slight differences in the thickness and refractive index of tissues to enhance the contrast at the edges of microstructural boundaries (25–27). The best source of coherent X-rays are synchrotron light sources (28), which additionally provide advantages over conventional μCT systems by reducing imaging times for an improved scan quality (with reduced to no beam hardening) and higher spatial resolution (29, 30).

Spondylo-megaepiphyseal-metaphyseal dysplasia is caused by homozygous mutations in human NK 3 Homeobox 2 (*NKX3.2*) gene (31, 32). Recently, the skeletal phenotypes associated with homozygous knockout mutants of the *nkx3.2* gene in zebrafish were characterized in detail using several techniques including X-ray microcomputed tomography (33, 34). These phenotypes included the fused jaw joint leading to an externally visible and permanently open jaw, loss of vertebral parapophyses, and defects in the occiput and Weberian apparatus (34).

Here, we combined diffusible iodine-based contrast enhancement (DICE) and propagation phase-contrast synchrotron radiation micro-computed tomography (PPC-SRμCT) to image late larval and juvenile *nkx3.2*$^{-/-}$ mutant and wild-type zebrafish. We obtained high-quality high-resolution 3D virtual histology datasets and characterized novel soft-tissue phenotypes in the muscles, ligaments, and inner ear that are associated with previously described skeletal defects.

Materials and methods

Ethical statement

All animal experimental procedures were approved by the local ethics committee for animal research in Uppsala, Sweden (permit number 5.8.18-18096/2019). All procedures for the experiments were performed in accordance with the animal welfare guidelines of the Swedish National Board for Laboratory Animals.

μCT scanning

μCT data from 1, 2, and 3 months post fertilization (mpf) wild-type zebrafish were obtained as part of a previous study (34). Fixed specimens were embedded in 1% agarose and scanned in 2mL

microcentrifuge tubes using a SkyScan 1172 (Bruker microCT, Belgium) at a voltage of 60kV, a current of 167µA, and an isotropic voxel size of 5.43µm.

Iodine staining

Zebrafish homozygous for the previously published *nkx3.2*^{uu2803} mutant allele (34) together with wild-type AB and *nkx3.2*$^{+/+}$ zebrafish were euthanized at 1, 2, and 3mpf with an overdose of MS-222 (300mg/L) and fixed in 4% paraformaldehyde. Specimens were rinsed in 1x phosphate-buffered saline and gradually dehydrated in 25%, 50%, 75% and 100% ethanol. Staining with iodine was performed overnight in 2mL microcentrifuge tubes (one fish per tube) with 1.5mL of 1% iodine solution in 100% ethanol according to the previously published protocol for I_2E staining (21). After staining specimens were transferred to 96% ethanol for scanning.

Synchrotron scanning

Iodine-stained zebrafish specimens were imaged using PPC-SRµCT (29) at beamline BM05 of the European Synchrotron Radiation Facility – Extremely Brilliant Source (ESRF-EBS) in France. They were imaged with two isotropic voxel sizes: 3µm and 0.727µm. The propagation distances were selected to optimize phase retrieval with a given photon energy (keV) and detector pixel size within the near-field Fresnel region (25, 35). The detector exposure times were optimized for the maximum dynamic range of the 16-bit image without saturation of the detector. The number of projections was optimized for high resolution and phase retrieval on the given detector pixel size (2048 x 2048) and the scanning mode (half-acquisition mode).

Medium-resolution configuration: 3µm voxel size

The specimens were imaged with a PCO Edge CLHS 4.2 camera using a magnifying optic based on a Canon 68mm F/D 2.8 Super Macro lens coupled to a 250µm-thick LuAG:Ce scintillator. The protocol of Hierarchical Phase-Contrast Tomography (HiP-CT) developed by Walsh et al. (36) was used to optimize the overall contrast of the data as well as the signal-to-noise ratio. The beam was filtered with 2.3mm of aluminum and 8 5mm bars of silicon dioxide. The resulting detected average energy was 78keV. In order to enlarge the lateral field of view, the samples were imaged in half acquisition, i.e. over 360 degrees around the center of rotation shifted by 900 pixels to the right side of the field of view. A total of 6000 projections, resulting from an accumulation of 4 sub-frames of 10ms each, were taken over 360 degrees. The specimens were placed at a propagation distance of 1.45m from the detector in order to maximize the phase-contrast effect. The relatively high energy results in the bones and the stained tissues having quite similar phase properties, making it possible to use a relatively simple approach for phase imaging.

High-resolution configuration: 0.727µm voxel size

The specimens were imaged with a PCO Edge 4.2 camera mounted on the Twinmic white-beam microscope system (Optique Peter) using a Mitutoyo 10x objective coupled to a 23µm-thick LSO scintillator. We used the side beam of BM05, which is produced by the last dipole of the synchrotron lattice before the short straight section that contains the dipole wiggler of BM05. This beam is partially superimposed with the main source of BM05, but on the side of the main beam. About 10mm of this beam with lower energy and higher coherence can be used for high-resolution imaging. It was filtered with 2.3mm of aluminum. The resulting detected average energy was 35keV. In total, 6000 projections of 40ms each were taken over 360 degrees, also in half-acquisition. The specimens were placed at a propagation distance of 180mm from the detector.

Reconstruction and segmentation

µCT data was reconstructed into 8-bit BMP image stacks using NRecon version 1.6.10 (Bruker microCT, Belgium). Tomographic slices were reconstructed from PPC-SRµCT scans using filtered back-projection algorithm using the software PyHST2 (37) coupled with a modified version (38) of single-distance phase retrieval (39). The different sub-volumes were ring-corrected (40), vertically concatenated, converted to 16 bits, cropped using in-house developed Matlab systems, and saved in jpeg2000 format for a 10x file size reduction without loss of data precision. Delta/beta ratios used in the reconstruction were 500 for 0.727µm voxel size scans and 1000 for 3µm voxel-size scans.

BMP and jpeg2000 image stacks were imported into VGStudio MAX version 3.5.1 (Volume Graphics, Germany) for manual segmentation and rendering. Tissue volumes were measured using the Porosity/Inclusion Analysis module.

Results

DICE-PPC-SRµCT reveals histological information about mineralized and soft tissues

Using conventional µCT without contrast enhancing agents can provide 3D data about the mineralized zebrafish skeleton, with the best results achieved in late juvenile or adults beyond 2-3mpf (Figures 1B–C"). As the younger juvenile skeleton is only weakly mineralized and therefore less X-ray dense, fewer skeletal elements can be resolved (Figures 1A–A").

By employing DICE-PPC-SRµCT we could obtain scan data with down to submicron voxel sizes and near-histological quality already at 1mpf (Figures 1D–F"; Supplementary Videos 1–3), allowing the visualization of range of soft tissues including the brain and spinal cord (Figures 2A, B), the retina (Figure 2C), the sensory organs in the semicircular canals (Figure 2D), organs such as the heart, kidney, and ovary (Figures 2E–G), teeth

(Figures 2H, I), and trunk musculature (Figure 2J). Cartilage could be observed at the cellular level, with chondrocyte lacunae appearing as dark (unstained) cavities containing bright stained nuclei (Figures 2K, N). All this was achieved while simultaneously retaining the histological information in the dense, mineralized elements including bones and otoliths (Figures 2L, M).

To demonstrate how these datasets can be used to uncover skeletal-associated soft tissue phenotypes, we scanned two wild-type and two *nkx3.2*$^{-/-}$ mutant zebrafish at 1mpf (late larva; 0.727µm voxel size) and 2mpf (juvenile; 3µm voxel size). These phenotypes are most likely the secondary result of the primary skeletal deformities we previously described (34): the jaw joint fusion leading to the open-mouth phenotype (Figure 3) and the deformities of the occiput and Weberian apparatus.

Identifying defects in jaw-associated musculature

As the jaw joint fusion characteristic of *nkx3.2*$^{-/-}$ mutants causes the lower jaw to be permanently locked in the open position (Figure 3), we chose to investigate whether this could have any secondary effects on the jaw-associated muscles at 2mpf. The zebrafish lower jaw is opened and closed primarily by two large muscles – the protractor hyoideus and adductor mandibulae, respectively (41, 42). The adductor mandibulae is divided into three main muscle bundles: A1, A2, and A3 (Figures 4A–D) (43), each with distinct attachment sites and functions that collectively serve to close the mouth. A1 is the maxillary component that has no connection to the mandible, instead connecting the maxilla to the

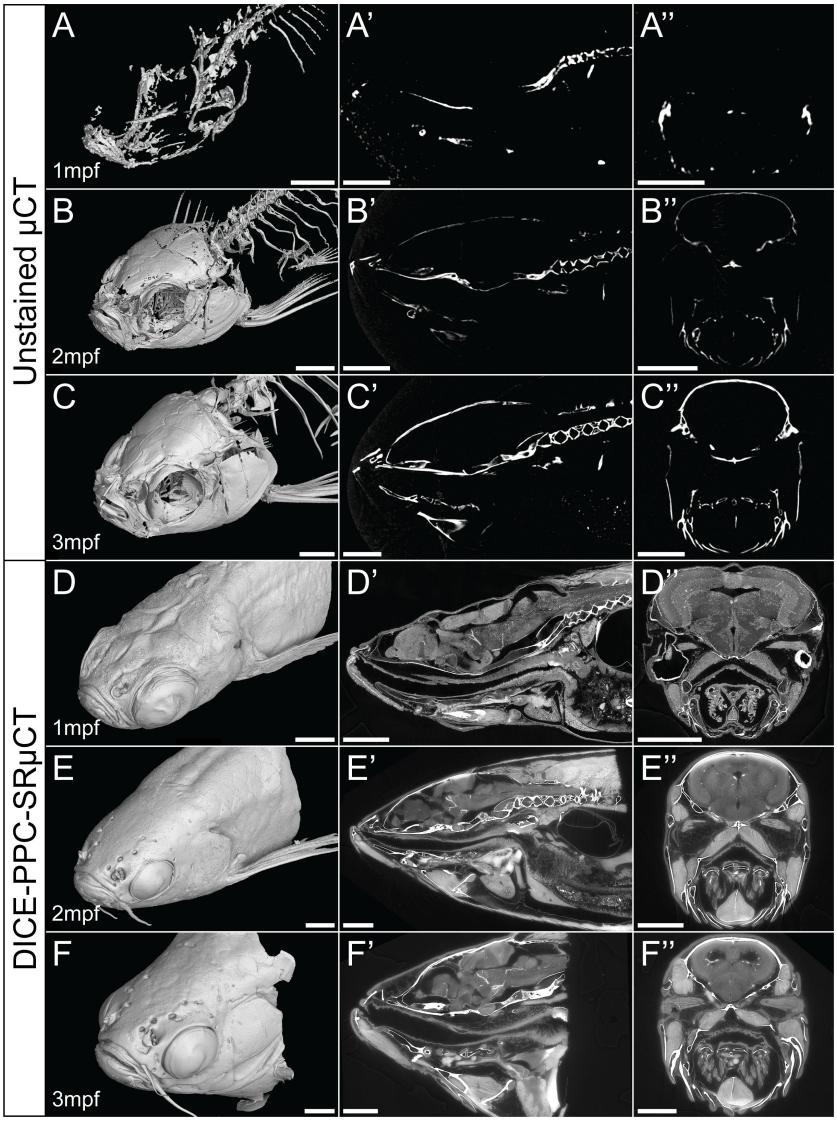

FIGURE 1
Conventional µCT only visualizes the zebrafish mineralized skeleton, while DICE-PPC-SRµCT adds soft-tissue information. **(A-C)** Volume renderings of 1-3mpf zebrafish scanned at a voxel size of 5.43µm using conventional µCT. **(D-F)** Volume renderings of 1-3mpf zebrafish stained with iodine and scanned at 0.727µm voxel size **(D)** and 3µm **(E, F)** using PPC-SRµCT. **(A'-F')** Sagittal virtual thin sections through the midline. **(A''-F'')** Transverse virtual thin sections through the head (immediately posterior to the eyes). Scale bars, 500µm **(A-A'', D-D'')** and 1mm **(B-B'', C-C'', E-E'', F-F'')**.

10.3389/fendo.2023.1108916

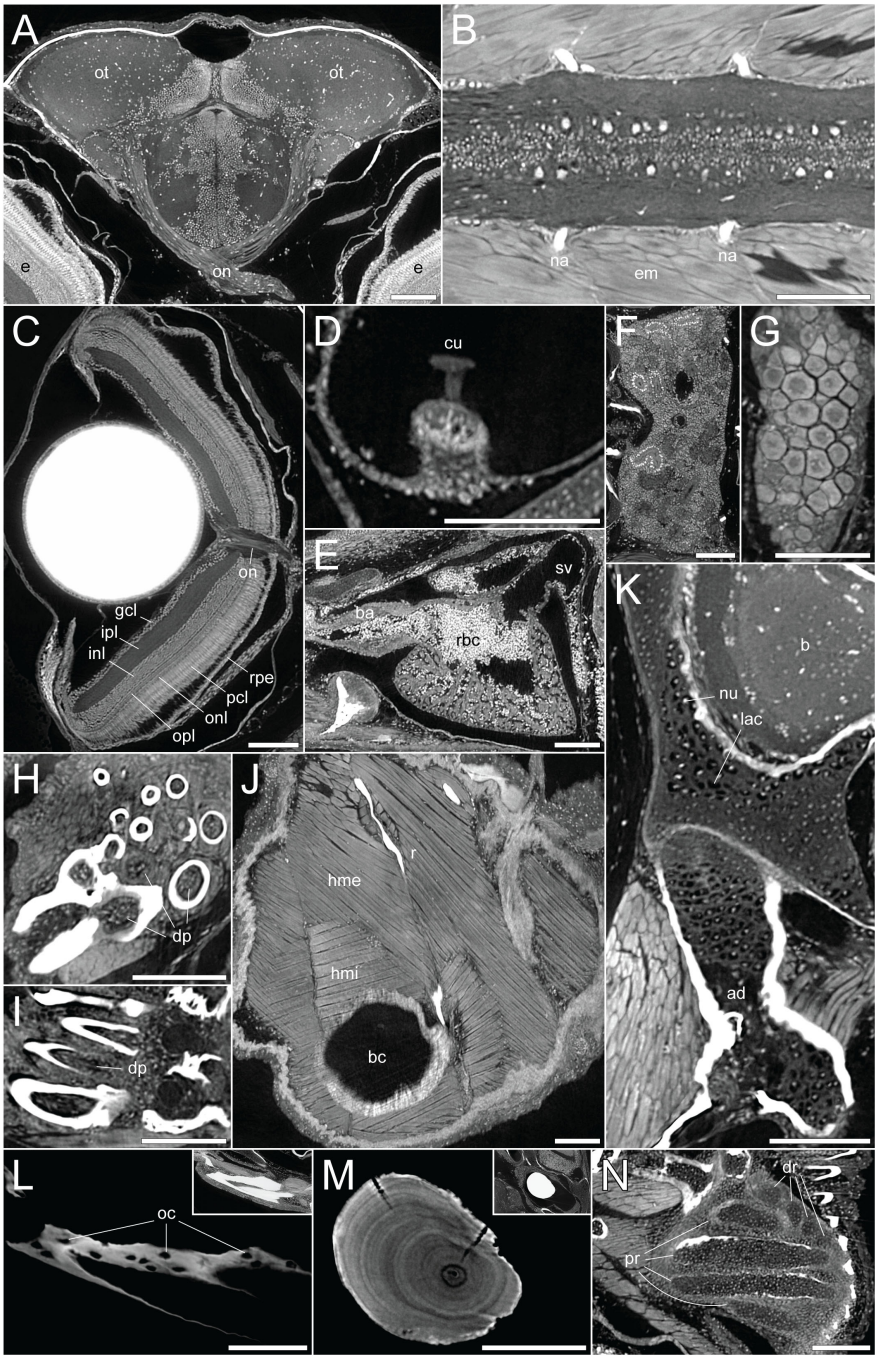

FIGURE 2
DICE-PPC-SRμCT at submicron resolution provides a detailed histological information. All images represent virtual thin sections from a 1mpf zebrafish scanned at 0.727μm voxel size. **(A)** Transverse view of the brain and optic nerves. **(B)** Longitudinal section through the spinal cord. **(C)** Transverse view of the eye, with the optic nerve and retinal layers visible. **(D)** Sagittal view of the crista ampullaris in the lateral semicircular canal. **(E)** Sagittal view of the heart. **(F)** Longitudinal view of the head region of the kidney. **(G)** Longitudinal view of the ovary. **(H, I)** Transverse and sagittal views of the pharyngeal teeth, with dental pulp visible. **(J)** Sagittal view of the two approximately perpendicular layers of hypaxial trunk musculature. **(K)** Sagittal view through the neurocranium (top) and hyomandibula (bottom), with visible chondrocyte lacunae and endochondral ossification of the hyomandibula. **(L)** Sagittal view through the dentary bone, using minimal projection with adjusted contrast to reveal osteocyte lacunae features in the bone. Inset image displays the same view but with comparable visualization settings to previous soft-tissue panels. **(M)** Sagittal section through the lapillus otolith, again with adjusted contrast to reveal the otolith microstructure showing growth rings. Inset image displays the same view but with comparable visualization settings to previous soft-tissue panels. **(N)** Section through the pectoral fin cartilaginous endoskeleton. ad, adipocytes; b, brain; ba, bulbus arteriosus; bc, body cavity; cu, cupula; dp, dental pulp; dr, distal radials; e, eye; em, epaxial muscle; gcl, ganglion cell layer; hme, hypaxial muscle (external); hmi, hypaxial muscle (internal); inl, inner nuclear layer; ipl, inner plexiform layer; lac, chondrocyte lacunae; na, neural arches; num, cell nuclei; oc, osteocytes; on, optic nerves; onl, outer nuclear layer; opl, outer plexiform layer; ot , optic tectum; pcl, photoreceptor cell layer; pr, proximal radials; r, rib; rbc, red blood cells; rpe, retinal pigmented epithelium; sv, sinus venosus. Scale bars, 100μm.

FIGURE 3
nkx3.2$^{-/-}$ zebrafish display the distinctive "open mouth" phenotype. Anterolateral and anterior volume renderings of DICE-PPC-SRμCT scanned *nkx3.2*$^{-/-}$ zebrafish at 1mpf (left) and 2mpf (right). Scale bars, 1mm.

quadrate and preopercle (Figure 4B) and functioning to retract the protruding upper jaw in concert as the rest of the adductor mandibulae complex retracts the mandible. A2 lies mesial to A1, connecting the posterior anguloarticular and dentary to the quadrate and preopercle (Figures 4A', C). A3 is mesial to A2, and connects the coronomeckelian bone on the mesial surface of the dentary *via* a tendon to a broad muscle insertion on the preopercle, metapterygoid, and hyomandibula (Figure 4D).

In the *nkx3.2*$^{-/-}$ mutant, the adductor mandibulae complex appears poorly formed as A1, A2, and A3 are difficult to differentiate from each other compared to the wild-type appearance of three distinctive bundles (Figures 4A'', E'', F''). Therefore, the 3D renderings of the mutant adductor mandibulae are displayed in single colors (Figures 4E-F'') and external morphology was used to attempt to define the muscle bundles. The major components of A1 and A2 appeared to be present, as well as the broad muscle insertions of A3 in the preopercle and hyomandibula. However, the tendon connecting A3 to the mandible appeared to be absent or malformed. The mutant also displayed additional abnormal muscle bundles or tendinous extensions not found in the wild-type (Figure 4E', F', arrowheads).

In both the left and right adductor mandibulae of the *nkx3.2*$^{-/-}$ mutant, the maxillary tendinous insertion of A1 is present but appears considerably reduced in size compared to the wild-type (arrows in Figures 4B, E', F'), while the ventral insertions appear different. In the absence of the jaw joint, the bones of the posterior dentary, anguloarticular, quadrate are disorganized and variably poorly shaped, making it difficult to assign definitive identities. However, the left A1 anteriormost ventral insertion is located unusually anteriorly in what would appear to be the posterior dentary (Figure 4E', asterisk), while the right A1 anteriormost posteroventral insertion is located more posteriorly, in what is more likely to represent the quadrate (Figure 4F'), more similar to the wild-type condition.

The protractor hyoideus connects the anterior dentary to the ceratohyal and hypohyals, linking the first arch to the second arch (Figure 4G). Associated with the protractor hyoideus is the intermandibularis anterior, connecting the paired dentary bones (Figure 4G). In the *nkx3.2*$^{-/-}$ mutant these muscles appear relatively normal in terms of gross morphology and insertion sites, with the notable exception of a portion of muscle fibers of the protractor hyoideus crossing the midline division of this paired muscle (Figure 4H), likely related to the lateral distortions in the orientation of the ceratohyals and basihyal observed in this individual.

Describing deformed and missing ligaments in the Weberian apparatus

The Weberian apparatus bones include vertebrae 1-4 and their modified ribs and neural arches (Figures 5, 6) that facilitate the transmission of vibrations from the swim bladder into the inner ear (44–46). Cartilage (blue) is present at 1mpf in the endochondrally ossifying parapophyses of both the Weberian apparatus and rib-bearing vertebrae (Figures 5A, C), in addition to the dorsal neural complex that can be clearly seen at 1mpf (Figure 5A) before gradually being endochondrally ossified into the anterior supraneurals and neural arches (Figure 6A) (44, 47, 48).

Connecting the modified ventral bones are ligaments that collectively form a chain between the swim bladder and inner ear. The anterior surface of the swim bladder (tunica externa) is connected *via* a large ligament ("triple" ligament, 48) to both the posterior tripus and os suspensorium, associated with vertebrae 3 and 4, respectively. The thick suspensor ligament connects the parapophyses of vertebrae 3 (tripus) and 4. Finally, the interossicular ligament connects the anterior process of the tripus to the scaphium *via* the intercalarium midway between them, dividing the interossicular ligament into anterior and posterior bundles. This wild-type organization of the Weberian skeleton and interossicular and suspensor ligaments (shades of purple) in a late larva and juvenile are shown in Figures 5A, 6A, along with sagittal virtual thin sections through the ligaments (Figures 5B, C, 6B, C).

In the 1mpf mutant the neural complex cartilage appears normal (Figure 5D). However, there is no parapophyseal cartilage associated with vertebrae 1 or 2, and dramatically less cartilage present in the parapophyses of vertebrae 3 and 4, consistent with our previous description (34). However, this late larval mutant is unusual compared to previously characterized mutants in that it has a small cartilaginous parapophysis in the first rib-bearing vertebrae (V5; Figure 5D), while all other rib-bearing vertebrae have no parapophyses as previously described (34). Other than this, the skeletal defects of the tripus, lateral process 2, and scaphium

10.3389/fendo.2023.1108916

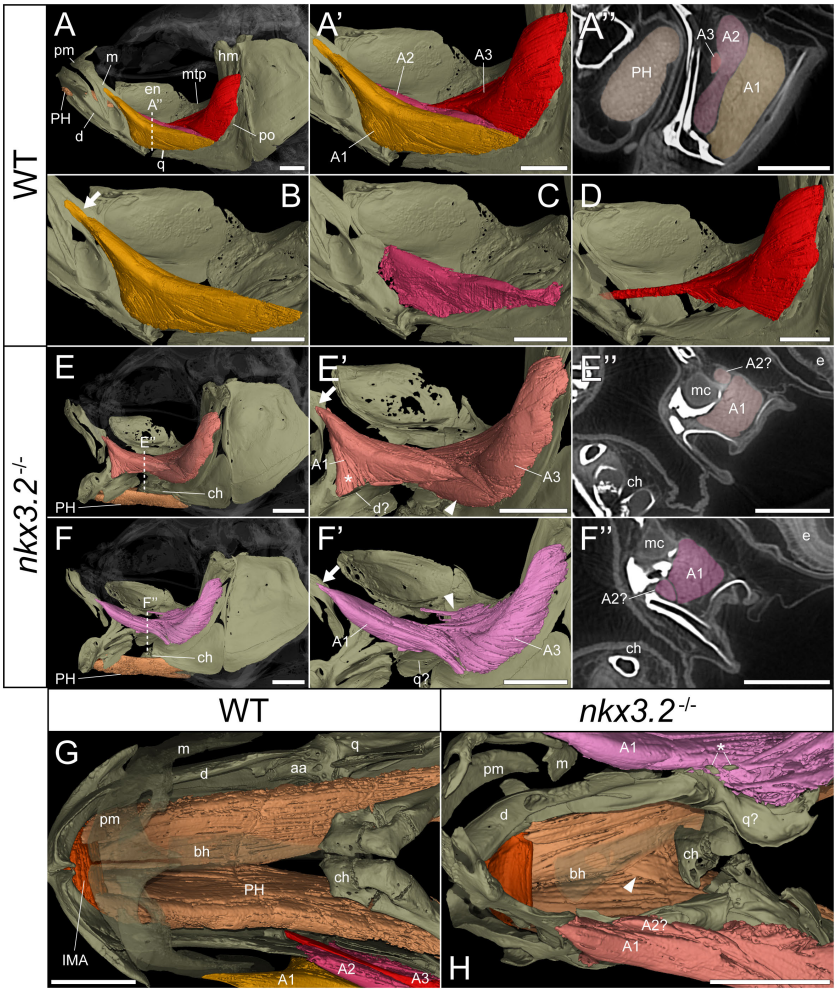

FIGURE 4
nkx3.2$^{-/-}$ zebrafish display defects in lower jaw-associated musculature. **(A)** Lateral volume rendering of the wild-type zebrafish head skeleton and relevant associated muscles. **(A')** Close up of the rendered adductor mandibulae muscle bundles A1-A3. **(A'')** False-coloured transverse virtual thin section [position indicated by dotted line in **(A)**] highlighting the protractor hyoideus muscle and distinct bundles of the adductor mandibulae. **(B–D)** Renderings of the isolated A1, A2, and A3 bundles of the adductor mandibulae, respectively. **(E, F)** The left and right lateral views of a single *nkx3.2*$^{-/-}$ zebrafish, with the panels in **(F-F'')** reversed to facilitate comparison. Arrows in **(B, E', F')** indicate the maxillary tendon of A1. Asterisk in **(E')** indicates the unusual anterior attachment site of the A1 bundle to the lower jaw. Arrowheads in **(E')** and **(F')** indicate the abnormal organization of muscle bundles. **(G, H)** Dorsal view of the lower jaw skeleton and associated musculature in wild-type and *nkx3.2*$^{-/-}$ fish, with the basihyal rendered transparent. In **(G)**, the maxilla and premaxilla were also rendered as partially transparent, and the right adductor mandibulae was removed to reveal the quadrate below. In **(H),** arrowhead indicates protractor hyoideus muscle fibers crossing the midline. Asterisk indicates ectopic ossifications embedded in the right adductor mandibulae. Both zebrafish are 2mpf and were scanned with a voxel size of 3µm using DICE-PPC-SRµCT. aa, anguloarticular; bh, basihyal; ch, ceratohyal; d, dentary; e, eye; en, endopterygoid; hm, hyomandibula; IMA, intermandibularis anterior; m, maxilla; mc, Meckel's cartilage; mpt, metapterygoid; PH, protractor hyoideus; pm, premaxilla; po, preopercle; q, quadrate. All scale bars, 500µm, except on virtual thin sections **(A'', E'',** and **F'')** 300µm.

(Figure 5D) are consistent with our previous description of the *nkx3.2*$^{-/-}$ mutant (34).

The swim bladder connection to the os suspensorium and posterior process of the tripus appears normal in the mutants, but the rest of the ligamentous auditory chain is highly disrupted (Figures 5D, 6D). The suspensor ligament between the tripus and parapophysis 4 was entirely absent in both the 1mpf (Figures 5D, F) and 2mpf (Figures 6D, F) mutants. The interossicular ligament also appeared to be absent in the 2mpf mutant (Figures 6D, E), while the 1mpf mutant possessed only a small piece of connective tissue resembling a potential ligament weakly connecting the tripus to the intercalarium (posterior interossicular), and extending ventrally to attach the intercalarium to the underdeveloped lateral process 2 (Figures 5D, E), a connection not found in the wild-types (Figures 5B, 6B).

Characterizing altered structures of the inner ear

The mature zebrafish inner ear is comprised of the three semicircular canals with sensory cristae for vestibular function, and three end organs with sensory macula with a primarily auditory function (49, 50). Each of the three end organs, the utricle, saccule,

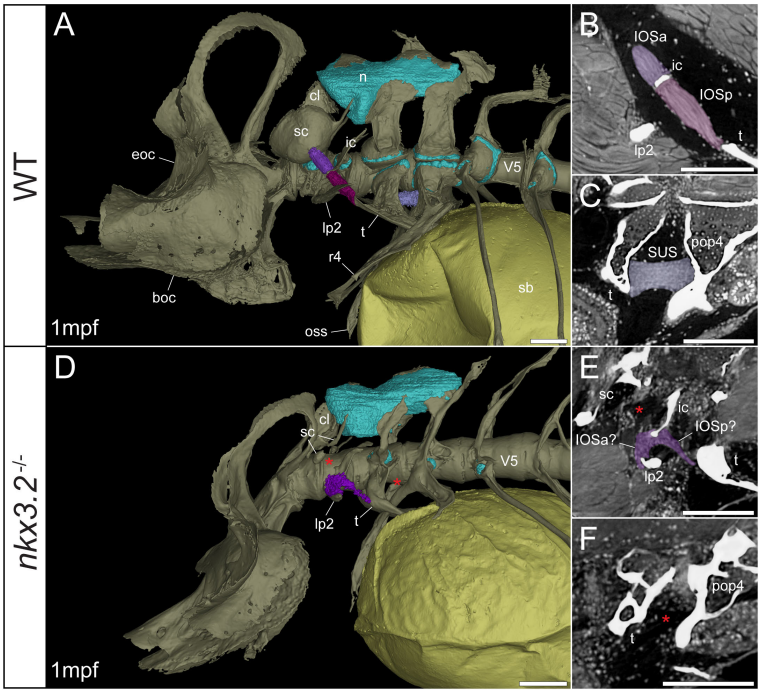

FIGURE 5
Late larval *nkx3.2*$^{-/-}$ zebrafish displays deformed and missing ligaments in the Weberian apparatus. **(A, D)** Lateral renderings of the occipital bones, Weberian apparatus, and anterior rib-bearing vertebrae (colored as bone) with associated cartilage (blue), ligaments (shades of purple), and swim bladder (yellow) of 1mpf wild-type and *nkx3.2*$^{-/-}$ zebrafish. Red asterisks in **(D)** indicate the absence of the anterior interossicular and suspensor ligaments. **(B, E)** False-coloured sagittal virtual thin sections through the interossicular ligament in wild-type and *nkx3.2*$^{-/-}$ zebrafish. Red asterisk in **(E)** indicates the absence of a ligamentous connection between the intercalarium and scaphium, as what may be anterior part of the interossicular ligament appears to be connected to lateral process instead. **(C, F)** False-coloured virtual thin sections through the suspensor ligament in wild-type and *nkx3.2*$^{-/-}$ zebrafish. The red asterisk in **(F)** indicates the absence of the suspensor ligament between the tripus and parapophysis 4. boc, basioccipital; cl, claustrum; eoc, exoccipital; ic, intercalarium; IOSa, anterior interossicular ligament; IOSp, posterior interossicular ligament; lp2, lateral process 2; n, neural complex cartilage; oss, os suspensorium; pop4, parapophysis 4; r4, rib 4; sb, swim bladder; sc, scaphium; SUS, suspensor ligament; t, tripus; V5, vertebrae 5. Scale bars, 100µm.

and lagena, possess a single sensory macula covered by a dense calcium carbonate otolith. The semicircular canals and utricle make up the pars superior, while the saccule and lagena comprise the pars inferior. The pars superior and inferior are connected *via* the small ductus sacculo-utricularis (51, 52). All of these inner ear canals are filled with a shared endolymphatic fluid. In this description, we use the term "sinus endolymphaticus" (Figures 7A, A', 8A, A') to refer to the space in the pars inferior that contains the endolymph.

As mentioned above, vibrations from the swim bladder travel anteriorly along the auditory chain until they reach the paired scaphia immediately posterior to the occiput (46). The gap between the scaphia and the sinus endolymphaticus of the inner ear is bridged by a second large sac containing perilymphatic fluid, the sinus perilymphaticus (also called sinus impar). The sinus perilymphaticus has paired atria that lie mesial to and partially surrounded by the cup-shaped scaphia, such that vibrations from the scaphia translate into motion of the perilymph (Figures 7A, A', E, 8A, A', E). The paired atria extend anteriorly before merging and entering the occiput *via* the cavum sinus impar, an opening between the posterior exoccipital and basioccipital bones that lies dorsal to the notochord (Figures 7D, 8D). The sinus perilymphaticus continues to extend anteriorly through the middle of the exoccipital, bounded ventrally by the basioccipital, until it reaches the midline of the transverse canal of the sinus endolymphaticus that connects the paired saccula. The perilymph and endolymph of these two compartments are separated by a thin membrane (52), but motion from the sinus perilymphaticus must be transmitted across this membrane to induce motion of the otoliths and stimulate the underlying sensory cells.

We segmented 3D models of the sinus endolymphaticus (green) and sinus perilymphaticus (magenta) in 1 and 2mpf wild-type zebrafish (Figures 7A, A', 8A, A'), and provide virtual thin sections that show the meeting point between these sacs (Figures 7B–D, 8B–D) and how the atria of the sinus perilymphaticus relate to the scaphia and claustra (Figures 7E, 8E). We previously described 3mpf *nkx3.2*$^{-/-}$ mutants displaying a closure/fusion of the cavum sinus impar between the exoccipital and basioccipital bones (34), and the same skeletal phenotype was observed in the 1 and 2mpf mutants included in this study. Here we extend this description by examining the effects of this phenotype on the sinus endolymphaticus and sinus perilymphaticus.

The 1mpf *nkx3.2*$^{-/-}$ mutant sinus perilymphaticus was extremely small and limited posteriorly (Figures 7F, F'), failing to extend out of the skull to reach the scaphia as a result of the closed

cavum sinus impar (Figure 7I). The only indication that this small space posterior to the transverse canal actually represented the sinus perilymphaticus was the presence of a thin membrane separating itfrom the transverse cana (Figures 7G, I), too dorsal to be seen in Figures 7H. On the posterior side of the closed cavum sinus impar, nothing resembling a perilymphatic sac could be observed, and no atria were observed in association with the claustra or reduced scaphia (Figure 7J). The phenotype in the 2mpf mutant was almost identical, except the sinus perilymphaticus was absent entirely (Figures 8F–J). The sinus endolymphaticus, on the other hand, appeared quite normal in shape and extent in mutants (Figures 7F, F', 8F, F').

Volume measurements of 3D segmented soft tissues provide information about growth trajectories

In addition to describing the shape of all of the above tissues qualitatively, the digital and high-resolution nature of the data makes it possible to acquire a wealth of additional quantitative data. Here, we used a simple measure, 3D volume, to describe the tissues and phenotypes. From the segmented volumes of the tissues displayed in the previous figures, precise volume measurements were performed and plotted in Figure 9. As zebrafish size can be variable even at identical ages, and our sample size was small, standard length was plotted against tissue volume in an attempt to enable to the comparison of approximate wild-type and mutant growth trajectories rather than comparing individuals.

By comparing the points and inferred growth trajectories of the wild-type and *nkx3.2*$^{-/-}$ mutants, it appears as though the adductor mandibulae and pars hyoideus muscles had their overall volumes relatively unchanged compared to the wild-type, while the intermandibularis anterior muscle volume was reduced (Figure 9A). The mutant Weberian ligaments are not as informative as only the 1mpf individual possessed just the interossicular ligament (the others being absent and given measured volumes of 0μm^3), but it nevertheless reiterates that this ligament appears to be reduced in volume compared to what might be expected in a comparable wild-type individual (Figure 9B). Finally, the mutant sinus endolymphaticus appears approximately unchanged in volume relative to wild-types, or only slightly reduced, while the sinus perilymphaticus is clearly dramatically reduced as described qualitatively above.

All three categories of wild-type tissues appeared remarkably internally consistent in the relative tissue volumes, as the ratio between the volumes of the adductor mandibulae, pars hyoideus, and intermandibularis anterior were almost unchanged at 1mpf and

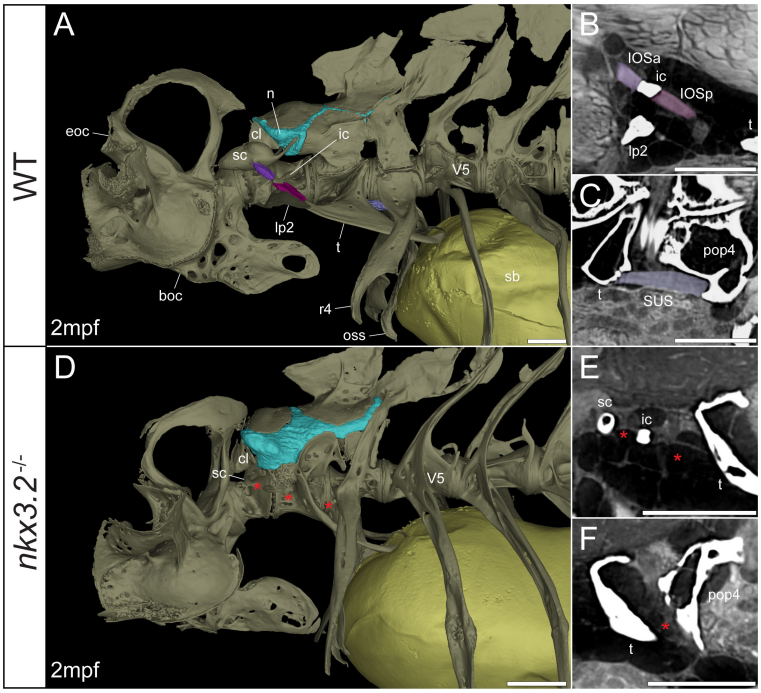

FIGURE 6
Juvenile *nkx3.2*$^{-/-}$ zebrafish displays missing ligaments in the Weberian apparatus. **(A, D)** Lateral renderings of the occipital bones, Weberian apparatus, and anterior rib-bearing vertebrae with associated cartilage (blue), ligaments (shades of purple), and swim bladder (yellow) of wild-type and *nkx3.2*$^{-/-}$ juvenile zebrafish. Red asterisks in **(D)** indicate the absence of the interossicular and suspensor ligaments. **(B, E)** False-coloured sagittal virtual thin sections through the interossicular ligament in wild-type and *nkx3.2*$^{-/-}$ zebrafish. Red asterisks in **(E)** indicate the absence of the interossicular ligament. **(C, F)** False-coloured virtual thin sections through the suspensor ligament in wild-type and *nkx3.2*$^{-/-}$ zebrafish. The red asterisk in **(F)** indicates the absence of the suspensor ligament between the tripus and parapophysis 4. boc, basioccipital; cl, claustrum; eoc, exoccipital; ic, intercalarium; IOSa, anterior interossicular ligament; IOSp, posterior interossicular ligament; lp2, lateral process 2; n, neural complex cartilage; oss, os suspensorium; pop4, parapophysis 4; r4, rib 4; sb, swim bladder; sc, scaphium; SUS, suspensor ligament; t, tripus; V5, vertebrae 5. Scale bars, 300μm.

2mpf (parallel growth trajectories in Figure 9A), and the same was true for the interossicular and suspensor ligaments (Figure 9B) and the sinus endolymphaticus and sinus perilymphaticus (Figure 9C), suggesting that within each category, the tissues increase in size at comparable rates as the fish grows.

Discussion

Whole-body histological examination in 3D is strongly desirable for characterization of organisms modeling skeletal diseases in order to carry out a rigorous comparison with human pathologies. Model organisms of small sizes like zebrafish currently display challenges in achieving high resolution datasets visualizing the interaction of the skeleton with the surrounding tissues. We applied diffusible iodine-based contrast enhancement (DICE) and propagation phase-contrast synchrotron radiation micro-computed tomography (PPC-SRμCT) to image late-larval and juvenile wild-type and *nkx3.2*$^{-/-}$ mutant zebrafish. The obtained datasets reveal high-quality, high-resolution virtual histological images of tissues and organs that can be segmented to get unprecedented 3D models of interaction between the mineralized skeleton and surrounding soft tissues.

In comparison, conventional μCT without a contrast enhancing agent provides little to no information about soft tissues. In addition, the best results for 3D segmentation of the bony skeleton are only achieved after 2 months post fertilization, because fewer skeletal elements can be resolved prior to a substantial degree of mineralization being completed. Iodine enhances contrast of soft tissues in addition to the mineralized skeleton (21, 24), whereas propagation phase contrast enhances the contrast at the edges of microstructural boundaries (25–27). The HiP-CT protocol of using a reference scan to reduce low-frequency background variation also further increases the soft-tissue contrast (36). Each of these three techniques independently enable the visualization of soft tissues in comparison to conventional μCT, and combined provide excellent image contrast for the relatively easy segmentation of the skeleton, soft tissues, and the boundaries between different tissue types. This can be advantageous for segmenting cartilage, muscle bundles, ligaments and tendons that are in direct contact with the mineralized skeleton.

By comparison, PTA enhances the contrast of soft tissues but does not seem to enhance the mineralized tissue (53, 54), leading to weaker contrast between mineralized and non-mineralized

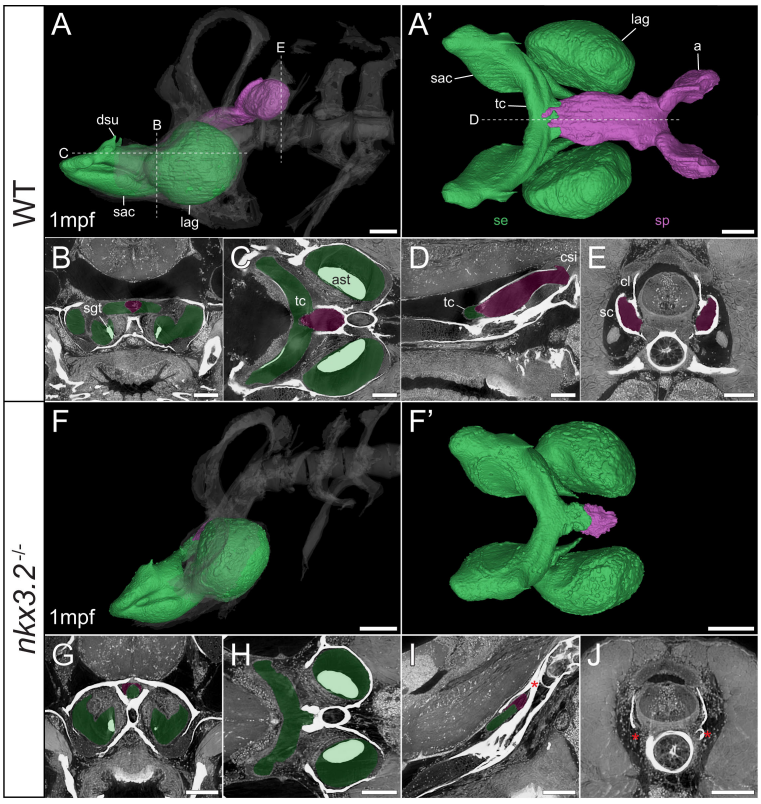

FIGURE 7
Late larval *nkx3.2*$^{-/-}$ zebrafish displays severe reduction of the sinus perilymphaticus. **(A, F)** Lateral rendering of the sinus endolymphaticus (green) and sinus perilymphaticus (magenta) in the context of the occiput and Weberian apparatus (white, transparent) in 1mpf wild-type and *nkx3.2*$^{-/-}$ zebrafish. **(A', F')** Anterodorsal renderings of the sinus endolymphaticus and sinus perilymphaticus (anterior to the left). False coloured transverse **(B, G)**, longitudinal **(C, H)**, and sagittal **(D, I)** virtual thin sections through the middle of the sinus endolymphaticus. Red asterisk in **(I)** indicates the blind posterior termination of the sinus impar. **(E, J)** False coloured transverse virtual thin sections through the atria of the sinus perilymphaticus. Red asterisks in **(J)** indicate the absence of the atria of the sinus perilymphaticus. Virtual thin section positions are indicated by labelled dotted lines in **(A, A')**. a, atrium; ast, asteriscus; cl, claustrum; csi, cavum sinus impar; dsu, ductus sacculo-utricularis; lag, lagena; sac, saccule; sc, scaphium; se, sinus endolymphaticus; sgt, sagitta; sp, sinus perilymphaticus; tc, transverse canal. Scale bars, 100μm.

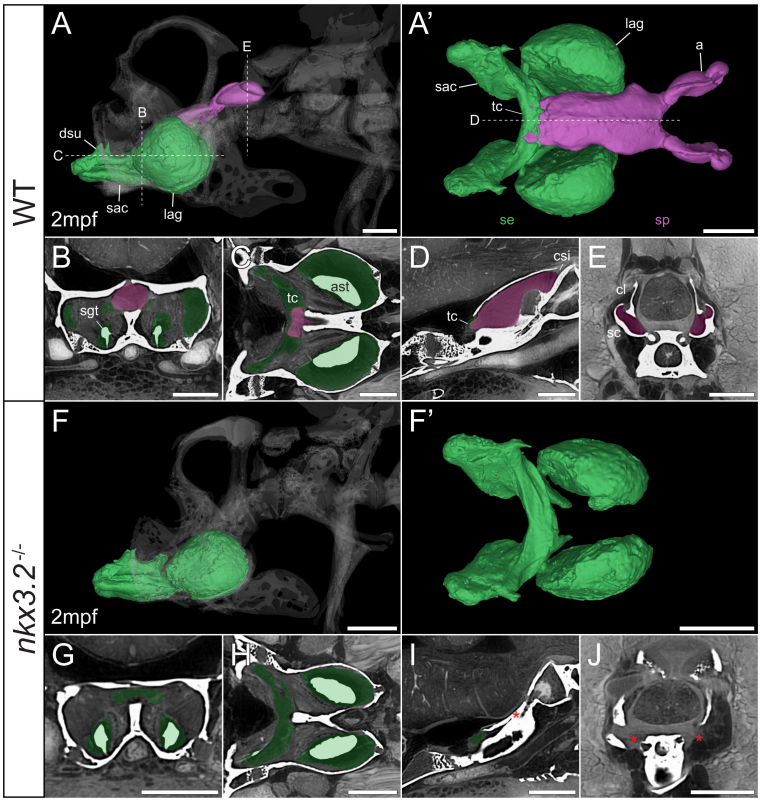

FIGURE 8
Juvenile *nkx3.2*$^{-/-}$ zebrafish displays complete absence of the sinus perilymphaticus. **(A, F)** Lateral rendering of the sinus endolymphaticus (green) and sinus perilymphaticus (magenta) in the context of the occiput and Weberian apparatus (white, transparent) in 2mpf wild-type and *nkx3.2*$^{-/-}$ zebrafish. **(A', F')** Anterodorsal renderings of the sinus endolymphaticus and sinus perilymphaticus (anterior to the left). **(B-D, G–I)** False coloured transverse, longitudinal, and sagittal virtual thin sections through the middle of the sinus endolymphaticus. Red asterisk in **(I)** indicates the blind posterior termination of the sinus impar. **(E, J)** False coloured transverse virtual thin sections through the atria of the sinus perilymphaticus. Red asterisks in **(J)** indicate the absence of the atria of the sinus perilymphaticus. Virtual thin section positions are indicated by labelled dotted lines in **(A, A')**. a, atrium; ast, asteriscus; cl, claustrum; dsu, ductus sacculo-utricularis; lag, lagena; sac, saccule; sc, scaphium; se, sinus endolymphaticus; sgt, sagitta; sp, sinus perilymphaticus; tc, transverse canal. Scale bars, 300µm.

tissues and making it harder to segment the skeleton and soft tissues on the basis of apparent density (brightness in the image). If the 3D segmentation of the interaction between mineralized and soft tissues is not the focus of the examination, PTA and iodine are capable of producing comparable high quality histological data down to the cellular level using PPC-SRµCT (24, 54). Particularly for analyses of absolute rather than relative tissue volumes, it should also be noted that I_2E causes shrinkage of many soft tissues due to the high concentration of ethanol, so other stains including PTA and pH-buffered I_2KI could be more suitable (55–57).

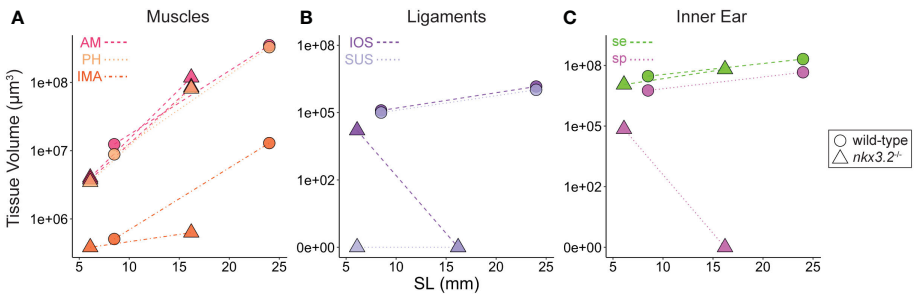

FIGURE 9
Volume measurements of 3D segmented soft tissues. Volume measurements of muscles **(A)**, Weberian ligaments **(B)**, and inner ear sacs **(C)**. Circles indicate wild-type tissues, while triangles indicate *nkx3.2*$^{-/-}$ tissues. Each point represents a single tissue volume measurement. Dotted lines connect corresponding tissues from 1mpf and 2mpf zebrafish of the same genotype to approximate growth trajectories. Different tissues are indicated by individual colors and line styles in agreement with the color codes used in the previous figures. Y-axes are log- or pseudolog-scaled. X-axes display standard length (mm). AM, adductor mandibulae; PH, protractor hyoideus; IMA, intermandibularis anterior; IOS, interossicular; SUS, suspensor; se, sinus endolymphaticus; sp, sinus perilymphaticus.

Applying DICE-PPC-SRμCT to the zebrafish model for *spondylo-megaepiphyseal-metaphyseal dysplasia* represented by homozygous *nkx3.2*$^{-/-}$ mutants not only revealed the detailed morphology of the mutants with characteristic open mouth phenotypes but also uncovered changes in the muscle organization around the fused jaw joint. Importantly, we observed that the adductor mandibulae and protractor hyoideus muscles had disrupted fiber/bundle organization, and some force-transmitting tendons appeared reduced, possibly indicative of jaw muscle disuse in the mutants due to the inability to articulate the jaws (33, 58, 59). Particularly notable is the apparent insertion of one of the 2mpf A1 muscles to the dentary rather than the quadrate, crossing the fused jaw joint. This could indicate that the loss of the joint identity in the skeleton weakens the boundaries of the molecular patterning zones of the muscle attachment sites, suggesting these attachment sites can be labile in response to an altered underlying skeleton (60).

Surprisingly, the volume measurements of the jaw muscles revealed that both the adductor mandibulae and protractor hyoideus muscles in the mutants appeared to be consistent with the growth trajectories of the wild-type fish, suggesting overall muscle volumes were unaffected by the open jaw phenotype. On the other hand, the intermandibularis anterior muscle with apparently normal morphology and attachment sites displayed an apparent reduction in volume at 2mpf compared to the wild-type, which could indicate that this muscle is more sensitive to disuse than the adductor mandibulae and protractor hyoideus. Together, the morphological, histological, and volume information are important for the characterization of muscle pathologies in a malformed skeleton, although a greater number of *nkx3.2*$^{-/-}$ specimens would have to be analyzed to draw statistically significant quantitative conclusions in this case.

We previously hypothesized that sound transmission from the swim bladder to the inner ear would be severely negatively affected by the deformation of the Weberian ossicles and closure of the cavum sinus impar on the basis of μCT data from adult mutants (34). This additional data from late larval and juvenile mutants that reveals the severe reduction and/or loss of Weberian ligaments and the sinus perilymphaticus strongly support this conclusion, as almost every connection in the auditory chain from swim bladder to inner ear is now demonstrated to be disrupted or missing altogether. Even though the Weberian apparatus is a morphological novelty of otophysan fishes (45), understanding the relationship between malformed bones and connected ligaments and the interaction between the heavily affected sinus perilymphaticus and apparently unaffected sinus endolymphaticus could have important implications for understanding the phenotypic outcomes in human pathologies involving similar bone-associated tissues.

These soft tissue phenotypes, in addition to those described above in the jaw musculature, are likely to be secondary effects of the malformed cartilage and bone of the skeleton that are the direct result of the *nkx3.2* knockout, as *nkx3.2* expression has not been described in these specific soft tissues. Axial ligaments are derived from the sclerotome (61, 62), where *nkx3.2* is a key regulator (63, 64), so we cannot rule out a direct effect of *nkx3.2* on axial fibrous tissues *via* disruption to the sclerotome. *nkx3.2* expression has also been described in association with the anterior notochord in juvenile zebrafish, although not with enough detail to distinguish precise tissues such as cartilage or ligaments (65).

Our histopathological findings in bone-associated soft tissues obtained by applying DICE-PPC-SRμCT demonstrates a great potential of this technique for the investigation of small fish skeletal disease models involving gene mutants and regulatory sequence mutants that often display subtle phenotypes (66), and also for skeleton-associated regeneration experiments and general developmental studies of, for example, mineralization progression. For some questions, particularly those involving adult fish and large soft tissues, conventional μCT combined with contrasting agents may be sufficient, as has been already shown for mouse (67) and in a limited number of zebrafish studies (e.g. 22, 68). However, 3D characterization of larval and juvenile tissues or those that require histological detail at least for now most probably will rely on the phase contrast capabilities and characteristic brightness of large synchrotron light sources, although as technologies advance these properties may become more accessible in lab-based facilities (27, 69, 70).

DICE-PPC-SRμCT scans generate a large volume of data (tens to hundreds of Gbs per specimen), and a large number of specimens can be scanned at a relatively high-throughput. Therefore, and in addition to the limited accessibility of synchrotron facilities to most researchers, key limiting factors can be the time, hardware, and software resources required to analyze the scans and generate relevant biological data by manual segmentation. However, in parallel to advances in imaging in recent years, various machine-learning image analysis techniques have been developed that can be applied to these large, complex datasets to obtain reproducible quantitative information in a significantly reduced timeframe (e.g. 53, 71–74).

In summary, we describe a novel protocol for the DICE-PPC-SRμCT of zebrafish larvae and juveniles, and use the *nkx3.2*$^{-/-}$ mutant line to demonstrate how the generated datasets can be used for the detailed histopathological and 3D analysis of phenotypes in skeletal-associated soft tissues. We encourage other small-fish researchers and the developmental biology community as a whole with access to conventional μCT or synchrotron light sources to explore the processes of development, growth, aging, and regeneration with the benefit of high-quality 3D histological data of soft tissues.

Data availability statement

The datasets presented in this study can be found in online repositories. The names of the repository/repositories and accession number(s) can be found below: doi.org/10.15151/ESRF-ES-642970891.

Ethics statement

The animal study was reviewed and approved by the local ethics committee for animal research in Uppsala, Sweden (permit number 5.8.18-18096/2019).

Author contributions

TH designed the study with contribution of SS and JL. Beamtime was granted through a successful application (LS3021) designed by SS with contribution from TH, JL, PT and KD. TH performed the staining. PT, KD, SS and JL performed the tomographic experiment. PT and KD reconstructed the data. JL segmented the data, and TH and JL analysed the data with contribution from SS. TH and JL wrote the manuscript, with contribution from SS, PT and KD. All authors contributed to the article and approved the submitted version.

Funding

TH was supported by *Vetenskapsrådet* (2022-04988), *Carl Tryggers Stiftelse*, and *Sven & Dagmar Salén Stiftelse*. SS was supported by *Vetenskaprådet* (2019-04595), *Inez Johanssons Stiftelse, Stiftelsen Lars Hiertas Minne*, and *Stiftelsen för Zoologisk Forskning*.

Acknowledgments

We thank Caroline Öhman-Mägi for µCT scanning, and Sifra Bijl for assisting with sample preparation for PPC-SRµCT scanning. Synchrotron beam time was obtained as part of proposal LS3021 (main applicant SS, co-applicants TH and JL) accepted at the European Synchrotron Radiation Facility – Extremely Brilliant Source (ESRF-EBS) in France on the beamline BM05.

Conflict of interest

The authors declare that the research was conducted in the absence of any commercial or financial relationships that could be construed as a potential conflict of interest.

Publisher's note

Supplementary material

The Supplementary Material for this article can be found online at: https://www.frontiersin.org/articles/10.3389/fendo.2023.1108916/full#supplementary-material

SUPPLEMENTARY VIDEO 1
Anterior to posterior transverse virtual thin sections through the wild-type 1mpf zebrafish obtained with DICE-PPC-SRµCT.

SUPPLEMENTARY VIDEO 2
Lateral sagittal virtual thin sections through the wild-type 1mpf zebrafish obtained with DICE-PPC-SRµCT.

SUPPLEMENTARY VIDEO 3
Dorsal-ventral longitudinal virtual thin sections through the wild-type 1mpf zebrafish obtained with DICE-PPC-SRµCT.

References

1. Zelzer E, Olsen BR. The genetic basis for skeletal diseases. *Nature* (2003) 423:343–8. doi: 10.1038/nature01659

2. Long F, Ornitz DM. Development of the endochondral skeleton. *Cold Spring Harb. Perspect Biol* (2013) 5:a008334–a008334. doi: 10.1101/cshperspect.a008334

3. Veilleux L-N, Trejo P, Rauch F. Muscle abnormalities in osteogenesis imperfecta. *J Musculoskelet Neuronal Interact* (2017) 17:1–7.

4. Veilleux L-N, Rauch F. Muscle-bone interactions in pediatric bone diseases. *Curr Osteoporos. Rep* (2017) 15:425–32. doi: 10.1007/s11914-017-0396-6

5. Kapp-Simon KA, Speltz ML, Cunningham ML, Patel PK, Tomita T. Neurodevelopment of children with single suture craniosynostosis: A review. *Childs Nerv. Syst* (2007) 23:269–81. doi: 10.1007/s00381-006-0251-z

6. Bonewald L. Use it or lose it to age: A review of bone and muscle communication. *Bone* (2019) 120:212–8. doi: 10.1016/j.bone.2018.11.002

7. Moutsopoulos HM, Zampeli E. Bone, cartilage, and soft tissue disorders. In: Moutsopoulos HM, Zampeli E, editors. *Immunology and rheumatology in questions*. Cham, Switzerland: Springer International Publishing, (2021) 175–87. doi: 10.1007/978-3-030-56670-8_12

8. Dietrich K, Fiedler IA, Kurzyukova A, López-Delgado AC, McGowan LM, Geurtzen K, et al. Skeletal biology and disease modeling in zebrafish. *J Bone Miner. Res* (2021) 36:436–58. doi: 10.1002/jbmr.4256

9. Marí-Beffa M, Mesa-Román AB, Duran I. Zebrafish models for human skeletal disorders. *Front Genet* (2021) 12:675331. doi: 10.3389/fgene.2021.675331

10. Howe K, Clark MD, Torroja CF, Torrance J, Berthelot C, Muffato M, et al. The zebrafish reference genome sequence and its relationship to the human genome. *Nature* (2013) 496:498–503. doi: 10.1038/nature12111

11. Howe DG, Bradford YM, Eagle A, Fashena D, Frazer K, Kalita P, et al. The zebrafish model organism database: new support for human disease models, mutation details, gene expression phenotypes and searching. *Nucleic Acids Res* (2017) 45:D758–68. doi: 10.1093/nar/gkw1116

12. Gonzales APW, Yeh J-RJ. . Cas9-based genome editing in zebrafish. In: Doudna JA, Sontheimer EJ, editors. *Methods Enzymology* 546:377–413. doi: 10.1016/B978-0-12-801185-0.00018-0

13. Sharma P, Sharma BS, Verma RJ. CRISPR-based genome editing of zebrafish, in: Singh, vijai (Ed.), progress in molecular biology and translational science. *Elsevier* (2021) pp:69–84. doi: 10.1016/bs.pmbts.2021.01.005

14. Mohideen M.-A.P.K., Beckwith LG, Tsao-Wu GS, Moore JL, Wong ACC, Chinoy MR, et al. Histology-based screen for zebrafish mutants with abnormal cell differentiation. *Dev Dyn.* (2003) 228:414–23. doi: 10.1002/dvdy.10407

15. Adissu HA, Estabel J, Sunter D, Tuck E, Hooks Y, Carragher DM, et al. Histopathology reveals correlative and unique phenotypes in a high throughput

mouse phenotyping screen. *Dis Model Mech* (2014). 7(5):515–24 doi: 10.1242/dmm.015263

16. Askary A, Smeeton J, Paul S, Schindler S, Braasch I, Ellis NA, et al. Ancient origin of lubricated joints in bony vertebrates. *eLife* (2016) 5:e16415. doi: 10.7554/eLife.16415

17. Copper JE, Budgeon LR, Foutz CA, van Rossum DB, Vanselow DJ, Hubley MJ, et al. Comparative analysis of fixation and embedding techniques for optimized histological preparation of zebrafish. *Comp Biochem Physiol Part C Toxicol Pharmacol* (2018) 208:38–46. doi: 10.1016/j.cbpc.2017.11.003

18. Misu A, Yamanaka H, Aramaki T, Kondo S, Skerrett IM, Iovine MK, et al. Two different functions of Connexin43 confer two different bone phenotypes in zebrafish. *J Biol Chem* (2016) 291:12601–11. doi: 10.1074/jbc.M116.720110

19. Charles JF, Sury M, Tsang K, Urso K, Henke K, Huang Y, et al. Utility of quantitative micro-computed tomographic analysis in zebrafish to define gene function during skeletogenesis. *Bone* (2017) 101:162–71. doi: 10.1016/j.bone.2017.05.001

20. Hur M, Gistelinck CA, Huber P, Lee J, Thompson MH, Monstad-Rios AT, et al. MicroCT-based phenomics in the zebrafish skeleton reveals virtues of deep phenotyping in a distributed organ system. *eLife* (2017) 6:e26014. doi: 10.7554/eLife.26014

21. Metscher BD. Micro CT for comparative morphology: Simple staining methods allow high-contrast 3D imaging of diverse non-mineralized animal tissues. *BMC Physiol* (2009) 9:11. doi: 10.1186/1472-6793-9-11

22. Babaei F, Hong TLC, Yeung K, Cheng SH, Lam YW. Contrast-enhanced X-ray micro-computed tomography as a versatile method for anatomical studies of adult zebrafish. *Zebrafish* (2016) 13:310–6. doi: 10.1089/zeb.2016.1245

23. Gignac PM, Kley NJ, Clarke JA, Colbert MW, Morhardt AC, Cerio D, et al. Diffusible iodine-based contrast-enhanced computed tomography (diceCT): An emerging tool for rapid, high-resolution, 3-d imaging of metazoan soft tissues. *J Anat.* (2016) 228:889–909. doi: 10.1111/joa.12449

24. Khonsari RH, Healy C, Ohazama A, Sharpe PT, Dutel H, Charles C, et al. Submicron imaging of soft-tissues using low-dose phase-contrast X-ray synchrotron microtomography with an iodine contrast agent. *Anat. Rec.* (2014) 297:1803–7. doi: 10.1002/ar.22997

25. Wilkins SW, Gureyev TE, Gao D, Pogany A, Stevenson AW. Phase-constrast imaging using polychromatic hard X-rays. *Nature* (1996) 384:335–8. doi: 10.1038/384335a0

26. Cloetens P, Pateyron-Salomé M, Buffière JY, Peix G, Baruchel J, Peyrin F, et al. Observation of microstructure and damage in materials by phase sensitive radiography and tomography. *J Appl Phys* (1997) 81:5878–86. doi: 10.1063/1.364374

27. Vågberg W, Larsson DH, Li M, Arner A, Hertz HM. X-Ray phase-contrast tomography for high-spatial-resolution zebrafish muscle imaging. *Sci Rep* (2015) 5:16625. doi: 10.1038/srep16625

28. Margaritondo G, Hwu Y. Imaging with coherent X-rays: From the early synchrotron tests to SYNAPSE. *J Imaging* (2021) 7:132. doi: 10.3390/jimaging7080132

29. Tafforeau P, Boistel R, Boller E, Bravin A, Brunet M, Chaimanee Y, et al. Applications of X-ray synchrotron microtomography for non-destructive 3D studies of paleontological specimens. *Appl Phys Mater Sci Process.* (2006) 83:195–202. doi: 10.1007/s00339-006-3507-2

30. Betz O, Wegst U, Weide D, Heethoff M, Helfen L, Lee W-K, et al. Imaging applications of synchrotron X-ray phase-contrast microtomography in biological morphology and biomaterials science. i. general aspects of the technique and its advantages in the analysis of millimetre-sized arthropod structure. *J Microsc.* (2007) 227:51–71. doi: 10.1111/j.1365-2818.2007.01785.x

31. Hellemans J, Simon M, Dheedene A, Alanay Y, Mihci E, Rifai L, et al. Homozygous inactivating mutations in the NKX3-2 gene result in spondylo-Megaepiphyseal-Metaphyseal dysplasia. *Am J Hum Genet* (2009) 85:916–22. doi: 10.1016/j.ajhg.2009.11.005

32. Simsek-Kiper PO, Kosukcu C, Akgun-Dogan O, Gocmen R, Utine GE, Soyer T, et al. A novel NKX3-2 mutation associated with perinatal lethal phenotype of spondylo-megaepiphyseal-metaphyseal dysplasia in a neonate. *Eur J Med Genet* (2019) 62:21–6. doi: 10.1016/j.ejmg.2018.04.013

33. Miyashita T, Baddam P, Smeeton J, Oel AP, Natarajan N, Gordon B, et al. nkx3.2 mutant zebrafish accommodate the jaw joint loss through a phenocopy of the head shapes of Paleozoic jawless fish. *J Exp Biol* (2020) 223:jeb216945. doi: 10.1242/jeb.216945

34. Waldmann L, Leyhr J, Zhang H, Öhman-Mägi C, Allalou A, Haitina T. The broad role of Nkx3.2 in the development of the zebrafish axial skeleton. *PloS One* (2021) 16:e0255953. doi: 10.1371/journal.pone.0255953

35. Cloetens P, Barrett R, Baruchel J, Guigay J-P, Schlenker M. Phase objects in synchrotron radiation hard x-ray imaging. *J Phys Appl Phys* (1996) 29:133–46. doi: 10.1088/0022-3727/29/1/023

36. Walsh CL, Tafforeau P, Wagner WL, Jafree DJ, Bellier A, Werlein C, et al. Imaging intact human organs with local resolution of cellular structures using hierarchical phase-contrast tomography. *Nat Methods* (2021) 18:1532–41. doi: 10.1038/s41592-021-01317-x

37. Mirone A, Brun E, Gouillart E, Tafforeau P, Kieffer J. The PyHST2 hybrid distributed code for high speed tomographic reconstruction with iterative reconstruction and *a priori* knowledge capabilities. *Nucl Instrum. Methods Phys Res Sect. B Beam Interact Mater At.* (2014) 324:41–8. doi: 10.1016/j.nimb.2013.09.030

38. Sanchez S, Ahlberg PE, Trinajstic KM, Mirone A, Tafforeau P. Three-dimensional synchrotron virtual paleohistology: A new insight into the world of fossil bone microstructures. *Microsc. Microanal.* (2012) 18:1095–105. doi: 10.1017/S1431927612001079

39. Paganin D, Mayo SC, Gureyev TE, Miller PR, Wilkins SW. Simultaneous phase and amplitude extraction from a single defocused image of a homogeneous object. *J Microsc.* (2002) 206:33–40. doi: 10.1046/j.1365-2818.2002.01010.x

40. Lyckegaard A, Johnson G, Tafforeau P. Correction of ring artifacts in X-ray tomographic images. *Int J Tomogr. Stat* (2011) 18:10.

41. Diogo R, Hinits Y, Hughes SM. Development of mandibular, hyoid and hypobranchial muscles in the zebrafish: Homologies and evolution of these muscles within bony fishes and tetrapods. *BMC Dev Biol* (2008) 8(24). doi: 10.1186/1471-213X-8-24

42. Tulenko FJ, Currie P. The zebrafish in biomedical research. *Elsevier* (2020) pp:115–21. doi: 10.1016/B978-0-12-812431-4.00012-9

43. Staab KL, Hernandez LP. Development of the cypriniform protrusible jaw complex in *Danio rerio*: Constructional insights for evolution. *J Morphol.* (2010) 271:814–25. doi: 10.1002/jmor.10836

44. Grande T, Young B. The ontogeny and homology of the weberian apparatus in the zebrafish danio rerio (Ostariophysi: Cypriniformes). *Zool J Linn Soc* (2004) 140:241–54. doi: 10.1111/j.1096-3642.2003.00097.x

45. Diogo R. Origin, evolution and homologies of the weberian apparatus: A new insight. *Int J Morphol* (2009) 27:333–54. doi: 10.4067/S0717-95022009000200008

46. Schulz-Mirbach T, Ladich F, Mittone A, Olbinado M, Bravin A, Maiditsch IP, et al. Auditory chain reaction: Effects of sound pressure and particle motion on auditory structures in fishes. *PloS One* (2020) 15:e0230578. doi: 10.1371/journal.pone.0230578

47. Bird NC, Mabee PM. Developmental morphology of the axial skeleton of the zebrafish, danio rerio (Ostariophysi: Cyprinidae). *Dev Dyn.* (2003) 228:337–57. doi: 10.1002/dvdy.10387

48. Bird NC, Richardson SS, Abels JR. Histological development and integration of the zebrafish weberian apparatus. *Dev Dyn.* (2020) 249:998–1017. doi: 10.1002/dvdy.172

49. Whitfield TT, Riley BB, Chiang M-Y, Phillips B. Development of the zebrafish inner ear. *Dev Dyn.* (2002) 223:427–58. doi: 10.1002/dvdy.10073

50. Abbas L, Whitfield TT. The zebrafish inner ear. In: Perry SF, Ekker M, Farrell AP, Brauner CJ, editors. *Zebrafish, fish physiology*. Adademic Press (2010). p. 123–71. doi: 10.1016/S1546-5098(10)02904-3

51. Evans HM. A contribution to the anatomy and physiology of the air-bladder and weberian ossicles in cyprinidae. *Proc R Soc Lond Ser B Contain. Pap. Biol Character* (1925) 97:545–76. doi: 10.1098/rspb.1925.0018

52. Bang PI, Sewell WF, Malicki JJ. Morphology and cell type heterogeneities of the inner ear epithelia in adult and juvenile zebrafish (Danio rerio). *J Comp Neurol* (2001) 438:173–90. doi: 10.1002/cne.1308

53. Weinhardt V, Shkarin R, Wernet T, Wittbrodt J, Baumbach T, Loosli F. Quantitative morphometric analysis of adult teleost fish by X-ray computed tomography. *Sci Rep* (2018) 8:16531. doi: 10.1038/s41598-018-34848-z

54. Ding Y, Vanselow DJ, Yakovlev MA, Katz SR, Lin AY, Clark DP, et al. Computational 3D histological phenotyping of whole zebrafish by X-ray histotomography. *eLife* (2019) 8:e44898. doi: 10.7554/eLife.44898

55. Buytaert J, Goyens J, De Greef D, Aerts P, Dirckx J. Volume shrinkage of bone, brain and muscle tissue in sample preparation for micro-CT and light sheet fluorescence microscopy (LSFM). *Microsc. Microanal.* (2014) 20:1208–17. doi: 10.1017/S1431927614001329

56. Li Z, Ketcham RA, Yan F, Maisano JA, Clarke JA. Comparison and evaluation of the effectiveness of two approaches of diffusible iodine-based contrast-enhanced computed tomography (diceCT) for avian cephalic material: diceCT FOR AVIAN CEPHALIC MATERIAL. *J Exp Zoolog. B Mol Dev Evol* (2016) 326:352–62. doi: 10.1002/jez.b.22692

57. Dawood Y, Hagoort J, Siadari BA, Ruijter JM, Gunst QD, Lobe NHJ, et al. Reducing soft-tissue shrinkage artefacts caused by staining with lugol's solution. *Sci Rep* (2021) 11:19781. doi: 10.1038/s41598-021-99202-2

58. Subramanian A, Kanzaki LF, Galloway JL, Schilling TF. Mechanical force regulates tendon extracellular matrix organization and tenocyte morphogenesis through TGFbeta signaling. *eLife* (2018) 7:e38069. doi: 10.7554/eLife.38069

59. Chen P, Chen Z, Mitchell C, Gao J, Chen L, Wang A, et al. Intramuscular injection of botox causes tendon atrophy by induction of senescence of tendon-derived stem cells. *Stem Cell Res Ther* (2021) 12:38. doi: 10.1186/s13287-020-02084-w

60. Hawkins MB, Henke K, Harris MP. Latent developmental potential to form limb-like skeletal structures in zebrafish. *Cell* (2021) 184:899–911.e13. doi: 10.1016/j.cell.2021.01.003

61. Williams S, Alkhatib B, Serra R. Development of the axial skeleton and intervertebral disc. In: Olsen BR, editor. *Current topics in developmental biology*, vol. pp . Elsevier (2019). p. 49–90. doi: 10.1016/bs.ctdb.2018.11.018

62. Bagnat M, Gray RS. Development of a straight vertebrate body axis. *Development* (2020) 147:dev175794. doi: 10.1242/dev.175794

63. Rodrigo I, Hill RE, Balling R, Münsterberg A, Imai K. Pax1 and Pax9 activate Bapx1 to induce chondrogenic differentation in the sclerotome. *Development* (2003) 130:473–82. doi: 10.1242/dev.00240

64. Ma RC, Jacobs CT, Sharma P, Kocha KM, Huang P. Stereotypic generation of axial tenocytes from bipartite sclerotome domains in zebrafish. *PloS Genet* (2018) 14: e1007775. doi: 10.1371/journal.pgen.1007775

65. Crotwell PL, Mabee PM. Gene expression patterns underlying proximal-distal skeletal segmentation in late-stage zebrafish, danio rerio. *Dev Dyn.* (2007) 236:3111–28. doi: 10.1002/dvdy.21352

66. Leyhr J, Waldmann L, Filipek-Górniok B, Zhang H, Allalou A, Haitina T. A novel cis-regulatory element drives early expression of Nkx3.2 in the gnathostome primary jaw joint. *eLife* (2022) 11:e75749. doi: 10.7554/eLife.75749

67. Handschuh S, Glösmann M. Mouse embryo phenotyping using X-ray microCT. *Front Cell Dev Biol* (2022) 10:949184. doi: 10.3389/fcell.2022.949184

68. Dimitriadi A, Beis D, Arvanitidis C, Adriaens D, Koumoundouros G. Developmental temperature has persistent, sexually dimorphic effects on zebrafish cardiac anatomy. *Sci Rep* (2018) 8:8125. doi: 10.1038/s41598-018-25991-8

69. Hornberger B, Kasahara J, Gifford M, Ruth R, Loewen R. A compact light source providing high-flux, quasi-monochromatic, tunable X-rays in the laboratory. In: Murokh A, Spiga D, editors. *Advances in laboratory-based X-ray sources, optics, and applications VII. presented at the advances in laboratory-based X-ray sources, optics, and applications VII*, vol. p . San Diego, United States: SPIE (2019). p. 2. doi: 10.1117/12.2527356

70. Huang J, Günther B, Achterhold K, Cui Y, Gleich B, Dierolf M, et al. Energy-dispersive X-ray absorption spectroscopy with an inverse Compton source. *Sci Rep* (2020) 10:8772. doi: 10.1038/s41598-020-65225-4

71. Lösel PD, van de Kamp T, Jayme A, Ershov A, Faragó T, Pichler O, et al. Introducing biomedisa as an open-source online platform for biomedical image segmentation. *Nat Commun* (2020) 11:5577. doi: 10.1038/s41467-020-19303-w

72. Arzt M, Deschamps J, Schmied C, Pietzsch T, Schmidt D, Tomancak P, et al. LABKIT: Labeling and segmentation toolkit for big image data. *Front Comput Sci* (2022) 4:777728. doi: 10.3389/fcomp.2022.777728

73. Lösel PD, Monchanin C, Lebrun R, Jayme A, Relle J, Devaud J-M, et al. Natural variability in bee brain size and symmetry revealed by micro-CT imaging and deep learning. *bioRxiv* (2022). doi: 10.1101/2022.10.12.511944

74. Wang A, Zhang Q, Han Y, Megason S, Hormoz S, Mosaliganti KR, et al. A novel deep learning-based 3D cell segmentation framework for future image-based disease detection. *Sci Rep* (2022) 12:342. doi: 10.1038/s41598-021-04048-3

frontiers | Frontiers in Endocrinology

TYPE Original Research
PUBLISHED 08 May 2023
DOI 10.3389/fendo.2023.1107339

OPEN ACCESS

EDITED BY
Erika Kague,
University of Bristol, United Kingdom

REVIEWED BY
Ignacio Fernández,
Spanish Institute of Oceanography (IEO), Spain
Pierre Le Pabic,
University of North Carolina Wilmington, United States
Paul Eckhard Witten,
Ghent University, Belgium

*CORRESPONDENCE
Hans-Martin Pogoda
pogodah@uni-koeln.de

RECEIVED 24 November 2022
ACCEPTED 15 March 2023
PUBLISHED 08 May 2023

CITATION
Pogoda HM, Riedl-Quinkertz I and Hammerschmidt M (2023) Direct BMP signaling to chordoblasts is required for the initiation of segmented notochord sheath mineralization in zebrafish vertebral column development.
Front. Endocrinol. 14:1107339.
doi: 10.3389/fendo.2023.1107339

Direct BMP signaling to chordoblasts is required for the initiation of segmented notochord sheath mineralization in zebrafish vertebral column development

Hans-Martin Pogoda[1]*, Iris Riedl-Quinkertz[1] and Matthias Hammerschmidt[1,2,3]

[1]Institute of Zoology – Developmental Biology, University of Cologne, Cologne, Germany, [2]Cluster of Excellence, Cellular Stress Responses in Aging-Associated Diseases (CECAD) Cluster of Excellence, University of Cologne, Cologne, Germany, [3]Center for Molecular Medicine Cologne (CMMC), University of Cologne, Cologne, Germany

The vertebral column, with the centra as its iteratively arranged building blocks, represents the anatomical key feature of the vertebrate phylum. In contrast to amniotes, where vertebrae are formed from chondrocytes and osteoblasts deriving from the segmentally organized neural crest or paraxial sclerotome, teleost vertebral column development is initiated by chordoblasts of the primarily unsegmented axial notochord, while sclerotomal cells only contribute to later steps of vertebrae formation. Yet, for both mammalian and teleostean model systems, unrestricted signaling by Bone Morphogenetic Proteins (BMPs) or retinoic acid (RA) has been reported to cause fusions of vertebral elements, while the interplay of the two signaling processes and their exact cellular targets remain largely unknown. Here, we address this interplay in zebrafish, identifying BMPs as potent and indispensable factors that, as formerly shown for RA, directly signal to notochord epithelial cells/chordoblasts to promote *entpd5a* expression and thereby metameric notochord sheath mineralization. In contrast to RA, however, which promotes sheath mineralization at the expense of further collagen secretion and sheath formation, BMP defines an earlier transitory stage of chordoblasts, characterized by sustained matrix production/*col2a1* expression and concomitant matrix mineralization/*entpd5a* expression. BMP-RA epistasis analyses further indicate that RA can only affect chordoblasts and their further progression to merely mineralizing cells after they have received BMP signals to enter the transitory *col2a1*/*entpd5a* double-positive stage. This way, both signals ensure consecutively for proper mineralization of the notochord sheath within segmented sections along its anteroposterior axis. Our work sheds further light onto the molecular mechanisms that orchestrate early steps of vertebral column segmentation in teleosts. Similarities and

differences to BMP's working mechanisms during mammalian vertebral column formation and the pathomechanisms underlying human bone diseases such as Fibrodysplasia Ossificans Progressiva (FOP) caused by constitutively active BMP signaling are discussed.

KEYWORDS

notochord, chordoblast, BMP, retinoic acid, vertebral body, centra, zebrafish, vertebral column

Introduction

Initially discovered as components of decalcified bone that are capable of inducing ectopic bio-mineralization upon *in vivo* administration into skeletal muscle (1, 2), Bone Morphogenetic Proteins (BMPs) are known to play multiple and diverse crucial roles in different steps of bone formation and homeostasis (3, 4). In the context of vertebral fusions in mice and humans, different effects of BMP signaling have been reported: Recessively inherited loss-of-function mutations in BMP13, also named GDF6 (5), or its close relative GDF3 (6) cause Klippel-Feil-Syndrome (KFS), characterized by abnormal fusion of any two of the first seven cervical vertebrae in the neck, but usually restricted to vertebrae C1 – C3, all of which result from aberrant segmentation along the embryo's developing axis during the first 3 to 8 weeks of gestation (7). In contrast, dominantly inherited gain-of-function mutations in the BMP receptor ACVR1/ALK2, which render the receptor constitutively active even in the absence of BMPs (8) and that are further activatable by Activin, a member of the other TGFβ superfamily subgroup (9), cause Fibrodysplasia Ossificans Progressiva (FOP) (9–11). FOP is characterized by multiple orthotopic (skeletal) and heterotopic ossifications, including orthotopic fusions at the level of lateral masses and spinous processes of cervical vertebrae, but, in contrast to KFS, not at the level of vertebral bodies themselves. Furthermore, in contrast to the rather early onset of cervical KFS defects, such orthotopic fusions in FOP are only constituted shortly after birth, but progress as the patients age (12).

Multiple and central roles during skeletogenesis have also been assigned to retinoic acid (RA), a derivative of vitamin A (13–15), which cooperates with BMPs to accelerate different processes of cartilage and bone formation and bone turnover *in vivo* (14, 16). To our knowledge, no mutations in genes encoding components or regulators of RA signaling have been assigned to human congenital vertebral malformations as yet, including wedge or hemivertebra as well as vertebral segmentation defects of any kind, most likely due to early lethality caused by such mutations in affected individuals (17). However, in mouse, gain of endogenous RA signaling caused by pharmacological inhibition of the RA-metabolizing enzyme Cyp26 has been shown to cause – among other defects (18) - similar FOP-like fusions of cervical vertebrae (19) as obtained upon gain-of-function of endogenous BMP signaling caused by loss-of-function mutations in the secreted BMP inhibitor Noggin (12, 20), pointing to a possible concerted action of RA and BMP signaling in promoting vertebral fusions. However, negative interplays between BMP and RA signaling have been described as well, including an inhibitory effect of RA- on BMP- signaling in the context of FOP (10) (see also Discussion).

Here, we study the cooperation of BMP and RA signaling during early development of vertebral centra anlagen in the zebrafish. Although initial steps of vertebra formation in teleosts are not driven by scleroblasts from the segmentally organized paraxial mesoderm *via* endochondral ossification as in amniotes, but instead by cells of a primarily unsegmented structure, the notochord (21–25), *via* the mineralization of a non-cartilaginous, type II collagen-rich extracellular matrix (ECM), gain of both RA or BMP signaling at early larval stages lead to an aberrant fusion of developing vertebral centra anlagen in zebrafish (19), somehow comparable to their aforementioned effects in mouse (12, 19, 20).

During larval stages, the notochord of teleosts consists of centrally positioned chordocytes and an outer epithelial layer of chordoblasts. Chordocytes are localized in inner regions of the notochord and are comparatively large cells with characteristic liquid-filled vacuoles. They align as horizontal stacks to provide the hydrostatic core part of the axial strut. The pile of such voluminous chordocytes gets encircled by a layer of rather flat, tightly linked chordoblasts. Thereby, the latter constitute the outer, epithelial border of the cellular notochord (26). Noteworthy, both notochordal cell-types are ontogenetically related, since chordoblasts segregate from early vacuolated notochord cells at the end of segmentation stages (24, 27). Aside from simply configuring the notochord epithelium, chordoblasts exhibit remarkable osteogenic properties during early vertebral column development in teleosts: like bona fide osteoblasts they unidirectionally secrete a collagenous matrix until it evenly envelopes the entire notochord, thereby constituting the so-called notochord sheath. The core part of the sheath consists of a collagen type II-based ECM. According to our own histological analyses (24, 27) the corresponding layers of collagen fibers encircle the notochord of early zebrafish larvae in an orientation perpendicular to the rostro-caudal axis of the organ. This central collagenous layer of the sheath (*elastica media*) itself is enveloped by a thin (inner) and thicker (outer) elastin-based basal lamina, the *elastica interna* and *elastica externa*, respectively. The chemical composition of the notochord sheath thus is very similar to that of cartilage matrix and designed to withstand the hydrostatic pressure

generated by the vacuolated chordocytes (28). Importantly, the notochord sheath can also serve as a substrate for mineralization (which accordingly can be compared with cartilage mineralization during chondral ossification), with iterative sections of it calcifying to form the chordacentra, repetitive mineralized ring-shaped fractions of the *elastica media* that serve as the precursor elements of the eventual vertebrae. Later, outer autocentra and vertebral arches are added to these chordacenta, mainly driven by sclerotomal cells derived from the paraxial somites (26, 28–30).

Of note, genetic ablation of zebrafish chordoblasts at a time point when a proper notochord sheath has already been formed, abrogates subsequent chordacentra mineralization (24). This demonstrates that chordoblasts do not solely produce notochord-derived ECM but later also actively fuel its mineralization. For this goal, segmentally arranged, ring-shaped clusters of chordoblasts start to express Ectonucleoside Triphosphate Diphosphohydrolase 5a (Entpd5a), an enzyme that is indispensable for ossification (31) and that provides inorganic mono-phosphate for matrix mineralization (23–25). Once metameric notochord sheath calcification has been initiated and dedicated chordacentra start to grow in length and thickness, the underlying chordoblasts progressively attenuate expression of collagens, while matrix proteins remain to be produced and secreted in intervertebral regions (24, 25). In this context, Wopat and colleagues were able to distinguish three subpopulations of chordoblasts: merely *collagen* genes-expressing, transitory *collagen*- and *entpd5a*-coexpressing, and *entpd5a*-positive, but *collagen*-negative cells (25). These findings point to an at least two-step developmental progression of chordoblasts from matrix-producing to matrix-mineralizing cells. A progression from matrix-producing to matrix-mineralizing properties has also been described for the transitioning of osteoblasts to pre-osteocytes (32, 33). During calvarial plate formation *via* intramembranous ossification in zebrafish, this transition has been shown to be driven by RA signaling (34), and a corresponding effect of direct RA signaling to chordoblasts has been shown to drive their transformation to mineralizing skeletogenenic cells during zebrafish backbone development (24). However, it remained unclear where exactly in this two-step process RA acts and how it interacts with BMP, for which a similar mineralization-promoting effect during zebrafish vertebral column formation had been formerly reported (19).

Performing detailed comparative analyses of zebrafish vertebral column defects caused by gain- or loss of BMP- or RA-signaling, we demonstrate that direct BMP signaling to chordoblasts promotes their transition from purely matrix-generating cells to the transitory cell type that simultaneously generates and mineralizes ECM. In contrast, RA promotes the progression of this transitory cell type to purely ECM-mineralizing cells. Epistasis analyses combining loss of BMP signaling with gain of RA signaling further indicate that RA can only do so after chordoblasts have entered the BMP-induced transitory stage. However, this consecutive action does not involve a stimulation of RA activity by BMP signaling.

In light of these findings, we discuss that, rather than RA (19, 22, 24, 35), it might be BMP signaling that qualifies as the initial pattern generator regulating the segmentation of the notochord sheath and thus the formation of iterative vertebral body anlagen from the foremost unsegmented chordoblast epithelium and notochord sheath. Similarities and differences between the roles of BMPs during vertebral column formation and segmentation in zebrafish versus mammals are discussed.

Materials and methods

Zebrafish lines

The following zebrafish lines were used: *Tg(R2-col2a1a:EGFP)*^{nu13Tg} to visualize *col2a1* expressing chordoblasts (27), *Tg(cyp26b1:YFP)*^{hu7426} to visualize RA-responsive chordoblasts (24), *Tg(col2a1a:CFP-NTR)*^{fr42Tg} to ablate *col2a1a* expressing chordoblasts (24), *Tg(hsp70:bmp2b)*^{fr13Tg} (36) and *Tg(hsp70:noggin3)*^{fr14Tg} (36) to globally induce *bmp2b* expression or to globally inhibit all endogenous BMP signaling upon heat-shocking (temporal control), respectively. The line *Tg(entpd5a:EGFP)*^{fr53Tg} was generated in the course of this study (details see below) with the goal to label chordoblasts that exhibit mineralizing activity. Larvae were taken for *in vivo* imaging or fixed for subsequent histology at the ages of 5, 6, 7 or 8 days post fertilization (dpf) with notochord lengths ranging from 3.2 to 3.6 mm, respectively. Ages of the specimens are specified in the figures. All zebrafish experiments were approved by the local and federal animal care committees in Cologne (LANUV Nordrhein-Westfalen: 84-02.04.2012.A251, 84-02.04.2012.A390, 81-02.04.40.2022.VG005, 81-02.04.2018.A282, 81-02.04.2022.A104; City of Cologne: 8.87-50.10.31.08.129).

RA, BMS493, Metronidazole and heat-shock treatments

A 10 mM stock solution of *all-trans* RA (Sigma; R2625) in DMSO as well as a corresponding working dilution was prepared as described (37). In order to globally activate RA signaling, wild-type or transgenic zebrafish larvae were incubated with final concentrations of 1 µM RA from 4 dpf until phenotypic evaluation or RNA extraction at 7 dpf or 8 dpf. For the reverse approach (global blockage of RA signaling) the pan-RAR antagonist BMS493 (Sigma; B6688) (38) using a 10 mM stock solution in DMSO was prepared. Transgenic larvae were incubated with a final concentration of 7 µM BMS493 from 4-6 dpf. As controls, siblings were treated with equivalent concentrations of ethanol (1 °/$_{oo}$)/ DMSO (0.1 °/$_{oo}$) (RA) or DMSO (0.7 °/$_{oo}$) alone (BMS493).

To show that chordoblasts are essential for BMP regulated notochord sheath mineralization it requires (a) the absence of the chordoblast layer while (b) simultaneously having a rather complete notochord sheath secreted in (c) otherwise intact larvae (d) at proper developmental stages. These conditions cannot be provided by any mutant or morphant background known to date. Thus, the approach of temporally-controlled chordoblast ablation was inevitable to answer that question. Treating Tg(*R2-col2a1a:cfp-nfsb*) larvae with Metronidazole (Mtz) as described below does not result in notable developmental retardation and affected tissues outside the notochord [e.g. paraxial mesoderm; see Figure S1 and

(24)]. For genetic cell ablation *via* the Nitroreductase-Metronidazole (Mtz) system, Mtz (Sigma-Aldrich; M3761) (39) was freshly dissolved in E2 embryo medium (15 mM NaCl, 0.5 mM KCl, 0.1 mM $MgSO_4$, 150 µM KH_2PO_4, 50 µM Na_2HPO_4) and replaced every day of treatment. For chordoblast ablation larvae were treated with 7 mM Mtz from 4-5 dpf and with 5 mM Mtz for the following 1.5 days. All treatments were performed in the dark in a 28°C incubator. For heat-shock experiments to globally induce the expression of the corresponding effector-transgenes Tg(*hsp70:bmp2b*) and Tg(*hsp70:noggin3*), the embryo medium was rapidly replaced by 40°C prewarmed medium. Subsequently, the larvae were left for 45 min in a 40°C incubator and then transferred back to 28°C for slow cool-down to standard conditions. In case of co-treatments with drugs, the reagents were left out of the embryo medium while heat-shocking.

Plasmid construction, injections and transgenesis

The *Tg(entpd5a:egfp)*^{fr53Tg} transgene was generated following standard procedures (40) using the BAC CH211-202H12 construct that had previously been reported to serve as a read-out for *entpd5a* expression (31). Plasmids for chordoblast-specific (de)activation of BMP signaling *(R2-col2a1a:dn-bmpr1b-p2a-dTomatoCAAX* and *R2-col2a1a:ca-bmpr1b-p2a-dTomatoCAAX)* were cloned using Multistep Gateway Recombineering system (Invitrogen) and the Tol2kit (41, 42). For the construction of dedicated middle-entry clones, the p2a-dTomatoCAAX sequence (Addgene) was first PCR amplified and hereby equipped with an *Xba*I site 5'-wards and a *Not*I-site at the 3'-side. Thereafter, the obtained fragment was cloned into pME-MCS (42) using *Xba*I and *Not*I restriction sites. The resulting intermediate-construct was digested with *Eco*RI/*Xba*I to be used as receiving vector in a ligation with *dn-bmpr1b* ORF from *Xenopus* as insert that was obtained *via Eco*RI/*Xba*I digest from a *hsp70:dn-bmpr1b-egfp* construct (43).

In preparation for the other middle-entry clone, the ORF of mouse *ca-bmpr1b*, which has been formerly shown to function properly also in zebrafish, was PCR-amplified from the *HSE:cBmpr1b, EGFP* construct (44), adding a *Spe*I site at its 5' and a *Xba*I site at its 3' end. Subsequently, the fragment was cloned in frame *via* these cut sites into the aforementioned and accordingly prepared pME-MCS-p2a-dTomatoCAAX vector.

The final *R2-col2a1a:ca-/dn-bmpr1b-p2a-dTomatoCAAX* constructs were generated *via* LR recombination of either of the two constructed middle-entry vectors together with p3E-polyA, pDestTol2CG and p5E-*R2-col2a1a* (24). All primers used for cloning procedures are listed below. Mosaic G0 larvae (Figures 3P–R) and the stable *entpd5a:egfp* transgenic line (Figures 1, 3, 4) were generated by standard injection and visual screening (fluorescence microscopy) procedures. Injection solutions contained nucleic acids (plasmid DNA, BAC DNA, Tol2mRNA respectively) at a concentration of 50 ng/µl each in 5% Phenol red (Sigma; P0290) and 1x Danieau buffer (17.4 mM NaCl, 0.21 mM KCl, 0.12 mM MgSO4, 0.18 mM $Ca(NO3)_2$, 1.5 mM HEPES, pH 7.6). Tg(*entpd5a:egfp*)-positive carriers were subsequently crossed to homozygous Tg(*hsp70:bmp2b*) and Tg(*hsp70:noggin3*) fish to generate the respective double-transgenic fish with which the experiments were conducted.

Tissue cryo-sectioning and immunofluorescence stainings

For cryo-sectioning samples fixed in 4% PFA (Sigma; P6148) and stored in 100% MeOH at -20°C were progressively rehydrated to PBST (PBS/0.1% Tween-20), embedded in a solution of PBS containing 1.5% low-melting agarose and 15% sucrose, and incubated overnight at 4°C in 30% sucrose in PBS. Tissue blocks covered in cryomatrix (VWR, Radnor, PA) were snap frozen in 2-methylbutane (Isopentane; Carl Roth, Karlsruhe, D) at -80°C. Sagittal as well as cross sections of 14 µm thickness were prepared from the specimen's anterior half of the abdominal domain using a Leica CM 1850 cryostat, collected on coated glass slides (Ultra Plus; VWR, Radnor, PA) and stored at –20°C until further processing. At least one hour prior to usage, frozen cryostat sections were thawed at room temperature. For subsequent immunofluorescence studies, sections were equilibrated by three washes of five minutes each in PBTX (PBS, 0.3% Triton-X) followed by at least two hours blocking in block solution (10% fetal calf serum, 1% DMSO in PBTX) at room temperature. Stainings were performed with the primary antibodies chicken anti-GFP (ThermoFisher Scientific, A-10262) and rabbit anti-phosphoSMad1/5/8 (Cell Signaling/NewEnglandBiolabs, #9511, http://zfin.org/ZDB-ATB-081015-1#summary), and the secondary antibodies goat-anti-chicken AlexaFluor-488 (ThermoFisher Scientific, A-11039) and goat-anti-rabbit AlexaFluor-555 (ThermoFisher Scientific, A-21428). Primary antibodies were diluted 1:500, secondary antibodies 1:1000 in block solution. Incubations with antibodies were carried out at 4°C over night, followed by six washes in PBTX for 15 minutes each. Control stains were performed on consecutive sections while omitting the incubation with the corresponding primary antibody. Prior to imaging, stained sections were mounted with Mowiol/Dapi mixture and left in the dark to dry at room temperature for 24 hours.

Imaging

Conventional fluorescent light microscopy was performed using a Zeiss AxioImager.M2 in combination with Axiovision 4.0 software. Confocal z-stacks were recorded using a Zeiss LSM 710 microscope. Fluorescent signals were excited by appropriate wavelengths of a 1-photon laser and detected sequentially in separate channels. For *in vivo* confocal imaging, whole larvae were anesthetized with 0.015% Tricaine and mounted in 1.5% low melting agarose/0.015% Tricaine in embryo medium. For subsequent image processing, ZEN *black* (Zeiss) and Photoshop CS4 (Adobe) software was used.

TEM analysis and alizarin red *in vivo* stains

For transmission electron microscopy (TEM) to assay notochord sheath diameter and integrity, 8 dpf zebrafish larvae

10.3389/fendo.2023.1107339

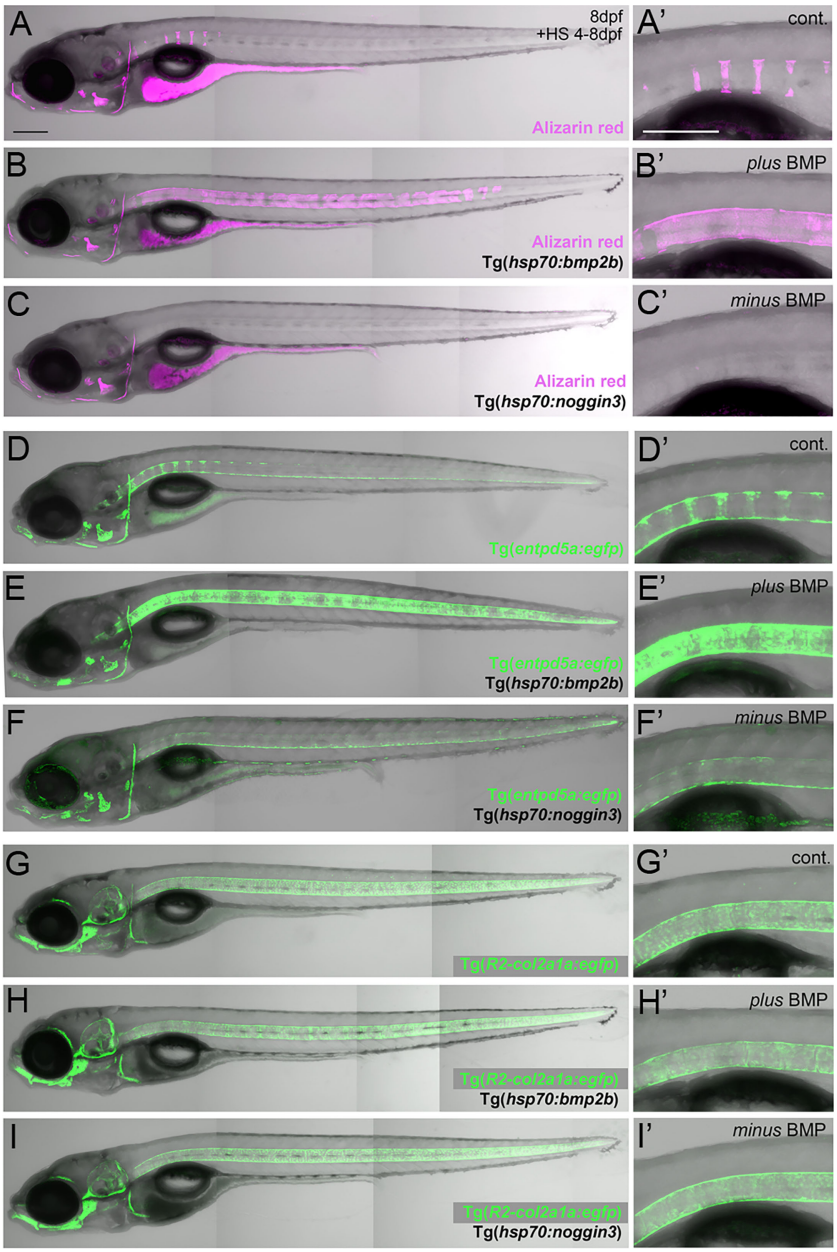

FIGURE 1
BMP regulates mineralization and *entpd5a* expression along the notochord. **(A–I)** Lateral views of zebrafish larvae shown in merged transmitted and fluorescent light channels with tissue staining and genotypes as indicated at an age of 8dpf. Alizarin red labels mineralized extracellular matrix (ECM) in magenta **(A–C)**. *entpd5a*-expressing cells are visualized by Tg(*entpd5a:egfp*) in green **(D–F)**, *col2a1*-expressing chondroblasts and chordoblasts by Tg(*R2-col2a1a:egfp*) in green **(G–I)**. Magnified views of the region right dorsal to the swim bladder from corresponding larvae are shown in **A'** o **I'**. All larvae have been heat-shocked once a day for 45 minutes at 40°C from 4-8 dpf. Note the ventral line of chordoblasts along the entire length of the notochord that remained EGFP positive after *noggin3* overexpression **(F, F')**, pointing to BMP-independent regulation in this particular notochordal subdomain. Scale bars: 200 µm.

with a notochord length of 3.5 mm were fixed in 2.5% glutaraldehyde and 2% PFA in 1x PBS firstly for 30 minutes at room temperature and then at 4°C overnight. Decalcification was not performed, since overall mineralization is little advanced at this early stage. Fixed specimens were then washed several times in 1x PBS and two times in 10% PBS, post-fixed with 1% osmium tetraoxide in 10% PBS for 1 hour at 4°C, washed three times in 10% PBS and incubated in 1% uranylacetate for 30 minutes at 4°C, dehydrated in a graded series of ethanol, and embedded in araldite (Hundsman Advanced Materials, Derry, NH). Ultrathin (70 nm) and consecutive semithin (750nm) cross-sections of the specimen's abdominal region were cut using the ultramicrotome Leica EM UC7. Ultrathin sections were mounted on pioloform-covered copper grids and post stained with aqueous uranyl acetate (2%, 10 minutes) and Reynolds' lead citrate (3.5 minutes). The samples were examined with the transmission electron microscope CM 10 (FEI Europe Main Office, Eindhoven, The Netherlands). Micrographs were taken with the ORIUS SC200W TEM CCD

camera using the software DigitalMicrograph that was also used for primary micrograph internal measurements (Gatan Inc., Pleasanton, CA). Semithin consecutive sections were collected on regular microscope slides (VWR) and stained with a filtered aqueous solution of 0.5% Azur II, 0.5% Methylene blue and 0.5% Borax for 30 seconds on a 70°C pre-warmed heating plate. After thoroughly rinsing the stained sections with distilled water, they were dried on a heating plate bevor mounting in Moviol and adding a cover slip.

Alizarin red stains on living larvae were performed as described (24). For ages and corresponding notochord lengths of stained larvae please see Materials and methods' paragraph "Zebrafish lines". Except for Figure 1 showing total larvae, the phenotypic evaluation of notochord sheath mineralization *via* Alizarin red stains was conducted at the prospective Weberian and abdominal domains.

qPCR

Per condition (Figure 2A), total RNA was isolated from trunks and tails of 3x30 larvae (N=3) of an age of 8 dpf that had been decapitated posterior of the inner ear, using Trizol Reagent (Thermo Fisher Scientific) with the PureLink RNA Mini Kit (Thermo Fisher Scientific), including on-column DNaseI. Quality and amount of the extracted RNA was determined *via* a Quantus™ fluorometer (Promega) by assaying 260/280nm and 260/230nm ratios. Gene expression was assayed using the Luna RT-qPCR Kit (New England Biolabs, E3006L) in combination with TaqMan assays (*col2a1a* (NCBI accession number XM_005166863.4: premade assay Dr03099270_m1; *entpd5a* (NCBI accession number XM_679770.8: custom made assay, forward primer AGCCCGGACTGTCAGCATAT, reverse primer TCAACAGCTGCACAATGGATTC, probe primer TATGCCTGAAAAGGGTGG on an ABI-PRISM 7500 Fast Detection system. As endogenous internal controls the housekeeping genes *ef1a* (assay ID Dr03432748_m1; NCBI accession number AM422110.2), *rps23* (assay ID Dr03430371_m1; NCBI accession number NM_001110121) and *ppiaa* (assay ID Dr03152038_m1; NCBI accession number NM_212758) have first been evaluated for their suitability in the context of applied conditions (controls, +RA, +BMP2b, +Noggin3) *via* the Excel-based tool *BestKeeper* (https://www.gene-quantification.de/bestkeeper.html; (45)): SDs of C_T values were 0.12 (*ef1a*), 0.19 (*rps23*) and 0.29 (*ppiaa*), SDs in regards to resulting fold change of expression level were 1.09 (*ef1a*), 1.14 (*rps23*) and 1.22 (*ppiaa*). Thus, all three chosen reference genes are within the range of stable expression and do not show critical changes in their activities for analyzed conditions. This was further confirmed *via* a gene stability test applying the *Genorm* algorithm (http://blooge.cn/RefFinder/?type=reference), which revealed same stability for *ef1a* and *rps23* (both 0.416), while the value for *ppiaa* was moderately inferior (0.435), with values closer to 0 representing higher stability. Based on this and the lower variances in C_T values we decided to use *ef1a* as internal reference gene for normalization.

For the final qPCR experiments, each condition was assayed in biological triplicates (N=3) and with technical triplicates (n=3) per biological sample. PCR conditions were set up according to the instructions given by the Luna RT-qPCR Kit that includes the cDNA synthesis step: reverse transcription for 10 minutes at 55°C, initial denaturation for 1 minute at 95°C, 42 cycles with 1 minute denaturation at 95°C and extension for 30 seconds at 60°C. Relative differences were calculated using the $\Delta\Delta C_T$ method *via* the 7500 Software version 2.3 (ABI). Subsequent statistical analysis of biological samples and experimental groups was conducted with Prism8.4.2 software (GraphPad Software).

Statistics

Statistical analyses were performed using Prism8.4.2 software (GraphPad Software). Data points of qPCR samples (Figure 2A) passed the D'Agostino and Pearson omnibus normality test and thus are not inconsistent with a normal distribution. Since subsequent F tests revealed significantly different variances among samples, Student t-test with Welch's correction was used for comparisons between each experimental group and its corresponding control group (*,**,***,****: statistically significant with $p < 0.05$, $p<0.01$, $p<0.001$, $p<0.0001$, respectively). Furthermore, statistical significance among the three experimental groups (+RA, +BMP2b, +Noggin3) per analyzed marker gene was determined by parametric Brown-Forsythe and Welch ANOVA tests with *post-hoc* Dunnett's T3 multiple comparison test (significance threshold of $p < 0.05$).

Notochord sheath thickness (Figure 2B) was measured using Fiji software. The mean values of five measured data points per biological sample were used for final statistical analysis, with N=3 biological samples per condition. Here, no inconsistence with a normal distribution was determined by the Shapiro-Wilk test. Testing for significance between shown groups was performed *via* Student t-tests with Welch's correction (significance threshold of $p < 0.05$).

Primers

entpd5a-egfp-F
ACCACCAGTCAAGCCTTCAGCTGTTTGCAGTGTCGGCGTG
GGAGAAAGAAACC**atggtgagcaagggcgaggag**

entpd5a-Kan-R
CCGGCAAAAAGCCACATGGACACCAACGTCAAGTGCAA
CATCTGCTGAGA**ggactagtctattccagaagtagtgaggag**

XbaI-P2A-F
TTAGTCTAGAGGCTCCGGAGCCACGAACTT

NotI-caax-R
TTAGGCGGCCGCTCAGGAGAGCACACACTTGC

SpeI-mAlk6CA-F
TTAGACTAGTCCACCATGCTCTTACGAAGCTCTGG

XbaI-mAlk6CA-R
TTAGTCTAGAGAGGCTAGCATAATCAGGAA

10.3389/fendo.2023.1107339

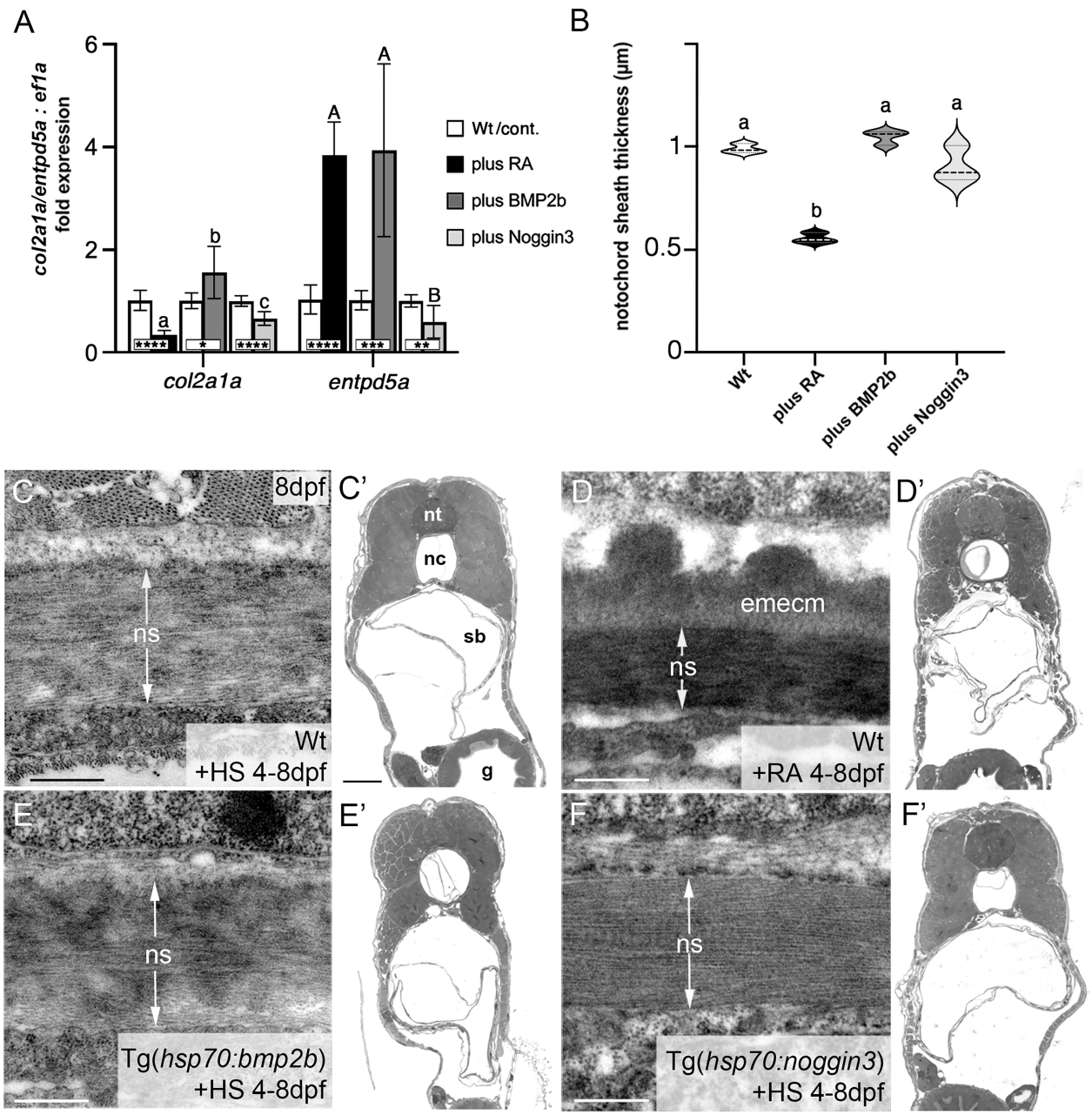

FIGURE 2
BMP has no major impact on *col2a1* expression and notochord sheath formation. **(A)** qPCR results for the matrix-generating gene *col2a1a* and the matrix-mineralizing gene *entpd5a* after RA exposure, BMP2b or Noggin3 overexpression, respectively. See main text for exact experimental conditions. Each shaded column indicates the ratio of expression levels between an experimental group and its specific control group set to a value of 1 (white columns), with the respective statistical significances determined *via* Student's t-test with Welch's correction and indicated as * (significant with $p<0.05$), ** (significant with $p<0.01$), *** (significant with $p<0.001$) and **** (significant with $p<0.0001$). In addition, the letter subscript system (small letters for *col2a1a*; capital letters for *entpd5a*) is used to indicate significances of differences between the different experimental groups, with groups with the same letters being not significantly different according to Brown-Forsythe and Welch ANOVA tests ($p < 0.0001$) with *post-hoc* Dunnett's T3 multiple comparison test ($p < 0.05$). **(B)** Quantitative analysis of notochord sheath thickness, based on measurements performed on TEM specimens as in **(C–F)**. Listed conditions have been obtained *via* drug treatment (RA) or by the aforementioned heat-shock inducible transgenes; violin plots of N=3 biological samples per condition from independent spawnings/treatments, with each N representing the mean value from 5 different sections per specimen; broken and dotted lines indicate mean and quartiles, respectively; experimental groups labeled with identical superscript letters are not significantly different according to Student's t-test with Welch's correction, $p < 0.05$. **(C–F)** TEM micrographs of cross-sections through the abdominal notochord sheath from larvae with genotypes and treatments as indicated; differences in the darkness of the notochord sheath are due to differences in its mineralization levels in the different conditions. **(C'–F')** show overviews of the corresponding semithin-sections indicating that the TEM images were taken at corresponding positions along the antero-posterior axis of the specimens. Scale bars: 0.5 µm **(C–F)**, 50 µm **(C')**; g, gut; nc, notochord; ns, notochordal sheath; nt, neural tube; emecm, external mineralized extracellular matrix; sb, swim bladder.

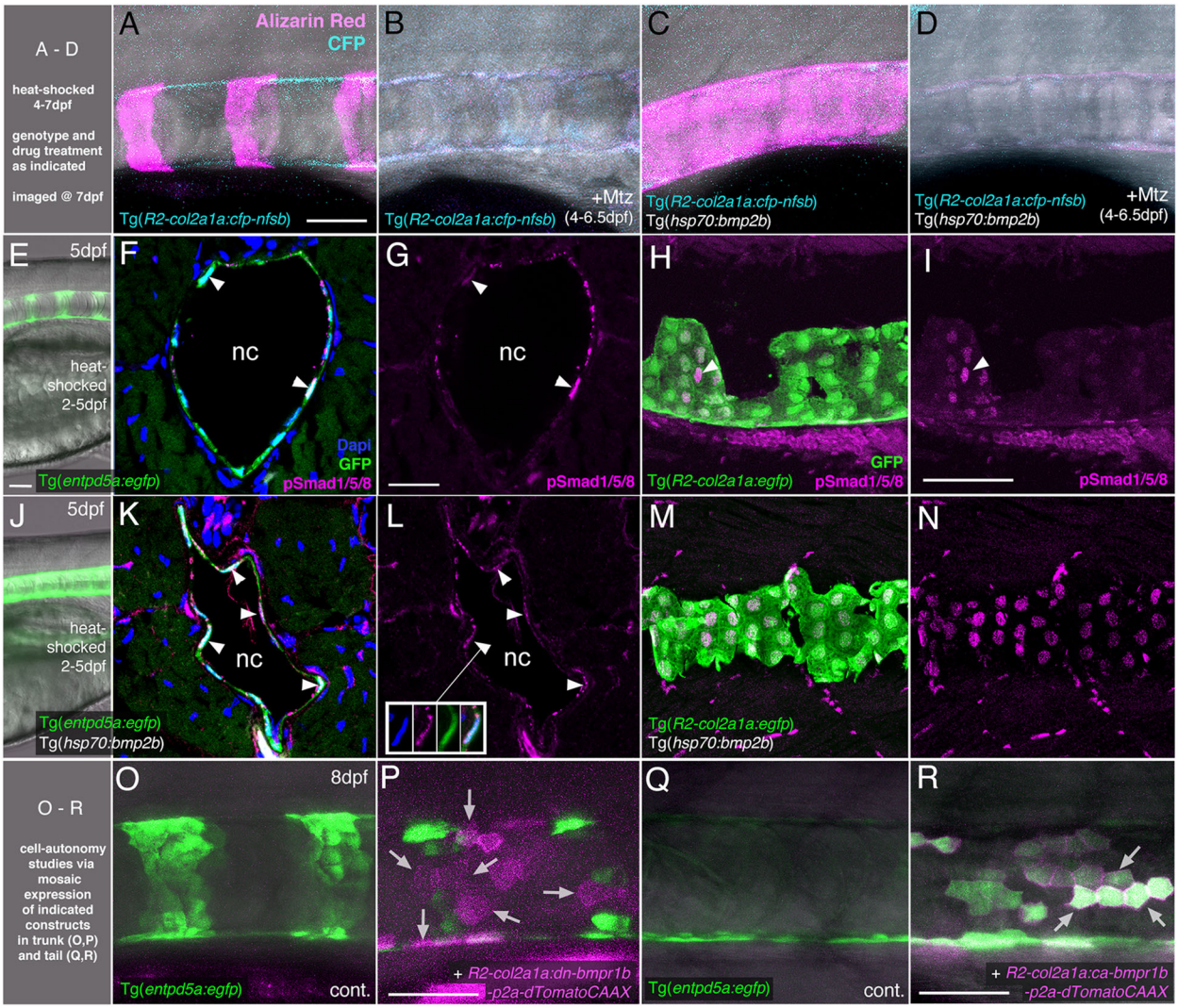

FIGURE 3
BMP directly targets chordoblasts to regulate Entp5a-mediated mineralization of the notochord sheath. **(A–D)** BMP induced hyper-mineralization of the notochord sheath requires an intact chordoblast layer. **(E–N)** Chordoblasts receive BMP signals as indicated by the presence of the responsible intracellular mediator pSmad1/5/8. Apart from chordoblasts, global overexpression of *bmp2b via* induction of Tg(*hsp70:bmp2b*) also resulted in the gain of pSmad1/5/8-positive cells within the myosepta, muscle tissue and the neural tube **(K-N)**. **(O–R)** Mosaic chordoblast-specific blockage or activation of the intracellular BMP signaling cascade alters *entpd5a* expression autonomously in targeted notochord epithelium cells. **(A–R)** Maximum intensity projections of confocal images with merged channels showing notochords and their immediate surroundings in live whole-mounts **(A–E, J, O–R)** and on stained cryosections **(F, H, K, M)**. **(G, I, L, N)** show corresponding single 555nm channels in magenta. **(E, J)** delineate overviews of those areas of heat-shocked larvae from which the sections presented in the corresponding rows were prepared. **(A–P)** have been assayed in the abdominal region at the level of the swim bladder, **(Q)** and **(R)** in the tail. **(A–E, H–J, M–R)** are lateral views with anterior to the left, **(F, G, K, L)** show transverse sections with dorsal upwards. Arrowheads in **(F, G, I, K, L)** point to exemplary chordoblasts with clear nuclear pSmad1/5/8 staining. Inset in **(L)** depicts magnified single channel images of pSmad1/5/8-positive chordoblast indicated in **(L)** by connected arrowhead. Arrows in **(P)** mark magenta-colored *dn-bmp1b-p2a-dTomatoCAAX* expressing cells that are located in a usually *entpd5a*-positive chordoblast cluster (compare with **(O)**), but that do not express the *entpd5a:egfp* transgene when BMP signal reception is blocked (N=5; n=28/39 dTomatoCAAX-positive, but EGFP-negative cells). Arrows in **(R)** point at a prominent group of chordoblasts that are triple positive for EGFP, the constitutively active BMP receptor Bmpr1b and dTomatoCAAX (N=2, 48 dTomatoCaax and EGFP double-positive of 53 dTomatoCAAX expressing chordoblasts). Ages, treatments, genotypes and color-coded markers as indicated. Scale bars: 50 µm **(A, E, I, O, P)**; 25 µm **(G)**. Mtz, Metronidazole; nc, notochord.

Results

Like RA, BMP signaling is required for notochord sheath mineralization

Zebrafish chordacentrum formation relies on segmented mineralization of the notochord sheath driven by chordoblasts (23–25). It starts anteriorly at the interface of the postcranial and cervical domains of the notochord. From there it progresses sequentially towards the posterior tip of the organ. Proper formation of chordacentra has been formerly shown to require retinoic acid (RA) signaling to chordoblasts, whereas gain of RA signaling leads to premature and ectopic notochord sheath mineralization and the fusion of chordacentra (19, 24, 35). To test whether BMP signaling has a similar impact on segmented notochord sheath mineralization, we made use of heat shock-

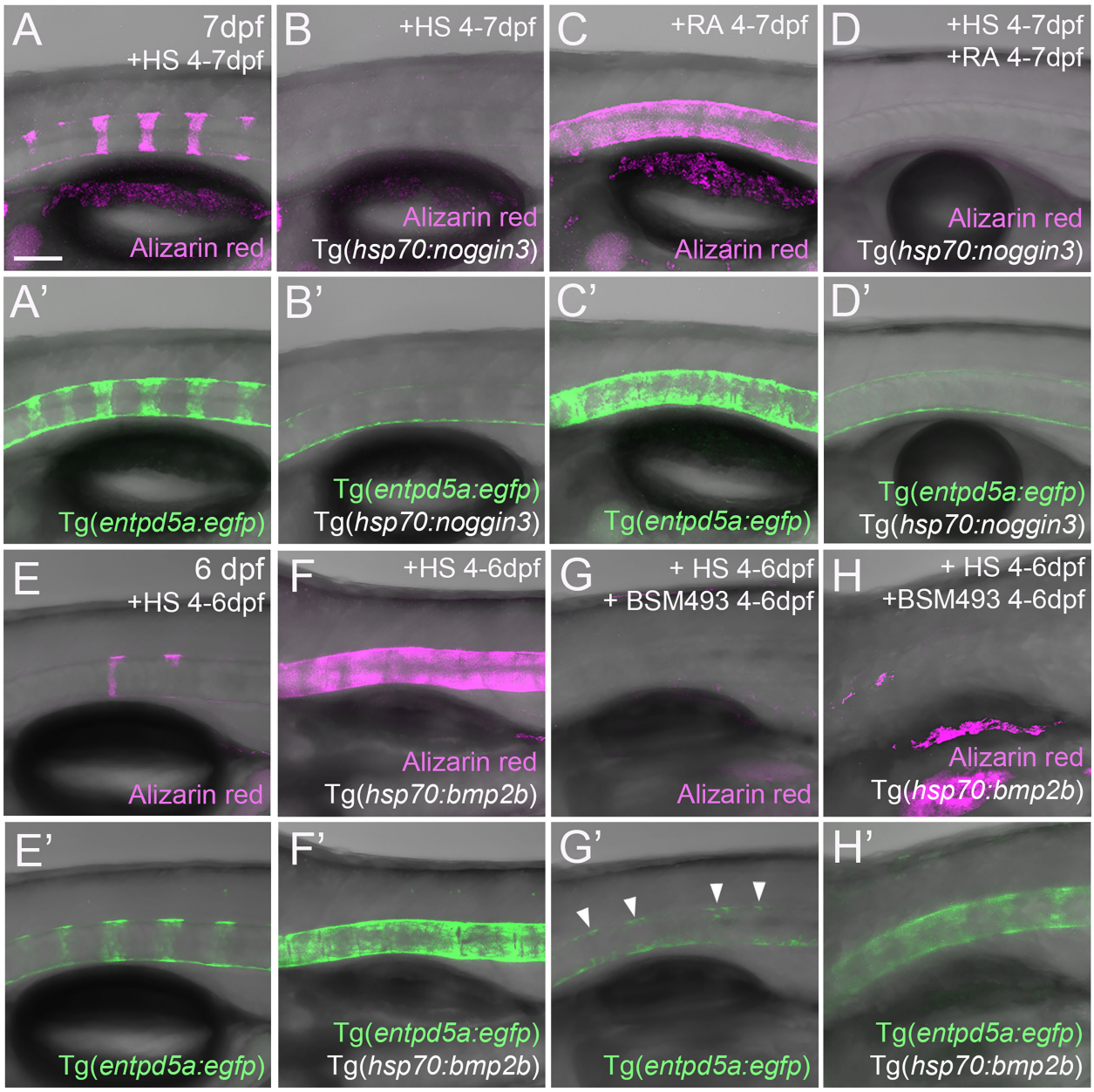

FIGURE 4
RA cannot promote notochord sheath mineralization when BMP signaling is blocked during initiation phases of mineralization. **(A–D')** RA fails to induce hyper-mineralization of the notochord sheath while BMP signaling is blocked. **(E–H')** BMP induced ectopic *entpd5a* activation cannot be hindered by interfering with the intra-cellular signal transduction of the RA pathway. **(A–H')** Lateral views of transgenic zebrafish larvae shown in merged transmitted and fluorescent light channels with tissue stainings, genotypes and treatments as indicated at an age of 7dpf **(A–D')** or 6dpf **(E–H')**. Heat-shocks were performed once a day for 45 minutes at 40°C. Arrowheads in **(G')** point to faintly EGFP-positive chordoblasts in areas of presumably segmented Tg (*entpd5a:egfp*) expression. Image-pairs X/X' show identical specimens. Scale bar (shown in **A**, applying to all panels): 100 µm.

inducible effector transgenes that allow for temporally controlled global hyperactivation or blockage of BMP signaling, respectively (36). In line with previous findings following an unbiased candidate approach (19), heat-shock induction of the *hsp70:bmp2b* transgene from 4 to 8 days post fertilization (dpf) robustly caused chordacentra fusion along the notochord (N=254/254) (Figures 1A–B'). In contrast, corresponding treatment of Tg (*hsp70:noggin3*) larvae to abrogate all endogenous BMP signaling caused the complete absence of sheath mineralization (N=163/163) (Figures 1C, C'). Thus, BMP is not only a potent but also an indispensable inducer of axial mineralization at this early phase of chordacentra development.

Ectonucleoside Triphosphate Diphosphohydrolase 5a (Entpd5a) has been formerly shown to be required for bone matrix ossification and notochord sheath mineralization in zebrafish (31). To investigate whether the effect of BMP signaling on notochord sheath mineralization might be due to a corresponding regulation of *entpd5a* expression in chordoblasts,

10.3389/fendo.2023.1107339

we generated a dedicated EGFP-based reporter transgene *via* BAC recombination following formerly described instructions (31) and established a transgenic *entpd5a:egfp*^{fr53Tg} line that recapitulates the recently reported activity of related transgenes (Figures 1D, D') (23, 25). In double transgenics, heat-shock activation of Tg(*hsp70:bmp2b*) from 4–8 dpf led to a strongly up-regulated and uniform, rather than segmented, expression of the *entpd5a:egfp* transgene along the entire notochord (N=189/189) (Figures 1E, E'). In contrast, corresponding activation of the *hsp70:noggin3* transgene led to strong reduction of segmented *Tg(entpd5a:egfp)* expression (N=273/273) (Figures 1F, F'). Together, this indicates that BMP signaling promotes *entdp5a* expression in chordoblasts and thereby notochord sheath mineralization, similarly to the formerly reported effect of RA (19, 24, 35).

Unlike RA, BMP signaling does not compromise notochord sheath production

We have formerly shown that upon treatment with RA, enhanced and premature mineralization of the notochord sheath by chordoblasts coincides with an attenuation of their matrix production, reflected by the loss of *col2a1* expression and a reduction in the thickness of the notochord sheath (24). To learn whether this also applies to the effect of BMPs on notochord sheath mineralization, we investigated *R2-col2a1a:egfp* transgene (27) expression under circumstances as described above for Tg (*entpd5a:egfp*). However, neither *R2-col2a1a:egfp*; *hsp70:bmp2b* nor *R2-col2a1a:egfp*; *hsp70:noggin3* double-transgenics displayed remarkable differences in axial Tg(*R2-col2a1a:egfp*) expression levels as detectable *via in vivo* imaging after heat-shock treatments from 4-8 dpf (N=46/46; N=62/62) (Figures 1G–I').

To validate these results, we performed qPCR studies of *entpd5a* and *col2a1a* transcripts with total RNA samples extracted from larvae treated with RA or after transgenic BMP overexpression, respectively (Figure 2A). For *entpd5a*, this approach confirmed the data obtained from the *in vivo* imaging of Tg(*entpd5a:egfp*) (Figures 1D–F), with gain of both RA or BMP signaling leading to an approximately 4fold increase in *entpd5a* expression (Figure 2A). For *col2a1a*, however, only RA treatment led to an approximately 3fold reduction of expression levels, whereas gain of BMP signaling even led to a subtle, but significant increase. Furthermore, loss of BMP signaling upon transgenic overexpression of Noggin3 resulted in moderately, but significantly reduced expression levels of both *col2a1a* and *entpd5a*. Corresponding differences between the effects of BMP and RA were also observed *via* our transmission electron microscopy (TEM) studies of the thickness of the notochord sheath (which mainly contains type II collagen encoded by *col2a1* from chordoblasts). Upon RA treatment, notochord sheath thickness was reduced almost by half, whereas no significant changes were observed by gain- or loss of BMP signaling (Figures 2B–F).

Taken together, we conclude that BMP signaling is a positive and indispensable regulator of early chordoblast-specific *entpd5a* expression and thereby of notochord sheath mineralization. However, and in difference to the properties of RA in the same context, it does not tune down *col2a1* expression and extracellular matrix (ECM) production in parallel. In light of the formerly described 2-step progression from ECM-generating to ECM-mineralizing chordoblasts (25) (see Introduction), we hypothesize that BMP signaling accounts for the first step, the transition to the transitory stage with both ECM-generating and ECM-mineralizing properties.

Chordoblasts are direct targets of BMP signaling

To further prove that the BMP-induced hyper-mineralization (Figure 1B) is indeed a consequence of altered activity of chordoblasts (and not other osteogenic cells as for instance scleroblasts), we tested whether BMP overexpression can induce the same phenotype in the absence of an intact notochord epithelium. To do so, we generated Tg(*R2-col2a1a:cfp-nfsb*); Tg (*hsp70:bmp2b*) double-transgenic larvae for temporally controlled and cell type-specific ablation of chordoblasts *via* the Metronidazole/Nitoreductase system (39). While leaving the overall integrity of the larvae intact (Figure S1 and (24)), Mtz treatment of Tg(*R2-col2a1a:cfp-nfsb*) larvae from 4 - 6.5 dpf resulted in the complete failure of notochord sheath mineralization, as assayed by Alizarin red staining at 7 dpf (N=81/81) (Figures 3A, B). This phenotype could not be alleviated or even converted into a hyper-mineralization upon concomitant Tg(*hsp70:bmp2b*) expression from 4-7 dpf (N=112/112), although the latter efficiently induced centra fusion of Tg(*R2-col2a1a:cfp-nfsb*) transgenics in the absence of Mtz (N=43/43; Figures 3C, D). Thus, BMP2b-induced mineralization of the notochord sheath depends on functional chordoblasts.

This effect of BMP signaling on chordoblasts could be either direct or indirect. To address these possibilities, we first performed immunofluorescence studies for phosphorylated Smad1/5/8 (pSmad1/5/8), the intracellular BMP signal transducer, in heat-shocked wild-type (Figures 3E–I) and Tg(*hsp70:bmp2b*) larvae (Figures 3J–N) at 5 dpf, when clearly segmented *entpd5a* expression in the chordoblast layer becomes apparent. Double labeling for transgene-encoded *entpd5a:egfp* (Figures 3F, G, K, L) or *col2a1:egfp* (Figures 3H, I, M, N) expression revealed nuclear pSmad1/5/8 staining in nearly all *entpd5a:egfp*-positive chordoblasts of wild-type (Figures 3F, G; N=4/4) and heat-shocked Tg(*hsp70:bmp2b*) larvae (Figures 3K, L; N=4/4) and in all *col2a1*-positive chordoblasts of heat-shocked Tg(*hsp70:bmp2b*) larvae (Figures 3M, N; N=5/5), whereas in *col2a1*-positive chordoblasts of wild-type larvae, nuclear pSmad1/5/8 was restricted to metamerically organized clusters that most likely correspond to their mineralizing subsets (Figures 3H, I; N=3/3).

Secondly, we performed chordoblast-specific cell-automomous loss- and gain-of-function studies, injecting dominant-negative or constitutively active versions of *bmpr1b* under the control of the chordoblast-specific *R2-col2a1a* enhancer element (*R2-col2a1a:dn-bmpr1b-p2A-dTomatoCAAX* or *R2-col2a1a:ca-bmpr1b-p2A-dTomatoCAAX*; (24, 27, 43, 44)) into *Tg(entpd5a:egfp)* embryos.

10.3389/fendo.2023.1107339

Even though we made use of the integration-facilitating Tol2 system (41, 42), resultant larvae were mosaic for the injected expression constructs. Larvae injected with the *R2-col2a1a:dn-bmpr1b-p2A-dTomatoCAAX* cassette displayed clearly disrupted Tg(*entpd5a:egfp*) expression in usually *entpd5a*-expressing chordoblast clusters (N=5; n=28/39 dTomatoCAAX-positive, but eGFP-negative cells) (Figures 3O, P). Vice versa, we were able to ectopically induce Tg(*entpd5a:egfp*) expression in the notochord epithelium after injecting the *R2-col2a1a:ca-bmpr1b-p2A-dTomatoCAAX* construct, with EGFP and dTomato double-positive chordoblasts even in more caudal regions of the notochord that had not developed any endogenous *entpd5a* expression at 8 dpf as yet (N=2, 48/53 double-positive chordoblasts) (Figures 3Q, R).

Together, this indicates that chordoblasts directly receive BMP signals, to which they respond by the initiation of *entpd5a* expression and notochord sheath mineralization. However, in contrast to RA signals, which according to our former studies are also directly received by chordoblasts (24), BMP signaling does not induce the termination of *col2a1* expression and notochord sheath formation.

RA cannot promote notochord sheath mineralization when BMP signaling is blocked during early phases of mineralization initiation

Given that both BMP and RA contribute to segmented *entpd5a* expression and notochord sheath mineralization, we wondered whether one acts *via* the other. To test this, we combined gain of function of one factor with loss of function of the other to perform epistasis analyses. To combine loss of BMP with gain of RA signaling, we compared Tg(*entpd5a:egfp*) activity and notochord sheath mineralization (via Alizarin red staining) in Tg(*hsp70:noggin3*) larvae with Tg(*hsp70:noggin3*)-negative siblings, both of which were heat-shocked and additionally treated with RA from 4-7 dpf or, as negative control, with DMSO. As in the studies shown in Figure 1, control-treated wild-type siblings showed the expected EGFP reporter expression in the rostral third of the notochord with up to eight mineralized chordacentra formed at 7 dpf (N = 58/58; Figures 4A, A'), whereas control-treated heat-shocked *hsp70:noggin3* transgenics lacked both markers, indicating successful blockage of the BMP pathway (N=74/74; Figures 4B, B'). Conversely, RA-treated wild-type larvae developed the expected hyper-mineralization/centra fusion phenotype (N=47/47, Figures 4C, C'), whereas RA-treated and heat-shocked *hsp70:noggin3* transgenics failed to show any RA-induced responses and displayed the pure BMP loss-of-function phenotype (N=118/118, Figures 4D, D').

In a reverse experiment, combining gain of BMP with loss of RA signaling, we compared Tg(*entpd5a:egfp*) activity and notochord sheath mineralization (via Alizarin red stains) in Tg(*hsp70:bmp2b*) larvae with Tg(*hsp70:bmp2b*)-negative siblings, both of which were heat-shocked and treated from 4-6 dpf with the pharmacological pan-RA receptor inhibitor BSM493 (38) or, as negative control, with DMSO. As in the studies shown in Figure 1, control-treated heat-shocked *hsp70:bmp2b* transgenics displayed continuous rather than metameric Tg(*entpd5a:egfp*) expression and Alizarin red incorporation along the notochord (N=21/21, Figures 4E, E', F, F'). Comparable uniform Tg(*entpd5a:egfp*) expression was also obtained upon concomitant BSM493-treatment (N=24/24; Figure 4H'), however, at considerably lower levels, consistent with the compromised metameric transgene expression in BSM493-treatment of wild-type siblings (N=20/20, Figure 4G'). Noteworthy, this moderate ectopic *entpd5a* activation was hardly able to induce notochord sheath mineralization (Figure 4H). In sum, RA cannot compensate for the loss of BMP in initiating *entpd5a* expression and consequently notochord sheath mineralization, while BMP cannot compensate for the loss of RA in reaching maximal *entpd5a* expression and thus sheath mineralization levels. In genetic terms, this categorizes BMP as being epistatic to RA in initiating *entpd5a* expression in chordoblasts for notochord sheath mineralization, and RA as being epistatic to BMP in potentiating Entpd5a production.

BMP and RA signaling do not act *via* each other

The described epistatic relationships between BMP and RA could mean that RA acts upstream of BMP, with RA inducing BMP signaling to initiate notochord sheath mineralization, but also that BMP acts upstream of RA, with BMP inducing RA signaling to potentiate *entpd5a* expression. This would imply a switch in the linear order of action of the two during the course of notochord sheath mineralization, with RA first acting upstream and later downstream of BMPs. This seems quite unlikely. To look into these options more directly, we studied whether gain of BMP signaling induces gain of RA signaling and/or vice versa. To address RA signaling, we determined the expression of the *cyp26b1:yfp* transgene, which has been used as an *in vivo* reporter for RA signal reception by zebrafish chordoblasts before (24). As previously reported, untreated Tg(*cyp26b1:yfp*) controls displayed iterative segments of the notochord epithelium labeled by YFP, overlapping with the sites of chordacentra mineralization visualized by alizarin red staining (N=12/12; Figures 5A, A', A''). Exposure of Tg(*cyp26b1:yfp*) transgenics to RA led to the expected expansion of *yfp* expression in the chordoblast layer that was accompanied by a hyper-mineralization of the notochord sheath (N=33, Figures 5B, B', B''). However, global Bmp2b overexpression in 4-7 dpf heat-shocked *hsp70:bmp2b* transgenics did not alter the segmented appearance of YFP-positive chordoblast clusters (N=54, Figure 5C), although it led to a similar notochord sheath hyper-mineralization (Figure 5C') as the YFP-expanding RA treatment (Figure 5B'). Thus, BMP does not drive notochord sheath mineralization by inducing or promoting RA signaling.

The reverse, however, also does not seem to be the case: in co-labeled untreated controls, transverse sections through vertebral regions display chordoblasts that are positive for both pSmad1/5/8 and Tg(*cyp26b1:yfp*) activity (N=3; Figures 5D–D''), whereas chordoblasts in intervertebral regions lack both pSmad1/5/8 and

10.3389/fendo.2023.1107339

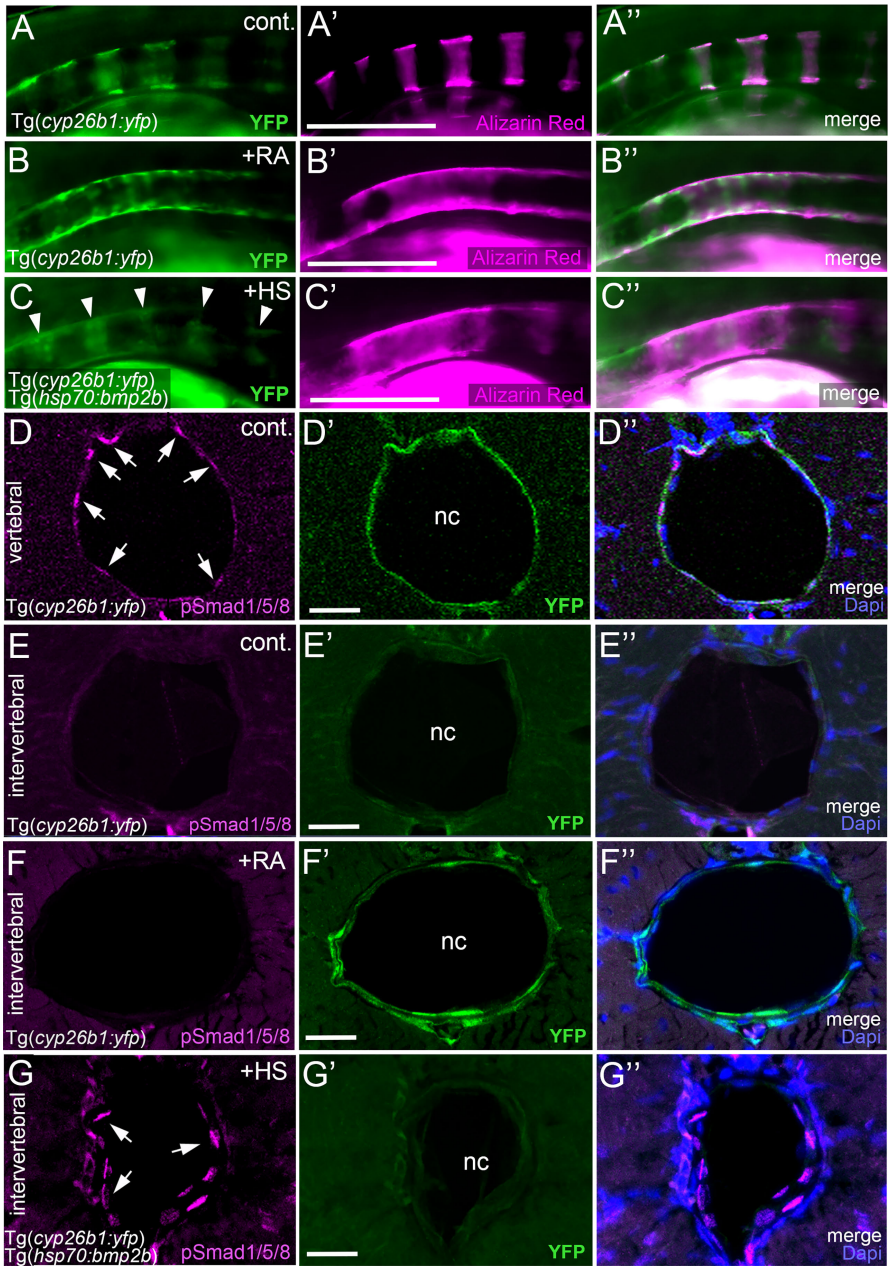

FIGURE 5
BMP and RA signaling do not act *via* each other. **(A–C'')** BMP-induced hyper-mineralization is not accompanied by an ectopic activation of the RA signaling reporter Tg(*cyp26b1:yfp*) in the notochord epithelium. Lateral views of notochords immediately dorsal to the swim bladder, anterior to the left. Images were taken by conventional fluorescent light microscopy and are shown as separate 488nm **(A–C)**, 555nm **(A'–C')** channels and with both channels merged **(A''–C'')**. The *cyp26b1:yfp* transgene **(A–C, A''–C''**, green**)** labels chordoblasts and serves as a readout for RA-responsiveness. Alizarin red stains the mineralized notochord sheath **(A'–C'**, **A''–C''** magenta**)**. Note the remaining segmented YFP signal after global overexpression of BMP2b (**C**, arrowheads). **(D–G'')** Exposure of larvae to 1 µM RA does not cause ectopic pSmad1/5/8 appearance at intervertebral positions of the chordoblast layer. Cross-sections through the abdominal notochord of 7 dpf control Tg(*cyp26b1:yfp*) **(D–E'')**, RA-treated Tg(*cyp26b1:yfp*) **(F–F'')**, and heat-shocked Tg(*cyp26b1:yfp*), Tg(*hsp70:bmp2b*) **(G–G'')** larvae co-stained *via* immunofluorescence labeling for the activated/phosphorylated BMP signal transducer pSmad1/5/8 and for YFP, encoded by the RA responder transgene. In untreated controls, pSmad1/5/8 reactivity is restricted to vertebral segments co-expressing the RA reporter transgene **(D–D'')** but absent from intervertebral spaces lacking Tg(*cyp26b1:yfp*) expression **(E–E'')**. Upon RA-treatment, such intervertebral domains (identified as such by the lack of pSmad1/5/8 activity) display ectopic Tg(*cyp26b1:yfp*) activity, although RA fails to induce ectopic pSmad1/5/8 reactivity **(F-F'')**. In contrast, as a positive control, ectopic pSmad1/5/8 reactivity in intervertebral regions, identified as such by the lack of Tg(*cyp26b1:yfp*) activity, is obtained by heat shock-induced ubiquitous Tg(*hsp70:bmp2b*) expression **(G-G'')**. Images represent single confocal slices shown as separate channels 555nm in magenta **(D–G)**, 488nm in green **(D'–G')** and merged with Dapi **(D''–G'')**. Arrows in **(D, G)** point at exemplary pSmad1/5/8 positive chordoblasts. Whole figure: Genotype, age, labeling and treatments as indicated. Heat-shocks were performed once a day for 45 minutes at 40°C from 4-7 dpf. RA was applied constantly from 4-7 dpf. Scale bars: 200 µm **(B)**; 20 µm **(D'–G')**. cont., vehicle-treated control; nc, notochord; HS, heat shock; RA, Retinoic acid.

Tg(*cyp26b1:yfp*) activity (N=3; Figures 5E–E"). Consistent with the data described above (Figures 5C–C"), upon forced ubiquitous BMP expression in Tg(*hsp70:bmp2b*) fish heat-shocked from 4-7 dpf, such intervertebral regions remained Tg(*cyp26b1:yfp*) negative, although displaying ectopic pSmad1/5/8 reactivity (N=5, Figures 5G–G"). In contrast, upon RA treatment, intervertebral regions have become positive for Tg(*cyp26b1:yfp*) activity while still lacking pSmad1/5/8 reactivity (N=7, Figures 5F–F"). Therefore, although BMP seems epistatic to RA in initiating *entpd5a* expression and notochord sheath mineralization (Figures 4A–D), RA does not seem to act *via* BMPs.

RA can promote notochord sheath mineralization independently of BMP signaling at later stages of vertebral column formation

An action of RA upstream of BMP to initiate *entpd5a* expression for notochord sheath mineralization also seems unlikely in the light of our formerly published data, according to which zebrafish larvae can respond to BMP overexpression by ectopic notochord sheath mineralization approximately two days earlier than to RA treatment (19). Thus, the epistatic relationship between RA and BMP revealed in the studies with combined loss of BMP and gain of RA activity described above (Figures 4A–D), might need to be interpreted differently. An alternative explanation could indeed be consecutive, temporally separated functions of the two, with RA only being able to promote chordoblasts and their mineralizing activity AFTER they have received BMP signals inducing a crucial earlier step of chordoblast differentiation. To test this notion, we performed the epistasis analyses described above (Figures 4A–D) at a later time window of vertebral development, co-treating larvae from 6-8 dpf, rather than from 4-7 dpf. Global overexpression of *noggin3* during that later time window arrested the mineralization process in a 6 dpf like-state, with beginning and subtle mineralizations of the first four to five centra (N=35, Figure 6B), compared to the stronger and posteriorly advanced mineralization of the first ten centra in non-transgenic controls (N=25, Figure 6A). Heat-shocked non-transgenic specimens hyper-mineralized their notochord sheath when exposed to RA from 6-8 dpf (N=33, Figure 6C). Remarkably and different to the corresponding experiment performed from 4-7 dpf (Figure 4D), upon combined Noggin3 and RA treatment from 6-8 dpf, the loss-of-BMP-function phenotype did not completely prevail over the gain-of-RA-function effect. Instead, we detected an intermediate phenotype with increased, but not fully normalized mineralization levels in the first seven centra and some signs of ectopic mineralization at the ventral side of the notochord (N=28, Figure 6D), indicating that later loss of BMP cannot fully abrogate RA-induced mineralization. In addition, compared to untreated siblings (Figure 6A), Tg(*R2-col2a1a:egfp*) expression in chordoblasts of double-treated larvae was diminished (Figure 6D), indicating that even in the absence of such late BMP signaling, RA can induce the progression of chordoblasts from matrix-producing to matrix-mineralizing cells.

Together with their differential effects on *col2a1* and *entpd5a* expression described above (Figures 1, 2), these data point to consecutive functions of BMP and RA during subsequent steps of chordoblast differentiation and activity. Hereby, BMP promotes the progression of purely matrix-producing to transitory matrix-producing and simultaneously matrix-mineralizing cells, while RA can only affect the latter (and later occurring) stage *via* further promoting its matrix-mineralizing capabilities while attenuating its matrix-producing activity. These findings are consistent with the former discovery of the corresponding three chordoblast subpopulations *via* FACS sorting of transgene-labeled chordoblasts and comparative transcriptome analysis (25). Along these lines, the incomplete normalization of the typical 8 dpf pattern of notochord sheath mineralization in larvae double-treated with Noggin3 and RA from 6-8 dpf would be due to the fact that at 6 dpf, not all usually mineralization-promoting chordoblasts along the notochord and within presumptive centra segments have received the pre-determining BMP signal as yet.

Discussion

It is certainly not surprising that a family of highly conserved signaling factors that have initially been identified as regulators of mammalian connective tissue mineralization (1, 2) (as reflected by their name: Bone Morphogenetic Proteins) take action in this particular function also in teleosts. Accordingly, BMP signaling has for instance been shown to have an impact on bone formation during zebrafish facial skeleton development (46) and fin regeneration (47). Also, as reported by us earlier, global BMP overexpression between 2 and 4 dpf leads to a fusion of vertebral centra in zebrafish larvae (19). In this follow-up study, we set out to shed further light on the endogenous function of BMP and its relationship to RA signaling in this developmental context.

Chordoblasts, the primary skeletogenic cells of the developing teleostean vertebral centra anlagen, are direct cellular targets of consecutive positive regulation by BMPs and RA

It was an unexpected and remarkable finding of recent years that the initial mineralization events in early teleost vertebral column development are not driven by sclerotome-derived osteoblasts, but by cells from the notochord, the chordoblasts (23–25). Noteworthy, the cellular and biochemical mechanisms underlying the formation of such chordacentra by chordoblasts are very similar to what we know from cells of the regular osteogenic lineage: secretion of a special extracellular matrix (ECM) followed by its bio-mineralization. In typical bone formation, osteoblasts secrete collagens and proteoglycans to generate a specialized ECM called osteoid as a first step. Subsequently, osteoblasts differentiate further to preosteocytes, which stop matrix production and instead initiate its calcification, thereby finalizing the process of ossification (32, 33). Chordoblasts

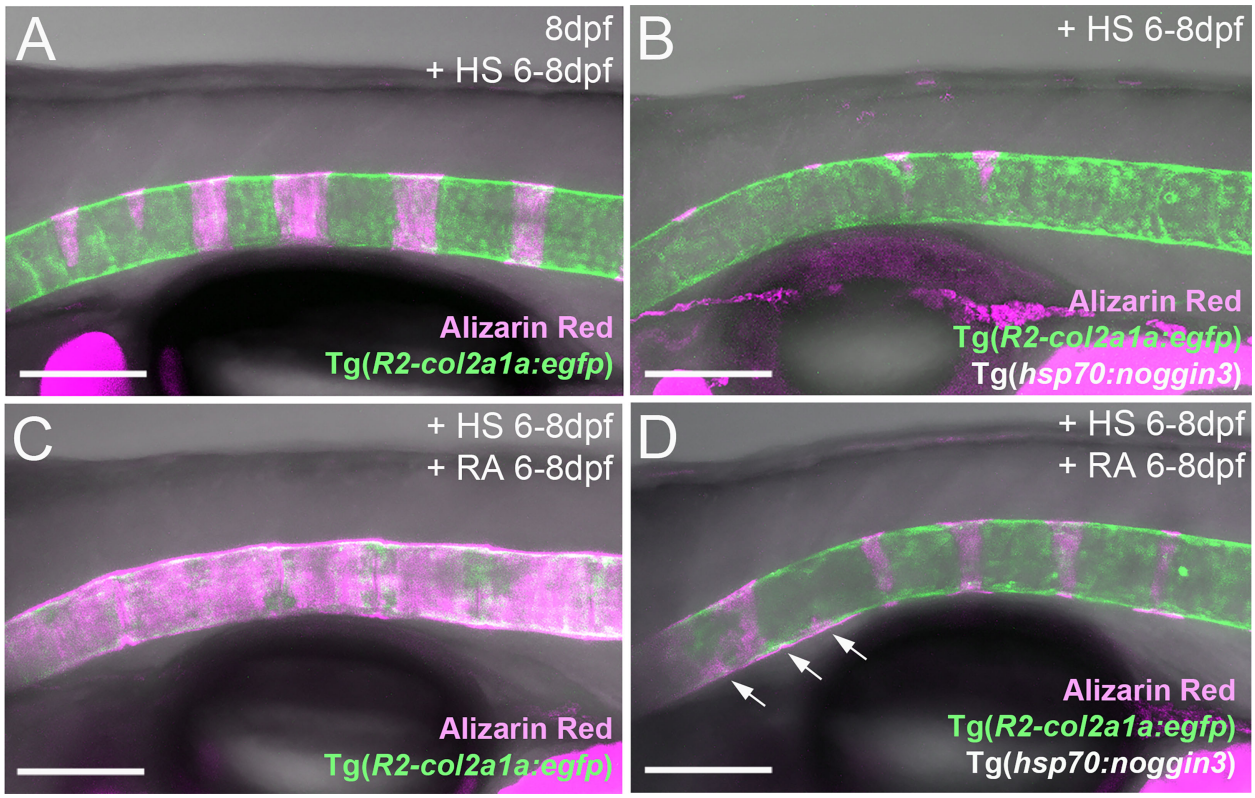

FIGURE 6
RA can promote notochord sheath mineralization independently of BMP signaling at later stages of vertebral column formation. **(A–D)** Blockage of BMP signaling with synchronous activation of the RA pathway from six to eight dpf results in larvae with less severe disrupted notochord sheath mineralization while chordoblasts show clear marks of RA responsiveness (decreased Tg(*R2-col2a1a:egfp*) activity and less distinct cellular morphology). Lateral views of transgenic zebrafish larvae shown in merged transmitted and fluorescent light channels with tissue staining, genotypes and treatments as indicated at an age of 8dpf **(A–D)**. Heat-shocks were performed once a day for 45 minutes at 40°C. Arrows in **(D)** point at zones of ectopic mineralization. Scale bars: 150 µm.

do basically the same (Figure 7): first, they secrete a type II collagen-based extracellular matrix, the notochord sheath; thereafter, they express *entpd5a* to allow for bio-mineralization of this sheath. Analogously to preosteocytes, the fully mineralizing chordoblasts gradually tune down matrix production (24, 25). Of note, the functional progression of chordoblasts from merely matrix-secreting towards merely mineralizing cells runs through a transitory phase. The latter is characterized by an onset of the Entpd5a-mediated mineralization process while notochord sheath production still pursues (25).

Here, we show that BMP – like RA - is capable of expanding *entpd5a* transcriptional activity in chordoblasts with the consequence of increased notochord sheath mineralization. But in contrast to RA, the BMP-induced effect is obviously not directly paralleled by a downregulation of matrix production. In fact, our results even point to a moderately positive impact of forced BMP signaling on *col2a1a* expression, contrasting the negative effect of increased RA signaling (Figure 2A), while the thickness of the notochord, again in contrast to the negative effect of RA signaling, is not significantly altered (Figure 2B). Thus, BMP's function is obviously not to silence chordoblasts' matrix secretion for the sake of mineralization, but to direct chordoblasts into that transitory phase of synchronized ECM secretion and mineralization – comparable to an early preosteocyte (32, 33). In contrast, RA is required for the next and subsequent step, inducing the progression of chordoblasts into a later stage characterized by aborted matrix production and elevated mineralizing activity (24), reflected by *col2a1a* downregulation, reduced thickness of the notochord sheath and several-fold *entpd5a* upregulation in RA-treated larvae (Figures 2A, B, 7). Accordingly, given the BMP-driven mineralization during the transitory phase, loss of RA signaling does not lead to a complete loss, but just severely reduced levels of notochord-intrinsic *entpd5a* activity (Figures 4E', G'), which seem higher than in the case of loss of BMP signaling (Figures 4A', B'). Such a consecutive function of BMP and RA also explains our former findings that zebrafish larvae can respond to BMP overexpression by ectopic notochord-sheath mineralization approximately two days earlier than to RA treatment (19). Furthermore, the epistasis analysis presented here indicates that chordoblasts need to run through this BMP-dependent transitory stage before becoming responsive to RA (Figure 7). Thus, RA treatment fails to induce an up-regulation of *entpd5a* expression in chordoblasts when they are co-exposed to high levels of the BMP inhibitor Noggin3 during early phases of vertebral column formation, when chordacentra mineralization is initiated (4 dpf; Figures 4A–D'), whereas approximately two days later, when at

10.3389/fendo.2023.1107339

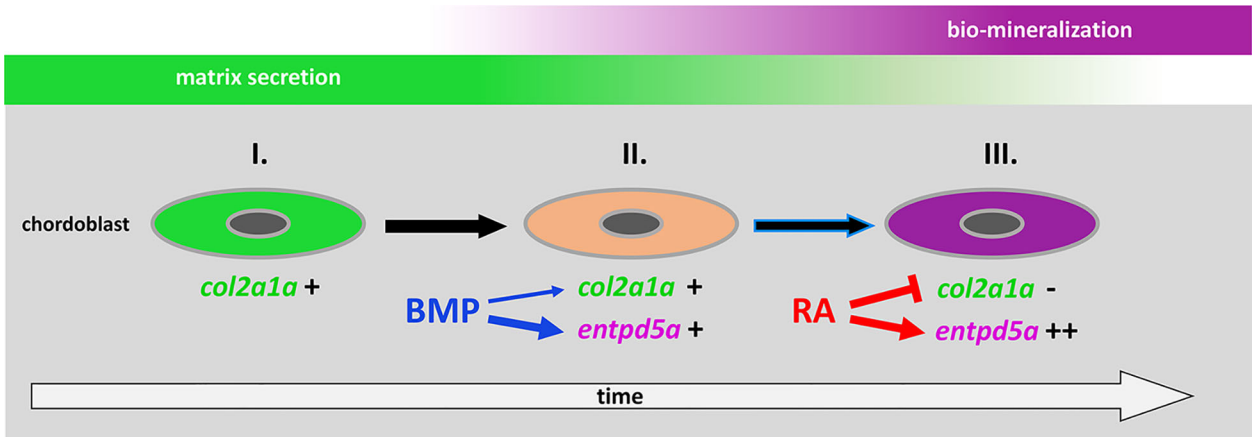

FIGURE 7
Proposed model for the consecutive roles of BMP and RA to induce the stepwise progression of chordoblasts from solely matrix-producing towards solely matrix-mineralizing cells. I. Chordoblast contribution to chordacentra formation starts with collagen II-based matrix (notochord sheath) production. II. Next, cells progress into a matrix-secreting and -mineralizing transitory stage induced by BMP, with an induction of *entpd5a* expression, required for matrix mineralization (thick blue arrow) and with some minor positive effect on *col2a1a* expression (thin blue arrow). III. Lastly, RA signaling enhances and maintains *entpd5a* transcription (thick red arrow), thereby reaching Entpd5a levels that allow for sustained bio-mineralization of the notochord sheath. At the same time RA represses *col2a1a* transcription to attenuate matrix secretion. Chordoblasts can only enter step III after they have experienced BMP signaling beforehand (black arrow with blue lining).

least some of the chordoblasts have received the BMP signal and have entered the transitory stage, RA can stimulate chordacentra mineralization in the absence of BMP signaling (Figure 6). Future single cell transcriptome analyses of chordoblasts under these different conditions will be necessary to reveal by which means the preceding BMP signaling prepares ground for the later RA signal. Apparently, it is not achieved by inducing RA signaling, for instance by activating the expression of RA-synthesizing Aldehyde Dehydrogenase enzymes, or by making chordoblasts competent for the reception of RA signals, for instance by inducing the production of RA receptors. Thus, BMP overexpression does not lead to enhanced RA signaling in chordoblasts, as indicated by the unaltered expression of the reporter transgene *cyp26b1:yfp* that labels RA-receiving cells (Figures 5A–C").

BMPs, rather than RA, might generate the metameric pattern in the initially unsegmented chordoblast layer of the notochord

A puzzling and still unresolved question is how the pattern of iterative *entpd5a* expressing segments within the otherwise uniform appearing chordoblast layer gets implemented in the first place. Different working-models have been proposed, ranging from a notochord-inherent molecular pattern generator up to an induction by external signals that are secreted by primarily segmented sources (22–26). To sort things out it is of course crucial to identify the involved molecular regulators, and RA as well as components of the Notch signaling system have already been implicated in this context (24, 25). Here, we provide evidence that BMP signaling also feeds into the molecular mechanisms that construct the early vertebral column anlage in zebrafish. Based on our data, BMP appears to direct chordoblasts from the merely ECM-producing into a transitory stage, thereby placing it functionally upstream of the RA-dependent manifestation of the merely mineralizing phase. Similarly, Notch signaling has been found to have impact on the initial transition from matrix-secreting to *entpd5a*-expressing chordoblasts (25). Further research is needed to dissect the functional and genetic correlation between BMP and Notch. In other contexts, ranging from vein formation in Drosophila wings (48) to zebrafish heart regeneration (49), Notch signaling has been reported to act upstream of BMP/Dpp signaling. However, as in the case of BMP and RA described here, corresponding epistasis analyses have to be taken with caution, as one factor being epistatic to another does not necessarily mean that it acts downstream, but could rather be involved in an earlier step of the biological process. Thus, temporally controlled double treatments at different time points are necessary to allow definitive answers.

In fact, based on its time of action, its functions and its formerly demonstrated diffusivity (50, 51), BMP itself might be the initial pattern generator during zebrafish vertebral column segmentation. Future research will aim to identify the specific BMP ligands and their cellular sources involved in these early steps of chordoblast activation and notochord epithelial segmentation. Analyses of secreted BMP inhibitors like Noggin, Chordin or Sclerostin (52) and their spatial distributions will further elucidate potential mechanisms to restrict the growth of individual centra along the anteroposterior axis of the notochord and to avoid centra fusions. Such inhibitors could for instance be expressed in a pattern complementary to that of the mineralization-inducing BMPs, thus in, or adjacent to, presumptive intervertebral regions (53). Alternatively, they could be co-expressed with the BMPs in, or adjacent to, presumptive vertebral regions, constituting a dynamic reaction-diffusion mechanism within the chordoblast layer,

similarly to how it has been formerly demonstrated for other activator-inhibitor systems during zebrafish embryogenesis (54, 55).

Similarities and differences in the roles of BMP and RA signaling during vertebral column formation in zebrafish versus mouse and human

Two prominent human syndromes display vertebral fusions caused by altered BMP signaling, which in both cases are restricted to cervical vertebrae of the neck: Klippel-Feil-Syndrome (KFS) caused by loss of GDF6 or GDF3, both BMP family members (5–7), thus contrasting our data that gain of BMP signaling causes chordacentra fusions in zebrafish, and Fibrodysplasia ossificans progressiva (FOP), caused by gain of BMP signaling *via* a mutated, constitutively active version of the BMP type I receptor ACVR1/ALK2 (9–11), consistent with our zebrafish data.

We can only speculate about the apparently opposite roles and effects of BMP signaling in human KFS versus human FOP and zebrafish chordacentra fusion. It has been reported that in difference to the thoracic and abdominal vertebrae, skeletogenic cells forming the KFS-affected cervical vertebrae derive from the neural crest rather than the somitic sclerotome (56). Thus, and in light of the much earlier manifestation of the vertebral fusion phenotype in KFS compared to FOP, resulting from early segmentation defects (see Introduction), it is tempting to speculate that in amniotes, GDF3/6 might play a specific early role in the development of such neural crest precursors that is not relevant in teleosts, where neural crest cells do not contribute to vertebra formation. Thus, BMP-induced chordacentra fusions in zebrafish, although similarly to KFS occurring at the level of the vertebral bodies/centra themselves, are definitively no model for human Klippel-Feil syndrome.

FOP is characterized by orthotopic and heterotopic ossifications at multiple sites, among them fusions at the level of lateral masses and neural arches of cervical vertebrae (ossification of the vertebral facet joints) (9–12), thus crucially contrasting the fusion type in KFS and in our zebrafish models described here, which are characterized by fusions at the level of the vertebral bodies/centra themselves. These orthotopic and heterotopic endochondral ossifications of FOP have been attributed to ALK2-mediated excessive chondrogenic differentiation of mesenchymal progenitor cells recruited to inflamed "flare-up" sites (57). Given that endogenous RA signaling has been known to be normally attenuated during chondrogenesis, that this attenuation is required for chondrogenic differentiation (58, 59) and that exogenous RA agonists can block chondrogenesis (60), it seemed feasible to prevent or alleviate such ossifications of FOP by blocking early ectopic chondrogenic differentiation processes *via* a pharmacological enhancement of RA signaling. And indeed, results obtained with the RA receptor γ (RARγ) agonist Palovarotene were so convincing that it has recently been approved for FOP therapy in human (61–63). Strikingly, the strong alleviation of heterotopic ossification defects in Palovarotene-treated genetic FOP mice was accompanied by significant reductions in pSmad1/5 levels (61, 63), suggesting that at the affected sites, RA normally acts upstream and as a negative regulator of BMP signaling. This is in striking contrast to our findings that during early mineralization steps of the developing vertebral column in zebrafish, BMP and RA have similar, rather than opposite effects, that BMP acts earlier, rather than as a mediator of RA, and that BMP and RA signaling do not affect each other. Furthermore, vertebral fusions in FOP are restricted to the neural arches (leaving the vertebral bodies unaffected) and to the cervical vertebrae, whereas in zebrafish, overexpression of BMP leads to fusions of the centra/vertebral bodies themselves and occurs along the entire length of the developing vertebral column.

In light of these differences, in addition to the long-known morphological differences between developing vertebral columns of amniotes and teleosts, as well as the strikingly different cellular contributions to vertebra formation in amniotes (neural crest- and sclerotome-derived chondrocytes and osteoblasts) versus teleosts (notochord-derived chordoblasts and sclerotome-derived osteoblasts) (28, 30), the mechanisms of early backbone formation and segmentation might appear so fundamentally different between the two clades that data obtained in zebrafish could be considered completely irrelevant for a better understanding of vertebral malformations in human.

On the other hand, it cannot be ruled out that the antagonistic correlation between RA and BMP signaling revealed in the mouse FOP models primarily applies to other sites of heterotopic ossifications, but not to the orthotopic ossifications in cervical vertebrae. Indeed, there is evidence that here, BMP and RA might act as partners, rather than opponents, similar to their cooperation during vertebral column development in zebrafish demonstrated in this work. Thus, in mouse, gain of endogenous RA signaling upon pharmacological inhibition of Cyp26 RA inhibitors leads to fusions of neural arches of cervical vertebrae (19) similar to those obtained by gain of endogenous BMP signaling upon genetic loss of the BMP inhibitor Noggin in mouse and FOP in human (12, 20). This suggests that at least some crucial, not well understood aspects of vertebral column segmentation and vertebrae fusion ARE mechanistically conserved among zebrafish, mouse and, possibly, human. More and more direct comparative studies of BMP and RA signaling during vertebral column formation in teleosts and mammals, including detailed expression pattern analyses of BMPs, BMP inhibitors, RA-synthesizing and RA-metabolizing Cyp26 enzymes, as well as cell type-specific loss-of-function experiments, will be necessary to unravel such conserved aspects within otherwise rather clade-specific and differential developmental programs (28).

Furthermore, future studies need to address whether for zebrafish, the concept of consecutive functions of BMP and RA for a stepwise transition of matrix-producing to matrix-mineralizing skeletogenic cells also applies to mineralizing tissues outside the notochord. Increased and precautious mineralization induced by gain of RA or loss of its inhibitor Cy26b1 have been reported for multiple other zebrafish bones, formed either *via* perichordal or intramembranous ossification, such as the ceratohyale and the opercle of the craniofacial skeleton (19), the fin rays (64) and the calvarial plates of the skull (34, 65). Of note, for the mouse skull, application of the BMP inhibitor Noggin has been shown to rescue RA-induced craniosynostosis (66), pointing to

mineralizing-promoting effects of both RA and BMP, contrasting their opposite effects during FOP and consistent with our data revealed here for the developing zebrafish vertebral column, but with a function of BMP downstream of RA that is opposite to the order revealed here for the zebrafish vertebral column.

Data availability statement

The original contributions presented in the study are included in the article/Supplementary Material. Further inquiries can be directed to the corresponding author.

Ethics statement

The animal study was reviewed and approved by LANUV Nordrhein-Westfalen.

Author contributions

H-MP and MH contributed to the conception and design of the study. IR-Q and H-MP performed the experiments, analyzed samples and collected data. H-MP conducted the statistical analysis. H-MP and MH wrote the manuscript. All authors contributed to the article and approved the submitted version.

Funding

This work was supported by the National Institutes of Health (R01GM63904 "Systematic Vertebrate Functional Genomics" to MH (main PI: Stephen C. Ekker, Mayo Clinic, Rochester, MN, USA).

Acknowledgments

We thank Dr. Sebastian Hess (Cologne University) for the excellent support and help during transmission electron microscopy. We thank Stefan Schulte-Merker (Münster University) for providing the *Tg(cyp26b1:YFP)*^{hu7426} and Rodney Dale (Loyola University Chicago) for the *Tg(R2-col2a1a:EGFP)*^{nu13Tg} line plus a *R2-col2a1a* 5'-entry construct. We are further grateful to David Kimelman (University of Washington, Seattle) for sending us plasmids with constitutively active and dominant-negative versions of *bmpr1*.

Conflict of interest

The authors declare that the research was conducted in the absence of any commercial or financial relationships that could be construed as a potential conflict of interest.

Publisher's note

All claims expressed in this article are solely those of the authors and do not necessarily represent those of their affiliated organizations, or those of the publisher, the editors and the reviewers. Any product that may be evaluated in this article, or claim that may be made by its manufacturer, is not guaranteed or endorsed by the publisher.

Supplementary material

The Supplementary Material for this article can be found online at: https://www.frontiersin.org/articles/10.3389/fendo.2023.1107339/full#supplementary-material

SUPPLEMENTARY FIGURE 1
Ablation of chordoblasts neither disrupts tissues outside the notochord nor does it impair overall integrity of the larvae. **(A, B)** Lateral view with anterior to the left of a wild-type control **(A)** and a Tg(*R2-col2a1a:CFP-NTR*) transgenic larva **(B)** both of them Mtz treated as indicated, at 7 dpf. Even though the chordoblast-ablated animal is a bit shorter than the control, it looks overall intact, has an inflated swim bladder and displays no signs of increased necrosis in tissues outside the notochord. **(A', B')** depict corresponding magnifications of notochords from the specimens shown in **(A, B)**. As in the control larva **(A')**, vacuolated chordocytes persist after chordoblast ablation upon Mtz application from 4dpf to 6.5dpf **(B')**. **(C, D)** Semi-thin transverse sections through posterior abdominal regions of Mtz-treated wild-type and Tg(*R2-col2a1a:CFP-NTR*) larvae. Except for the collapse of the notochord that is caused by the chordoblast ablation in combination with the applied histology procedures, all other tissues of Mtz-treated *R2-col2a1a:CFP-NTR* transgenic larvae appear unaffected **(D)**. Scale bars: 200 µm **(A, B)**, 100 µm (A', B'), 20 µm **(C, D)**. Abbreviations: nc = notochord, ns = notochord sheath.

References

1. Urist MR, Strates BS. Bone morphogenetic protein. *J Dent Res* (1971) 50(6):1392–406. doi: 10.1177/00220345710500060601

2. Dimitriou R, Giannoudis PV. Discovery and development of bmps. *Injury* (2005) 36(Suppl 3):S28–33. doi: 10.1016/j.injury.2005.07.031

3. Wu X, Shi W, Cao X. Multiplicity of bmp signaling in skeletal development. *Ann N Y Acad Sci* (2007) 1116:29–49. doi: 10.1196/annals.1402.053

4. Wu M, Chen G, Li YP. Tgf-beta and bmp signaling in osteoblast, skeletal development, and bone formation, homeostasis and disease. *Bone Res* (2016) 4:16009. doi: 10.1038/boneres.2016.9

5. Tassabehji M, Fang ZM, Hilton EN, McGaughran J, Zhao Z, de Bock CE, et al. Mutations in Gdf6 are associated with vertebral segmentation defects in klippel-feil syndrome. *Hum Mutat* (2008) 29(8):1017–27. doi: 10.1002/humu.20741

6. Ye M, Berry-Wynne KM, Asai-Coakwell M, Sundaresan P, Footz T, French CR, et al. Mutation of the bone morphogenetic protein Gdf3 causes ocular and skeletal anomalies. *Hum Mol Genet* (2010) 19(2):287–98. doi: 10.1093/hmg/ddp496

7. Frikha R. Klippel-feil syndrome: A review of the literature. *Clin Dysmorphol* (2020) 29(1):35–7. doi: 10.1097/MCD.0000000000000301

8. Mucha BE, Hashiguchi M, Zinski J, Shore EM, Mullins MC. Variant bmp receptor mutations causing fibrodysplasia ossificans progressiva (Fop) in humans show bmp ligand-independent receptor activation in zebrafish. *Bone* (2018) 109:225–31. doi: 10.1016/j.bone.2018.01.002

9. Meng X, Wang H, Hao J. Recent progress in drug development for fibrodysplasia ossificans progressiva. *Mol Cell Biochem* (2022) 477(10):2327–34. doi: 10.1007/s11010-022-04446-9

10. Pignolo RJ, Pacifici M. Retinoid agonists in the targeting of heterotopic ossification. *Cells* (2021) 10(11). doi: 10.3390/cells10113245

11. Smilde BJ, Botman E, de Ruiter RD, Smit JM, Teunissen BP, Lubbers WD, et al. Monitoring and management of fibrodysplasia ossificans progressiva: Current perspectives. *Orthop Res Rev* (2022) 14:113–20. doi: 10.2147/ORR.S337491

12. Schaffer AA, Kaplan FS, Tracy MR, O'Brien ML, Dormans JP, Shore EM, et al. Developmental anomalies of the cervical spine in patients with fibrodysplasia ossificans progressiva are distinctly different from those in patients with klippel-feil syndrome: Clues from the bmp signaling pathway. *Spine (Phila Pa 1976)* (2005) 30(12):1379–85. doi: 10.1097/01.brs.0000166619.22832.2c

13. Weston AD, Hoffman LM, Underhill TM. Revisiting the role of retinoid signaling in skeletal development. *Birth Defects Res C Embryo Today* (2003) 69 (2):156–73. doi: 10.1002/bdrc.10010

14. Adams SL, Cohen AJ, Lassova L. Integration of signaling pathways regulating chondrocyte differentiation during endochondral bone formation. *J Cell Physiol* (2007) 213(3):635–41. doi: 10.1002/jcp.21262

15. Green AC, Martin TJ, Purton LE. The role of vitamin a and retinoic acid receptor signaling in post-natal maintenance of bone. *J Steroid Biochem Mol Biol* (2016) 155(Pt A):135–46. doi: 10.1016/j.jsbmb.2015.09.036

16. Cowan CM, Aalami OO, Shi YY, Chou YF, Mari C, Thomas R, et al. Bone morphogenetic protein 2 and retinoic acid accelerate in vivo bone formation, osteoclast recruitment, and bone turnover. *Tissue Eng* (2005) 11(3-4):645–58. doi: 10.1089/ten.2005.11.645

17. Giampietro PF, Raggio CL, Blank RD, McCarty C, Broeckel U, Pickart MA. Clinical, genetic and environmental factors associated with congenital vertebral malformations. *Mol Syndromol* (2013) 4(1-2):94–105. doi: 10.1159/000345329

18. Roberts C. Regulating retinoic acid availability during development and regeneration: The role of the Cyp26 enzymes. *J Dev Biol* (2020) 8(1). doi: 10.3390/jdb8010006

19. Laue K, Janicke M, Plaster N, Sonntag C, Hammerschmidt M. Restriction of retinoic acid activity by Cyp26b1 is required for proper timing and patterning of osteogenesis during zebrafish development. *Development* (2008) 135(22):3775–87. doi: 10.1242/dev.021238

20. Brunet LJ, McMahon JA, McMahon AP, Harland RM. Noggin, cartilage morphogenesis, and joint formation in the mammalian skeleton. *Science* (1998) 280 (5368):1455–7. doi: 10.1126/science.280.5368.1455

21. Fleming A, Keynes R, Tannahill D. A central role for the notochord in vertebral patterning. *Development* (2004) 131(4):873–80. doi: 10.1242/dev.00952

22. Harris MP, Arratia G. Patterning the spine. *Elife* (2018) 7. doi: 10.7554/eLife.37288

23. Lleras Forero L, Narayanan R, Huitema LF, VanBergen M, Apschner A, Peterson-Maduro J, et al. Segmentation of the zebrafish axial skeleton relies on notochord sheath cells and not on the segmentation clock. *Elife* (2018) 7. doi: 10.7554/eLife.33843

24. Pogoda HM, Riedl-Quinkertz I, Lohr H, Waxman JS, Dale RM, Topczewski J, et al. Direct activation of chordoblasts by retinoic acid is required for segmented centra mineralization during zebrafish spine development. *Development* (2018) 145(9). doi: 10.1242/dev.159418

25. Wopat S, Bagwell J, Sumigray KD, Dickson AL, Huitema LFA, Poss KD, et al. Spine patterning is guided by segmentation of the notochord sheath. *Cell Rep* (2018) 22 (8):2026–38. doi: 10.1016/j.celrep.2018.01.084

26. Grotmol S, Kryvi H, Nordvik K, Totland GK. Notochord segmentation may lay down the pathway for the development of the vertebral bodies in the Atlantic salmon. *Anat Embryol (Berl)* (2003) 207(4-5):263–72. doi: 10.1007/s00429-003-0349-y

27. Dale RM, Topczewski J. Identification of an evolutionarily conserved regulatory element of the zebrafish Col2a1a gene. *Dev Biol* (2011) 357(2):518–31. doi: 10.1016/j.ydbio.2011.06.020

28. Witten PE, Hall BK. *The notochord: Development, evolution and contributions to the vertebral column*. Boca Raton: Taylor & Francis Group (2022). p. 266.

29. Bensimon-Brito A, Cardeira J, Cancela ML, Huysseune A, Witten PE. Distinct patterns of notochord mineralization in zebrafish coincide with the localization of osteocalcin isoform 1 during early vertebral centra formation. *BMC Dev Biol* (2012) 12:28. doi: 10.1186/1471-213X-12-28

30. Fleming A, Kishida MG, Kimmel CB, Keynes RJ. Building the backbone: The development and evolution of vertebral patterning. *Development* (2015) 142(10):1733–44. doi: 10.1242/dev.118950

31. Huitema LF, Apschner A, Logister I, Spoorendonk KM, Bussmann J, Hammond CL, et al. Entpd5 is essential for skeletal mineralization and regulates phosphate homeostasis in zebrafish. *Proc Natl Acad Sci U.S.A.* (2012) 109(52):21372–7. doi: 10.1073/pnas.1214231110

32. Franz-Odendaal TA, Hall BK, Witten PE. Buried alive: How osteoblasts become osteocytes. *Dev Dyn* (2006) 235(1):176–90. doi: 10.1002/dvdy.20603

33. Dallas SL, Bonewald LF. Dynamics of the transition from osteoblast to osteocyte. *Ann N Y Acad Sci* (2010) 1192:437–43. doi: 10.1111/j.1749-6632.2009.05246.x

34. Jeradi S, Hammerschmidt M. Retinoic acid-induced premature osteoblast-to-Preosteocyte transitioning has multiple effects on calvarial development. *Development* (2016) 143(7):1205–16. doi: 10.1242/dev.129189

35. Spoorendonk KM, Peterson-Maduro J, Renn J, Trowe T, Kranenbarg S, Winkler C, et al. Retinoic acid and Cyp26b1 are critical regulators of osteogenesis in the axial skeleton. *Development* (2008) 135(22):3765–74. doi: 10.1242/dev.024034

36. Chocron S, Verhoeven MC, Rentzsch F, Hammerschmidt M, Bakkers J. Zebrafish Bmp4 regulates left-right asymmetry at two distinct developmental time points. *Dev Biol* (2007) 305(2):577–88. doi: 10.1016/j.ydbio.2007.03.001

37. Begemann G, Marx M, Mebus K, Meyer A, Bastmeyer M. Beyond the neckless phenotype: Influence of reduced retinoic acid signaling on motor neuron development in the zebrafish hindbrain. *Dev Biol* (2004) 271(1):119–29. doi: 10.1016/j.ydbio.2004.03.033

38. Isales GM, Hipszer RA, Raftery TD, Chen A, Stapleton HM, Volz DC. Triphenyl phosphate-induced developmental toxicity in zebrafish: Potential role of the retinoic acid receptor. *Aquat Toxicol* (2015) 161:221–30. doi: 10.1016/j.aquatox.2015.02.009

39. Curado S, Stainier DY, Anderson RM. Nitroreductase-mediated Cell/Tissue ablation in zebrafish: A spatially and temporally controlled ablation method with applications in developmental and regeneration studies. *Nat Protoc* (2008) 3(6):948–54. doi: 10.1038/nprot.2008.58

40. Bussmann J, Schulte-Merker S. Rapid bac selection for Tol2-mediated transgenesis in zebrafish. *Development* (2011) 138(19):4327–32. doi: 10.1242/dev.068080

41. Kawakami K, Shima A. Identification of the Tol2 transposase of the medaka fish oryzias latipes that catalyzes excision of a nonautonomous Tol2 element in zebrafish danio rerio. *Gene* (1999) 240(1):239–44. doi: 10.1016/s0378-1119(99)00444-8

42. Kwan KM, Fujimoto E, Grabher C, Mangum BD, Hardy ME, Campbell DS, et al. The Tol2kit: A multisite gateway-based construction kit for Tol2 transposon transgenesis constructs. *Dev Dyn* (2007) 236(11):3088–99. doi: 10.1002/dvdy.21343

43. Pyati UJ, Webb AE, Kimelman D. Transgenic zebrafish reveal stage-specific roles for bmp signaling in ventral and posterior mesoderm development. *Development* (2005) 132(10):2333–43. doi: 10.1242/dev.01806

44. Row RH, Kimelman D. Bmp inhibition is necessary for post-gastrulation patterning and morphogenesis of the zebrafish tailbud. *Dev Biol* (2009) 329(1):55–63. doi: 10.1016/j.ydbio.2009.02.016

45. Pfaffl MW, Tichopad A, Prgomet C, Neuvians TP. Determination of stable housekeeping genes, differentially regulated target genes and sample integrity: Bestkeeper–Excel-Based tool using pair-wise correlations. *Biotechnol Lett* (2004) 26 (6):509–15. doi: 10.1023/b:bile.0000019559.84305.47

46. Windhausen T, Squifflet S, Renn J, Muller M. Bmp signaling regulates bone morphogenesis in zebrafish through promoting osteoblast function as assessed by their nitric oxide production. *Molecules* (2015) 20(5):7586–601. doi: 10.3390/molecules20057586

47. Smith A, Avaron F, Guay D, Padhi BK, Akimenko MA. Inhibition of bmp signaling during zebrafish fin regeneration disrupts fin growth and scleroblasts differentiation and function. *Dev Biol* (2006) 299(2):438–54. doi: 10.1016/j.ydbio.2006.08.016

48. Sotillos S, De Celis JF. Interactions between the notch, egfr, and decapentaplegic signaling pathways regulate vein differentiation during drosophila pupal wing development. *Dev Dyn* (2005) 232(3):738–52. doi: 10.1002/dvdy.20270

49. Wang W, Hu YF, Pang M, Chang N, Yu C, Li Q, et al. Bmp and notch signaling pathways differentially regulate cardiomyocyte proliferation during ventricle regeneration. *Int J Biol Sci* (2021) 17(9):2157–66. doi: 10.7150/ijbs.59648

50. Pomreinke AP, Soh GH, Rogers KW, Bergmann JK, Blassle AJ, Muller P. Dynamics of bmp signaling and distribution during zebrafish dorsal-ventral patterning. *Elife* (2017) 6. doi: 10.7554/eLife.25861

51. Zinski J, Bu Y, Wang X, Dou W, Umulis D, Mullins MC. Systems biology derived source-sink mechanism of bmp gradient formation. *Elife* (2017) 6. doi: 10.7554/eLife.22199

52. Winkler DG, Sutherland MK, Geoghegan JC, Yu C, Hayes T, Skonier JE, et al. Osteocyte control of bone formation *Via* sclerostin, a novel bmp antagonist. *EMBO J* (2003) 22(23):6267–76. doi: 10.1093/emboj/cdg599

53. Ofer L, Dean MN, Zaslansky P, Kult S, Shwartz Y, Zaretsky J, et al. A novel nonosteocytic regulatory mechanism of bone modeling. *PloS Biol* (2019) 17(2): e3000140. doi: 10.1371/journal.pbio.3000140

54. Chen Y, Schier AF. Lefty proteins are long-range inhibitors of squint-mediated nodal signaling. *Curr Biol* (2002) 12(24):2124–8. doi: 10.1016/s0960-9822(02)01362-3

55. Muller P, Rogers KW, Jordan BM, Lee JS, Robson D, Ramanathan S, et al. Differential diffusivity of nodal and lefty underlies a reaction-diffusion patterning system. *Science* (2012) 336(6082):721–4. doi: 10.1126/science.1221920

56. Matsuoka T, Ahlberg PE, Kessaris N, Iannarelli P, Dennehy U, Richardson WD, et al. Neural crest origins of the neck and shoulder. *Nature* (2005) 436(7049):347–55. doi: 10.1038/nature03837

57. Culbert AL, Chakkalakal SA, Theosmy EG, Brennan TA, Kaplan FS, Shore EM. Alk2 regulates early chondrogenic fate in fibrodysplasia ossificans progressiva heterotopic endochondral ossification. *Stem Cells* (2014) 32(5):1289–300. doi: 10.1002/stem.1633

58. Weston AD, Rosen V, Chandraratna RA, Underhill TM. Regulation of skeletal progenitor differentiation by the bmp and retinoid signaling pathways. *J Cell Biol* (2000) 148(4):679–90. doi: 10.1083/jcb.148.4.679

59. Weston AD, Chandraratna RA, Torchia J, Underhill TM. Requirement for rar-mediated gene repression in skeletal progenitor differentiation. *J Cell Biol* (2002) 158 (1):39–51. doi: 10.1083/jcb.200112029

60. Pacifici M, Cossu G, Molinaro M, Tato F. Vitamin a inhibits chondrogenesis but not myogenesis. *Exp Cell Res* (1980) 129(2):469–74. doi: 10.1016/0014-4827(80)90517-0

61. Chakkalakal SA, Uchibe K, Convente MR, Zhang D, Economides AN, Kaplan FS, et al. Palovarotene inhibits heterotopic ossification and maintains limb mobility and growth in mice with the human Acvr1(R206h) fibrodysplasia ossificans progressiva (Fop) mutation. *J Bone Miner Res* (2016) 31(9):1666–75. doi: 10.1002/jbmr.2820

62. Hoy SM. Palovarotene: First approval. *Drugs* (2022) 82(6):711–6. doi: 10.1007/s40265-022-01709-z

63. Shimono K, Tung WE, Macolino C, Chi AH, Didizian JH, Mundy C, et al. Potent inhibition of heterotopic ossification by nuclear retinoic acid receptor-gamma agonists. *Nat Med* (2011) 17(4):454–60. doi: 10.1038/nm.2334

64. McMillan SC, Zhang J, Phan HE, Jeradi S, Probst L, Hammerschmidt M, et al. A regulatory pathway involving retinoic acid and calcineurin demarcates and maintains joint cells and osteoblasts in regenerating fin. *Development* (2018) 145(11). doi: 10.1242/dev.161158

65. Laue K, Pogoda HM, Daniel PB, van Haeringen A, Alanay Y, von Ameln S, et al. Craniosynostosis and multiple skeletal anomalies in humans and zebrafish result from a defect in the localized degradation of retinoic acid. *Am J Hum Genet* (2011) 89 (5):595–606. doi: 10.1016/j.ajhg.2011.09.015

66. Wang W, Zhou C, Feng Z, Li H, Zhang Y, Bao B, et al. Plga-based control release of noggin blocks the premature fusion of cranial sutures caused by retinoic acid. *Appl Microbiol Biotechnol* (2019) 103(1):291–301. doi: 10.1007/s00253-018-9457-8

frontiers | Frontiers in Endocrinology

TYPE Original Research
PUBLISHED 29 May 2023
DOI 10.3389/fendo.2023.1122351

OPEN ACCESS

EDITED BY
Christoph Winkler,
National University of Singapore, Singapore

REVIEWED BY
Sarah Kelly McMenamin,
Boston College, United States
David Karasik,
Bar-Ilan University, Israel

*CORRESPONDENCE
Franziska Knopf
franziska.knopf@tu-dresden.de

RECEIVED 12 December 2022
ACCEPTED 09 May 2023
PUBLISHED 29 May 2023

CITATION
Fleischhauer L, López-Delgado AC, Geurtzen K and Knopf F (2023) Glucocorticoid effects in the regenerating fin reflect tissue homeostasis disturbances in zebrafish by affecting Wnt signaling. *Front. Endocrinol.* 14:1122351. doi: 10.3389/fendo.2023.1122351

Glucocorticoid effects in the regenerating fin reflect tissue homeostasis disturbances in zebrafish by affecting Wnt signaling

Lisa Fleischhauer[1,2], Alejandra Cristina López-Delgado[1,2], Karina Geurtzen[1,3] and Franziska Knopf[1,2]*

[1]CRTD – Center for Regenerative Therapies, TU Dresden, Dresden, Germany, [2]Center for Healthy Aging, Faculty of Medicine Carl Gustav Carus TU Dresden, Dresden, Germany, [3]Laboratory of Clinical and Experimental Endocrinology, Department of Chronic Diseases, Metabolism and Ageing, KU Leuven, Leuven, Belgium

As a treatment for various immune-mediated diseases, the use of glucocorticoids as anti-inflammatory and immunosuppressive agents is common practice. However, their use is severely hampered by the risk of the development of adverse effects such as secondary osteoporosis, skin atrophy, and peptic ulcer formation. The exact molecular and cellular mechanisms underlying those adverse effects, which involve most major organ systems, are not yet fully understood. Therefore, their investigation is of great importance to improve treatment regimens for patients. Here, we investigated the effects of the glucocorticoid prednisolone on cell proliferation and Wnt signaling in homeostatic skin and intestinal tissue and compared them to the anti-regenerative effects in zebrafish fin regeneration. We also investigated a potential recovery from the glucocorticoid treatment and the impact of short-term treatment with prednisolone. We identified a dampening effect of prednisolone on Wnt signaling and proliferation in highly proliferative tissues, namely the skin and intestine, as well as reduced fin regenerate length and Wnt reporter activity in the fin. The presence of the Wnt inhibitor Dickkopf1 was enhanced in prednisolone treated skin tissue. A decreased number of mucous producing goblet cells was observed in the intestine of prednisolone treated zebrafish. Unexpectedly, proliferation in bone forming osteoblasts of the skull, homeostatic scales, as well as the brain was not decreased, opposite to the observed effects in the skin, fin, and intestine. Short-term treatment with prednisolone for a few days did not significantly alter fin regenerate length, skin cell proliferation, intestinal leukocyte number and proliferation of intestinal crypt cells. However, it affected the number of mucous-producing goblet cells in the gut. Likewise, discontinuation of prednisolone treatment for a few days saved the skin and intestine from a significant reduction of skin and intestinal cell proliferation, intestinal leukocyte number and regenerate length, but did not

rescue goblet cell number. The suppressive effects of glucocorticoids in highly proliferative tissues may be relevant in the context of their therapeutic applications in patients with inflammatory diseases.

KEYWORDS

glucocorticoid, zebrafish, fin regeneration, Wnt signaling, cell proliferation, skin, intestine, goblet cell

1 Introduction

Glucocorticoids (GCs) are a group of commonly used potent therapeutic agents to treat immune-mediated diseases in humans, because of their anti-inflammatory and immunosuppressive functions. Due to their lipophilic character, GCs can freely diffuse through the cell membrane and directly bind to the glucocorticoid receptor (GR) located in the cells' cytoplasm. Upon binding to the GR, GCs lead to a conformational change and the translocation of the GR into the nucleus. In the nucleus, the GR either interacts with other DNA-bound transcription factors or directly binds to DNA sequences known as GC response elements to exert the signaling molecule's function (1). *Via* the GR-DNA interaction, GCs increase gene expression of anti-inflammatory proteins such as Lipocortin-1, Interleukin-1 receptor, and Interleukin-10 (2). Depending on the type and physiological state of the cell, the GR can regulate many physiological functions including energy homeostasis, embryonic and postembryonic development, and the stress response (3). GCs show several adverse effects that involve most major organ systems. In particular, long-term use of GCs is associated with a rapid and pronounced decrease in bone mineral density and an increased fracture risk. This undesired consequence is a common form of secondary osteoporosis and is known as GC-induced osteoporosis (4). Depending on their potency and the duration of the therapy, GCs have been shown to be an inducer of numerous cutaneous side effects. Skin atrophy is the most frequent side effect of long-term topical treatment, by which the skin becomes thin and fragile. Atrophy of the skin affects all parts of the skin and results in increased permeability of the stratum corneum barrier, the outermost layer of the epidermis, accounting for increased transepidermal water loss (2). This effect was reported to be a result of GCs suppressing cutaneous cell proliferation and protein synthesis in particular of keratinocytes and dermal fibroblasts (5). Ultimately, GC treatment can result in irreversible stretch marks and disturbed wound healing (2). Furthermore, the use of GCs in combination with non-steroidal anti-inflammatory drugs is associated with a twofold increase in the risk of gastrointestinal adverse reactions among patients and a significant rise in the risk of developing peptic ulcer disease (6). Nevertheless, GCs are a regular treatment option for patients with inflammatory intestinal diseases such as Bowel's disease (7).

Zebrafish have become an important model organism to study vertebrate development, mimic human diseases and investigate complex tissue regeneration, the latter due to their spectacular capability to regenerate various organs even after extensive trauma (8, 9). Genetic and chemical screens can be performed at low cost, and the identification and investigation of gene function in zebrafish is feasible because of their genetic amenability. The amputated part of the zebrafish fin is readily replaced and therefore provides a valuable model to study regeneration (10). Previously, effects of sustained GC-treatment on bone regeneration have been investigated by using the zebrafish fin, skull and spine. Rapid anti-inflammatory, bone inhibitory and anti-regenerative effects were observed upon treatment with the synthetic GC prednisolone in injured bone. These effects were characterized by a reduction of innate immune cells (macrophages), reduced fin regenerate length, impaired osteoblast (bone matrix forming cell) proliferation and their diminished differentiation (11). Anti-osteogenic effects were discovered in tissues undergoing high rates of proliferation, while bone volume was unaltered in the uninjured spine after a 2-month GC treatment (11). Studies on mice documented an induction of autophagy and partially even apoptosis of osteoblasts and terminally differentiated osteoblasts (osteocytes) in the presence of GCs (12, 13). Furthermore, a continued reduction in osteoblast activity subsequent to an elevation in osteoclast activity, as well as an increase of Wnt/β-catenin antagonists such as Dickkopf1 and Sclerostin were observed upon GC treatment (14, 15). Expression of Wnt inhibitor genes by osteocytes during the exposure with GC were identified (12, 13).

Wnt signaling is a signaling pathway that plays a key role in regulating proliferation and differentiation in a wide variety of cell types. This signaling pathway can be classified into i) β-catenin-dependent canonical Wnt signaling and ii) β-catenin-independent non-canonical Wnt signaling. Canonical Wnt/β-catenin signaling regulates gene expression very early during the fin regeneration process and plays an important role in blastemal cell proliferation (16, 17). In the mammalian intestine and skin, Wnt signaling is a crucial regulator of organ development and adult homeostasis. It controls epidermal cell fate specification, morphogenesis, and hair follicle induction during skin development in mammals and is crucial for scale development and regeneration in teleost fish (18, 19). Later on, it regulates epidermal stem cell activation, maintenance and fate determination (19). At the base of mammalian intestinal crypts, rapidly cycling stem cells are marked by the expression of LGR5, which is a receptor that enhances Wnt/β-catenin signaling. LGR5+ cells are necessary for intestinal homeostasis by continuously generating new cells of the intestinal epithelium and Wnt signaling is essential for this process

to happen (20). In clinical studies focusing on patients receiving initial GC therapy to treat systemic autoimmune disease, an increase of Wnt co-receptor inhibitors in the early phase of therapy along with a subsequent reduction of the ratio of Wnt to Wnt-ligand inhibitors could be observed in the serum, suggesting a suppressive effect of GCs on Wnt/β-catenin signaling leading to impaired bone formation (15, 21).

The above findings suggest that side effects of GC treatment on bone, skin and intestinal tissue might result from impaired cell proliferation, differentiation, and deprived Wnt signaling. However, the effects that GCs exert on Wnt signaling and cell proliferation beyond bone tissue in zebrafish are not well understood. Moreover, the reversibility of putative inhibitory effects on the above tissues is not yet described. This study aimed to close this knowledge gap by examining Wnt signaling and cell proliferation in the zebrafish skin, intestine and bone tissue in conjunction with fin regenerates undergoing GC treatment. Immunohistochemistry was performed on zebrafish tissues of individuals carrying a Wnt signaling reporter that had been exposed to high dose prednisolone treatment (22). In order to test for the reversibility of Wnt- and proliferation suppressive effects GC treatment was discontinued in some specimens. Proliferation and the intensity of the Wnt signaling reporter were used as readouts for tissue growth. To investigate the impact of prednisolone on proliferation and Wnt signaling in injured tissue, an assessment of treatment effects on fin regeneration was included, by examining regenerate length and Wnt activity in the fin's proliferation zone. The resulting data show that reduced Wnt activity and regenerate length correlate well with defects in intestinal organ proliferation and reduced Wnt signaling in the skin.

2 Methods

2.1 Transgenic fish lines

For all the performed immunohistochemical experiments the transgenic zebrafish line Tg(*7xTCF-XIa.Siam*:nlsmCherry)^{ia5} (22) was used as a Wnt reporter line. In these zebrafish, the expression of the monomeric Cherry protein (mCherry) is under the control of seven multimerized TCF responsive elements upstream of the minimal promoter of the *Xenopus laevis* direct β-catenin target gene *siamois*, leading to mCherry fluorescence in Wnt signaling+ cells (22). mRNA used for RT-PCR expression analysis of Wnt/Notch/Fgf target genes and *dickkopf1b* was isolated from a different transgenic reporter zebrafish line [Tg(*Ola.Sp7:NLS-GFP*)^{zf132};Tg(*mpeg*:mCherry)^{gl23}] (23, 24).

2.2 Fish husbandry, fin clipping and GC treatment

All procedures were performed in accordance with the animal handling and research regulations of the Landesdirektion Sachsen (permit numbers AZ DD25-5131/354/87, DD25-5131/450/4, 25-5131/496/56 and amendments). Fish were bred and maintained as described (25). The caudal fin of the zebrafish was clipped and left to regenerate under different treatment conditions. Directly after amputation zebrafish were either treated for 21 days with dimethylsulfoxide (DMSO) or 50 μM prednisolone as described previously (11, 26). In two other groups zebrafish were treated for 17 days with DMSO followed by 4 days of prednisolone treatment (short-term treatment) or alternatively for 17 days with prednisolone followed by 4 days of DMSO treatment (recovery). To isolate mRNA from regenerating caudal fins, treatment was performed for 7 days starting directly after amputation.

2.3 Imaging of fin regenerates

Regeneration of the fin was imaged in 0.02% MS222 (Merck)-anaesthetized individuals with a Zeiss SteREO Discovery.V12 stereomicroscope equipped with a AxioCam MRm and AxioVison software version 4.7.1.0. at 9, 14, 17, and 21 days post amputation (dpa), respectively. Imaging was reduced to a minimum of time points to ensure low experimental burden to the animals and started at 9 dpa as suppression of fin regenerate growth by prednisolone is robust at this stage (11).

2.4 Immunohistochemistry

2.4.1 Fixation and decalcification of zebrafish

Zebrafish were euthanized at 21 dpa by using 0.1% MS222 and head and trunk regions were separately fixed in 4% paraformaldehyde (PFA, Electron Microscopy Sciences, 15710) in phosphate buffered saline (PBS) at 4°C overnight. The next day, specimens were transferred to a 1:1 mix of 4% PFA/PBS and Osteosoft (Merck) for one day. Thereafter, samples were transferred to Osteosoft for one additional day, after which they were transferred to PBS at 4°C for a 4-day wash. PBS was then exchanged with fresh PBS and remained in it for another three days, after which paraffin embedding was performed.

2.4.2 Paraffin embedding and sectioning

Histological slides of the zebrafish tissues embedded in paraffin were generated by the histology facility of the CMCB (Center for Molecular and Cellular Bioengineering, Susanne Weiche and colleagues). First, the samples were dehydrated and infiltrated by using the 13:45 hour-program in the Microm STP 420D Tissue Processor (Thermo Fisher Scientific^{TM} Inc.). Then, the samples were washed for 2 minutes with distilled water before they were dehydrated in an ascending ethanol (EtOH) series (45 minutes 40% EtOH, 45 minutes 70% EtOH, three times 60 minutes 96% EtOH, two times 60 minutes 100% EtOH). Finally, the samples were incubated twice in xylene for 50 minutes and infiltrated with Paraffin for four rounds for 60 minutes each time.

Paraffin-embedded zebrafish slides (1 μm transverse head sections, 2 μm sagittal trunk sections) at different stages (9, 14, 17 and 21 dpa) were generated with the help of the Rotary Microtome Microm HM 355 S (Thermo Fisher Scientific^{TM} Inc.) by the histology facility of the CMCB (Susanne Weiche and colleagues).

2.4.3 Rehydration of paraffin-embedded tissue slides

Paraffin slides were immersed in xylene (Carl Roth) two times for 10 minutes to remove paraffin from the tissue sections. Successively, xylene was removed by immersion in a decreasing EtOH-series (100%, 95%, 70%, 50%) twice in 100% EtOH for 10 minutes followed by lower concentrations of EtOH once for 5 minutes each (Fisher Chemical). After a final rinse in deionized water (dH_2O), the samples were rehydrated in wash buffer (1xPBS) for 10 minutes.

2.4.4 Antigen retrieval

Antigen retrieval was performed on slides before adding the primary antibody mix of dsRed, Proliferating-Cell-Nuclear-Antigen (PCNA) and Phospho-Histone H3 (PH3). Similarly, antigen retrieval was carried out before immunohistochemistry with Dickkopf1 (Dkk1) antibody. Staining for L-plastin was completed without antigen retrieval. Antigen retrieval was performed with the help of the histology facility of the CMCB (Susanne Weiche). After rehydration, slides were put into a heat cycler with 10 mM sodium citrate pH6. The samples were gradually heated up to 110°C in a DC-Module (Zytomed) and kept for 5 minutes at this temperature. Following this, the slides were left in the cycler for 30 minutes to cool down until immunohistochemistry was performed.

2.4.5 Blocking, antibody treatment and DAPI staining

The rehydrated, and antigen retrieved (in case for dsRed, PCNA and PH3), tissue sections were incubated in blocking buffer (10% NGS, normal goat serum, Gibco, 16210-064) for 30 minutes at room temperature (RT), to prevent unspecific binding of the primary antibody to the samples. Following this, the tissue sections were incubated with primary antibody mix against dsRed (rabbit, polyclonal, 1:500, Clontech, 632496), PH3 (rabbit, polyclonal, 1:400, Merck Millipore, 06-570), and PCNA (mouse, IgG2a, 1:1000, Dako, M087901-2) or with a primary antibody against L-plastin (rabbit, polyclonal, 1:500, courtesy of Michael Brand) or Dkk1 (rabbit, 1:435, aviva systems biology, San Diego, USA, ARP55048_P050, with reactivity to zebrafish Dkk1 protein according to the manufacturer, raised against the following amino acids of the human DKK1 protein: CARHFWSKICKPVLKEGQ VCTKHRRKGSHGLEIFQRCYCGEGLSCRIQKD) alone, diluted in blocking buffer at 2-8°C overnight. The next day, the surplus primary antibody was removed by washing the slides 3 times for 15 minutes with washing buffer (1xPBS). Secondary antibodies Alexa Fluor 555 goat anti-rabbit (1:800, Invitrogen, A21428) and Alexa Fluor 488 goat anti-mouse (1:800, Invitrogen, A11029) were diluted in 1xPBS and applied for 60 minutes at RT. Again, the slides were washed 3 times for 15 minutes with washing buffer (1xPBS), to remove the surplus antibody. Lastly, DAPI (4',6-Diamidino-2-phenylindol, 1:5000 of 1 mg/ml stock in 1xPBS) was added to the slides and the samples were incubated for 2-5 minutes at RT, to stain cell nuclei. The slides were rinsed once with 1xPBS and mounted with an anti-fade mounting media (Vectashield®). Slides were stored at 2-8°C until visualization with the widefield fluorescence microscope.

2.5 Imaging of tissue sections, image analyses, and image processing

Images were obtained using an inverted Zeiss Axio Imager (widefield fluorescence mode) at a magnification of 40X. Mitotic nuclei were detected very rarely which is why PCNA was solely used as a readout for cell proliferation. This is in line with the fact that many more cells express PCNA during the cell cycle than PH3, which is only detectable during mitosis (27, 28). Images were acquired using identical settings for different groups. Image contrast, brightness, exposure and blacklevel were adjusted using the same settings across samples using GNU Image Manipulation Program (GIMP, GIMP 2.10.22). Intensity measurements of the mCherry signal in fin and skin were conducted using the Plot Profile Tool in Image J/Fiji Software. In the fin, the intensity was measured along the second, third and fourth fin ray of 5 to 8 individuals per group. In all other analyses of the skin, intestine, brain and skull, 5 individuals were used per group. Both sexes of the same age and housing conditions were used, with a maximum of 25% males per experimental group. We did not investigate sex-specific differences in our analyses. For the assessment of PCNA, Dkk1 and mCherry signal in the skin, different skin regions of the zebrafish head were assessed. The most representative regions of the data were chosen for figures. For measurements of mCherry signal in the skin, the plot profile tool was used on maximum width of 300 in Image J/Fiji Software (ImageJ 2.3.0/1.53q). Intensity was measured on three different areas per image starting from the outermost layer of the skin and proceeding inwards. First, two sections were analyzed each, with three measurements per section. From this, one fish average was calculated and used for the statistical analysis. Proliferating cell quantification and leukocyte quantifications was performed using the Image J/Fiji (ImageJ 2.3.0/1.53q) cell counter tool. PCNA+ cells were counted per microscopic image, if not stated otherwise. Overlay of different channel images was performed using Image J/Fiji Software (ImageJ 2.3.0/1.53q) and images were arranged with GIMP. The scheme displaying scale anatomy was created using DrawboardPDF (Drawboard 6.36.34.0).

2.6 RT-PCR

RNA samples were generated from fins at 7 dpa treated with DMSO or Prednisolone from 0 to 7 dpa using Trizol as described (11). cDNA was synthetized with the Transcriptor First Strand cDNA Synthesis Kit (Roche, 04897030001) according to the manufacturer's instructions. RT-PCR was performed using DreamTaq Green DNA-Polymerase (Thermo Scientific, EP0713). Thermal cycling conditions recommended by the supplier were followed and 35 cycles were used. Primers used were the following (5'-3'): *fosl1b* Fw CCAGTGGTTTCTGCAGTCTT, *fosl1b* Rv AGCTGCTACCCTGTTCCTTT (amplicon size 244 bp), *dkk1b* Fw AATGACCCTGACATGATTCAGC, *dkk1b* Rv AGGCT TGCAGATTTTGGACC (amplicon size 213 bp) (29), *etv5b* Fw CGTTACAATGAGCAGGGTGT, *etv5b* Rv CGTCATACCC AAAACCCTCA (amplicon size 181 bp), *her6* Fw AGCTGCAT

GACACAGATCAA, *her6* Rv AGCTGGAAACCCCCATATAC (amplicon size 212 bp), *actb* Fw TTCACCACCACAGCCG AAAGA, *actb* Rv TACCGCAAGATTCCATACCCA (amplicon size 223 bp). We quantified *dkk1b* expression as this orthologue of human DKK1 has previously been shown to be expressed in regenerating zebrafish fins (17).

2.7 Statistical analyses

Graphpad Prism 9.2.0 for Windows 10 (Graphpad Software, La Jolla California) and R-studio (RStudio 2022.02.1 + 461) were used for statistical analysis and data visualization. Sampled data was tested for normal distribution using the Shapiro-Wilk test. Subsequently, normally distributed data was analyzed by parametric testing, using One-way ANOVA followed by a *post-hoc* Dunnett's multiple comparison test or a two-tailed t-test. Data which did not follow a normal distribution was analyzed by non-parametric testing, using the Kruskal-Wallis test and *post hoc* Dunn's multiple comparison. P-values ≤ 0.05 were considered statistically significant. Data were expressed as mean ± SEM (Standard Error of the Mean) for plot profiles and as mean ± SD (Standard Deviation) for all other graphs. We calculated group averages and SEM/SD based on the number of used individuals in the respective groups in order to display inter-individual variation. The respective required fish averages were calculated from a minimum of 2 sections and 3 fin rays, respectively, per individual. In case of PCNA+ skull osteoblast quantification, 1 section per individual was used; for PCNA+ scale forming cell quantification 6 scales on one section were analyzed per individual For details, see figure legends.

3 Results

3.1 GC treatment decreases fin regenerate length and affects Wnt signaling in the growth zone of the fin

The effect of prednisolone on regeneration and cell proliferation was analyzed by assessing fin regenerate length and Wnt signaling activity in the fin regenerate. Zebrafish were treated for 17 days post amputation (dpa) with prednisolone or DMSO as a control. In order to determine a possible recovery from prednisolone treatment, treatment with prednisolone was stopped at 17 dpa in a subset of zebrafish which were then incubated for 4 days with DMSO. In another subset of zebrafish, a 4-day prednisolone treatment was performed on previously DMSO treated zebrafish from 17 dpa onwards, in order to test for the impact of a short-term treatment during the late regeneration phase. This treatment regime was chosen to allow for sustained suppression of regeneration in terms of regenerate length with growth being stalled in prednisolone treated zebrafish starting at 17 dpa (11). Furthermore, with a total time of 21 days, the experimental burden on animals was reduced to a minimum, considering that longer treatments do not enhance anti-regenerative effects any further [see Figure 1H in (11)]. Regenerate length was measured at 9, 14, 17, and 21 dpa (Figure 1). For all treatments, an increase in regenerate length over time could be observed. Exclusive prednisolone treatment led to a significant reduction in the regenerate length compared to the control DMSO treatment at all-time points. While the fins of zebrafish treated with DMSO regenerated about 1700 µm, fins of prednisolone-treated zebrafish only regenerated 1300 µm within 12 days (from 9 dpa to 21 dpa). Discontinuation of prednisolone treatment after 17 days had a similar effect as prednisolone treatment during the last four days of the experiment; however, it did not significantly alter regenerate length in comparison to the 21-day DMSO control treatment (Figure 1).

Next, the effect of prednisolone on Wnt signaling was assessed by quantifying the signal strength of the Wnt signaling reporter mCherry along the fin ray from the tip of the regenerate down to the amputation plane in the same Tg(*7xTCF-XIa.Siam*:nlsmCherry)^{ia5} zebrafish (22). This allowed the determination of a Wnt-active zone (a region at the fin tip displaying relatively high mCherry expression) in these zebrafish, in addition to assessing signal intensity along the proximo-distal axis of the regrowing tissue (Figures 2, 3). Importantly, Wnt signaling activity correlates with proliferation rates in regenerating zebrafish fins (17). In all fins, no matter the treatment, mCherry signal strength decreased over time, likely reflecting decreased proliferation rates occurring towards completion of regeneration. In comparison to the DMSO control, treatment with prednisolone resulted in a reduced Wnt-reporter signal (lower maximum fluorescence intensity) as well as a shorter Wnt-active zone (see boxes and arrows in Figure 2) at 9 dpa. At 14 dpa, Wnt signaling strength (maximum fluorescence intensity) in both treatment groups was similar, however, a reduction in the length of the Wnt-active zone in the prednisolone-treated zebrafish remained. This difference diminished over time, as the Wnt-active zone length reduced in size up to 21 dpa. Discontinuation of prednisolone treatment, as well as short-term prednisolone treatment in the late regeneration phase showed similar effects, resulting in modest suppression of Wnt activity at 21 dpa.

In order to confirm that Wnt signaling was affected by GC treatment, we performed RT-PCR on prednisolone and control treated regenerating fins. Indeed, *fosl1b (FOS like 1, AP-1 transcription factor subunit b)*, an orthologue to the human Wnt target *FOSL1* (30) was expressed at reduced levels after prednisolone treatment, as were targets of other signaling pathways (Figure 4). This supports the hypothesis that Wnt signaling is reduced upon high GC exposure.

3.2 GC treatment leaves cell proliferation in homeostatic skull bone, scales and brain tissue unaffected

The fact that prednisolone treatment affected regrowth and Wnt signaling as well as osteoblast proliferation during fin regeneration, as reported previously (11), led us to investigate whether proliferation of osteoblasts was altered in homeostatic conditions. Proliferation in cells along the skull bone was generally low, and there was no significant reduction of PCNA staining in these cells (Figures 5A, B). Scales were used as a second readout for bone matrix forming cell proliferation. Cells lining scale

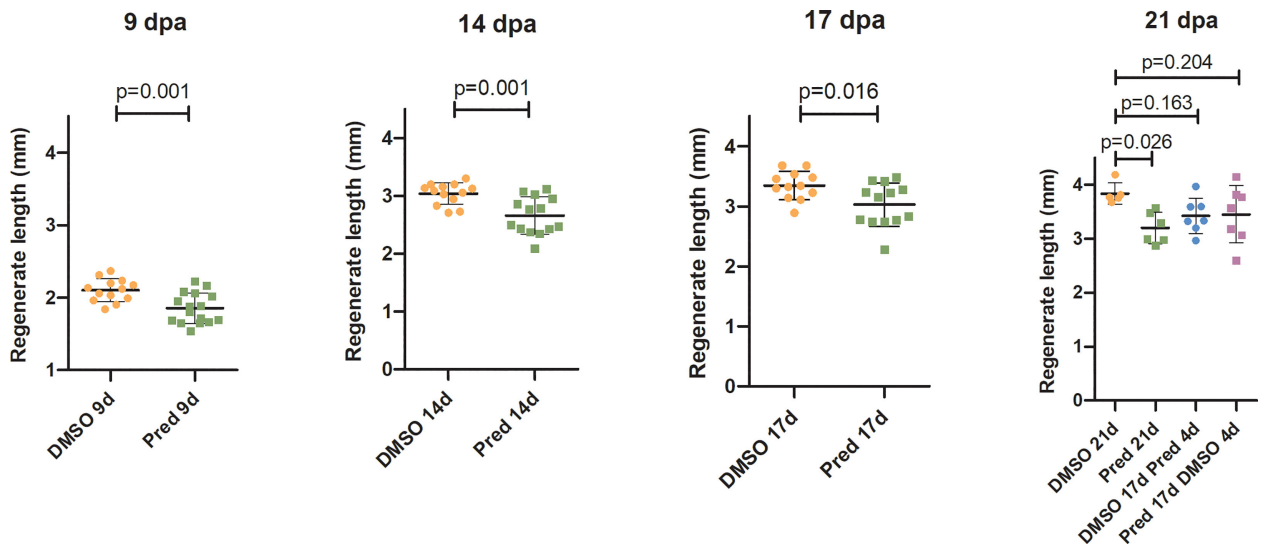

FIGURE 1
Quantification of fin regenerate length during the course of regeneration. Bars represent mean ± SD of fin outgrowth after amputation under different treatment conditions, measured at different times post amputation. Each dot represents one biological replicate. Parametric testing because of normal distribution of data. Statistical significance at 9 dpa, 14, dpa and 17 dpa was tested by two-tailed t-tests and at 21 dpa by *post-hoc* Dunnett's multiple comparison after one-way ANOVA. $n^{(DMSO,9dpa)}$ = 13 (10 females, 3 males), $n^{(Pred,9dpa)}$ = 16 (12 females, 4 males), $n^{(DMSO,14dpa)}$ = 13 (10 females, 3 males), $n^{(Pred,14dpa)}$ = 14 (12 females, 2 males), $n^{(DMSO,17dpa)}$ = 12 (10 females, 2 males), $n^{(Pred,17dpa)}$ = 13 (12 females, 1 male), $n^{(DMSO\ 21d,21dpa)}$ = 5 (4 females, 1 male), $n^{(Pred\ 21d,21dpa)}$ = 6 (6 females), $n^{(DMSO\ 17d\ Pred\ 4d,21dpa)}$ = 7 (6 females, 1 male), $n^{(Pred\ 17d\ DMSO\ 4d,21dpa)}$ = 7 (6 females, 1 male).

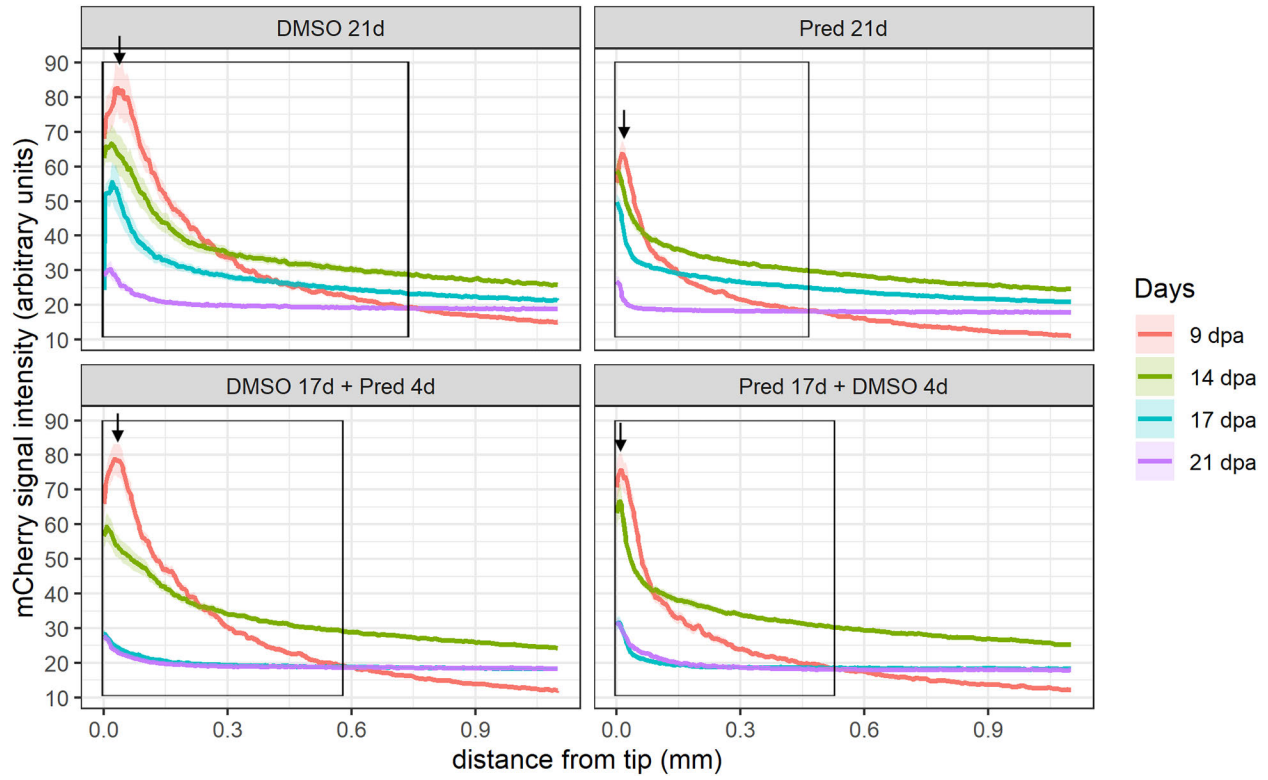

FIGURE 2
Quantification of the *7xTCF-Xia.Siam*:nlsmCherry Wnt reporter expression in the fin regenerate. Lines represent mean ± SEM of mCherry signal intensity for the four different treatments measured at 9 dpa, 14 dpa, 17 dpa, and 21 dpa. Signal was measured from the tip towards the amputation plane. Boxes indicate "Wnt-active zone" at 9 dpa, defined as levels beyond baseline expression levels detected at 21 dpa (i.e. point of intersection of 9 dpa curve with 21 dpa curve). $n^{(DMSO\ 21d,9/14/17/21dpa)}$ = 5 (4 females, 1 male); $n^{(Pred\ 21d,9dpa)}$ = 8 (6 females, 2 males), $n^{(Pred\ 21d,14dpa)}$ = 7 (6 females, 1 male), $n^{(Pred\ 21d,17/21dpa)}$ = 6 (6 females); $n^{(DMSO\ 17d\ Pred\ 4d,9/14dpa)}$ = 8 (6 females, 2 males), $n^{(DMSO\ 17d\ Pred\ 4d,17/21dpa)}$ = 7 (6 females, 1 male); $n^{(Pred\ 17d\ DMSO\ 4d,9dpa)}$ = 8 (6 females, 2 males), $n^{(Pred\ 17d\ DMSO\ 4d,14/17/21dpa)}$ = 7 (6 females, 1 male).

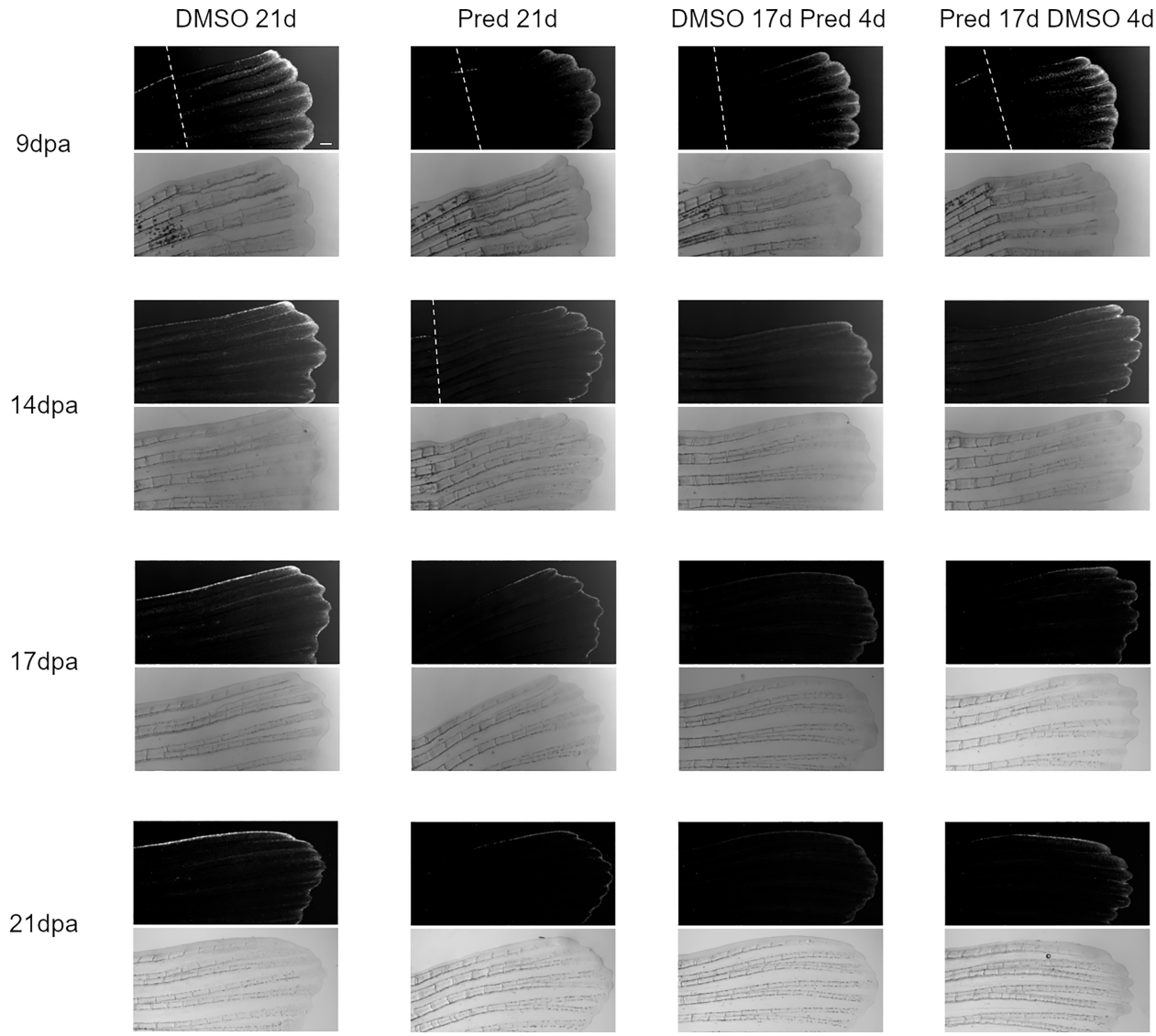

FIGURE 3
Images of the mCherry-fluorescent Wnt-active zone in zebrafish fin regenerates. The *7xTCF-Xia.Siam:*nlsmCherry expression is detectable due to mCherry fluorescence (upper rows). Corresponding brightfield images are shown below. Within one treatment group, the same individual is shown across time points. From left to right: fish underwent 21 days of DMSO, 21 days of prednisolone, 17 days of DMSO followed by 4 days of prednisolone and 17 days of prednisolone followed by 4 days of DMSO treatment. Scalebar 200 µm. The white dotted lines indicate amputation planes in the fluorescence view of the fins. $n^{(DMSO\ 21d,9/14/17/21dpa)} = 5$ (4 females, 1 male); $n^{(Pred\ 21d,9dpa)} = 8$ (6 females, 2 males), $n^{(Pred\ 21d,14dpa)} = 7$ (6 females, 1 male), $n^{(Pred\ 21d,17/21dpa)} = 6$ (6 females); $n^{(DMSO\ 17d\ Pred\ 4d,9/14dpa)} = 8$ (6 females, 2 males), $n^{(DMSO\ 17d\ Pred\ 4d,17/21dpa)} = 7$ (6 females, 1 male); $n^{(Pred\ 17d\ DMSO\ 4d,9dpa)} = 8$ (6 females, 2 males), $n^{(Pred\ 17d\ DMSO\ 4d,14/17/21dpa)} = 7$ (6 females, 1 male).

matrix and cells being located in the growth zone of the scale did not show any significant reduction in PCNA staining (Figure 6). Another tissue, which was unaffected by prednisolone treatment was the brain (telencephalon) which did not show any significant changes in proliferation (Figures 7A, B).

3.3 GC treatment decreases cell proliferation in the skin and intestine, as well as Wnt signaling in the skin

To assess whether the effects of prednisolone on Wnt signaling and tissue growth in the fin reflect the status of signaling pathway activity and potentially tissue turnover in highly proliferative tissues, immunohistochemical staining was performed against mCherry (Wnt signaling reporter) and PCNA in the skin and intestine of treated zebrafish. Furthermore, Dkk1, a Wnt inhibitor, was detected by immunohistochemistry in skin tissue. Changes in cell proliferation could be observed in the skin and intestine, along with the respective changes in Wnt signaling reporter activity and increased Dkk1 presence in the skin (Figures 8–11). Wnt signaling reporter staining was undetectable in the intestine (Figure 12), pointing at either lacking expression or too low-level expression of the reporter to be detected with the used immunohistochemistry protocol. 21 days of prednisolone treatment resulted in a strong decrease of Wnt signaling in the skin compared

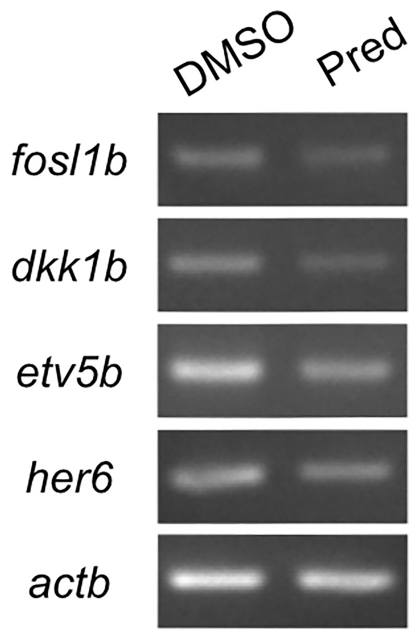

FIGURE 4
RT-PCR on Wnt, Fgf and Notch target genes and the Wnt signaling inhibitor *dkk1b*. 7-day prednisolone treatment after fin amputation reveals suppression of *fosl1b* (Wnt target gene), *etv5b* (*ETS variant transcription factor 5b*, Fgf target gene) and *her6* (*hairy-related 6*, Notch target gene) in fin regenerates. Likewise, *dkk1b* levels are reduced.

to the DMSO control (Figure 8A). Prednisolone treatment led to a reduction of the reporter signal to less than half of the control in the outermost layer of the skin (Figure 8B). In line with this, basal skin tissue showed more prominent expression of Dkk1 in prednisolone treated zebrafish (Figure 9). Of note, Dkk1 protein was also detected in skin mucous cells of our samples (asterisks in Figure 9). Discontinuation of the treatment during the last four days partly reversed the effect of suppressed Wnt reporter activity in the skin. Importantly, treatment with prednisolone during only the last four days of the experiment resulted in a similar level of Wnt signaling as was seen in zebrafish which had experienced a 17-day treatment with prednisolone followed by a 4-day recovery period. These results correlate with our findings of suppressed Wnt signaling in fin regeneration.

Analyses of PCNA+ cells in the skin showed a significant reduction in cell proliferation after 21-day prednisolone treatment (average of 10 ± 2.5 PCNA+ cells) in comparison to the DMSO control with an average of 24 ± 9.68 PCNA+ cells per skin section (Figures 10A, B). On the other hand, a stop of prednisolone treatment during the last four days resulted in no significant reduction in the PCNA+ cell number (average of 18 ± 7.01 PCNA+ cells). Similarly, skin proliferation was not significantly decreased by a 4-day prednisolone treatment (average of 11 ± 6.8 PCNA+ cells).

Analysis of PCNA+ cells in the crypts of the intestine revealed reduced cell proliferation in samples treated with prednisolone for 21 days (Figures 11A, B). On average, only 6 ± 6.8 cells per crypt were PCNA+ after 21-day prednisolone treatment as compared to an average of 23 ± 9.6 PCNA+ cells after 21 days of DMSO treatment. Discontinued prednisolone treatment did not significantly impact crypt cell proliferation (8 ± 5.1 PCNA+ cells) in comparison to the DMSO control; similarly, PCNA+ cell number was not significantly altered by short-term prednisolone treatment (10 ± 4.2 PCNA+ cells). In contrast, assessment of the number of goblet cells per crypt revealed their significant reduction in all prednisolone treatment conditions (Figures 11A, C). While the

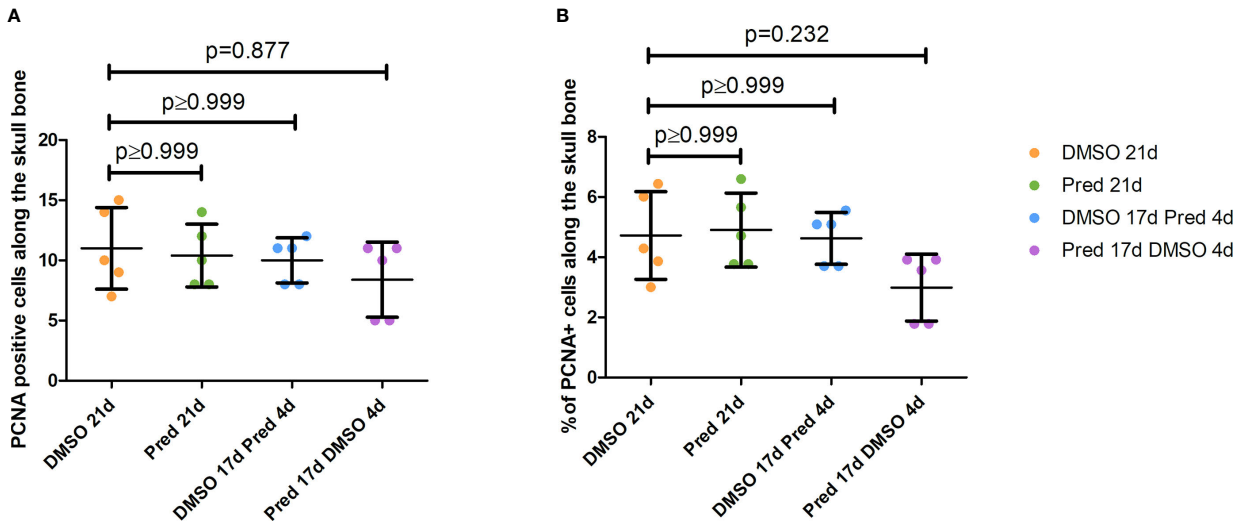

FIGURE 5
Quantification of PCNA positive cells along the skull bone of the zebrafish. **(A)** Total number of PCNA+ cells lining the skull bone. **(B)** Percentage of PCNA+ cells lining the skull bone (normalized to all cells lining the skull bone). Data are mean ± SD of PCNA positive cells lining bone in the different groups (21 days of DMSO, 21 days of prednisolone, 17 days of DMSO followed by 4 days of prednisolone and 17 days of prednisolone followed by 4 days of DMSO treatment). Each dot represents one biological replicate. Non-parametric testing because of non-normal distribution of the data. Statistical significance was tested by *post-hoc* Dunn's multiple comparison after Kruskal-Wallis test. n=5 (4 females, 1 male in DMSO 21d, DMSO 17d Pred 4d, Pred 17 d DMSO 4d; 5 females in Pred 21d) in all groups with 1 section per individual.

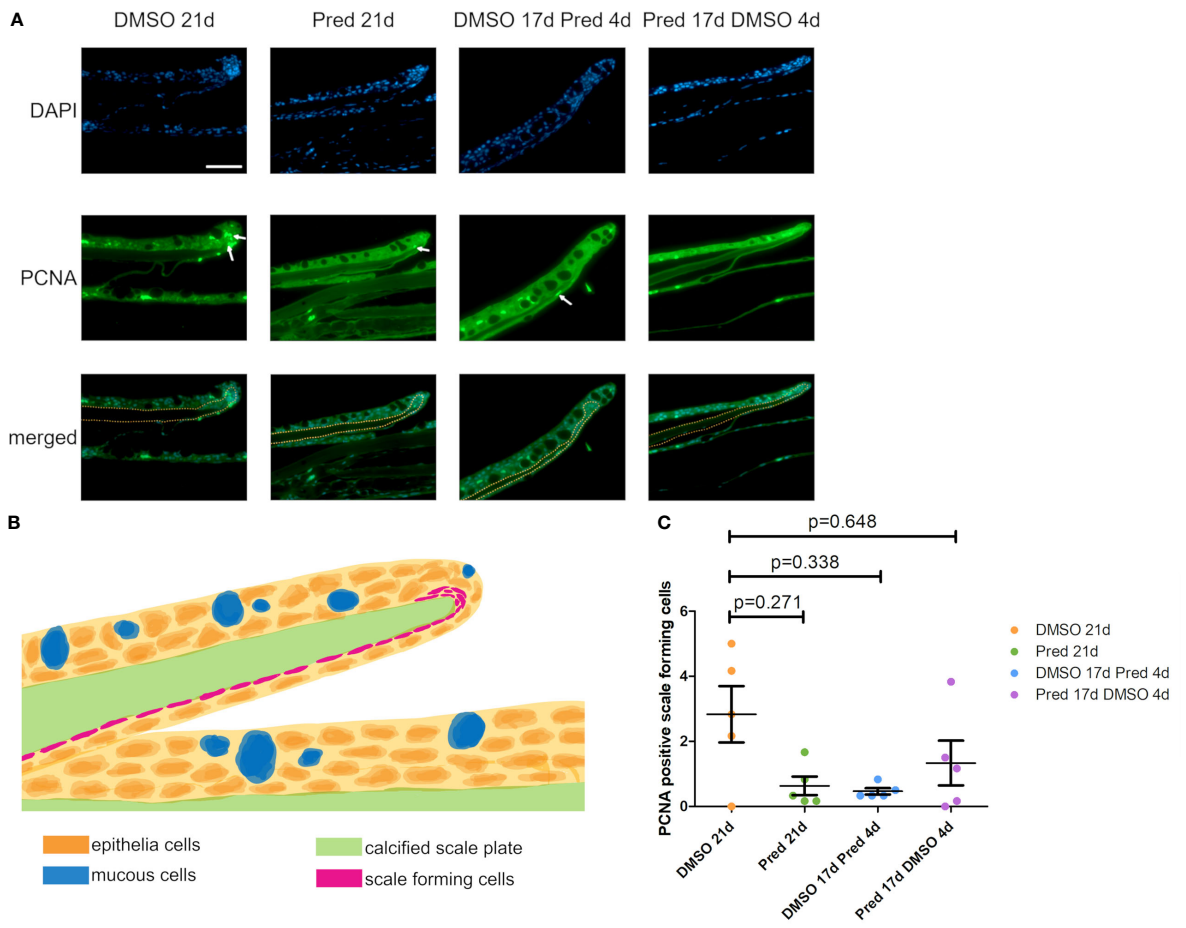

FIGURE 6
Proliferation of scale forming cells after treatment. **(A)** Immunohistochemical staining against PCNA and nuclear counterstain with DAPI. From left to right: fish underwent 21 days of DMSO, 21 days of prednisolone, 17 days of DMSO followed by 4 days of prednisolone and 17 days of prednisolone followed by 4 days of DMSO treatment. Scalebar 50 µm. White arrows indicate some PCNA+ cells. Yellow dotted lines outline the calcified scale plate together with the scale forming cells. **(B)** Schematic section view of a zebrafish scale in the zebrafish trunk. The calcified scale plate (green) is enclosed by the skin epithelium containing layers of epithelial (orange) and mucous cells (blue). The scale-forming cells (magenta) are in close proximity to the calcified scale plate. They cover the lower side of the scale and are located in higher number at the scale tip (in the marginal zone). **(C)** Quantification of PCNA+ scale forming cells in the different groups (21 days of DMSO, 21 days of prednisolone, 17 days of DMSO followed by 4 days of prednisolone and 17 days of prednisolone followed by 4 days of DMSO treatment). Data are mean ± SD of PCNA+ scale forming cells. Each dot represents one biological replicate. Non-parametric testing because of non-normal distribution of the data. Statistical significance was tested by *post-hoc* Dunn's multiple comparison after Kruskal-Wallis test. n=5 (4 females, 1 male in DMSO 21d, DMSO 17d Pred 4d, Pred 17 d DMSO 4d; 5 females in Pred 21d) in all groups with 1 section per individual.

control treatment with DMSO showed an average of 10 ± 0.69 goblet cells per crypt, the number of goblet cells was reduced to an average of 7 ± 1.14 by 21-day treatment with prednisolone, 8 ± 0.52 by 17-day prednisolone + 4-day DMSO treatment and 6 ± 0.67 goblet cells by short-term prednisolone treatment.

3.4 GC treatment reduces leukocytes in the intestine

L-plastin is a cross-linking protein for actin filaments, specifically found in the cytosol of leukocytes (31). To investigate the influence of prednisolone on immune cells in the intestine the number of L-plastin+ cells per crypt was assessed as a readout for leukocytes (Figures 13A, B). A significant reduction of leukocytes was observed after 21 days of prednisolone treatment. While DMSO treatment for 21 days resulted in an average of 36 ± 6.2 L-plastin+ cells per crypt, prednisolone treatment resulted in an average of 13 ± 4.7 L-plastin+ cells. Discontinuation of prednisolone treatment after 17 days (4-day recovery) saved the intestine from a significant reduction of L-plastin+ cell number compared to DMSO treatment, with an average of 28 ± 2.37 L-plastin+ cells, suggesting reversibility of leukocyte suppression. Likewise, 4-day prednisolone treatment did not significantly suppress leukocyte number in the intestine, indicating that longer treatment is required to reduce intestinal leukocyte number.

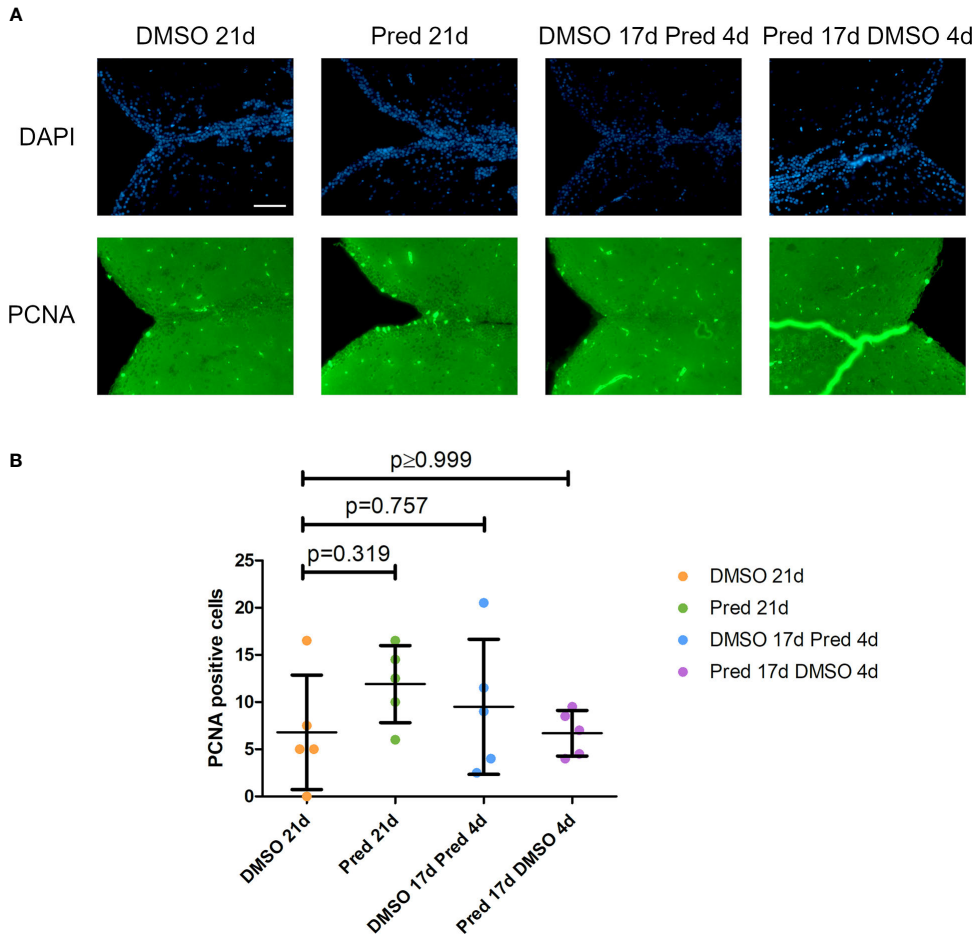

FIGURE 7
Cell proliferation in the telencephalon of zebrafish. **(A)** Immunohistochemical staining against PCNA and nuclear counterstain with DAPI. From left to right: fish underwent 21 days of DMSO, 21 days of prednisolone, 17 days of DMSO followed by 4 days of prednisolone and 17 days of prednisolone followed by 4 days of DMSO treatment. Scalebar 50 µm. **(B)** Quantification of PCNA+ cells in the telencephalon. Data are mean ± SD of PCNA+ cells in the different groups (21 days of DMSO, 21 days of prednisolone, 17 days of DMSO followed by 4 days of prednisolone and 17 days of prednisolone followed by 4 days of DMSO. Each dot represents one biological replicate. Parametric testing because of normal distribution of the data. Statistical significance was tested by *post-hoc* Dunnett's multiple comparison after one-way ANOVA. n=5 (4 females, 1 male in DMSO 21d, DMSO 17d Pred 4d, Pred 17 d DMSO 4d; 5 females in Pred 21d) in all groups with 2 sections per individual.

4 Discussion

Here, we studied the effects of GC treatment in zebrafish, a teleost species which shows life-long proliferation capacity in a variety of tissues such as the fin which grows at the fin tips (32). After injury, proliferation capacity is strongly boosted during regeneration of the fin and many other organs (33), allowing for the distinction between low-level tissue proliferation during adult growth and tissue homeostasis and regenerative settings characterized by much higher proliferation rates and induction of pro-regenerative signaling cascades (34). Therefore, we assessed the impact of the GC prednisolone on Wnt signaling and cell proliferation in different homeostatic zebrafish tissues as well as regenerating fin tissue. We also investigated the potential recovery of a 17-day prednisolone treatment and the impact of short-term treatment with prednisolone.

Assessment of regenerate length and Wnt reporter signal in the growing fin was used to determine the effect of prednisolone on growth mirroring proliferation during regeneration. As shown previously, regeneration and cell proliferation in the fin are negatively affected by prednisolone treatment (11). Furthermore, Wnt signaling is known as a mitogenic pathway in numerous tissues (35) allowing for high rates of proliferation. Treatment with prednisolone for 21 days after amputation diminished fin regenerate length significantly, both in a previous study (11) and the study at hand. Likewise, treatment with the GC dexamethasone exerted an inhibitory effect on fin regrowth and brain regeneration (36, 37). Here, we show that prednisolone treatment results in a reduction of the Wnt-active proliferation zone of fin regenerates. A study focusing on human neural progenitor cells in cell culture demonstrated that dexamethasone induces upregulation of the Wnt signaling inhibitor DICKKOPF1 (DKK1) (38). This upregulation is

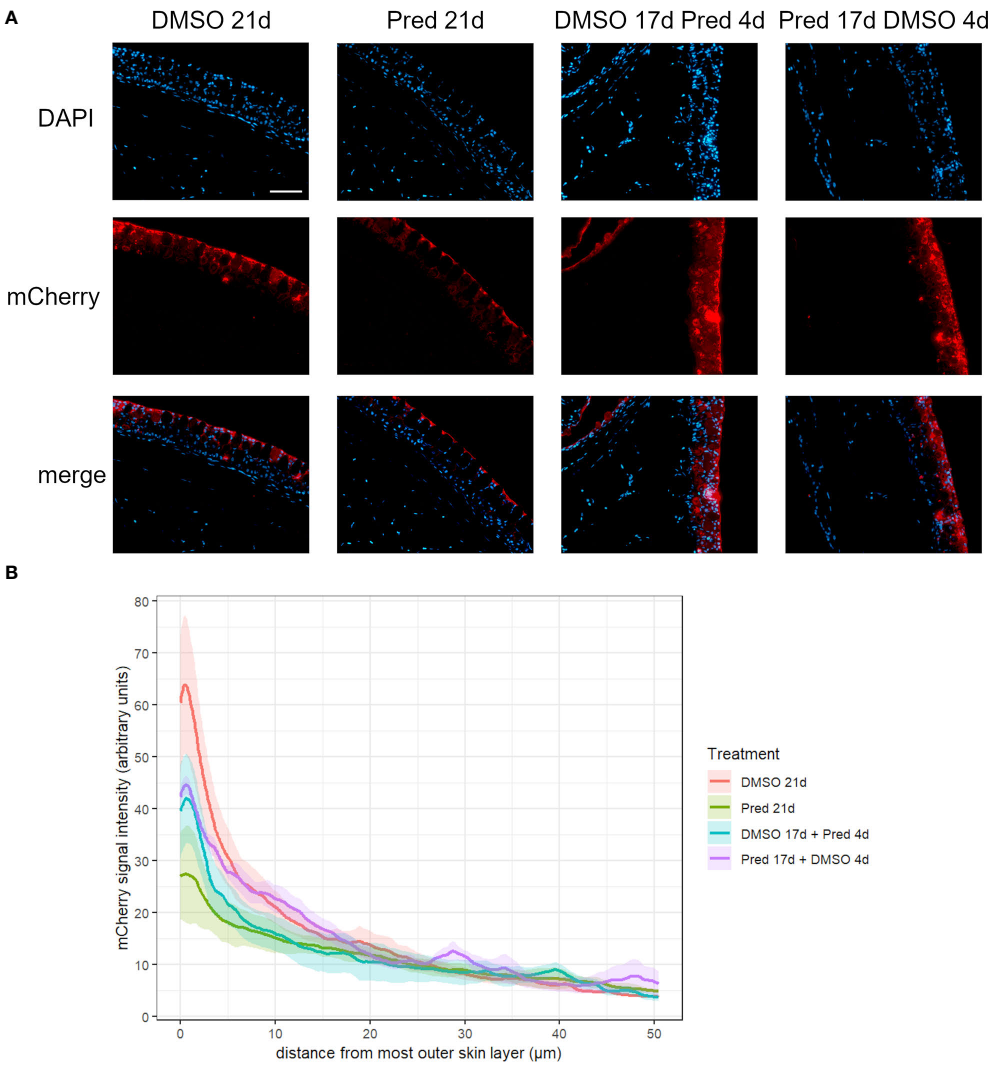

FIGURE 8
Wnt signaling in the skin of zebrafish. **(A)** Immunohistochemical staining against the Wnt-reporter mCherry and nuclear counterstain with DAPI. From left to right: fish underwent 21 days of DMSO, 21 days of prednisolone, 17 days of DMSO followed by 4 days of prednisolone and 17 days of prednisolone followed by 4 days of DMSO treatment. Scalebar 50 µm. **(B)** Quantification of the *7xTCF-Xia.Siam:*nlsmCherry Wnt reporter expression in the skin. Lines represent mean ± SEM of mCherry signal intensity for fish that underwent 21 days of DMSO, 21 days prednisolone, 17 days DMSO followed by 4 days prednisolone and 17 days of prednisolone followed by 4 days of DMSO treatment. Signal was measured from the outermost layer towards the inner layers of the skin. Average skin thickness is around 50 µm. n=5 (4 females, 1 male in DMSO 21d, DMSO 17d Pred 4d, Pred 17 d DMSO 4d; 5 females in Pred 21d) in all groups with 2 sections per individual.

due to increased transcription of *DKK1* mRNA through the action of dexamethasone, in a dose- and time-dependent manner, which was also shown in primary cultured human osteoblasts (38, 39). This effect could be circumvented by adding the GR antagonist mifepristone (38, 40). The inhibitory effect of GCs on Wnt signaling is in line with our findings of suppressed Wnt reporter gene expression in the growth zone of the regenerate along with the observed reduced expression of *fosl1b* in prednisolone treated fin regenerates. The observed reduction in Wnt signaling (along with changes in Fgf and Notch target gene expression, see Figure 4) indicates that proliferation could no longer be sustained, which resulted in shorter growth of the fin regenerates.

Immunohistochemistry revealed negative effects of prednisolone on cell proliferation and Wnt signaling in the skin and intestine. First, 21 days of prednisolone treatment reduced Wnt signaling in the skin compared to the control. Previous reports have shown that GCs lead to a thinning of the epidermis by inhibiting the proliferation and migration of keratinocytes (41). Furthermore, Wnt signaling is known to play an important role in tissue homeostasis and stem cell activation of the skin (42). For example, aberrations in Wnt signaling were found to be essential for the initiation and progression of keratinocyte carcinoma by increasing tumor cell proliferation (42). This leads to the assumption that GCs might exert their negative effects on the epidermis at least partly by influencing Wnt signaling. In line with this, GC treatment increased the presence of Dkk1 in the basal part of the skin, indicating that GCs suppress Wnt signaling in the skin by increasing Dkk1 expression in zebrafish.

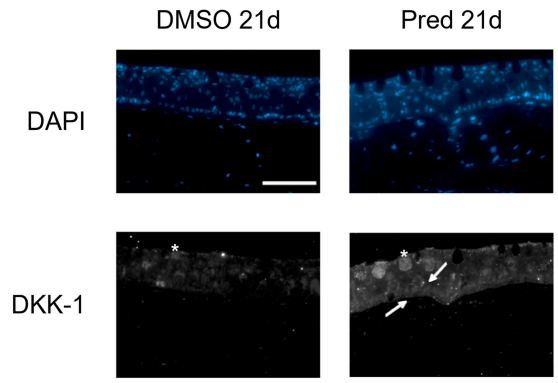

FIGURE 9
Dkk1 expression in the skin of zebrafish. Immunohistochemical staining against Dkk1 and nuclear counterstain with DAPI in zebrafish that underwent 21 days of DMSO or 21 days of prednisolone treatment. 4 out of 5 zebrafish with prednisolone treatment showed stronger staining in the basal portion of skin than DMSO treated zebrafish (4 out of 5 DMSO treated zebrafish with weak staining in the basal portion of the skin). Scale bar 50 µm. Arrows point to brighter signal in the basal portion of the skin. Asterisks indicate mucous cells. n=5 (4 females, 1 male in DMSO 21d, 5 females in Pred 21d) in both groups with 5 sections per individual.

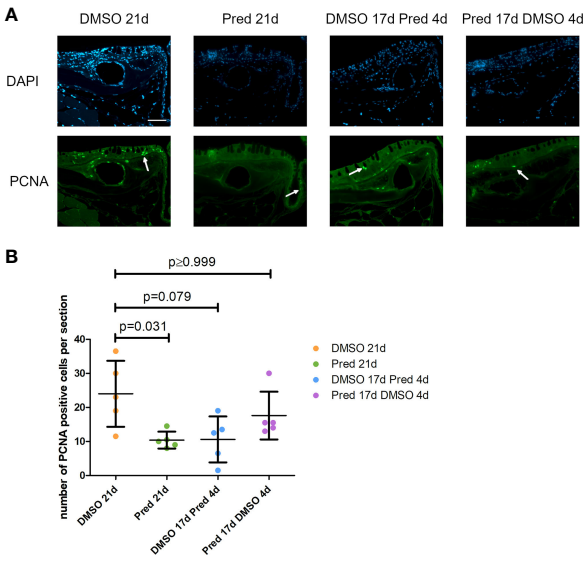

FIGURE 10
Cell proliferation in the skin of zebrafish. **(A)** Immunohistochemical staining against PCNA and nuclear counterstain with DAPI. From left to right: fish underwent 21 days of DMSO, 21 days of prednisolone, 17 days of DMSO followed by 4 days of prednisolone and 17 days of prednisolone followed by 4 days of DMSO treatment. Scalebar 50 µm. White arrows indicate PCNA+ cells. **(B)** Quantification of PCNA + cells in the skin. Data are mean ± SD of PCNA+ cells per section for the treatment conditions 21 days of DMSO, 21 days of prednisolone, 17 days of DMSO followed by 4 days of prednisolone and 17 days of prednisolone followed by 4 days of DMSO. Each dot represents one biological replicate. Non-parametric testing because of non-normal distribution of the data. Statistical significance was tested by *post-hoc* Dunn's multiple comparison after Kruskal-Wallis test. n=5 (4 females, 1 male in DMSO 21d, DMSO 17d Pred 4d, Pred 17 d DMSO 4d; 5 females in Pred 21d) in all groups with 2 sections per individual.

Second, homeostatic tissue turnover in the intestine and skin was negatively affected by prednisolone treatment. 21-day prednisolone treatment significantly reduced the number of proliferating cells in the intestinal crypts compared to the control. Similarly, significant reduction of skin cell proliferation was only observed after 21-day treatment, indicating a recovery potential of the skin and intestine which both did not show any significant impairment of proliferation in the remaining test groups. Notably, formation of goblet cells per crypts was reduced in all conditions of prednisolone treatment. During undisturbed mammalian homeostasis, these cells are continuously renewed every three to five days from the highly proliferative stem cells at the base of the crypts (43). Both reduction of proliferation and impaired differentiation might contribute to decreased goblet cell number in excess GC conditions. Moreover, in line with its immunosuppressive function, prednisolone treatment significantly lowered the cell number of intestinal leukocytes; however only if administered for a sufficient amount of time. Leukocyte reduction is likely caused by GC-induced apoptosis of lymphocytes (44), at least partially, and might be involved in the antiproliferative effect which prednisolone exerts on the intestinal tissue. If so, this would be in line with the known importance of immune cells during tissue zebrafish regeneration as cells supporting stem and progenitor cell proliferation and subsequent differentiation (45, 46).

Notably, we did not detect a clear Wnt signaling reporter activity in the zebrafish intestine. This may indicate that cell turnover in zebrafish crypts does not strongly depend on Wnt signaling; alternatively, there might be issues of Wnt signaling reporter expression in the intestine or with our staining protocol. Peron et al. (47) reported that Signal transducer and activator of transcription 3 (Stat3) is expressed in a Wnt-dependent fashion in intestinal crypts in zebrafish (47) which points to the relevance of Wnt signaling in zebrafish gut homeostasis. To resolve this discrepancy, staining for Wnt signaling components should be performed in the future, in particular, because a potential interaction of the GR with STAT3 was already described (48, 49). Moreover, a report on the expression of IL-10 in human B cells suggests an induction of substantial STAT3 by GC *via* direct interaction of the GR with STAT3 (50).

The maintenance of stem cells and differentiation into specific cell lineages, like the goblet cells, is orchestrated by a complex interplay of multiple pathways, not only the Wnt/β-catenin pathway. This also includes pathways such as PI3-kinase/Akt and Notch signaling (51, 52). Taken together, we observed a correlative impairment of Wnt signaling and cell proliferation due to prednisolone treatment in homeostatic skin, a reduction of proliferation in the intestinal crypts, as well as suppressed Wnt signaling and diminished growth under regenerative conditions in the fin. Of note, we did not detect increased *dkk1b* levels in regenerating fins treated with prednisolone for 7 days by RT-PCR (Figure 4), indicating that other mechanisms than enhanced *dkk1b* expression drive Wnt suppression during fin regeneration. Despite

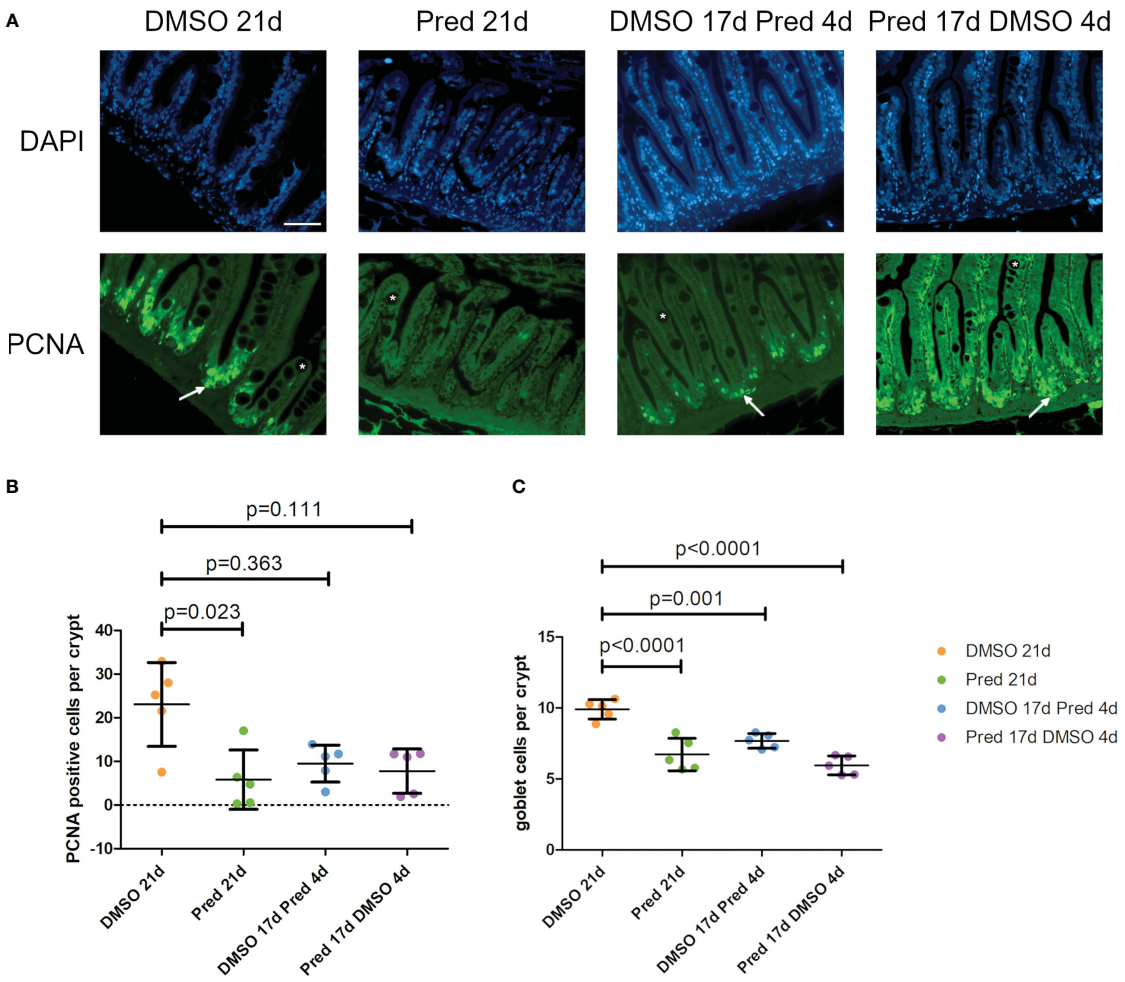

FIGURE 11
Cell proliferation and goblet cell number in the crypts of the intestine. **(A)** Immunohistochemical staining against PCNA and nuclear counterstain with DAPI. From left to right: fish underwent 21 days of DMSO, 21 days of prednisolone, 17 days of DMSO followed by 4 days of prednisolone and 17 days of prednisolone followed by 4 days of DMSO treatment. White asterisks indicate goblet cells and white arrows indicate PCNA+ cells in the crypts. Scalebar 50 µm. Sample "Pred 17d DMSO 4d" showed increased autofluorescence. **(B)** Quantification of PCNA+ cells per crypt in the intestine. Data are mean ± SD of PCNA+ cells per crypt for the treatment conditions 21 days of DMSO, 21 days of prednisolone, 17 days of DMSO followed by 4 days of prednisolone and 17 days of prednisolone followed by 4 days of DMSO. Each dot represents one biological replicate. Non-parametric testing because of non-normal distribution of the data. Statistical significance was tested by *post-hoc* Dunn's multiple comparison after Kruskal-Wallis test. n=5 (4 females, 1 male in DMSO 21d, DMSO 17d Pred 4d, Pred 17 d DMSO 4d; 5 females in Pred 21d) in all groups with 3 sections per individual. **(C)** Quantification of goblet cells per intestinal crypt. Data are mean ± SD of goblet cells per crypt for the treatment conditions 21 days of DMSO, 21 days of prednisolone, 17 days of DMSO followed by 4 days of prednisolone and 17 days of prednisolone followed by 4 days of DMSO. Each dot represents one biological replicate. Parametric testing because of normal distribution of the data. Statistical significance was tested by *post-hoc* Dunnett's multiple comparison after one-way ANOVA. n=5 (4 females, 1 male in DMSO 21d, DMSO 17d Pred 4d, Pred 17 d DMSO 4d; 5 females in Pred 21d) in all groups with 8 sections per individual.

these tissue-specific differences of Wnt suppression mechanisms, our study indicates that the status of regenerating fins, which are convenient to study due to their accessibility and transparency, can serve as a first approximation to the status of other proliferative tissues (the skin and intestine), and that proliferation and Wnt signaling are both under control of the stress response in these tissues. It remains to be tested whether the anti-proliferative effects of prednisolone in the mentioned tissues are downstream of suppressed Wnt signaling or whether both, Wnt inhibition and suppression of proliferation, occur independently of each other. However, a study on human osteosarcoma cells shows that the GR represses cyclin D1, the function of which is required for cell cycle G1/S transition, by targeting Tcf-β-catenin, thereby providing evidence for a direct link between GC and Wnt signaling in cell cycle repression by GR (53). This is supported by findings in the osteoblast-like cells MC3T3-E1, which show that the inhibitory effect of GCs on the cell cycle during osteoblast differentiation is mediated both in a Wnt-independent manner and by abrogation of Wnt signaling, which involves actions up- and downstream of GSK3β. Both mechanisms employed by GCs contribute to the

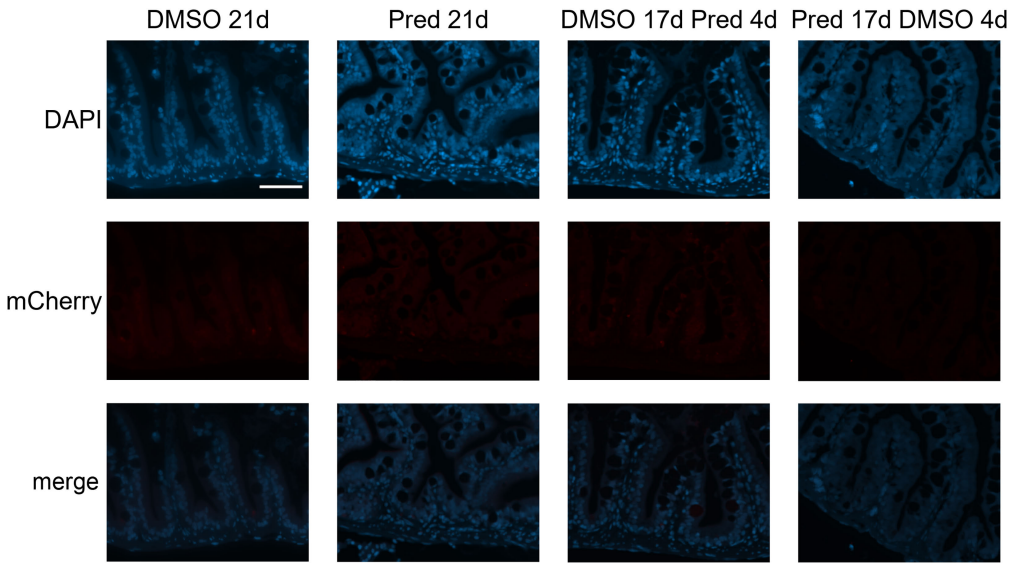

FIGURE 12
Absence of mCherry specific staining in Wnt-reporter *7xTCF-Xia.Siam*:nlsmCherry zebrafish intestine. Immunohistochemical staining against the Wnt-reporter mCherry and nuclear counterstain with DAPI. From left to right: fish underwent 21 days of DMSO, 21 days of prednisolone, 17 days of DMSO followed by 4 days of prednisolone and 17 days of prednisolone followed 4 days of DMSO treatment. With our staining method, we were unable to detect mCherry+ cells in the intestine of transgenic reporter zebrafish. Scalebar 50 µm. n=5 (4 females, 1 male in DMSO 21d, DMSO 17d Pred 4d, Pred 17 d DMSO 4d; 5 females in Pred 21d) in all groups with 3 sections per individual.

attenuation of the G1-S cell cycle transition by suppression of the LEF/TCF transcriptional activity (54).

Third, we hypothesized that discontinuation of prednisolone treatment after 17 days and a recovery period of 4 days would be sufficient for a partial reversal of the prednisolone induced effects. This generally seems to be the case, as suppression of fin regeneration, proliferation, L-plastin+ cell infiltration, and Wnt signaling reporter activity in the skin were not as pronounced in case prednisolone treatment was either discontinued or lasted only a few days. Our data indicate that a 4-day treatment at the given dose is not sufficient to suppress these parameters in the studied tissues. A remarkable exception to this were the intestinal goblet cells whose number significantly decreased in all prednisolone treatment conditions, which suggests that their function is extremely sensitive to increased GC levels. In case of the skin, it is likely that the minimum time to achieve significant suppression of Wnt signaling would correlate with the time which is needed for fin regeneration to be significantly impaired, which is 7 days of treatment (11). In this regard, it will be interesting to further compare the effects of short and sustained GC treatment (and recovery thereof) in fin regeneration and tissue turnover of highly proliferative tissues.

Last but not least, we show here that treatment with prednisolone did not affect uninjured, homeostatic zebrafish bone in terms of bone forming cell proliferation. Proliferation of cells lining bone matrix was overall low and not further reduced by GC treatment as shown in skull bone and homeostatic scales. Similarly, parts of the brain did not change the number of proliferating cells, opposite to the observed effects in the skin, fin, and intestine. Both tissue types (bone and brain) exhibit low levels of proliferation in uninjured conditions. Thus, our observations agree with a previous study which suggested that GCs mainly exert their negative effects in highly proliferative tissues (11). Studies on methylprednisolone observed its ability to cross the blood-brain barrier, however just at a low rate (55). Therefore, caution is warranted as the actual concentration of prednisolone in the brain of treated zebrafish is not known in our experiments. Further experiments are needed to test the effects of prednisolone treatment on proliferation in brain tissue. Of note, brain-injured zebrafish show decreased levels of stem cell proliferation upon treatment with dexamethasone, a more potent GC, an effect that is linked to immunosuppression (36).

Taken together, we identified a dampening effect of prednisolone on Wnt signaling and proliferation in highly proliferative tissues in homeostasis and regeneration. Our study raises interesting questions for future research: What is the minimal time which is required for the intestine to recover goblet cell number? Do individuals treated with GC show intestinal barrier dysfunction? Do longer treatments with GCs affect proliferation of stem and progenitor cells in the brain (36)? How does GC treatment influence other pathways that are involved in intestinal proliferation and differentiation besides Wnt signaling, such as Notch- and Fgf-signaling? Does prednisolone affect Wnt signaling in fin and skin tissue directly, or does immunosuppression play

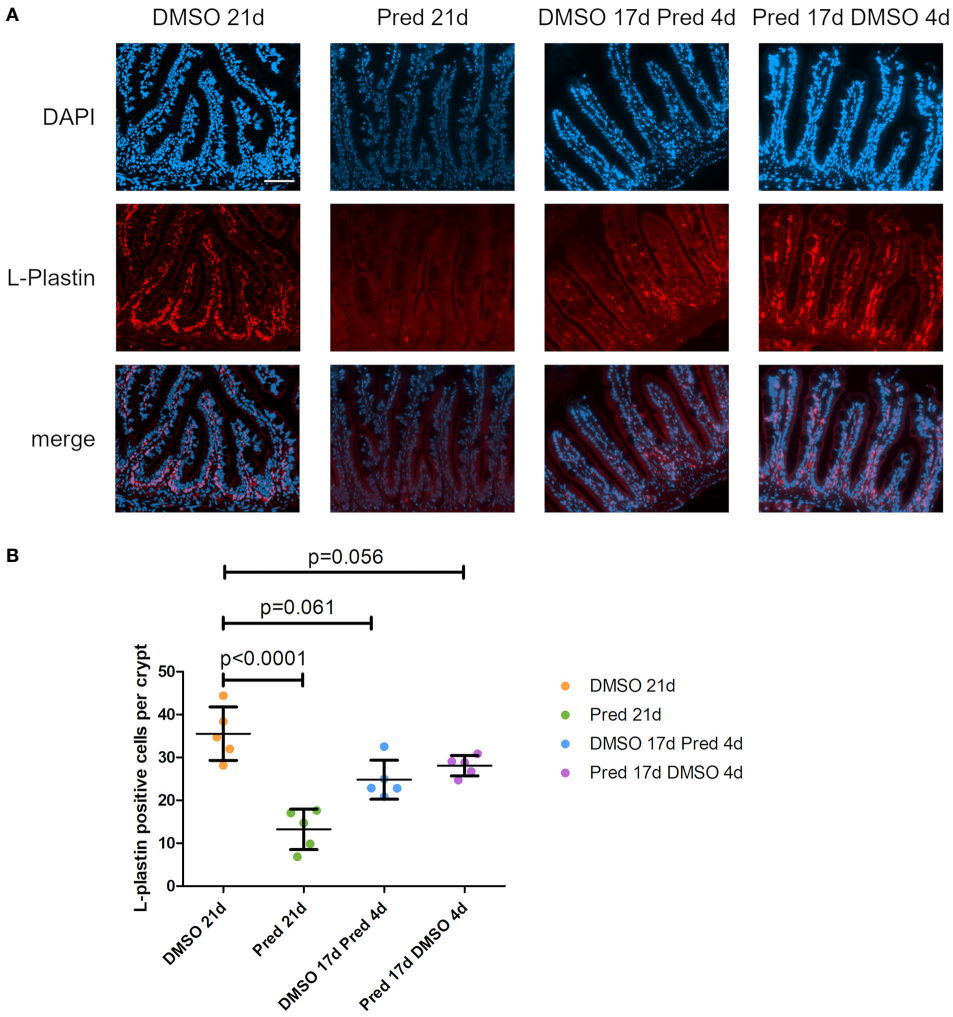

FIGURE 13
Leukocytes in the zebrafish intestine. **(A)** Immunohistochemical staining against L-Plastin and nuclear counterstain with DAPI. From left to right: fish underwent 21 days of DMSO, 21 days of prednisolone, 17 days of DMSO followed by 4 days of prednisolone and 17 days of prednisolone followed by 4 days of DMSO treatment. Scalebar 50 µm. **(B)** Quantification of L-Plastin+ cells per crypt of the zebrafish intestine. Data are mean ± SD of L-Plastin+ cells in the 4 groups (21 days of DMSO, 21 days of prednisolone, 17 days of DMSO followed by 4 days of prednisolone and 17 days of prednisolone followed by 4 days of DMSO). Each dot represents one biological replicate. Parametric testing because of normal distribution of the data. Statistical significance was tested by *post-hoc* Dunnett's multiple comparison after one-way ANOVA. n=5 (4 females, 1 male in DMSO 21d, DMSO 17d Pred 4d, Pred 17 d DMSO 4d; 5 females in Pred 21d) in all groups with 5 sections per individual.

a role? Addressing these questions will increase our understanding of the adverse effects of GCs which may help to reduce their impact in the future. Furthermore, this and future studies will also underscore the use of the fin regeneration paradigm to study adverse effects of frequently prescribed drugs in tissues with high cell turnover.

Data availability statement

The original contributions presented in the study are included in the article/supplementary material. Further inquiries can be directed to the corresponding author.

Ethics statement

The animal study was reviewed and approved by Landesdirektion Sachsen.

Author contributions

Experiments were designed by FK, performed and analyzed by LF, ACL-D, KG, and FK. LF, ACL-D and FK interpreted data and all authors edited the manuscript. LF wrote the first draft of the manuscript. LF and FK accept responsibility for the integrity of data

analysis. All authors contributed to the article and approved the submitted version.

Funding

This work was supported by the DFG Transregio 67 (project 387653785), the DFG SPP 2084 µBone (project KN 1102/2-1) and the EXU transCampus funding program (tC2020_02_MED). The heat cycler for antigen retrieval (CMCB techology platform) was funded by EFRE Sachsen. The Article Processing Charges (APC) were funded by the joint publication funds of the TU Dresden, including Carl Gustav Carus Faculty of Medicine, and the SLUB Dresden as well as the Open Access Publication Funding of the DFG. The work at the TU Dresden is co-financed with tax revenues based on the budget agreed by the Saxonian Landtag.

Acknowledgments

We are very grateful to Susanne Weiche from the Histology facility of the CMCB technology platform for technical assistance. We would like to thank the Light Microscopy core facility at the CMCB technology platform at the TU Dresden for their support. We are grateful to the members of the Knopf laboratory, Michael Brand, Heiner Grandel, Anja Machate, Suzanne Manthey, Mareike Albert and Annika Kolodziejczyk for discussion, sharing reagents, technical support and help in establishing the tissue fixation and decalcification protocols.

Conflict of interest

The authors declare that the research was conducted in the absence of any commercial or financial relationships that could be construed as a potential conflict of interest.

Publisher's note

References

1. Vandewalle J, Luypaert A, De Bosscher K, Libert C. Therapeutic mechanisms of glucocorticoids. *Trends Endocrinol Metab* (2018) 29(1):42–54. doi: 10.1016/j.tem.2017.10.010

2. Schäcke H, Döcke W-D, Asadullah K. Mechanisms involved in the side effects of glucocorticoids. *Pharmacol Ther* (2002) 96(1):23–43. doi: 10.1016/S0163-7258(02)00297-8

3. Sacta MA, Chinenov Y, Rogatsky I. Glucocorticoid signaling: an update from a genomic perspective. *Annu Rev Physiol* (2016) 78(1):155–80. doi: 10.1146/annurev-physiol-021115-105323

4. den Uyl D, Bultink IEM, Lems WF. Advances in glucocorticoid-induced osteoporosis. *Curr Rheumatol Rep* (2011) 13(3):233–40. doi: 10.1007/s11926-011-0173-y

5. Pérez P, Page A, Bravo A, Del Río M, Giménez-Conti I, Budunova I, et al. Altered skin development and impaired proliferative and inflammatory responses in transgenic mice overexpressing the glucocorticoid receptor. *FASEB J* (2001) 15(11):2030–2. doi: 10.1096/fj.00-0772fje

6. Piper JM, Ray WA, Daugherty JR, Griffin MR. Corticosteroid use and peptic ulcer disease: role of nonsteroidal anti-inflammatory drugs. *Ann Internal Med* (1991) 114 (9):735–40. doi: 10.7326/0003-4819-114-9-735

7. Bruscoli S, Febo M, Riccardi C, Migliorati G. Glucocorticoid therapy in inflammatory bowel disease: mechanisms and clinical practice. *Front Immunol* (2021) 12. doi: 10.3389/fimmu.2021.691480

8. Marques IJ, Lupi E, Mercader N. Model systems for regeneration: zebrafish. *Development* (2019) 146(18):dev167692. doi: 10.1242/dev.167692

9. Dietrich K, Fiedler IA, Kurzyukova A, López-Delgado AC, McGowan LM, Geurtzen K, et al. Skeletal biology and disease modeling in zebrafish. *J Bone Mineral Res* (2021) 36. doi: 10.1002/jbmr.4256

10. Pfefferli C, Jaźwińska A. The art of fin regeneration in zebrafish. *Regeneration* (2015) 2(2):72–83. doi: 10.1002/reg2.33

11. Geurtzen K, Vernet A, Freidin A, Rauner M, Hofbauer LC, Schneider JE, et al. Immune suppressive and bone inhibitory effects of prednisolone in growing and regenerating zebrafish tissues. *J Bone Mineral Res* (2017) 32(12):2476–88. doi: 10.1002/jbmr.3231

12. Xia X, Kar R, Gluhak-Heinrich J, Yao W, Lane NE, Bonewald LF, et al. Glucocorticoid-induced autophagy in osteocytes. *J Bone Mineral Res* (2010) 25 (11):2479–88. doi: 10.1002/jbmr.160

13. Yao W, Dai W, Jiang JX, Lane NE. Glucocorticoids and osteocyte autophagy. *Bone* (2013) 54(2):279–84. doi: 10.1016/j.bone.2013.01.034

14. Yao W, Cheng Z, Busse C, Pham A, Nakamura MC, Lane NE. Glucocorticoid excess in mice results in early activation of osteoclastogenesis and adipogenesis and prolonged suppression of osteogenesis: a longitudinal study of gene expression in bone tissue from glucocorticoid-treated mice. *Arthritis Rheumatism* (2008) 58(6):1674–86. doi: 10.1002/art.23454

15. Kawazoe M, Kaneko K, Nanki T. Glucocorticoid therapy suppresses wnt signaling by reducing the ratio of serum Wnt3a to wnt inhibitors, sFRP-1 and wif-1. *Clin Rheumatol* (2021) 40(7):2947–54. doi: 10.1007/s10067-020-05554-x

16. Kawakami Y, Rodriguez Esteban C, Raya M, Kawakami H, Marti M, Dubova I, et al. Wnt/β-catenin signaling regulates vertebrate limb regeneration. *Genes Dev* (2006) 20(23):3232–7. doi: 10.1101/gad.1475106

17. Stoick-Cooper CL, Weidinger G, Riehle KJ, Hubbert C, Major MB, Fausto N, et al. Distinct wnt signaling pathways have opposing roles in appendage regeneration. *Dev (Cambridge England)* (2007) 134(3):479–89. doi: 10.1242/dev.001123

18. Aman AJ, Fulbright AN, Parichy DM. Wnt/β-catenin regulates an ancient signaling network during zebrafish scale development. *eLife* (2018) 7:e37001. doi: 10.7554/eLife.37001

19. Veltri A, Lang C, Lien W-H. Concise review: wnt signaling pathways in skin development and epidermal stem cells. *Stem Cells* (2018) 36(1):22–35. doi: 10.1002/stem.2723

20. Chen D, Xie R, Shu B, Landay AL, Wei C, Reiser J, et al. Wnt signaling in bone, kidney, intestine, and adipose tissue and interorgan interaction in aging. *Ann New York Acad Sci* (2019) 1442(1):48–60. doi: 10.1111/nyas.13945

21. Kawazoe M, Kaneko K, Shikano K, Kusunoki N, Nanki T, Kawai S. Glucocorticoid therapy causes contradictory changes of serum wnt signaling-related molecules in systemic autoimmune diseases. *Clin Rheumatol* (2018) 37(8):2169–78. doi: 10.1007/s10067-017-3689-3

22. Moro E, Ozhan-Kizil G, Mongera A, Beis D, Wierzbicki C, Young RM, et al. *In vivo* wnt signaling tracing through a transgenic biosensor fish reveals novel activity domains. *Dev Biol* (2012) 366(2):327–40. doi: 10.1016/J.YDBIO.2012.03.023

23. Spoorendonk KM, Peterson-Maduro J, Renn J, Trowe T, Kranenbarg S, Winkler C, et al. Retinoic acid and Cyp26b1 are critical regulators of osteogenesis in the axial skeleton. *Development* (2008) 135(22):3765–74. doi: 10.1242/dev.024034

24. Ellett F, Pase L, Hayman JW, Andrianopoulos A, Lieschke GJ. mpeg1 promoter transgenes direct macrophage-lineage expression in zebrafish. *Blood* (2011) 117(4): e49–56. doi: 10.1182/blood-2010-10-314120

25. Brand M, Granato M, Nuesslein-Volhard C. Keeping and raising zebrafish. In: Nuesslein-Volhard C, Dahm R, editors. *Zebrafish: a practical approach*. New York: Oxford University Press (2002). p. 7–37.

26. Geurtzen K, Knopf F. Adult zebrafish injury models to study the effects of prednisolone in regenerating bone tissue. *J visualized experiments: JoVE* (2018) 140: e58429. doi: 10.3791/58429

27. Schönenberger F, Deutzmann A, Ferrando-May E, Merhof D. Discrimination of cell cycle phases in PCNA-immunolabeled cells. *BMC Bioinf* (2015) 16(1):180. doi: 10.1186/s12859-015-0618-9

28. Sherman J, Wang R. Rapid profiling of G2 phase to mitosis progression by flow cytometry in asynchronous cells. *Cell Cycle* (2020) 19(21):2897–905. doi: 10.1080/15384101.2020.1827510

29. Ramachandran R, Zhao XF, Goldman D. Ascl1a/Dkk/beta-catenin signaling pathway is necessary and glycogen synthase kinase-3beta inhibition is sufficient for zebrafish retina regeneration. *Proceedings of the National Academy of Sciences of the United States of America* (2011) 108(38):1585815863. doi: 10.1073/pnas.1107220108

30. Thorfve A, Dehne T, Lindahl A, Brittberg M, Pruss A, Ringe J, et al. Characteristic markers of the WNT signaling pathways are differentially expressed in osteoarthritic cartilage. *CARTILAGE* (2011) 3(1):43–57. doi: 10.1177/1947603511414178

31. Morley SC. The actin-bundling protein l-plastin: a critical regulator of immune cell function. *Int J Cell Biol* (2012) 2012:935173. doi: 10.1155/2012/935173

32. Itou J, Kawakami H, Burgoyne T, Kawakami Y. Life-long preservation of the regenerative capacity in the fin and heart in zebrafish. *Biol Open* (2012) 1(8):739–46. doi: 10.1242/bio.20121057

33. Gemberling M, Bailey TJ, Hyde DR, Poss KD. The zebrafish as a model for complex tissue regeneration. *Trends Genet* (2013) 29(11):611–20. doi: 10.1016/j.tig.2013.07.003

34. Wehner D, Weidinger G. Signaling networks organizing regenerative growth of the zebrafish fin. *Trends Genet* (2015) 31(6):336–43. doi: 10.1016/j.tig.2015.03.012

35. Steinhart Z, Angers S. Wnt signaling in development and tissue homeostasis. *Development* (2018) 145(11):dev146589. doi: 10.1242/dev.146589

36. Kyritsis N, Kizil C, Zocher S, Kroehne V, Kaslin J, Freudenreich D, et al. Acute inflammation initiates the regenerative response in the adult zebrafish brain. *Science* (2012) 338(6112):1353–6. doi: 10.1126/SCIENCE.1228773

37. Sharif F, Steenbergen PJ, Metz JR, Champagne DL. Long-lasting effects of dexamethasone on immune cells and wound healing in the zebrafish. *Wound Repair Regeneration* (2015) 23(6):855–65. doi: 10.1111/wrr.12366

38. Moors M, Bose R, Johansson-Haque K, Edoff K, Okret S, Ceccatelli S. Dickkopf 1 mediates glucocorticoid-induced changes in human neural progenitor cell proliferation and differentiation. *Toxicological Sci* (2012) 125(2):488–95. doi: 10.1093/toxsci/kfr304

39. Ohnaka K, Taniguchi H, Kawate H, Nawata H, Takayanagi R. Glucocorticoid enhances the expression of dickkopf-1 in human osteoblasts: novel mechanism of glucocorticoid-induced osteoporosis. *Biochem Biophys Res Commun* (2004) 318 (1):259–64. doi: 10.1016/j.bbrc.2004.04.025

40. Meszaros K, Patocs A. Glucocorticoids influencing wnt/β-catenin pathway; multiple sites, heterogeneous effects. *Molecules* (2020) 25, 1489. doi: 10.3390/molecules25071489

41. Stojadinovic O, Lee B, Vouthounis C, Vukelic S, Pastar I, Blumenberg M, et al. Novel genomic effects of glucocorticoids in epidermal keratinocytes: inhibiton of apoptosis, interferon gamma pathway, and wound healing along with promotion of terminal differentiation. *J Biol Chem* (2007) 282(6):4021–34. doi: 10.1074/jbc.M606262200

42. Lang CMR, Chan CK, Veltri A, Lien W-H. Wnt signaling pathways in keratinocyte carcinomas. *Cancers* (2019) 11:1216. doi: 10.3390/cancers11091216

43. Barker N. Adult intestinal stem cells: critical drivers of epithelial homeostasis and regeneration. *Nat Rev Mol Cell Biol* (2014) 15(1):19–33. doi: 10.1038/nrm3721

44. Smith LK, Cidlowski JA. Glucocorticoid-induced apoptosis of healthy and malignant lymphocytes. *Prog Brain Res*. (2010) 182:1–30. doi: 10.1016/S0079-6123(10)82001-1

45. Bosak V, Murata K, Bludau O, Brand M. Role of the immune response in initiating central nervous system regeneration in vertebrates: learning from the fish. *Int J Dev Biol* (2018) 62(6-7–8):403–17. doi: 10.1387/ijdb.180033vb

46. Geurtzen K, Lopez-Delgado AC, Duseja A, Kurzyukova A, Knopf F. Laser-mediated osteoblast ablation triggers a pro-osteogenic inflammatory response regulated by reactive oxygen species and glucocorticoid signaling in zebrafish. *Development* (2022) 149(8):dev199803. doi: 10.1242/dev.199803

47. Peron M, Dinarello A, Meneghetti G, Martorano L, Facchinello N, Vettori A, et al. The stem-like Stat3-responsive cells of zebrafish intestine are wnt/β-catenin dependent. *Development* (2020) 147(12):dev188987. doi: 10.1242/dev.188987

48. Zhang Z, Jones S, Hagood JS, Fuentes NL, Fuller GM. STAT3 acts as a Co-activator of glucocorticoid receptor signaling *. *J Biol Chem* (1997) 272(49):30607–10. doi: 10.1074/jbc.272.49.30607

49. Duan HO, Simpson-Haidaris PJ. Cell type-specific differential induction of the human γ-fibrinogen promoter by interleukin-6 *. *J Biol Chem* (2006) 281(18):12451–7. doi: 10.1074/jbc.M600294200

50. Unterberger C, Staples KJ, Smallie T, Williams L, Foxwell B, Schaefer A, et al. Role of STAT3 in glucocorticoid-induced expression of the human IL-10 gene. *Mol Immunol* (2008) 45(11):3230–7. doi: 10.1016/j.molimm.2008.02.020

51. Stanger BZ, Datar R, Murtaugh LC, Melton DA. Direct regulation of intestinal fate by notch. *Proc Natl Acad Sci* (2005) 102(35):12443–8. doi: 10.1073/pnas.0505690102

52. van der Flier LG, Clevers H. Stem cells, self-renewal, and differentiation in the intestinal epithelium. *Annu Rev Physiol* (2009) 71(1):241–60. doi: 10.1146/annurev.physiol.010908.163145

53. Takayama S, Rogatsky I, Schwarcz LE, Darimont BD. The glucocorticoid receptor represses cyclin D1 by targeting the tcf-β-Catenin complex *. *J Biol Chem* (2006) 281(26):17856–63. doi: 10.1074/jbc.M602290200

54. Smith E, Frenkel B. Glucocorticoids inhibit the transcriptional activity of LEF/TCF in differentiating osteoblasts in a glycogen synthase kinase-3β-dependent and -independent manner *. *J Biol Chem* (2005) 280(3):2388–94. doi: 10.1074/jbc.M406294200

55. Chen TC, Mackic JB, McComb JG, Giannotta SL, Weiss MH, Zlokovic BV. Cellular uptake and transport of methylprednisolone at the blood-brain barrier. *Neurosurgery* (1996) 38(2):348-54. doi: 10.1097/00006123-199602000-00023

Frontiers in Endocrinology

Explores the endocrine system to find new therapies for key health issues

The second most-cited endocrinology and metabolism journal, which advances our understanding of the endocrine system. It uncovers new therapies for prevalent health issues such as obesity, diabetes, reproduction, and aging.

Discover the latest Research Topics

See more →

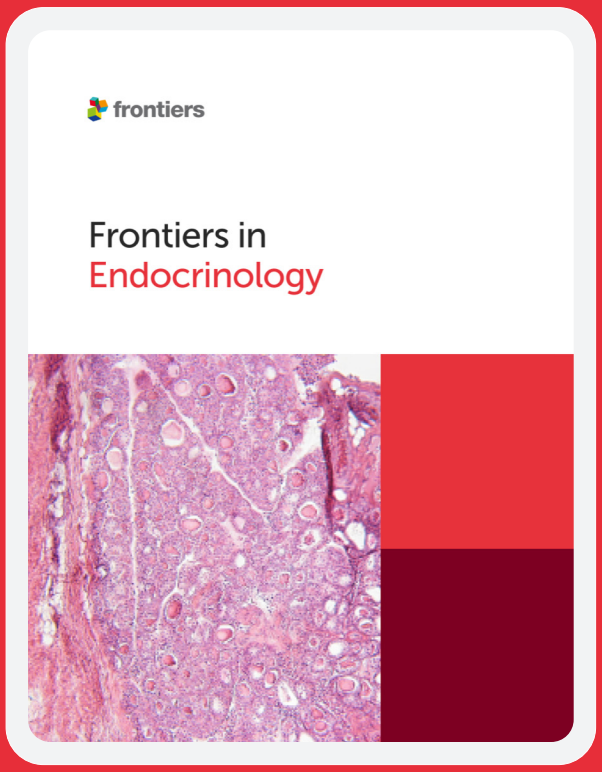

Frontiers

Avenue du Tribunal-Fédéral 34
1005 Lausanne, Switzerland
frontiersin.org

Contact us

+41 (0)21 510 17 00
frontiersin.org/about/contact